

ABSTRACT

MERA, ROBERTO JAVIER. Analysis and Prediction of West African Moist Events during the Boreal Spring of 2009. (Under the direction of Fredrick H.M. Semazzi).

Weather and climate in Sahelian West Africa are dominated by two major wind systems, the southwesterly West African Monsoon (WAM) and the northeasterly (Harmattan) trade winds. In addition to the agricultural benefit of the WAM, the public health sector is affected given the relationship between the onset of moisture and end of meningitis outbreaks. Knowledge and prediction of moisture distribution during the boreal spring is vital to the mitigation of meningitis by providing guidance for vaccine dissemination. The goal of the present study is to a) develop a climatology and conceptual model of the moisture regime during the boreal spring, b) investigate the role of extra-tropical and Convectively-coupled Equatorial Waves (CCEWs) on the modulation of westward moving synoptic waves and d) determine the efficacy of a regional model as a tool for predicting moisture variability.

Medical reports during 2009, along with continuous meteorological observations at Kano, Nigeria, showed that the advent of high humidity correlated with cessation of the disease. Further analysis of the 2009 boreal spring elucidated the presence of short-term moist events that modulated surface moisture on temporal scales relevant to the health sector.

The May moist event (MME) provided insight into interplays among climate anomalies, extra-tropical systems, equatorially trapped waves and westward-propagating synoptic disturbances. The synoptic disturbance initiated 7 May and traveled westward to the coast by 12 May. There was a marked, semi-stationary moist anomaly in the precipitable water field (kg m^{-2}) east of 10°E through late April and early May, that moved westward at the time of

the MME. Further inspection revealed a mid-latitude system may have played a role in increasing the latitudinal amplitude of the MME.

CCEWs were also found to have an impact on the MME. A coherent Kelvin wave propagated through the region, providing increased monsoonal flow and heightened convection. A Tropical Depression-type (TD-type) system developed on May 7 at 20°E and traveled westward with the MME. As this system progressed westward it induced important changes in surface moisture. The TD-type and Kelvin waves underwent phase coupling over central Nigeria (8°E), strengthening the westward-moving feature on May 9. Further evidence is presented that an ER wave also contributed to the development of the TD-type system.

The Weather Research and Forecasting Model (WRF) was employed to simulate the environment during 2009 in seasonal and real-time forecast modes. WRF was configured during the 2006 boreal spring, given the increase in meteorological information through the Africa Monsoon Multidisciplinary Analyses project. The model simulated the moist events but tended to have a dry bias and a 2-day delay of the MME for the seasonal simulation. Real-time simulations were able to simulate the MME better than the seasonal run, temporally and spatially.

The ensemble simulations served as a testbed for a new tool for the analysis of ensemble prediction skill called the extended ROC (EROC) method. The EROC retains the appealing simplicity of the traditional ROC method and the ability of the EV method to provide evaluation of the performance of an ensemble climate prediction system (EPS) for a hypothetical end user defined by the cost-loss ratio ($\mu = C/L$). Seasonal simulations varied in their useable skill, with Bamako (Mali) as the location with the highest value.

This study has revealed that moist events could be of crucial importance to meningitis mitigation. The systems constituting the MME represent predictable phenomena that can be forecasted days in advance. Real-time model simulations were able to diagnose the event 10 days in advance.

Analysis and Prediction of West African Moist Events during the Boreal Spring of 2009

by
Roberto Javier Mera

A dissertation submitted to the Graduate Faculty of
North Carolina State University
in partial fulfillment of the
requirements for the Degree of
Doctor of Philosophy

Marine, Earth and Atmospheric Sciences

Raleigh, North Carolina

2010

APPROVED BY:

Dr. Fred H. M. Semazzi
Committee Chair

Dr. Arlene G. Laing

Dr. Anantha R. Aiyyer

Dr. Lian Xie

Dedication

I dedicate this work to my loving wife, my mother, my father, my brothers, friends and all who believed in me. And to New Orleans and Guayaquil...for everything.

Biography

Roberto Javier Mera was born in the city of Guayaquil, Ecuador, in 1978. He moved to New Orleans, USA, in 1990 where he attended Benjamin Franklin High School and graduated with honors in 1997. Roberto decided to drastically change the scenery by becoming a student at the University of North Carolina at Asheville where he would fulfill his desire to become a meteorologist. After an unfortunate hiatus in 1998 and 1999, he returned to school in the 2000 fall semester where he continued with his studies in meteorology. He was in the Dean's List on several semesters and became a member of the Sigma Delta Pi National Hispanic Honor Society. He graduated in 2003 with a major in Meteorology and a minor in Spanish. He began his master's studies in Atmospheric Science at North Carolina State University in the fall of 2003. Roberto has served as a research assistant at NC State and participated in research conducted at Purdue University. In 2008, Roberto became an intern at the NOAA National Climatic Data Center to work with the University of North Carolina at Asheville on the development of a new Master's Degree in Climate Change and Society. Roberto received an Outstanding Teaching Assistant Award in 2008. He spent two months at the National Center for Atmospheric Research in 2010 to conduct valuable research for his PhD. His interests include teaching, model skill and value measurements, regional climate modeling, climate-society interactions.

Acknowledgements

I would like to acknowledge my committee chair, Dr Fred Semazzi for all of his support, and my advisory committee: Arlene Laing, Lian Xie, Anantha Aiyyer. Also to everyone at UCAR that made this such a wonderful project to be a part of and to the Climlab crew.

Table of Contents

	Page
List of Figures	xii
List of Tables	xxxiii
1 Introduction.....	1
1.1 Sahelian West Africa	1
1.2 The Meningitis-Climate Link	3
2 Recent Climatology of the Moisture Regime during the Boreal Spring.....	11
2.1 Introduction.....	11
2.2 Datasets	13
2.2.1 Gridded Reanalysis	13
2.2.1 Gridded Observations	15
2.3 Air mass sources and the moisture budget during the boreal spring	16
2.3.1 Back-trajectory analysis of source points	17
2.3.1.1 Circulation patterns affecting air parcel trajectories.....	19
2.3.1.2 Vertical profile of the atmosphere during the boreal spring.....	22
2.3.2 Variability of humidity along parcel trajectories.....	25
2.3.2.1 Source points and moisture during the early spring.....	26
2.3.2.2 Source points and moisture during the mid-spring.....	28
2.3.2.2 Source points and moisture during the late spring.....	31
2.4 Characterization of convection during the transition season	34
2.4.1 The pre-onset of the monsoon and the Intertropical Front	34

2.4.2	Variability of convection along the Gulf of Guinea	37
2.4.3	Variability of convection over the Sahel	39
2.5	A conceptual model of the boreal spring	44
2.5.1	General features of the boreal spring	44
2.5.2	Conditions during the early spring	47
2.5.3	Conditions during the mid spring	48
2.5.4	Conditions during the late spring	49
2.6	Conclusions	50
3.	West African Climate and Meningitis Epidemics during 2009	81
3.1	Introduction	81
3.2	Datasets and Methodology	82
3.2.1	Epidemiological data	82
3.2.2	In-situ and gridded meteorological data	83
3.2.3	Methodology	83
3.3	Results	85
3.3	Conclusions	87
4.	Large Scale Patterns affecting Short-term Moist Events during April and May 2009	98
4.1	Introduction	98
4.2	Data and Methodology	100
4.2.1	Datasets	100
4.2.2	Methodology	102

4.3 Large Scale Anomalies during 2009.....	105
4.3.1 Low-level Circulation Anomalies.....	105
4.3.2 Moisture anomalies during 2009	106
4.3.2 Precipitation.....	108
4.3.2 Summary	109
4.4 Convectively coupled Equatorial waves.....	112
4.4.1 Equatorial wave Theory.....	113
4.4.2 Equatorial Phenomena during 2009.....	116
4.4.2.1 ER and MJO.....	118
4.4.2.2 Kelvin waves.....	121
4.4.2.3 TD-type disturbances	122
4.4 Conclusions.....	124
5. Development and Propagation of a Moist Event during May 2009	150
5.1 Introduction.....	150
5.2 Datasets and Methodology	152
5.2.1 Datasets	152
5.2.2 Methodology	152
5.3 Synoptic Evolution and Large-Scale forcing.....	153
5.3.1 MME in Observations and Reanalysis.....	154
5.3.1.1 Surface and Sounding Observations	154
5.3.1.2 Precipitation	155
5.3.1.3 Local Circulation and Moisture in the Reanalysis	156

5.3.2 Large-Scale Circulation Anomalies.....	156
5.3.2.1 Daily Moisture Anomalies.....	159
5.3.2.2 Large-scale Synoptic Environment.....	160
5.3.2.3 Qualitative analysis.....	162
5.3.2.4 Summary.....	164
5.4 Convectively coupled Equatorial waves.....	164
5.4.1 Kelvin waves.....	166
5.4.2 TD-type disturbances.....	171
5.4.3 Equatorial Rossby	173
5.4.4 Relationships among Equatorial Waves during the MME	174
5.4.4.1 Kelvin and TD-Type.....	174
5.4.4.2 Equatorial Rossby and TD-type.....	178
5.4.4.2 Intraseasonal systems.....	179
5.5 Forcing from the Extratropics.....	179
5.5.1 Horizontal Analysis	189
5.5.1.1 Mass Circulation.....	189
5.5.1.2 Potential Vorticity.....	192
5.5.2 Vertical Analysis	193
5.6 Further investigation and conclusions	193
5.6.1 Large scale effects.....	194
5.6.2 Low-level moisture convergence and the African Easterly Jet	195

5.6.2 Summary and Conclusions	197
6. Simulation and prediction of moist events during the boreal spring	259
6.1 Introduction.....	259
6.2 Model description.	262
6.2.1 Dynamical core model physics	262
6.2.2 Atmospheric Radiation schemes.....	263
6.2.2.1 Community Atmosphere Model	263
6.2.2.2 Rapid Radiative Transfer Model (RRTM) Longwave.....	264
6.2.2.3 Goddard shortwave	264
6.2.3 Land Surface model schemes.....	264
6.2.3.1 Noah Land Surface Model	264
6.2.3.2 5-layer Thermal Diffusion	265
6.2.3.3 Rapid Update Cycle (RUC) Model LSM.....	265
6.2.4 Planetary Boundary Layer schemes.....	266
6.2.4.1 Yonsei University (YSU) PBL	266
6.2.4.2 Mellor-Yamada-Janjic (MYJ).....	267
6.2.5 Microphysics schemes	268
6.2.5.1 WRF Single-Moment 3-class (WSM3) scheme	268
6.2.5.2 WSM6 scheme	268
6.2.5.3 Kessler scheme.....	269
6.2.5.4 Purdue Lin scheme.....	269
6.2.6 Cumulus Parameterization schemes	270

6.2.6.1 Kain-Fritsch scheme	270
6.2.6.2 Betts-Miller-Janjic scheme	270
6.2.6.3 Grell-Devenyi ensemble scheme	271
6.2.7 Surface layer schemes.....	272
6.2.8 Boundary conditions	272
6.2.8.1 NCEP Final Analyses	272
6.2.8.2 GFS Real time.....	273
6.3 Data and Methods	273
6.3.1 Validation datasets.....	273
6.3.1.1 In-Situ Observations	274
6.3.1.2 Gridded Reanalysis and Observations	275
6.3.2 Model domains and configuration	276
6.3.3 Model physics parameterization sensitivity experiment.....	277
6.3.4 Real-time forecasts and seasonal hindcasts	278
6.4 Results.....	280
6.4.1 Simulations during 2006.....	280
6.4.1.1 Qualitative Analysis.....	280
6.4.1.2 Quantitative Analysis.....	284
6.4.2 Simulations during 2009	286
6.4.2.1 Moist Events	286
6.4.2.2 Surface Humidity	289
6.4.2.3 Real-time Forecasts.....	291

6.5 Conclusions.....	293
7. An extended procedure for implementing the relative operating characteristic graphical method	323
7.1 Introduction.....	323
7.2.1 Traditional ROC graphical method.....	325
7.2.2 The EV graphical method	327
7.2 EROC procedure.....	334
7.2.1 Construction of generalized baselines	334
7.2.2 End-user eligibility limits	340
7.2.3 Interpretation of EROC area under graph.....	345
7.2.4 The Semazzi-Mera skill score.....	351
7.2.5 Further geometrical interpretation of the connection between the EV and ROC graphs.....	354
7.3 Application of EROC.....	356
7.3.1 Economic Benefits of Environmental Prediction for West Africa	356
7.3.2 Datasets and methodology	359
7.3.3 Results.....	362
7.3.3.1 Seasonal simulations.....	362
7.3.3.2 Real-time simulations	363
7.4 Conclusions.....	365
7.4 APPENDIX.....	367
References.....	383

List of Figures

Figure 1.1	African Human Footprint (courtesy of National Geographic. URL: http://ngm.nationalgeographic.com/ngm/0509/feature1/zoomify/).....	7
Figure 1.2	The meningitis belt in Africa (shown in dark orange) extends from Senegal to Ethiopia. (Map courtesy U.S. Centers for Disease Control and Prevention.).....	8
Figure 1.3	Comparison of meningitis cases over West Africa (top), absolute humidity (g kg-1) (center), and mean maximum temperature during (bottom) 1977, 1978 and 1979. After Greenwood et al. (1984).....	9
Figure 1.4	NNRP 2000-2009 climatology of Mean sea level pressure and 925 hPa winds for (a) January and (b) July. The dotted line represents the boundary between dry Saharan air and the moist monsoon.....	10
Figure 2.1	Adapted from Parker et al. (2005): Vertical schematic of the boreal summer West African Monsoon at its strongest point. Source: AMMA International Science Plan (http://science.amma-international.org/science/docs/AMMA_ISP_May2005.pdf)	55
Figure 2.2	(a) Sample of air parcel trajectory analysis. (b) Matrix of back-trajectory analysis end points and topography of the region.....	56
Figure 2.3	Time series of surface RH (%) at 10°N, 11°N, 12°N, 13°N,14°N, and 15°N in the NCEP/NCAR reanalysis.....	57
Figure 2.4	Trajectory analysis endpoints (black circles), surface relative humidity and winds for P1 (a), P2 (b) and P3 (c).....	58

Figure 2.5	Distribution of air parcel source points in the (a) horizontal and (b) vertical viewpoints.....	59
Figure 2.6	Horizontal distribution of source regions by geographical location for P2 (a) and P3 (b)	60
Figure 2.7	Vertical distribution of air mass source regions for P1 (a), P2 (b) and P3 (bottom).....	61
Figure 2.8	Three-dimensional schematic of the large scale airflow during the boreal spring.....	63
Figure 2.9	Geopotential height for P1 at 700 hPa (a) and 700 hPa-ZMR (b), 850 hPa (c) and 850 hPa-ZMR (d), 925 hPa (e) and 925 hPa-ZMR (f)	64
Figure 2.10	Geopotential height for P2 at 700 hPa (a) and 700 hPa-ZMR (b), 850 hPa (c) and 850 hPa-ZMR (d), 925 hPa (e) and 925 hPa-ZMR (f)	65
Figure 2.11	Geopotential height for P2 at 850 hPa (a) and 850 hPa-ZMR (b), 925 hPa (c) and 925 hPa-ZMR (d)	66
Figure 2.12	Vertical profile of the atmosphere at the prime meridian showing specific humidity (shaded), meridional wind (solid contours), zonal wind (grey dash-dot) and isentropes (yellow, dashed) for the February 2000-2009 average (a) and the April 2000-2009 average (b)	67
Figure 2.13	Vertical profile of the atmosphere at the prime meridian showing the zonal wind for the April 2006 (a) and 2009 (b) and June 2006 (c) and 2009 (d). The black solid line denotes 0 m/s to specify change in east-west regime.....	68

Figure 2.14	Source points during P1 for points below 650 hPa (a), between 650 and 750 (b), and between 750 and 850 hPa (c)	69
Figure 2.15	Vertical trajectory of air parcels with endpoints averaged at 10°N and 15°N.	
Figure 2.16	Composite trajectories for points along 10°N (green), 11°N (magenta), 12°N (yellow), 13°N (orange), 14°N (purple) and 15°N (gray)	70
Figure 2.17	Source points during P2 for points below 750 hPa (a), between 750 and 850 (b), and between 850 and 925 hPa (c)	71
Figure 2.18	Vertical trajectory of air parcels with endpoints averaged at 10°N and 15°N.	
Figure 2.19	Composite trajectories for points along 10°N (green), 11°N (magenta), 12°N (yellow), 13°N (orange), 14°N (purple) and 15°N (gray)	72
Figure 2.20	Source points during P3 for points above 850 hPa (left), and below 850 (right)	73
Figure 2.21	Mean 2000–2009 monthly rainfall fields (mm day-1) for (a) April and (b) May. Rainfall values are derived from CMAP data. The NCEP–NCAR 925-hPa wind field is expressed in vectors and its scale (9 ms-2). The black line represents the zero isoline of the zonal wind component to delineate the domain of the monsoon wind. Thin curves display mean sea level pressure isolines (expressed in hPa minus 1000)	74
Figure 2.22	Time series of mean 2000–2009 pentad rainfall fields (mm day-1) during February-July for grid boxes averaged at 10°N-12.5°N (solid red) and 12.5°N-15°N. Rainfall values are derived from CMAP data.....	75

Figure 2.23	Kelvin wave-filtered outgoing longwave radiation (OLR) variance for March 15 – June 15 averaged for the 2000-2009 period.....	76
Figure 2.24	Hovmoller diagram of April-May meridional wind component at 850 hPa for 15°N latitude points during 2009.....	77
Figure 2.25	Three-dimensional schematic of airflow, dynamical and surface structures during the early boreal spring.....	78
Figure 2.26	Three-dimensional schematic of airflow, dynamical and surface structures during the mid boreal spring.....	79
Figure 2.27	Three-dimensional schematic of airflow, dynamical and surface structures during the late boreal spring.....	80
Figure 3.1	Recapitulative map of cumulative Meningitis attack rates at week 1 - 17, 2009. Plot shows districts in epidemic (red) and alert (yellow). Source: Multi-disease Control Center, Ouagadougou, Burkina-Faso, World Health Organization.....	91
Figure 3.2	States used for meningitis data (names in dark grey) and meteorological stations used to analyze climate relationship (names in black).....	92
Figure 3.3	Relative humidity anomaly for the change in humidity from the March 23-30 week to March 31-April 5. The solid line represents the 40% humidity threshold for the March 31 – April 5 week. Red circles denote districts in <i>epidemic</i> and black circles are districts in <i>alert</i>	93

Figure 3.4	Comparison of districts reporting <i>epidemic</i> in the state of Borno (Nigeria) during March and April of 2009 (solid line) and the concurrent observed relative humidity (bars) at the station in N'Djemena (Chad)94
Figure 3.5	(a) Comparison of districts reporting <i>epidemic</i> in the state of Kano (Nigeria) during March and April of 2009 (solid line) and the concurrent observed relative humidity (bars) in Kano. (b) Histogram of AR and observed relative humidity in Kano.....95
Figure 3.6	Comparison of districts reporting <i>epidemic</i> in the states of Sokoto and Kibbe (Nigeria) during March and April of 2009 (solid line) and the concurrent observed relative humidity (bars) at the station in Gaya (Niger)96
Figure 3.7	Time series of observed relative humidity (%) for Kano, Nigeria during March-May 2009 (solid, black) and the 7-day moving average (red, dashed)97
Figure 4.1	Relative Humidity (%) observations at Bamako (blue), Deodougou (brown), Niamey (dark red)126
Figure 4.2	Climatology of Geopotential height and winds at 925 hPa. for April 2000-2009 (a), 2009 (b). Geopotential height and wind anomalies for 2006 (c) and 2009 (d)127
Figure 4.3	Geopotential height (m) and wind anomalies ($m s^{-1}$) for 2009 relative to recent climatology.....128
Figure 4.4	Total atmospheric column precipitable water anomalies (a) during April 15 – May 15 2009 compared to the climatological period 2000-2009.

	Climatological conditions are shown for perspective (b) as well as 2009 (c)	128
Figure 4.5	FNL-derived April 2009 anomaly relative to recent climatology for precipitable water (kg m^{-2} shaded) and surface temperature (K, contour)	130
Figure 4.6	Time-longitude Hovmoller plot of precipitable water averaged for points averaged between $10^{\circ}\text{N} - 15^{\circ}\text{N}$ and spanning from $40^{\circ}\text{E}-40^{\circ}\text{W}$ for (a) NNRP and (b) FNL	131
Figure 4.7	Estimated precipitation totals (mm) for April 2009 in (a) CMAP and (b) TRMM. Anomalies are shown accordingly for CMAP (c) and (d) TRMM	132
Figure 4.8	Estimated precipitation totals (mm) for May 2009 in (a) CMAP and (b) TRMM. Anomalies are shown accordingly for CMAP (c) and (d) TRMM	133
Figure 4.9	FNL-derived recent climatology (2000-2009) of potential temperature (K) at (a) 925 hPa and (c) 850 hPa averaged for April 15 – May 15. Anomalies for 2009 are shown for (b) 925 hPa and (d) 850 hPa levels	134
Figure 4.10	NCEP Operational Dataset mean sea level pressure (hPa) anomalies for April 30 (a), May 1 (b), 2 (c) and 3 (d)	135
Figure 4.11	NCEP OLR for March 15 – June 15 2009 averaged for all points between 2.5°S and 7.5°S . Only values lower than 240K are shaded for clarity	136

Figure 4.12	After Wheeler and Kiladis (1999). Symmetric component of OLR. Contour interval is 0.1, and shading begins at a value of 1.1 for which the spectral signatures are statistically significantly above the background at the 95% level (based on 500 dof). Superimposed are the dispersion curves of the even meridional mode-numbered equatorial waves labeled for the various waves of interest in the present study. Frequency spectral bandwidth is 1/96 cpd	137
Figure 4.13	MJO-filtered OLR variance $(W m^{-2})^2$ for (a) spring 2000-2009 and (b) 2009.....	138
Figure 4.14	MJO-filtered OLR $(W m^{-2})$ averaged for 2.5°S to 7.5°N from 80°W to 80°E for the period April 1 – May 20 2009.....	139
Figure 4.15	Equatorial Rossby wave filtered OLR variance for March 15 – June 15 averaged for the 2000-2009 period.....	140
Figure 4.16	Equatorial Rossby wave filtered OLR variance $(W m^{-2})^2$ for (a) April and May 2009 and (b) April 20 – May 20 2009.....	141
Figure 4.17	Equatorial Rossby filtered OLR $(W m^{-2})$ averaged for 12.5°N to 15°N from 80°W to 80°E for the period April 1 – May 20 2009	142
Figure 4.18	Kelvin wave-filtered OLR variance for March 15 – June 15 averaged for the 2000-2009 period.....	143
Figure 4.19	Kelvin wave filtered OLR variance $(W m^{-2})^2$ for (a) April and May 2009 and (b) April 20 – May 20 2009.....	144

Figure 4.20	Kelvin-filtered OLR ($W m^{-2}$) averaged for $2.5^{\circ}S$ to $7.5^{\circ}N$ from $80^{\circ}W$ to $80^{\circ}E$ for the period April 1 – May 20 2009.....	145
Figure 4.21	TD-type wave-filtered OLR variance ($W m^{-2}$) ² for March 15 – June 15 averaged for the 2000-2009 period.....	146
Figure 4.22	TD-type variance ($W m^{-2}$) ² for (a) March 15 – June 15 2009 and (b) April 2009.....	147
Figure 4.23	TD-type filtered OLR ($W m^{-2}$) averaged for $5^{\circ}N$ to $10^{\circ}N$ from $80^{\circ}W$ to $80^{\circ}E$ for the period April 1 – May 20 2009.....	148
Figure 4.24	Observed relative humidity (RH, %) and area averages of TD-type filtered OLR ($W m^{-2}$) at Bamako (top left), Niamey (bottom left), and Kano (bottom right) for the period April 1 – May 20. Small arrows denote significant TDs found in Fig. 3.33. TD1 and MME are also labeled. A locator map is also shown for reference.....	149
Figure 5.1	Top left: circles show the locations: Bamako (red), Ouagadougou (blue) and Niamey (green). Observed relative humidity during the mid-May moist event for Bamako (top right), Ouagadougou (bottom left), Niamey (bottom right)	200
Figure 5.2	MeteoSat Infrared image of tropical plume associated with the moist event in May 5-10, 2009.)	201
Figure 5.3	Time series of water vapor mixing ratio at 925 hPa for Niamey (dashed, diamonds), N'Djamena (solid, triangles), and Agadez (squares)	202

Figure 5.4 Time series of mean sea level pressure (hPa) for Niamey (long dashed, diamonds), Ouagadougou (short dashed, circles), and Tambacounda (solid, triangles).)203

Figure 5.5 TRMM estimated total accumulated precipitation associated with the moist event in May 5-10, 2009 (a), and time-longitude Hovmoller plot (b) of daily accumulated precipitation (mm) averaged for 10-15°N. Dashed line denotes westward progression of the disturbance204

Figure 5.6 Synoptic evolution over tropical West Africa on (a) 5, (b) 6, (c) 7, (d) 8, (e) 9, (f) 10 and (g) 11 May 2009. Solid lines indicate mean sea level pressure contoured every 1 hPa and shading depicts total atmospheric column precipitable water (kg m^{-2}). 10m winds are also shown as vectors. The RH40 isoline is marked by a thick dash-dot line.....205

Figure 5.7 Time-longitude Hovmoller plot of precipitable water averaged for all points at 15°N and spanning from 40°E-40°W for (a) NNRP and (b) FNL.....206

Figure 5.8 Time-longitude Hovmoller plot of meridional wind averaged for all points at 15°N and spanning from 40°E-40°W for (a) NNRP and (b) FNL.....207

Figure 5.9 Sequence of total atmospheric column precipitable water 3-day running mean anomalies during 2009 compared to the climatological period 2000-2009. Presented are (a) 2, (b) 3, (c) 4, (d) 5, (e) 6, (f) 7, (g) 8, (h) 9, (i) 10, (j) 11, (k) 12, (l) 13, (m) 14 and (n) 15 of May 2009.....208

Figure 5.10 Time-longitude Hovmoller plots of 3-day running mean of total atmospheric column precipitable water using FNL data for all points spanning from 40°E-40°W at (a) 10°N, (b) 12.5°N, (c) 15°N, and (d) 17.5°N.....212

Figure 5.11 Large-scale Synoptic evolution of MME on (a) 5, (b) 6, (c) 7, (d) 8, (e) 9, (f) 10 and (g) 11 May 2009. Solid lines indicate 925 hPa geopotential height and shading depicts total atmospheric column precipitable water (kg m^{-2}) 3-day running mean of anomalies (2009-climatology). 200 hPa winds are also shown as vectors. The thick dash-dot line represents the ITF (0 ms^{-1} , Sultan and Janicot 2003 definition)213

Figure 5.12 *Meteosat-7* IR images at 1800 UTC for the duration of the MME (May 4 – May 11). Dates are marked on the images216

Figure 5.13 TRMM-derived view of mid-May tropical – extra-tropical interaction event. The dates shown are May 4 (a), 5 (b), 6 (c), 7 (d), 8 (e), 9 (f), 10 (g) and 11 (h)217

Figure 5.14 NCEP OLR-derived view of mid-May tropical – extra-tropical interaction event. The dates shown are May 4 (a), 5 (b), 6 (c), 7 (d), 8 (e), 9 (f), 10 (g) and 11 (h)218

Figure 5.15 Time-longitude Hovmoller plot of NCEP OLR anomaly (2009 - recent climatology) for March 15 – June 15 2009 averaged for all points between 2.5°S and 7.5°S. Only negative values are shown for clarity.....219

Figure 5.16 Kelvin-filtered OLR (W m^{-2}) averaged for equator to 5°N from 80°W to 80°E for the period April 1 – May 20. Dashed diagonal line shows the eastward

	progression of the waves. Wave name designations are labeled accordingly.....	220
Figure 5.17	Unfiltered 3B43 TRMM daily accumulate precipitation (mm) averaged for equator to 7.5°N from 80°W to 80°E for the period April 1 – May 20. Vertical lines denote the approximate position of Africa. Dashed diagonal line shows the eastward progression of the wave	221
Figure 5.18	NNRP-derived (a) velocity potential at (200 hPa) at the equator, (b) FNL ω at 500 hPa at 1 Pa intervals, (c) zonal wind ($m s^{-1}$) at 850 hPa and (d) zonal wind ($m s^{-1}$) at 925 hPa averaged for 2.5°S to 7.5°N from 80°W to 80°E for the period April 1 st – May 20 th . Vertical lines denote the approximate position of Africa. Dashed diagonal line shows the eastward progression of the wave.....	222
Figure 5.19	Time-longitude Hovmoller diagram of the MME Kelvin wave filtered from the OLR (shaded) averaged for 2.5°S – 7.5°N along with the 200 hPa velocity potential at the equator (solid contour) and westerly 850 hPa zonal wind (dash dot). Only positive values are shown for zonal winds and negative values for the velocity potential so that it corresponds with the convective signal.....	223
Figure 5.20	Vertical view of MME Kelvin wave (K1) on May 7 with the profile taken at the equator. Vertical velocity is shown (shaded) along with pseudo-vectors of zonal wind ($m s^{-1}$) and vertical velocity ($Pa*100$)	224

Figure 5.21	(top to bottom) Time sequences of NCEP OLR and Kelvin-filtered OLR. Date (t_0) is when the tropical-extratropical interaction is at its maximum. Kelvin-filtered positive anomalies are shown in contours; NCEP OLR is shaded for lower radiation values (i.e. strong convection).....	225
Figure 5.22	(a) TD-type filtered OLR ($W m^{-2}$) averaged for $10^{\circ}N - 15^{\circ}N$ from $80^{\circ}W$ to $80^{\circ}E$ for the period March 27 – May 20 th . Diagonal dashed line denotes convective portion of TD-types. Westward systems < 10 day period (b) also shown for perspective.....	226
Figure 5.23	Time-longitude Hovmoller plot of ER-filtered OLR ($W m^{-2}$) for (a) $17.5^{\circ}N$ and (b) $7.5^{\circ}S$ from $80^{\circ}W$ to $80^{\circ}E$ for the period April 1 – May 20. Dashed diagonal line shows the westward progression of the wave. Wave name designation is labeled accordingly.....	227
Figure 5.24	Time-longitude Hovmoller plot of 850 meridional wind ($m s^{-1}$) $10^{\circ}N - 10^{\circ}S$ difference for April – May 2009 for $80^{\circ}W$ to $80^{\circ}E$	228
Figure 5.25	Time-longitude Hovmoller plot of TD-type (contour) and Kelvin (shaded) filtered OLR ($W m^{-2}$) averaged for $10^{\circ}N - 15^{\circ}N$ from $80^{\circ}W$ to $80^{\circ}E$ for the period April 1 – May 20 for 2009. TD1 is labeled and K1 is marked with a diagonal dashed line over the convective portion.....	229
Figure 5.26	Time sequences of Kelvin-filtered OLR (shaded) and TD-type (contoured every $10 W m^{-2}$ from $-10 W m^{-2}$; only negatives shown for clarity). TD-type activity was determined by filtering OLR in the period of 2–7.5 days with westward wavenumber of 6–20 used to capture easterly waves during the	

northern summer (see Kiladis et al. 2006). Weak and potentially spurious signals are suppressed, and only significant phases of both Kelvin waves and TD-types are displayed (i.e., magnitudes greater than one standard deviation). Dates and times are labeled on the bottom right (data is in twice daily format). K1 and K2 are labeled in black and TD1 is labeled in red.....230

Figure 5.27 Time series for TD-type and Kelvin filtered OLR ($W m^{-2}$) along with the sum of the two taken as area averages for the period 1800 UTC May 5 – 1800 UTC May 11 of 2009.....234

Figure 5.28 Time-longitude Hovmoller plot of TD-type (contour) and ER (shaded) filtered OLR ($W m^{-2}$) averaged for $10^{\circ}N - 15^{\circ}N$ from $80^{\circ}W$ to $80^{\circ}E$ for the period April 1 – May 20 for 2009. TD1 is labeled and ER1 is marked with a diagonal dashed line over the convective portion.....235

Figure 5.29 Time sequences of ER-filtered OLR (shaded) and TD-type (contoured every $10 W m^{-2}$ from $-10 W m^{-2}$; only negatives shown for clarity). Weak and potentially spurious signals are suppressed, and only significant phases of both ER waves and TD-types are displayed (i.e., magnitudes greater than one standard deviation). Dates and times are labeled on the bottom right (data is in twice daily format). ER1 is labeled in black and TD1 is labeled in red.....236

Figure 5.30 Day t0 of Time series for TD-type and Kelvin filtered OLR ($W m^{-2}$) along with the sum of the two taken as area averages for the period 1800 UTC May 5 – 1800 UTC May 11 of 2009.....239

Figure 5.31	Time sequences of filtered OLR with the peak date (t_0) on May 7 2009. We show (a) the MJO-filtered OLR, (b) the Kelvin-filtered OLR, and (c) the equatorial Westward-propagating <30 day filtered OLR fields over the whole tropics from $t_0 - 20$ to $t_0 - 10$ days; (d) the sum of the three signals	240
Figure 5.32	Time sequences of filtered OLR with the peak date (t_0) on May 7 2009 for the sum of ER and MJO over the whole tropics from $t_0 - 20$ to $t_0 - 10$ days.....	241
Figure 5.33	MJO (shaded) and Kelvin (contour) filtered NCEP OLR averaged for 2.5°S-7.5°N for April 1 – May 20 2009. K1, K2 and the April and May MJOs are labeled accordingly (MJO1 and MJO2 respectively). Vertical lines denote approximate location of Africa. Possible MJO Kelvin trigger is also labeled.....	242
Figure 5.34	200-mb streamfunction daily anomaly (contour), rotational wind, and OLR anomalies (shaded) for total OLR (left column) and ER-filtered OLR (right column). Dates are labeled. Contour interval is $10 \times 10^6 \text{ m}^2 \text{ s}^{-1}$, with negative contours dashed and in black and positive contours in red. Rotational wind anomalies are presented as vectors.....	243
Figure 5.35	200-mb velocity potential (contoured) and OLR anomalies (shaded) for total OLR (left column) and ER-filtered OLR (right column). Dates are labeled. Contour interval is $2 \times 10^5 \text{ m}^2 \text{ s}^{-1}$, with negative contours dashed and in black	

and positive contours in red. Rotational wind anomalies are presented as vectors.....247

Figure 5.36 200-mb divergence (contoured) and OLR anomalies (shaded) for total OLR (a) and ER-filtered OLR (b). Dates are labeled. Contour interval is $2 \times 10^5 \text{ m}^2 \text{ s}^{-1}$, with negative contours dashed and in black and positive contours in red. Rotational wind anomalies are presented as vector.....251

Figure 5.37 200-mb divergent wind and OLR anomalies (shaded) for total OLR (a) and ER-filtered OLR (b) for t0.....252

Figure 5.38 200-mb PV in PV units ($= 1 \times 10^6 \text{ m}^2 \text{ s}^{-1} \text{ K kg}^{-1}$). Contour interval is 0.1 PV units between 22.0 and 12.0, and 1 PV unit otherwise wind and OLR anomalies (shaded) for total OLR (a) and ER-filtered OLR (b) for t0253

Figure 5.39 200-mb mass circulation shown by the vectors. The contour interval is $1 \times 10^{-2} \text{ Pa s}^{-1}$, and the vectors are scaled such that a 1 m s^{-1} meridional divergent wind is equal to a $-5 \times 10^{-2} \text{ Pa s}^{-1}$ vertical motion. (a) Apr 17 – May 27 2000-2009. (b) Day t0 (c) t0-climatology.....254

Figure 5.40	Moisture convergence at 850 hPa (shaded) and starting on May 5 (a), 6 (b), 7 (c), 8 (d), 9 (e) and 10 (f). Arrow denotes the tropical plume	255
Figure 5.41	The African Easterly Jet at 700 hPa as given by FNL zonal wind (m s^{-1}) for the May climatology (2000-2009) (a), May 7 (b), 8 (c), 9 (d), 10 (e), 11 (f)	256
Figure 5.42	Representation of the AEJ core at 0°E as given by FNL zonal wind (m s^{-1}) for May 2 (dash-dot), May 8 (solid) and May 16 (dotted)	257
Figure 5.43	Schematic of MME during (a) the interaction between tropics and extratropics (-2d) and after the Kelvin/TD-type phasing (+2d)	258
Figure 6.1	Model resolution of relative humidity (%) over Ghana for (a) WRF at 30 km and (b) NNRP at $2.5^{\circ}\times 2.5^{\circ}$. Blue outlines denote country boundaries. State boundaries are shown in black contours	299
Figure 6.2	Locations chosen for comparative analysis with in-situ information	300
Figure 6.3	Model domain configuration showing inner and outer domain for seasonal and real-time simulations.....	301
Figure 6.4	Accumulated precipitation (mm) for April 2006. Labels denote the data analyzed: TRMM, CMAP and physics parameterizaion ensemble members defined in Table 6.1	302
Figure 6.5	Average temperature ($^{\circ}\text{C}$) for April 2006. Labels denote the data analyzed: ECMWF, NNRP, FNL and physics parameterizaion ensemble members defined in Table 6.1.....	303

Figure 6.6	Time series of relative humidity (%) during May 2006 for in-situ observations over the city of (a) Niamey and (b) Bamako (black, solid), and area averages of ensemble members E1 (red, solid), E2 (purple, short dash), E5 (dark blue, dotted), E10 (long dash) and E14 (dash dot)304
Figure 6.7	Time series of the diurnal variability of relative humidity (%) during May 23-28 2006 at 6 hr intervals for in-situ observations over the city of Niamey (black, solid), and area averages of ensemble members E1 (black, long dash) and E2 (purple, short dash)305
Figure 6.8	Accumulated precipitation during April 29 – May 5, May 6-12, May 13-19. TRMM is shown in (a), (c) and (e) while WRF is shown in (b), (d) and (f) for the dates shown306
Figure 6.9	Time longitude Hovmoller diagram of accumulated precipitation during April 11 – May 20 for 20°W-20°E for all points spanning 25°W-20°E. Points along 10N are shown for (a) TRMM and (b) WRF and for 10-15N average for (c) TRMM and (d) WRF. Vertical line denotes approximate location of the coast of West Africa307
Figure 6.10	Time-longitude Hovmoller meridional wind (m s-1) in the WRF inner domain for April 11 – May 20 2009 averaged for all points between 10N and 15N.....308

Figure 6.11	Sequence of accumulated precipitation (mm) from the WRF simulation. Dates are from May 6 to May 14 and are shown at the top of each figure. This vantage point shows the delayed progression of the TD1 event within the MME	309
Figure 6.12	925 hPa mixing ratio from (a) AIRS satellite for May 6-12 at 1330 UTC and WRF at 1200 UTC (b), AIRS for 1330 UTC May 13-19 (c) and WRF at 1200 UTC (d)	310
Figure 6.13	Time longitude Hovmoller diagram of accumulated precipitation in the outer domain averaged for points between 2.5°S and 7.5°N (shaded) and 10°N-15°N (contour). The domain spans longitudes 39°W-49°E	311
Figure 6.14	Time series of observed relative humidity (%) at Kano, Nigeria (solid) and area average of WRF output over the region (dash). The period shown is April 1 – May 30 2009	312
Figure 6.15	Time series of dewpoint temperature (°C) for observed (solid) and WRF-simulated (dotted) for (a) Niamey, (b) Bamako, (c) Tambacounda and (d) Ouagadougou. Dashed red line denotes 15°C isoline for the ITD	313
Figure 6.16	Scatter plots for WRF-derived dewpoint temperature versus observed for (a) Niamey, (b) Bamako, (c) Tambacounda and (d) Ouagadougou	314
Figure 6.17	Mixing ratio at 925 hPa for April 15-22, 2009 for (a) AIRS 1330 UTC and (b) WRF 1200 UTC.....	315

Figure 6.18	Forecasted westward-propagating event during May 7, 2009. (a) Change in RH (% , shaded) and 40% line (contour). (b) Daily accumulated precipitation and 933 hPa winds. Contour delineates the ITF	316
Figure 6.19	Time series of observed (solid) relative humidity (%) at Kano and area average of model output for WRF ensemble average (blue circles) for (a) April 28 – May 4 and (b) May 1–7. Unlabeled contours are individual ensemble member.....	317
Figure 6.20	Time series of observed (solid) relative humidity (%) at Niamey and area average of model output for WRF ensemble average (blue circles) for (a) May 1-7 (b) May 8-13. Unlabeled contours are individual ensemble members	318
Figure 6.21	Time series of observed (solid, black squares) relative humidity (%) at Bamako and area average of model output for WRF ensemble average (tan, burgundy circles) for May 3-16. Unlabeled contours are individual ensemble members.....	319
Figure 6.22	Time series of observed (solid, black squares) relative humidity (%) at Kano and area average of model output for WRF ensemble average (tan, burgundy circles) for May 3-16. Unlabeled contours are individual ensemble members.	
Figure 6.23	Time series of observed (solid, black squares) relative humidity (%) at Bamako and area average of model output for WRF ensemble	

	average (tan, burgundy circles) for May 3-16. Unlabeled contours are individual ensemble members.....	320
Figure 6.23	Time series of observed (solid, black squares) relative humidity (%) at Niamey and area average of model output for WRF ensemble average (tan, burgundy circles) for May 3-16. Unlabeled contours are individual ensemble members.....	321
Figure 6.24	Time series showing attack rates (black/white), observed RH (blue), WRF-simulated RH (red) and NCEP/NCAR reanalysis RH (green) during March-April 2009.....	322
Figure 7.1	ROC Diagram based on synthetic hit-rate and false-alarm data computed from (7.24)	373
Figure 7.2	Economic value graph based on the ROC graph in Fig. 7.1	374
Figure 7.3	Algorithm for the EROC graphical method	375
Figure 7.4	EROC diagram based on synthetic hit-rate and false-alarm data computed from (7.24): $V_{\min} =$ (a) 0 and (b) 0.2.....	376
Figure 7.5	Comparison of relationship between V and ΔH from $\Delta H\beta$ calculated in this study and $\Delta H/\beta$ from Semazzi and Mera (2006)	377
Figure 7.6	Comparison of relationship between V and ΔH from $\Delta H\beta$ calculated in this study and $\Delta H/\beta$ from Semazzi and Mera (2006)	378

Figure 7.7	(a) EROC graph based on modification of Fig. 7.4, and (b) corresponding economic value graph with forward trail	379
Figure 7.8	(a) EROC graph based on modification of Fig. 7.4, and (b) corresponding economic value graph with backward trail	380
Figure 7.9	EROC plots for (a) Bamako, (b) Niamey and (c) N'Djamena.....	381
Figure 7.10	EROC graph for real-time WRF simulations of the 3-day running mean of RH40 over the stations listed in Table 7.4	382

List of Tables

Table 2.1	Date 40% RH threshold is crossed in NNRP at each latitude inside the study area.....	53
Table 2.2	Geographical regions used in source point analysis	54
Table 3.1	Sample of typical MDSC meningitis data	89
Table 3.2	Definition of weeks in the MDSC weekly reports during 2009.....	90
Table 6.1	List of Physics parameter sensitivity ensembles	296
Table 6.2	MAE for each ensemble member at the cities listed	297
Table 6.3	WRF MAE for relative humidity (%) at each city	298
Table 7.1	Forecast model contingency matrix	369
Table 7.2	User Expense Matrix	370
Table 7.3	Predictive and Reactive vaccination costs from Parent du Châtelet et al. (2001) and derived ratios used in EROC	371
Table 7.4	Locations of station observations used in the real-time simulation model skill analysis	372

Chapter 1

Introduction

1.1 Sahelian West Africa

Sahelian West Africa exists at a crossroads of climate regimes: to the north are the wide expanses of the Sahara Desert and to the south lies the Guinea rain forest and the Atlantic Ocean. This transition region of the continent (spanning from 15°N to 20°N and from Senegal in the west to the Sudan in the east) is highly populated and has undergone a significant degree of human impact (see the “human footprint” map in Fig. 1.1). These changes in the environment translate into increased farming and exposure to severe climate events such as the drought during the 1960-1980 period, which translated into augmented mortality risk for the population and stunted economic development (Dilley et al. 2005). Decreased rainfall and its impact on the agricultural community is also coupled with other important climatic events affecting the inhabitants of the Sahel. Dry conditions associated with the “Harmattan” northeasterly winds emanating from the Sahara Desert have also been found to play a role in the spread of meningitis outbreaks throughout the length of Sahelian

West Africa during the dry season in the boreal winter and spring (Molesworth et al., 2003). Therefore, the study of the moisture regime over this portion of the continent has received increased interest given recent efforts in addressing epidemics.

Knowledge and prediction of moisture distribution during the boreal spring is vital to the mitigation of meningitis by providing guidance for vaccine dissemination. Yet the boreal spring has received little attention in the literature; in contrast to the summer monsoon which has been the subject of numerous studies (Eltahir and Gong 1996, Sultan and Janicot 2003, Gu and Adler 2004, Hagos and Cook 2007, Hagos and Cook 2009, Drobinski et al. 2009, among others) and field campaigns [e.g., GATE (Kuettner and Parker 1976) AMMA (Parker et al 2008)].

As the primary driver for precipitation, the monsoon is a vital component of the socio-economic environment of the region. In addition to the relationship between the onset of monsoon moisture and end of meningitis outbreaks in West Africa (Moore 1992, Molesworth et al. 2003, Sultan et al. 2005, Thomson et al. 2006), other areas of the public health sector such as malaria (Breman et al. 2001, 2004), as well as agriculture [impact of locust infestation (Drake and Farrow 1988, Tipping 1995, Roffey and Magor 2003, Maiga 2005)] are also highly sensitive to the shift of moisture regime in the region (Lélé and Lamb, 2010).

1.2 The Meningitis-Climate link

The risk of mortality from climate-related diseases and their impact on socio-economic stability and sustainable development is one of the most important areas of study across sub-Saharan Africa. Meningococcal meningitis, for example, has been a problem in Africa for the past 100 years, where *Neisseria meningitidis* is endemic and periodically epidemic (Greenwood 1999). The World Health Organization and the Meningitis Environmental Risks Information Technologies (MERIT) initiative have determined that the Meningitis Belt is vulnerable to a number of risk factors that include climate, socio-demographic and immunologic. The Meningitis Belt (Fig. 1.2) is a geographic area of Sub-Saharan Africa prone to disease epidemics. The Belt stretches from Senegal in the west coast of Africa eastward to Ethiopia and north-to-south from 15°N latitude to 10°N. This region was first defined by Lapeyssonnie (1963) and is characterized by seasonal epidemics during the dry season (boreal winter and spring), which usually stop with the onset of the monsoon. The area has also been affected by large epidemics with a frequency of 8-12 years, culminating in a massive epidemic in which close to 200,000 cases were reported in 1996 (Greenwood et al. 1999, Broutin et al. 2007).

Based on past and recent literature, it is assumed that dry and windy weather conditions during the early boreal winter might cause damage to the mucous membranes of the human respiratory system and/or inhibits mucosal immune facilitating the transfer of the bacterium to the meninges and thus create propitious conditions to the triggering of meningitis epidemics (Greenwood et al. 1984, Moore 1992, de Chabaliere et al. 2000). Much of what is

known about the climate/environmental factors relevant to meningitis has been based on annual and seasonal data. Meningitis epidemics tend to occur in sectors of West Africa that exhibit particular environmental characteristics. For instance, epidemics have been rarely reported from the humid forested or coastal regions, even when neighboring areas are severely affected (Molesworth et al. 2003). Ongoing research indicates that along with moisture (relative and absolute humidity), incidence of the disease can also be affected by land-cover type (e.g. arid, semi-arid, tropical forest), dust loading in the atmosphere and surface temperature. An example of humidity-climate link is provided in Fig. 1.3, based on Greenwood et al. (1984). Notice in this figure the precipitous decline in meningitis with the advent of increased absolute humidity.

The critical variables associated with meningitis outbreaks are very low humidity and dusty conditions (Besancenot et al 1997); while cessation occurs with the onset of rains (Molesworth et al. 2003). Sultan et al. (2005) found a strong correlation between the timing of the epidemic onset in Mali and the winter wind maximum but could not differentiate low and high incidence years. Yaka et al. (2008) found that variations in surface winds can explain 25% of the year-to-year differences in meningitis outbreaks in Niger. Thomson et al. (2006) suggested that anomalies in annual meningitis incidence at the district level in Burkina Faso, Niger, and Mali were related to monthly climate anomalies. Although questions remain about the initiation of outbreaks, a clear pattern has emerged in the cessation of the disease, brought about by the advent of moist conditions.

While there is no consensus on which measure of humidity and other environmental variables correlate best with meningitis incidence, a few studies do provide some guidance. For example, Greenwood et al. (1984) used absolute humidity and mean maximum temperature while Thomson et al. (2006) examined rainfall, satellite-derived dust loading, and vegetation indices. Besancenot et al. (1997) identified three meteorological conditions associated with the Harmattan regime and meningitis epidemics: minimal mean temperature of no more than 20 °C, a mean relative humidity of no more than 40%, and the presence of at least three days of dust haze. The present study uses the 40% surface relative humidity (RH40) as a threshold for alleviation of epidemic conditions.

Our study is based during the transition period, which is marked by an important meridional gradient in surface humidity that pushes northward with the advancement of the seasonal cycle. We utilize the notion that there exists a robust and actionable climate/meningitis relationship given the strong correlation between the start of the rainy season and the abrupt decline in the transmission of the disease (Molesworth et al., 2003). Given our focus on the shift from dry season to monsoonal conditions, it is imperative to recognize the two regimes that define the change from dry season to the monsoon. In order to illustrate this, we use 925 hPa wind (zonal and meridional components) and mean sea level pressure data from the NCEP/NCAR reanalysis (NNRP, described in Chapter 2) averaged for the 2000-2009 decade to compare two opposing regimes: in (Fig. 1.4a) we have the Harmattan season at its height during the month of January and in (Fig. 1.4b) we present the conditions in July during the height of the West Africa Monsoon (WAM). During the heart of

the dry season (January), strong northeasterly flow reaches the Gulf of Guinea coast bringing warm, dry air emanating from the Sahara desert. Conversely, during the fully-fledged monsoon, southwesterly winds reach the northern boundary of the Sahel (20°N, Sultan and Janicot 2003). It is the interface between these two wind regimes that creates the background conditions associated with the northward progression of the moisture front. Our focus throughout this study will address only the conditions during the height of observed epidemics in 2009 and their eventual collapse in relation to the onset of humidity.

In order to better recognize the variability of moisture during the boreal spring and to improve prediction of critical thresholds in the moisture regime, this study attempts to answer the following questions:

- What are the large-scale features that influence moisture variability during the boreal spring?
- What are the effects of extra-tropical synoptic systems?
- How might intraseasonal circulations and their interactions with synoptic weather systems influence the moisture regime?
- Can regional climate/weather models be used for the prediction of weather and climate for meningitis efforts?

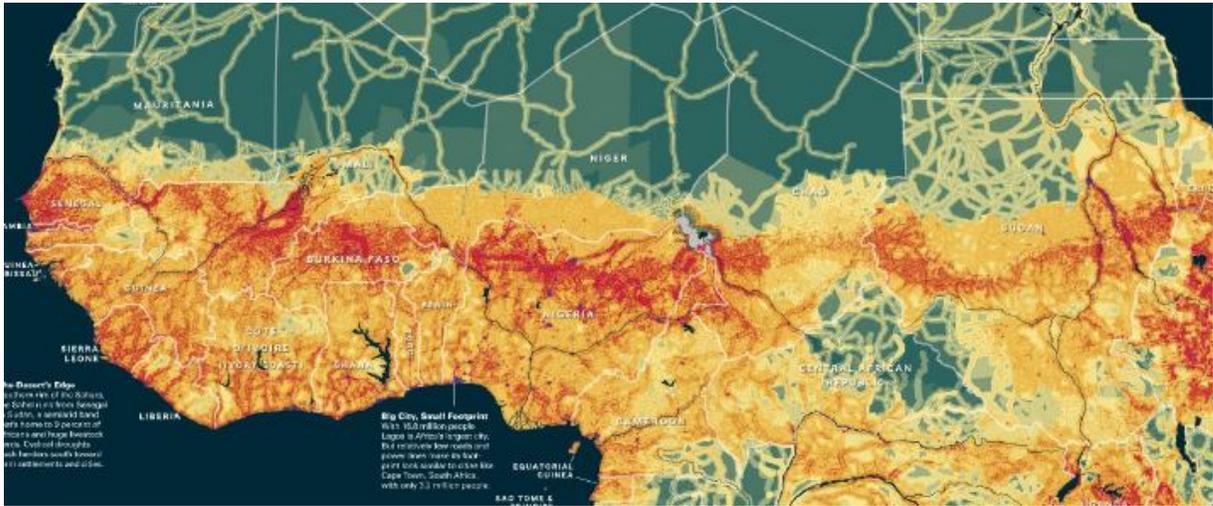


Figure 1.1: African Human Footprint (courtesy of National Geographic. URL: <http://ngm.nationalgeographic.com/ngm/0509/feature1/zoomify/>)

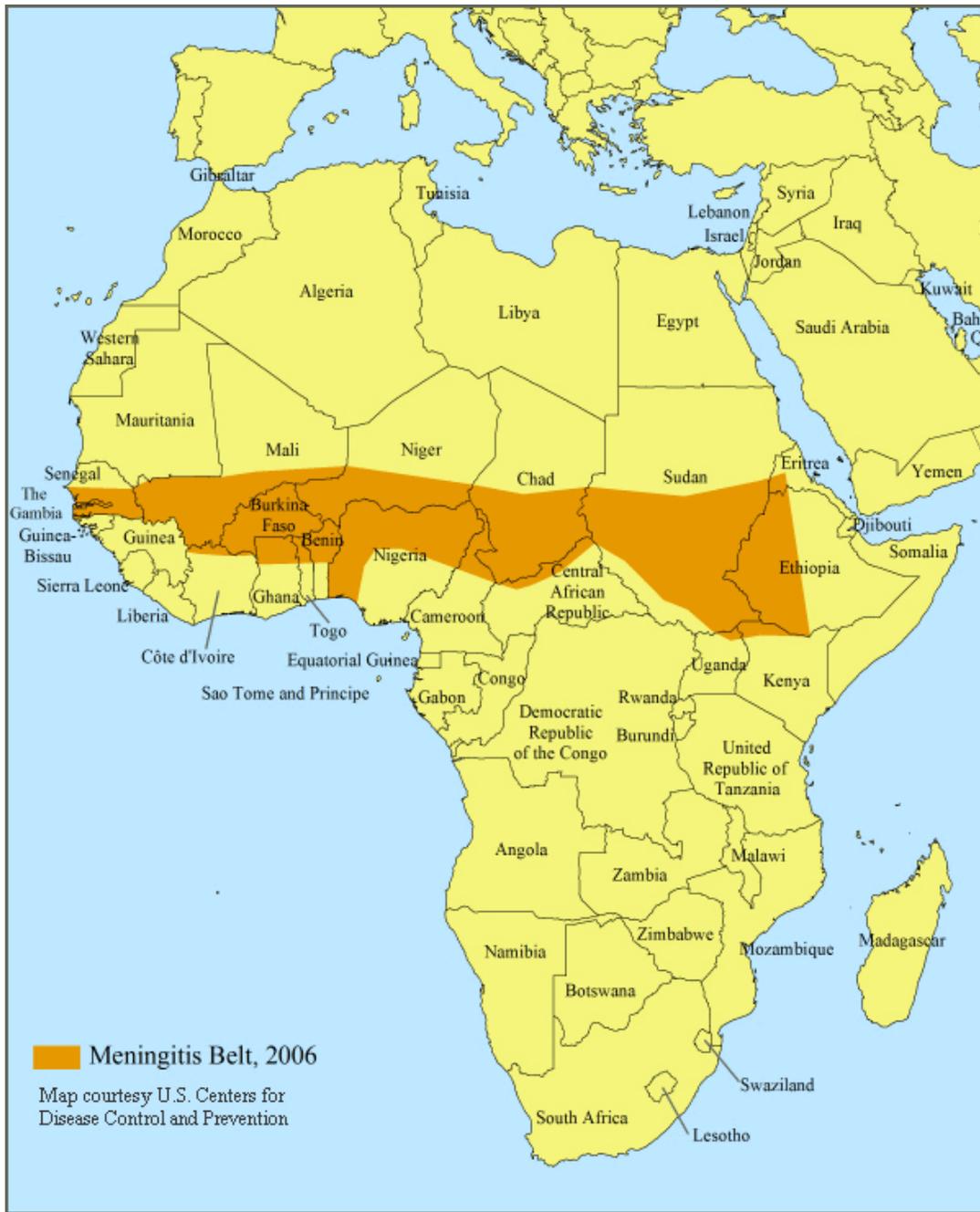


Figure 1.2: The meningitis belt in Africa (shown in dark orange) extends from Senegal to Ethiopia. (Map courtesy U.S. Centers for Disease Control and Prevention.)

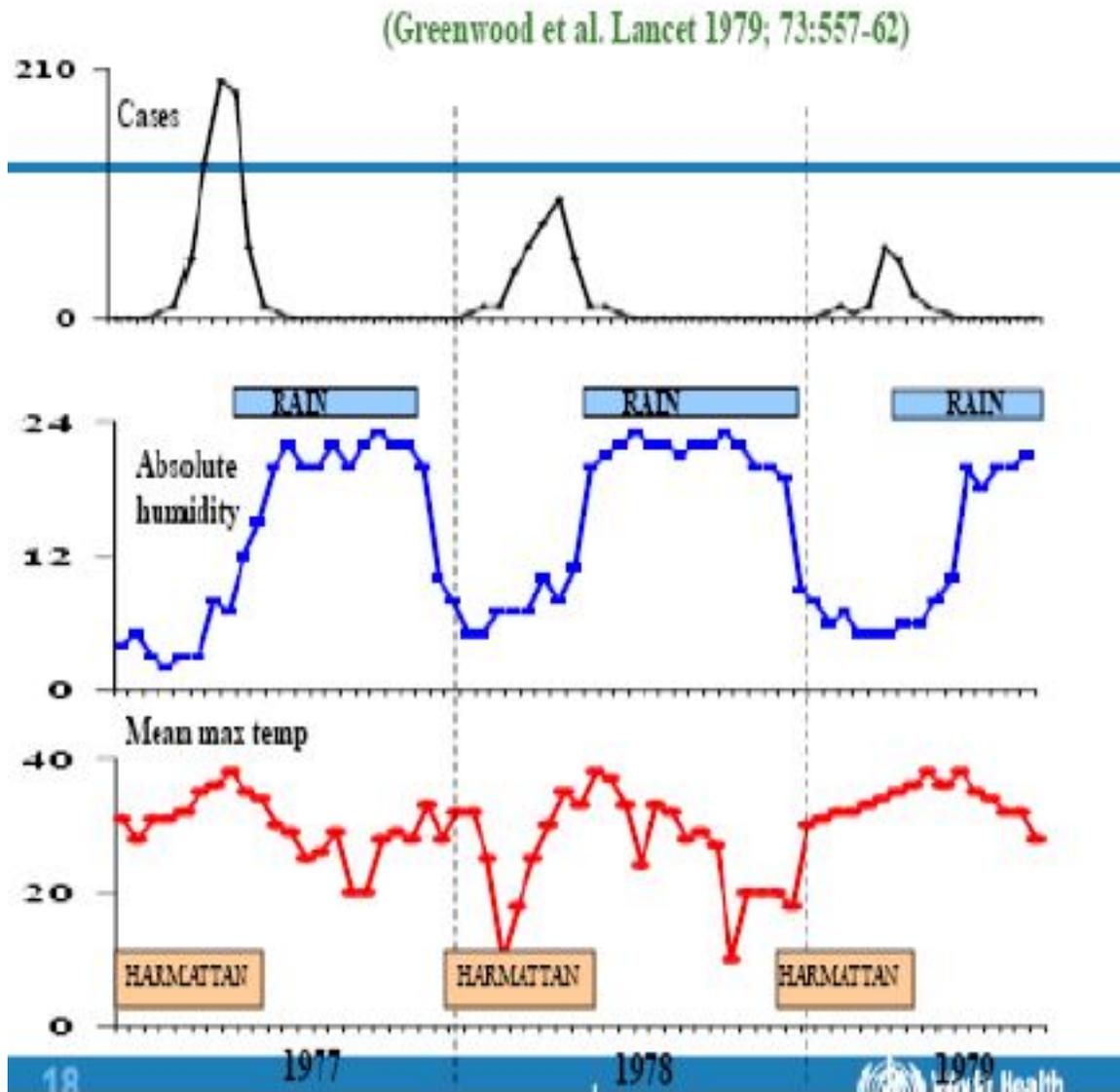


Figure 1.3: Comparison of meningitis cases over West Africa (top), absolute humidity (g kg⁻¹) (center), and mean maximum temperature during (bottom) 1977, 1978 and 1979. After Greenwood et al. (1984).

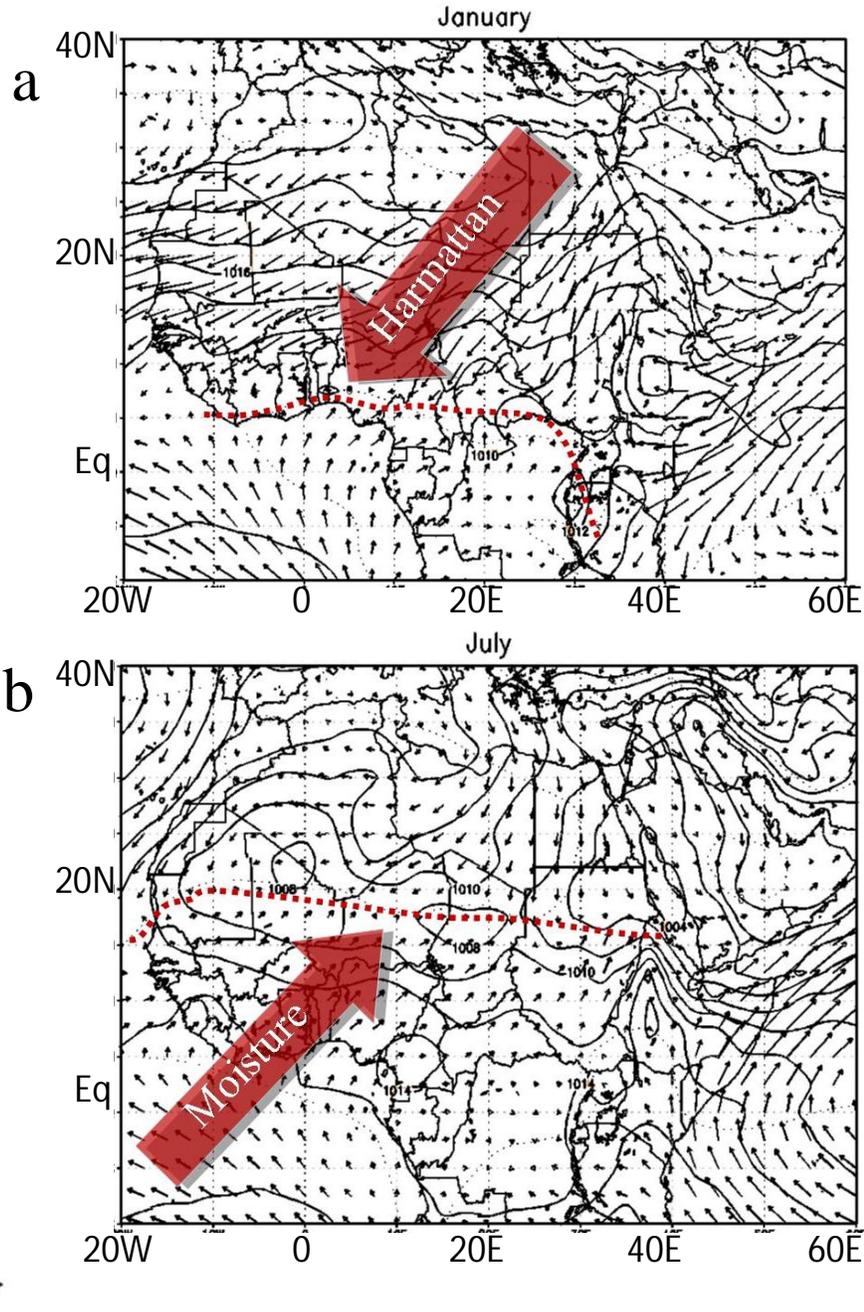


Figure 1.4: 2000-2009 climatology of Mean sea level pressure and 925 hPa winds for (a) January and (b) July. The dotted line represents the boundary between dry Saharan air and the moist monsoon.

Chapter 2

Recent Climatology of the Moisture

Regime during the Boreal Spring

2.1 Introduction

The West Africa Monsoon (WAM) is characterized by two seasons, the pre-onset and the onset (Le Barbe´ et al. 2002; Redelsperger et al., 2002; Sultan and Janicot, 2003). During the pre-onset period of the WAM, precipitation associated with the Intertropical Convergence Zone (ITCZ) is confined to the Gulf of Guinea coast at 5°N, which coupled with the northward migration of the northern limit of the southwesterly winds of the monsoon, [also known as the intertropical front (ITF)] marks the beginning of the rainy season over the Sudano–Sahelian zone (Sultan and Janicot, 2003; Gu and Adler, 2004; Gu, 2009). The monsoon onset is characterized in the literature as the arrival of the ITCZ at 10°N (Sultan and Janicot 2000; Le Barbe´ et al., 2002; Sultan and Janicot, 2003b), leading to major changes in the atmospheric circulation over West Africa.

Due to the scope of the present study, it is important to understand the mechanisms involved in the West Africa circulation pattern during the boreal spring. We chose the ten

year period of 2000-2009 due to the increased availability of district-level meningitis data (described in Chapter 3) as well as increased resolution of boundary conditions for regional climate model simulations (Chapter 5). For our purposes, we define the boreal spring as the period spanning from mid-March through mid-June. During this period, the WAM reaches its pre-onset stage and is followed by the onset (late June) and the subsequent summer monsoon from July through September. The pre-onset of the monsoon is closely linked with the position of the ITF in West Africa (Sultan and Janicot, 2003b; Lélé and Lamb, 2009), and the various interactions that govern its state and the associated atmospheric and ocean patterns. In this study, we will state the fundamental differences between the occurrences of the spring monsoon and the summer monsoon, the interactions governing its dynamics, and its natural variability.

During the boreal summer, the monsoon is characterized by the propagation of African Easterly Waves (AEWs), which are governed by the state of the African Easterly Jet (AEJ), the Tropical Easterly Jet (TEJ) and the Saharan Heat Low (SHL). During this time period, the confluence of the southwesterly monsoon and the northeasterly Harmattan winds (represented by the ITF) is as far north as 20°N and the precipitation maximum is located near 10°N in the southern fringes of the Sahel. In this stage of the WAM, the Atlantic marine ITCZ, along with the confluence of the southeasterly and northeasterly surface winds, is at its northernmost latitude and the easterly surface winds over the central Atlantic are weak (Hagos and Cook, 2009). The vertical structure of the WAM's dynamical components is presented in Fig. 2.1 by taking a vertical profile from 10°S to 40°N using the prime meridian

as a constant. Some important features to note are the AEJ located at 10°N and 600 hPa, the ITCZ's position within the Sahel, the subsidence incurred at the Gulf of Guinea coast, and the deep, dry convection over the Sahara. We will use these definitions in the following sections as we analyze the various source regions of the air mass over West Africa during the boreal spring.

This chapter is set up as follows: Section 2 describes the datasets used to characterize atmospheric moisture during the boreal spring. We address air mass sources in Section 3. In Section 4 we describe the role of convection during the transition from the dry season to the monsoon. We construct a conceptual model for the West Africa Monsoon during the boreal spring in Section 5. We present concluding remarks for this portion of our work in Section 6.

2.2 Datasets

2.2.1 Gridded Reanalysis

We address the sparse and discontinuous nature of in-situ observations throughout Sahelian West Africa (Parker et al., 2008) by employing reanalysis information to investigate the large scale climatology of the boreal spring in this sector of the African continent. We use the National Centers for Environmental Prediction / National Center for Atmospheric Research (NCEP/NCAR) reanalysis (NNRP) product (Kalnay et al. 1996) due to its continuous availability through 2000-2009.

The NRRP dataset (Kalnay et al. 1996) provides a gridded analysis of the global observational network of meteorological variables (wind, temperature, geopotential height, humidity on pressure levels, surface variables) and flux variables such as precipitation rate and radiative and turbulent fluxes. The reanalysis uses a “frozen” state-of-the-science analysis and forecast system at a triangular spectral truncation of T62 to perform data assimilation throughout the period 1948 to present. Data are reported on a $2.5^\circ \times 2.5^\circ$ grid every 6 hours (0000, 0600, 1200, and 1800 UTC), on 17 pressure levels from 1000 to 10 hPa as well as the surface level, which are adequate resolutions for investigating synoptic weather systems as well as climate dynamics.

There are important differences between NRRP and other datasets such as the European Center for Medium-Range Forecasts (ECMWF) ERA-15 and ERA-40 (Uppala et al. 2005), which have increased skill on some aspects of the atmosphere over tropical Africa. For example, Trenberth and Guillemot (1998) concluded that there exists a negative bias in tropical precipitation, indicating the possibility that divergent circulation is too weak. Recent work by Trenberth et al. (2001) also found that large discrepancies with ECMWF temperatures existed in the lower troposphere, which indicates that changes in the satellite observing system may have adversely affected the ECMWF reanalyses, especially in the Tropics. This, in turn, would also be reflected in atmospheric humidity. Some of the more contemporary work on tropical Africa climate dynamics has been based on NRRP. Such work includes the study of the AEJ by Afiesimama (2007) and Wu (2009), intraseasonal variability over Northern Africa (Mathews 2004), and the WAM dynamics (Mounier et al.

2008). This continued use of the reanalysis product over the same locations as the present study gives us confidence in the application of this dataset for our purposes, especially since it covers the entirety of our period of interest. We also recognize that there exists an updated version of NNRP, the NCEP - DOE reanalysis 2 data set Kistler et al. (2001), but this information is available only until 2008, making it unusable for our study of the 2009 northern spring.

2.2.3 Gridded observations

The investigation of atmospheric humidity regime dynamics over the African continent requires a basic understanding of precipitation over the continent, as moisture fronts emanating from convective events can penetrate the dry Saharan air during the dry season as well as the transition period (Knippertz and Fink 2008, Flamant et al. 2009). Our study also analyzes the structure and variability of intraseasonal phenomena that modulates synoptic-scale convective events. Therefore, it is important to complement our data sources with gridded precipitation analysis.

We utilize the Climate Prediction Center Merged Precipitation Analysis (CMAP) for monthly and seasonal analysis. CMAP merges observations from rain gauges with precipitation estimates from several satellite-based algorithms (infrared and microwave) and is enhanced by NCEP-NCAR reanalysis precipitation. The analyses are on a $2.5^\circ \times 2.5^\circ$ grid and covers the 1979-2009 period. Comparisons of the CMAP with the merged analysis of

Huffman et al. (1995) reveal good agreement over the global land areas and over tropical and subtropical oceanic areas (Xie and Arkin, 1997).

2.3 Air mass sources and the moisture budget during the boreal spring

In the present study, we use surface humidity values to determine moisture conditions relevant to meningitis management in the region for the 2000-2009 decade. We use the relative humidity data available from NNRP to diagnose conditions at the surface for a predetermined area of study that is bounded by 10°W - 10°E and 10°N - 15°N (Fig. 2.2b) . On Fig. 2.3 we present time series for the average relative humidity (RH, %) for grids points along each of the latitudes bounded by our box, i.e. 9.5°N - 10.5°N for the 10°N latitude and so on. We note that the change in RH at the surface is highly variable, as is the threshold (40%, Besancenot et al. 1997) currently used for meningitis mitigation in the region (see Table 2.1). The meningitis-climate link and the motivation behind this particular threshold will be expanded on in Chapter 3.

Within our domain, areas to the south (10°N and 11°N) see changes from dry to moist conditions earliest due to the seasonal progression of the Intertropical Convergence Zone (ITCZ) and the disturbed weather associated with it. This also marks the general position of the ITF, which remains at a quasi-stable position between 10°N and 12°N from late March through mid May. Most of the variability of the ITF occurs during the mid-April to mid-June

window as the ITF continues its progression northward to 15°N at the end of June, which is also the start of the West African monsoon (Sultan and Janicot, 2003b).

The length of the period used in this study reflects the need to analyze the dynamics at a daily scale due to the high variability of the system and because monthly averages tend to generalize conditions in the atmosphere to a degree that is unusable for the various applications (health, agriculture, etc.). For the sake of brevity, we have constricted our analysis to 19-day periods before (P1, January 27 – February 15), during (P2, April 15 – May 4), and after (P3, June 11 – 30) the passage of the ITF through the region. This has allowed us to get an overall perspective of the climatology of the region during its different phases.

As seen in Fig. 2.4, our region of study is completely immersed in the dry Saharan air during P1 (2.4a), partially within the moist environment of the WAM during P2 (2.4b), and almost entirely outside of the desert air in P3 (2.4c). Also note the strength and direction of the prevailing winds during these periods: strong northeasterlies for P1, a mix of northerly and northeasterlies for points north of the 40% line and WAM southwesterlies to the south for P2, and southwesterlies for P3 even for points that remain below 40%.

2.3.1 Back-trajectory analysis of source points

In order to understand the overall mechanism for atmospheric moisture and air flow of the WAM during the boreal spring, it becomes imperative to understand the sources of air mass. Using a five day back-trajectory technique (example in Fig. 2.2a), and utilizing horizontal and vertical wind components from the NNRP, we computed the sources of air parcels for

the points in Fig. 2.2b. We have chosen the 925 hPa level as our endpoint surface to circumvent noise generated in the reanalysis below 925 hPa, where parcels can intercept the ground (1000 hPa). Using our predetermined dates (P1, P2, and P3), we constructed averages for each of the points throughout each period. The source points vary in spatial scale both in their horizontal and vertical components. In Figure 2.5a we show the horizontal distribution of source points for February (P1, solid diamonds), April (P2, circles), and June (P3, triangles). Figure 2.6b represents the vertical profile of the source points. Note that for P1 the majority of source points are tightly clustered north of 30°N in North Africa. For P2, the spread of source points is much more scattered in nature and extends from north of 30°N to south of the equator. In contrast with P1, the P3 source points are tightly clustered south of the equator over the Gulf of Guinea and points south.

Further analysis of the source points for each of the periods shows the proportion of air parcels from each of the geographical areas (Fig. 2.6) adjacent to and including the study area delineated in Fig. 2.2b. We have chosen not to show P1 since they are all clustered over North Africa. We define these geographical regions in Table 2.2. We may discern that the majority of source points (44%) in P2 (Fig. 2.6a) emanate from the NW Sahara region and is in accordance with 2.5a, where we there is a set of points clustered within 30°N-40°N and 18W-0°E. Some of these points are located over Europe (8%). The second highest density (20%) occurs over the South Atlantic region, with 14% for the Gulf of Guinea (GOG) and 8% within our box (Sahel). Smaller percentages represent areas like the GOG coast, North-east Tropical Atlantic (NETA) and NE Sahara. In contrast with P2, P3 (Fig 2.6) has the

majority of source points (73%) located over the South Atlantic, and a smaller percentage (20%) from the GOG.

In terms of the vertical profile of source points (Fig. 2.5b), we see that the P1 source points are tightly clustered in the mid levels of the atmosphere between 750hPa and 650hPa and north of 30°N. The P2 points, in contrast are scattered from 650 at 30°N to the lower levels of the atmosphere (<850hPa) south of the equator. The source points for P3 are nearly all emanating from the lower levels of the atmosphere and south of the equator. An analysis of the overall distribution also allows us to view the vertical source regions quantitatively (Fig. 2.7). As the season progresses and the southerly flow associated with the monsoon pushes northward into West Africa and our region of study, the percentage of source regions shifts from a majority of mid to upper levels during P1 (85%), to a higher percentage of lower level source points in during P2 (44%), until the majority of air parcels are oceanic in nature and between 925 hPa and 850 hPa (58%) although a fair amount are still descending from mid levels of the atmosphere between 850 hPa and 650 hPa. In the next section of this study, we will characterize the general circulation patterns associated with air parcel trajectories and offer a hypothesis that describes the vertical motion associated with the source points above 850 hPa.

2.3.1.1 Circulation patterns affecting air parcel trajectories

During the boreal spring, the bulk of the precipitation is limited to the coast along the Gulf of Guinea at 5°N, where the ITCZ resides. Additionally, most of the region is governed by dry,

dusty Harmattan winds emanating from the Sahara desert. We present a three-dimensional view of the major characteristics governing the spring WAM in Fig. 2.8. This schematic allows us to view the interaction between the two ocean basin anticyclones (Azores and St. Helena), with the equatorial trough and the Equatorial Trough (ET) clearly placed between the two high pressures. The nature of the airflow is also easier to contemplate as can be seen with the descending air from the mid-latitudes and northern Africa being contracted around the Azores and the St Helena anticyclones as it descends into the ET. The descending air would be undergoing adiabatic compression, effectively increasing its temperature whilst maintaining its initial moisture content until it reaches the boundary layer. The monsoon flow is also present as a low-level air parcel trajectory, as derived from Fig. 2.5.

Some of the leading theories concerning the dynamics of deserts include their association with the descending branches of Hadley cells and the self-induction effect through albedo enhancement which exists when a desert has formed or is forming (Charney, 1975). Additionally, it has been found that the descending air from the mid-latitudes into North Africa can be traced to isentropic descent in subtropical deserts and eastern ocean basins on the eastern flank of subtropical highs. The isentropic descent can be attributed to the intense latent heat release in the wet summer monsoon regions to the east (Asian monsoon), which instigates isentropic descent to the west (Rodwell and Hoskins, 1996; Rodwell and Hoskins, 2001). We will show how this mechanism may account for the descending air in section gaorghajrg3.

We present a horizontal view of the overall circulation pattern at different levels in the atmosphere for P1-P3 in Figs. 2.9-2.11, for the levels at which our air parcels originate (Fig. 2.6b). During P1, the subtropical high over the Atlantic and Europe is largely responsible for strong northwesterly flow over Europe and northern portions of Africa at 700hPa (where we removed the zonal mean; ZMR hereafter) as it streams towards a trough in the eastern Mediterranean (Fig. 2.9a-b). As we work our way down the vertical levels of the atmosphere (850 hPa) we can discern the large scale flow around the Azores anticyclone and its overall extent over much of northwest Africa (Fig. 2.9.c-d). This subtropical high forces airflow around it from Libya (northwesterly) to Chad (northeasterly flow) and acts to enhance the Harmattan winds experienced at the surface over West Africa (Fig. 2.9e). The ZMR at this level also shows the northwesterly flow over the northern coast of Africa as well as weak monsoon flow limited to the GOG (2.9f).

As the season progresses (Fig 2.10), the influence of the Azores anticyclone weakens over north central and northeastern Africa and the smaller Libyan anticyclone exerts its influence over the Saharan desert, where the ZMR also shows lower heights over the continent forcing convergence off the northwest Africa at 850hPa (Fig. 2.10c -d). At 700hPa, during the P2 period (Fig. 2.10a-b), a wide region of anticyclonic flow is present from the West coast of Africa to the Sudan in the east and from the GOG to the northern Sahel as the surface begins to warm and deep, dry convection indicative of the Saharan desert develops and begins to shift northward. This also allows the West African Heat Low (WAHL) to further develop (Fig. 2.10e-f), increasing convergence at 10°N and inducing the isolated

regions of moist convection associated with the pre-onset of the WAM (Sultan and Janicot, 2003b).

Once the ITF has reached 15°N during P3, much of the air associated with the region emanates from the South Atlantic Ocean and the Gulf of Guinea with weak southerly flow at 850hPa (Fig. 2.11a-b) that becomes stronger at 925hPa (Fig. 2.11c-d). The Libyan anticyclone has shifted northward along with its influence over the region and the SHL has strengthened, increasing low level convergence and enhancing cross equatorial flow from the Atlantic Ocean. We do not show the 700 hPa level since no parcels originate there in our back-trajectory analysis.

2.3.1.2 Vertical profile of the atmosphere during the boreal spring

As alluded to in Section 2.3.1.1 of this portion of the study, descending vertical motion and northerly flow tend to bring dry, mid to upper level air into the region of interest and as far south as the Gulf of Guinea. In Figure 2.13, we show a vertical profile of the atmosphere taken at the prime meridian for the February and April 2000-2009 averages of specific humidity (shaded), meridional wind (solid contours), zonal wind (dash-dot) and potential temperature (dashed contours). During February (2.12a), parcels in the mid-levels of the atmosphere descend following isentropes (lines of equal potential temperature), with dry <4 kg/kg specific humidity into the turbulent Saharan Air Layer (SAL) below 700 hPa, where it undergoes further mixing with warm, dry desert air. We also show that the monsoon

westerlies are limited to the GOG and that the AEJ is centered at 650 hPa and 3°N latitude in February.

During April (2.12b), the isentropic descent penetrates further south with the advent of strong convection in the vicinity of the ITF and progressive heating of the desert. The low-level southerly winds grow stronger and penetrate further north along with the ITF (now at 14°N as denoted by the zonal wind contour set at 0 m/s to denote change in east-west regime). The AEJ is also stronger and farther north at 5°N.

The motion of air parcels as described above can be attributed to more complex dynamics than the Hadley or Walker overturning circulation (Diaz, personal communication). In contrast with the Hadley circulation, this descending air is primarily of mid-latitude origin and occurs on the eastern flank of the dominant Azores subtropical high (Rodwell and Hoskins, 2001). However, whereas recent studies have focused on the role of the SAL and the Azores High in localizing isentropic descent along the African coast and its influence on tropical cyclogenesis, here we stress its influence in dictating the strength of the dry season over the Sahel and points south (see Figs. 2.9-2.11).

There is evidence from in-situ data during the period of monsoon onset between May and June which suggests a strengthening of descent over the east Mediterranean and Sahara as the monsoon heating moves northward with the seasonal cycle (Lezine and Casanova, 1991). In a study by Rodwell and Hoskins (1996), it was argued that the adiabatic descent in the vicinity of subtropical highs would imply a reduction in relative humidity and convection and a lowering of the level of radiative emission to space that could lead to a local diabatic

enhancement of the descent over the eastern Mediterranean and Sahara. The year-round and relatively cold SSTs in the eastern subtropical north Atlantic are likely to reinforce the lack of penetrative convection through changes to the moist static energy (Neelin and Held 1987) and other mechanisms, effectively helping to maintain the atmospheric descent in the region. In a study by Lindzen and Hou (1988), it was shown that meridional displacements of the maximum in zonal-mean surface temperature may be responsible for the main characteristics of the summer and winter Hadley cells. Further, it was argued that in the winter hemisphere, there could be strong zonal-mean subtropical descent associated with radiative cooling and a strong equatorially displaced subtropical jet. Vertical cross sections of the zonal winds (Fig. 2.13) also indicate strong variability and southward progression of the subtropical jet during anomalous years and months. The subtropical jet also displays different structures during June of 2006 (1.15°C) and 2009 (2.13d), with 2009 extending further south and lower in the troposphere.

As the seasonal cycle progresses, the intense heating of the Sahara desert causes the monsoon circulation to begin and initiates rainfall over the Sahel. This occurs due to an enhancement of the meridional circulation associated with the SHL, which causes increased convective inhibition in the ITCZ through intrusion of dry and subsiding air from the north, and increased potential instability through a greater inland moisture advection and a higher monsoon depth (Sultan and Janicot, 2003a,b). The increase in monsoon depth is induced by a stronger cyclonic circulation in the low levels, higher vertical wind shear due to westerly monsoon wind and a strengthening of the midlevel AEJ.

2.3.2 Variability of humidity along parcel trajectories

In the preceding sections we presented findings concerning the source of air parcels over the Sahelian zone of West Africa and we described the nature of the atmosphere as a result of compressional warming and transport of dry upper-level air. The monsoon flow, however, is a low level flow below 925 hPa that has a strong relationship with the SSTs in adjacent areas of the Atlantic Ocean. The variability of moisture at the surface is thus the end result of complex interactions between the atmosphere at horizontal and vertical scales as well as with the dynamics of the adjacent ocean basin.

The variability of the SST over the eastern tropical Atlantic experiences a strong annual cycle that is partly controlled by the seasonal progression of the WAM and the associated St Helena anticyclone (Hagos and Cook, 2009). During the spring, the sun is directly over the GOG, the trade winds are weak, and a band of high SSTs lies along the equator from 10°S to 5°N. As the year progresses, the trade winds along the equator intensify, followed by a rapid decline of SSTs over the eastern equatorial Atlantic. Seasonal cycles bring climatological levels of moisture into the region, but this shift is highly variable in spatial and temporal scales. Within the following subsections, we characterize the moisture at the source points for each point in our matrix, the change in relative humidity as the parcels advect into our study region, and we show results on composite back-trajectories.

2.3.2.1 Source points and moisture during the early spring

During the early spring period (March 15 – April 15), the monsoon flow is weak and moisture is confined to the GOG coast, which is experiencing warm SSTs. The ITF is at its southernmost point and the AEJ is located at 3°N and near 700 hPa. The majority of the air over the Sahelian region can be traced back to northern Africa, Europe and the North Atlantic. In order to view events preceding the structure of the early spring, we use a simple average during P1 for the source point for each of our 126 points and we separate them according to their height in the atmosphere. In Fig. 2.14 we present three different levels (600 hPa, 700 hPa, 850 hPa) with specific humidity as the background and corresponding winds. Overlaid are the source points during P1 that occurred below 650 hPa (a), between 650 hPa and 750 hPa (b), and between 750 hPa and 850 hPa (c). Even though there is significant generalization due to the wide range of source points in the vertical (see Fig. 2.5b), we can still discern the relative dryness of the source regions. Even at their highest level of moisture (850 hPa), parcels do not cross the 4 kg/kg isoline.

Further analysis using the parcel back-trajectory procedure has allowed us to develop a vertical profile of the pathway by which air from this location of the atmosphere reaches the 925 hPa surface in Sahelian West Africa (Fig. 2.15). Here, we average all end points along 10°N and along 15°N and all their associated trajectories to construct a composite trajectory for each group of points at each of the two latitudes. We show that parcels are, on average, originating between 810 hPa and 675 hPa from points north of 30°N . For the 10°N group of parcels, the starting relative humidity is between 40-50% and its final humidity is below

20%. Due to the inherent definition of relative humidity and its dependency on temperature, it is important to recognize the generally cold conditions at this height [below 0°C (not shown)] in the atmosphere and the data indicates that the air descended dry-adiabatically to 925 hPa.

Another important aspect generated from the vertical analysis is the different “moisture trajectories” taken by both latitudinal groups. Points at 15°N, for instance, have their source much higher in the atmosphere and at much drier conditions. Conversely, points at 10°N tend to be slightly moister in their origin, although at the surface they are below 20% relative humidity. This suggests more mixing may be involved and that the horizontal trajectories may differ at this latitude from points further north.

We attempt to address the above question in Figure 2.16 by compiling the composite trajectories at each latitude within our matrix of points (10°N, 11°N, 12°N, 13°N, 14°N, 15°N) and mapping it onto the 850 hPa specific humidity field. It follows that latitudinal averages from 10°N to 12°N follow the clockwise airflow from northern Libya, descending through Chad and westward into their end points in West Africa. Latitudinal averages from 13°N to 15°N initiate their motion further west into Tunisia and Algeria following the same clockwise flow but farther west. As our analysis suggests, further scrutinization of parcel trajectory is required to understand the mixing of air masses that may be occurring and the synoptic conditions that may be affecting their advection. It is clear, however, that certain groups of end points are affected by different climatological conditions. This is more so during the shift from the dry season to the monsoon. Note that for latitudinal averages close

to the equator, the specific humidity in the vicinity of their point of origin sits within a slightly moister pocket and this may contribute to the higher relative humidity shown for 10°N in Fig. 2.16.

2.3.2.2 Source points and moisture during the mid-spring

As the season progresses to the middle of spring in the northern hemisphere, the waters of the GOG begin to cool with the relaxation of trade winds as discussed in Hagos and Cook (2009). At the same time, waters off West Africa (NETA) begin to warm. With increased solar radiation, the Saharan desert rapidly warms and induces a stronger SHL and equatorial trough, which in turn creates a pressure gradient between the higher pressure over the ocean and the lower pressure over the land. This results in a stronger monsoon flow and a waning of the Harmattan flow. At this point of the year, air is still flowing from the northeast into parts of the Sahel but it is mostly from the mid to lower levels of the atmosphere from northern latitudes. The increased baroclinicity also induces a stronger AEJ and causes it to move north to 6°N and higher in the atmosphere to 650 hPa. As a result of the stronger monsoonal flow, the ITF shifts northward. This also allows for transient westward-propagating disturbances to develop along the point of convergence between the Harmattan and the WAM.

We again employ a simple average during P2 for the source point for each of our 126 points and we separate them according to their height in the atmosphere. In Figure 2.17 we present three different levels (700 hPa, 850 hPa, 925 hPa) with specific humidity as the

background and corresponding winds. Overlaid are the source points during P2 that occurred below 750 hPa (a), between 750 hPa and 850 hPa (b), and between 850 hPa and 925 hPa (c). Even though there is significant generalization due to the wide range of source points in the vertical (see Fig. 2.5b, much higher than P1), we can still discern the relative dryness of the source regions to the north and the moister, oceanic source points to the south. Indeed, the higher variability of source points during P2 enhances the complexity and natural variability of the ITF during the pre-onset of the WAM. Parcels emanating from northern latitudes do not cross the 4 kg/kg isoline even at their highest level of moisture (850 hPa). Another important aspect indicated in this figure is the geographical and vertical positioning of source points and their inherent humidity: points north of the end point matrix tend to have their source higher in the atmosphere, points in the immediate vicinity tend to come from lower in the atmosphere, and points south of our study area begin their trajectories in the much moister locations over the tropical Atlantic waters.

In order to highlight the variability of humidity described above, we employ an analysis of the vertical structure of parcel trajectories. As was done with end points during P1, we averaged all end points along 10°N and along 15°N and all their associated trajectories to construct a composite trajectory for each group of points at each of the two latitudes (Fig. 2.18). We show that parcels at 15°N are, on average, originating around 750 hPa from points between 25°N and 30°N with a starting relative humidity between 40-50% and a final humidity is below 20% at 925 hPa. For the 10°N group of parcels, most originate below 850 hPa and have a relative humidity above 60% with a final number 50-60%. This high

humidity is an important factor for meningitis mitigation in the region since it has crossed the 40% threshold (see Section 2.6).

In contrast with P1, the vertical analysis for P2 shows vastly different “moisture trajectories” taken by both latitudinal groups. Points at 15°N, for instance, have their source much higher in the atmosphere and at much drier conditions. This is similar to the parcel trajectories in P1 for 10°N in scale and moisture. Both initiate above 40% but decrease to below 20% at the 925 hPa surface, indicating a similar circulation pattern may be at work and also suggesting that the overall structure of the climatological flow associated with the different points in our matrix has shifted north. The structure for parcel trajectories averaged for end points at 10°N stems from the tropical Atlantic Ocean south of the GOG coast with much higher humidity. As shown in Fig. 2.18, these parcels are much closer to the surface in their origin and with appreciably heightened humidity. This indicates that the pre-onset of the WAM has fully developed over the region and that widespread precipitation is likely to be occurring (Sultan and Janicot, 2003b).

In order to track the horizontal progress of parcel trajectories at the various latitudes within our end point matrix, we again construct composite trajectories for each of the 6 latitude lines (Fig. 2.19). Note that this plot is noticeably different and more complex than Fig. 2.16. This is due to the presence of the ITF within our end point matrix and the different trajectories taken by each of the points. Our method for averaging parcels at each latitude tends to fall apart in P2 due to the various components at work in the whole of West Africa and the adjacent regions. We can still retrieve some information from this analysis, however:

1) parcel trajectories shift from south of GOG at the lower latitudes to over the Sahel for the middle latitudes in our matrix, and to over the Sahara for points in the northernmost latitude of our matrix. 2) parcels at 14°N and 15°N follow roughly the same clockwise circulation pattern over the desert as those for all parcel trajectories in P1. 3) Southerly trajectories emanate from moister environments whilst northern trajectories tend to propagate from much drier locations.

2.3.2.3 Source points and moisture during the late spring

As the boreal spring transitions into summer, many of the important attributes of the summer monsoon are present. For example, AEWs, an integral part of the summer monsoon are now one of the prevalent sources of precipitation and moisture in the region. As evidenced from Fig. 2.20, the main source of air parcels during this period has now shifted to be purely oceanic in nature, from the equatorial Atlantic. Additionally, most of these parcels originate around and below 850 hPa (see Fig. 2.5b). This region of the atmosphere, including 850 hPa is considerably moist even for points south of 10°S (>6 kg/kg). Note that the source points have a slight southwest to northeast tilt in accordance with the flow in the atmosphere. This flow eventually shifts to a southwest to northeast tilt near the coast and within West Africa, indicating the start of the WAM. The stronger monsoon flow has shifted the ITF further north (see Fig. 2.4c), and most of the points within our matrix are now above the 40% threshold except for the extreme northeastern sector.

For the sake of brevity and due to the scope of this study, we have elected not to compute the parcel trajectories for P3. There is sufficient evidence from the preceding analysis that parcels during this time period are oceanic and lower tropospheric in nature in accordance with the monsoon flow. We note that the Sahelian climate is now increasingly affected by AEWs that propagate from their genesis locations in the Ethiopian Highlands and that undergo significant flux as they traverse the width of the African continent and are modified by the equatorial central Africa (Tetzlaff and Peters, 1988; Laing and Fritsch, 1993; Lin and Robertson, 2005; Laing et al., 2008). At this point of the year, the increasing precipitation at 10°N causes subsidence along the coast of the GOG, effectively suppressing precipitation in the region. Ultimately, the shift of the precipitation maxima leads to the characteristic monsoon “jump,” but there exist many important variables that have to be explored in order to determine the causality of the sudden shift of the ITCZ to a new, quasi-stable position at 10°N (Sultan and Janicot 2000; Le Barbe´ et al. 2002; Sultan and Janicot, 2003a,b; Hagos and Cook, 2007; Okumura and Xie, 2004; Ramel et al., 2006; and Sijikumar et al., 2006; Eltahir and Gong, 1996).

It is also clear from the preceding analysis that the variability of moisture onset is related to intraseasonal phenomena that modulates humidity over the region as well as its sources. An essential variable of these intraseasonal phenomena is the presence of convection over West Africa during the dry season as well as the transition season. Convection within the area of interest can induce cold pool outflow from Mesoscale Convective Systems (MCS) that is able to increase monsoon flow from the ocean (Flammant et al. 2009). Conversely,

increased convection in equatorial Africa or the GOG induces sinking motion over the Sahel. We address these mechanisms in the following section.

2.4 Characterization of convection during the transition season

The onset of rainfall is an important variable for the population in Sahelian West Africa due to its influences in areas such as health, through the spread and cessation of infectious diseases like malaria and meningitis (Molesworth et al. 2003), and agriculture by influencing planting dates (Ati et al. 2002) and locust migration (Roffey and Magor 2003, Maiga 2005). Isolated rain events can modify the moisture content of the environment (Knipertz and Fink 2009) and induce or be the precursor to increased humidity (Flamant et al. 2009). Therefore, it is important to characterize the nature of moist events during the transition period from the dry season to the monsoon.

Meteorological signals prior to the start of the monsoon are weak at a regional scale because the initiation of rainfall over the Sudano–Sahelian zone is seldom abrupt in nature and is usually preceded by a succession of isolated precipitation systems of uncertain intensity interspersed with dry periods of varying duration (Omotosho et al., 2000; Ati et al. 2002). Past and concurrent studies have been aimed at successfully diagnosing the interannual and intraseasonal variability of the WAM rains in order to elucidate the causes of elongated dry and wet periods. Much of this work has been focused on the overall structure of the WAM throughout its lifetime and the AEWs that constitute the majority of its representation at the surface and throughout the atmosphere (Burpee 1972; Janicot 1992; Le

Barbe et al. 2002; Sultan et al. 2003; Sultan and Janicot 2003a; Grist 2002; Rowell and Milford, 1993; Hsieh and Cook, 2005; Kiladis et al., 2006; Parker et al., 2005a; among others). Further, the characteristic shift in the Intertropical Convergence Zone (ITCZ) from latitude 5°N to 10°N (Hagos and Cook, 2007; Drobinski et al., 2005; Le Barbe et al., 2002; Sultan and Janicot, 2003b) has also been explored in order to determine its predictability and variability in interannual scales and as forced by the general circulation.

Although only a limited amount of previous studies have focused on the rains during the pre-onset, many of the same background climatological information, both on intraseasonal and longer scales, can be applied to their study. This includes important aspects such as the location of the ITF, convectively-coupled equatorial waves (CCEWs), state of SST in adjacent Atlantic Ocean waters, SHL dynamics and mid-latitude systems.

2.4.1 The pre-onset of the monsoon and the Intertropical Front

In order to understand the persistence, strength and variability of the early season WAM rains, it is important to analyze the behavior of the Intertropical Front (ITF). As introduced by Hamilton and Archbold (1954), Eldridge (1957), Hare (1977), and later expanded on by Sultan and Janicot (2003) and Lélé and Lamb (2010), the ITF is an integral part of the buildup and retreat of the WAM. Lélé and Lamb (2010) postulated that the location of the ITF in April could be used as a predictor for the advancement of the leading edge of the southwest monsoon flow during the May-June period. Sultan and Janicot (2003b) diagnosed

this critical feature as one where the first isolated precipitation systems occur ahead of the WAM.

The ITF, which is also defined in the literature as the Intertropical Discontinuity (ITD), is strongly affected by the variability of the West African or Sahara Heat Low (SHL). As described in Section 2.3 of this study, the SHL is an extension of the equatorial trough and the pressure gradient between the SHL and the subtropical anticyclone controls the strength of the Harmattan. Recent studies suggest that the monsoon onset is partly controlled by the SHL dynamics (Sultan and Janicot, 2003; Drobinski et al., 2005; Parker et al., 2005a; Ramel et al., 2006; Sijikumar et al., 2006). Another of the more important aspects of the WAM, and which affects the position of the ITF, is the existence of the African Easterly Jet (AEJ). The jet forms as a consequence of the dry, hot environment of the Sahara and the cooler and moister conditions in the Gulf of Guinea (Cook, 1999 and references therein). The AEJ is considered to be instrumental in creating an environment in which African wave disturbances develop through baroclinic and barotropic instability.

The definition of the ITF, in terms of the variables used to derive its location and behavior, is calculated differently in recent studies. Lélé and Lamb (2010) used daily temperature, humidity, and rainfall data at 10-day (dekad) resolution to calculate concurrent monthly ITF-rainfall relations. In Sultan and Janicot (2003), the position of ITF was derived using the 925 hPa zero isoline of the zonal wind (denoting a change in the east-west regime). We will use Sultan and Janicot's (2003b) definition of the ITF for this study since they

isolate short rains at the northern boundary as an important feature in the progression of the WAM.

The progression of early-season precipitation along the leading edge of the monsoon wedge also delineates the start of the WAM for points along its boundary, which, in turn, can be used by the local population for health and agricultural applications. Because of its south-to-north progression due to the seasonal solar cycle, monsoon rains will occur earlier for points closer to the Gulf of Guinea (March) and later (late June) for points along 15°N . We again focus on the time of greatest impact for meningitis mitigation: April and May during 2000-2009. We use CMAP-derived precipitation (see Section 2.2.3) and NNRP variables (Section 2.2.2) to denote the relative position of the ITF and heat low during these months (Fig. 2.21). The zero isoline of the zonal wind at 925 hPa is used as a proxy for the location of the ITF in accordance with Sultan and Janicot (2003b).

The month of April (Fig. 2.21a) is characterized by precipitation higher than 4 ms^{-2} (indicative of steadier rains, Sultan and Janicot 2003b) being limited to the GOG coast, the heat low is at its maximum over southern Chad and the ITF positioned along 12°N . For the month of May (Fig. 2.21b), heavier precipitation is present farther inland (9°N), the heat low is an elongated trough extending from eastern Mali to Chad and the ITF undulates about the 15°N latitude from 10°E westward. We attempt to diagnose the influx of moisture on a meridional scale in Fig. 2.22, where we show the mean 2000-2009 rainfall time series (mm day^{-1}) during the February-July period is plotted using area averages of grid boxes bounded by 10°W - 10°E and 10°N - 12.5°N and 12.5°N - 15°N . There is an important change in the

slope of the northern box at May 10th, where the slope during the March 30th – May 10th is 0.01 mm and May 10th – June 15th is 0.05 mm. This change in the slope suggests that isolated events increase in frequency within the core of the Sahel from early May and then rapidly in late May to June. We should note that this finding is in accordance with Sultan and Janicot (2003b) except that their data was for 1968-1990 and using daily rain gauge amounts supplied by Institut de Recherche pour le Developpement (IRD), thus increasing the robustness of their study whilst suggesting further exploration of intraseasonal variability of convection during this time of the year.

2.4.2 Variability of convection along the Gulf of Guinea

Points along the Gulf of Guinea (GOG) are likely to be affected by southwesterly flow injecting moisture into the region during the start of the boreal spring, which can be dependent on the SSTs to the immediate south and large scale circulation governing the synoptic pattern in the region. The sensitivity of precipitation along southern portions of West Africa (along 5°N) to SSTs occurs due to weak southwesterlies that induce weakening of upwelling in the GOG (Adedokun, 1978). Additionally, the Walker circulation (Walker, 1924 and subsequent) can also have an impact in this region by enhancing (suppressing) precipitation patterns through increased (decreased) ascent of air as the system oscillates due to natural variability (Adedokun, 1978).

Other external forcings on the response of precipitation patterns along the GOG coast can be attributed to pronounced tropical Pacific El Niño events (Lamb and Pepler 1990), such as

the year 1983, which included a drought that extended from the Soudano-Sahel equatorward to the GOG coast (Ward 1998, Nicholson and Grist 2001, Nicholson and Webster 2007, Nicholson 2008). Further, Gu (2009) found that there was coherent intraseasonal variability of convective and dynamic propagating features that are closely associated with the global tropical (eastward-propagating) intraseasonal mode, i.e., the Madden-Julian Oscillation [MJO, (Madden and Julian, 1994)]. The study found that areas bounded by 10°N-10°S were highly affected by a 30-80 day cycle in accord with the MJO; this included coastal sections of the GOG and oceanic points south.

In addition to the longer-scale variability due to the MJO, Gu and Adler (2004) found that shorter-period eastward-propagating precipitation signals dominate the precipitation regime at 5°N during the April-June period. This precipitation pattern may be associated with the Kelvin-type tropical waves forced by warm SSTs in the equatorial Atlantic (Wheeler and Kiladis 1999) or formed in the eastern Pacific or in association with the MJO (Mekonnen et al. 2008). Indeed, a large portion of the equatorial variability can be attributed to Kelvin wave activity (Kiladis et al. 2009). The presence of Kelvin waves is at its peak during the boreal spring over West Africa (Wheeler and Kiladis 1999) with a clear center of highest variance along the GOG coast from Ghana into central Cameroon. There is considerable variability on monthly timescales as well as seasonal and their effect can extend into the Sahel as the boreal spring gives way to summer. We will explore CCEWs in more detail in Chapter 4.

2.4.3 Variability of convection over the Sahel

The influence of the Walker circulation can affect convective precipitation throughout West Africa (Adedokun, 1978), but other processes account for a wider portion of the variability away from the Gulf of Guinea. For Sahelian West Africa, episodes of deep convection during the rainy season occur in the presence of moderate vertical shear of the horizontal wind. This is commonly associated with the AEJ, and the disturbances that are dynamically linked to this midlevel feature (Nicholson and Grist, 2006). Certain environmental factors, such as vertical wind shear buoyant energy, low-level jets, and latitude determine whether convection organizes into these systems (Laing and Fritsch 1993). The frequency of cloud clusters and the amount of rainfall associated with them is modulated by transient synoptic-scale AEWs (Houze and Betts 1981; Thompson et al. 1979). This mechanism, however, is not considered to be a main source of precipitation during the pre-onset period of Sahelian rains (Grist, 2002). Indeed, Grist (2002) cited the Subtropical Jet (STJ) as a feature that explains the occurrence of precipitation during the spring and stated that there are few accounts of easterly waves during March and April (records from the Tropical Prediction Center that state that between 1968 and 1979 of easterly wave season, there is no record of an easterly wave at Dakar before 30 April).

The literature on the subject of boreal spring convection also reveals a shift in the focus away from equatorial regions. The southward penetration of westerly disturbances into West Africa has been documented in past studies (Flohn 1975; Thorncroft and Flocas 1997). During the boreal spring, the STJ has its mean core position much closer to tropical Africa, at

around 25°N, with mean westerly speeds up to 16–24 ms⁻¹ at 200 hPa over 15°N (Grist 2000). The synoptic scale systems associated with this mechanism affect variables such as soil moisture and vegetation feedbacks. Indeed, dry season precipitation patterns have been found to have important impacts in the region (Knippertz and Fink 2008, 2009). They constitute a potentially-predictable source of precipitation during the dry season that could affect the progression of the ITF and WAM. In Knippertz and Fink (2008), their case study of a January precipitation event in West Africa associated with a mid-latitude disturbance in 2004 occurs in a year that saw the ITF arrive at 15°N 23 days in advance of the climatology. We note that the proximity of boreal winter extra tropical synoptic phenomena is likely to have a significant impact on the nature of convection over the region during our period of study. Indeed, a series of mid-latitude events exerted their influence on Sahelian West Africa during early May 2009. This interaction is explored in more detail in Chapter 4.

The ITF plays an integral role in the development of convective systems during the boreal spring. Gravity currents associated with westward-propagating convective systems in the ITF region are also often observed to be widespread and to propagate on long distances over the Sahel and the Sahara (Flamant et al., 2007). At the beginning of the monsoon season, these convective systems produce conditions favorable to the monsoon progression towards the north by cooling and moistening the surface north of the ITF. Flamant et al. (2007) postulates that these systems could play a role in the monsoon onset mechanism and can be considered an important component of the monsoon cycle in pre-onset conditions.

The impact of strong convective events is highlighted by Flamant et al. (2009), where they detail the influence of cold pool outflows generated by downdrafts in convective systems persists as a coherent dynamic and thermodynamic structure over two study days, influencing a front at least 1000 km long and 200 km wide across southern Mali. The positive feedback associated with the cold pool generated by this convective system, which brought moisture north over the northern Sahel and into the southern fringes of the Sahara, effectively cooled the desert surface and added to the evolution of the WAM onset.

Convective complexes that propagate westward during the pre-onset of Sahelian rains in April, May and June are also subject to modulation from interactions with orographic features (Fig. 2.2b) such as the Jos Plateau (Nigeria), the Darfur mountains (Sudan), and the Ethiopian Highlands (Tetzlaff and Peters, 1988; Laing and Fritsch, 1993; Laing et al., 2008). We note that some westward-propagating systems occurring near the start of the pre-onset of the WAM can have an important impact on the moisture content of the atmosphere as the season progresses from dry conditions into the rainy season. Although these systems may not propagate with the same strength, and may even dissipate as they reach the west coast of Africa as Grist (2002) suggests, they can be strongly modulated by orographic interactions in the same manner as their boreal summer counterparts. One such example is a strong westward-propagating disturbance during early May, 2009. We show the progression of this event in the Hovmoeller plot of the NNRP-derived meridional wind component at 850 mb at 15°N (Fig. 2.23). Precipitation associated with this convective system was recorded from Kano, Nigeria, to Niamey, Niger, and Bamako, Mali. This system also caused permanent

changes in atmospheric moisture in the vicinity of Kano, Nigeria and is the greatly expanded upon in Chapter 3, as it has direct consequence on meningitis mitigation.

One important, and potentially dramatic feedback associated with early season convective systems is their diurnal variability. The general diurnal cycle across tropical continents shows that the peak of precipitation occurs in the late afternoon to early evening (Yang and Slingo, 2001). Mohr (2004) used data from the Tropical Rainfall Measuring Mission (TRMM) satellite Microwave Imager to examine the diurnal cycle in sub-Saharan Africa for May–September, 1998–2001 and found that the diurnal cycle of precipitation varied geographically, intra-seasonally, and interannually. The study also found that this diurnal variability seemed to be influenced by the frequency and life cycles of organized convective systems.

The diurnal variability of the WAM is also explored in detail by Parker et al. (2005b), in which it is shown that there is a coherent diurnal cycle of the winds associated with the WAM. Their study finds that the lower-tropospheric monsoon circulations and boundary-layer mixing that characterizes the baroclinic region over West Africa is driven by the interplay between the diurnal cycle of the SHL (which drives the circulation) and the diurnal cycle of boundary-layer convective turbulence (which tends to suppress the circulation). Further, the diurnal cycle of transport and mixing is found to be a key process that influences the continental water budget over West Africa. This has implications both for the initiation of the WAM and for the wet season itself. Parker et al. (2005b) also recognized that the importance of the diurnal cycle of the WAM circulations varies with the surface temperature

of the heat low to the north, and that the time at which this variation may be particularly important is the period leading up to the monsoon onset. The timing of deep convective events, for example, could change the water budget of the system by moistening the soil and modifying surface fluxes.

Another essential aspect that can determine the feedback sign (positive or negative) is the contribution by land surface processes. Charney (1975) suggested a significant role for vegetation in the dynamics of rainfall over the Sahel by implying that the rainfall-producing circulation over this region is sensitive to changes in the state of vegetation at the desert border with the Sahara. Walker and Rowntree (1977) investigated the effect of soil moisture conditions on circulation and rainfall in West Africa. Within the studies addressing the impact of vegetation cover (e.g., Charney et al. 1975; Xue and Shukla 1993), it is generally concluded that the desertification near the sub-Saharan desert border reduces rainfall within the region of vegetation perturbation and increases rainfall south of the perturbation region. The soil moisture–rainfall interactions are often found to be able to sustain rainfall anomaly and thus provide a positive feedback (e.g., Walker and Rowntree 1977; Yeh et al. 1984; Zheng and Eltahir 1997b). Convective systems during the start of the WAM can create important feedbacks by inducing higher amounts of soil moisture that, in turn, generate changes in vegetation, which can also be a precursor for the sustainability of stronger and longer-lived convective systems to follow.

2.5 A Conceptual Model of the West Africa Monsoon during the boreal spring

The preceding work has illustrated the many facets that govern the variability of moisture over Sahelian West Africa during the transition season as the Harmattan retreats and gives way to the summer monsoon. We use this knowledge to develop a conceptual model of the boreal spring in order to acquire a more complete view of the multi-scale interactions at play during this time of the year. Due to the complexity of the interactions at work, and the spatial and temporal scales related to the various components of the system, we will divide the conceptual model into separate stages of development and the dynamical interplays involved.

2.5.1 General features of the boreal spring

The large scale components of the circulation during the spring, such as the Azores and St Helena anticyclones and the Saharan Heat Low, and the winds resulting from pressure gradients of these systems (Harmattan, monsoonal flow) were reviewed and analyzed in Section 2.2.2. The Azores and the Libyan anticyclones in the northern hemisphere and the St. Helena Anticyclone in the Southern Hemisphere serve as centers of action dominating the atmospheric circulation over West Africa (Adedokun, 1978; Dohnneur, 1970). The Azores high is more permanent than the Libyan anticyclone, whilst the St. Helena anticyclone often oscillates north in the boreal summer and south in the winter. These large scale systems, coupled with the Sahara Heat Low (SHL) directly affect the variability of the monsoon and Harmattan winds.

The general circulation is complimented by smaller but integral dynamical features and land surface conditions that determine the state of the atmosphere over West Africa during the boreal spring. One such feature is the AEJ, which varies from a position of about 3N and 700 hPa in mid March to about 9°N and 600 hPa in mid June (Afiesiamama, 2007). Equally important to the overall mechanics of the monsoon are the waters of the Gulf of and the North East Tropical Atlantic (NETA). Indeed, much of the variability and some dramatic, historical events involving the WAM are derived from the SSTs in these two regions (Vizy and Cook, 2001; Janicot et al., 1998; Xie and Carton, 2004; Hagos and Cook, 2007a,b).

In Section 2.4.3 we learned that another group of relevant surface features includes the meridional difference in land cover from the forests close to the GOG, moving northward to the grasslands of the Sahel and arriving at the desert in the Sahara. The precipitation and induced circulation stemming from the tropical jungles of equatorial Africa as well as the terrain in eastern Africa aid in the maintenance and development of AEWs as they traverse the width of the continent into the Sahel on their way to the Atlantic Ocean (Tetzlaff and Peters, 1988; Laing and Fritsch, 1993; Laing et al., 2008). Teleconnections and interactions with mid-latitude systems and the general circulation also determine the state of the WAM during the spring. For instance, it has been shown that mid-latitude systems can extend their influence deep into the tropics, causing anomalous precipitation in the region during the dry season (Knippertz and Fink 2008 and 2009). Points closer to the GOG are also intimately tied with phases of the Walker Circulation and the Madden-Julian Oscillation (Adedokun, 1978).

We presented a three-dimensional view of the major characteristics governing the spring WAM in Fig. 2.8. This idealized projection of the large scale features shows the interaction between the two ocean basin anticyclones (Azores and St. Helena), with the equatorial trough and the SHL clearly placed between the two high pressures. The nature of the airflow is also easier to contemplate as can be seen with the descending air from the mid-latitudes and northern Africa being contracted around the Azores high and the St Helena high as it descends into the equatorial trough. The descending air would be undergoing adiabatic compression, effectively increasing its temperature and would also be low in moisture. The monsoon flow is also present as a low-level air parcel trajectory, as derived from our analysis in Section 2.3.1. We characterize this flow as being lower tropospheric in nature (925 hPa) with a clear oceanic source over the equatorial Atlantic and which is intimately-linked with the state of surface temperatures of the water.

The variability of the SST over the eastern tropical Atlantic experiences a strong annual cycle that is partly controlled by the seasonal progression of the WAM and the associated St Helena anticyclone (Hagos and Cook, 2009). During the spring, the sun is directly over the GOG, the trade winds are weak, and a band of high SSTs lies along the equator from 10°S to 5°N. As the year progresses, the trade winds along the equator intensify, followed by a rapid decline of SSTs over the eastern equatorial Atlantic. This warming and cooling of the SSTs is highly asymmetric, with the latter taking only three months and the former seven months (Xie and Carton 2004). Conversely, in the northeastern tropical Atlantic, April–August is a period of rapid warming (Hagos and Cook, 2009).

The change in SST over the GOG is particularly important for the onset of the WAM and is one of the primary sources of precipitation variability along the coast at 5°N (Adedokun, 1978). The relationship between GOG SSTs and the summer monsoon tend to have important feedbacks on each other. Mitchell and Wallace (1992), for example, proposed that the onset of the WAM is instrumental in initiating the rapid cooling over the equatorial region. According to their study using observational analysis of SSTs, surface winds, and outgoing longwave radiation (OLR), the intensification of the northward wind stress across the equator induces a remote response, bringing colder water to the surface just south of the equator to form the characteristic equatorial cold tongue. Another important argument the authors pose is that the marked equatorial asymmetry in the annual mean SST distribution, with warmer waters in the northern tropics, may partly be due to the continental geometry. In the case of Africa, the GOG coastline is parallel to the trade winds near the equatorial region favors upwelling and advection of cold water, while the north–south alignment of the west coast of northern Africa favors weakening of the easterly trades.

2.5.2 Conditions during the early boreal spring

As we alluded to in the previous section and as derived using the back-trajectory analysis (Section 2.3.2.1), the start of the spring monsoon is marked by strong northerly to north-easterly airflow that often descends from mid to upper levels of the atmosphere over North Africa, Europe and the North Atlantic. This time of the year sees only a limited amount of

southwesterly monsoonal air from the Atlantic Ocean. In Figure 2.24, we present the primary attributes of the early spring atmosphere adjacent to West Africa.

During the early spring period (March 15 – April 15), the monsoon flow is weak and precipitation is confined to the GOG coast, which is experiencing warm SSTs. The ITF is at its southernmost point, and the AEJ is located at 3°N and near 700 hPa. The majority of the air over the Sahelian region can be traced back to northern Africa, Europe and the North Atlantic (red arrow). Also present during this time of the year is an active Subtropical Jet (STJ), which can sometimes bring disturbances that can enhance precipitation throughout the region (Knippertz and Fink 2008 and 2009).

2.5.3 Conditions during the mid-boreal spring

We show how the advancement of the WAM changes conditions over West Africa and adjacent regions in Fig. 2.25. As the season progresses to the middle of spring in the northern hemisphere, the waters of the GOG begin to cool with the relaxation of trade winds as discussed in Hagos and Cook (2009). At the same time, waters off West Africa (NETA) begin to warm. With increased solar radiation, the Saharan desert rapidly warms and induces a stronger SHL and equatorial trough, which in turn creates a pressure gradient between the higher pressure over the ocean and the lower pressure over the land. This results in a stronger monsoon flow and a waning of the Harmattan flow. At this point of the year, air is still flowing from the northeast into parts of the Sahel but it is mostly from the mid to lower levels of the atmosphere over the vicinity of Egypt. The increased baroclinicity also induces

a stronger AEJ and causes it to move north to 6°N and to 650 hPa. As a result of the stronger monsoonal flow, the ITF shifts northward. This also allows for transient, westward-propagating disturbances (crescent shape in Fig. 2.25), which we discuss in Section 2.4 and is expanded upon in Chapter 3 of this study.

2.5.4 Conditions during the Late Boreal Spring

In the last section of our discussion of the development of the spring WAM and its transition to the summer monsoon, we see that many of the important attributes of the summer monsoon are present (Fig. 2.26). For example, AEWs, an integral part of the summer monsoon are now one of the prevalent sources of precipitation in the region. As evidenced from Fig. 2.6b, we also note that the main source of air parcels during this period has now shifted to be purely oceanic in nature, both from the equatorial Atlantic as well as the south Atlantic and the NETA off West Africa. We note that the NETA has undergone modest warming and that the Azores high has drifted further north. The stronger monsoon flow also shifts the ITF further north, as well as the dynamical response of the AEJ, which now sits at 9°-10°N and 600 hPa by mid July. The SHL has also shifted north and west in accord with the climatic changes. Further, the Sahelian climate is now increasingly affected by AEWs that propagate from their genesis locations in the Ethiopian Highlands and that undergo significant flux as they traverse the width of the African continent and are modified by the equatorial central Africa (Tetzlaff and Peters, 1988; Laing and Fritsch, 1993; Lin and Robertson, 2005; Laing et al., 2008).

During the late boreal spring, the increasing precipitation at 10°N causes subsidence along the coast of the Gulf of Guinea, effectively suppressing precipitation in the region, and returning the system to the one shown in schematic form in Fig. 2.1. Ultimately, the shift of the precipitation maxima leads to the characteristic monsoon “jump,” but there exist many important variables that have to be explored in order to determine the causality of the sudden shift of the ITCZ to a new, quasi-stable position at 10°N (Sultan and Janicot 2000; Le Barbe´ et al. 2002; Sultan and Janicot, 2003; Hagos and Cook, 2007; Okumura and Xie, 2004; Ramel et al., 2006; and Sijikumar et al., 2006; Eltahir and Gong, 1996). This particular point of research is beyond the focus of the present study. Instead, we apply our conceptual model the different phases of the boreal spring to the ultimate motivation of our research: meningitis and the climate of West Africa. This relationship is explored in further detail within the confines of the present study for the 2009 season in Chapter 4.

2.6 Conclusions

The preceding analysis has provided a better perspective on the large scale dynamics which represent conditions over Sahelian West Africa during the boreal spring. We constructed a three-dimensional conceptual model of the boreal spring separated into early, middle and late stages which shows the main circulation patterns responsible for air mass origin over the Sahel and the small-scale features that affect moisture variability. Using our parcel trajectory technique, we have shown that the majority of the air parcels for locations experiencing dry, desert-type conditions stem from the mid-latitudes and the mid to upper troposphere.

Conversely, areas experiencing moist conditions contain air masses that are oceanic and lower tropospheric in nature. It is recognized that the five-day back-trajectory analysis contains inherent generalization due to the resolution of the reanalysis product utilized (NNRP). However, previous research using this reanalysis product over this part of the planet has yielded significant contributions to the understanding of the atmosphere over a region with few resources to maintain a well-equipped array of meteorological observation stations. This dataset also contains the entirety of our period of study: 2000-2009. NNRP's accessibility and the considerable documentation supporting it give us confidence in our analysis.

A section of this study was aimed at recognizing the persistence of rainfall and the strength of feedbacks associated with the initiation and evolution of convection during the dry-to-rainy season transition. We postulate that the feedbacks generated by convective systems during the pre-onset of the West Africa Monsoon are highly dependent on the location within the area of interest: points closer to the Gulf of Guinea are owe much of their variability to the SSTs to the immediate south and convectively-coupled equatorial waves, whilst points within the Sahel exist at a crossroads of different factors: the behavior of the Intertropical Front, the evolution and propagation of African Easterly Waves, mid-latitude systems, land surface interactions and the diurnal structure of precipitation patterns. Further analysis of the 2000-2009 period also showed that isolated westward-propagating events were present during this time of the year and could exert significant influence on the moisture front dynamics.

Knowledge and prediction of moisture regime climatology and dynamics is a vital component of the greater scope of this research: to provide guidance for health efforts in Sahelian West Africa. In particular, prediction of atmospheric moisture at the 2-15 day scale has been targeted as a method to help appropriate scarce vaccine where environmental conditions are still favorable for disease epidemic. In the following chapter, we use meteorological and epidemic data to explore the moisture-meningitis interface during the boreal spring of 2009.

Table 2.1: Date 40% RH threshold is crossed in NNRP at each latitude inside the study area.

Latitude	Date Threshold is crossed
10°N	24-Mar
11°N	18-Apr
12°N	29-Apr
13°N	5-Jun
14°N	21-Jun
15°N	29-Jun

Table 2.2. Geographical regions used in source point analysis.

Geographical Region	Bounding coordinates
NW Sahara	15°N-35°N, 18W-10°E
NE Sahara	15°N-35°N, 10°E-30°E
Europe	35°N-60°N, 10°W-40°E
North Atlantic	20°N-60°N, 18W-60°W
Northeast Tropical Atlantic (NETA)	5°N-20°N, 18W-30°W
Sahel	10°N-15°N, 10°W-10°E
Gulf of Guinea (GOG)	5°S-5°N, 10°W-10°E
GOG Coast	5°N-10°N, 12W-10°E
South Atlantic	20S-5°S, 12W-10°E

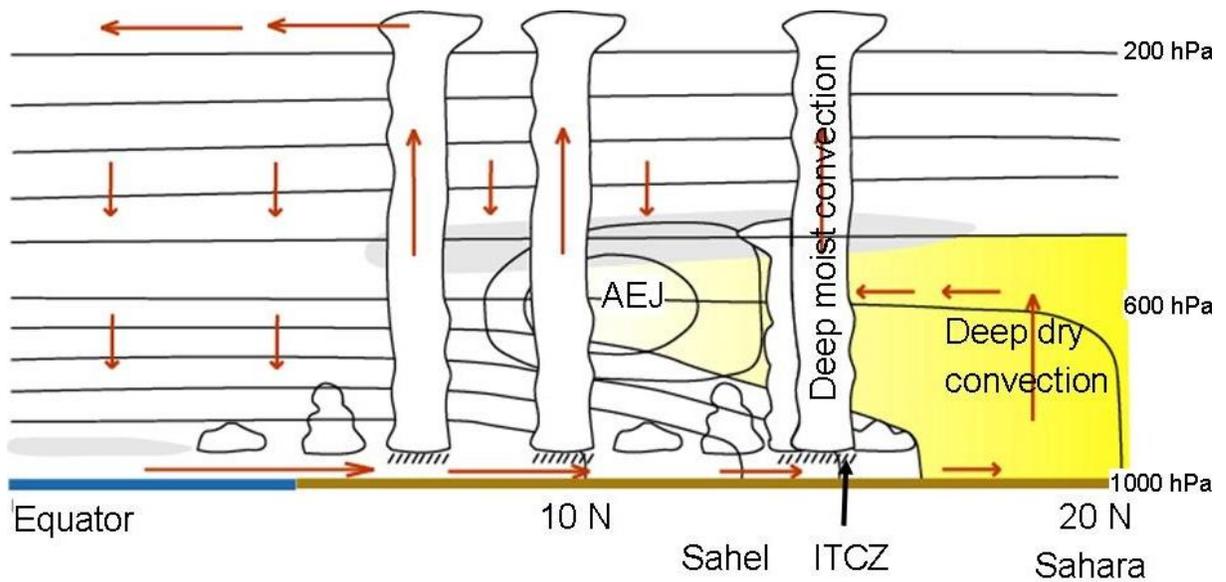


Figure 2.1: Adapted from Parker et al. (2005): Vertical schematic of the boreal summer West African Monsoon at its strongest point. Source: AMMA International Science Plan (http://science.amma-international.org/science/docs/AMMA_ISP_May2005.pdf).

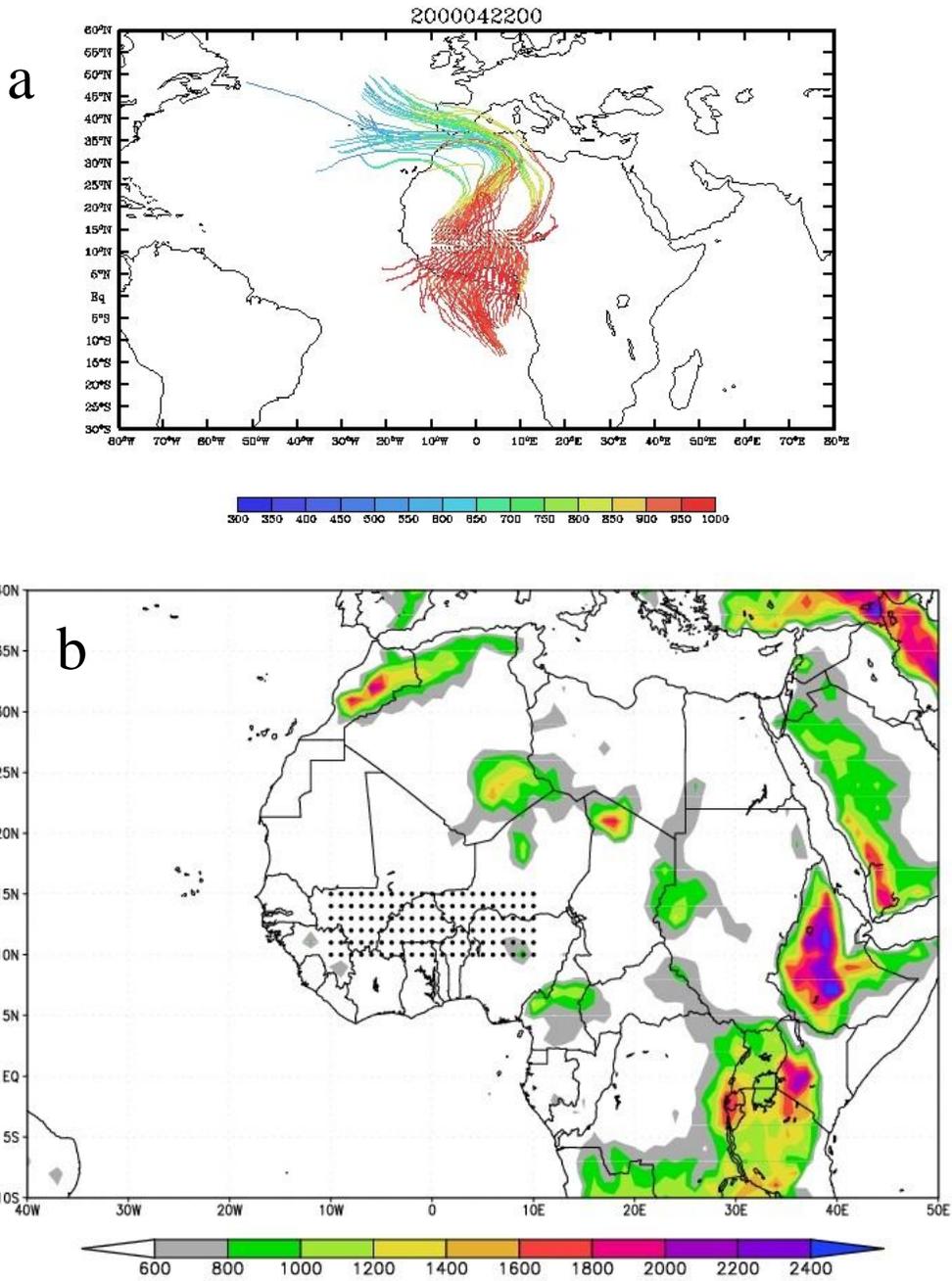


Figure 2.2: (a) Sample of air parcel trajectory analysis. (b) Matrix of back-trajectory analysis end points and topography of the region.

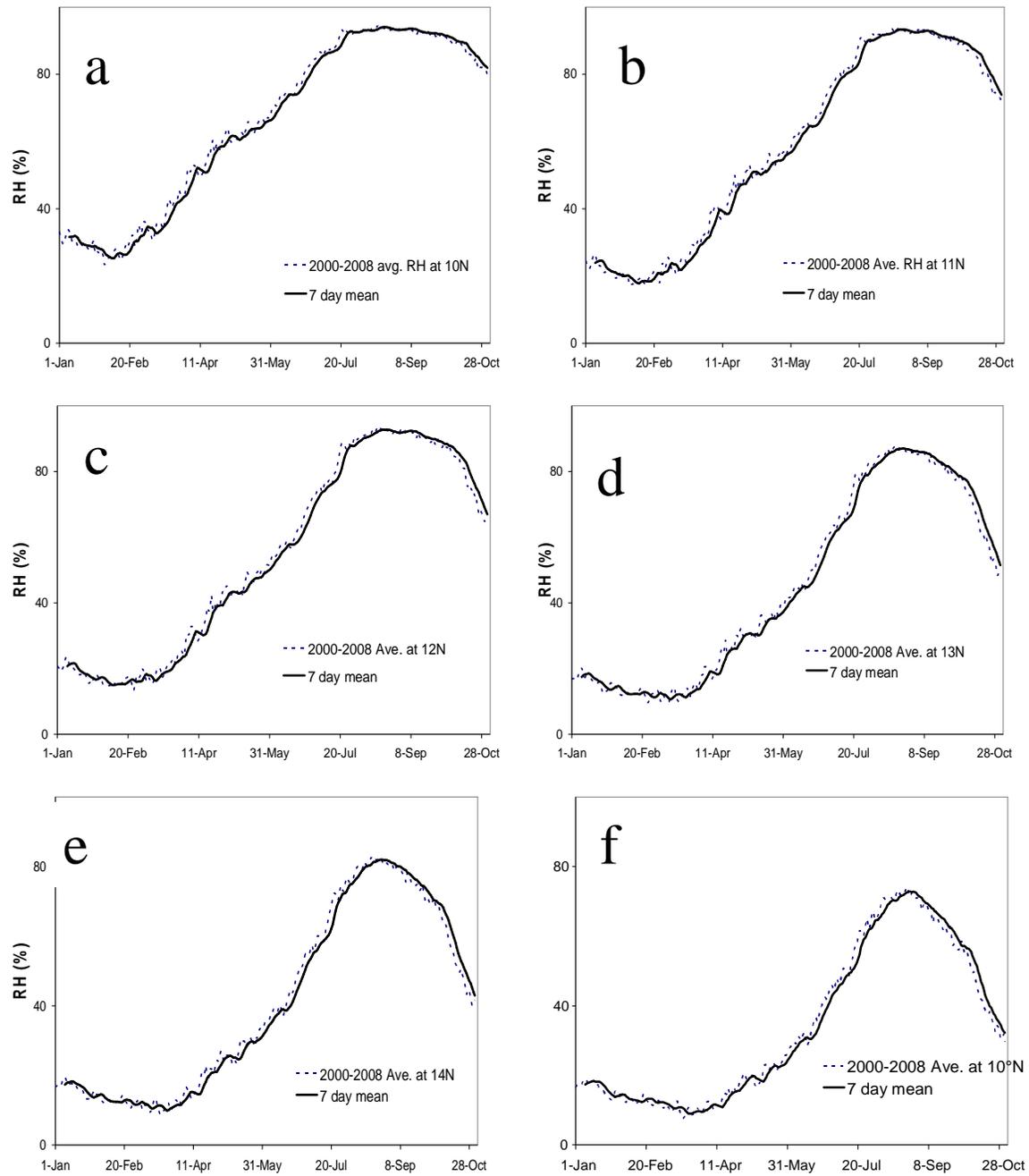


Figure 2.3: Time series of surface RH (%) at 10°N, 11°N, 12°N, 13°N, 14°N, and 15°N in the NCEP/NCAR reanalysis.

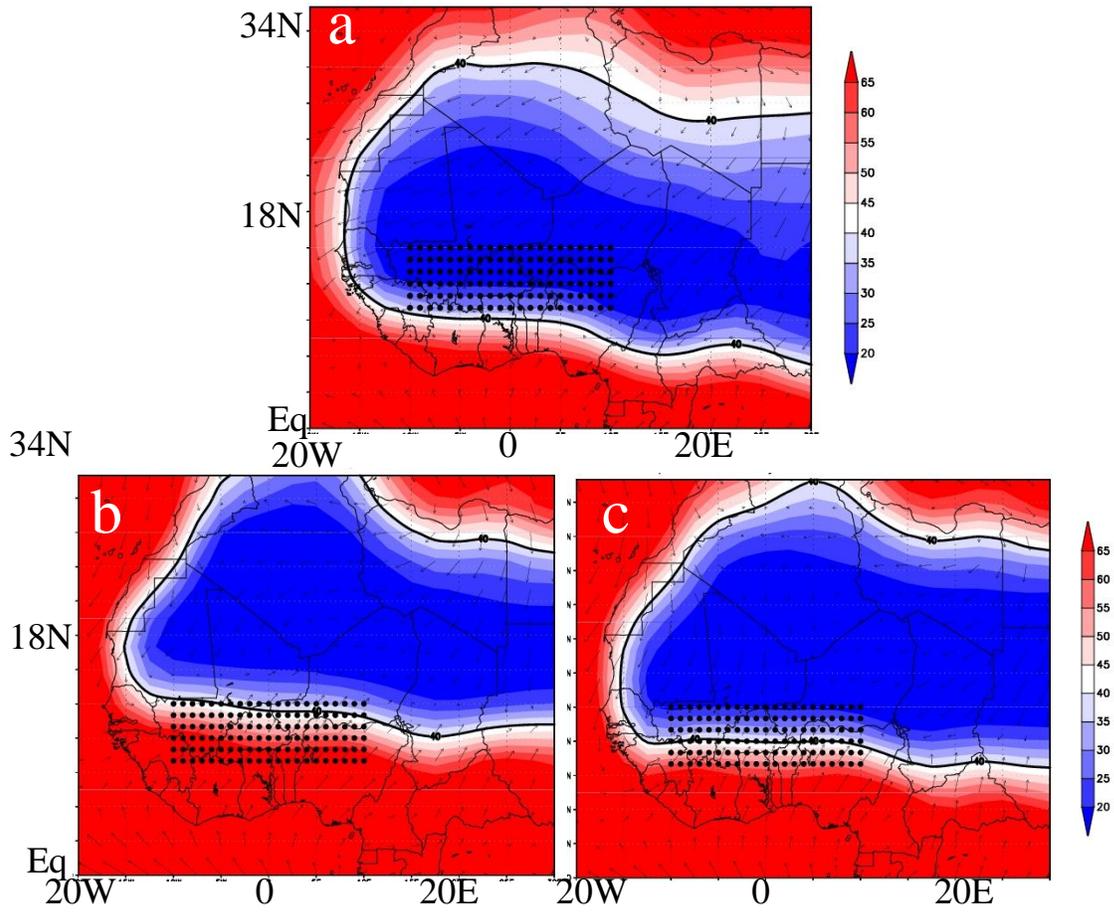


Figure 2.4: Trajectory analysis endpoints (black circles), surface relative humidity and winds for P1 (a), P2 (b) and P3 (c).

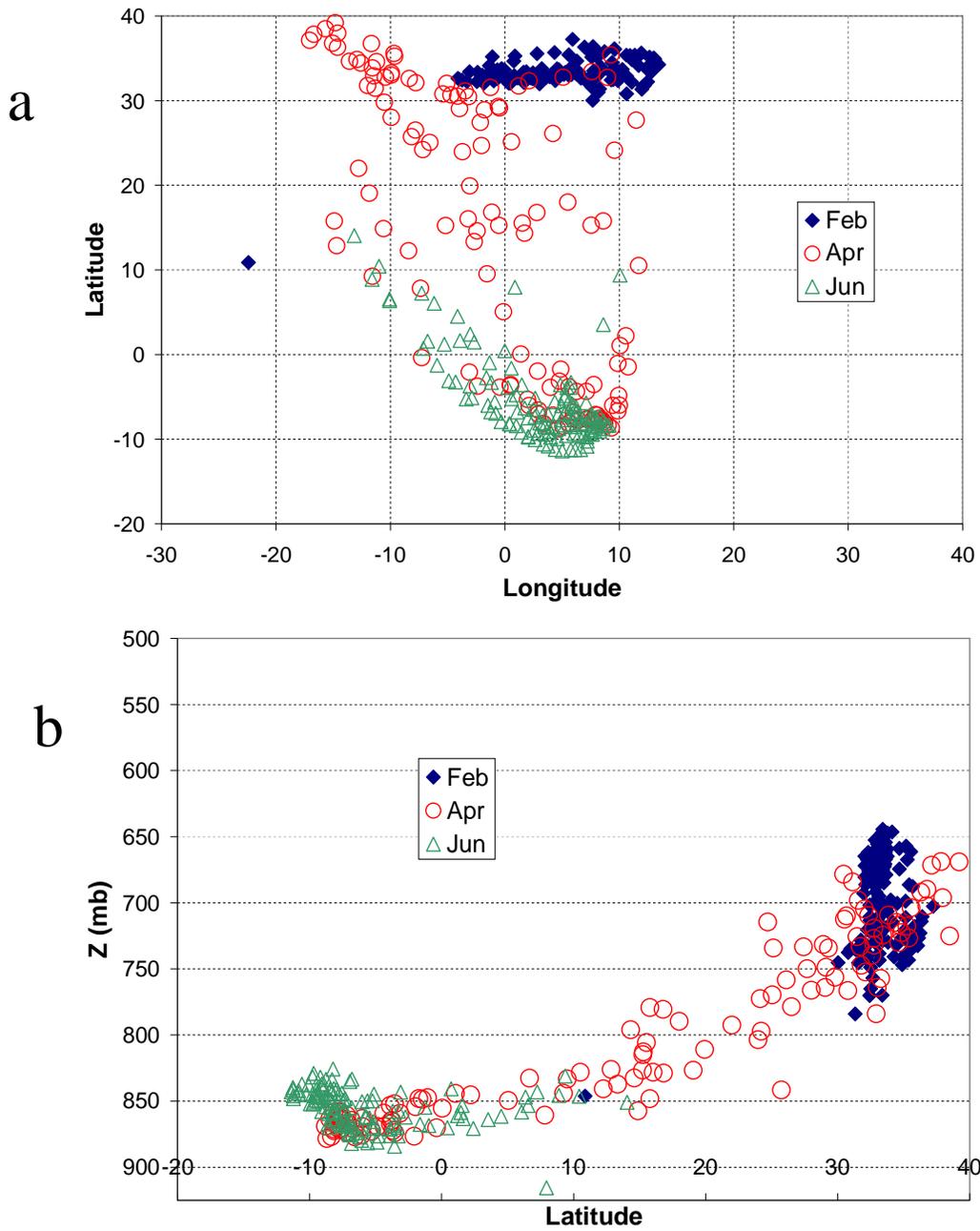


Figure 2.5: Distribution of air parcel source points in the (a) horizontal and (b) vertical viewpoints.

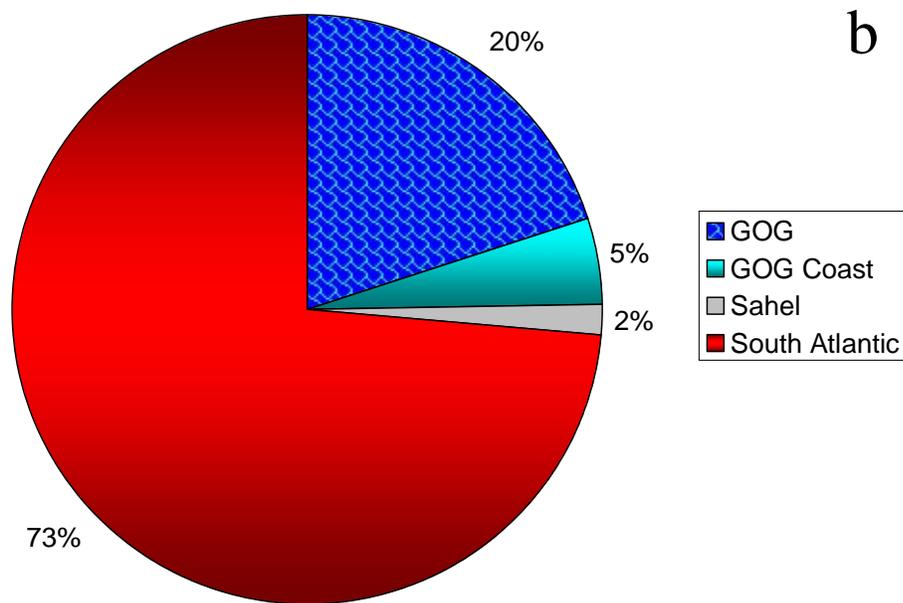
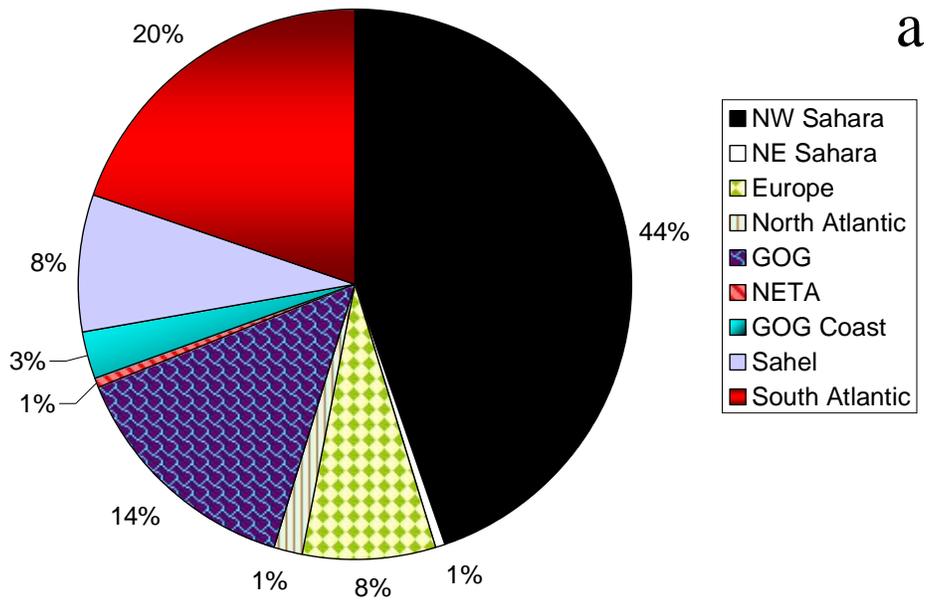


Figure 2.6: Horizontal distribution of source regions by geographical location for P2 (a) and P3 (b).

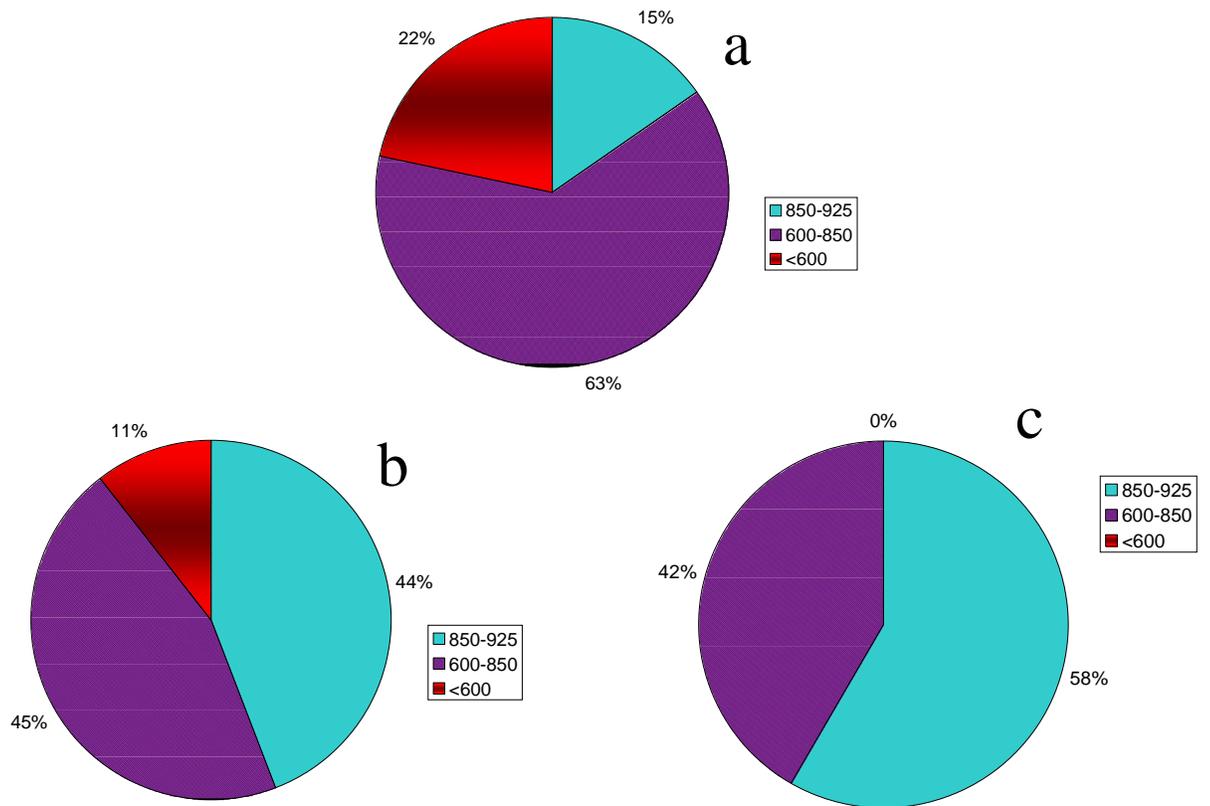


Figure 2.7: Vertical distribution of air mass source regions for P1 (a), P2 (b) and P3 (bottom).

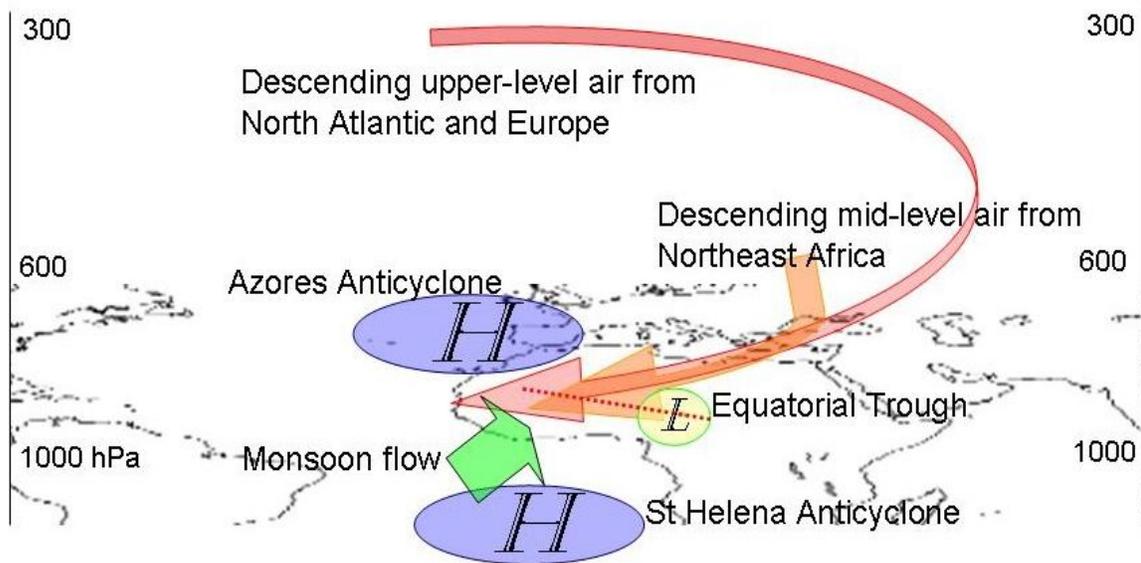


Figure 2.8: Three-dimensional schematic of the large scale airflow during the boreal spring.

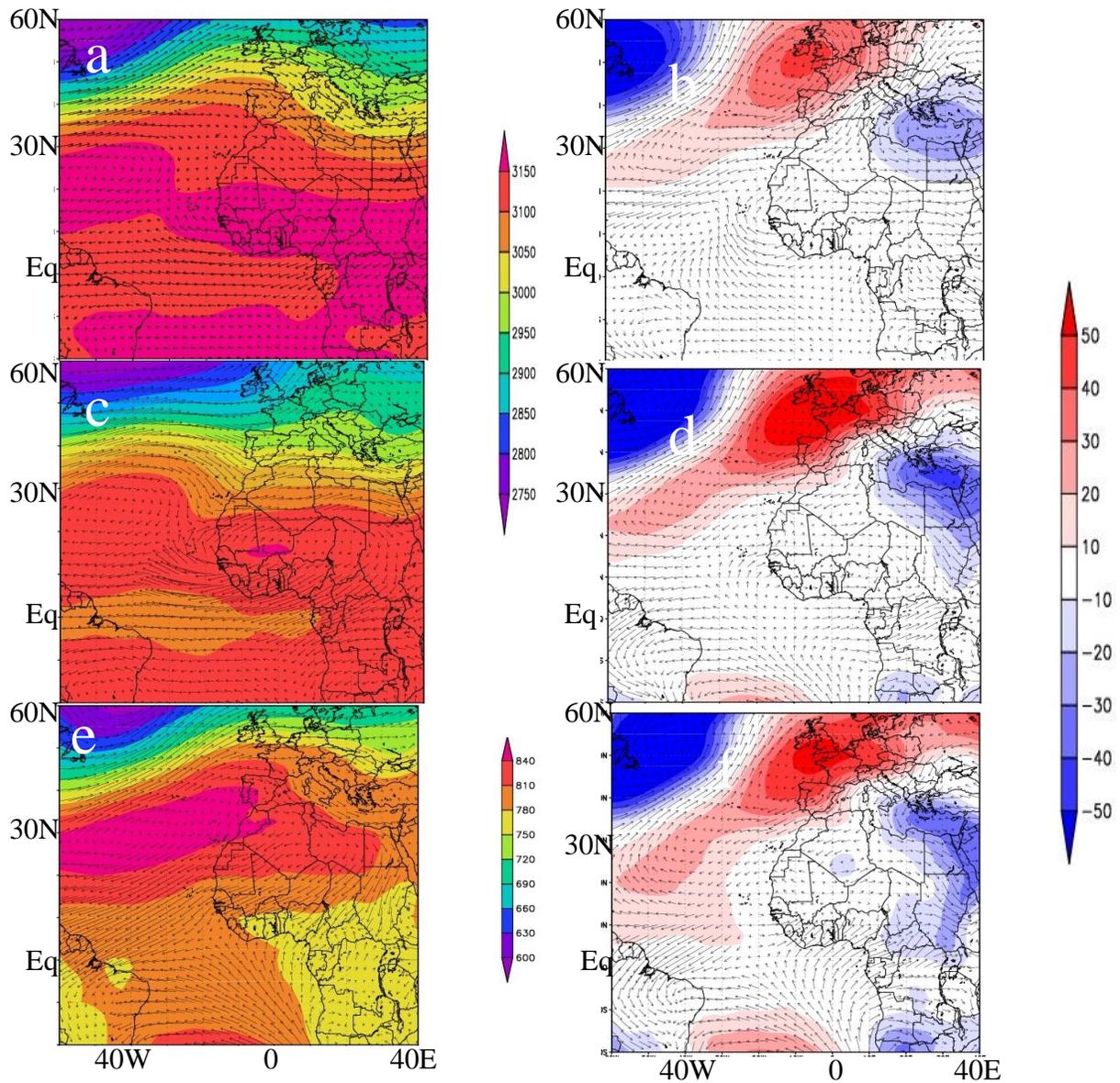


Figure 2.9: Geopotential height for P1 at 700 hPa (a) and 700 hPa-ZMR (b), 850 hPa (c) and 850 hPa-ZMR (d), 925 hPa (e) and 925 hPa-ZMR (f).

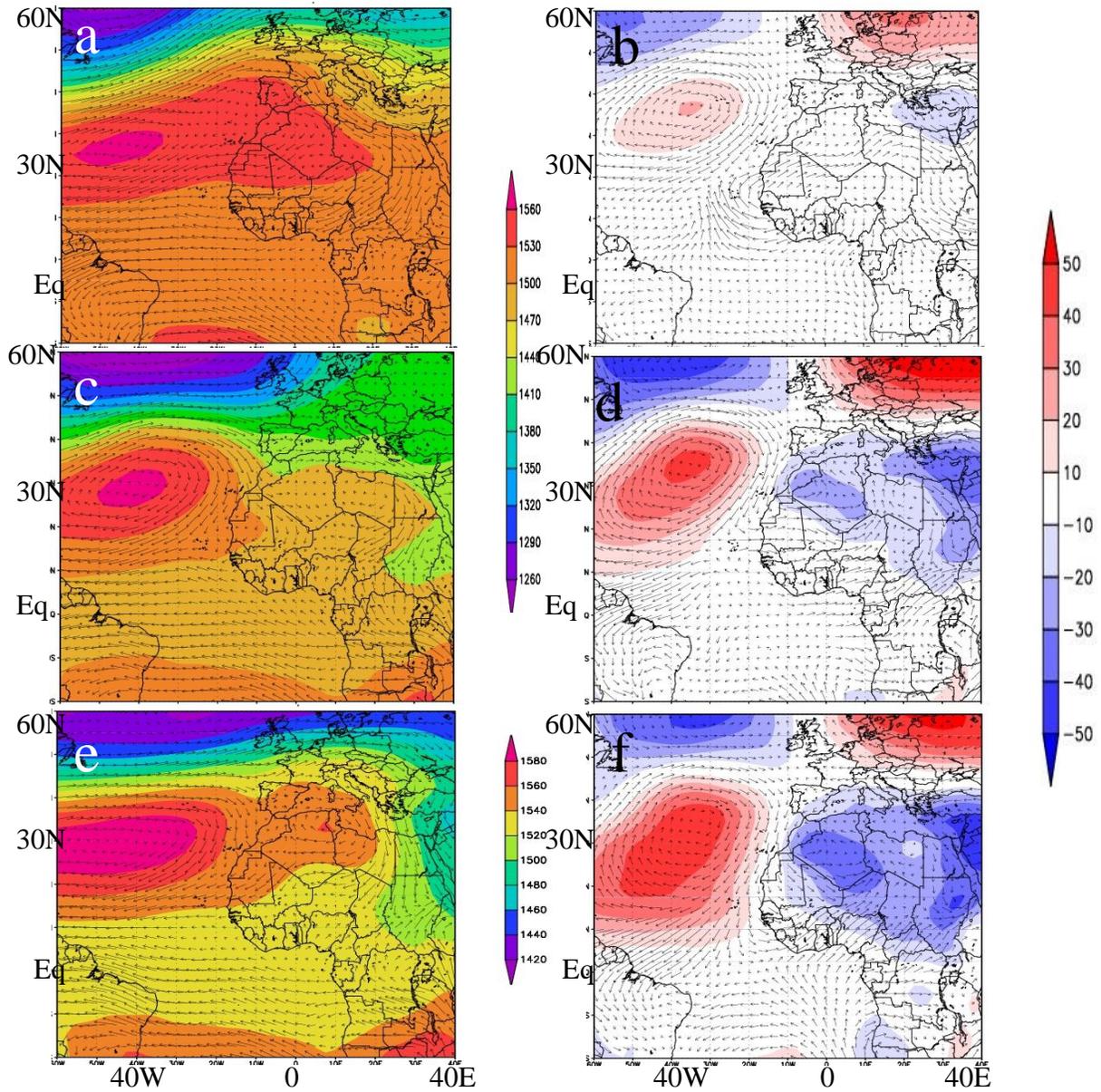


Figure 2.10: Geopotential height for P2 at 700 hPa (a) and 700 hPa-ZMR (b), 850 hPa (c) and 850 hPa-ZMR (d), 925 hPa (e) and 925 hPa-ZMR (f).

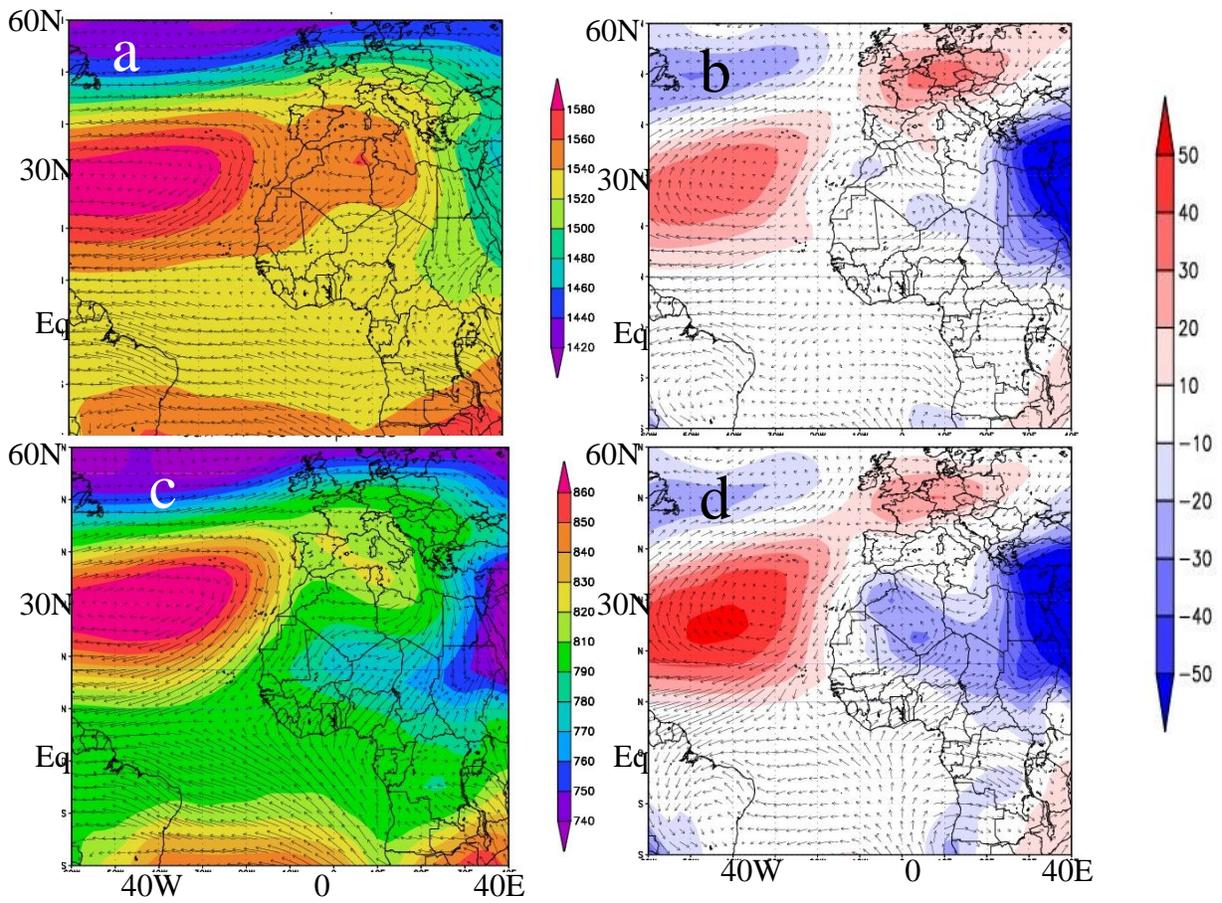


Figure 2.11: Geopotential height for P2 at 850 hPa (a) and 850 hPa-ZMR (b), 925 hPa (c) and 925 hPa-ZMR (d).

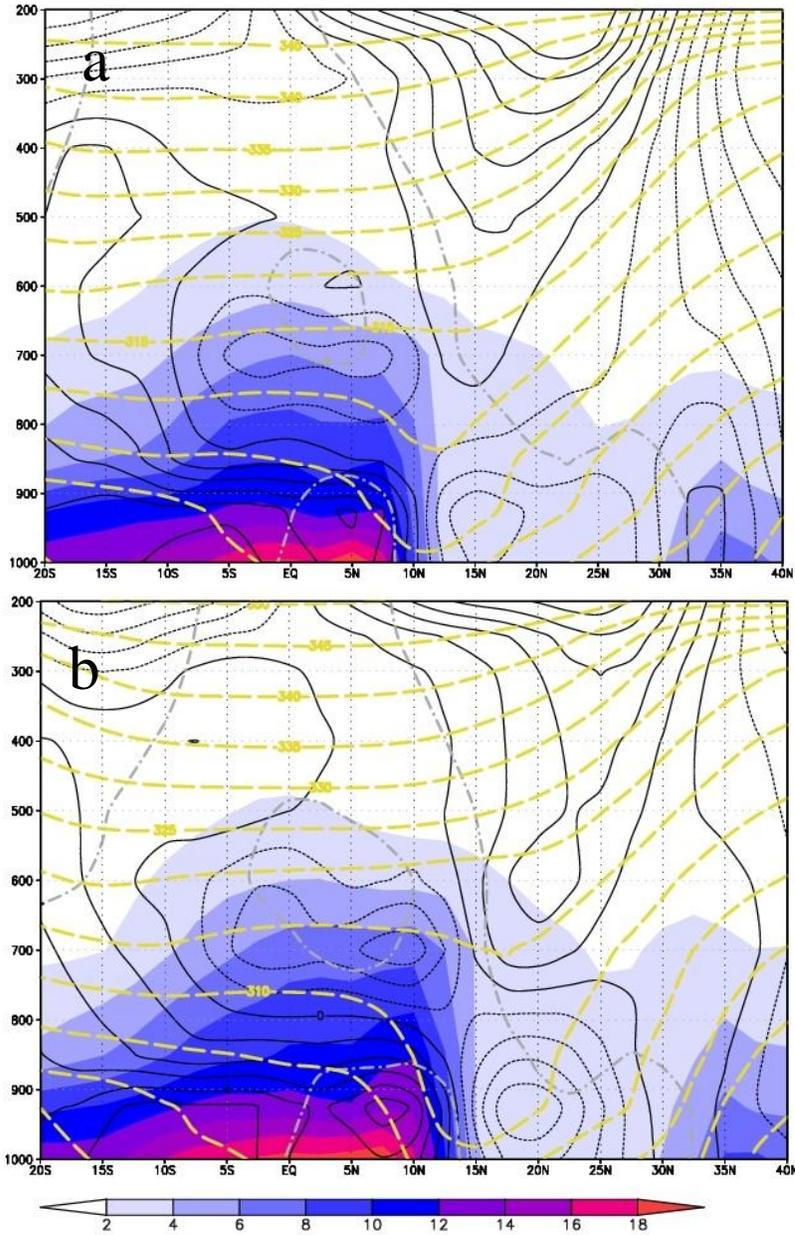


Figure 2.12: Vertical profile of the atmosphere at the prime meridian showing specific humidity (shaded), meridional wind (solid contours), zonal wind (grey dash-dot) and isentropes (yellow, dashed) for the February 2000-2009 average (a) and the April 2000-2009 average (b).

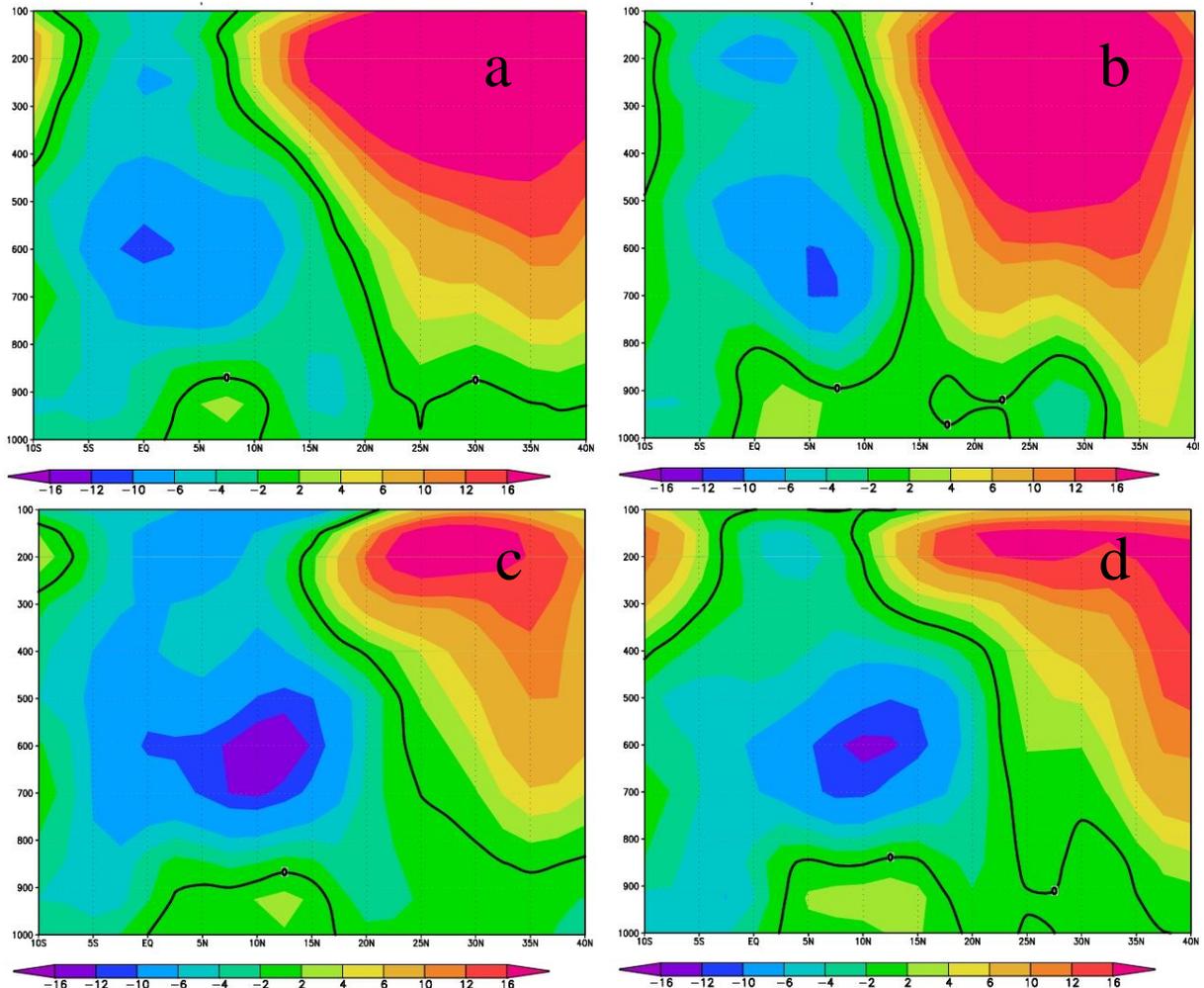


Figure 2.13: Vertical profile of the atmosphere at the prime meridian showing the zonal wind for the April 2006 (a) and 2009 (b) and June 2006 (c) and 2009 (d). The black solid line denotes 0 m/s to specify change in east-west regime.

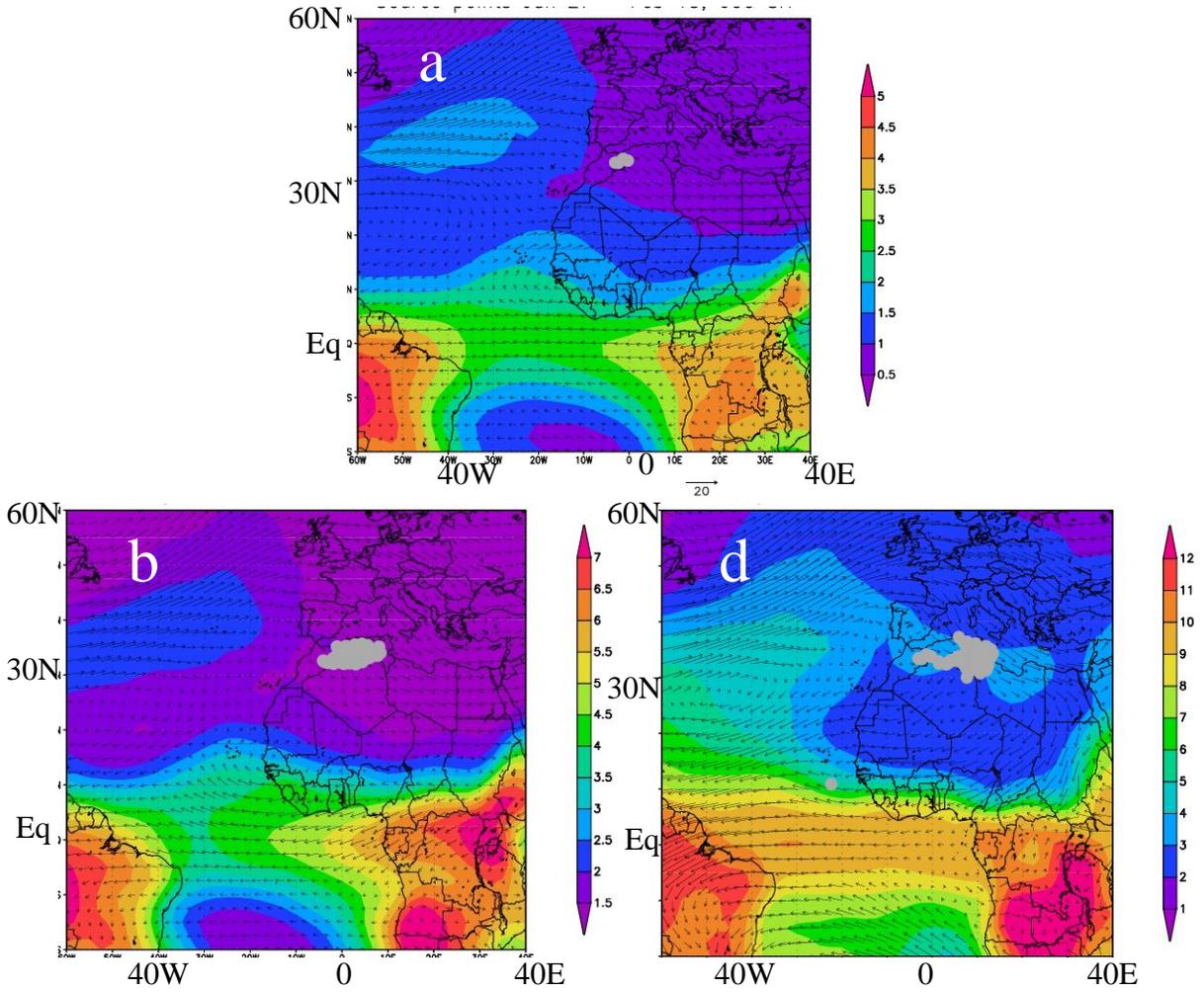


Figure 2.14: Source points during P1 for points below 650 hPa (a), between 650 and 750 (b), and between 750 and 850 hPa (c).

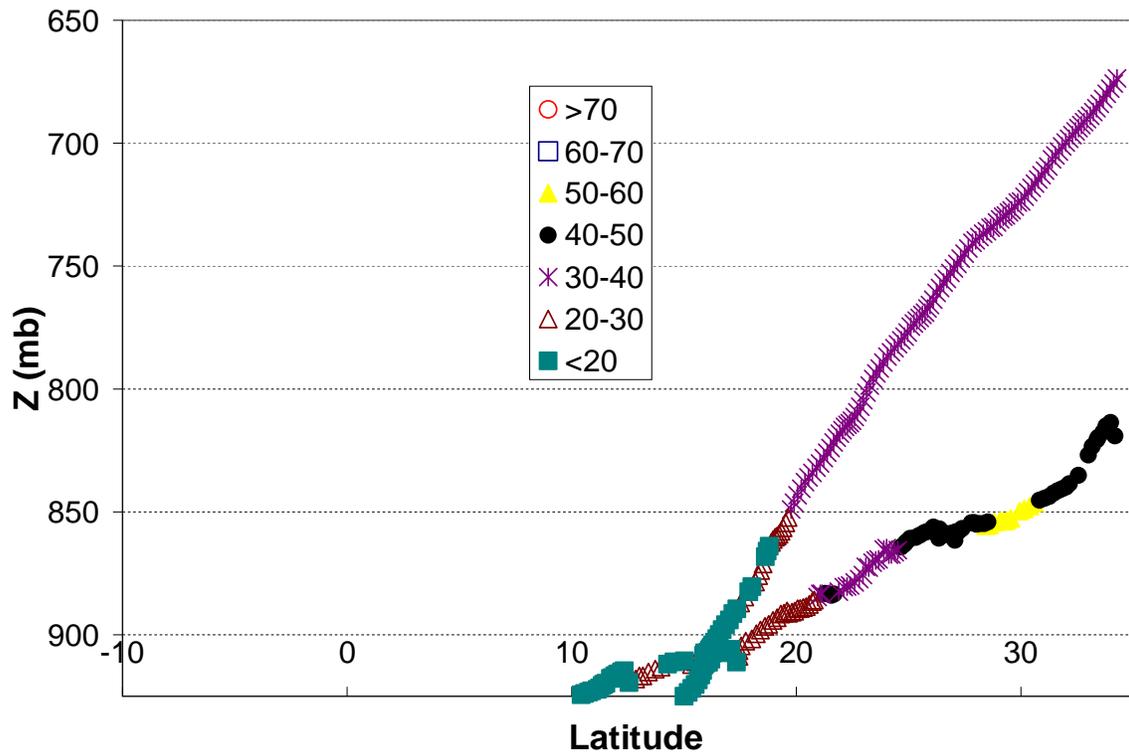


Figure 2.15: Vertical trajectory of air parcels with endpoints averaged at 10°N and 15°N.

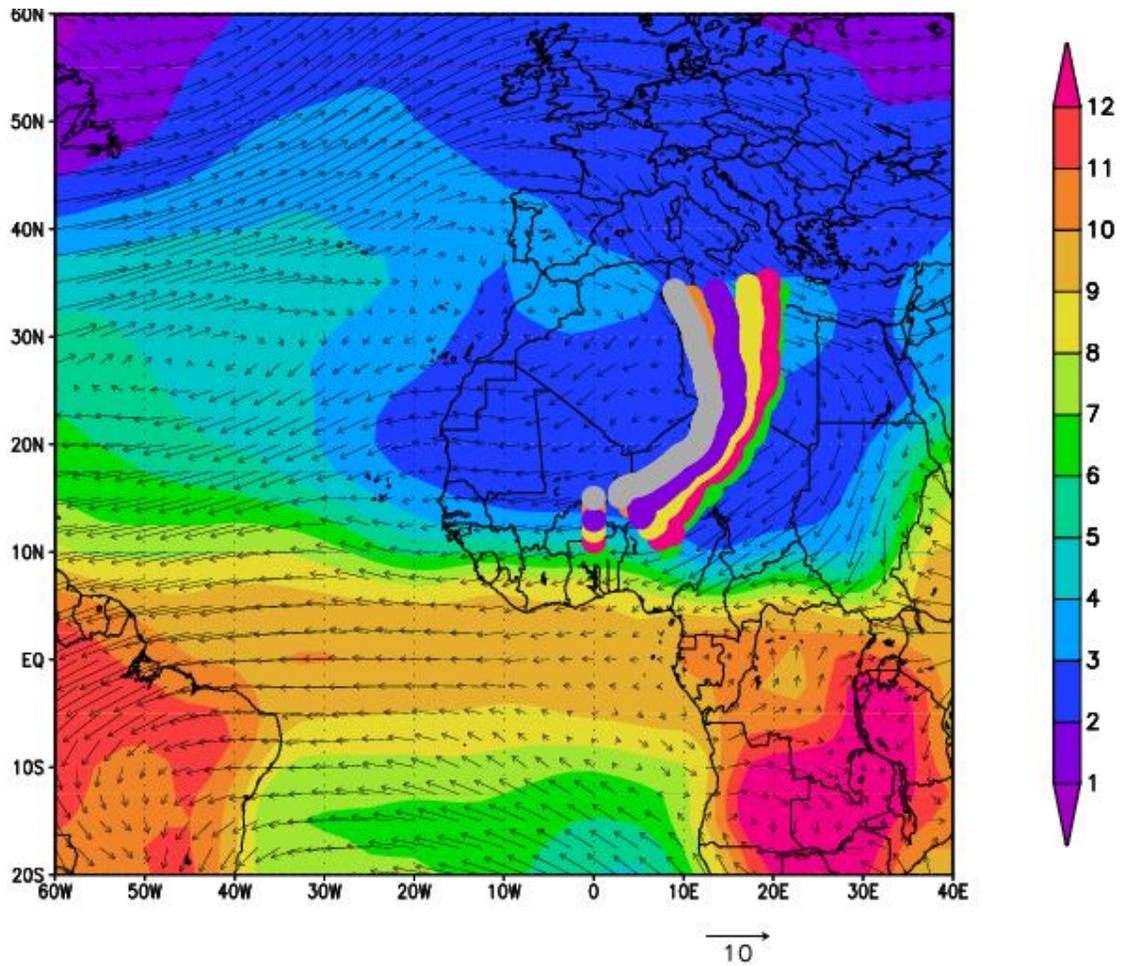


Figure 2.16: Composite trajectories for points along 10°N (green), 11°N (magenta), 12°N (yellow), 13°N (orange), 14°N (purple) and 15°N (gray).

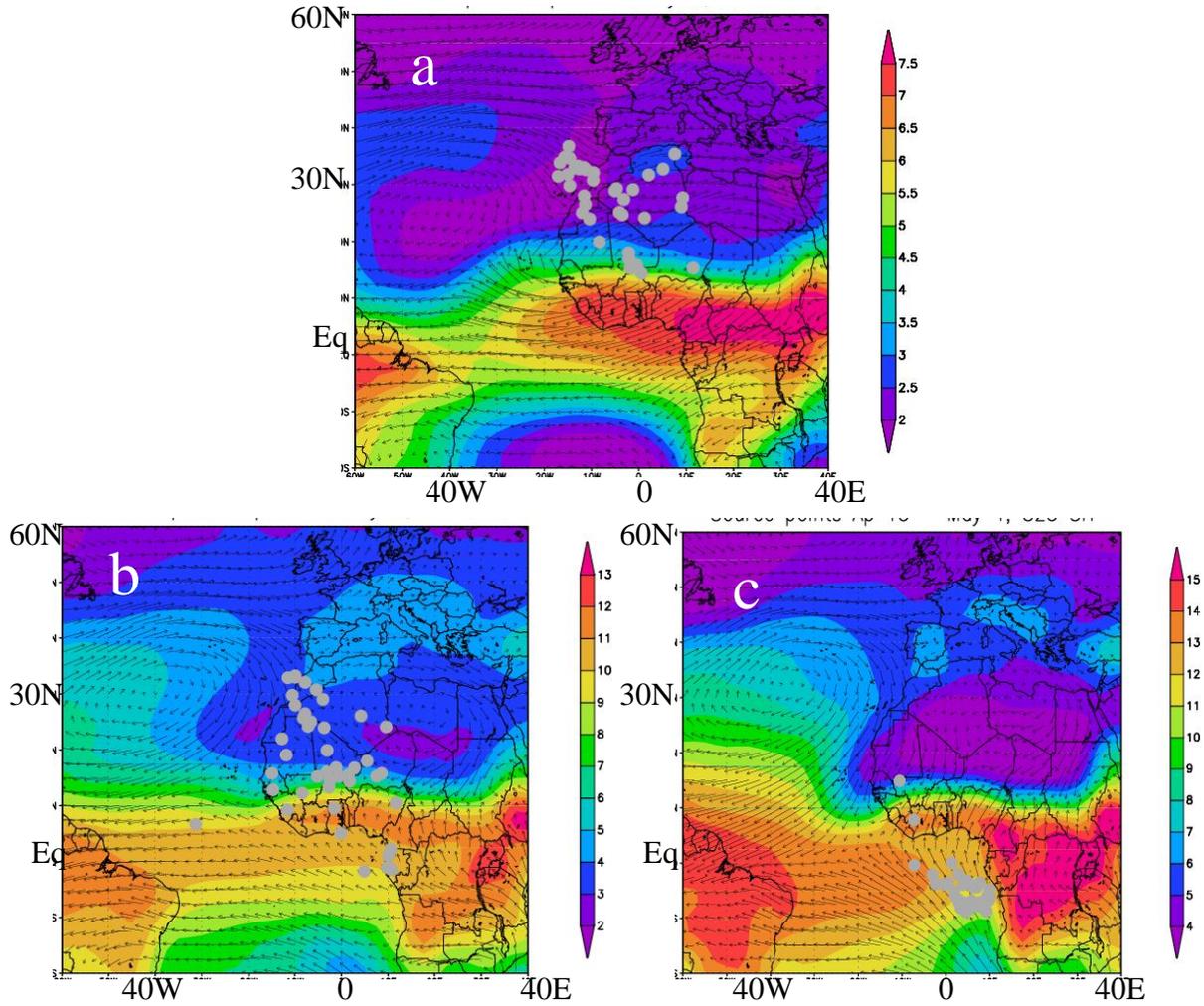


Figure 2.17: Source points during P2 for points below 750 hPa (a), between 750 and 850 (b), and between 850 and 925 hPa (c).

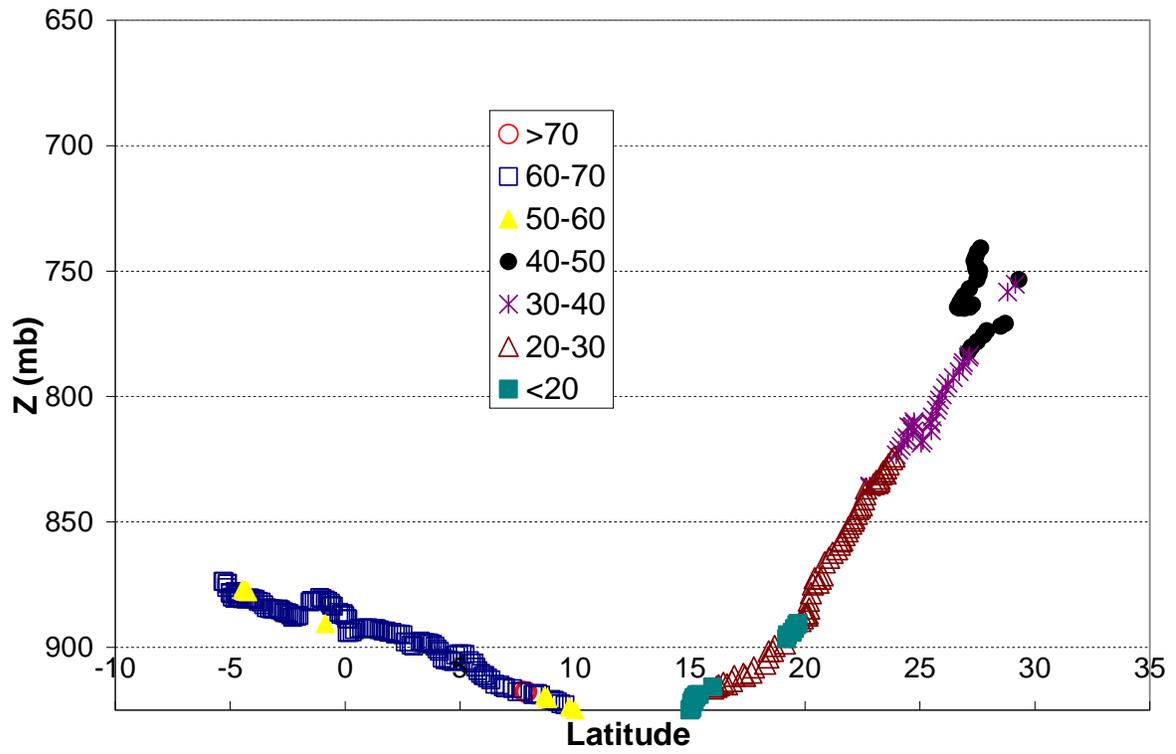


Figure 2.18: Vertical trajectory of air parcels with endpoints averaged at 10°N and 15°N.

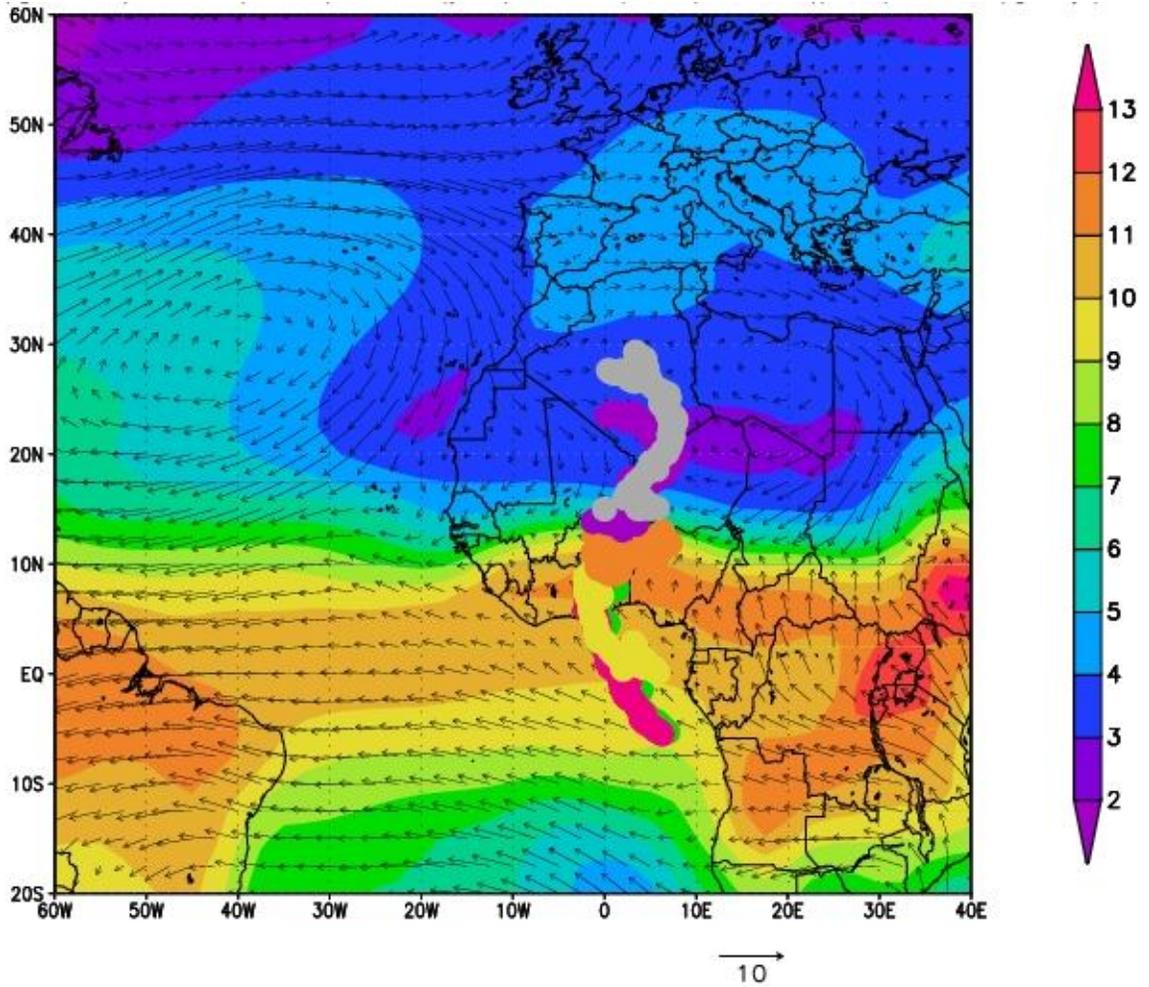


Figure 2.19. Composite trajectories for points along 10°N (green), 11°N (magenta), 12°N (yellow), 13°N (orange), 14°N (purple) and 15°N (gray).

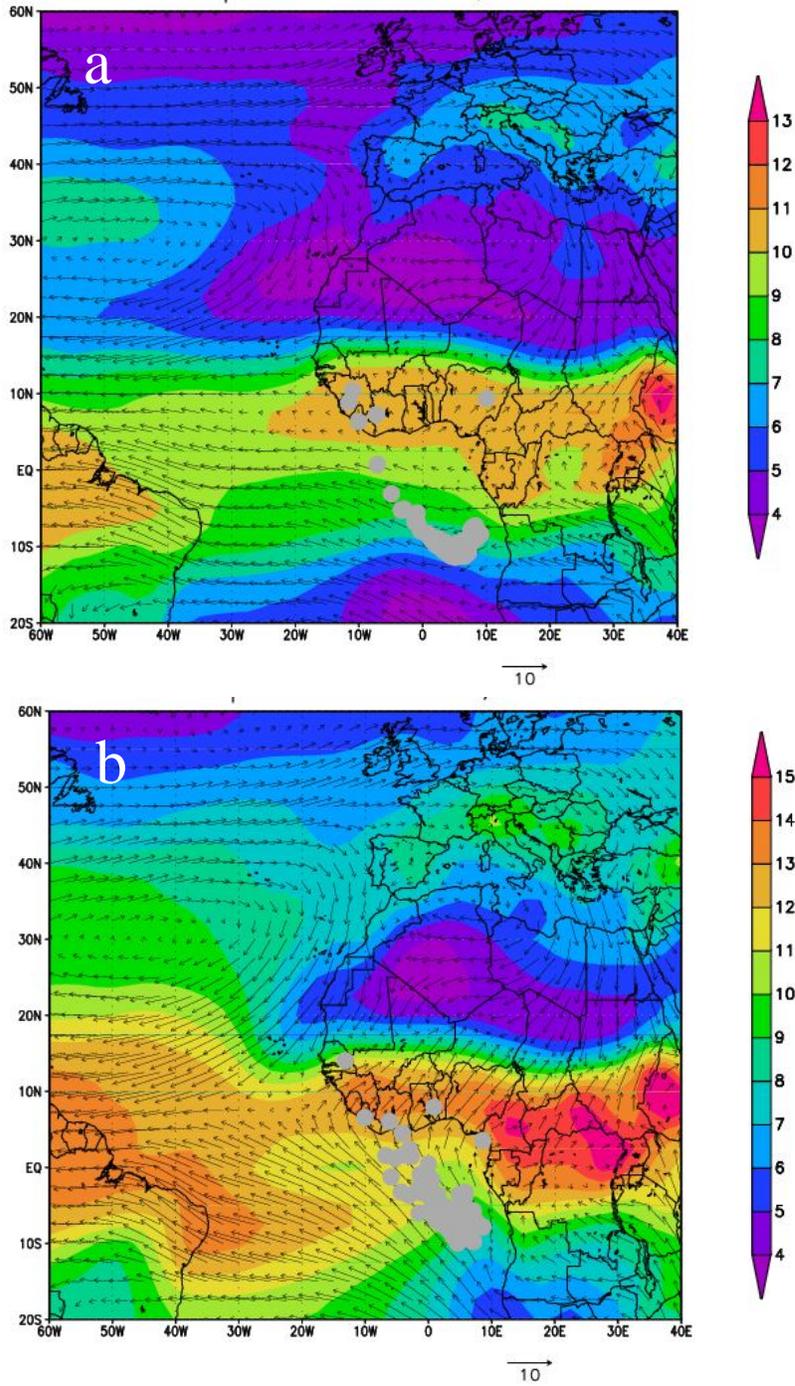


Figure 2.20: Source points during P3 for points above 850 hPa (left), and below 850 (right).

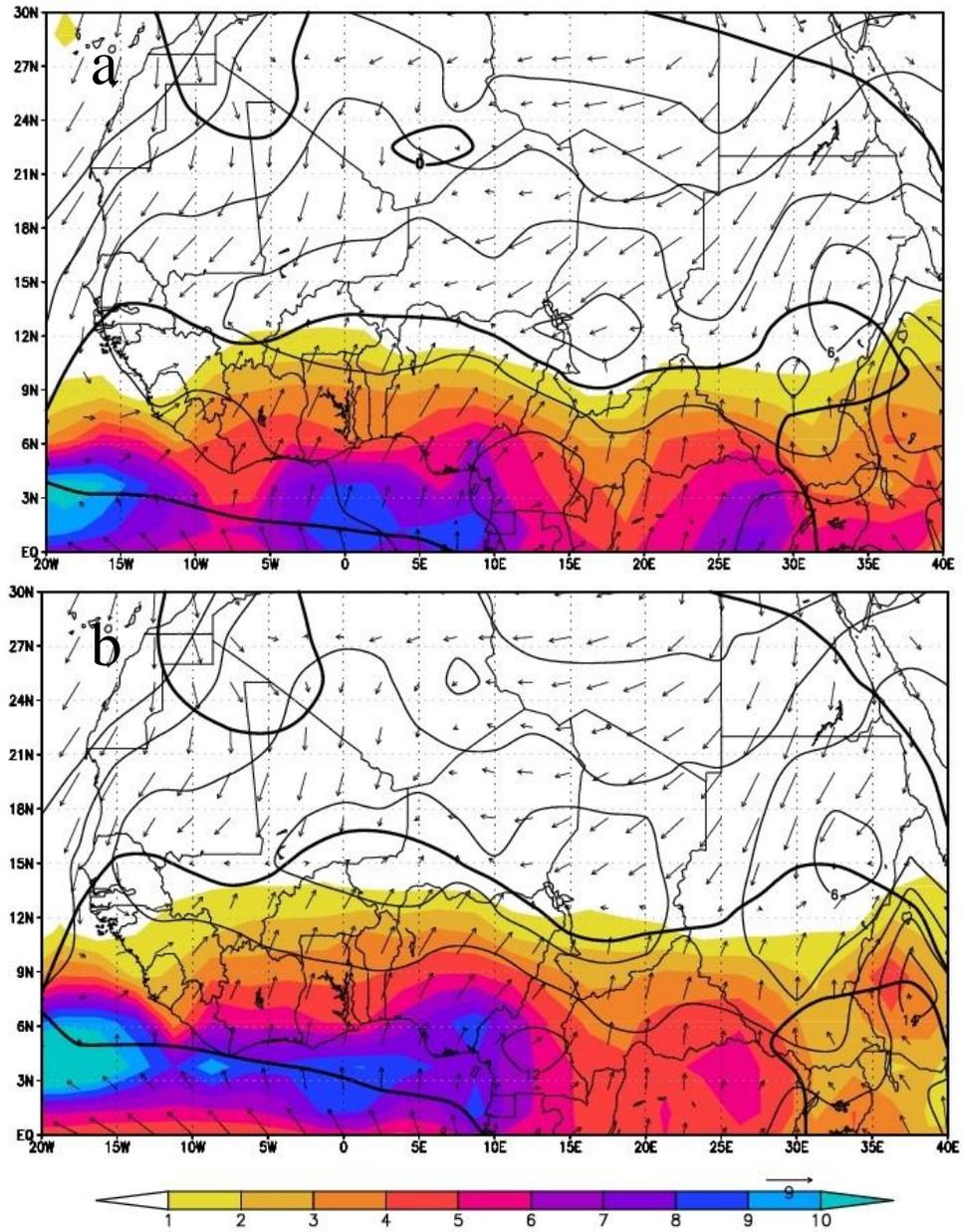


Figure 2.21: Mean 2000–2009 monthly rainfall fields (mm day⁻¹) for (a) April and (b) May. Rainfall values are derived from CMAP data. The NCEP–NCAR 925-hPa wind field is expressed in vectors and its scale (9 ms⁻²). The black line represents the zero isoline of the zonal wind component to delineate the domain of the monsoon wind. Thin curves display mean sea level pressure isolines (expressed in hPa minus 1000).

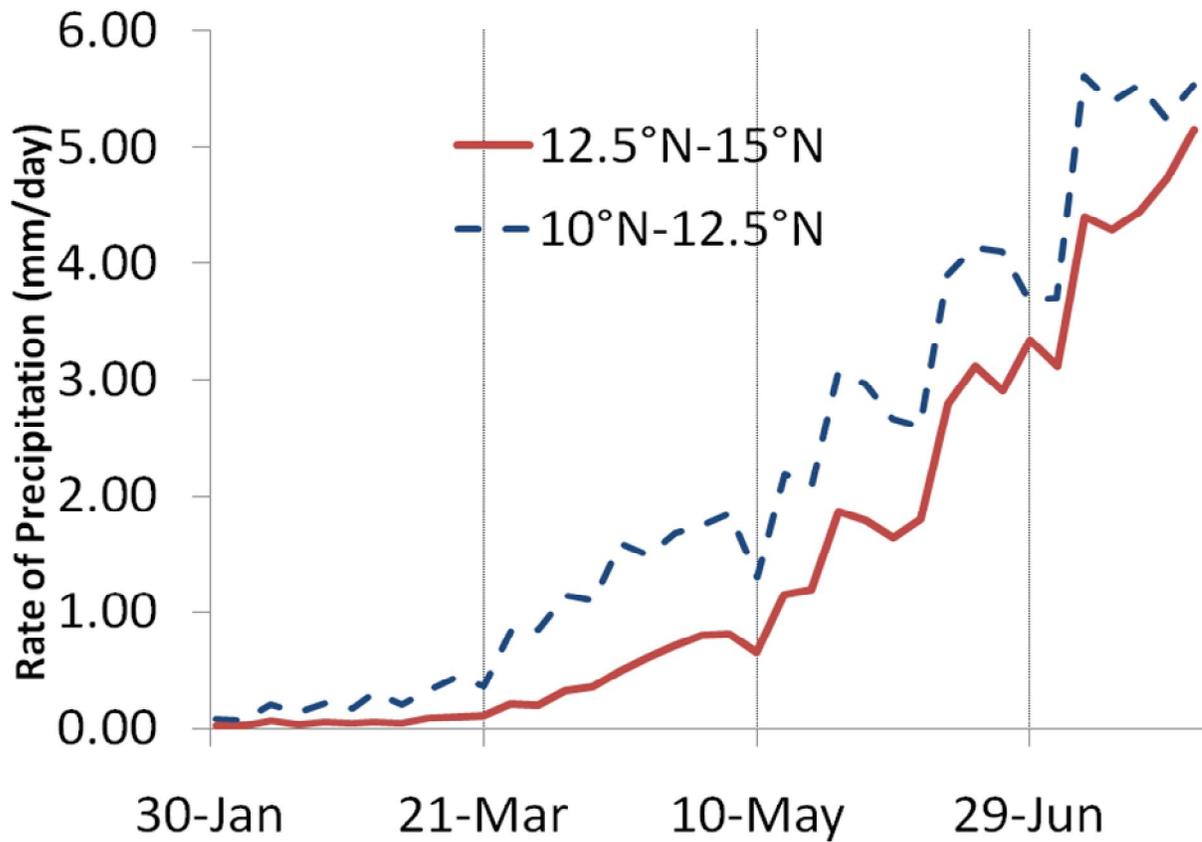


Figure 2.22: Time series of mean 2000–2009 pentad rainfall fields (mm day⁻¹) during February–July for grid boxes averaged at 10°N–12.5°N (solid red) and 12.5°N–15°N. Rainfall values are derived from CMAP data.

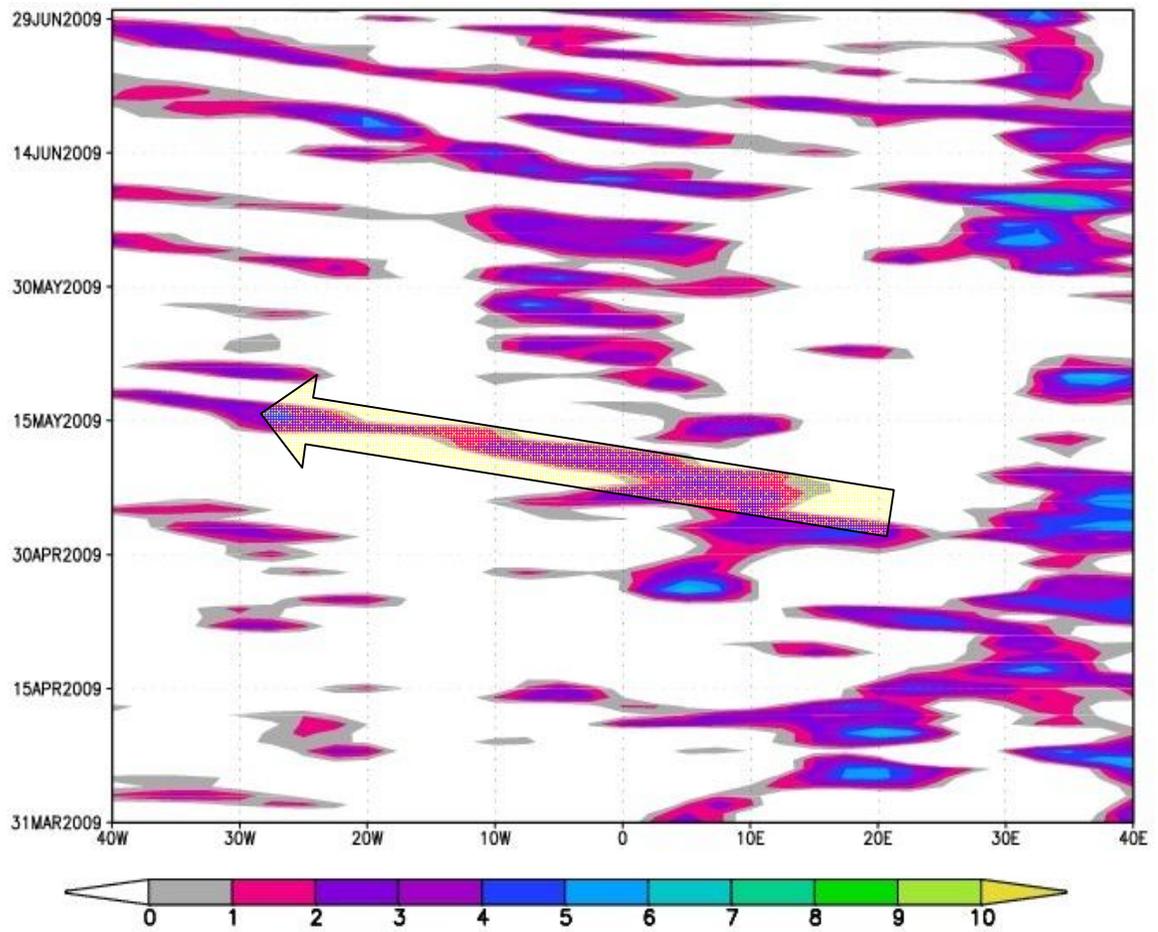


Figure 2.23: Hovmoller diagram of April-May meridional wind component at 850 hPa for 15°N latitude points during 2009.

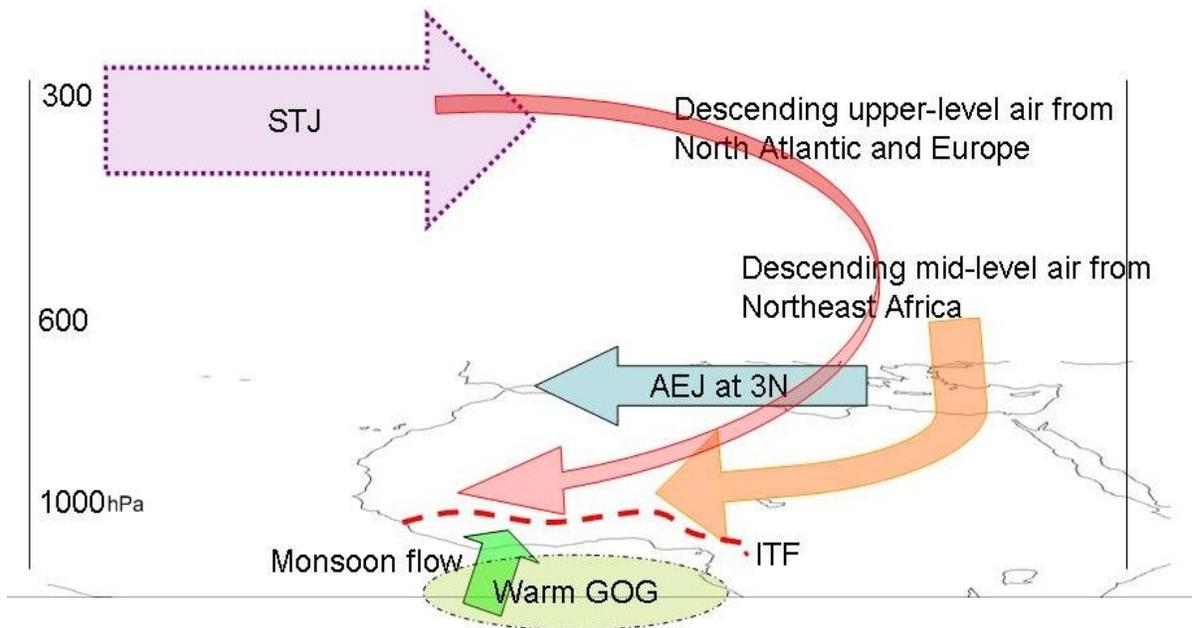


Figure 2.25: Three-dimensional schematic of airflow, dynamical and surface structures during the early boreal spring.

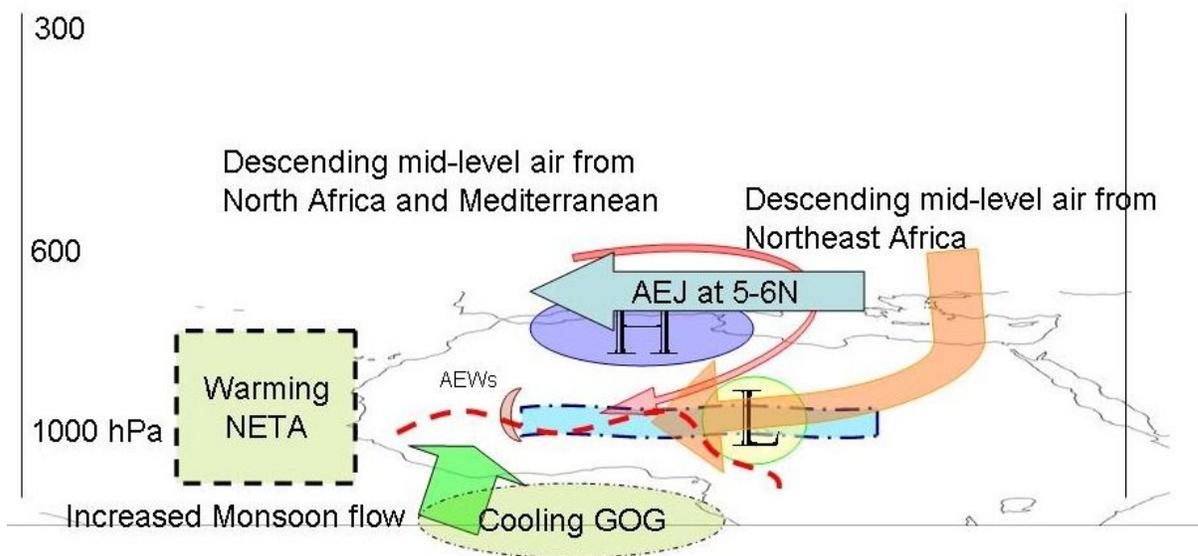


Figure 2.26: Three-dimensional schematic of airflow, dynamical and surface structures during the mid boreal spring.

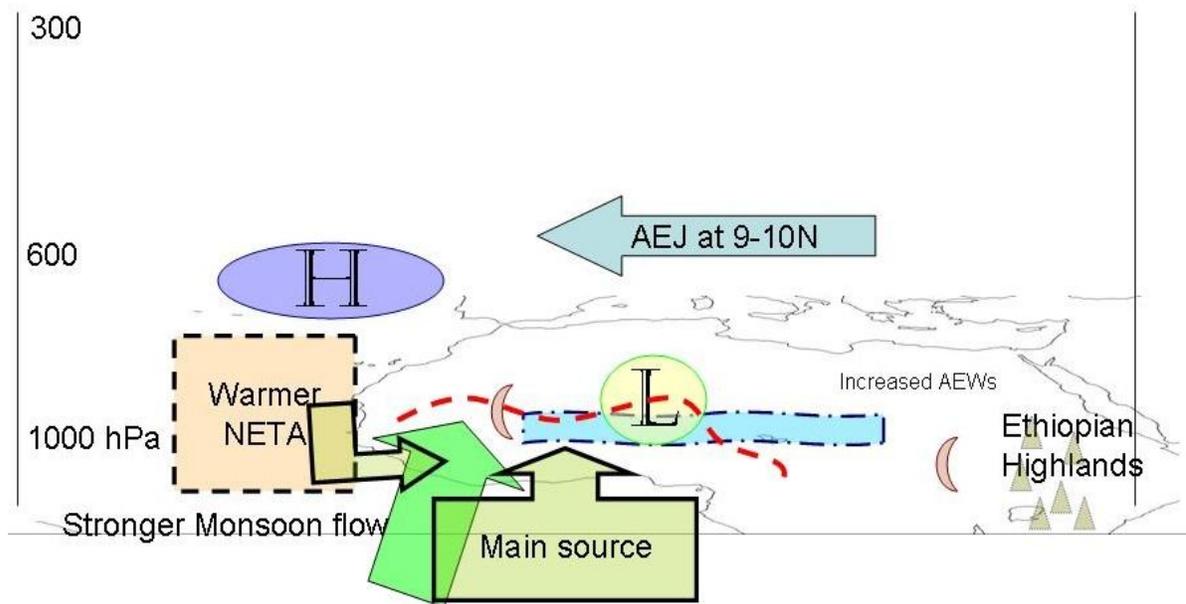


Figure 2.27: Three-dimensional schematic of airflow, dynamical and surface structures during the late boreal spring.

Chapter 3

West African Climate and Meningitis

Epidemics during 2009

3.1 Introduction

During the first 11 weeks of 2009 (January 1- March 15), a total of 24,868 suspected cases, including 1,513 deaths, were reported to the World Health Organization (WHO) by countries of the Meningitis Belt. More than 85% of the cases occurred in one epidemic foci, encompassing Northern Nigeria and Niger (WHO, 2009). Throughout this time period, highly-detailed, district-level data on disease cases, alert rates and epidemic rates for Nigeria became available to the public through the WHO on a weekly basis. This data, coupled with continuous in-situ weather observations throughout the length of the boreal spring for the cities of Kano (Nigeria), N'Djamena (Chad) and Gaya (Niger) allowed for a detailed investigation of the meningitis-climate interface during 2009. In the following sections we describe the data utilized, its merits and applications and we provide evidence for a relationship between epidemic dynamics and the state of the atmosphere during the boreal spring of 2009.

3.2 Datasets and Methodology

3.2.1 Epidemiological data

The meningitis epidemiological data used in this study is reported to the WHO via the Multi-Disease Surveillance Center (MDSC) based out of Ouagadougou in the country of Burkina Faso. Details on the diagnosis used for meningitis can be found in WHO (2000). Meningitis information is aggregated at different spatial scales from the health unit to the country level and is released on a weekly basis. This surveillance is aimed at achieving early detection and control of meningitis epidemics at the level of health districts. The reports database is available online on the WHO website and has already been used by Broutin et al. (2007) for a comparative study of meningitis dynamics across nine African countries and Yaka et al. (2008) to investigate the climate-disease interface.

The key constituents in the MDSC reports used in this study are presented in Table 3.1. An important variable provided by the MDSC meningitis reports is the disease's attack rate, which is defined as follows:

$$AR = c / 100,000 \text{ per week}, \quad (1.1)$$

where AR is the attack rate and c is the number of cases reported and the 100,000 is the population unit based on USGS total population estimate. The AR is then used to determine the number of districts that are in *alert* or *epidemic*, which are defined as the threshold in $AR > 5$ for districts in alert and $AR > 10$ for districts in epidemic.

The present study utilizes the *alert*, *epidemic* and AR values to investigate the disease's relationship with atmospheric conditions such as relative humidity. We chose the data from

stations in northern Nigeria during 2009 due to the volume of meningitis incidence throughout the majority of the districts in the country and grouped them by state (districts in Benin and Niger had smaller *AR* numbers than Nigeria). In Fig. 3.1 we are able to appreciate the geographical extent of meningitis epidemics in Nigeria during 2009. Note that this figure represents cumulative *AR* for week 17 of the year (see Table 3.2 for definition of meningitis weekly reports). We chose 4 different states: Kano, Borno, Kibbe and Sokoto given the high incidence of the disease and relative distance from one another in order to achieve a good representation of disease dynamics in different sectors along the northern boundary of the country. Kibbe and Sokoto are grouped together in order to allow for a better comparison with meteorological data available at a nearby station and also because of their irregular geopolitical shapes.

It should be noted that MDSC data quality is debatable (Yoksas, personal communication), as it may rely on outdated population estimates and could be incomplete (underreported cases) due to lack of resources in less accessible regions. However, this information is highly-detailed for 2009 and MDSC data from previous years has been repeatedly used by recent epidemiology-climatology interface studies (e.g. Broutin et al. 2007, Yaka et al. 2008).

3.2.2 In-situ and gridded meteorological data

Due to the lack of stable monitoring throughout much of Sahelian West Africa (Parker et al., 2008), it was difficult to acquire meteorological conditions from surface stations at each one

of the aforementioned Nigerian states. Even though recent efforts have been aimed at improving observations throughout the region (Redelsperger et al. 2006), the sparse nature of continuous data streams limits the spatial coverage of meteorological stations. Only Kano, Nigeria was collocated with the Nigerian state chosen for epidemiological data (also called Kano). We chose to use nearby stations Gaya (Niger) for the Kebbi-Sokoto states average and N'Djemena (Chad) for Borno due to the lack of concurrent coverage of meteorological data within those particular regions. In Fig. 3.2 we show the different Nigerian states used along with the location for each of the weather stations.

Gridded datasets such as NNRP are good sources of information for surface conditions but their resolution ($2.5^\circ \times 2.5^\circ$) is too coarse for our purposes. For instance, when mapping *AR* over Nigeria for week 14 (early April), we find that the reanalysis product is too moist for the RH40 threshold in relation to the epidemic situation (Fig. 3.3). The figure shows the change in relative humidity from week 13 to week 14 (March 23-30 and March 31-April 5 respectively). The RH40 line is averaged for week 14 with red dots representing districts in *epidemic* and black dots are districts in *alert*. This overestimation of local humidity can be a drawback for disease mitigation, as it would suggest that the environmental predictors defined in the literature (e.g. Besancenot et al. 1997, Molesworth et al. 2003) are less favorable for an epidemic to continue. There is certain value to using reanalysis products due to their spatial coverage and Fig. 3.3 also shows how states such as Borno, Sokoto and Kibbe are all within the dry sector and also contain districts reporting *epidemic* or *alert*. It is also worthwhile to note that the information from the reanalysis products has also been used to

drive regional atmospheric models (Chapter 4 and 5) with some success and that the incompatible resolution situation can be ameliorated to the extent that dynamical downscaling could be used to provide forecasts on environmental proxies for meningitis efforts.

3.2.2 Methodology

The months of March and April of 2009 provided a significant amount of information from the health sector (MDSC reports) that can be analyzed alongside observed environmental conditions for portions of the Meningitis Belt that were afflicted by epidemics during these months. We use the average *AR*, *alert* and *epidemic* numbers of all reporting districts in each state for our analysis. The RH40 threshold is employed to delineate the boundary between moist monsoon-type conditions and the dry season Harmattan regime and we compare weekly averages of surface humidity values from the three stations against reported meningitis data for the chosen states for each week. This allows for a *qualitative* approach for exploring the relationship between the disease and the environment. This approach is necessary due to the scarcity of quality observations in 2009 and the scale incompatibility with reanalysis products.

3.3 Results

The analysis presented here suggests there is a strong relationship between surface humidity and the *AR* and epidemic reports within the states chosen in our study. For the state of Borno

(Fig. 3.4), the number of stations reporting epidemic increased dramatically from 10 in mid-March (week 12) to 50 in early April (week 14). At the same time (weeks 12-14), the humidity values at N'Djamena (closest continuous station) remained well below the RH40 threshold and hovered around 20%. The peak in stations reporting *epidemic* is followed by a small decrease during in week 15. In week 16, however, the number of districts in *epidemic* collapsed to 2 and then to 1 in week 17. The *AR* values also showed a considerable decrease from weeks 12-13 (24.94) to week 17 (5.65). Meanwhile, humidity values rose to 38.9% in week 15 and crossed the RH40 threshold in weeks 16 and 17.

We find the same pattern for the state of Kano (Nigeria) (Fig. 3.5a), where the number of districts reporting *epidemic* reached 21 in week 14 and collapsed to just 7 in week 16. Note that the humidity level was well below the RH40 threshold until week 16, suggesting that a shift in the moisture regime could have played a role in changing the epidemic dynamics for this particular state. Kano is unique in our analysis in that its meteorological observations are located within the state itself in the city of Kano. Further, the number of districts is much larger (41, 9.69 million inhabitants) compared to that of Borno (8 districts, 1.3 million) or the combined Sokoto-Kibbe states (21, 4.5 million). The state's relative size is also smaller in surface area ($2/3$ of the other states), effectively increasing its population density. This combination allows for further inspection of the disease-climate interface: in Fig. 3.5b we present further evidence of the humidity-meningitis link with a histogram of weekly *AR* values alongside concurrent observed relative humidity. Note that *AR* is high when humidity values are far below the RH40 threshold but have a corresponding collapse when the

atmosphere has moistened for a long enough period and entered the monsoon regime. This anticorrelation is evident in many of the previous studies conducted on this subject (e.g. Molesworth et al. 2003).

The states of Sokoto and Kibbe (SK hereafter) in northwestern Nigeria (Fig. 3.6) were combined to get a better appreciation of the scale of the meningitis epidemic during 2009 and were chosen due to their proximity to the city of Gaya in extreme southern Niger. For SK, we opted for the use of the *number* of stations reporting meningitis given the lower amounts of disease incidence in comparison with Kano and Borno. Using a variable like *epidemic* or *alert* does not yield numbers greater than 4. The *AR* variable is also not an adequate reference point for our analysis since it has a secondary spike in mid April even though only two stations were reporting the epidemic. From Fig. 3.5 we learn that the same process occurring in Kano and Sokoto is also present in the northwest sector of Nigeria. Incidence of the disease is higher during periods of lower humidity and rapidly collapse with the advent of the monsoon moisture as the humidity figures reach the RH40 threshold. There is a secondary, albeit small, spike of meningitis in mid April but the overall pattern is the same as in Figs. 2.32 and 2.33.

3.4 Conclusions

The preceding analysis explored the relationship between meningitis and West African climate during the boreal spring. Throughout the spring months of 2009, highly-detailed meningitis data became available for the country of Nigeria. This, coupled with a well-

maintained in-situ observation station in the northern city of Kano and nearby locations (Gaya, Niger and N'Djamena, Chad) allowed for a robust view of the moisture-epidemic interface. Exploring Figure 2.33b we ask this question: What mechanisms account for the sharp increase in humidity during mid April? If we explore the observations in Kano a bit further we find that there were three distinct spikes in humidity (Fig. 3.7). It should be noted that every time each one of these events occurred, the humidity regime was elevated to a new level (red dashed line denote the 7-day moving average). These features (moist pulses) are present for the majority of the reporting stations in the Sahel as well as the reanalysis (Fig. 2.23, Chapter 2). Their effect on surface humidity is uneven and related to the proximity of the station to moisture sources. Therefore, it has become evident that these systems should be studied in more detail, as they could contain inherent predictability that can be exploited by forecasting agencies involved with decision-makers in areas affected by meningitis.

Table 3.1: Sample of typical MDSC meningitis data.

	Cases	Death	Lethality (%)	District in Alert	District in Epidemic
Benin	3	0	7.9	0	0
Nigeria	2227	32	2.9	24	41
Niger	550	56	5.8	7	3
Total	2780	88	5.53	31	44

Table 3.2. Definition of weeks in the MDSC weekly reports during 2009.

Reported week	Corresponding days
Week 10	2-8 March
Week 11	9-15 March
Week 12	16-22 March
Week 13	23-29 March
Week 14	30 March – 5 April
Week 15	6-12 April
Week 16	13-19 April
Week 17	20-26 April

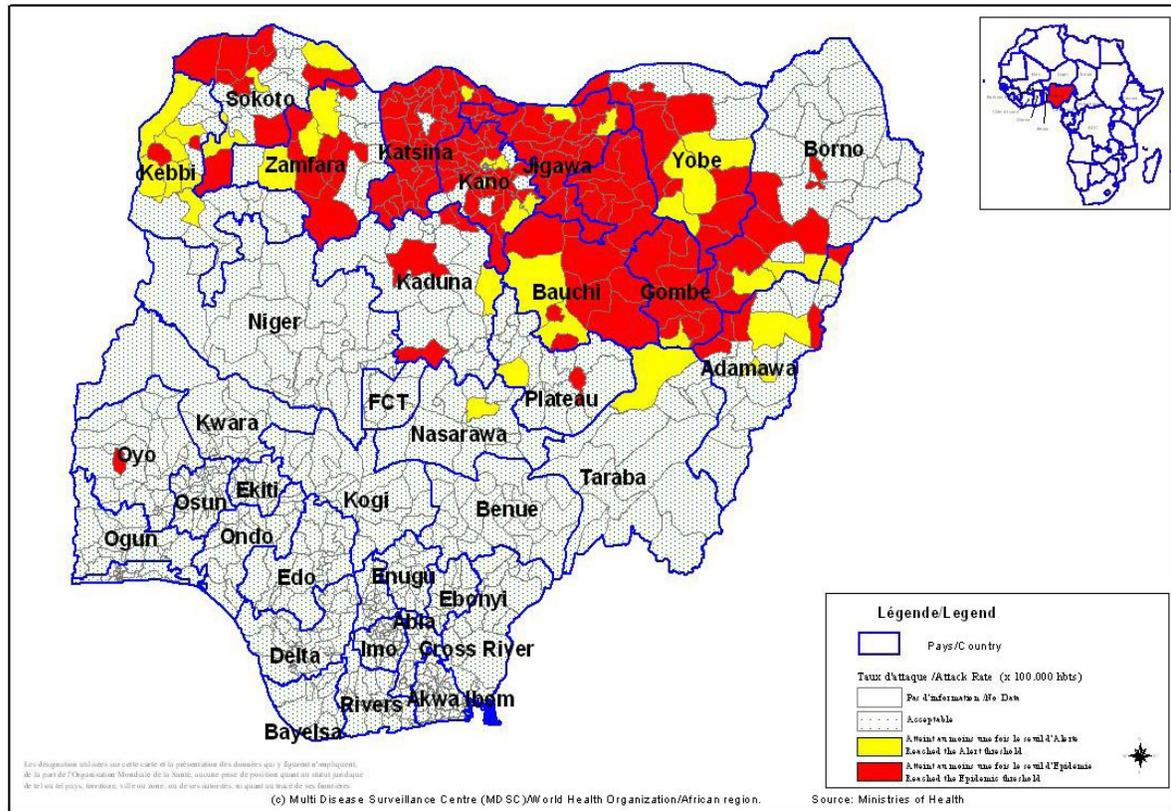


Figure 3.1: Recapitulative map of cumulative Meningitis attack rates at week 1 - 17, 2009. Plot shows districts in epidemic (red) and alert (yellow). Source: Multi-disease Control Center, Ouagadougou, Burkina-Faso, World Health Organization.

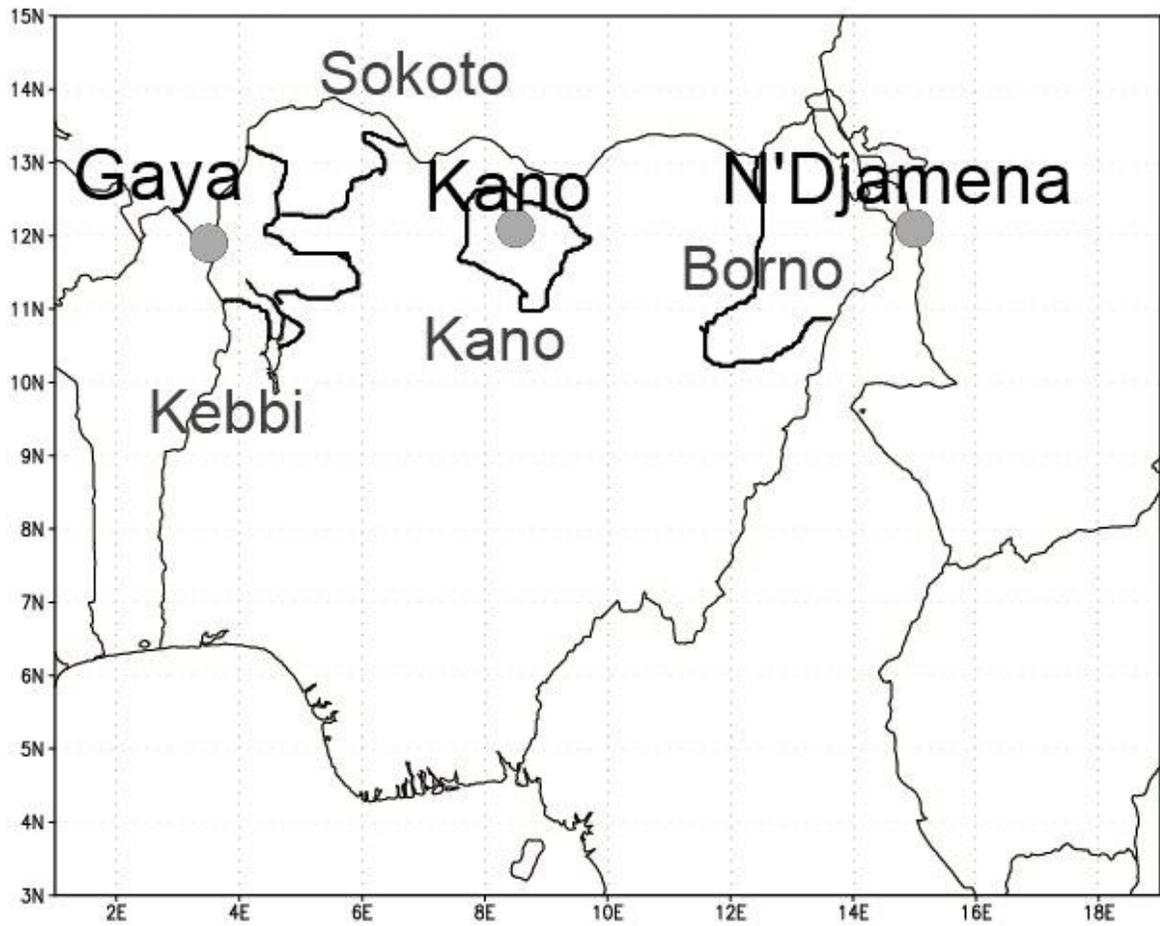


Figure 3.2: States used for meningitis data (names in dark grey) and meteorological stations used to analyze climate relationship (names in black).

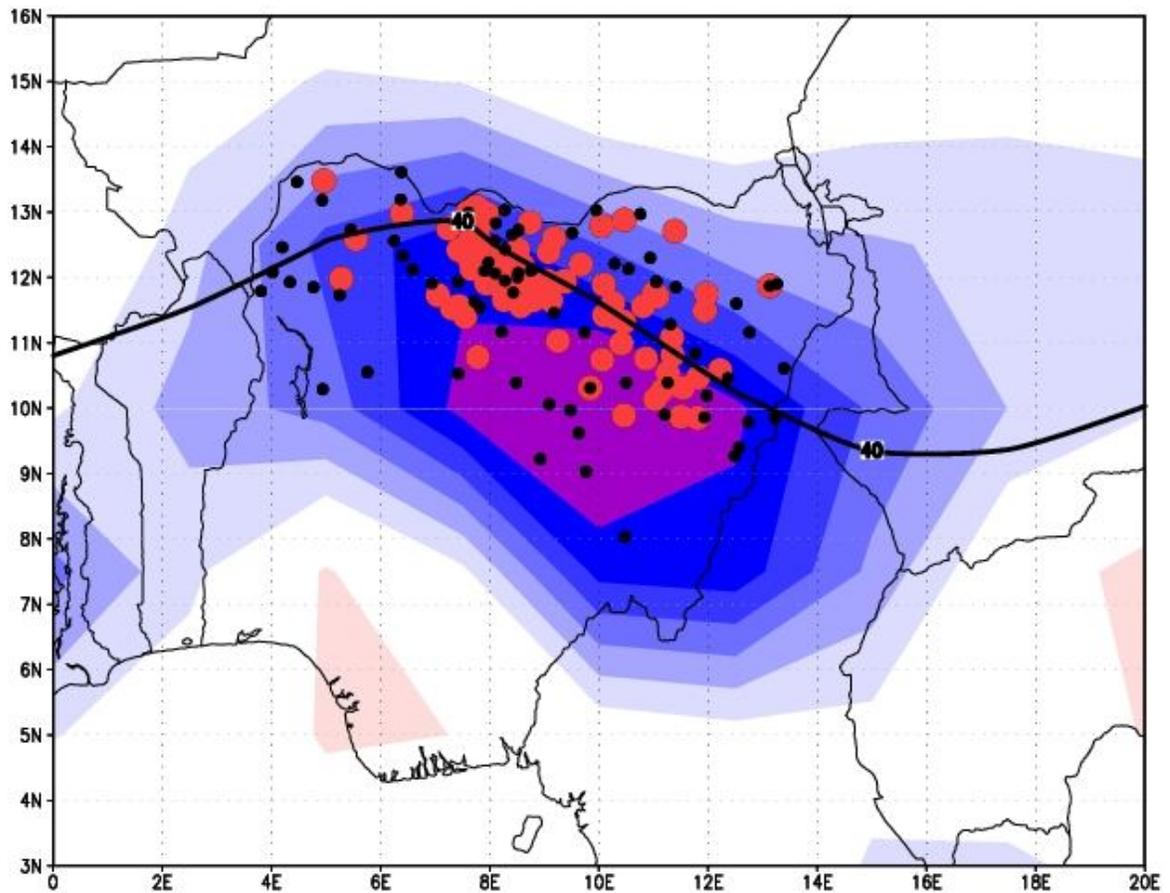


Figure 3.3: Relative humidity anomaly for the change in humidity from the March 23-30 week to March 31-April 5. The solid line represents the 40% humidity threshold for the March 31 – April 5 week. Red circles denote districts in *epidemic* and black circles are districts in *alert*.

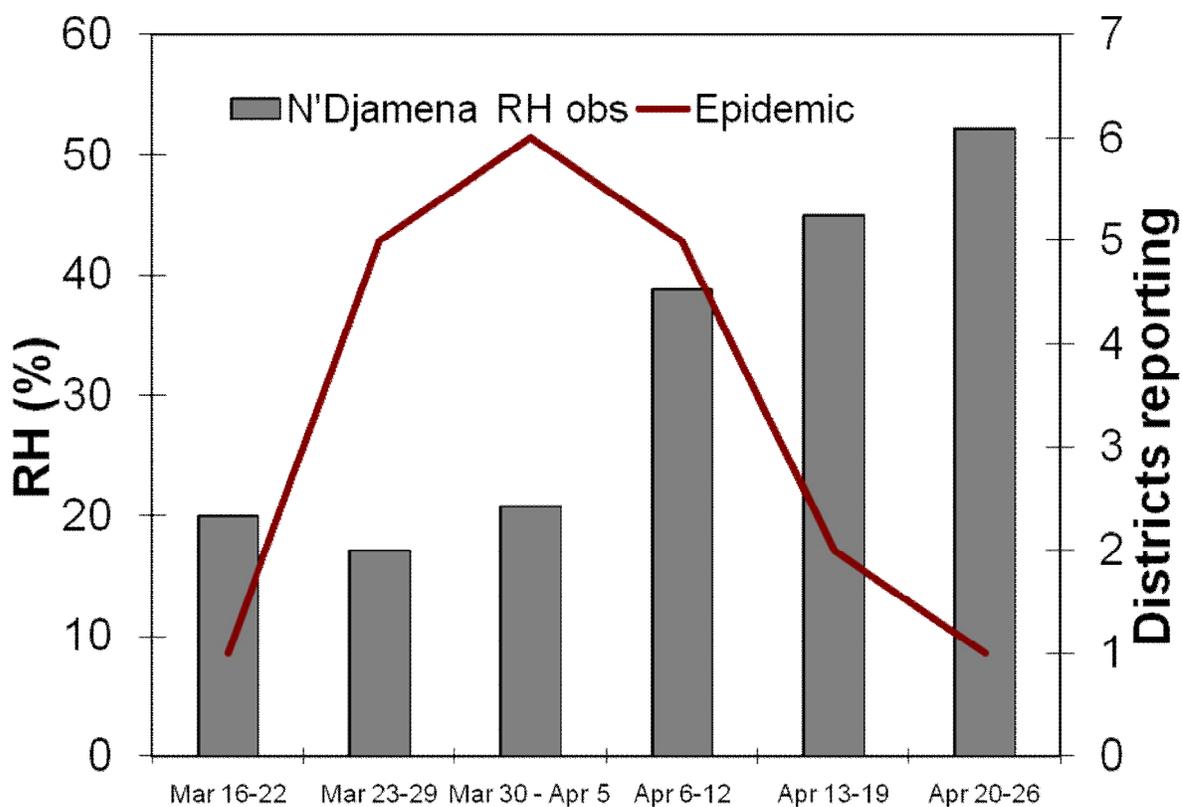


Figure 3.4: Comparison of districts reporting *epidemic* in the state of Borno (Nigeria) during March and April of 2009 (solid line) and the concurrent observed relative humidity (bars) at the station in N'Djemena (Chad).

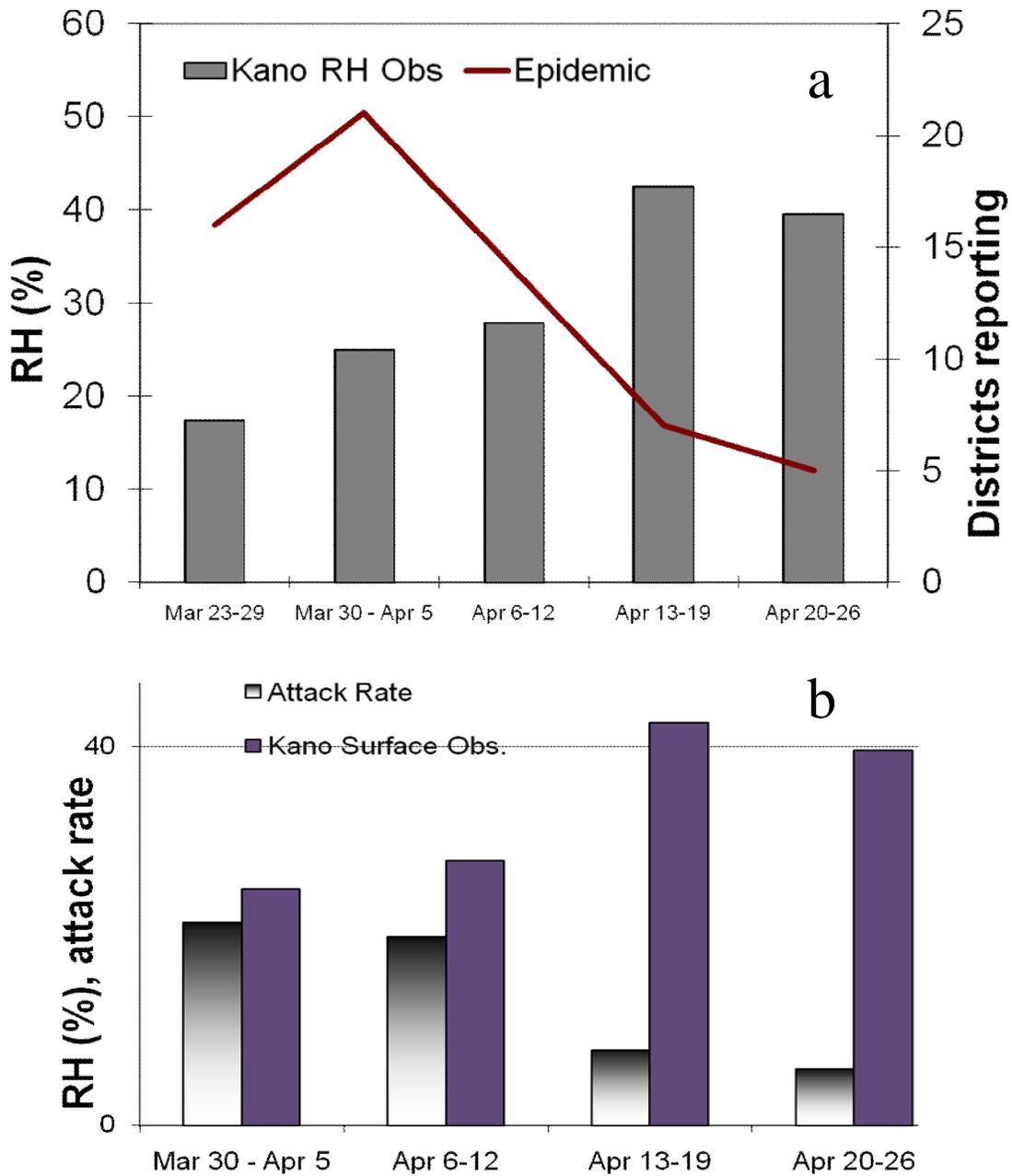


Figure 3.5: (a) Comparison of districts reporting *epidemic* in the state of Kano (Nigeria) during March and April of 2009 (solid line) and the concurrent observed relative humidity (bars) in Kano. (b) Histogram of AR and observed relative humidity in Kano.

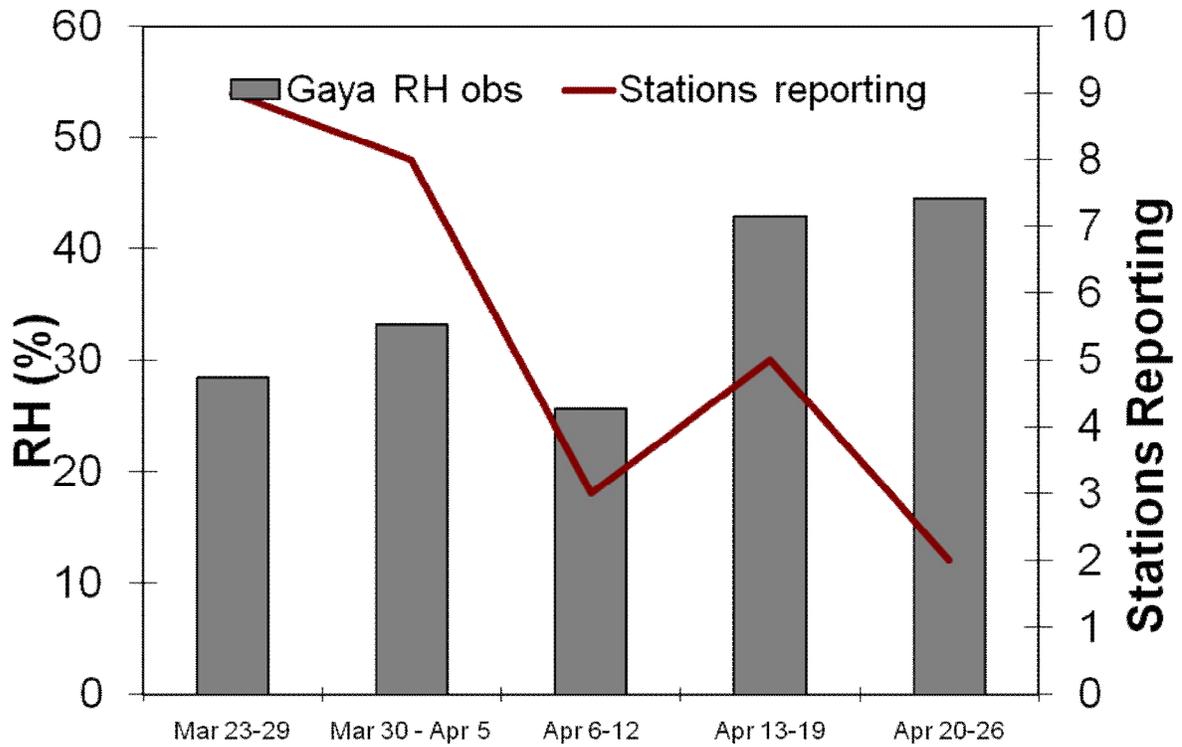


Figure 3.6: Comparison of districts reporting *epidemic* in the states of Sokoto and Kibbe (Nigeria) during March and April of 2009 (solid line) and the concurrent observed relative humidity (bars) at the station in Gaya (Niger).

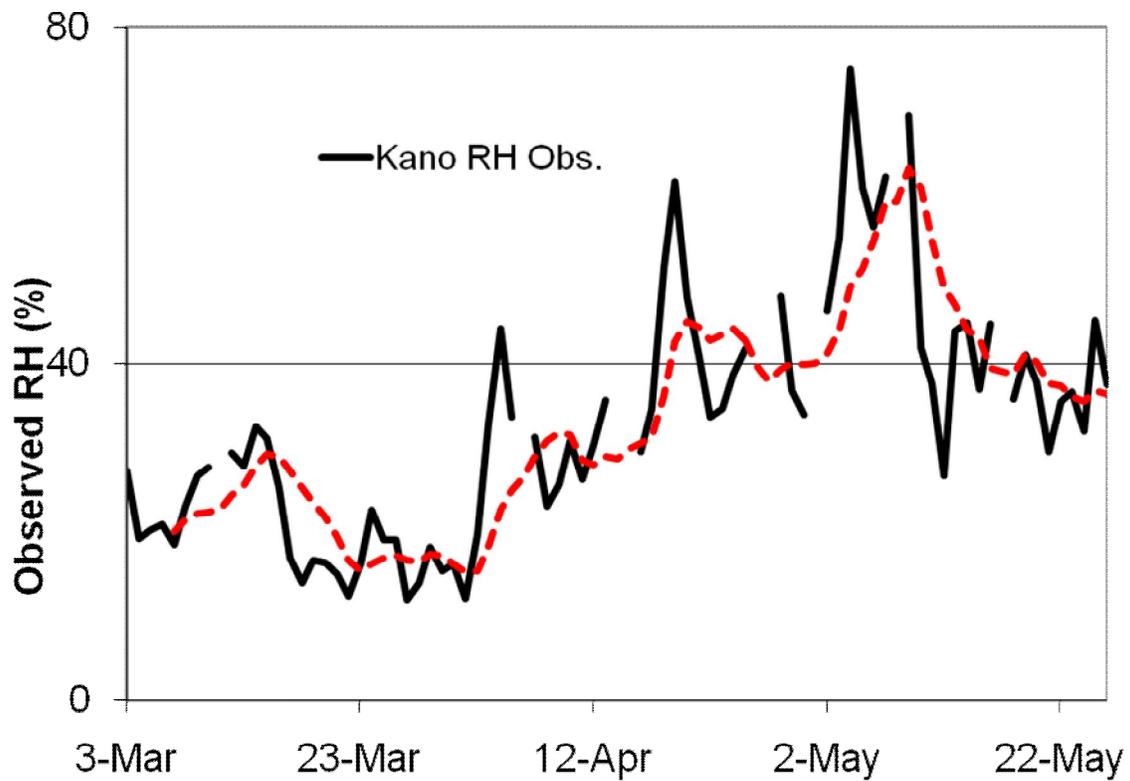


Figure 3.7: Time series of observed relative humidity (%) for Kano, Nigeria during March-May 2009 (solid, black) and the 7-day moving average (red, dashed).

Chapter 4

Large Scale Patterns affecting Short-term

Moist Events during April and May 2009

4.1 Introduction

Sahelian West Africa is characterized by a monsoon climate and receives the majority of its annual precipitation during the boreal summer, when the intertropical convergence zone (ITCZ) is at its northernmost point (Hastenrath 1991). This northward migration of the ITCZ is due to strong, moist southwesterly flow from the Gulf of Guinea (GOG) that penetrates deep into the continent in response to the intensification of the Sahara Heat Low (Hamilton and Archbold 1945; Griffiths 1972; Leroux 1983a,b, 2001; Buckle 1996). Although the rainfall that occurs during the summer monsoon often receives significant attention due to its far-reaching implications on the local economy and livelihood, the start of the rains is another important subject of research within the climate dynamics of this sector of the continent (Eltahir and Gong 1996, Sultan and Janicot 2000, Le Barbe´ et al. 2002, Sultan and Janicot 2003, Gu and Adler 2004, Hagos and Cook 2007, Gu 2009 (hereafter G09)), as it has direct impact on the community (Ati et al. 2002). The onset of monsoon humidity, for

example, has a robust documented link with the cessation of meningitis epidemics over the region (Molesworth et al. 2003).

At the end of Chapter 3 the presence of strong moist pulses were shown to occur over the city of Kano during April and May of 2009 (Fig. 3.7) and it was postulated that they could have played a role in the rapid decline of meningitis cases within the state of Kano, Nigeria. These moist pulses are present throughout the March-May 2009 observational period at different locations within the Meningitis Belt of Sahelian West Africa (Fig. 4.1). As can be discerned, the moist events become more frequent and stronger later in the period. This poses important questions that will be addressed in the present chapter as well as Chapter 5: Can these systems have an effect on the whole of West Africa? What large scale forcings govern their development and predictability? Was 2009 unique in terms of their frequency and strength?

A brief description of the large scale moist anomalies during the boreal spring of 2009 are provided in this chapter along with analysis of CCEW activity during this time period. Datasets and methodology are presented in section 4.2, observed moist anomalies are included in section 4.3, section 4.4 describes the theory of CCEWs and provides details on systems progressing through the region during the transition season of 2009; conclusions are provided in section 4.5.

4.2 Data and Methodology

4.2.1 Datasets

The complexity of the interactions at work in the present study requires the use of multiple data sources: in-situ and gridded observations as well as reanalysis. In addition to information from the NNRP dataset (details were provided in Chapter 2, Section 2.2), this study also employs the $1.0^\circ \times 1.0^\circ$ NCEP Global Forecast System (GFS) Final (FNL) analyses from 2000 to 2009. This analysis is available at six hourly intervals on 26 pressure levels and is used to drive regional models such as the Weather Research and Forecasting Model (WRF, Chapter 4). The FNL version uses the GFS model, but the data assimilation system is run at three hours past synoptic time to allow more data to be assimilated and to use a shorter forecast lead time. Presumably, these factors provide improvements over the operational analysis. This dataset has been used for comparative purposes in research ranging from the characterization of the South American Low Level Jet within the analysis data (Mejia et al. 2006) to the study of energy transformation and diabatic processes in AEWs (Ross et al. 2009). The higher resolution provided by this dataset allows for more spatial detail on the various climatic components of the West African boreal spring.

The investigation of atmospheric humidity regime dynamics over the African continent requires a basic understanding of precipitation over the continent, as moisture fronts emanating from convective events can penetrate the dry Saharan air during the dry season as well as the transition period (Knippertz and Fink 2008, Flamant et al. 2009). Our study also analyzes the structure and variability of intraseasonal phenomena that modulates synoptic-

scale convective events. Therefore, it is important to complement our data sources with gridded precipitation and Outgoing Longwave Radiation (OLR) analysis.

Data from Tropical Rainfall Measuring Mission (TRMM) products [3B43 (monthly) and 3B42 (daily)] is employed for the analysis of intraseasonal phenomena as well as climatology (respectively). The TRMM (Kummerow 1998, 2000) precipitation estimate (algorithm 3B43) is one of the operational products of TRMM. The purpose of 3B43 algorithm is to produce the best-estimate precipitation rate (mm/hr) and root-mean-square (RMS) precipitation-error estimates from TRMM and the monthly accumulated Climate Assessment and Monitoring System (CAMS) or Global Precipitation Climatology Centre (GPCC) rain gauge analysis (TRMM product 3A45). These gridded estimates have a calendar month temporal resolution and a $0.25^\circ \times 0.25^\circ$ spatial resolution that extends from 50°S to 50°N . The 3B42 daily data is derived using TRMM information along with GMS, GOES-E, GOES-W, Meteosat-7, Meteosat-5, and NOAA-12 data to produce daily accumulated rainfall products with the same spatial resolution as 3B43.

The TRMM products outlined above have been validated against rain gauge and ground-based radar data over the Tropics on a monthly scale (Adler et al. 2000, 2003). However, it is important to recognize some of the inherent errors found in TRMM. For example, Nicholson et al. (2003) found a very small overall bias (14%) over West Africa for the daily product during May–September, although the June bias peaked at 120% in the year examined (1998). The monthly product was also analyzed by Adeyewa and Nakamura (2003) and they found that TRMM has a large overestimation in the tropical-rain-forest region of Africa in

December–January–February and in March–April–May. Further, and more importantly for our purposes, the authors also found that there was a high bias for all algorithms in the dry seasons when rainfall is minimal. Although these are significant biases, we should note that our work is not directly based on precipitation but instead on the state of moisture in the atmosphere. Given this caveat, and that the use of this hydrometeor product as a complementary dataset, the biases reported in previous work has only a minimal effect on our results.

In order to study intraseasonal aspects of the transition from Harmattan to the monsoon, we also employ NCEP twice-daily outgoing longwave radiation (OLR). This dataset is derived from polar orbital Television and Infrared Observation Satellite–National Oceanic and Atmospheric Administration (TIROS–NOAA) satellites, which established a quasi-complete series of OLR at the top of the atmosphere and at a resolution $2.5^\circ \times 2.5^\circ$ latitude–longitude (Grueber and Krueger 1984). The OLR dataset is used to represent large-scale deep tropical convection and we use space-time filtering technique (Section 4.2.2) to retrieve information on convectively-coupled equatorial waves (CCEW). We employ NNRP in unison with OLR in subsequent analyses given their compatible resolution.

4.2.2 Methodology

The climatology of moisture during the northern spring of 2009 is explored in this chapter in terms of large scale background anomalies and intraseasonal phenomena such as CCEWs and

mid-latitude systems. Spatio-temporal averages and anomalies (event subtracted from climatology) are employed to characterize background climate forcings and tropical disturbances are derived using wavenumber-frequency filtering.

The wavenumber–frequency filtering technique is applied to the NOAA OLR data following the method of WK99 to obtain MJO, Kelvin, ER and Tropical Depression (TD-Type) signals. This technique is particularly useful for the study of zonally propagating waves, as it decomposes a field of data dependent on time and longitude into wavenumber and frequency components for eastward and westward propagating waves, as well as zonal-mean fluctuations (Hayashi 1982). This method has also been successfully applied in other studies based on OLR (e.g., SK02; SK03a; SK03b; Mekonnen et al. 2008), and on precipitable water data (Roundy and Frank 2004). We should state that our main results are based on spectral quantities that have been calculated for many successive overlapping (by 2 months) 96-day segments of the multiyear raw OLR dataset that is identical to that used in WK99. The results are not sensitive to this overlap. Following WK99, to help prevent aliasing, the first three harmonics of the seasonal cycle are removed. As in their work, for each segment the mean and linear trends are removed in time by a least squares fit, and the ends of the series are tapered to zero. The tapering provided data windowing and helped to minimize the effects of spectral leakage, and the overlapping of segments minimizes the loss of data by the tapering. Complex Fast Fourier Transforms (FFTs) were performed in longitude to obtain Fourier coefficients (in zonal planetary wavenumber space), after the tapering procedure, for each time and for each latitude. The FFTs allow us to obtain the

wavenumber-frequency spectrum for each latitude. Finally, the OLR power is averaged over all available segments of the 30-yr record (1979-2009), and is summed for the latitudes between 30°S and 30°N. The resulting effective bandwidth is 1/96 cycles per day (cpd) in frequency, and 1 unit zonal wavenumber.

The interest in eastward propagating (Kelvin, MJO) and westward propagating (TD-Type, ER) waves requires that the OLR spectrum be separated into antisymmetric and symmetric components. Linear equatorial waves are either symmetric or antisymmetric about the equator depending on the parameter considered. In WK99's decomposition procedure, the gridded fields (e.g., OLR) that are a function of latitude, φ , can be written as:

$$\text{OLR}(\varphi) = \text{OLRA}(\varphi) + \text{OLRS}(\varphi), \quad (3.1)$$

where

$$\text{OLRA}(\varphi) = [\text{OLR}(\varphi) - \text{OLR}(-\varphi)]/2 \quad (3.2)$$

is the antisymmetric component and

$$\text{OLRS}(\varphi) = [\text{OLR}(\varphi) + \text{OLR}(-\varphi)]/2 \quad (3.3)$$

is the symmetric component. It is also the case that, in such a linear decomposition, when the power in the antisymmetric and symmetric components are summed, and also summed over the same latitudes in both hemispheres, then this power is identical to the power of the total field summed for the same latitudes. By studying the latitudinally summed power of the antisymmetric and symmetric components WK99's procedure accounts for all the variance of the total field for these latitudes.

Finalizing this portion of the methodology, it should be noted that the OLR power spectral results that were presented in section 3 of WK99 extend up to a planetary wavenumber 15 and from a frequency of 1/96 cpd to 0.8 cpd, a range for which they estimate the dataset has useful information. The authors also mention that only three obviously erroneous peaks in the power spectra could be detected within the range studied: at eastward wavenumber 14 and periods of 9 and 4.5 days, and also at westward wavenumber 14 and a period around 1.27 days; these peculiar peaks can be explained by the 14 swaths recorded per day by the satellite system, the slow precession of the orbit that takes about 9 days, and the folding of various harmonics about the frequency of 0.5 cpd.

4.3 Large Scale Anomalies during 2009

As a preface to analyzing the shift in the moisture regime for length of the Sahel, findings on important climate anomalies during this time period are presented in this section. It should be noted that important differences during April and May of 2009 may have played a role in the short-term events that could have influenced the collapse of meningitis within the country of Nigeria.

4.3.1 Low-level Circulation Anomalies

There existed important anomalous patterns in the atmospheric circulation during April and May of 2009. Most notably, April exhibited a strong anomalous low pressure center in the 925 hPa geopotential field in the NNRP dataset at [20°N, 23°E] (Fig. 4.3d) as compared to

the 2000-2009 climatology (Fig. 4.2a). Also, for perspective, the same field is presented in Fig. 4.3d but for April 2006 (Fig. 4.2c). Note that the opposite is the case in 2006: an anomalous high pressure is centered over the same region. Also on these plots is the approximate location of the ITF (change in zonal wind domain at 925 hPa) as defined by Sultan and Janicot (2003). Note that the ITF is pulled north by the anomalous low into northern Niger and Chad in 2009 (solid line). Although this indicates an early shift in the ITF compared to the climatological position of this feature (dash dot), it may not necessarily be reflected on surface humidity.

Due to the nature of the present analysis, the transition period has a critical point from mid-April to mid-May. Thus, we provide a wider look at the anomalies during 2009 that take into account the entirety of the period. As can be appreciated in Fig. 4.3, the anomalous low pressure at this height has lessened in intensity but is still a major focal point in the large scale circulation. Also note the strong northeasterly flow over the western side of the Sahel. This would favor a drier environment. Subsequent sections and Chapter 5 will explore this location in more detail, as it could have implications on the propagation of short-term events as well as their prediction.

4.3.2 Moisture Anomalies during 2009

The interest in atmospheric moisture motivates provides motivation to characterize its distribution during the transition period and how these conditions compare to the recent climatology of the region. The structure of total atmospheric column precipitable water (kg

m^{-2}) is first examined using FNL data during the April 15 – May 15 2009 period (Fig. 4.6). This period was chosen since it contains the strong moist pulses experienced over the observational record (Fig. 4.1). Climatological values of precipitable water during the 2000-2009 period are displayed in Fig. 4.4b and in Fig. 4.4c is the corresponding plot for 2009. The difference between these two plots is provided in Fig. 4.4a, where a strong positive anomaly can be discerned over southern Chad, western Sudan and eastern Nigeria. Just as important is the fact that this positive anomaly extends northward into northern Chad and northwestward into northern Niger and the vicinity of the Air Mountains. This excess moisture has significant implications in terms of diabatic heating and vertical motion in the region.

Mapped together with precipitable water (contoured) in figure 4.5, the surface temperature (K) field (shaded) has a significant gradient adjacent to the location of maximum moisture anomalies. The warm anomalies are also collocated with the anomalous low pressure center during this month; this would favor increased flow into this location. The significance of this sustained anomaly could have played a crucial role in the development of a strong moist event that originated in this region during the first half of May 2009. This will be analyzed in more detail in Chapter 5.

Another vantage point for the analysis of the total amount of precipitation present in the atmosphere is to investigate its propagation throughout the period. Westward-propagation of moist pulses is discernable in Fig. 4.6 using time-longitude Hovmoller plots of total atmospheric column precipitable water (kg m^{-2}) for (a) NNRP and (b) FNL from 40°E to

40°W and spanning from 1 April, 2009 to 31 May, averaged for latitudes 10°N-15°N. The figure shows clear westward propagation of 4 different events that initiate between 20°E and 40°E on during April and May. Although the FNL display is drier than NNRP for the eastern portion of the domain, the same patterns are still discernable. One particular event in May (mentioned above) initiates close to 35°E with markedly high amounts of moisture, especially at 10°E in both datasets/. This event has considerably better resolution in the FNL, providing detail on its scale relative to the background conditions. Interestingly, the continuously high moisture values east of 20°E through the month of April are clear in both datasets. Also visible is the continuously dry conditions west of 0°E, which echoes the analysis of anomalous conditions during the April 15 – May 15 period. It is not until the May event that conditions in this region approach values found in the eastern Sudano-Sahel.

4.3.3 Precipitation

Precipitation is an important factor the present analysis given the influence of moisture advection and cold pool dynamics associated with convective events (Flamant et al., 2009). Thus, a clear understanding of rain patterns during the period of study is crucial for the detection and prediction of moist pulses that travel the width of Sahelian West Africa.

Precipitation patterns are derived from two datasets for this analysis: TRMM 3B43 (monthly) and CMAP. The latter is used due to the compatible scale with OLR information and NNRP whilst the former is more useful for comparisons with regional model output in Chapter 6. During April, both CMAP (Fig. 4.7a) and TRMM (Fig. 4.7c), precipitation values

>50 mm of accumulated rainfall remained south of 10°N but with a distinct maximum of >250 mm in south central Nigeria. Totals derived from TRMM confirm this signal but to a lesser extent (~200 mm at 4°E), slightly to the southwest of where CMAP had located the event. Also on TRMM, given its higher resolution, is the presence of higher localized precipitation values within the country of Ghana, as well as pockets of >50 mm in isolated parts of southern Chad, extreme northeastern Chad and a small portion of western Sudan.

Perhaps more useful for the current analysis, the April 2009 anomaly relative to the 2000-2009 average for the same month shows important features of interest (Fig. 4.7b,d). In CMAP (Fig. 4.7b), for example, the increased precipitation over Nigeria, described above, is also visible as a strong positive anomaly encompassing much of the country, with especially high values southwest of the Jos Plateau. Slight positive anomalies (<40 mm) are also present over southern Chad, parts of the Central African Republic and western Sudan. Another feature worth noting is the southward shift in the ITCZ, where negative values are present off the Atlantic coast of Liberia, Sierra Leone and Cote d'Ivoire. Mirroring this anomaly is a positive signal straddling the equator. This signal is also prevalent in TRMM (Fig. 4.7d), where strong negative values (<140 mm) can be seen in the same location along with positive anomalies further south along the equator. Also present in TRMM are the higher accumulation rates over much of the southwest quadrant of Nigeria, parts of Ghana and Togo and also over northern sectors of Cote d'Ivoire. Perhaps more relevant to the preceding large scale anomalies in atmospheric moisture (section 4.3.2), however, are the positive anomalies over the southern half of Chad, southwestern Sudan, and most of the Central African

Republic. This further supports the large scale moist anomalies discussed above and provides more insight into anomalous patterns that could influence short term events and meningitis outbreaks.

The month of May was similar to April in both CMAP (Fig. 4.8a) and TRMM (Fig. 4.8c) except for a northward seasonal shift in precipitation such that areas north of 10N have begun seeing precipitation amounts >50 mm. Nearly all of Chad is below the 50 mm threshold in CMAP (Fig. 4.8a) and a large pocket of rainfall is present over Nigeria (as in April). The output from TRMM (Fig. 4.8c) places the rainfall maximum over the Jos Plateau in accordance with climatology due to orographic effects. Another small rainfall maximum signal (>200 mm) is present over Sierra Leone. In addition, small pockets of >50 mm are present in parts of Niger, Mali and Chad. These, as was alluded to in Section 4.3.2 above and which is explored in further detail in Chapter 5, are probably related to one particular event during the early half of May.

In terms of anomalies relative to the 2000-2009 period, April exhibited a similar structure to May in that there is a southward shift of the higher precipitation values associated with the ITCZ. Inspecting figure 4.8b, positive anomalies remain south of the GOG coast, whilst negative anomalies persist along the coast itself, as given by CMAP. Two small pockets of positive anomalies are present, however, one in Nigeria and the other in the Sierra Leone/Guinea region adjacent to the Guinea Highlands. The higher-resolution image derived from TRMM (Fig. 4.8d) also shows interesting patterns in anomalous precipitation during the month of May. Some key features are the increased precipitation seen over the Jos Plateau

and points north that lie in the state of Kano, Nigeria, as well as the Guinea Highlands maximum that was found in CMAP-derived anomalies. Worth noting, also, are small pockets of >20 mm over central Chad, northwest Niger and western Mali, which could be attributed to the May event that crossed this region as described in the Hovmoller plot in Fig. 4.6.

4.3.4 Summary

The preceding analysis has highlighted the main attributes of the 2009 boreal spring in terms of low level circulation, moisture anomalies and precipitation patterns. This analysis concentrated during the transition period of April-May. The most important feature was a localized region of anomalous moisture in the southern Chad-Sudan region. Interestingly, this period of study was also marked by negative θ anomalies in the Nigeria-Chad-Sudan area from April 15 – May 15 as given by the FNL data at the 925 and 850 hPa levels compared to the climatological period 2000-2009 (Fig. 4.9). It is possible that the two features may be linked and that it could have affected the continuously-dry atmosphere for points west of 0°E and the much moister conditions found from Nigeria to the Sudan, which started around the first half of April with short-lived moist events.

Large scale upper level phenomena also affecting this region could emanate from the mid-latitudes. Figure 4.10 hints at a possible connection between weather patterns over Sahelian West Africa and a mid-latitude event over northern portions of the continent during late April 28 – May 1. It is conceivable that extratropical systems such as the one in Fig. 4.10 may have contributed to the evolution of short-term moist events and this possibility is

supported by previous work on tropical-extratropical interactions (Winstanley 1970; Flohn 1975; Fink and Knippertz 2003, Knippertz 2005, Knippertz and Fink 2008).

Another large scale factor that could influence low level moisture during this time period is the presence of equatorially trapped waves. Indeed, the westward-propagation of the short-term systems in Fig. 4.6 and the persistent moist-dry dipole between the eastern and western Sahel could be explored by including this type of tropical phenomena in the present analysis.. One possibility that is explored in Chapter 5 is ER activity during this time period may have played a role in the persistence, and eventual westward shift, of the moist anomaly over the eastern Sahel. In the following section CCEWs are described in more detail and their possible role in determining the propagation and intensity of short term moist events is also explored.

4.4 Convectively Coupled Equatorial Waves

Equatorially trapped waves account for a significant portion of the synoptic-scale convective variability in the tropics (Gruber 1974; Zangvil 1975; Takayabu 1994; Pires et al. 1997; Wheeler and Kiladis 1999, hereafter WK99; Wheeler et al. 2000, hereafter WKW00). In chapter 2 it was shown that one of the important sources of variability for tropical Africa comes from equatorial waves such as the MJO, Kelvin and Equatorial Rossby (ER) disturbances.

Although the majority of the research conducted on moisture patterns over West Africa has been focused on mesoscale convective systems (Laing and Fritsch 1993, 1997; Hodges

and Thorncroft 1997; Mathon and Laurent 2001; Mathon et al. 2002), synoptic-scale easterly waves (Reed et al. 1977; Duvel 1990; Thorncroft and Hoskins 1994a,b; Diedhiou et al. 1999; Kiladis et al. 2006; Hall et al. 2006), and interannual and decadal time scales (Lamb 1978a,b; Nicholson 1978; Newell and Kidson 1984; Folland et al. 1986; Rowell et al. 1995; Ward 1998; Janicot et al. 2001; Rowell 2001; Giannini et al. 2003), recent work has also addressed equatorially-trapped phenomena such as Kelvin waves (Matthews 2004, hereafter M04; Mounier et al. 2007; Mekonnen et al. 2008) and Equatorial Rossby waves (M04; Janicot et al. 2009, hereafter J09). These systems were found to play an integral role in the evolution of and northward shift of the moisture front as spring gave way to summer over Sahelian West Africa in 2009.

4.4.1 Equatorial Wave Theory

Convectively-coupled equatorial waves (CCEWs) first became apparent with the advent of satellite technology in the 1960s. This new technology and the ability to perform time-longitude analysis of convection over the tropics elucidated the presence of synoptic-scale westward-propagating disturbances within the ITCZ (Chang 1970). During the same decade, fundamental advances in the understanding of tropical motions were made through the development of the theory of equatorially trapped waves (Matsuno 1966; Lindzen 1967).

Since the present study relies on important notions acquired by the derivation of equatorial disturbances in Matsuno (1966), it is imperative to review this knowledge briefly. Equatorial wave theory starts with a separation of the primitive equations, linearized about a

basic state with no vertical shear, governing small motions in a three-dimensional stratified atmosphere on an equatorial β -plane, into the “vertical structure” equation and “shallow water” equations (Matsuno 1966; Lindzen 1967). The equatorial wave modes are the zonally (and vertically) propagating, equatorially trapped solutions of the shallow water equations, which are characterized by four parameters: meridional mode number n , frequency ν , planetary zonal wavenumber s , and “equivalent depth” h of the layer of fluid (“shallow water”). In this case, h is related to the internal gravity wave speed as $c = \sqrt{g/h}$, and acts as a separation constant linking the vertical structure equation and the shallow water equations. The h variable is also related to the vertical wavelength of free (dry) waves, and to the meridional scaling through the relation for the equatorial Rossby radius, $R_e = (\sqrt{g/h}/\beta)^{1/2}$, where β is the latitudinal gradient of the Coriolis parameter.

The theoretical dispersion relation fully characterizes a wave, given the meridional mode number and wave type, provided two out of n , s , and h variables are specified. The theory also argues that tropical waves that are forced by, and those that control, the convective heating are internal modes with wavelike vertical structures. The resulting solutions of the shallow water equations are either symmetric or antisymmetric about the equator. For the divergence or temperature field, which is presumably related to the convection, modes of odd meridional mode number n (as in Matsuno 1966) are symmetric, whereas those of even n are antisymmetric. Later studies (WK99; Kiladis et al. 2006) showed that the horizontal structures of CCEWs and dispersion characteristics corresponded to Matsuno’s (1966)

solutions for equatorially-trapped waves: Kelvin, equatorial Rossby, mixed Rossby-gravity, and inertigravity waves.

The work of WK99 allowed for the disambiguation of different CCEWs from satellite observation products such as precipitation (TRMM) or outgoing longwave radiation (OLR). Their wavenumber-frequency filtering technique has allowed for multiple studies in this sector of tropical meteorology. For instance, Straub and Kiladis (2002, 2003a,b, hereafter SK02 and SK03a,b) studied the role of Kelvin waves on the convective activity within the Pacific ITCZ. Wang and Fu (2007) researched Kelvin waves reaching central Africa from the Atlantic during northern spring, while Mekonnen et al. 2008 provided evidence of Kelvin waves crossing West Africa during the boreal summer. M04 showed also that the MJO has a large scale influence on overall African monsoon activity.

It is essential to note that although recent studies by Nguyen and Duvel (2008) and Wang and Fu (2007) inspect the role of CCEWs like Kelvin waves during the boreal spring, these studies are reserved for equatorial Africa and the Atlantic ITCZ, respectively. Less attention has been given to Sahelian West Africa during this time of the year given the prevalence of the dry season. However, in G09 it was found that regional intraseasonal convective signals over the Tropical Atlantic-West Africa domain during March-June are closely associated with the global tropical (eastward-propagating) intraseasonal mode, i.e. the MJO. This echoes a similar finding for the fully-fledged summer monsoon in M04. It should also be noted that G09's focus was on areas along the GOG coast and not necessarily points inland, but their results provide valuable information for the purposes of the present study. Also,

G09 did not find faster-moving Kelvin-type structures to play as large a role as the MJO, but they acknowledged their possible contribution to convection. Additionally, and perhaps more importantly for the present work, Kelvin waves are most active during the boreal spring (WK99). Other wave types, such as TD-type (tropical depression), are classified as hybrid waves in Kiladis et al. (2009) and also as a primarily-summer feature, but one which would nonetheless appear to have a presence in the mid-to-late spring. They, along with the MJO and ER waves are found to be consistently crucial in the moisture dynamics over this portion of the continent. It is their phasing with one another as well as interactions with other phenomena (mid-latitude systems) which motivates their inclusion in this work. Evidence for their role throughout the boreal spring will be presented in this chapter in subsequent sections, as well as case of particular significance during May 2009 in chapter 5.

4.4.2 Equatorial Phenomena during 2009

The occurrence of westward-propagating features first became evident with a forecasted event during mid-May (described in Chapter 5). This prompted an analysis of humidity in in-situ observations to validate the forecast (Fig. 3.7 in Chapter 3). Analysis of unfiltered 2009 NCEP OLR data, averaged over $2.5^{\circ}\text{S} - 7.5^{\circ}\text{N}$ in a time-longitude Hovmoller plot, reveals the signature of a coherent eastward propagating feature (Fig. 4.11). OLR has been used in the literature for the analysis of equatorially-trapped disturbances (WK99, Kiladis et al 2009, Mekonnen et al 2008, Nguyen and Duvel 2008). When employing this dataset, emphasis has

been placed on the WAM but important inferences were also made about the boreal spring (Nguyen and Duvel 2008, Wang and Fu 2007).

Concurrently with the eastward-propagating convective signatures on Fig. 4.11, moist events of varying strengths begin westward propagation along 10°N-15°N from the 20°E longitude and points east (Fig. 4.6). It is clear that multiple systems affected convection in the region, which suggests they should be investigated in order to determine which role, if any, they played in the development and progression of the moisture front. It is thus imperative to understand the various types of disturbances that are filtered from the NCEP OLR fields. In section 4.2.2 some of the basics of space time filtering were presented as well as the identification of different waves. Figure 4.12 is a modified version of Fig. 1 in WK99 that shows regions of wavenumber–frequency filtering calculated to separate Kelvin, TD-type, MJO and ER. Notice that the symmetric component of OLR about the equator is used in this work in order to separate the waves of interest.

The spectrum on Fig. 4.12 elucidates the existence of a peak corresponding to the Kelvin wave, lying along equivalent depth curves of around 20–50 m (Matsuno 1966). This corresponds to an eastward phase speed of around 15 m s^{-1} . There exists another peak of interest visible in the domain of westward propagating signals between periods 2 and 6 days and zonal wavenumbers 6 to 20 with average speeds of 8 ms^{-1} . Kiladis et al. (2006) showed that this “TD” signal represents easterly waves in Africa. Also on this plot is the Kelvin within a period of 2.5–17 days, and eastward wavenumber 1–14, as in SK02, WK99 and WKW00. Mekonnen et al. (2008) also found that the phase speed of the Kelvin wave

changes as it propagates across different regions of the globe. The waves are faster over the central and eastern Pacific ($\sim 24 \text{ m s}^{-1}$) and slow down over Africa (14 m s^{-1}). In WKW00, it was surmised that the slowing of the waves is suggestive of stronger coupling between the dynamical and convective signatures. Additionally, Mekonnen et al. (2008) also observed that the wave periodicity decreased from about 8 days over the Pacific and the Atlantic to about 4 days over central and eastern Africa.

Two other features of interest can be found on Fig. 4.12: MJO and Equatorial Rossby (ER). The MJO is discernible in the figure as an eastward propagating system that is separate from the Kelvin wave signal even at wavenumber 1, with a spectral gap in the power ratio occurring at a period of about 25 days. Globally, the $n = 1$ ER wave activity explains somewhat less convective variance than the MJO or the convectively coupled Kelvin wave (WK99), yet over tropical Africa these systems can influence important modes of intraseasonal variability of convection (Janicot et al. 2009, hereafter J09).

4.4.2.1 ER and MJO

The MJO has been found to be an integral part of large scale convective signals over tropical Africa (M04, J09). Their activity is reserved mostly to the Indian Ocean and the Western Pacific, and this can also be seen for the recent climatology (2000-2009) in terms of variance during the March 15 – Jun 15 period (Fig. 4.13a). For this analysis, the technique developed in WK99 is utilized to filter for the MJO within the period of 30-60 days and eastward (positive) wavenumbers 1 and 2. A narrow band of increased variance ($>70 \text{ (W m}^{-2}\text{)}^2$) does

stretch through the equatorial Africa and the GOG coast. Variance was markedly higher (>90 $(W m^{-2})^2$) along $5^{\circ}N$ within the same locations during the spring of 2009 (Fig. 4.13b), suggesting the MJO may have influenced the climate of the region.

In the unfiltered analysis of the OLR dataset (Fig. 4.11), longer-varying convective signals appear to be in place during April and May of 2009. Indeed, a weak MJO (Fig. 4.14) was found to be traversing the region from April 14 to May 20 according to observations recorded over tropical Africa by the Climate Prediction Center (CPC, http://www.cpc.noaa.gov/products/precip/CWlink/MJO/ARCHIVE/PDF/mjo_evol-status-fcsts-20090706.pdf). The possible role of this particular MJO in terms of intraseasonal convective signals during April and May is explored further in Chapter 5.

Analysis of ER waves has been found to be more difficult than the other CCEWs due, in part, to their slow speeds and broad spatial scales, which allow them to be modulated by propagation through varying background wind states such as the MJO (Kiladis et al. 2009). Another potential complication noted by Kiladis et al. (2009) is that the ER spectral peak in Figure 4.12 lies partially in the MJO region (Roundy and Frank, 2004). Nevertheless, westward propagating features related to ER have been found to strongly affect modes of convection over tropical Africa during the boreal summer, and, as this study suggests, during the boreal spring as well. ERs have also been linked with the formation of easterly waves, i.e. TD-type signals (Kiladis et al. 2009), and may have affected these type of phenomena during 2009.

The space-time filtering technique is applied to the OLR dataset to filter for ER waves at 6 – 30 days and westward (negative) wavenumbers 1 – 10. The variance of ER during the 2000-2009 period (Fig. 4.15) reveals that, as is the case with the MJO, most of the activity occurs over the Indian Ocean and points east, although a narrow band of increased variance ($>80 \text{ (W m}^{-2}\text{)}^2$) along 15°N does affect Sahelian Africa. For the spring of 2009, the variance did not extend as far west as the recent climatology and stops short at the prime meridian (Fig. 4.16a). There is a pocket of higher variance from southeastern Chad [20°E] to western Ethiopia [40°E]. During the critical transition period between April 20 through May 20 (Fig. 4.16b), which saw the significant drift in moisture in Fig. 4.6, the pocket of higher variance ($>200 \text{ (W m}^{-2}\text{)}^2$) is even more pronounced, partly due to the short time period but also for significant activity over this location. To illustrate this, Fig. 4.17 displays a time-longitude Hovmoller plot of ER-filtered OLR (W m^{-2}) averaged for 12.5°N to 15°N (highest activity during the boreal spring, Roundy and Frank 2004) from 80°W to 80°E for the period April 1 – May 20 2009. Two separate convective phase ER signatures are present: 60°E to 0°E in early April and another from 40°E to 30°W from April 21 to May 20. Also present is the dry phase of the second ER disturbance, which is most prominent from 10°E to 40°E starting on May 6. This particular ER wave is of great interest to the present work, as it was found to have profound impacts on the strong moist event in Fig. 4.6.

4.4.2.2 Kelvin waves

Kelvin waves are most active during the boreal spring (WK99). The WK99 technique is once again employed to filter for the Kelvin waves within the period of 2.5–17 days and eastward wavenumber 1–14. The location of highest variance during the spring (March 15 – June 15 2000-2009) is shown in Fig. 4.18, where the highest values (variance of $>220 \text{ (W m}^{-2}\text{)}^2$) are located along the GOG coast from 15°W to western Central African Republic. As can be seen, most of the activity during the recent period has had the majority of impact over coastal regions.

The months of April and May in 2009 were characterized by a wide belt of Kelvin wave activity (variance, $(\text{W m}^{-2})^2$) that stretched from the GOG into southern portions of Sahelian West Africa (Fig. 4.19a). When the April 20 – May 20 period of 2009 is isolated in the variance plot (Fig. 4.19b), Kelvin wave activity becomes more apparent near the equator between 0°E and 20°E . This activity can also be seen in a time-longitude Hovmoller plot (Fig. 4.20) of Kelvin-filtered OLR (W m^{-2}) averaged for -2.5°S to 7.5°N . One Kelvin wave, in particular, had a significant influence on convection during early May (also visible in 4.11 as the eastward-propagating convective signature). The month of April was also quite active in the region, with at least 4 coherent waves ($<-10 \text{ ms}^{-1}$) between 20°W and 20°E . This could have influenced westward-propagating features similar to African Easterly Waves (AEWs) as described in Mekonnen et al. (2008).

4.4.2.3 TD-type disturbances

Space-time filtering was once again applied to the original NCEP OLR dataset to derive TD-type disturbances that correspond with easterly waves (EW) at the 2-6 day westward peak and zonal wavenumbers 6-20 (similar to that in Kiladis et al. 2006). EWs are off-equatorial westward propagating Rossby gyres that appear within the trade wind field of the ITCZ over the northern hemisphere (Kiladis et al. 2009). These features are primarily active over the Pacific and Atlantic sectors, but they also tend to occur over sub-Saharan Africa during the monsoon season.

The variance $(W m^{-2})^2$ of TD-type disturbances during the northern spring (March 15 – June 15) for the 2000-2009 period is presented in Fig. 4.21 in order to highlight activity of this class of waves during the recent period. This analysis is consistent with TD-type filtered OLR variance in Roundy and Frank (2004) and it highlights the occurrence of EWs during this time period from 20°E to 40°W, with particularly high variance ($>160 (W m^{-2})^2$) between 15°W and 0°E.

TD-type activity during the entire spring of 2009 is shown in Fig. 4.22a, where the peak in variance is similar to that in the recent climatology (Fig. 4.21). Note, however, that the overall variance does not extend as far west as the climatology and that the belt is generally wider longitudinally than the climatology. The month of April is highlighted in Fig. 4.22b due to the large number of westward propagating events present in the reanalysis (Fig. 4.6) as well as the observations (Fig. 4.1). Two peaks in variance $(W m^{-2})^2$ are present during this month: one over the Atlantic south of the GOG coast between 5°W and 15°W and a second

one along 10°N from 10°W to 0°E. This could be highly significant, as it would suggest that a number of systems have crossed the region at this latitude.

The westward propagating features traveling north of 10°N are discernable in a time-longitude Hovmoller diagram of TD-type filtered OLR averaged for 5°N-10°N and spanning 80°W to 80°E from April to May (Fig. 4.23). During the latter half of April, there was a succession of short-lived (20°E to 10°W), strong negative anomalies that could account for some of the moisture spikes experienced at more southerly regions of the Sahel (i.e. Kano, Fig. 3.7). Then, in early May, a significant, coherent disturbance initiated much farther east than its April counterparts (>40°E instead of 20°E). This feature (hereafter TD1) is connected temporally with the increase in humidity values throughout most of the populated region of the Sahel (see Fig. 4.1). In Fig. 4.24, the observed RH (%) for three separate stations (Bamako, Niamey, Kano) is displayed along with area averages of TD-type filtered OLR (W m^{-2}) over each city. The arrows on the plots point to coherent TD-type disturbances that are propagating over each of the locations, with TD1 highlighted to show its influence throughout the region. It is found that the spikes in humidity tend to coincide with particularly strong, negative TD-type filtered anomalies. This adds to the theory that short-term moist events could be related to EWs.

4.5 Conclusions

The role of climate anomalies over Sahelian Africa during the boreal spring has been explored. During April 2009, strong positive anomalies were found in the precipitable water (kg m^{-2}) field in FNL and NNRP datasets in the eastern Sahel [20°E - 40°E , 10°N - 17.5°N], along with strong negative anomalies in the same field west of 0°E , between 10°N and 20°N . Several westward-propagating moist events traversed the region during April but their latitudinal impact was limited to points closer to the coast. These events were found to be coinciding with TD-type system signatures in the filtered OLR analysis.

The break in dry anomalies for much of the region west of 0°E did not occur until a particularly strong iteration of moist anomalies. The May moist event (MME hereafter) brings large amounts of moisture to the western Sahel (Fig. 4.6) and is supported by observations (Fig. 4.24). Within this figure, the MME is highlighted for each of the three stations along with TD-type anomalies. It is found that a particularly strong event (TD1) could have played a role in the westward propagation of moisture. The preceding analysis has also shown that coherent and relevant equatorially trapped waves were present during this time period: a strong Kelvin wave along with negative (convective) anomalies in the ER and MJO fields. It is the possibility of interplay between these equatorial waves as well as the underlying climate anomalies that have dictated the state of the moisture front throughout the transition season. One event in particular, the MME, brought about significant change to the width of the Sahel: it transported large amounts of moisture into dry areas so that, in theory,

the threat of meningitis could have been reduced. More resources are devoted to the study of the MME in chapter 5.

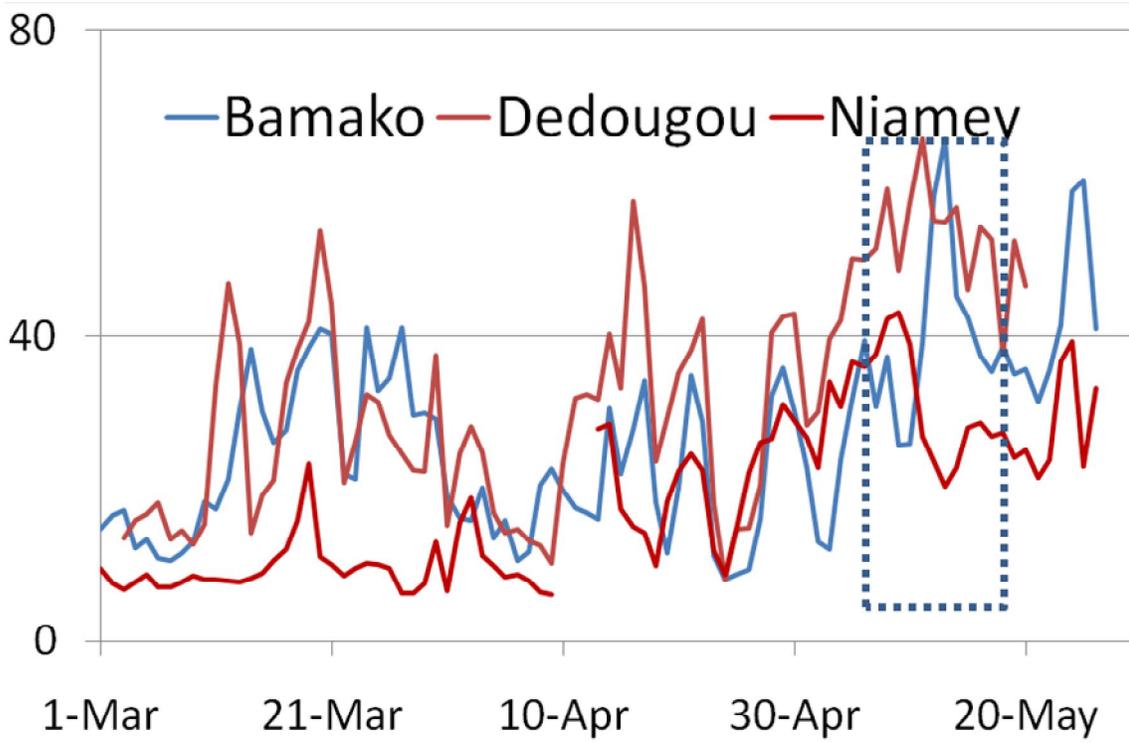


Figure 4.1: Relative Humidity (%) observations at Bamako (blue), Deodogou (brown), Niamey (dark red).

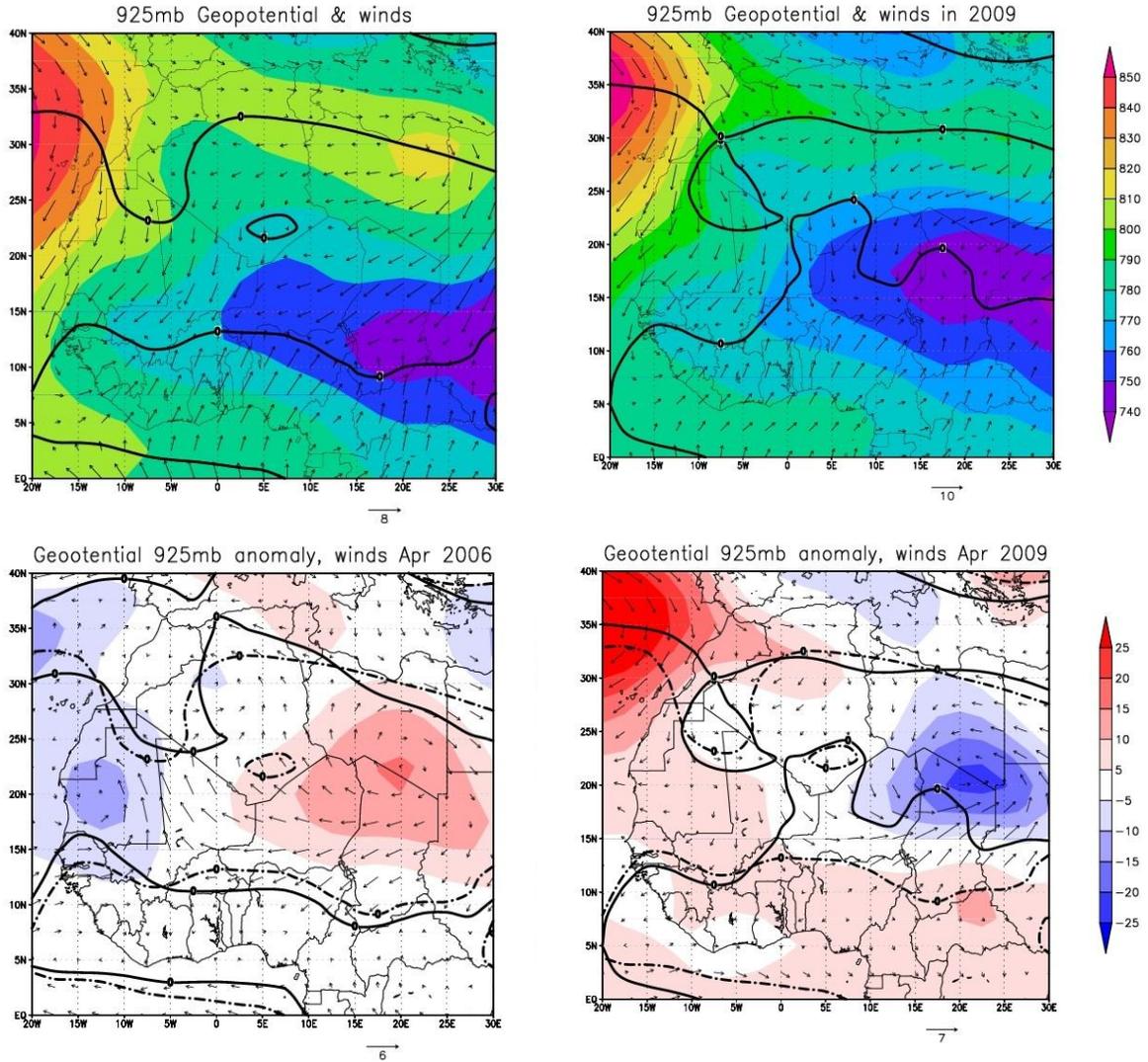


Figure 4.2. Climatology of Geopotential height and winds at 925 hPa. for April 2000-2009 (a), 2009 (b). Geopotential height and wind anomalies for 2006 (c) and 2009 (d).

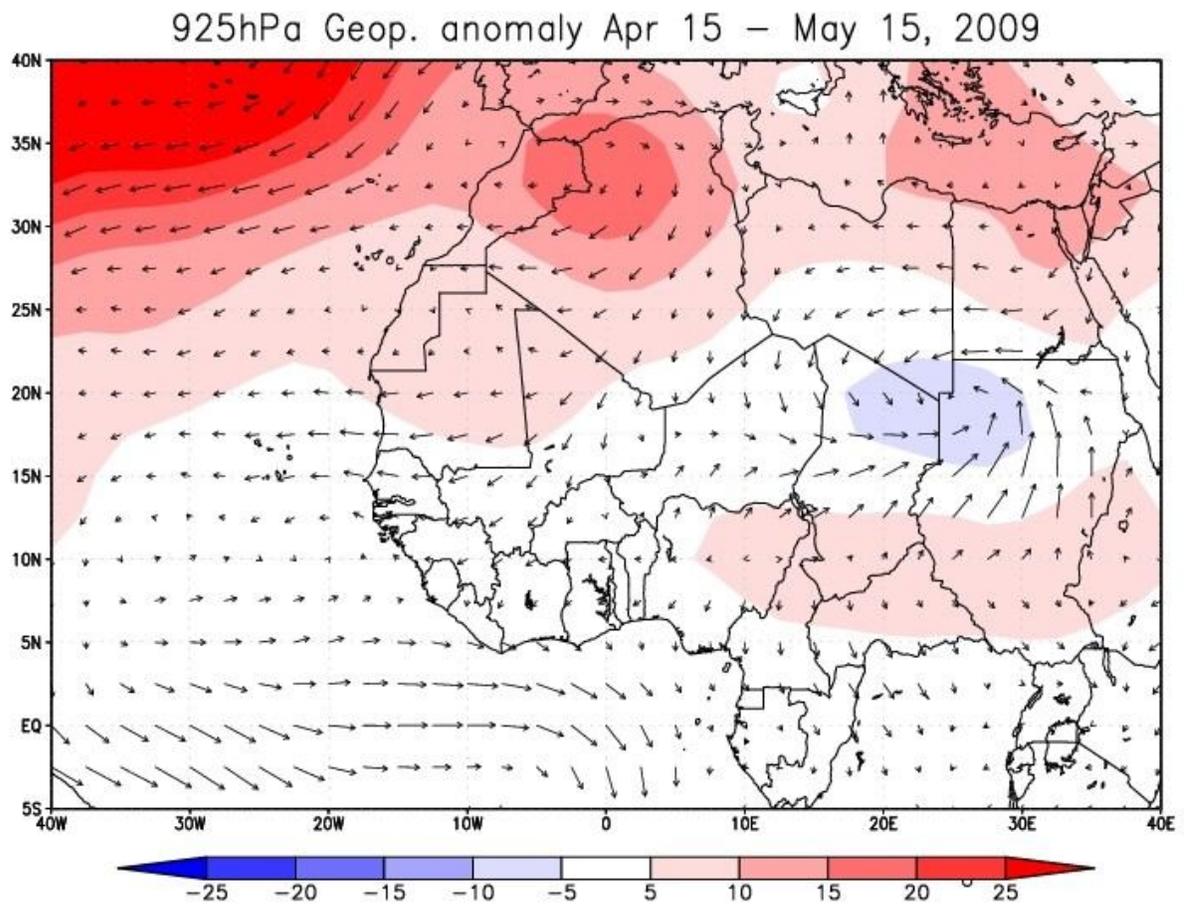


Figure 4.3: Geopotential height (m) and wind anomalies (m s^{-1}) for 2009 relative to recent climatology.

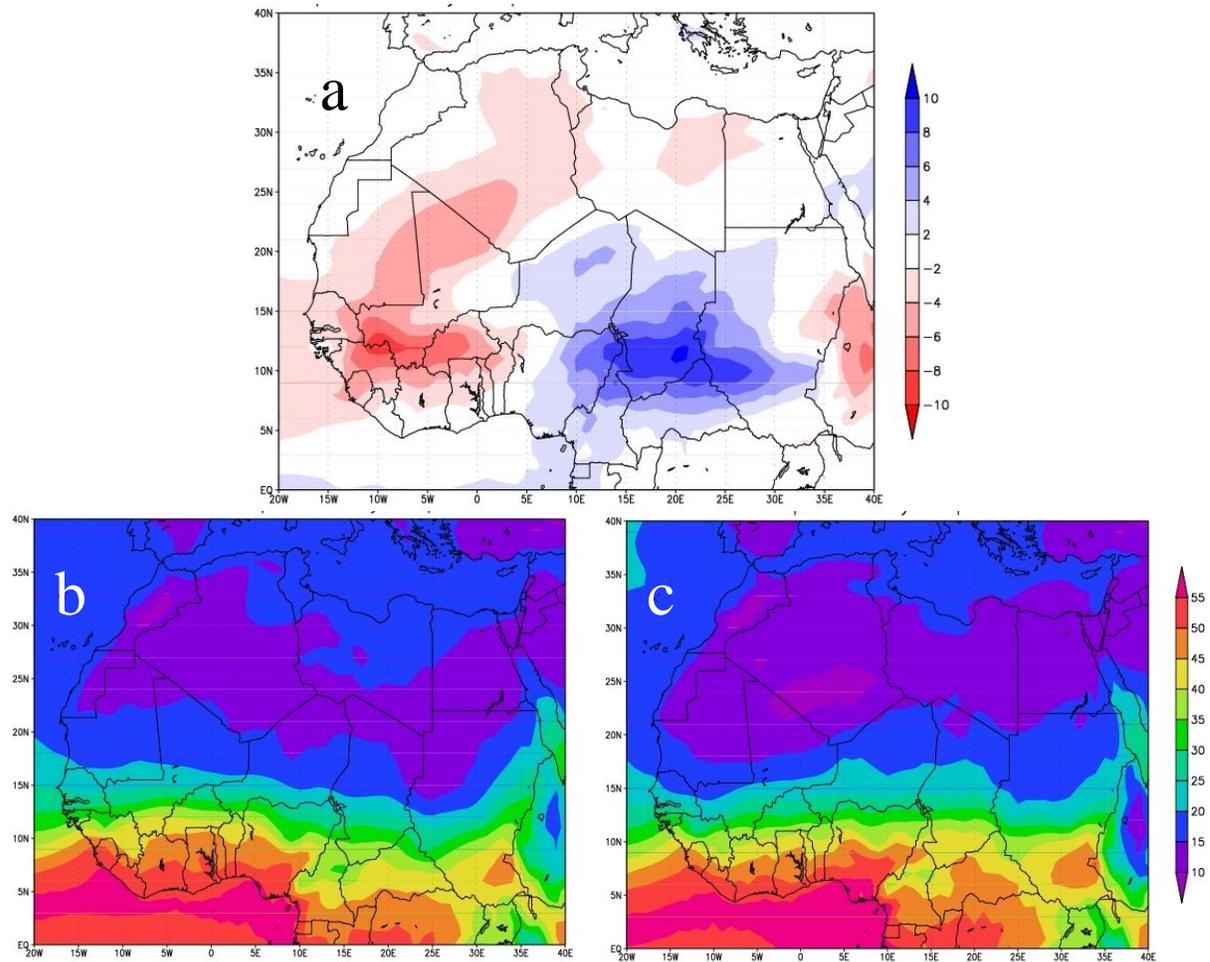


Figure 4.4: Total atmospheric column precipitable water anomalies (a) during April 15 – May 15 2009 compared to the climatological period 2000-2009. Climatological conditions are shown for perspective (b) as well as 2009 (c)

2009-clm Surface temp. anomaly, prH2O

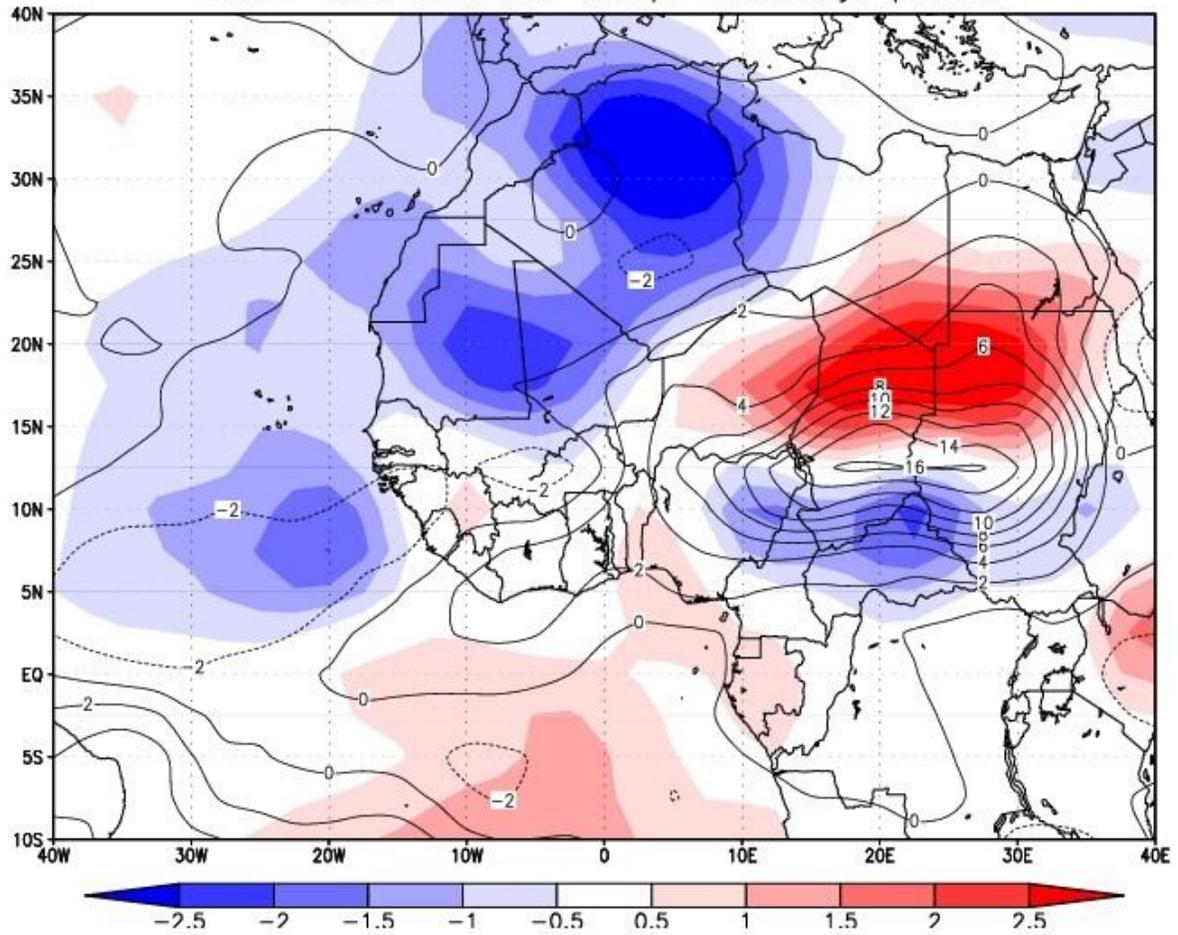


Figure 4.5: FNL-derived April 2009 anomaly relative to recent climatology for precipitable water (kg m^{-2} shaded) and surface temperature (K, contour).

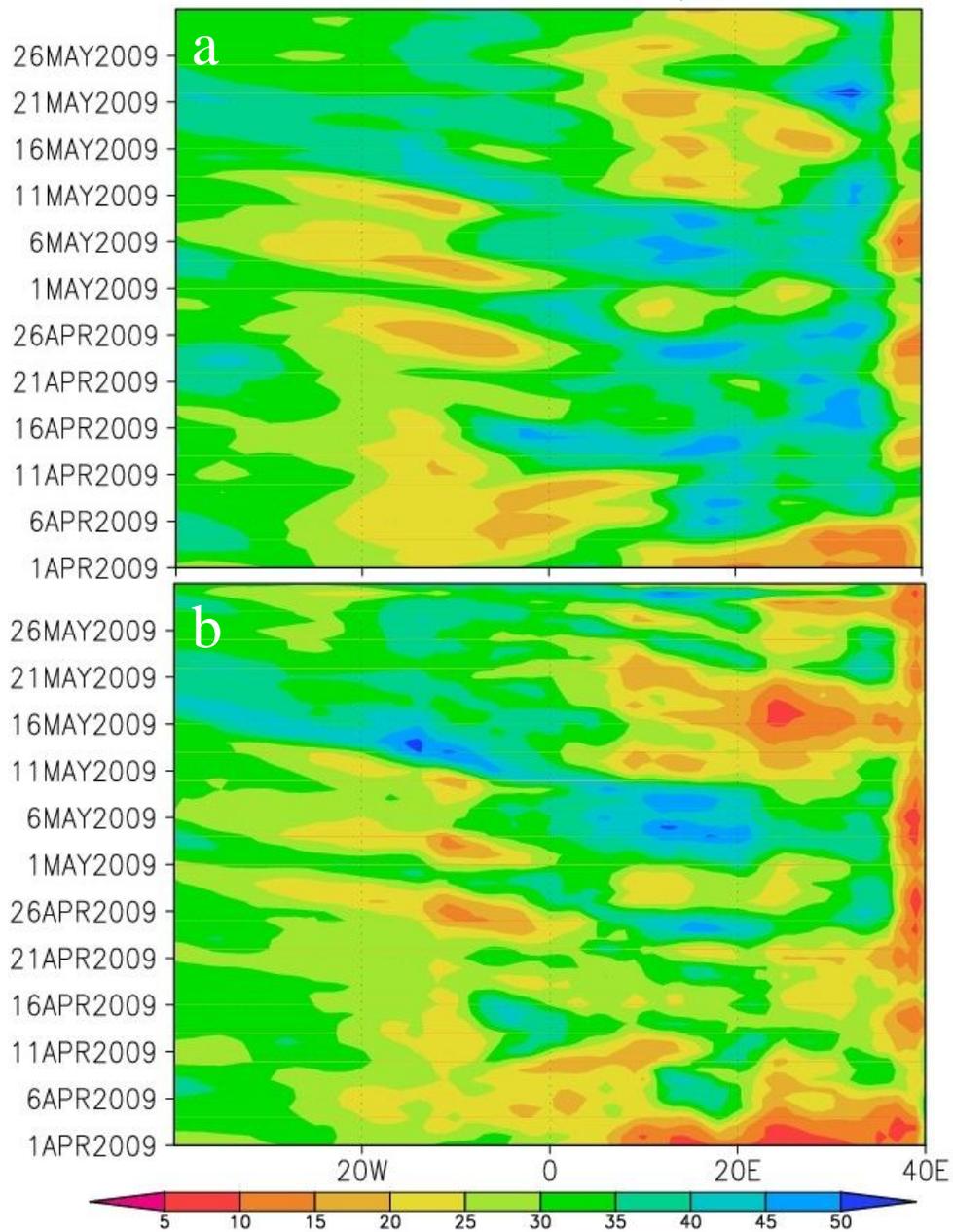


Figure 4.6: Time-longitude Hovmoller plot of precipitable water averaged for points averaged between 10°N - 15°N and spanning from 40°E-40°W for (a) NNRP and (b) FNL.

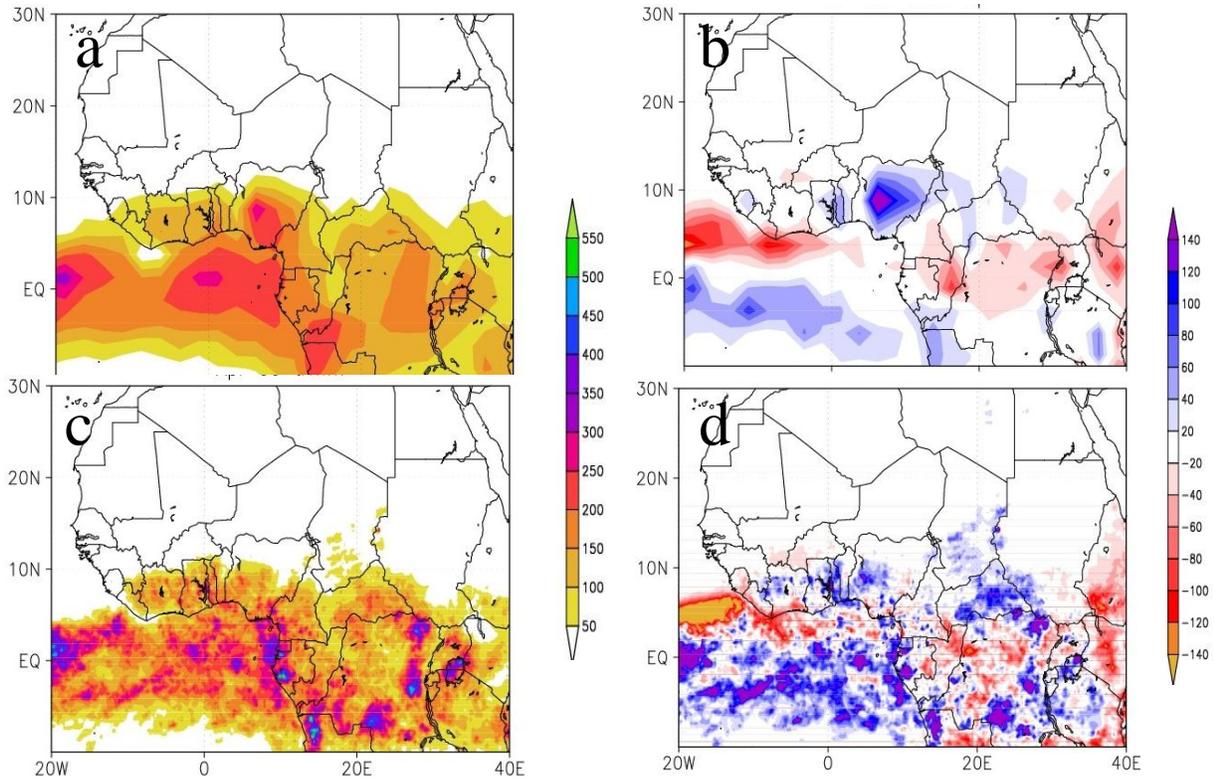


Figure 4.7: Estimated precipitation totals (mm) for April 2009 in (a) CMAP and (b) TRMM. Anomalies are shown accordingly for CMAP (c) and (d) TRMM.

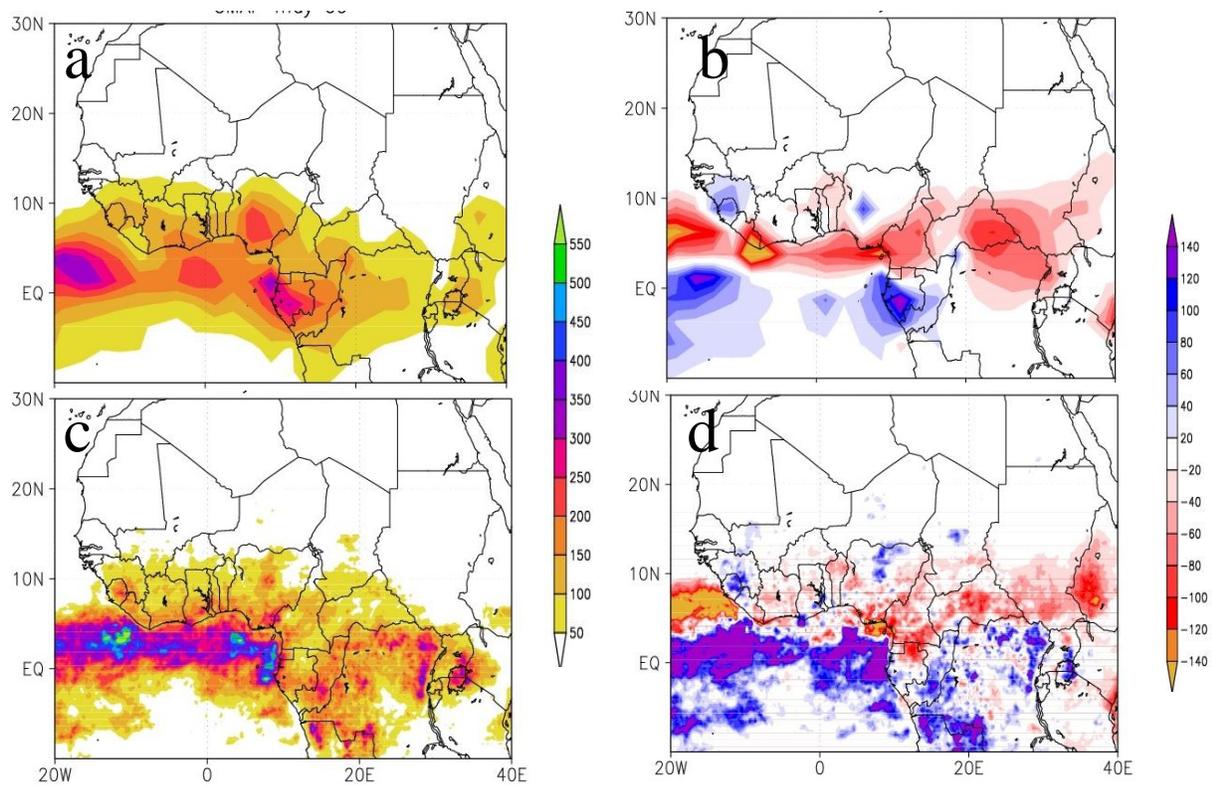


Figure 4.8: Estimated precipitation totals (mm) for May 2009 in (a) CMAP and (b) TRMM. Anomalies are shown accordingly for CMAP (c) and (d) TRMM.

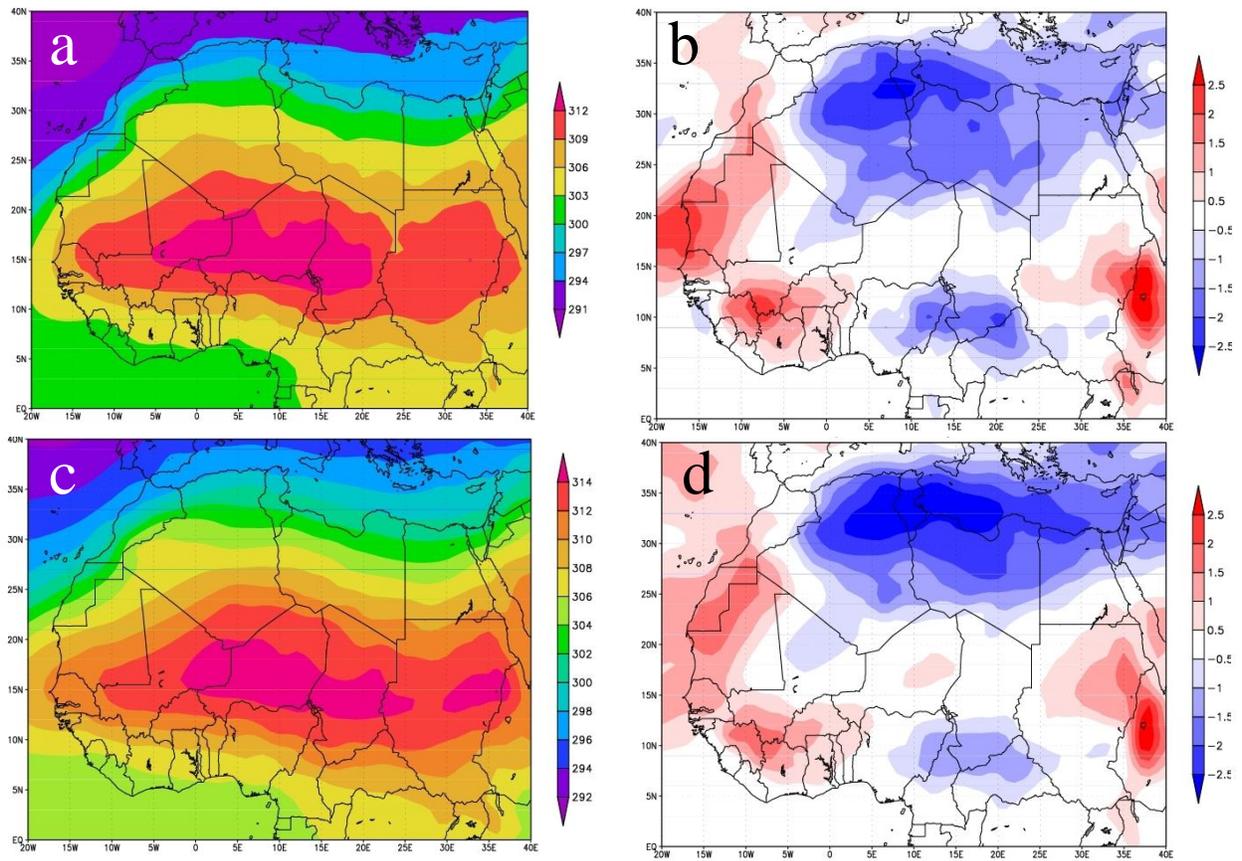


Figure 4.9: FNL-derived recent climatology (2000-2009) of potential temperature (K) at (a) 925 hPa and (c) 850 hPa averaged for April 15 – May 15. Anomalies for 2009 are shown for (b) 925 hPa and (d) 850 hPa levels.

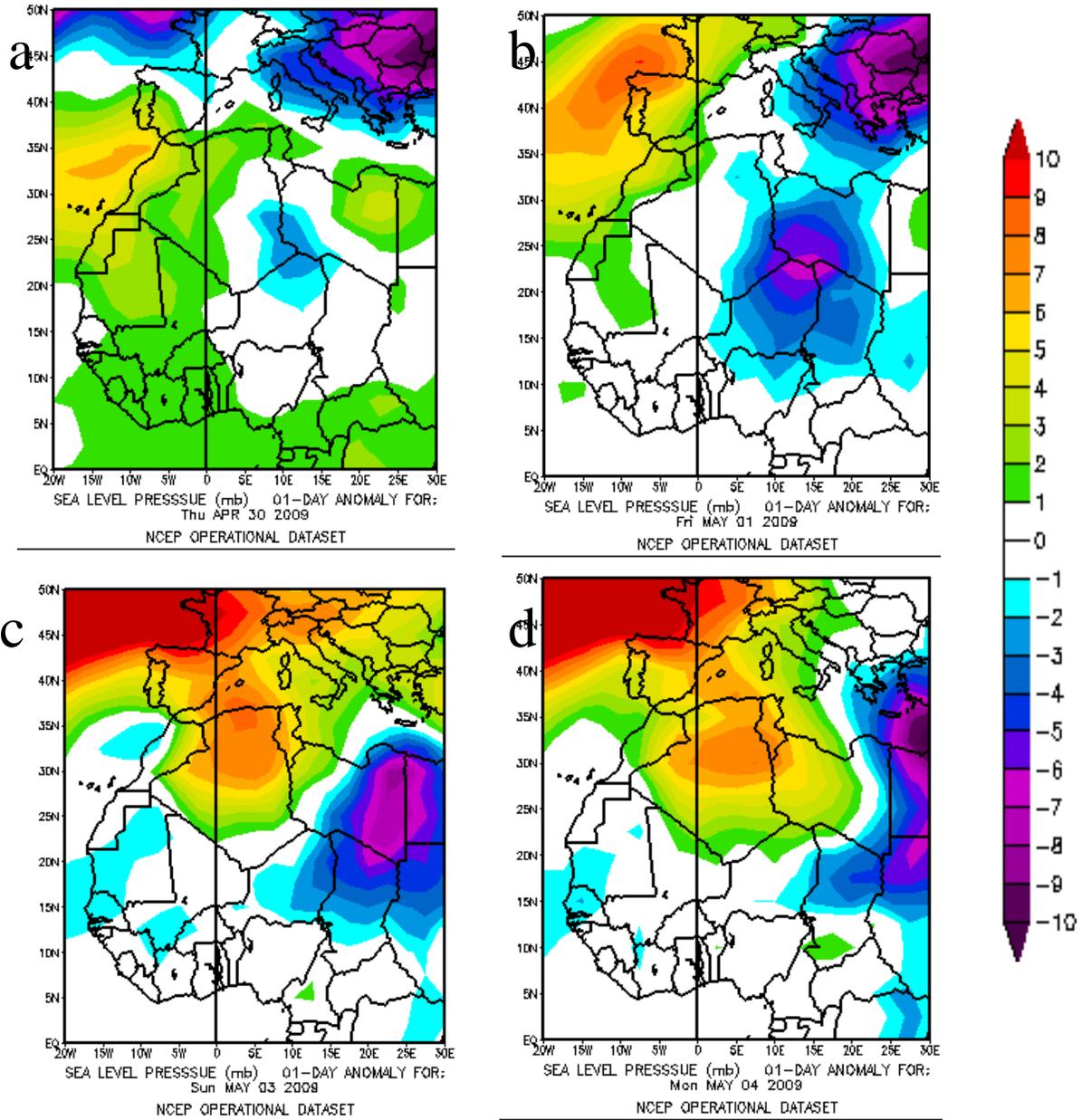


Figure 4.10: NCEP Operational Dataset mean sea level pressure (hPa) anomalies for April 30 (a), May 1 (b), 2 (c) and 3 (d).

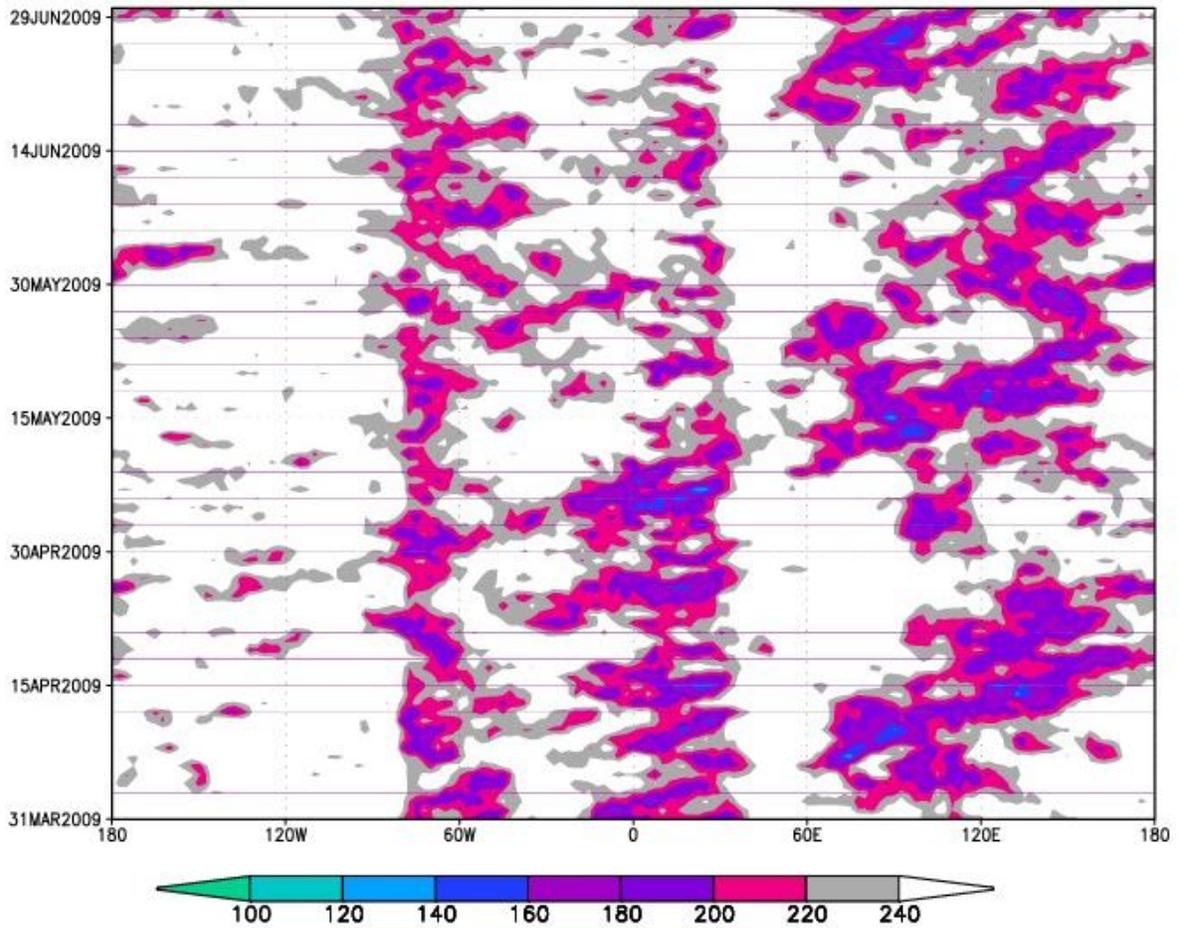


Figure 4.11: NCEP OLR for March 15 – June 15 2009 averaged for all points between 2.5°S and 7.5°S. Only values lower than 240K are shaded for clarity.

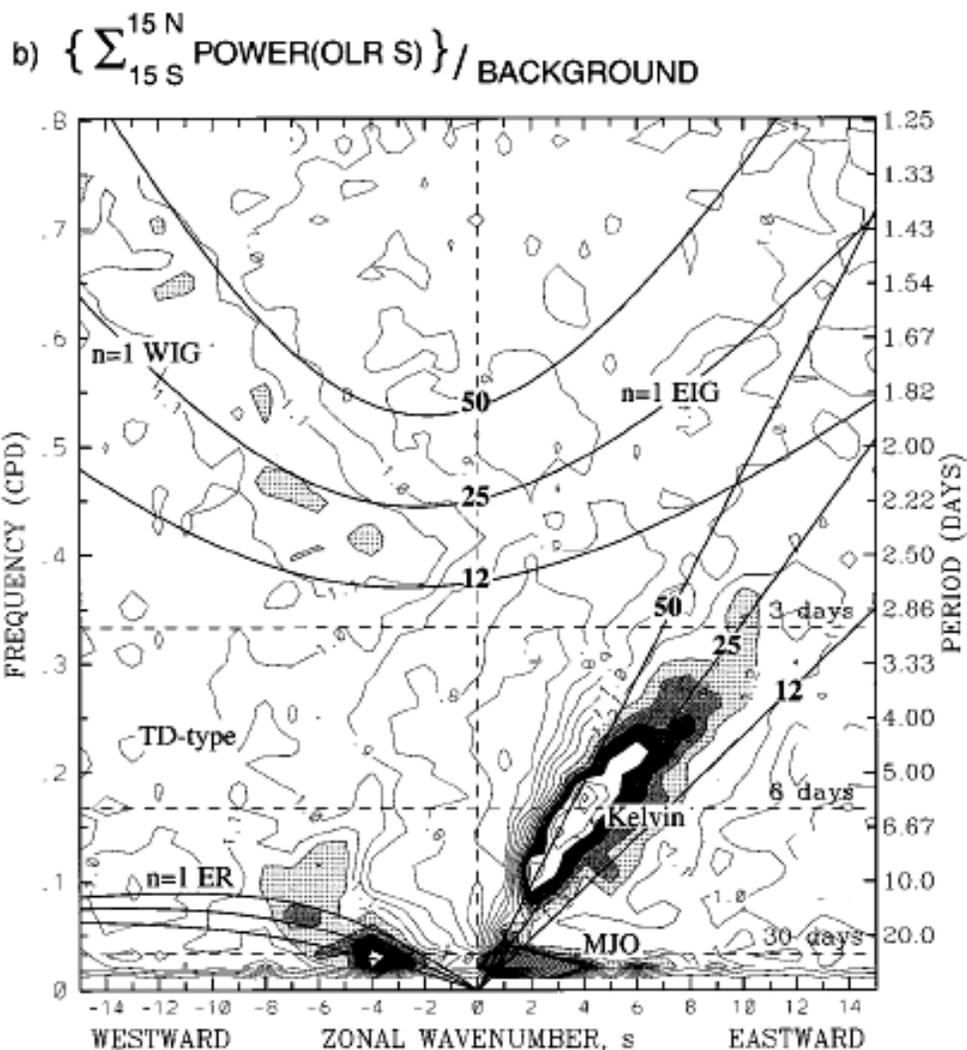


Figure 4.12: After Wheeler and Kiladis (1999). Symmetric component of OLR. Contour interval is 0.1, and shading begins at a value of 1.1 for which the spectral signatures are statistically significantly above the background at the 95% level (based on 500 dof). Superimposed are the dispersion curves of the even meridional mode-numbered equatorial waves labeled for the various waves of interest in the present study. Frequency spectral bandwidth is 1/96 cpd.

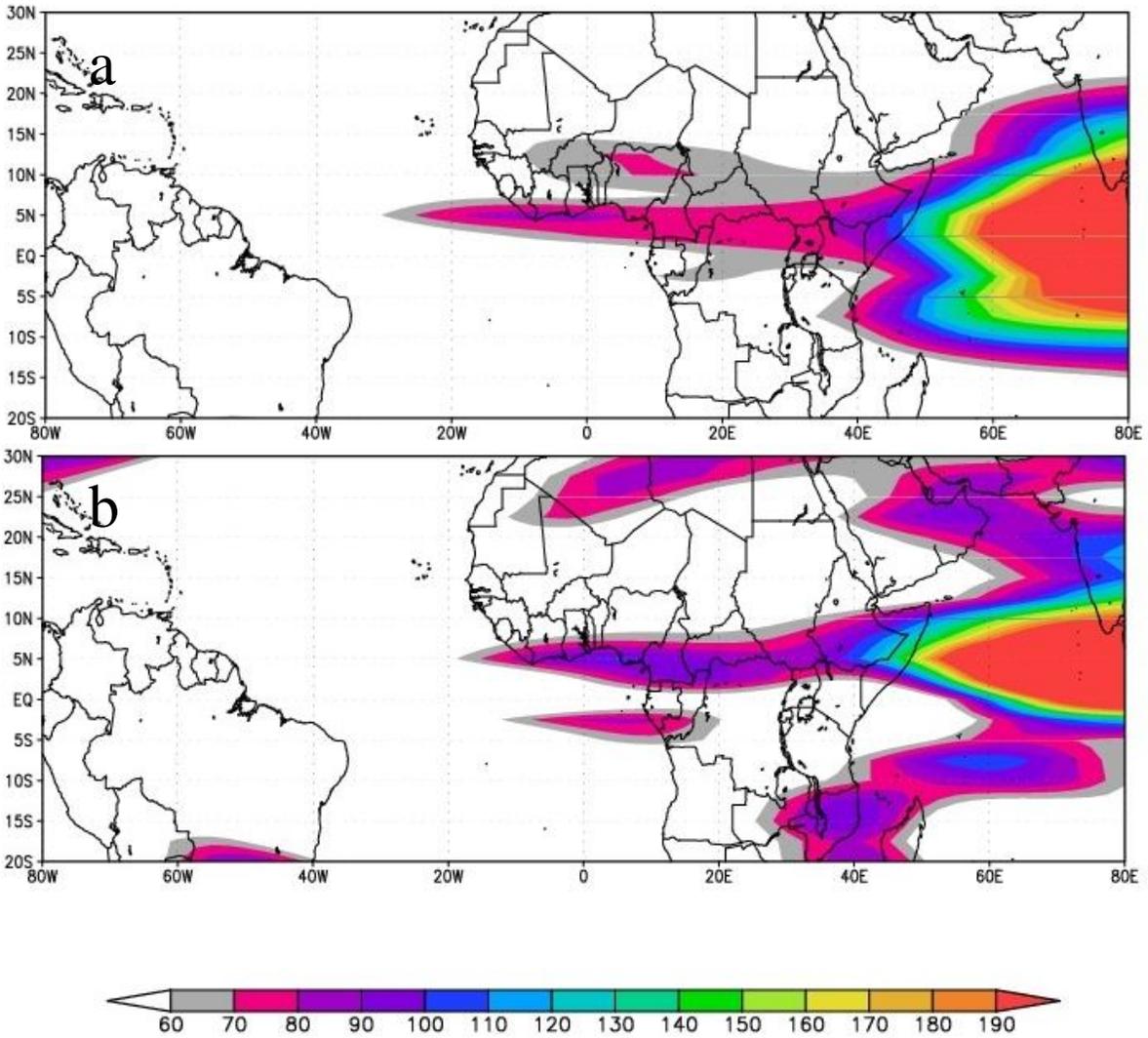


Figure 4.13: MJO-filtered OLR variance ($\text{W m}^{-2})^2$ for (a) spring 2000-2009 and (b) 2009.

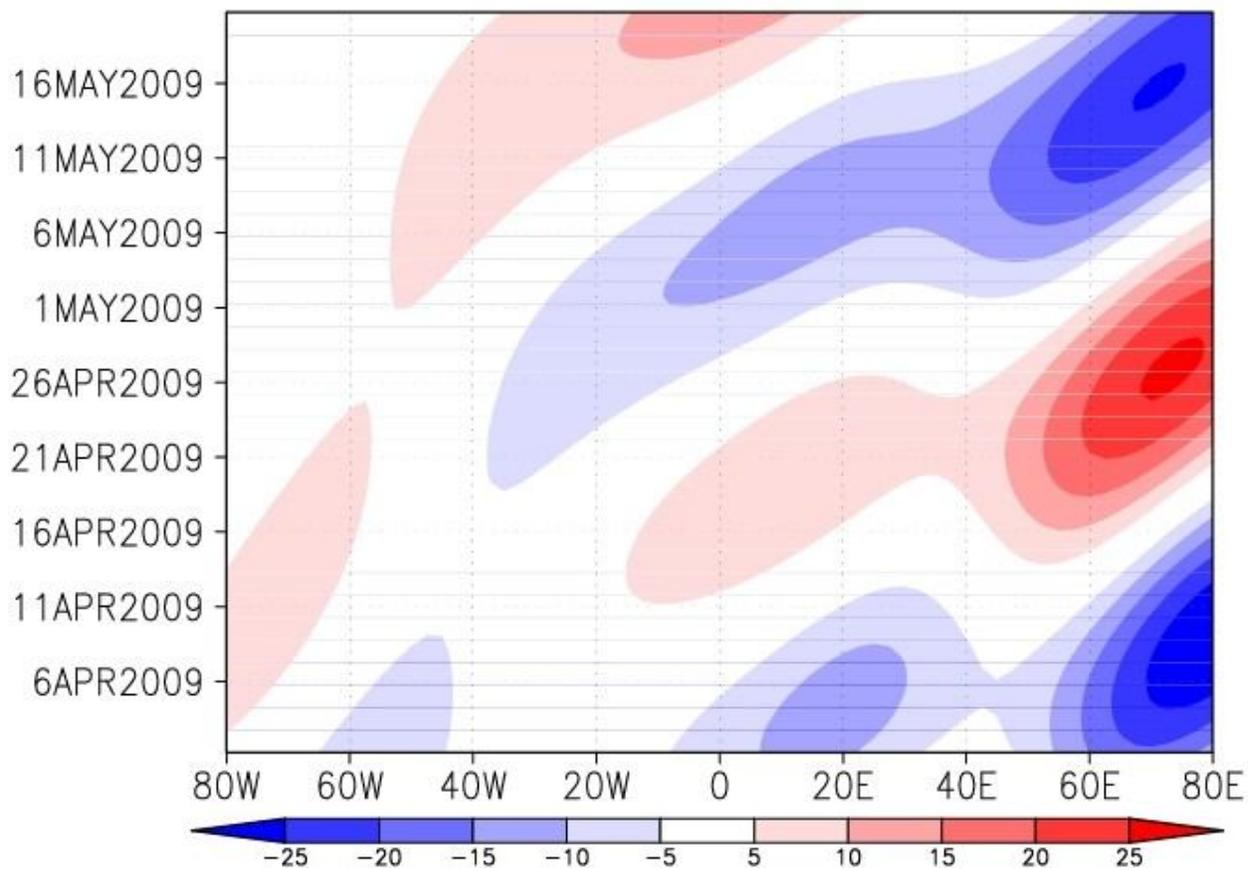


Figure 4.14: MJO-filtered OLR (W m^{-2}) averaged for 2.5°S to 7.5°N from 80°W to 80°E for the period April 1 – May 20 2009.

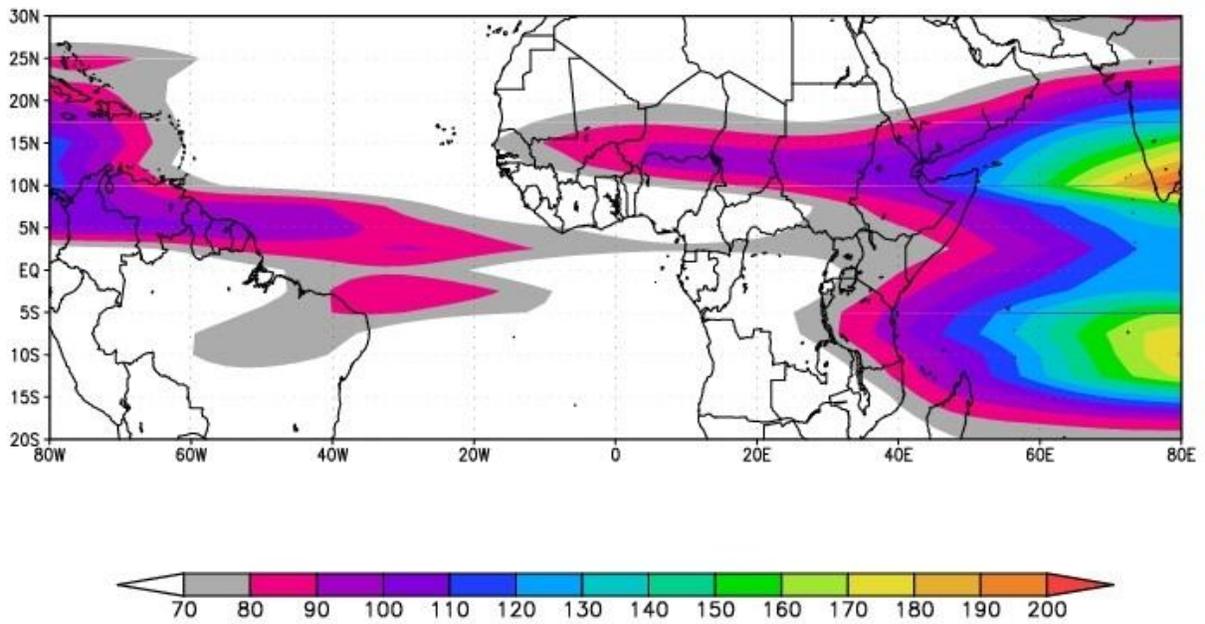


Figure 4.15: Equatorial Rossby wave filtered OLR variance for March 15 – June 15 averaged for the 2000-2009 period.

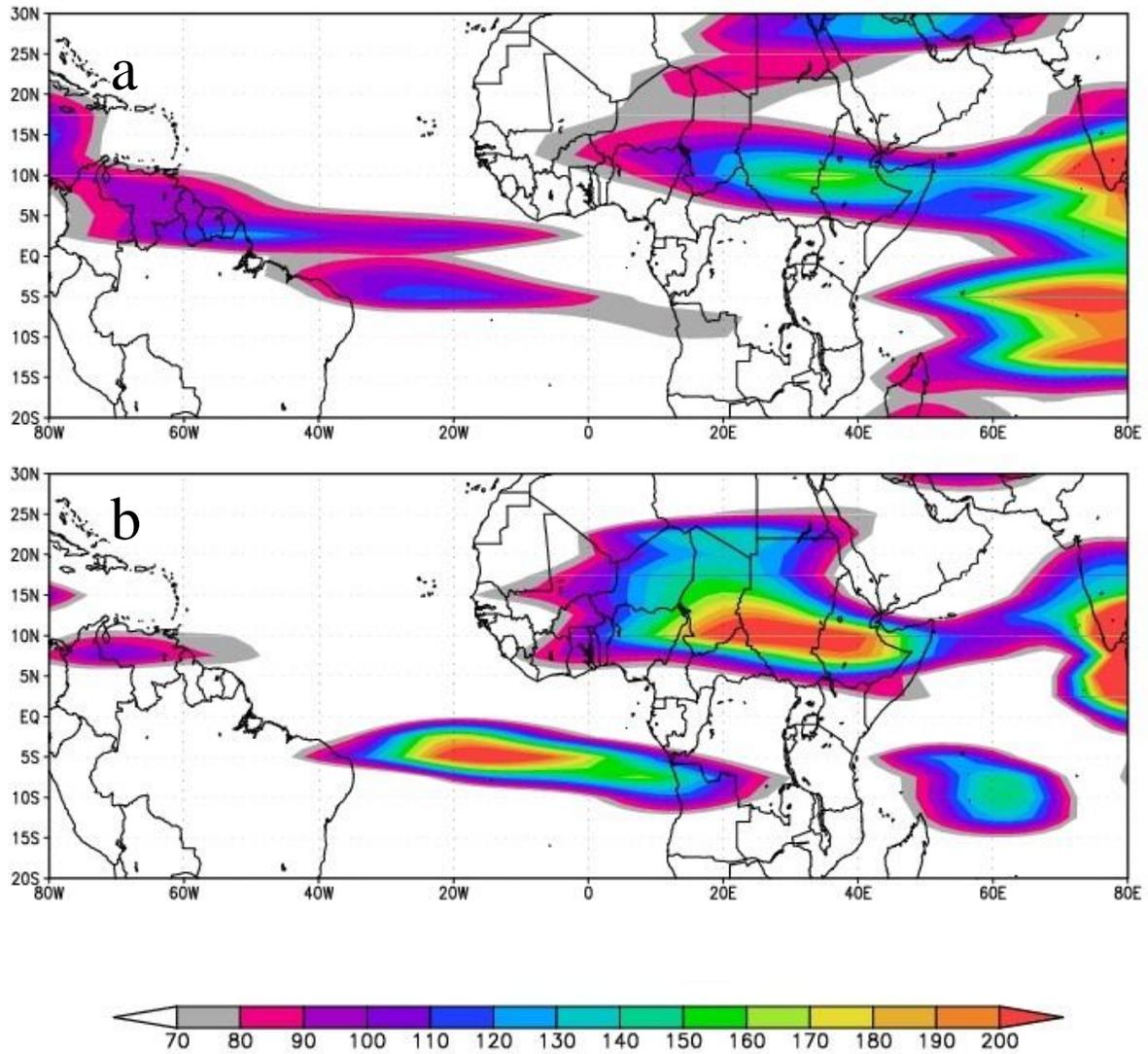


Figure 4.16: Equatorial Rossby wave filtered OLR variance $(W m^{-2})^2$ for (a) April and May 2009 and (b) April 20 – May 20 2009.

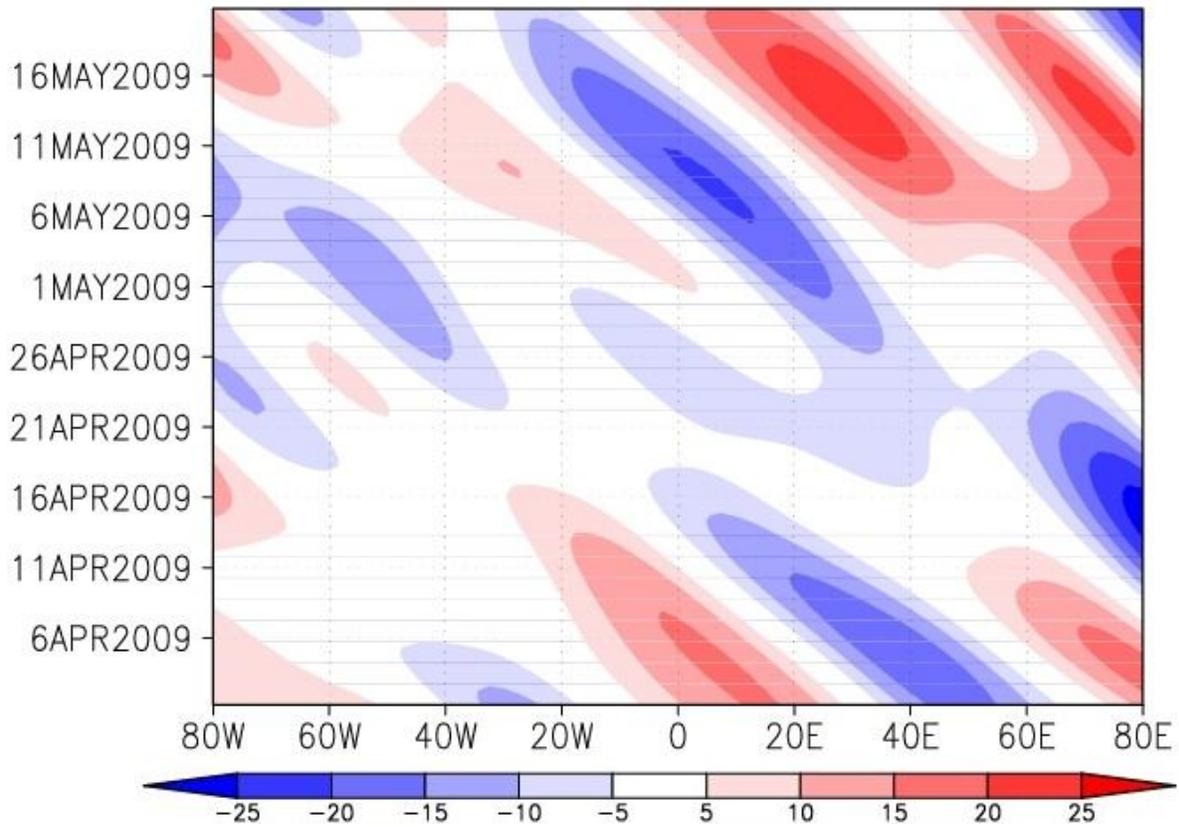


Figure 4.17: Equatorial Rossby filtered OLR (W m^{-2}) averaged for 12.5°N to 15°N from 80°W to 80°E for the period April 1 – May 20 2009.

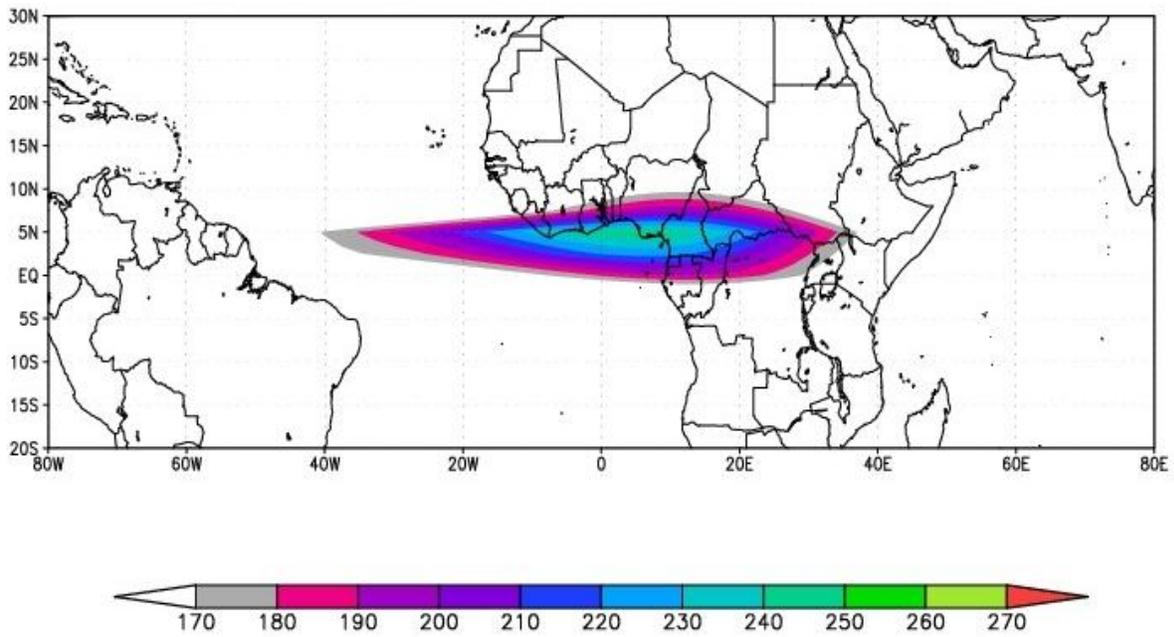


Figure 4.18: Kelvin wave-filtered OLR variance for March 15 – June 15 averaged for the 2000-2009 period.

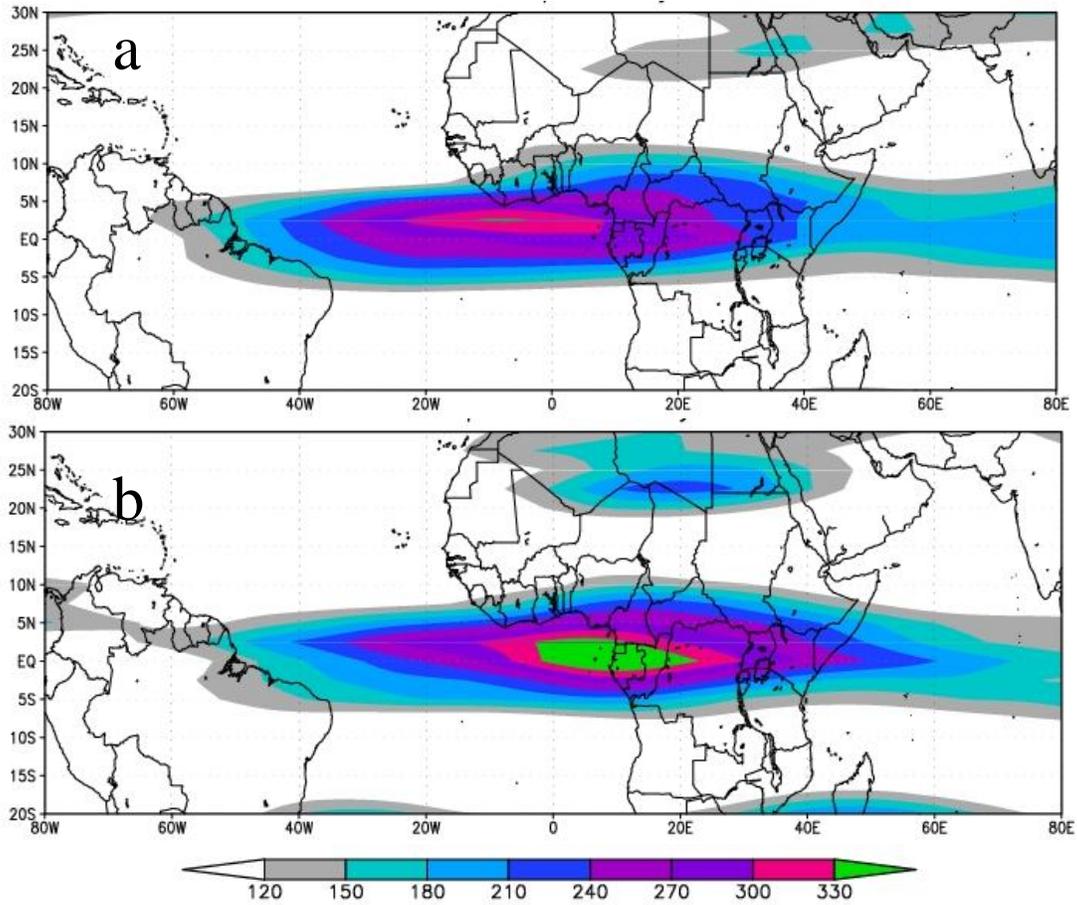


Figure 4.19: Kelvin wave filtered OLR variance (W m^{-2}^2) for (a) April and May 2009 and (b) April 20 – May 20 2009.

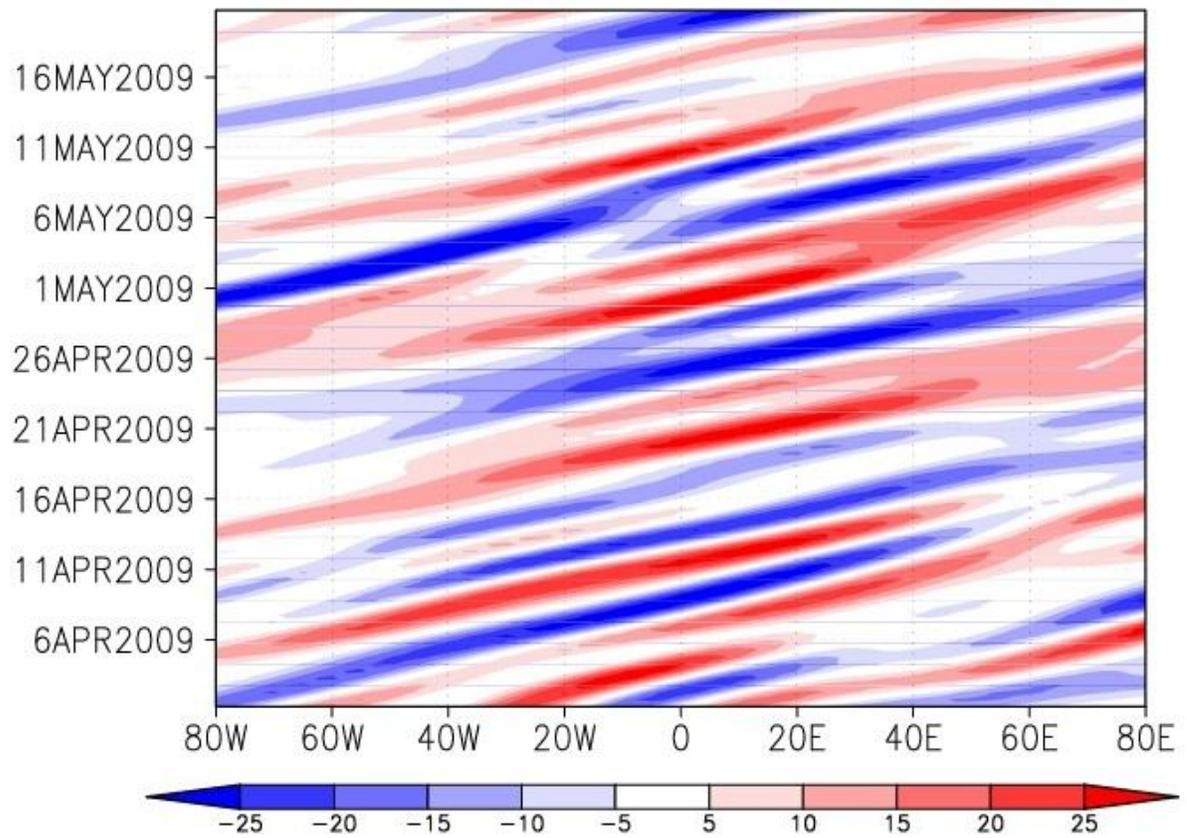


Figure 4.20: Kelvin-filtered OLR ($W m^{-2}$) averaged for 2.5°S to 7.5°N from 80°W to 80°E for the period April 1 – May 20 2009.

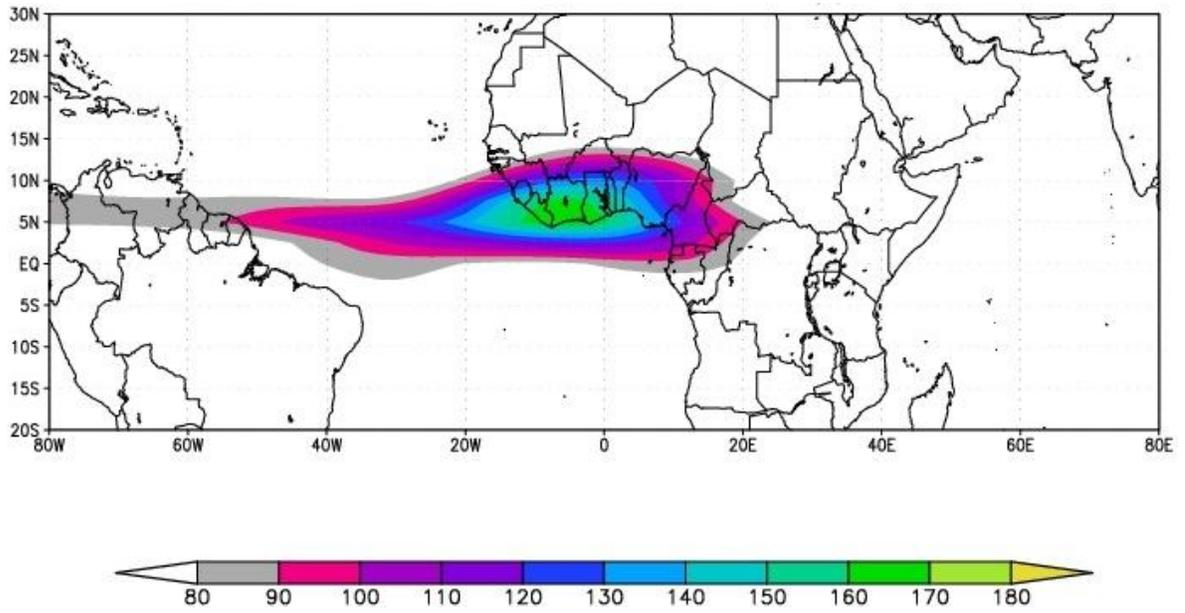


Figure 4.21: TD-type wave-filtered OLR variance (W m^{-2})² for March 15 – June 15 averaged for the 2000-2009 period.

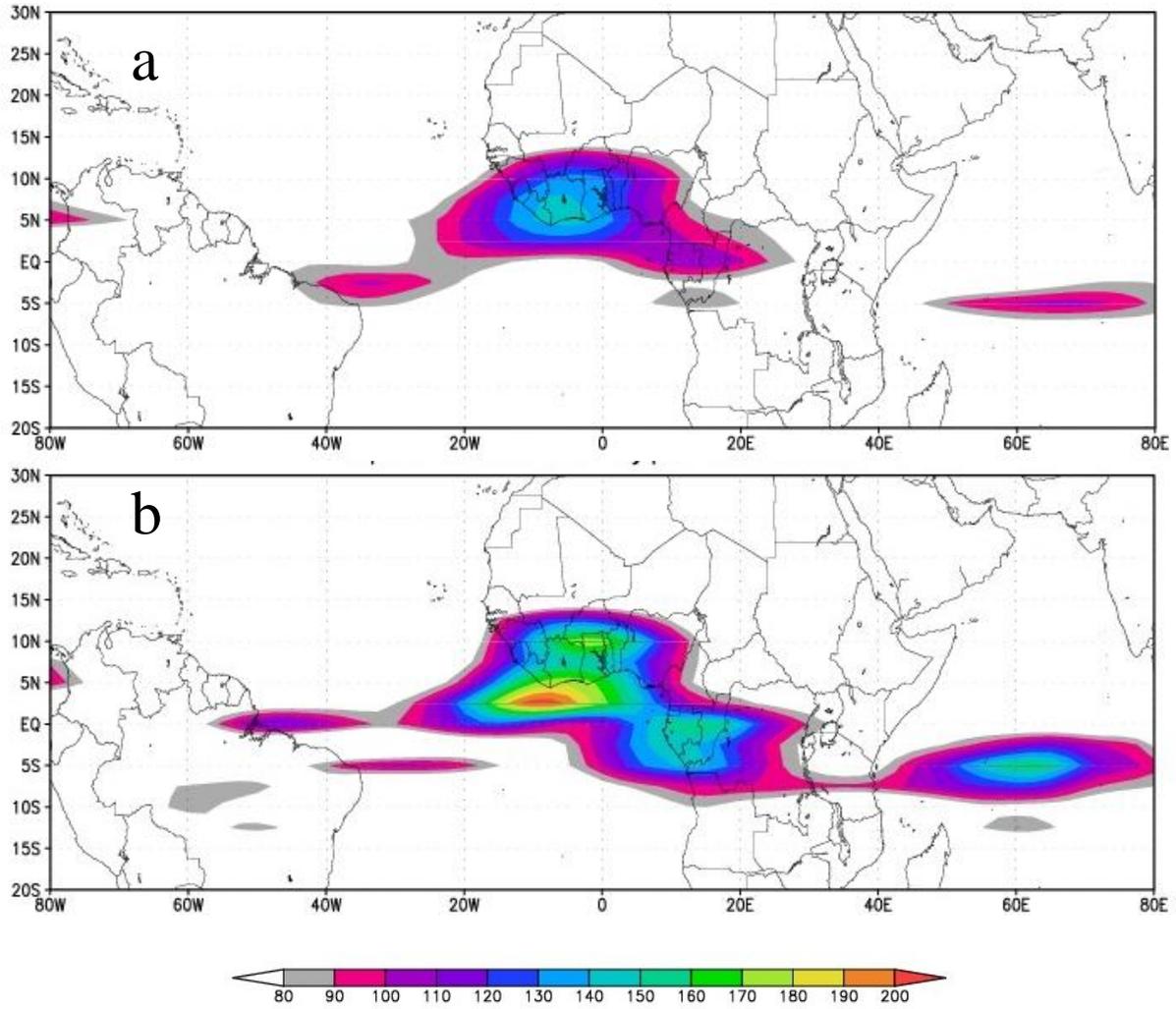


Figure 4.22: TD-type variance (W m^{-2})² for (a) March 15 – June 15 2009 and (b) April 2009.

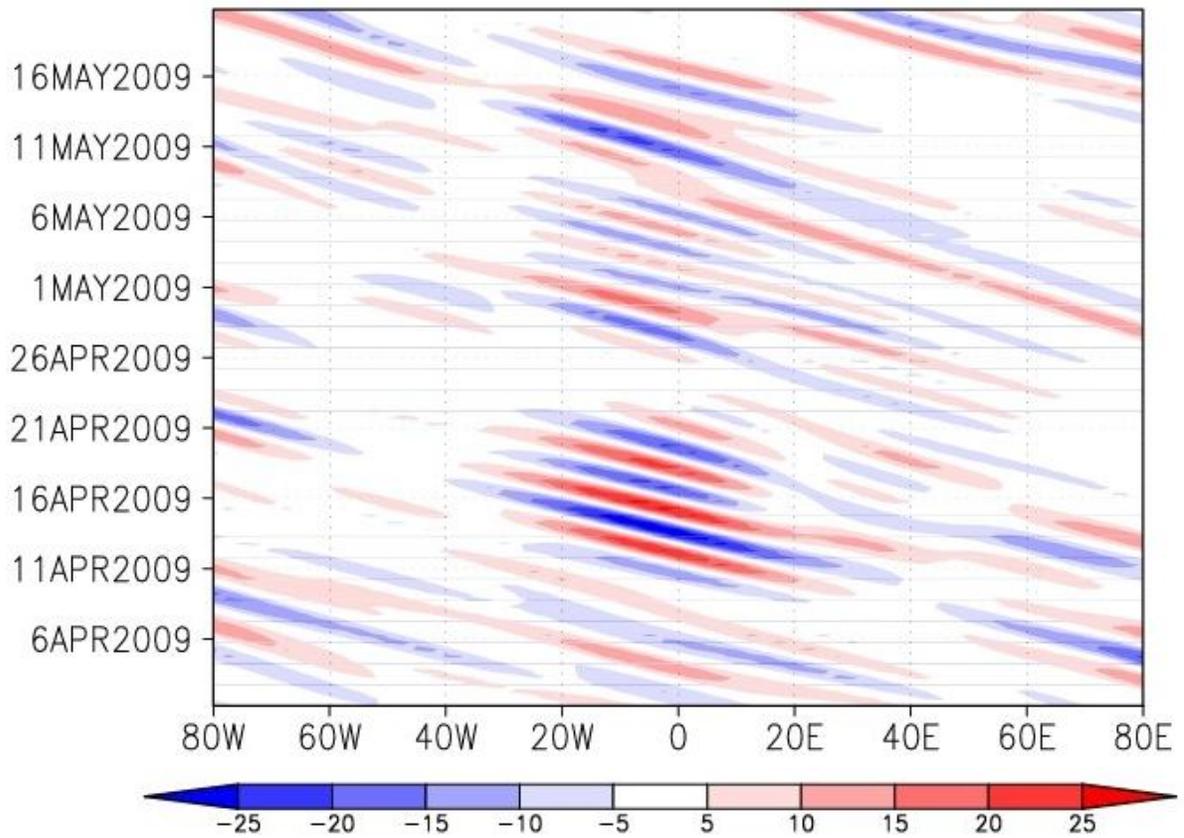


Figure 4.23: TD-type filtered OLR (W m^{-2}) averaged for 5°N to 10°N from 80°W to 80°E for the period April 1 – May 20 2009.

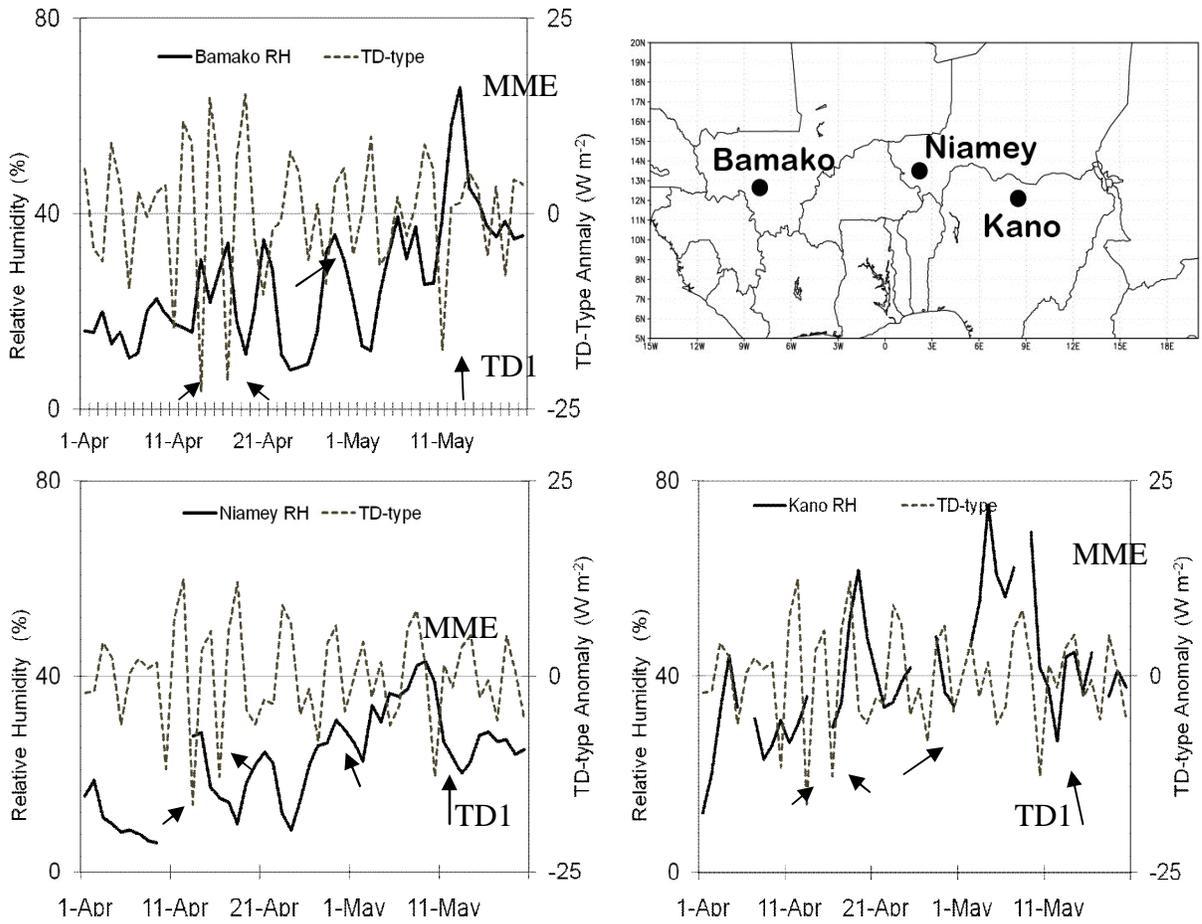


Figure 4.24: Observed relative humidity (RH, %) and area averages of TD-type filtered OLR ($W m^{-2}$) at Bamako (top left), Niamey (bottom left), and Kano (bottom right) for the period April 1st – May 20th. Small arrows denote significant TDs found in Fig. 3.33. TD1 and MME are also labeled. A locator map is also shown for reference.

Chapter 5

Development and Propagation of a Moist Event during May 2009

5.1 Introduction

At the end of Chapter 4, the presence of strong moist pulses were shown to occur over the cities of Kano (Nigeria), Niamey (Niger), Bamako (Mali) during April and May of 2009 (Fig. 4.24) and it was postulated that they could be related to TD-type systems traversing the region. Exploring Fig. 4.24 further, it is clear that the strong moist event during early May (May Moist Event, MME) pushed the moisture content of the atmosphere far above the RH40 threshold for an elongated period of time (10 days in the observations at Kano). The question then arises as to whether these systems can modulate the moisture over West Africa and about their inherent predictability, with a direct application to meningitis efforts. The data from observations reveal that the MME is present throughout the width of our region of interest (Fig. 5.1). Note that the strength of the MME varies according to a location's proximity to the ocean and that the timing of the event has a clear westward progression (i.e. occurs in Niamey, the easternmost city, first). Further, the stations in Fig. 5.1 (Ouagadougou,

Niamey, Bamako) all reside within the Meningitis Belt and along with Kano reported incidences of the disease in 2009 (with the exception of Bamako).

The scale of the MME can be better appreciated in Fig. 5.2 with a Meteosat satellite photograph in the Infrared band on May 8 at 1800 UTC. Note that there are several important factors visible: i) cloud-cover and precipitation from the Gulf of Guinea (GOG) to the southern Sahel, ii) a strong convective signal over the GOG possibly associated with equatorial phenomena (e.g. Kelvin waves), and iii) a trail of clouds that extends from West Africa deep into the Mid-latitudes over the Arabian peninsula and beyond. Indeed, this particular system hints that it contains a wealth of information on interactions between the tropics and extra-tropics and its influence over Sahelian West Africa could have important implications for meningitis mitigation in the region. This chapter explores this system in detail and is structured as follows. Section 5.2 includes the data and methodology utilized. Section 5.3 focuses on the synoptic evolution of the MME in observations and reanalysis products. The possible impact of convectively-coupled equatorial waves is investigated in Section 5.4. Section 5.5 addresses the role of forcing from the extra-tropics, theoretical background and results. Further exploration of the MME along with a summary is presented in section 5.6

5.2 Data and Methodology

5.2.1 Datasets

Details on the various data sources utilized in this chapter are provided in Chapter 4, Section 4.2. Thus, for the sake of brevity, the data sources will only be listed along with the motivation for their application. The reanalysis data employed includes both NNRP and FNL. Data from FNL is used to investigate various dynamical fields associated with the MME given its higher resolution (compared to NNRP). Surface and upper air observations are used to validate reanalysis products and were acquired from the NOAA National Climatic Data Center (NCDC, <http://www.ncdc.noaa.gov/oa/climate/climatedata.html#daily>). The National Oceanic and Atmospheric Administration (NOAA) outgoing longwave radiation (OLR) data are used to represent large-scale deep tropical convection. Information from NNRP is employed in unison with OLR in the analyses given their compatible resolution. Daily data from the TRMM 3B42 products is used to characterize precipitation and cloud structure associated with the event. Finally, *Meteosat-7* images in the IR channel (10.8 μm) are utilized (such as Fig. 5.2) for comparative purposes.

5.2.2 Methodology

The nature of the MME, in terms of its spatial scale, requires a thorough exploration of the relative roles played by CCEW, mid-latitude systems and the background conditions. Thus, methods similar to those utilized in Chapter 4 apply to this chapter as well: spatio-temporal averages and anomalies to characterize background climate forcings and wavenumber–

frequency filtering on the NOAA OLR data following the method of WK99 to obtain MJO, Kelvin, ER and TD-Type signals. This technique is discussed in more detail in Chapter 4. space-time filtering technique (Section 4.2.2) to retrieve information on convectively-coupled equatorial waves (CCEW) from the OLR dataset.

The dynamics of extra-tropical forcing from the mid-latitude system in question is explored by analyzing the role of upper-level Rossby wave activity during this time period. Work by Kiladis (1998), Kiladis and Weickmann (1992a,b, 1997) and Tomas and Webster (1994) serve as a guideline for the analysis presented here: horizontal (850 and 200 hPa) and vertical structure as well as wave propagation. Moisture convergence at 925, 850 and 200 hPa is also analyzed.

5.3 Synoptic Evolution and Large Scale Forcing

The following two subsections provide an analysis of the synoptic evolution during the period 5-10 May 2009. The first portion of this subsection concentrates on the nature of the moist event in tropical West Africa within the observational record and the reanalysis products. The latter part places this event into the context of the large-scale circulation present during that time period and the background forcings that may have played a role in the development and propagation of this important feature.

5.3.1 MME in Observations and Reanalysis

5.3.1.1 Surface and Sounding Observations

Section 5.1 of this chapter described the recording of the MME throughout the width of Sahelian West Africa (Fig. 5.1). This was a convective event that propagated westward from 20°E in central Chad [20°E] to the coast of Senegal [18°W]. The bulk of the literature regarding convective systems and associated circulation patterns is generally reserved for the boreal summer and for the full extent of the WAM. A few studies have, however, investigated the variability of moisture during the heart of the boreal spring (Omotosho et al. 2000, Ati et al. 2002, Sultan and Janicot 2003, Nguyen and Duvel 2008, Lélé and Lamb 2010). For example, Lélé and Lamb (2010) postulated that the location of the ITF in the month of April could be used as a predictor for the advancement of the leading edge of the southwest monsoon flow into West Africa during the May-June period. Sultan and Janicot (2003) used a slightly different approach as they diagnosed this important dynamical feature as one where the first isolated precipitation systems occur ahead of the WAM.

Evidence for the moisture pulse associated with the MME can be found in atmospheric soundings in the lower levels of the atmosphere (925 hPa). Figure 5.3 displays sounding data for water vapor mixing ratio (g/kg) over Agadez [17.0°N, 8.0°E], Niamey [13.5°N, 2.2°E] and N'Djamena [12.1°N, 15.0°E]. Note the strong moist pulse early in the period over N'Djamena (station furthest east) occurring at 0000 UTC on May 7. There is a smaller but noticeable spike in the drier (northern Sahel) Agadez station at 1200 UTC on May 8. Finally, Niamey sees a small spike on May 9. Although continuous data for all the desired variables

is notoriously hard to attain, some of the more reliable stations such as Niamey provide important information such as mean sea level pressure (MSLP). Evidence for a low pressure center associated with the MME is presented in Fig. 5.4. Along with Niamey, data is plotted for Ouagadougou [12.4°N, 1.5°W] and Tambacounda [13.8°N, 13.7°W]. A clear dip in MSLP is present in both Niamey and Ouagadougou on May 9, which corresponds with the spike in moisture at 925 hPa in Fig. 5.3. Also, notice that the pressure falls in Tambacounda in the far western portion of our domain as the MME system progresses to the Atlantic coast of Senegal [18°W]. It is also important to state that the dates of May 7 and May 9 have particular implications in terms of concurrent synoptic phenomena and will be addressed in detail in subsequent sections.

5.3.1.2 Precipitation

The magnitude of the MME can be better appreciated in terms of precipitation in Fig. 5.5a using data from the 3B42 daily TRMM product (see Section 4.2 in Chapter 4 for details). Note that significant amounts of precipitation (>5 mm) reach as far north as Agadez and significant rainfall totals stretches westward to the city of Bamako in Mali. Places like Niamey, N'Djamena and Ouagoudogou are all deep within the envelope of precipitation, which can also imply increased humidity where dry season conditions had been prevalent until the MME. Using the Hovmoeller time-longitude technique further elucidates the westward propagation of the event (Fig. 5.5b). In this figure, daily precipitation totals are tracked back from 20°E on May 1 to 15°W by May 16.

5.3.1.3 Local Circulation and Moisture in the Reanalysis

The spatial scale of moisture fields associated with this particular event as well as the dearth of observations throughout the region requires the exploration of other datasets, such as reanalysis. The strength of the monsoon circulation is known to experience a distinct diurnal cycle, whereby monsoon-like conditions penetrate far inland during nighttime and retreat closer to the coast during the day. Within this cycle, the heat low peaks in the afternoon, given weak surface winds due to the turbulent boundary layer, and the moist southwesterlies are strongest in the morning (Parker et al. 2005). Previous studies (e.g. Knippertz and Fink 2008) opted to construct surface maps at 1200 UTC using observations and taking advantage of the daytime coverage. Given the scope of the present study, however, and the need to know the average humidity for a given day, reanalysis information is deemed more appropriate, with the mean conditions for the day as the variable of choice. Another motivation for this selection is the nature of some of the datasets utilized (i.e. OLR, TRMM), which are daily or bi-daily in nature.

Further corroborating with precipitation values and surface observations is the nature of circulation associated with the MME. Figure 5.6 presents a series of synoptic maps of the main region of interest: 20°W-30°E and 5°N-20°N during May 5 – 11. Within this window is the entirety of the Sahel plus coastal regions for perspective. Also included are surface winds (10m) and the RH40 isoline in order to track surface humidity.

At the beginning of synoptic development on May 5 (Fig. 5.6a), the RH40 isoline reaches deep into the Sahel east of 15°E, covering much of southern Chad and all of Nigeria. On May 6 (Fig. 5.6b), the moisture east of 15°E shifts further south but the overall state of humidity remains above 30mm of precipitable water. Also note that the RH40 line has drifted slightly northward (~1° latitude) but it remains south of cities like Ouagadougou, Bamako and Niamey. Moisture in northern Chad and Sudan increases once again on May 7 (Fig. 5.6c) with high surface humidity (RH40) over northeast Chad. Strong cross-isobar northwesterly flow is also present in the northeast corner of the domain. On May 8, increased southerly flow into eastern Niger forces moisture northward at 15°E (Fig. 5.6d). This is also reflected in the RH40 line, which reaches its northernmost point at this time. The westward advancement of the MME is clearly visible on May 9 (Fig. 5.6e) as the eastern edge (east of 15°E) of the event becomes drier with stronger Harmattan winds and the central portion of the domain (5-10°E) becomes moister. Areas west of 5°E also become much drier, especially in places like Bamako, Mali (<10 kg m⁻² precipitable water). This figure also shows stronger monsoonal flow in south central Niger and a corresponding northward shift in the RH40 line.

As the MME continues its westward track (May 10, Fig. 5.6f), the return flow over much of Chad, Sudan, and eastern Niger becomes stronger and brings increasingly drier air into the region. The moist pulse is over the city of Niamey in western Niger and its effect can now be felt over most of Burkina Faso as well. Note that the RH40 has crossed over Niamey and is consistent with surface observations (Fig. 5.1). Finally, on May 11 (Fig. 5.6g), the MME reaches the western Sahel and induces an increase in humidity over southern Mali (Bamako).

Note also on this figure that much drier conditions are prevalent for the eastern two thirds of the domain as the Harmattan increases its influence over the region.

The westward propagation of moisture is shown in Fig. 5.7 with a Hovmoeller time-longitude plot of daily average of total atmospheric column precipitable water (kg m^{-2}) along 15°N as given by (5.7a) NNRP and (5.7b) FNL from 40°E to 40°W and spanning from 1 April, 2009 to 31 May. Latitude 15°N was chosen given the relative dryness of the environment during this time of the year along this latitude throughout the width of the continent, which allows for clarity of the moist event. The figure shows a clear westward propagation with markedly high amounts of moisture, especially at 10°E . The increased southerly flow associated with the MME is shown in Fig. 5.8, where the meridional component of the wind at 850 hPa is plotted using a time-longitude Hovmoller plot. The MME is noticeably prevalent in this figure as it starts at 20°E with strong southerly flow and continues westward in time to the Atlantic coast of West Africa on May 14.

5.3.2 Large-scale Circulation and Anomalies

The large-scale environment constitutes another important scale in the analysis of the MME. Details on the underlying climate anomalies were provided in Chapter 4: strong moist anomalies over the eastern Sudano-Sahel and Darfur Mountains [10°N - 15°N , 20°E - 40°E] and an anomalous low pressure center at 925 hPa over the eastern Sahara [20°N , 23°E] (Fig. 4.3d). Also discussed in Chapter 4, were CCEWs active during the time of the MME. This section explores climate anomalies at the daily scale relevant to the MME.

5.3.2.1 Daily Moisture Anomalies

Shorter-term moisture anomalies elucidate more information to support the evidence of this major system. Figure 5.9 shows a sequence of plots of the progression of the moisture anomaly through the width of the region. A 3-day running mean was chosen for each day beginning on 2 May through 15 May 2009 due to the documented meningitis threshold in humidity of at least three days to break the Harmattan regime (Besancenot et al. 1998). Notice how the beginning of the period is marked by strong negative moisture anomalies over much of West Africa with a small amount of positive anomalies over Nigeria, southern Chad and western Sudan (Fig. 5.9a). Positive anomalies undergo intensification in the running mean through May 5 (Figs. 3.9b,c) as their area of coverage expands. Also notice positive anomalies over the eastern Mediterranean and northeast Africa (Egypt) in association with a mid-latitude disturbance. On May 6 (Fig. 5.9d), a diagonal extension of moist anomalies from its center over the nation of Chad spreading northeast into the Red Sea; this also continues to occur from May 7 through the 10 (Figs. 3.9e-h). The strong moist anomalies begin a northwestward expansion on May 9-10 (Figs. 3.9g,h) and on 11 May (Fig. 5.9i) it spreads into western Niger whilst shrinking in size. At the same time, the strong positive anomaly over Nigeria-Chad-Sudan (east of 10°E) subsides and becomes negative on 12 May (Fig. 5.9j). As the westward-propagating anomaly moves towards the Senegalese coast through Mali and Mauritania, strong negative anomalies build over much of the region from Nigeria to the Sudan (Figs. 3.9k).

Another vantage point of the strong positive anomaly during the beginning of the period (May 2-11) is presented in Fig. 5.10 using time longitude Hovmoller diagrams. Starting with conditions averaged for 10°N latitude from 20°W to 40°E on Fig. 5.10a, we notice the aforementioned positive anomaly that ranges from 5°E to 35°E and is stationary in the 3-day running mean until May 10. The westward propagation of this feature is more prevalent at 12.5°N (Fig. 5.10b) starting on May 10 from 5°E to 20°W. Also notice how the positive anomaly strengthens on May 13 at 10°W. At 15°N (Fig. 5.10c), there is a clear connection between the positive anomaly over the eastern Sahel and the westward progression of this feature beginning on May 9. We find that it is at this latitude where the anomalous moisture has the highest impact for the duration of the MME. Also consider that the impact of the MME was present farther north (17.5°N, Fig. 5.10d), with a clear westward progression starting on 9 May.

5.3.2.2 Large-scale Synoptic Environment

The view of the MME is now expanded in the context of the large-scale synoptic situation in order to explore other factors that may be driving the westward progression of the moisture anomaly. In Fig. 5.11 we show the large-scale synoptic evolution of conditions during the MME (May 5 – 11). The figures contain 3-day running mean moisture anomalies (shaded, as in Figs. 3.10 and 3.11), wind vectors at 200 hPa to indicate upper level atmospheric flow, geopotential height at 925 hPa to delineate features such as the SHL and other dynamical

components, and the 925 hPa 0 ms⁻¹ isoline that represents the location of the ITF (see Sultan and Janicot 2003).

At the beginning of the period (May 5, Fig. 5.11a), upper level flow is nearly zonal for most of North Africa and there exists a positive diagonal moist anomaly (as in Fig. 5.9) stretching from Nigeria to the Arabian Peninsula. The geopotential height also shows three smaller centers of low pressure within the equatorial trough (Mali, Niger and Chad). On May 6 (Fig. 5.11b), an upper level trough begins to form off the Mediterranean coast of Libya and the geopotential height shows a low pressure center in southern Algeria and northern Niger near the Haggar Mountains. On May 7 (Fig. 5.11c), the upper level trough of extra-tropical origin digs further into Libya into extreme northern Chad and induces a northward shift in the moist anomalies. Also notice how the ITF reaches farther north into Mali and Niger but humidity over Mali is still seeing negative anomalies. May 8 (Fig. 5.11d) sees a continuation of the upper level trough coupled with a westward shift of the moisture anomalies as well as a low pressure center over northern Niger. On May 9 (Fig. 5.11e), the upper level system begins to move eastward and a low pressure center in the 925 hPa geopotential field moves westward pulling along the moist anomalies. Also in this figure we can discern how the low-level circulation is interacting with the negative anomalies to its east as it brings northerly winds into the region while the eastern edge has more southerly flow that transports moisture into the Sahel. May 10 and 11 (Figs. 3.11f,g) portray the dissipation of the system as the moist anomalies weaken in their westward shift over the western portion of the northern

Sahel (Mali, Mauritania). At the same time, the extra-tropical disturbance has shifted farther east and north taking the moist anomalies into the Arabian Peninsula.

5.3.2.3 Qualitative Analysis

Having provided some of the synoptic details on the MME, it is also essential to view the system in an unfiltered status (i.e. imagery) to gain a different perspective on the factors at work. This subsection provides qualitative details on the development and propagation of the MME and its various components.

The cloudiness associated with the MME is shown in Fig. 5.12 with the aid of *Meteosat-7* IR images at 1800 UTC. The time 1800 UTC was chosen since this is the time of highest convective activity of a given day. Note the strong low pressure center over Asia Minor in the northeastern part of the image for May 4. On May 5, the characteristic tropical plume (TP) form; this feature was found repeatedly in previous tropical-extratropical interaction studies such as McGuirk et al. (1988) and Knippertz and Fink (2008). On May 7 and 8 the TP strengthens, aided by the trough as the systems reaches, and possibly interacts, with the anomalous moisture over the eastern Sudano-Sahel. The westward-propagating Sahelian feature associated with the MME is clearly visible on May 9 – May 11. Worth noting as well is the large amount of cloudiness over the GOG. This is in association with a convectively-coupled Kelvin wave that will be discussed in more detail in Section 5.4.

Another vantage point to further scrutinize the progression of the event is achieved through the use of daily 3B42 TRMM-derived precipitation totals (mm) (Fig. 5.13). The base

of the analysis with this dataset was set to 0 mm in order to elucidate the structure of convection and associated cloud cover. Most notable in this view of the MME is the clear impact of the mid-latitude short wave associated with the upper-level trough (Figs. 5.13c,d). One possible impact of the extratropical influence in this event could be the extension in the latitudinal range of the westward propagation of the MME, given the strong amount of convection near [15°N, 20°E]. It is postulated that this enhancement of convection farther north at the edge of the Sahel which, coupled with the more southerly component of the MME, helped the event cover a much larger latitudinal range and brought about significant changes in surface moisture.

Further corroborating with the above analysis is a view of the event using NCEP OLR in Fig. 5.14. The vantage point is widened with this dataset in order to see how the extratropical feature may also be exerting influence on CCEWs. Notice the large signature of convection in the OLR field that traverses the width of the Atlantic from the Brazilian Amazon Basin to equatorial Africa. Enhancement of convection at [15°N, 20°E] in association with the extratropical feature is again visible in Fig. 5.14c-e for May 6 – 8. One other important occurrence with the MME is the development of an OLR structure reminiscent of the Gill solution (Gill 1980) found in composite analysis by M04 and J09 for the intraseasonal structure of convection during the boreal summer and G09 during the spring. It is argued that the mid-latitude system aided in the development of the structure by initiating the TP and enhancing the latitudinal extent of the OLR structure.

5.3.2.4 Summary

The preceding analysis has highlighted the complexity of the MME and the potential impact of this large change in moisture throughout the breadth of the Sudano-Sahel region. Figure 5.9 hints at a possible connection between this system and a mid-latitude event over northern portions of the continent. It is conceivable that this system may have contributed to the evolution of the MME and this possibility is supported by previous work on tropical-extratropical interactions (Winstanley 1970; Flohn 1975; Kiladis 1998; Fink and Knippertz 2003, Knippertz 2005, Knippertz and Fink 2008). The larger-scale westward propagation of the event, including the semi-stationary positive anomaly over the Nigeria-Chad-Sudan region (Fig. 5.11) also suggests that there may be an equatorial component to the event. The westward propagation of the large-scale moist anomaly was estimated at 3.88 ms^{-1} . In the following sections of this work the roles of the mid-latitude system is explored as well CCEWs and the propagation of the MME on shorter timescales.

5.4 Convectively Coupled Equatorial Waves

The occurrence of westward-propagating features first became evident with a forecasted event during mid-May (described in Chapter 4). This prompted an analysis of humidity in in-situ observations to validate the forecast (Fig. 2.35 in Chapter 2). Inspecting figures 5.12 – 5.14, it is found that there is a strong signature of convection in the GOG that could be related to eastward-propagating equatorial disturbance. Analysis of unfiltered 2009 NCEP

OLR data, averaged over $2.5^{\circ}\text{S} - 7.5^{\circ}\text{N}$ and subtracted from the 2000-2009 mean, reveals the signature of this eastward propagating feature (Fig. 5.15).

As discussed in Section 4.4.2 in Chapter 4 and as can be seen on Fig. 5.15, an MJO and an associated Kelvin wave are observed traversing the region during this part of May 2009. Also at this time, a synoptic-scale moist event starts its westward propagation along 15°N from the 20°E longitude (Figs. 5.7 and 5.8). It was previously argued in Chapter 4 that several features were present during the time of the MME: a weak MJO, a coherent Kelvin wave, an ER and a TD-type system. The latter was shown to be occurring alongside moist events throughout the observations (Fig. 4.24 in Chapter 4). It is thus imperative that the various components of CCEWs' influence during the MME be analyzed in more detail. In the following subsections, individual waves are analyzed in various dynamical fields and compared to their theoretical counterparts.

There exists another peak of interest visible in the domain of westward propagating signals between periods 2 and 6 days and zonal wavenumbers 6 to 20 with average speeds of 8 ms^{-1} . Kiladis et al. (2006) showed that this "TD" signal represents easterly waves in Africa and, as shall be seen in the course of subsequent sections, this constitutes a major component of the MME. Also on this plot is the Kelvin within a period of 2.5–17 days, and eastward wavenumber 1–14, as in SK02, WK99 and WKW00.

Two other features of interest can be found on Fig. 5.22: MJO and Equatorial Rossby (ER). The MJO is discernible in the figure as an eastward propagating system that is separate from the Kelvin wave signal even at wavenumber 1, with a spectral gap in the power ratio

occurring at a period of about 25 days. Although we don't separate ER waves directly in our analysis, we propose that they may still influence the MME through the slower westward propagation of the moist anomaly found in section 3.3.2. Globally, the $n=1$ ER wave activity explains somewhat less convective variance than the MJO or the convectively coupled Kelvin wave (WK99), yet over tropical Africa these systems can influence important modes of intraseasonal variability of convection (Janicot et al. 2009, hereafter J09).

5.4.1 Kelvin Waves

In Chapter 4, it was shown that the months of April and May in 2009 were characterized by a wide belt of Kelvin wave activity (variance, $(W\ m^{-2})^2$) that stretched from the GOG into southern portions of Sahelian West Africa (Fig. 4.19a). One Kelvin wave, in particular, had a significant influence on convection during the MME and we can see its signature as the fast, eastward-propagating feature in Fig. 5.15. Kelvin waves were retrieved from the OLR information using the WK99 technique and the latitudes of highest activity ($0^{\circ}N$ - $5^{\circ}N$) during April 20 – May 20 (Fig. 4.19b) were chosen in order to investigate individual waves at their peak. A strong, coherent Kelvin wave (hereafter K1) emerged from the dataset (Fig. 5.16). This plot shows that K1 emerges from South America [$80^{\circ}W$] on ~30 April and, as it reaches the eastern Atlantic ($\sim 30^{\circ}W$) on May 3, a secondary Kelvin wave (hereafter K2) forms within the GOG. This secondary wave strengthens as it reaches equatorial Africa ($\sim 10^{\circ}E$) before the first wave.

Further investigation of the Kelvin waves reveals that both K1 and K2 have speeds estimated at 16-17 m s⁻¹, consistent with past research (Yang et al. 2007; Kiladis et al. 2009). Mekonnen et al. (2008) also found that the phase speed of the Kelvin wave changes as it propagates across different regions of the globe. The waves are faster over the central and eastern Pacific (~24 m s⁻¹) and slow down over Africa (14 m s⁻¹), thus placing K1 and K2 within the envelope of Kelvin wave definition. In WKW00, it was surmised that the lowering of speed of the waves is suggestive of stronger coupling between the dynamical and convective signatures. Additionally, Mekonnen et al. (2008) also observed that the wave periodicity decreased from about 8 days over the Pacific and the Atlantic to about 4 days over central and eastern Africa, and this is evident as K1 begins to interact with the continent at 10°W.

It is also found that K1 was much stronger and also quite coherent as it propagated from the Indian Ocean in mid April (this will be shown in section 5.4.3), which motivates further investigation of K1's impact in other meteorological variables. One of the primary influences of Kelvin waves, in general, is the development of enhanced convection in the tropics. Figure 5.17 provides a time-longitude Hovmoller diagram of daily 3B43 TRMM-derived accumulated precipitation (mm) plotted for the period April 1 – May 20, averaged over 0°N - 7.5°N and spanning 80°W to 80°E. Notice the clear eastward progression of the precipitation in association with the Kelvin wave.

Kelvin waves are also present in wind, vertical velocity (ω) and divergence terms. The MME Kelvin wave, K1, is no different. When analyzing the ω , velocity potential (χ) and the

zonal wind at lower level (925 and 850 hPa) it is shown that the eastward signature of the wave is continuously present in all instances (Fig. 5.18). The velocity potential at 200 hPa (Fig. 5.18a) is a measure of the irrotational velocity and is indicative of strong convection in areas of divergence (Boer 1995; Molinari et al. 1997). This variable arises from the shallow water equations in Matsuno (1966):

$$\frac{\partial u}{\partial t} - \beta y u + \frac{\partial \phi}{\partial x} = 0 \quad (5.1)$$

$$\frac{\partial v}{\partial t} + \beta y u + \frac{\partial \phi}{\partial x} = 0 \quad (5.2)$$

$$\frac{\partial \phi}{\partial t} + c^2 \left(\frac{\partial u}{\partial x} + \frac{\partial v}{\partial y} \right) = 0 \quad (5.3)$$

where u and v are the perturbation velocities, $c^2(=gH)$ is the square of the pure gravity wave speed for a mean depth H and $\phi (=gh)$ is the perturbation geopotential where h is surface deviation. Matsuno (1966) also states that u , v and ϕ all have the factor $e^{i(kx-wt)}$. For a Kelvin wave, $v=0$ and the solutions for u and ϕ are:

$$u = U_0 \exp(-ay^2) \quad (5.4)$$

$$\phi = cU_0 \exp(-ay^2) \quad (5.5)$$

where $a = \beta/2c$ and U_0 is an arbitrary amplitude. In his derivation of χ , Hendon (1996) states that Kelvin waves propagate nondispersively eastward according to:

$$\omega = kc \quad (5.6)$$

and where the e-folding decay is given by:

$$Y_L = a^{-1/2} \quad (5.7)$$

The velocity potential (χ) is assumed to also have the factor $e^{i(kx-wt)}$ and is derived by expressing the horizontal divergence in terms of the Laplacian of χ , such that:

$$\nabla \cdot V = \frac{\partial^2 \chi}{\partial y^2} - k^2 \chi = ik \exp(-ay^2) \quad (5.8)$$

The solution thus becomes:

$$\chi = \frac{1}{4} \left(\frac{\pi}{a} \right)^{1/2} \exp(-i\pi/2 + k^2/4a) \times \left\{ \exp(ky) \left[1 - \operatorname{erf} \left(\sqrt{a}y + \frac{k}{2\sqrt{a}} \right) \right] + \exp(-ky) \left[1 + \operatorname{erf} \left(\sqrt{a}y - \frac{k}{2\sqrt{a}} \right) \right] \right\} \quad (5.9)$$

The eastward progression of this dynamical feature is consistent with the definition of Kelvin waves (e.g. Mekonnen et al. 2008). Values exceed $-9 \times 10^{-6} \text{ m}^2 \text{ s}^{-1}$ for this dynamical feature over the equator throughout the propagation of K1's convective phase.

Also consistent with χ is the ω field, which is defined as:

$$\omega = \frac{dp}{dt} \quad (5.10)$$

where dp is the change in pressure over time (dt). Strong upward motion ($< -0.14 \text{ Pa s}^{-1}$) is present in the mid troposphere (500 hPa) at the equator as given by the NNRP data (Fig. 5.18b) during the passage of K1 convective phase. Further, the zonal winds associated with Kelvin waves tend to be characterized by anomalous shift from easterlies to westerlies (WKW00). In Fig. 5.18c the NNRP zonal winds for 850 hPa display the clear signature of eastward propagation of this shift, which is averaged in this case for $2.5^\circ\text{S} - 7.5^\circ\text{N}$. When all

unfiltered fields are mapped together (Fig. 5.19), it is clear that all of the anomalies are collocated with the filtered OLR Kelvin signal.

Another view of the main Kelvin wave associated with the MME (K1) is further analyzed in its vertical extent in Fig. 5.20. This figure displays the strong vertical motion that is consistent with description of Kelvin waves in the literature (WKW00, Mounier et al. 2007). Also notice the subsidence to its immediate west and east (albeit only at more shallow levels of the troposphere for the eastward portion).

It is often advisable to show the general impact of Kelvin waves on actual convection over the tropics (e.g. Mounier et al. 2008). In this instance the influence of Kelvin waves on the overall NCEP OLR fields is displayed as a series of plots (Fig. 5.21). The analysis is centered on May 7, given the important increased convection over the whole of Africa on this date (t_0). This also coincides with the possible interaction occurring with the extratropics. Only negative values of Kelvin-filtered data are shown for clarity as well as lower numbers from the OLR ($< 260 \text{ W m}^{-2}$). At -4d, K1 is over northeastern South America [40°W], collocated with the positive Kelvin anomalies (the twice-daily Kelvin data was averaged into daily in order to match the NCEP OLR field). Convection increases over West Africa at -2d as a secondary Kelvin disturbance (K2) propagates through the GOG and approaches the coast of equatorial Africa [10°E , (Cameroon, Gabon, and Equatorial Guinea)]. K1, the primary Kelvin disturbance, has moved off the South American coast along with the highest area of convection. Also note that at -2d the structure of convection over the continent is reminiscent of the summertime 10–25-day signal of intraseasonal variability found by

Mounier et al. (2008). At t_0 this signal becomes even more prevalent as the convection reaches farther north into Senegal as well as into equatorial Africa (i.e. the Congo Basin). This event is echoed in J09's analysis of the 25-90 day cycle, in which they show the interaction between the MJO, Kelvin and ER signals. More resources will be devoted to this subject in Section 5.4.4 to elucidate whether this type of interaction is also occurring during the MME. At +2d, K1 has a large meridional extent that stretches it far north into Nigeria [12°N] along with the more intense convection in the unfiltered OLR. This particular date also marks another potentially important interaction (phasing) with a TD-type disturbance alluded to at the end of Chapter 4 in Fig. 4.24. As time progresses to +4d, most of the convection along with the Kelvin wave is over central Africa, whilst a small pocket of lower OLR moves westward through Mali, Guinea and the Ivory Coast on the western edge of the GOG.

5.4.2 TD-type Disturbances

Tropical Depression or TD-type disturbances were first introduced within this work in Chapter 4. Space-time filtering was applied to the original NCEP OLR dataset to derive TD-type disturbances that have been shown correspond with EWs (Kiladis et al. 2009). It was shown that the spring of 2009 (Fig. 4.22a) was near climatology in terms of variance (W m^{-2}), but that April had high activity at 10°N from 10°W to 0°E. Figure 4.23 shows that May was not as active as May but that one particular wave was prominent for a wide longitudinal scale. Further analysis of this feature reveals that this is a significant event for the 10°N –

15°N belt for 80°W to 80°E (Fig. 5.22a). Here, the color scheme is altered to highlight the event. It is again evident that this event propagated with marked coherence ($< -8 \text{ W m}^{-2}$ anomaly) from as far east as 40°E.

It should be recognized that this TD-Type event (TD1) is also present in other OLR fields. As in Kiladis et al. (2006), the objective is to show TD-type signal is reproducible in other datasets. Given this premise, the OLR was filtered without screening for wavenumbers for < 10 day westward propagation (Fig. 5.22b). This dataset, although noisier in comparison to the TD-type, corroborates with the hypothesis that this event is related to summertime EWs, even if it may not share all aspects.

Further, TD1 is estimated to be moving at 8 m s^{-1} and has a period of 3-4 days, consistent with previous studies (Reed and Recker, 1971; Reed et al., 1977; Thompson et al., 1979; Kiladis et al. 2009). The importance of TD1, in that it is connected temporally with the increase in humidity values throughout most of the populated region of the Sahel (see Fig. 5.1) and that it is also present in other related fields such as precipitable water (Kg m^{-2}) (Fig. 5.7) and southerly meridional wind (m s^{-1}) (Fig. 5.8), motivates deeper investigation into how this system may have interacted, or benefited from, events in the larger and longer scales that were found to be prevalent during the same time period (moist anomalies in the eastern Sahel, extratropical interactions, and Kelvin wave activity). These potential interactions are explored further in Section 5.4.4.

5.4.3 Equatorial Rossby

At the end of Section 5.4.2 it was suggested that larger scale components could also be exerting their influence on the TD1 during the MME. Section 5.4.1 reviewed one such large scale type of system: Kelvin waves. It was shown that a particular Kelvin wave (K1) was traversing the region during the same time period. It is also found that ER disturbances were active within the eastern side of the domain (east of 20°E). Figure 4.16b in Chapter 4 displays increased variance ($W m^{-2}$)² within this region and also a signature of ER west of 20°E, in areas affected by negative moisture anomalies until the passage of the MME. It was found that an ER wave's negative phase (ER1 hereafter) propagated from 40E to 20W around the time of the MME (Fig. 4.17 in Chapter 4). Further investigation of this feature (Fig. 5.23) reveals that ER1 is more prevalent in terms of negative filtered anomalies ($< -20 W m^{-2}$) at 17.5°N (Fig. 5.23a) and begins its propagation at 40°E. From Kiladis et al (2009) and references therein, ER tend to be recognized as cyclone pair structures. This is also the case with ER1: strong negative filtered OLR anomalies propagate along 7°S during the same time period (Fig. 5.23b).

ER disturbances are notoriously difficult to detect (Kiladis et al. 2009) since their spectral peak lies partially within the MJO region. Unfiltered analysis of other fields tends to be insufficient for ER waves. In Fig. 5.24, the difference between meridional wind at 10°N and 10°S at 850 hPa is taken and it reveals a clear westward propagating feature around the time of the MME that is traveling westward at a speed of $4.34 m s^{-1}$, which consistent with the $4.5 m s^{-1}$ speed of cyclone pair phenomena found in Kiladis et al. (2009) Fig. 17. The faster-

moving (8 m s^{-1}) structure of TD1 is also visible here, suggesting the possibility of ER1's role in the development of TD1. This possible relationship is explored in the next section.

5.4.4 Relationships among Equatorial Waves during the MME

Interactions (phasing, forcing, enhancement) among different equatorial wave systems have been the centerpiece of a wide array of previous studies on the WAM (Ward 1998; Rowell 2001; Janicot et al. 2001; M04; Mounier et al. 2007,2008; Mekonnen et al. 2006,2008; J09; G09). CCEWs and tropical moisture also interact with mid-latitude systems (Flohn 1975; Nicholson 1981; McGuirk et al. 1988; Kiladis 1998 Knippertz 2005; Knippertz and Fink 2008). Are these types of interactions present during the MME? So far, some evidence has been provided for interfacing among various structures such as large scale subsidence and χ , ITCZ moisture, and longer scale westward shifts in moist anomalies. In the following, further support for these interactions is provided.

5.4.4.1 Kelvin and TD-type

Recent work on CCEWs has been aimed at understanding how longer-scale phenomena (duration in days, not phase speed) such as Kelvin waves can have on AEWs during the summer monsoon. Mekonnen et al. (2008), for example, examined a case study over Africa in August 1987 and found that an enhanced Kelvin wave disturbance was linked with the development of a series of AEWs, although this type of interaction is deemed to have low

frequency on any given season (Berry et al. 2007). The first portion of this analysis is thus devoted to the possibility of Kelvin – TD-type interaction within the region of interest.

A time-longitude Hovmoller plot is presented in Fig. 5.25 in order to see the effect of equatorial wave interaction on the environment over the more populated region of the Sahel, which displays Kelvin filtered OLR (shaded, $W m^{-2}$) averaged for $10^{\circ}N$ - $15^{\circ}N$. Overlaid on the Kelvin waves are TD-type features that are contoured only at $10 W m^{-2}$ in order to acquire information on only the more coherent systems. This threshold was chosen because it was found to be one standard deviation from the mean. TD1 and K1 have been labeled to show how they intersect at $10^{\circ}E$ during the MME (May 9). Notice that there is another TD – Kelvin crossing much earlier in the period in mid April. It is found, however, that this particular event did not influence surface humidity to the extent that MME had. This is illustrated in Chapter 4 (Fig. 4.24), where three different time series of observed RH (%) at Bamako, Niamey and Kano are plotted along with area averages of TD-type OLR over each location. Only Kano breaks the RH40 line with the April TD systems. For Niamey and Bamako this does not occur until TD1 approaches the cities. This supports the evidence that MME was the first system to cause significant changes in moisture for the highly populated portion of the Sahel.

It is possible, from the evidence presented, that TD1 could have undergone strengthening due to phasing with K1. This question is first approached with a sequence of plots (Fig. 5.26) showing Kelvin waves (shaded) and TD-type systems (contour). For this time sequence of figures, only values greater than one standard deviation are plotted for the TD-type-filtered

OLR ($\sim 10 \text{ W m}^{-2}$). Kelvin-filtered OLR is contoured every 5 W m^{-2} . Only negative numbers from the two wave types are utilized for the sake of clarity. Dash-dot contours were chosen for the TD-type systems at -10 and -15 W m^{-2} but solid contours for -20 W m^{-2} in order to show intensification.

During May 4, K1 is on the western side of the tropical Atlantic and K2 has begun to form in the GOG. Most TD-types are relatively weak, including one over northern Nigeria. K2 strengthens on May 5 while K1 retains its strength over the central tropical Atlantic. At this point, K2 reaches the western coast of equatorial Africa (i.e. Cameroon) and interacts with a southerly track ($< 5^\circ\text{N}$) TD-type system. Notice also that this TD-type system seems to have a “twin” on the other side of the equator and could be considered to be a Rossby couplet and is indicative of another type of equatorial wave: Equatorial Rossby (ER) or Mixed Rossby-Gravity (MRG). It has been found that MRG, TD-type along with ER $n=1$ waves coexist within a continuum, with some disturbances shifting from one type to another and developing hybrid structures as they transition (Takayabu and Nitta, 1993; Dunkerton and Baldwin, 1995; Yang et al., 2007; Kiladis et al. 2009). This has potential implications for the MME, as one type of disturbance could transition in its dynamics. However, this is beyond the scope of this study and will be addressed in future work.

As the systems evolve on May 6, K2 has gained strength as it progresses through equatorial Africa (i.e. Congo Basin, centered at 15°E) while K1 approaches the west coast of Africa [18°W]. Notice, also, that K1 has a significant meridional range as it stretches as far north as the coast of Senegal [15°N] with a -35 W m^{-2} OLR signal. At 1800 UTC on May 7,

the first signs of TD1 become visible as the system begins to develop in the western Sudan as it is possibly triggered by the northern portion of K2. TD1 remains far to the south at 0600 UTC on May 8 as it propagates along $\sim 7^{\circ}\text{N}$ over southern Chad [20°E]. Meanwhile, K1 maintains its strength over most of the GOG coast and as far north as 15°N . This remains consistent in other fields such as precipitation (Fig. 5.13e) and unfiltered OLR (Fig. 5.14e). TD1 begins to strengthen at 1800 UTC on May 8 and 0600 UTC on May 9 as it approaches K1. Also notice at 1800 UTC May 8 that there is a secondary TD-type filtered feature just to the north of TD1 and it merges with the system at 0600 UTC May 9. Thus, TD1 grows in its latitudinal range and spans from the GOG (5°N) to northern Niger in the vicinity of Agadez [17°N , 8°E], whose meteorological station recorded heightened humidity values ($+1 \text{ g kg}^{-1}$ in mixing ratio, Fig. 5.3). It is argued that the northward growth of TD1 occurs due to its interaction with convection over northern Chad in association with the forcing from the extratropics, which will be reviewed in Section 5.5 of this chapter.

The main interaction between K1 and TD1 occurs at 1800 UTC May 9. Here, the northern edge of K1 intersects the TD-type system over central Nigeria, close to the Jos Plateau (10°N , 8°E). Notice that a pocket of $< -20 \text{ W m}^{-2}$ has formed within the TD1 envelope as the system gains in strength, presumably, through its interaction with the Kelvin wave. The result of this interface is a stronger TD1 on May 10 as it moves westward with a significant northern edge that traverses most of Niger and Mali until it reaches the west coast of Africa over Sierra Leone on May 11. Meanwhile, K1 continues its eastern propagation without losing much strength in the process.

The point at which the two systems of interest, K1 and TD1, meet can be further scrutinized by analyzing the possibility of phase coupling of the two systems over central Nigeria. To do this, an area averages [9°N-11°N, 7°E-9°E] of both fields is taken and the data is presented as a time series in Fig. 5.27. From this vantage point, it can be seen that a moderate Kelvin wave is traversing the area during May 5 and 6 (filtered OLR at $< -10 \text{ W m}^{-2}$). TD-type signals do not reach the 10 W m^{-2} magnitude cutoff used previously until 1800 UTC May 9. The Kelvin-filtered signal, on the other hand, begins at 0600 UTC May 8 and is consistent with the geographical extent of K1 on Fig. 5.26. As the sum the two signals is taken, the total OLR from the two systems is -30.8, -39.1 and -24.2 W m^{-2} at May 9 0600 UTC, 1800 UTC and May 10 0600 UTC respectively. Notice also that both signals reach their lowest points in the filtered OLR nearly simultaneously, thus adding to the evidence of phase coupling and its perceived role in the strengthening of TD1.

5.4.4.2 Equatorial Rossby and TD-type

There is evidence to suggest that the ER in question (ER1) may also be contributing to the development of the TD-type system (TD1). Previous research suggests there exist important relationships between ER waves and tropical cyclogenesis (TD-type systems) (Frank and Roundy 2006; Bessafi and Wheeler 2006; Molinari et al. 2007). When evident, cyclogenesis events tend to cluster to the east of the ER wave trough, with ER waves also subject to the deformation effects of varying zonal flow as described in Kiladis et al. (2009) for MRG waves.

During the MME, ER1 and TD1 cross paths between 20°E and 0°E as the ER wave propagates westward (Fig. 5.28). In fact, TD1 begins its formation during periods of large negative OLR anomalies given by the filtered ER dataset. This figure is similar to Fig. 5.25 in that it is the average OLR anomaly for each filtered field between 10°N-15°N, a region crucial for this study. Also visible in this figure is the fact that TD1 strengthens (i.e. has values $< 10 \text{ W m}^{-2}$) on the eastern side of ER1 at 20°E.

Another important outcome of ER1's presence during the event is that TD1 remained within the envelope of negative ER-filtered OLR anomalies until 10°W. The phasing with K1 was much shorter in comparison due to the relative speed of both types of disturbances (Fig. 5.25). In order to better illustrate ER1's possible influence on TD1 on spatial scales, the same analysis carried out in Fig. 5.26 is presented in Fig. 5.29. Note that the northern sector of the developing of TD1 (May 8) is enhanced ($< -10 \text{ W m}^{-2}$ anomalies) east of ER1. On May 9, this is even more evident, as the northern part of TD1 is within some of the larger negative values of ER1. This continues to be the case on May 10 and May 11, where points north of 10N within the TD1 negative anomalies always lie within the ER.

5.4.4.3 Intraseasonal Systems

During the past decade, Kelvin waves have increasingly been studied to diagnose intraseasonal variability of the West Africa Monsoon because of their synoptic scale nature. More recent work by M04, Mounier et al. (2007), Mekonnen et al. (2008), G09, and J09 has explored how this type of wave interacts with longer-scale phenomena such as the MJO and slower, westward moving ERs. Significant progress has thus been made in understanding

dominant modes of variability over this portion of the continent which dictates the distribution of precipitation during the monsoon season. However, of the more recent work mentioned above, only one has explored intraseasonal variability in the equatorial Atlantic and West Africa: G09. Yet their study was primarily concerned with events off the GOG coast and in correspondence with the first monsoon, which appears during March–June (Le Barbe´ et al. 2002; Redelsperger et al. 2002). Still, their analysis showed that at their day 0 peak, enhanced convection covered the entire tropical Atlantic-equatorial Africa.

As a first step in this analysis we introduce the more important figures from recent research which shows the peak in intraseasonal variability for M04 (Fig. 5.30), J09 (Fig. 5.30b) and G09 (Fig. 5.30c). Notice that all figures converge more or less as the same OLR pattern over West Africa as a 90° clockwise rotation of the letter “Y” (although G09’s diagram deviates somewhat; also consistent with the Gill solution in Gill 1980). In the case of J09, the authors also provided sequences of Kelvin, ER and MJO signals by employing Spatial Empirical Orthogonal Function (SEOF) analysis (Richman 1986) on the 25–90-day bandpass filtered June–September OLR values over the domain 10°S–30°N, 30°W–30°E for the period 1979–2000. They concluded that the warm pool created by the MJO over the western Pacific 20 days prior to the peak developed Rossby and Kelvin waves that traveled a circuit around the globe before converging over Africa. Similarly, G09 also utilized EOF analysis of daily OLR anomalies passed through a 20–100 day band-pass Lanczos filter over the domain 10°S–20°N, 35°W–30°E but for the March-June period. His analysis also concluded that a convergence of ER and Kelvin signals along with depressed convection

Indian Ocean – Western Pacific in association with the MJO brought about the same peak of activity over the region of interest at day t_0 . This, perhaps, is more significant to the present study since the time period is nearly equal. In the published work by M04, the nearly-identical EOF pattern was also determined to have intrinsic global effects since the MJO warm pool in the Western Pacific was again present and, as a response to the heightened convection over Africa at day t_0 , OLR signals of reduced convection over the warm pool had moved farther northward to 10° – 15° N.

Earlier in this study (section 5.3.2.3), reference was made to this mode of variability as perhaps being present within West Africa at the time of the MME. Indeed, as Fig. 5.14 shows, negative OLR activity took the form of Fig. 5.30(a-c). The question then becomes: Is this pattern consistent with equatorial wave anomalies? This study is limited the occurrences of CCEWs as given by the datasets available for the April-May period of 2009 and does not take into account modes of variability. The spatio-temporal and wavenumber filtering does provide robust results, however, and this is shown in Fig. 5.31. As in J09, the question is approached by providing sequences of the three most prominent waves found to be the source of peak activity: ER, Kelvin and MJO.

The MJO is the dominant mode of intraseasonal variability in the tropics (MJO; Madden and Julian 1994) and research on this time scale for the monsoon has made crucial links between this dynamical feature and the anomalies in the general circulation that allow for the peak signal in Fig. 5.30a-c at t_0 for each experiment. This study uses same paradigm found in J09, G09 and M04 and analyze OLR anomalies at 5-day intervals. The peak (t_0) occurs on

May 7 2009. At -20d the MJO is in a strong negative OLR phase in the eastern Indian and western Pacific oceans. Low positive anomalies reside over West Africa. Positive anomalies are present over the Arabian Peninsula and the western Indian Ocean, which corresponds to the first mode in the EOF analysis by J09, although their positive signal exceeds the one found here. There are two Kelvin waves of moderate strength during this time, but perhaps most intriguing is the ER, which has a strong negative signal off West Africa but also positive anomalies over most of tropical Africa. Kelvin waves were deemed to have only limited effect on the intraseasonal mode in J09, but the occurrence and timing of K1 cannot be overlooked. As for the ER signal, a similar pattern can be seen in J09, with positive anomalies over the continent. The overall pattern of the sum of the three signals (hereafter SUM) is of mostly positive anomalies ($>35 \text{ W m}^{-2}$) over equatorial Africa, with a small negative anomaly at $[10^\circ\text{N}, 10^\circ\text{E}]$. M04 also had a similar signal on his -20d, except that the negative OLR signal is in the northern hemisphere. Further, lagged regression map of OLR anomalies in G09 also echo the finding in the present work.

Although the -15d may not explicitly represent the modes found in the literature, some information remains the same: the MJO, for instance, shifts farther east and positive OLR anomalies become more prevalent over the Indian Ocean. Slight negative ER ($< 10 \text{ W m}^{-2}$) anomalies are also present centered over $[10^\circ\text{N}, 10^\circ\text{E}]$. Curiously, the Kelvin convective signal is strongly negative over the same regions as the ER. This this may be due to a mid-latitude system crossing the region during this time, which has similar phase speeds and

wavenumbers as the Kelvin waves. However, regions of positive OLR in the SUM are similar to the regressed OLR pattern in G09.

A similar pattern to -15d can be found for SUM at -10d, strong, isolated negative OLR signal limited to the GOG and over the Sahara desert. ER and Kelvin negative anomalies are also present over the same region, but the MJO strongly resembles the one in J09. At -5d, convective anomalies are found east of 20°E from 10°N to 30°N whilst west of 20°E, there are strong positive anomalies. The MJO begins a negative phase over equatorial Africa, in a manner similar to that in J09. Even in their study, however, the sum of the signals do not specify especially strong convective anomalies over West Africa itself. Do note, however, that a strong positive signal is present in the ER data as a diagonal structure from 10E (Nigeria) to 40E (Eritrea), which is collocated with negative precipitable water analysis over this region in Section 5.3.2.1 (Fig. 5.10).

At t_0 , the SUM shows a pattern reminiscent to that found in the recent literature and which is highlighted in Fig. 5.14. Perhaps the only deviation from the composite is the small pocket of neutral filtered OLR (between -10 and 10 $W m^{-2}$) over Nigeria. Inspecting the Kelvin field, it is found that subsidence associated with K2 and ahead of K1 (see Fig. 5.20) may be the cause for this cancelation in the overall signal. However, the unfiltered OLR pattern found in Fig. 5.14, with the characteristic “Y” shape, strongly suggests that the interactions between the different waves converged at t_0 to initiate the pattern of peak convection over tropical Africa in both boreal summer and spring iterations.

The negative anomalies in the ER field at t_0 also show a connection with the extratropical system, once again adding to the evidence of the interaction. The MJO signal is also beginning to become more prevalent in the western Indian Ocean, and is in accordance with the J09 analysis. Also worth noting is the westward progression of ER in their analysis, with a similar pattern found in the diagram provided in Fig. 5.31.

The dates +5d and +10d are included for perspective and also to show how the overall activity diminishes substantially after the apex of convection. Positive filtered Kelvin signals as well as deepening anomalies in the primary MJO region is consistent with J09's strengthening MJO, especially given its 30-60 day period that is intrinsic the MJO definition. G09 also finds the same signal over the western Indian Ocean, as does M04 for +10d. The SUM has the bulk of the negative anomalies at the Senegalese coast ($\sim 15^\circ\text{W}$) and is collocated with the exit region for TD1 for +5d. The ER signal in J09 occurs over the same area as ER in the present analysis, which strongly corresponds with TD1.

It was deduced in J09 that Kelvin waves do not feature in the intraseasonal peak in the convective mode of variability. Thus, the Kelvin signal is removed from the sum and only the MJO and ER are kept in Fig. 3.32. Note that at t_0 the "Y" shape is clearer and the neutral OLR anomaly over Nigeria is erased. Instead, the sum of the signals in this figure is much more reminiscent to that in the observations (Fig. 5.14), and also of the work in G09, J09 and M04. This suggests that although K1 had a prominent impact on the MME, the areal span of the event as a continent-wide structure meant that longer-varying signals provided larger contributions.

It is clear from the preceding details of wave interaction that a characteristic “peak” event of convection, as given by M04, J09 and G09 may be occurring during the development of the MME. The more recent work on intraseasonal variability (i.e. J09) suggests that a strong warm pool in the MJO mode excites the surrounding atmosphere and may give rise to both ER and Kelvin waves (something intrinsic in MJO dynamics). These waves circumvent the equatorial plane and converge over Africa. Was K1 triggered by the April MJO (-20d)? Figure 5.33 presents a time-longitude Hovmoller plot of MJO (shaded) and Kelvin (contour) filtered OLR information. The April MJO is labeled as MJO1 and the May MJO as MJO2. MJO1 was observed and documented by the NOAA Climate Prediction Center (CPC, http://www.cpc.noaa.gov/products/precip/CWlink/MJO/ARCHIVE/PDF/mjo_evol-status-fcsts-20090706.pdf) and determined to be a strong iteration of this phenomenon. Notice that K1 forms near the eastern edge of the MJO1 signal in late April close to the international dateline and propagates eastward through the Pacific Ocean. K1 gains strength over South America ($< -20 \text{ W m}^{-2}$) and continues as a coherent feature through the tropical Atlantic and equatorial Africa. Such a finding has important implications in terms of forecasting, as the observance of an MJO could be used as guidance to identify possible coherent Kelvin waves that are able to affect the climate of Sahelian West Africa directly or via interaction with other features such as TD-type disturbances, ER waves, or mid-latitude systems. This analysis also leads to the conclusion that SSTs over the Atlantic may not have factored in the overall structure of K1, given its coherent long-lived nature.

5.5 Forcing from the Extratropics

The transition from dry to moist conditions has important interannual variability and the progression of the moisture front is susceptible to intraseasonal phenomena such as mid-latitude system intrusions (Knippertz and Fink 2009) and CCEWs (Wang and Fu 2007, Mounier et al. 2008, Nguyen and Duvel 2008). A great volume of work exists that provides the integral dynamical links between circulation in the mid-latitudes and tropical convection dynamics. Previous research has shown that the transport of Rossby wave energy into the Tropics from higher latitudes is an integral feature of the general circulation. Stationary and transient eddies are essential features of the momentum balance of the atmosphere and allows for poleward transport of westerly momentum at low latitudes (Jeffreys 1926) and for driving tropical motions (e.g., Mak 1969; Zangvil and Yanai 1980; Yanai and Lu 1983; Wilson and Mak 1984; Zhang and Webster 1992; Magaña and Yanai 1995). Rossby wave activity propagating into the Tropics has been shown to occur in regions of mid-latitude westerly flow that penetrates into low latitudes (e.g., Kiladis and Weickmann 1992a,b, 1997; Kiladis 1998; Hsu and Lin 1992; Tomas and Webster 1994).

In a study of relationships between convection in the tropics and global circulation at 200 mb, Kiladis and Weickmann (1992a,b) and Kiladis (1998) demonstrated that strong convective anomalies over the Pacific during the northern winter were modulated by upper-level Rossby wave activity. This type of convective activity over the Pacific tends to occur ahead of upper-level troughs propagating into the Tropics from the vicinity of the Asian jet exit region. These OLR signals typically evolve into “cloud band” or “tropical plume”

signatures in the southwesterly flow ahead of the troughs, of the type seen on satellite photos extending from the ITCZ into western North America (e.g., McGuirk et al. 1987; McGuirk et al. 1988; Iskenderian 1995). Tropical convective anomalies at the ITCZ have been shown to be associated with the advection of high potential vorticity (PV) into the Tropics, with upward motion observed in the region of positive PV advection. A study by Tomas and Webster (1994) also recognized strong PV signals in combination with cross-equatorial wave activity during northern winter. Equatorward-propagating Rossby wave activity associated with ITCZ convection has also been shown to occur in the eastern Pacific during the boreal spring and in the Atlantic during the boreal winter, when belts of upper tropospheric westerlies extend from high latitudes into the tropics.

The role of mid-latitude systems during the dry season in West Africa has recently been explored in more detail, as these features can have an important influence on the population of the region (Knippertz and Fink 2008, 2009). Extra-tropical systems can interact with tropical moisture from the GOG and cause strong precipitation events with substantial impacts on the local residents: rotting of harvests stored in the open air (e.g. cotton), greening of pastures in the open savannah, changes in soil moisture.

While dry season precipitation studies have been focused on occurrences deep within the boreal winter (January), their connection with mid-latitude systems can occur during the boreal spring as well (Andreas Fink, personal communication). However, studies during the transition season on equator-penetrating mid-latitude systems are confined to subtropical North Africa. These systems take the form of diagonal troughs that extend from deep into the

Sahel and northward to the Mediterranean (Flohn 1975, Nicholson 1981). The troughs are accompanied by tropical plumes (TPs) comprised of high and mid-level clouds (as in Fig. 5.2) connecting the tropics and subtropics (McGuirk et al. 1988). The characteristic TPs tend to form along the equatorward flank of subtropical jet (STJ) streaks (Knippertz 2005). Boreal winter and spring rainfall events in the central Sahara have been attributed to “Saharan disturbances,” surface lows that move westward in tropical West Africa and then cross the Sahara toward the Mediterranean Sea on an anticyclonic trajectory (Dubief and Queney 1935). In Nicholson (1981), these systems were referred to as Soudano-Sahelian depressions and suggested an interaction of diagonal troughs with low-level African easterly waves (AEWs).

There exists further evidence that extra-tropical systems can couple with intraseasonal equatorial phenomena such as Kelvin waves (SK02a) and ER waves (Kiladis and Wheeler 1995; Kiladis 1998; Hoskins and Yang 2000; Yang et al. 2007). Most work on this type of interaction, however, is limited to oceanic domains and has not been addressed over the continent of Africa for this time of the year. Other interactions with tropical circulation patterns such as the MJO have important global influences (e.g. Donald et al. 2006) but have not been addressed for the boreal spring and over the region of interest. It is possible that tropical-extratropical interactions may constitute an important factor in the development of the MME. From the Meteosat images in Fig. 5.12 it is clear that a strong TP is present and that the large signal of convection over the GOG is likely related to CCEW phenomena.

In Section 5.3, it was postulated that Mid-latitude systems tend to interact with tropical weather phenomena over Africa (Knippertz and Fink 2008). It will now be shown how a strong upper level disturbance provided divergence aloft as well as vertical motion to the region experiencing the moisture anomaly described in subsection 5.3.2.1 and contributed to the evolution of the MME. To illustrate the influence of the extratropical disturbance, this study follows work by Kiladis (1998) and explores a variety of dynamical fields that could have contributed to the hypothesized interaction.

5.5.1 Horizontal Analysis

This section examines the horizontal structure of the synoptic-scale circulation at 200 hPa that is associated with the MME. Although these circulations are not filtered in time and space nor regressed to specific phenomena (such as OLR anomalies), it will be shown that dynamics occurring are highly consistent and typical of the type of equatorward-propagating wave activity shown to affect tropical convection in previous research such as Kiladis (1998).

5.5.1.1 Mass Circulation

Following the same paradigm as in Kiladis (1998), the first field of interest is the streamfunction at 200 hPa. Unlike Kiladis (1998), analysis for 850 hPa will not be carried out in the present work and will be addressed in future research. Figure 5.34 shows the sequence of 200-mb streamfunction and rotational wind anomalies for May 7 (t_0) and -4d, -2d, +2d and +4d times. Anomalies are relative to the daily mean during the 2000-2009 period.

Observed daily OLR is provided on the left and ER anomalies are provided on the right. ER was chosen since it highlights previous findings concerning forcing from the extratropics (reviewed in Kiladis et al. 2009). Only anomalies lower than -260 W m^{-2} (observed) and -10 W m^{-2} (ER) are analyzed for clarity.

Four days (-4d) before the peak of the MME (May 7) circulations are present as an anticyclone over the mid Atlantic Ocean, a weaker one over North Africa / southern Europe, the Middle East, and a fourth one over East Africa [eq, 40°E] with an cyclonic anomalies over central Asia and the north Atlantic. There is a weak wave train over northern Eurasia. There is no clear quadrupole as is found in Kiladis (1998) at this time.

A clearer quadrupole begins to form at -2d, as a strong anticyclone exerts its force over much of West Africa west of the prime meridian. A small trough remains over northern Africa, with cyclonic anomalies over the Arabian Peninsula and an anticyclone over Eastern Europe. Note, however, that at the structure is not directly related to the increased convection in the unfiltered OLR, as it is mainly to the south of the West African anticyclone. This is also a region of strong northerly flow at 200 hPa.

At t_0 , the structure of the streamfunction and rotational wind resembles that in Kiladis (1998) more so than the previous two days analyzed. Now, stronger anticyclonic anomalies are present to the immediate west of the heightened OLR anomalies over northern Chad [20°N , 20°E]. Note also that the ER-filtered OLR anomalies undergo significant intensification at this date as well over the same location. Also note that the wave trains in the northern sector have also strengthened in terms of anticyclonic circulations over northern

Eurasia. Two days later (+2d), cyclonic flow continues to intensify at [20°N, 20°E], as the anticyclone over West Africa propagates to the northeast and weakens. The unfiltered OLR signal is still peaking over the TP to the immediate east of the cyclonic anomalies and the ER peak is centered below them. The TP (OLR peak) has shifted to the northeast and is in agreement with the same type of shift found to be occurring with the ITCZ in Kiladis (1998). By +4d, the anticyclonic flow has weakened substantially even though cyclonic anomalies are still present over northeast Africa. The streamfunction is, at this point, no longer affecting convection over Africa in terms of the total OLR. However, the location of the ER maximum is still located in the east side of the anticyclonic anomalies.

It should be noted that, although some of the same patterns found in Kiladis (1998) appear to be present during the MME, there are important differences that may also be having an impact, such as the arrangement of the quadrupole, which is structurally dissimilar in the present work. This warrants further work with filtered upper level wind data that would elucidate clearer relationship between the systems and could identify the interaction with more detail.

Another method that can diagnose possible interaction between the systems is presented in Fig. 5.35 through the use of velocity potential. In this view, at t_0 there is a clear strengthening of divergence at [20°N, 20°E] that advances from -4d and begins to dissipate at +2d. This correlates with the heightened negative unfiltered OLR over the same location, and perhaps more importantly, with the strengthening and development of the ER. Further, Fig. 5.36 provides a view of divergence over the region. Note that the highest divergence occurs

over the [20°N, 20°E] location at t0. This is also found in Kiladis (1998), although their study used regressed values, but it provides confidence that the qualitative pattern of the divergence field is well-captured by the NNRP data, given that it is independent of the OLR information.

The divergent wind (Fig. 5.37) also provides an interesting perspective on the location of the theorized interaction point. Strong divergence is located over [20°N, 20°E], where the ER is developing, as well as over the GOG in conjunction with the K1 Kelvin wave. As was found in Kiladis (1998), significant convergence occurs at the junction between the tropical outflow and divergent outflow from the storm track trough off the coast of northwest Africa. It is possible that these transient events could play an important role in the vorticity balance of this region, but this is to be further explored in future work.

5.5.1.2 Potential Vorticity

Finalizing the horizontal analysis is a look at potential vorticity (PV). Unlike in Kiladis (1998), this study does not utilize isentropes (isentropic potential vorticity, IPV) for the analysis and is limited to an isobaric procedure at 200 hPa. It is argued that PV at this level (200 hPa) corresponds to the 350-K θ surface used in Kiladis (1998), where regressed horizontal distribution of IPV corresponding to the streamfunction pattern in their work, which, they argue, is the case at all latitudes. PV is defined as follows:

$$PV = \frac{1}{\rho} \zeta_a \bullet \nabla \theta \quad (5.11)$$

For the present study, the PV is derived from wind components at all levels of the atmosphere along with θ . No anomalies are taken and only the observed PV field is mapped

at 200 hPa in “PV units” ($= 1 \times 10^6 \text{ m}^2 \text{ s}^{-1} \text{ K kg}^{-1}$). As in Kiladis (1998), a positively tilted “trough” of high PV air is present immediately northwest of the OLR anomaly in Fig. 5.38. Previous dates (not shown) depict this signal originating as a small trough initiated over northwest Europe, which propagated southeastward and was followed by a rapid amplification and equatorward propagation from western Europe into the Tropics. This evolution is related to that found in Kiladis (1998) and by Kiladis and Weickmann (1992b) quite closely, although the use of regressed values and anomalies relative to the climatology may elucidate clearer relationship with past work. Further analysis of the vertical structure is provided in the next section, and it is found to be a better representation of the dynamics at work.

5.5.2 Vertical Analysis

A short review of the vertical analysis using ω and divergent wind shows large scale anomalies (Fig. 5.39) for t_0 compared to the recent climatology. The strong divergence hints at the involvement of the extratropical system on the strong negative OLR signal. This is in agreement with Kiladis (1998) except that it extends much farther north. This may be due to the large scale convergence aloft over Europe.

5.6 Further Investigation and Conclusions

We have explored the role of various features that are found in the MME, as well as possible interactions that may have aided in the development of the system. This section is dedicated

to add to previous examinations within the context of prediction and how this information could potentially be used for modeling similar events. We also provide a conceptual model along with conclusions.

5.6.1 Large Scale Effects

We have reviewed the possible role of background conditions such as the anomalous moisture present over the eastern Sudano-Sahel in section 3.3.2. We have also hinted that some of the CCEW structures could explain these large-scale anomalies. The ER in subsection 5.4.3, for example, was collocated with the anomalies in the moisture field in Section 5.3.2.1.

The findings highlighted here have important consequences on the prediction of moist events since extratropical systems have inherent predictability due to baroclinicity (Holton, 2004) and recent work over Africa has yielded positive results (Knippertz and Fink, 2008). Indeed, the mid-latitude system that preceded the interaction highlighted in the MME caused significant pressure falls across a wide portion of the northern half of the continent during late April. It's important to note that this figure represents actual forecasts by NCEP and elucidates the ability of state-of-the-science models to predict extratropical phenomena. This system, however, was limited in its impact on surface moisture over most of the reporting stations, possibly due to the ER and associated subsidence over the region. Nevertheless, its impact on the stationary moist anomaly over the eastern Sahel cannot be overlooked.

5.6.2 Low-level Moisture Convergence and the African Easterly Jet

Within the context of prediction there are other factors that are also crucial to understanding the MME's impact on surface moisture. For example, moisture convergence (g kg^{-1}) at 850 hPa shows important characteristics of this event (Fig. 5.40, using FNL-derived data), such as the divergence associated with the TP and the convergence to its south and west. The TP is a prominent feature at this level in terms of moisture convergence and is present throughout the period shown (May 5-10). Also notice that our starting date for Fig. 5.40 is shifted by a day in order to show the progression of TD1 through the central and western Sahel. The large scale moist anomaly can also be seen as a deep center of increased moisture on May 6 is at its peak on May 4 (a), with values $>1 \text{ g kg}^{-1} \text{ s}^{-1}$. There is marked increased moisture convergence ($>1.5 \text{ g kg}^{-1} \text{ s}^{-1}$) on May 6 (b) and 7 (c) over Niger and Chad in association with the mid-latitude – moist anomaly interaction. The progression of moisture convergence is clear on May 9 (e) and 10 (f), as the system shifts to the west, so that by May 10 it is essentially a moisture front spreading its influence throughout the Sahel. Indeed, the convective activity in this region is a key factor in the growth and meridional extent of the westward-moving portion of the MME.

Another important feature that is dynamically linked to AEWs, or in our case a TD-type disturbance, is the African Easterly Jet (AEJ). During the northern summer, AEWs grow both north and south of the African Easterly Jet (AEJ). The two main tracks, noted over West Africa at 5°N and 15°N , converge over the Atlantic on latitude 17.5°N (Diedhiou et al. 1999). In our case, TD1 is most prominent in the vorticity and meridional wind field at 15°N .

We present a horizontal view of the state of the AEJ during the evolution of the TD1 in Fig. 5.42. The climatology for the 2000-2009 period is shown in (Fig. 5.42a) for perspective. To derive the location of this feature, we use FNL zonal wind (m s^{-2}) to maintain continuity with the rest of the work. We also find that it is comparable to NNRP (another dataset used in this study). In this sequence of figures, we see that the AEJ is most active at 8°N west of the prime meridian on May 7 (Fig. 5.41b). A strengthening ($+5 \text{ m s}^{-1}$) in easterly zonal winds east of 5°E occurs on May 9 (Fig. 5.41d) in association with the developing TD and, possibly with the enhanced convection over Nigeria during the westward-propagating disturbance's interaction with K1. May 10 (Fig. 5.41e) shows a pocket of stronger ($>15 \text{ m s}^{-1}$) winds within the AEJ centered at 5°E . This core shifts westward with TD1 to 5°W and strengthens further ($>20 \text{ m s}^{-1}$) along 10°N .

The above analysis displays how the AEJ is also responding to the TD1 in the MME and we find that the core temporarily shifts north of its climatological location (8°N during May, Afiesimama 2007). In Fig. 5.42, we show a vertical cross section taken at the prime meridian (0°E) from 10°S to 30°N for May 2 (dash-dot), May 8 (solid) and May 16 (dotted). Note that at 0°E the jet core at this longitude is at 3°N (-5 degrees from climatology). It moves to its climatological position a day before the TD1-K1 phasing and then elongates and exhibits a temporary double core on May 16 (6 days after TD1 crosses 0°E). Clearly, with this analysis we can show that the MME has reverberated through the majority of dynamical fields associated with the West Africa Monsoon. Changes in SSTs are not considered in this study but warrant attention in future work.

5.6.3 Summary and Conclusions

This chapter has been dedicated to the analysis of a particular moist event during early May of 2009. We highlighted this event due to the fact that it was able to cause a temporally-significant change in the moisture regime for areas north of 12°N such as Niamey, Niger and Bamako, Mali. This event was also the first of the season to actually bring enough moisture to break the RH40 barrier that is one of the proxies for the cessation of meningitis epidemics throughout Sahelian West Africa. The MME provided us with a wealth of knowledge about possible predictability of these types of occurrences, especially given that moisture spikes over Kano, Nigeria, during the month of April were partly responsible for the shift from Harmattan to monsoon conditions.

The case study in this chapter also showed how the timing of certain events (mid-latitude systems penetrating the tropics, MJO evolution, Kelvin wave activity) corroborated to produce a coherent structure capable of changing surface moisture over the parched land of the dry season Sahel. Thus, we find that MME is comprised of 3 separate but equally important components: anomalous semi-stationary moisture over the eastern Sahel, a mid-latitude system, and CCEWs (Kelvin and TD-type). We illustrate the main constituents of the MME in Fig.

In our conceptual model (Fig. 5.43), we divide it into the anomalous moisture and extratropical interaction phase (-2d) phase and after the CCEW interaction phase (+2d). At -2d, the anomalous dipole of moist eastern Sahel and dry western Sahel is prevalent and has

been a standing feature for at least 5 days. We found that this feature was associated with a <30 day filtered OLR signal moving westward with a phase speed around 3.88 ms^{-1} , slower than the 4.5 m s^{-1} found in Kiladis et al. (2009), but this may be due effects of the background mean winds or interaction with convection and orography. Also at this time, the main Kelvin wave (K1) is approaching the GOG. The ITF is delineated by the 15°C dewpoint temperature isoline (Pospichal et al. 2009).

The anomalous moisture would play a crucial role in the interaction between tropics and extratropics as a mid-latitude anticyclone at 200 hPa penetrates to 20°N . This interface allows for increased convection on -2d and the development of a tropical plume (TP) on the eastern flank of the trough, as well as the ER. The CCEW portion of our conceptual model shows the TD-type system (TD1) developing in southern Chad and phasing with the increased convection in an area that roughly covers (10°E - 20°E , 10°N - 20°N). The Kelvin wave also acts to provide increased monsoonal flow.

At t_0 , the moment of highest interaction between different CCEWs, the meridional range of convection stretches from 5°N to 20°N , bringing the first sustained influx of moisture to most of the region. The Kelvin (K1), ER (ER1) and TD-type (TD1) systems are in phase over central Nigeria, increasing convection and further strengthening the shorter-period system. Also visible at this point is the northeastward shift of the upper level trough as its influence over the region subsides.

As the extratropical system exits northeast Africa during +2d, subsidence from ER to the east becomes prevalent from 15°E east, which reignites the Harmattan and dry conditions

sweep over regions that have seen continuous monsoon-type weather for at least a week. The Kelvin wave traverses equatorial Africa during this point and the TD-type system continues to modulate surface moisture for points west of 5°E. This shift allows for further penetration of the ITF and RH40 lines into locations that have remained within the Harmattan air mass until this point (i.e. Niamey, Bamako, Ouagadougou).

The work provided in this chapter elucidates the possibility of inherent predictability in systems such as the MME. Indeed, recent work on extratropical forcing of dry season precipitation has found good skill (significant 0.77 temporal correlation of area averages to GPCP by the ERA-40 reanalysis). Overall, however, skill in tropical weather forecasting has lagged that in midlatitudes, and current daily to weekly tropical forecasts have only modest credibility with the majority of users (Smith et al., 2001). In terms of CCEWs, forecasting is limited by the extent to which they can be detected in real time. The filtering typically employed to extract the waves in research studies such as ours is applied after the fact. The real-time filtering of Wheeler and Weickmann (2001) is a step in the right direction but it is limited in the wave types that can be resolved by the technique. Recent work with numerical forecast models has demonstrated improvements in model initialization over the tropics by projecting observations onto the theoretical structures of CCEWs (Yang et al., 2003) using four dimensional variational data assimilation. Our focus thus turns to the prediction of the various systems that corroborated in the development of the MME, and we devote the next chapter to this endeavor.

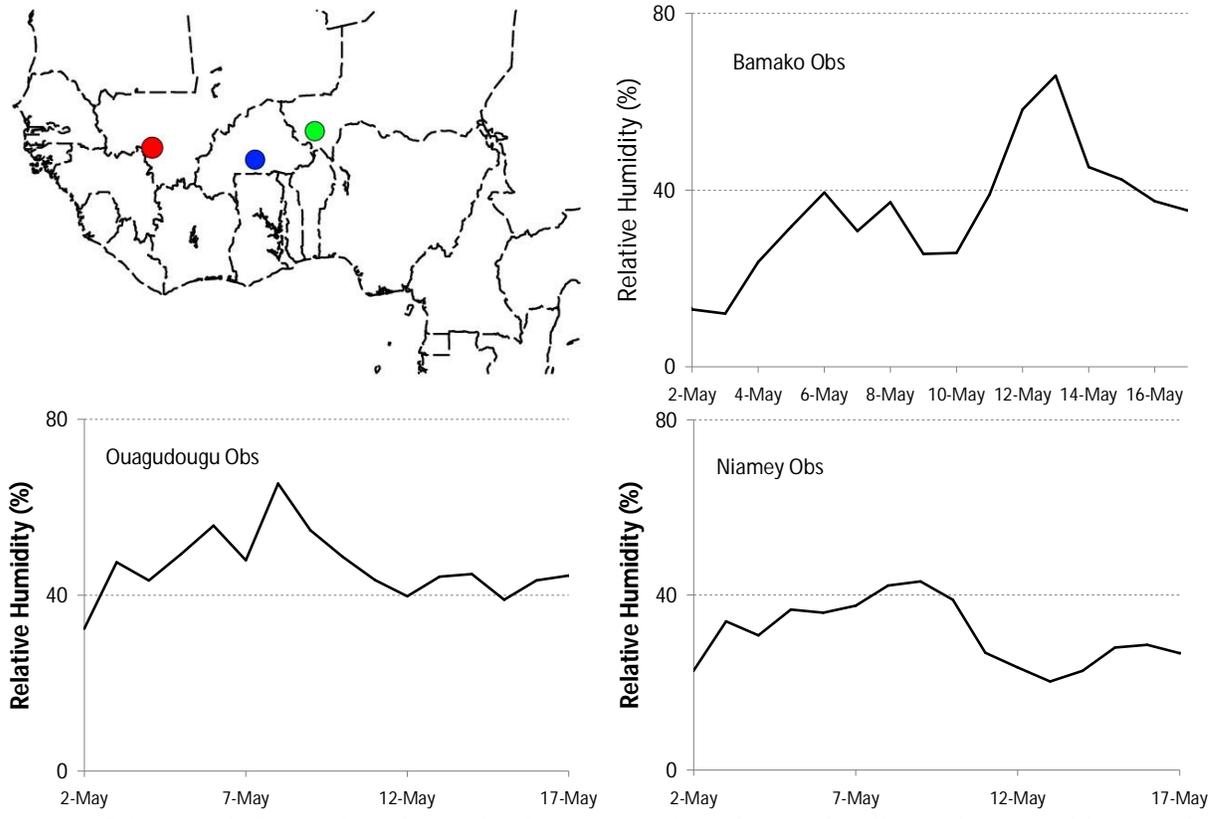


Figure 5.1: Top left: circles show the locations: Bamako (red), Ouagadougou (blue) and Niamey (green). Observed relative humidity during the mid-May moist event for Bamako (top right), Ouagadougou (bottom left), Niamey (bottom right).

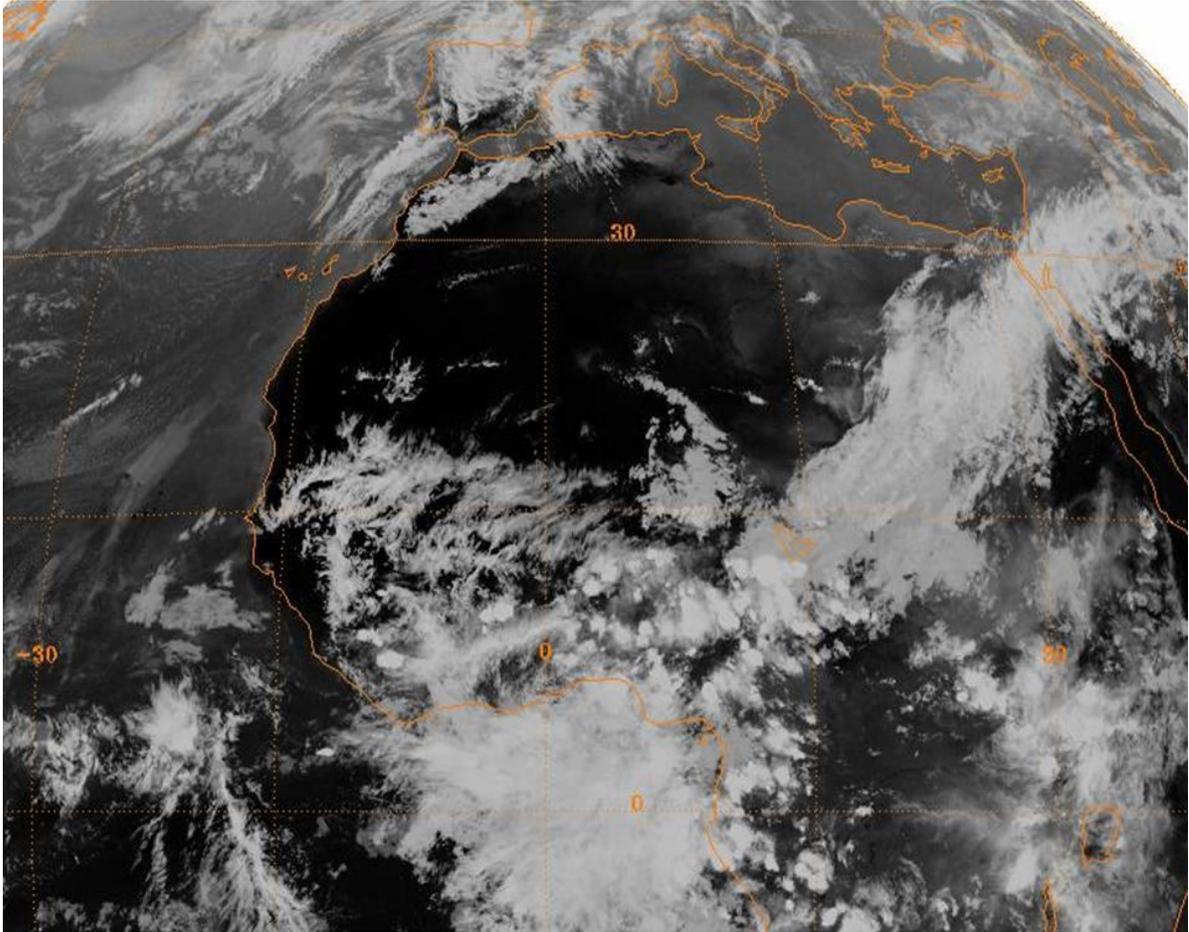


Figure 5.2: MeteoSat Infrared image of tropical plume associated with the moist event in May 5-10, 2009.

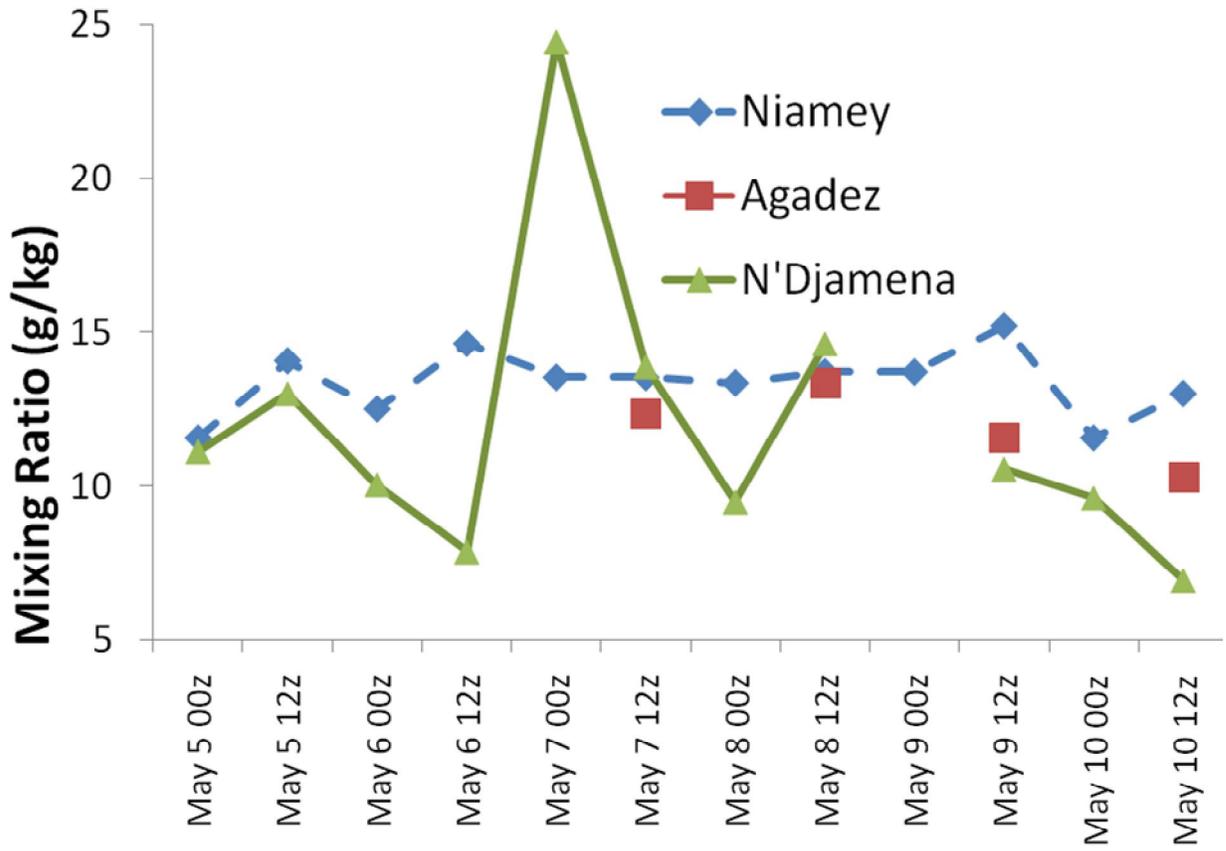


Figure 5.3: Time series of water vapor mixing ratio at 925 hPa for Niamey (dashed, diamonds), N'Djamena (solid, triangles), and Agadez (squares).

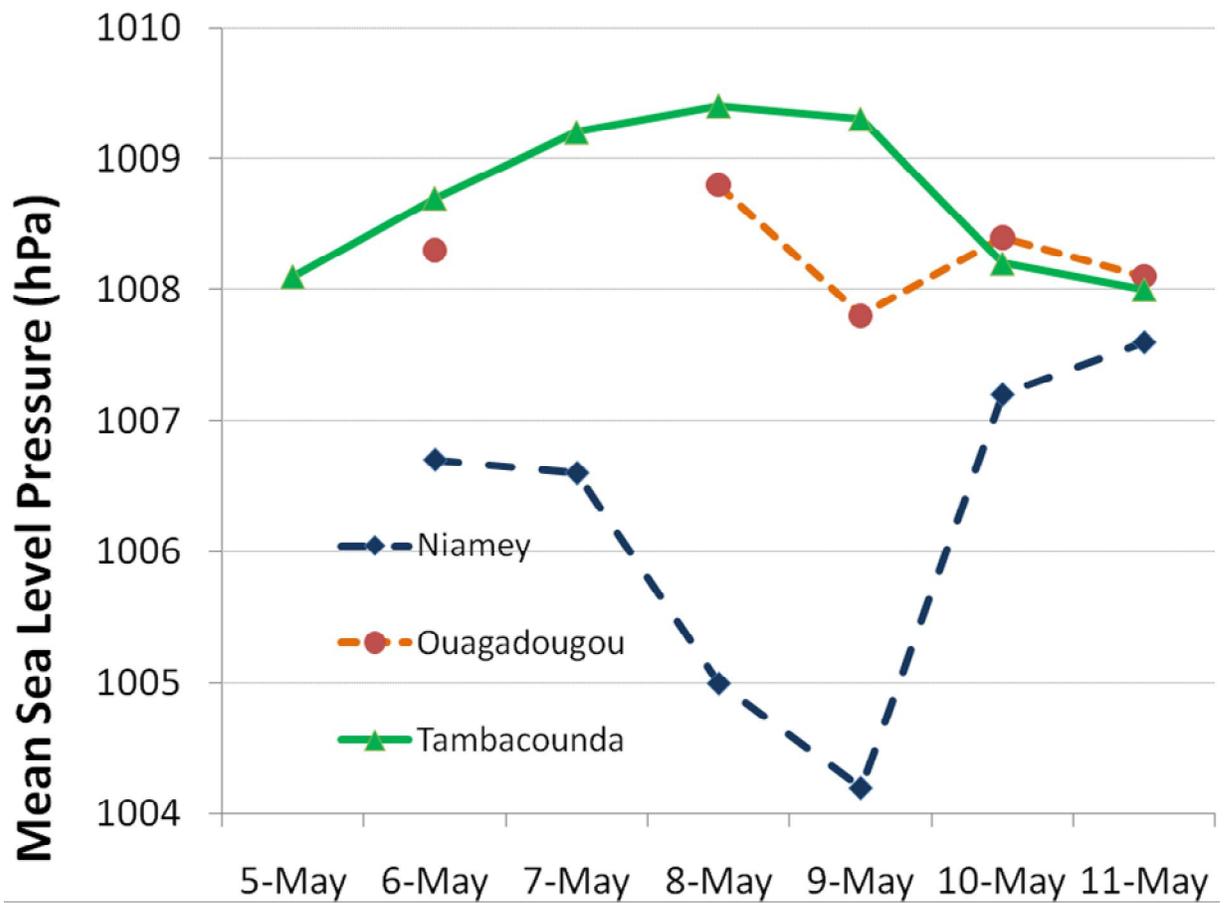


Figure 5.4: Time series of mean sea level pressure (hPa) for Niamey (long dashed, diamonds), Ouagadougou (short dashed, circles), and Tambacounda (solid, triangles).

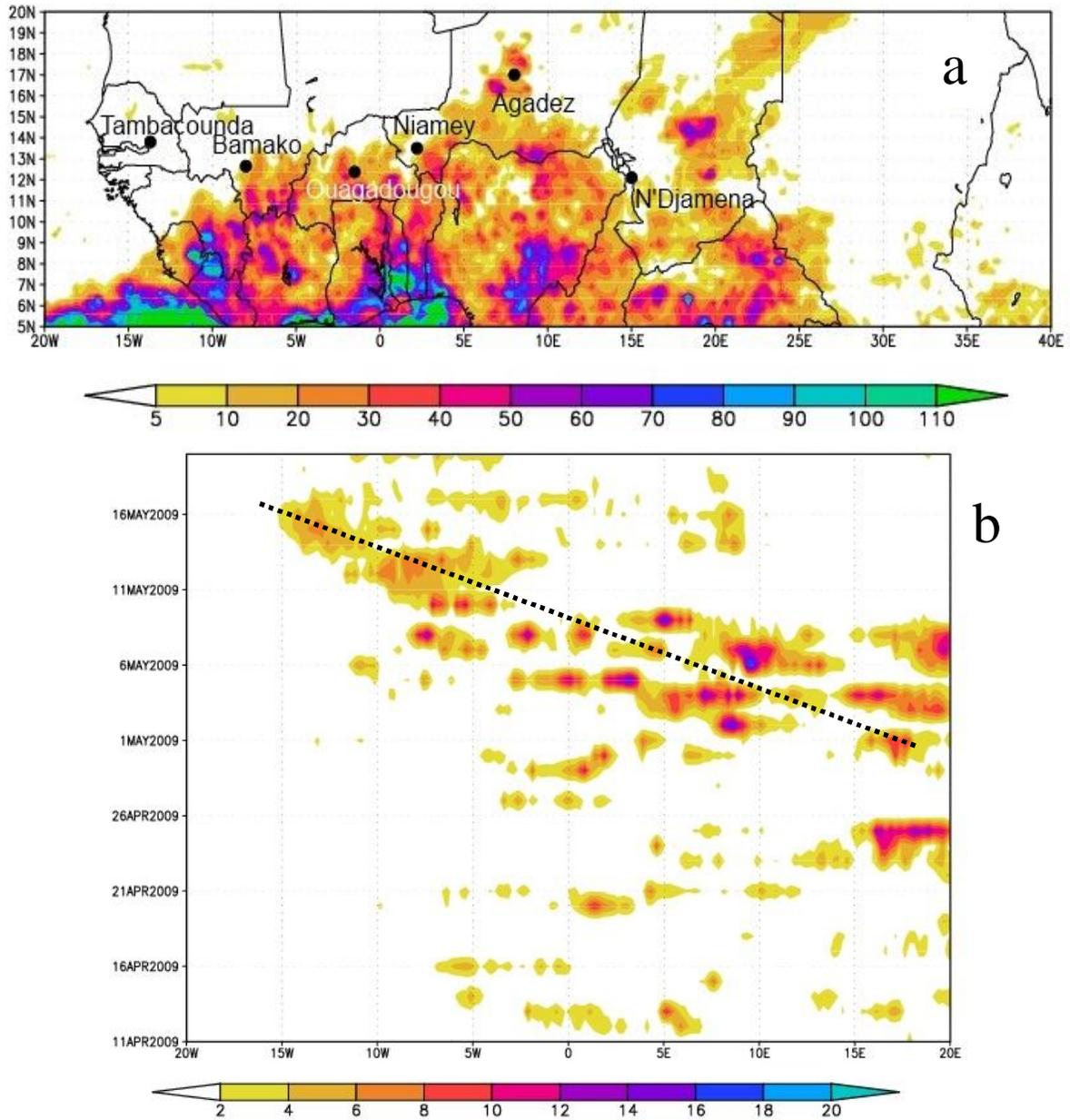


Figure 5.5: TRMM estimated total accumulated precipitation associated with the moist event in May 5-10, 2009 (a), and time-longitude Hovmöller plot (b) of daily accumulated precipitation (mm) averaged for 10-15°N. Dashed line denotes westward progression of the disturbance.

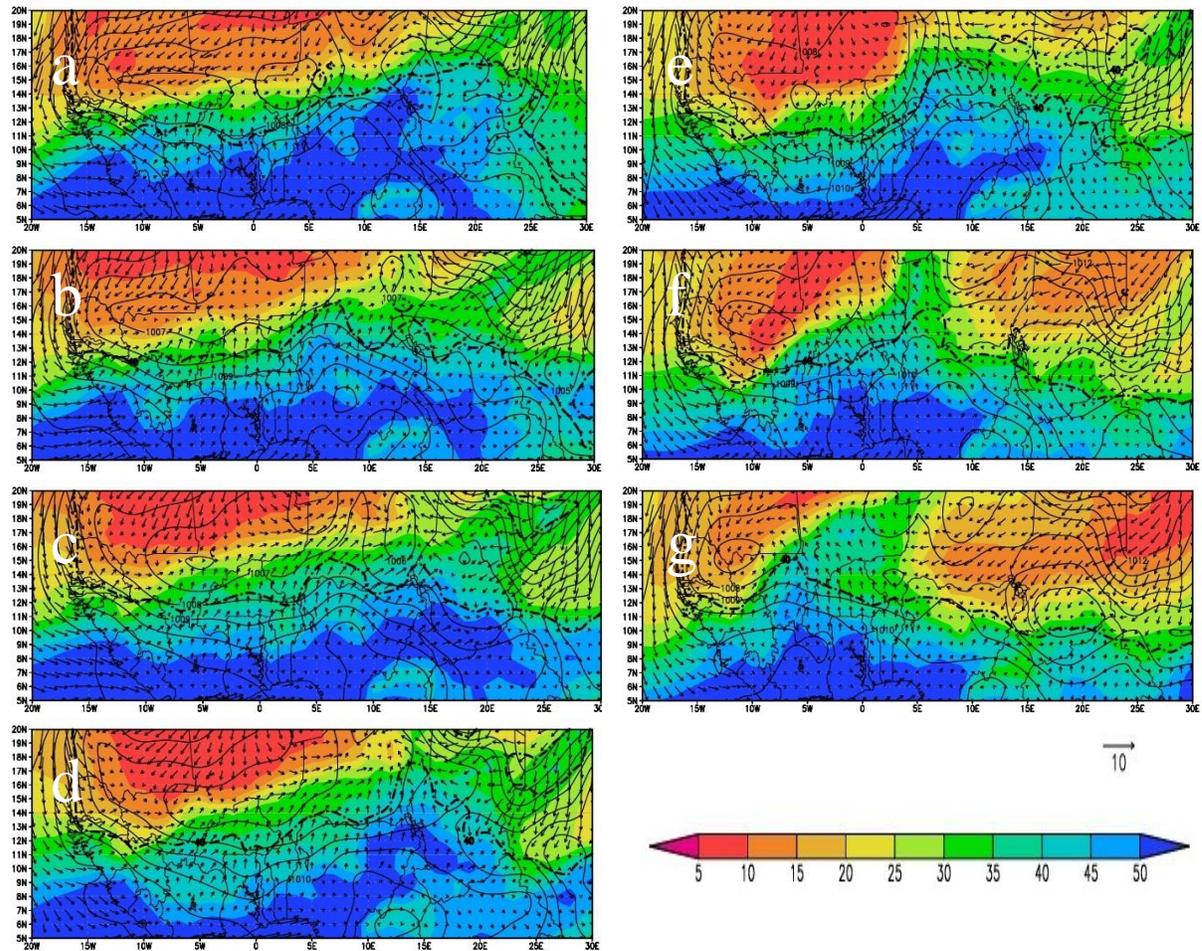


Figure 5.6: Synoptic evolution over tropical West Africa on (a) 5, (b) 6, (c) 7, (d) 8, (e) 9, (f) 10 and (g) 11 May 2009. Solid lines indicate mean sea level pressure contoured every 1 hPa and shading depicts total atmospheric column precipitable water (kg m^{-2}). 10m winds are also shown as vectors. The RH40 isoline is marked by a thick dash-dot line.

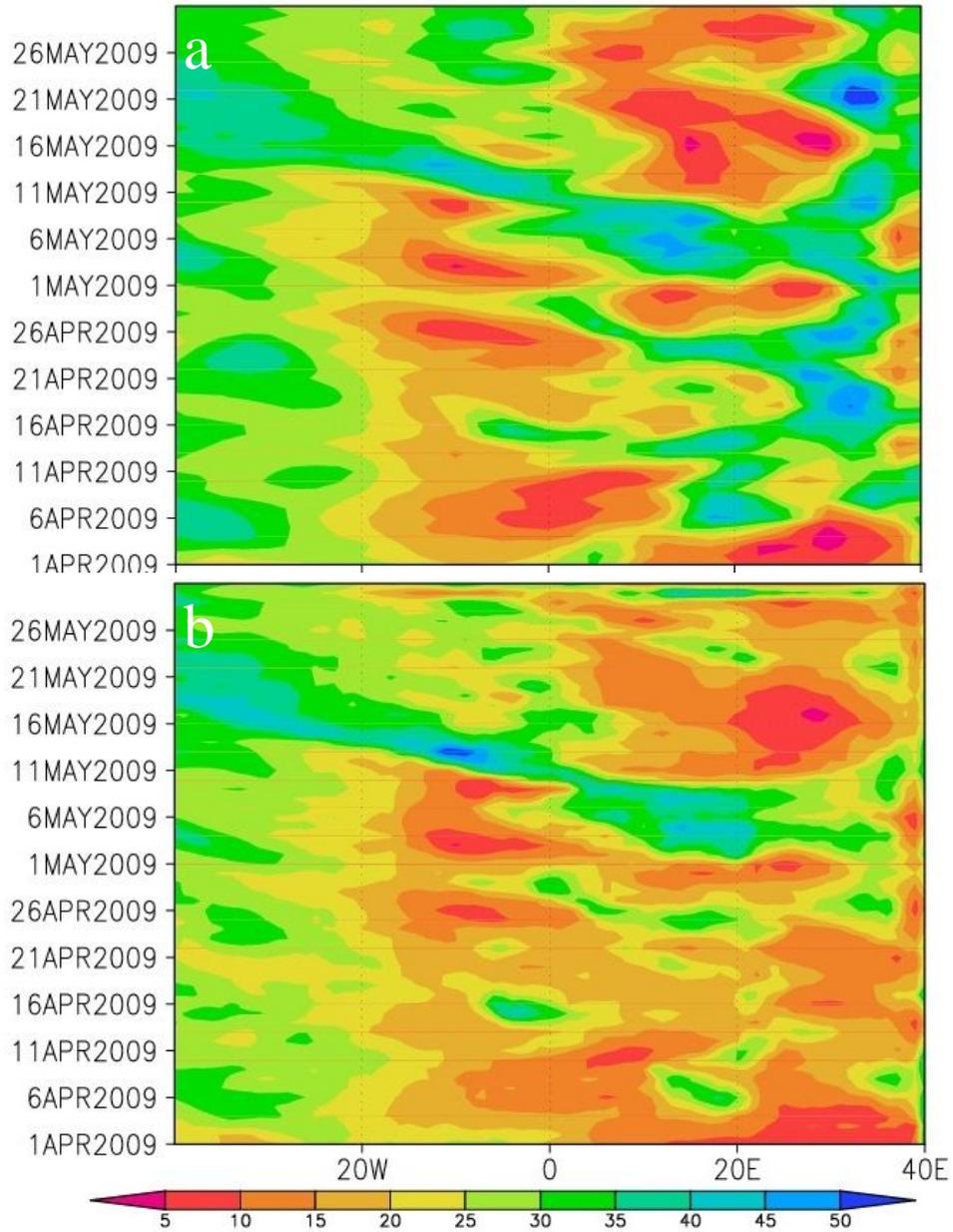


Figure 5.7: Time-longitude Hovmoller plot of precipitable water averaged for all points at 15°N and spanning from 40°E-40°W for (a) NNRP and (b) FNL.

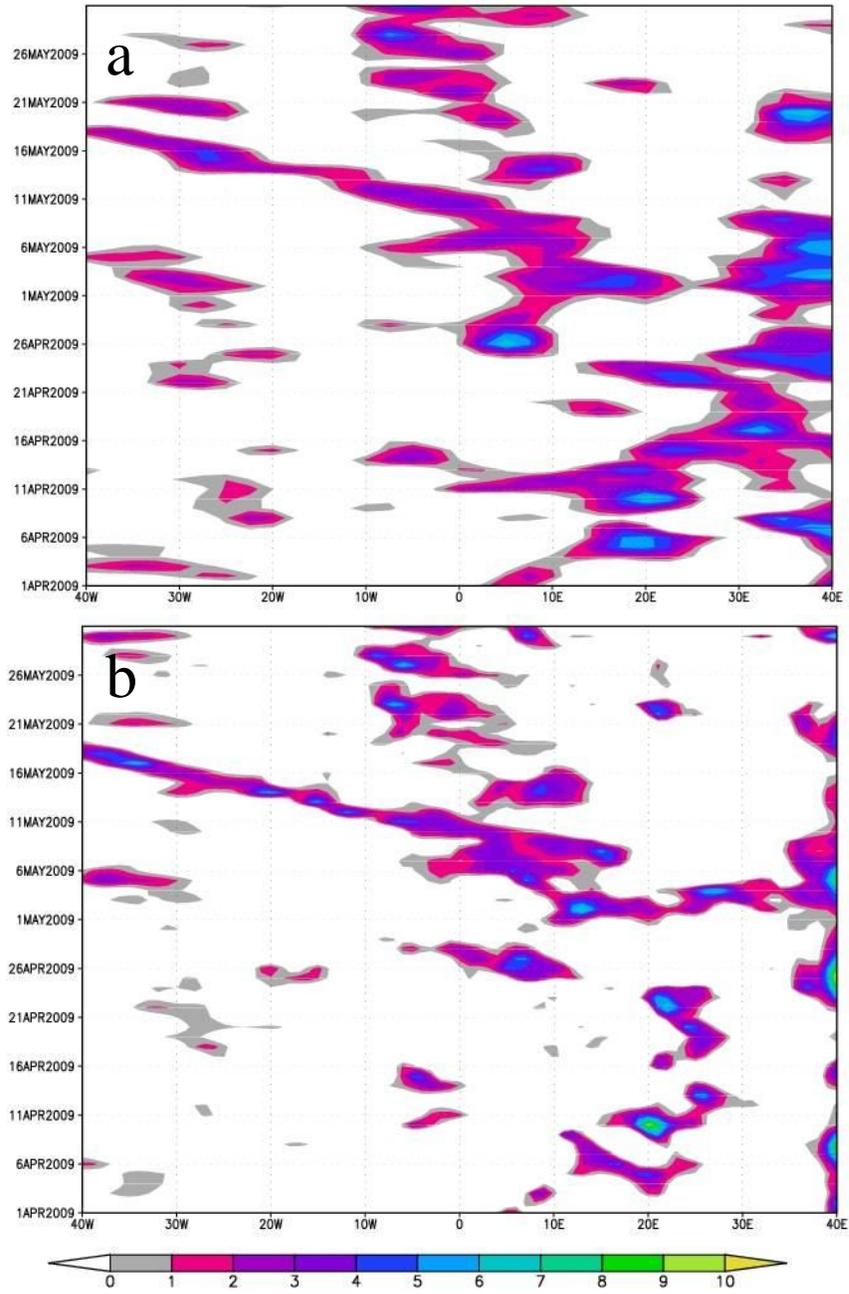
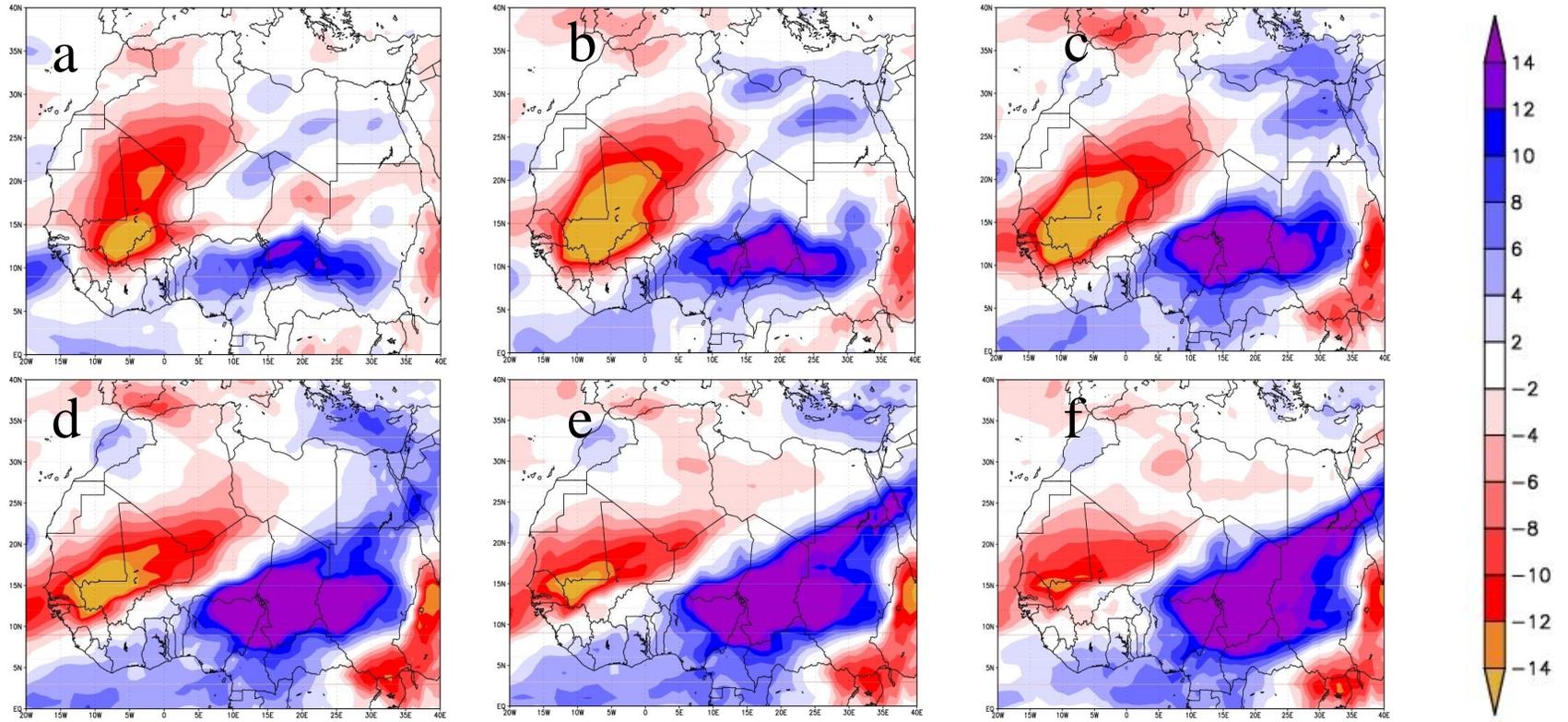
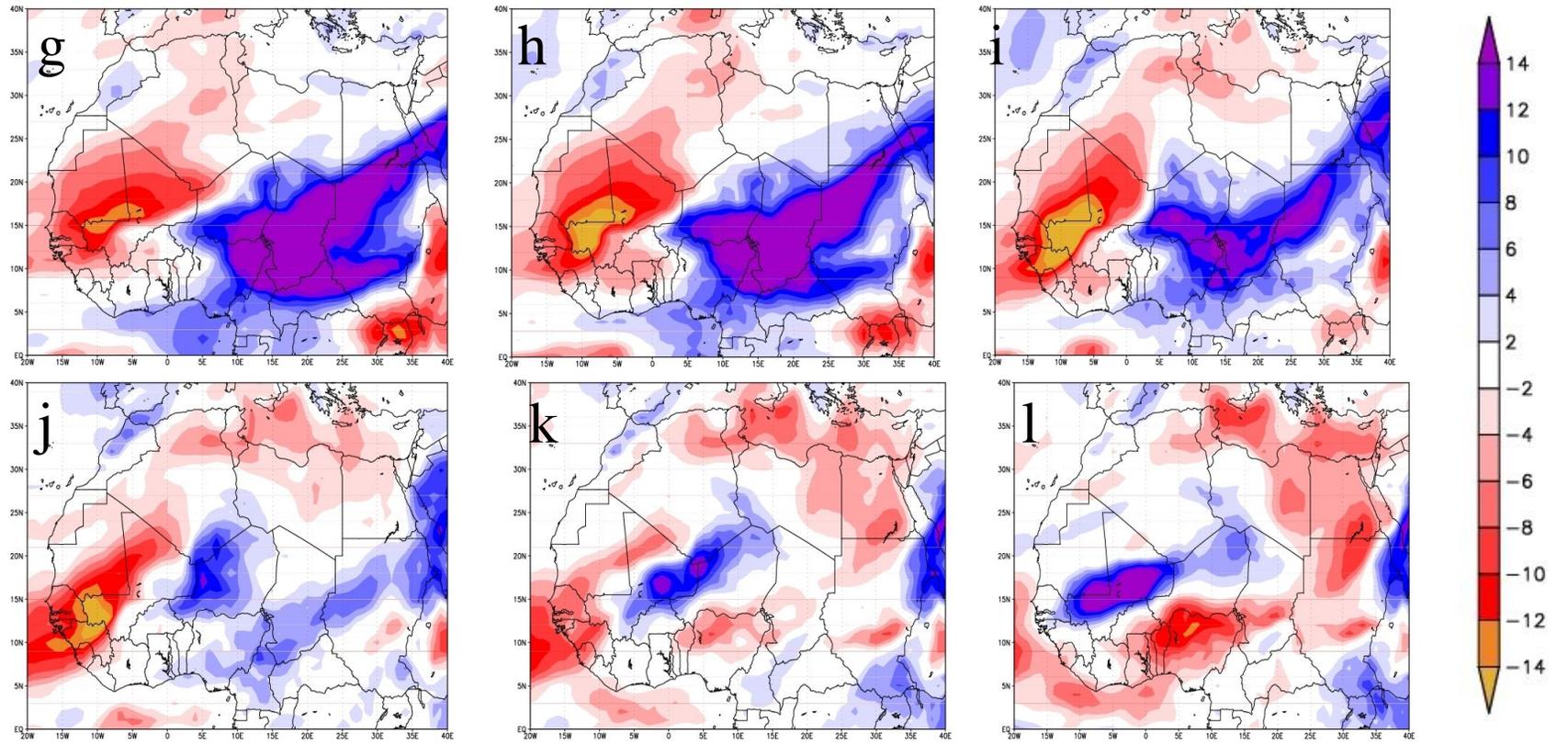
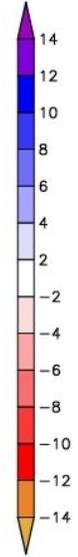
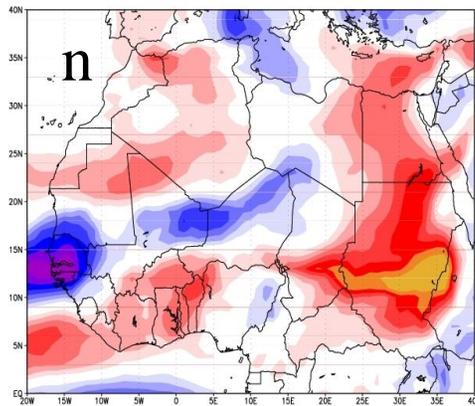
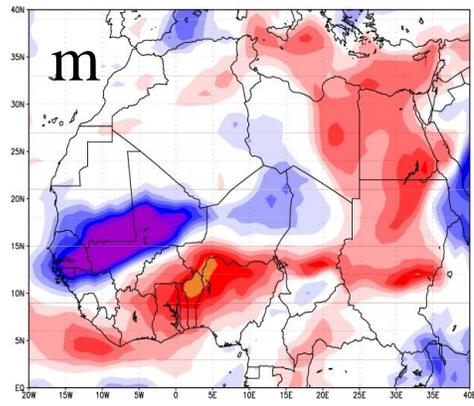


Figure 5.8: Time-longitude Hovmöller plot of meridional wind averaged for all points at 15°N and spanning from 40°E-40°W for (a) NNRP and (b) FNL.

Figure 5.9: Sequence of total atmospheric column precipitable water 3-day running mean anomalies during 2009 compared to the climatological period 2000-2009. Presented are (a) 2, (b) 3, (c) 4, (d) 5, (e) 6, (f) 7, (g) 8, (h) 9, (i) 10, (j) 11, (k) 12, (l) 13, (m) 14 and (n) 15 of May 2009.







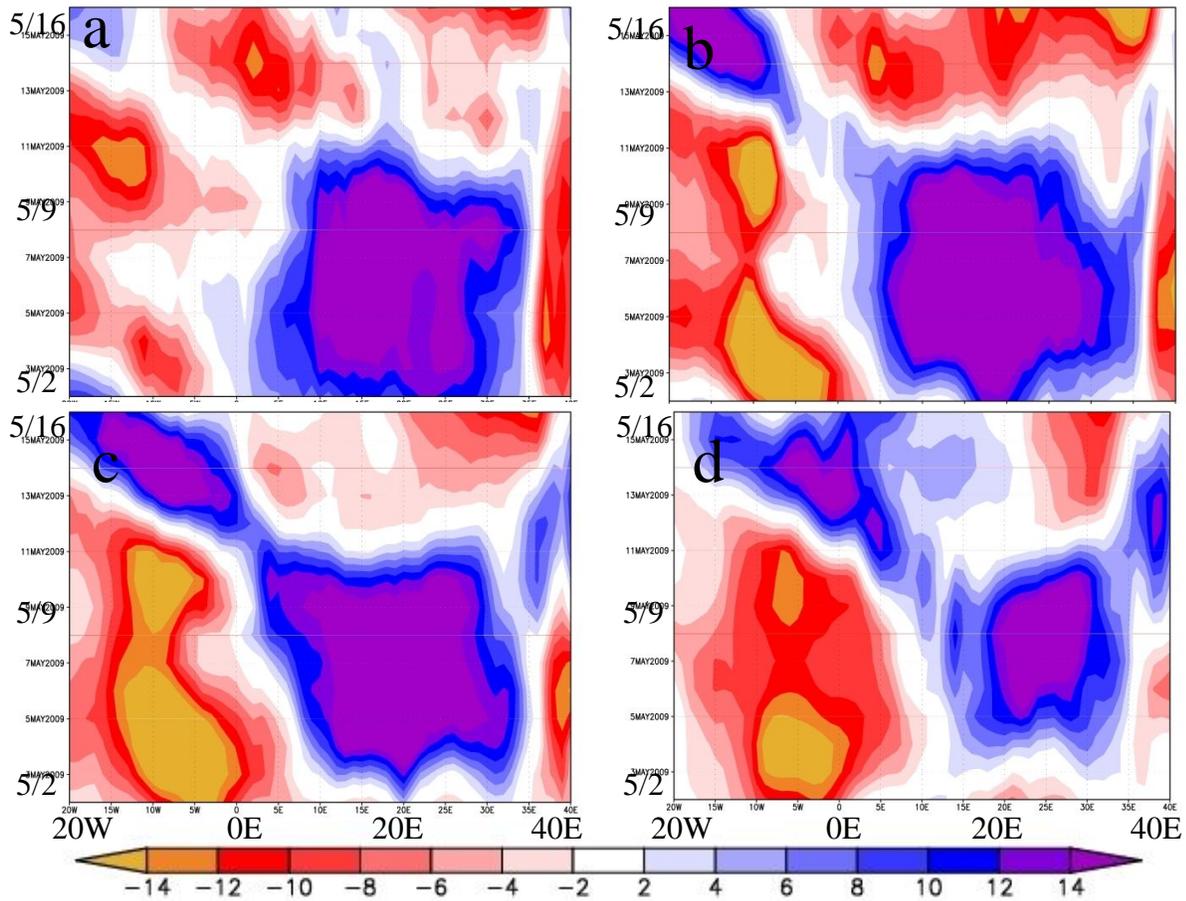
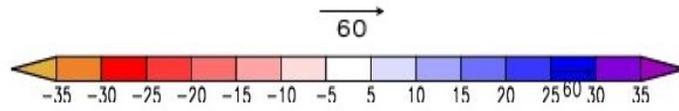
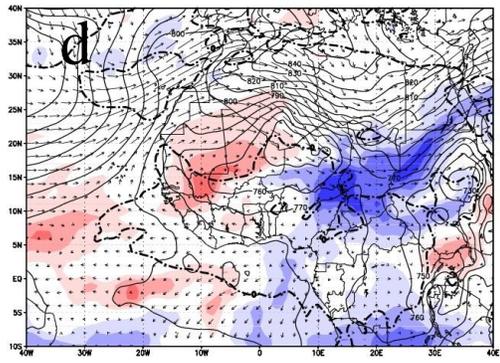
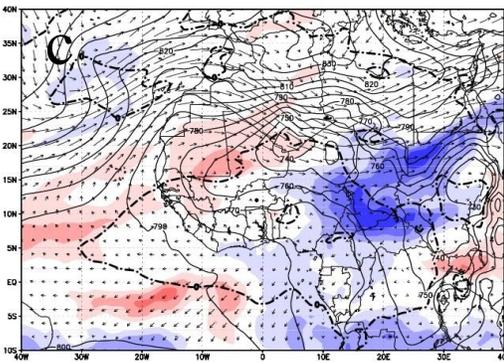
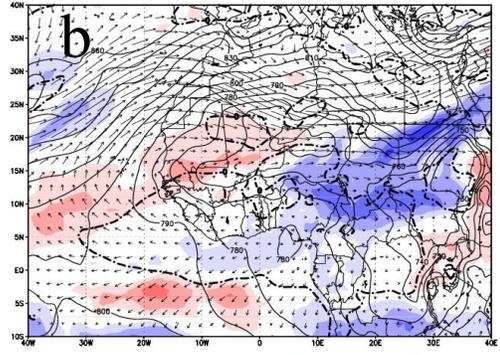
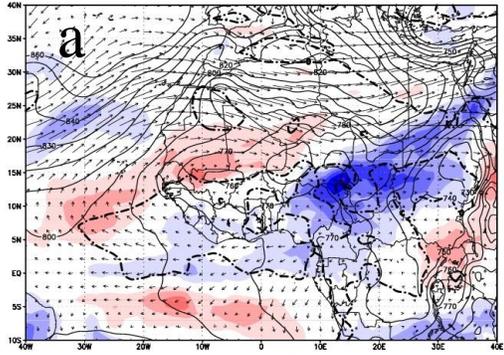
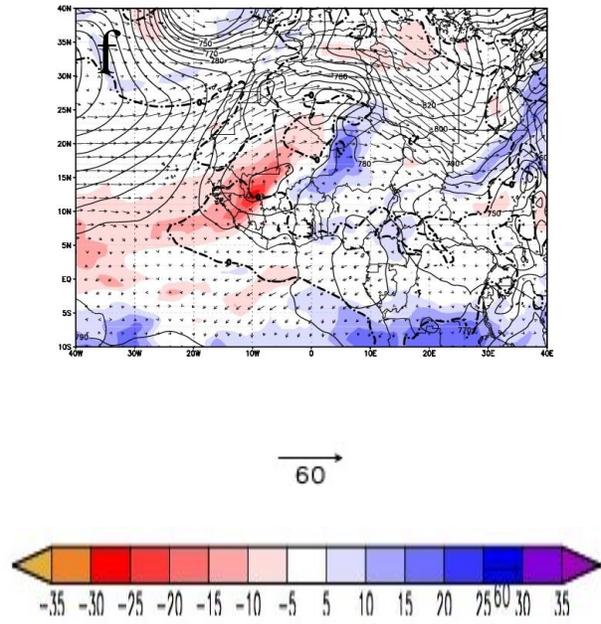
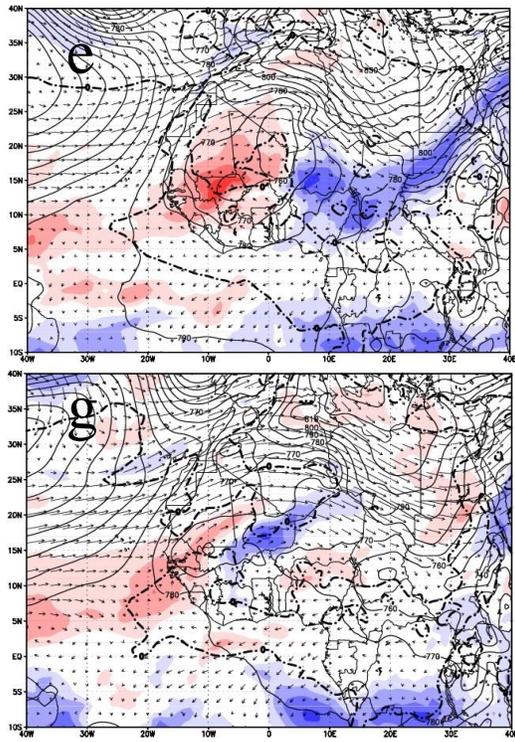


Figure 5.10: Time-longitude Hovmöller plots of 3-day running mean of total atmospheric column precipitable water using FNL data for all points spanning from 40°E-40°W at (a) 10°N, (b) 12.5°N, (c) 15°N, and (d) 17.5°N.

Figure 5.11: Large-scale Synoptic evolution of MME on (a) 5, (b) 6, (c) 7, (d) 8, (e) 9, (f) 10 and (g) 11 May 2009. Solid lines indicate 925 hPa geopotential height and shading depicts total atmospheric column precipitable water (kg m^{-2}) 3-day running mean of anomalies (2009-climatology). 200 hPa winds are also shown as vectors. The thick dash-dot line represents the ITF (0 ms^{-1} , Sultan and Janicot 2003 definition).





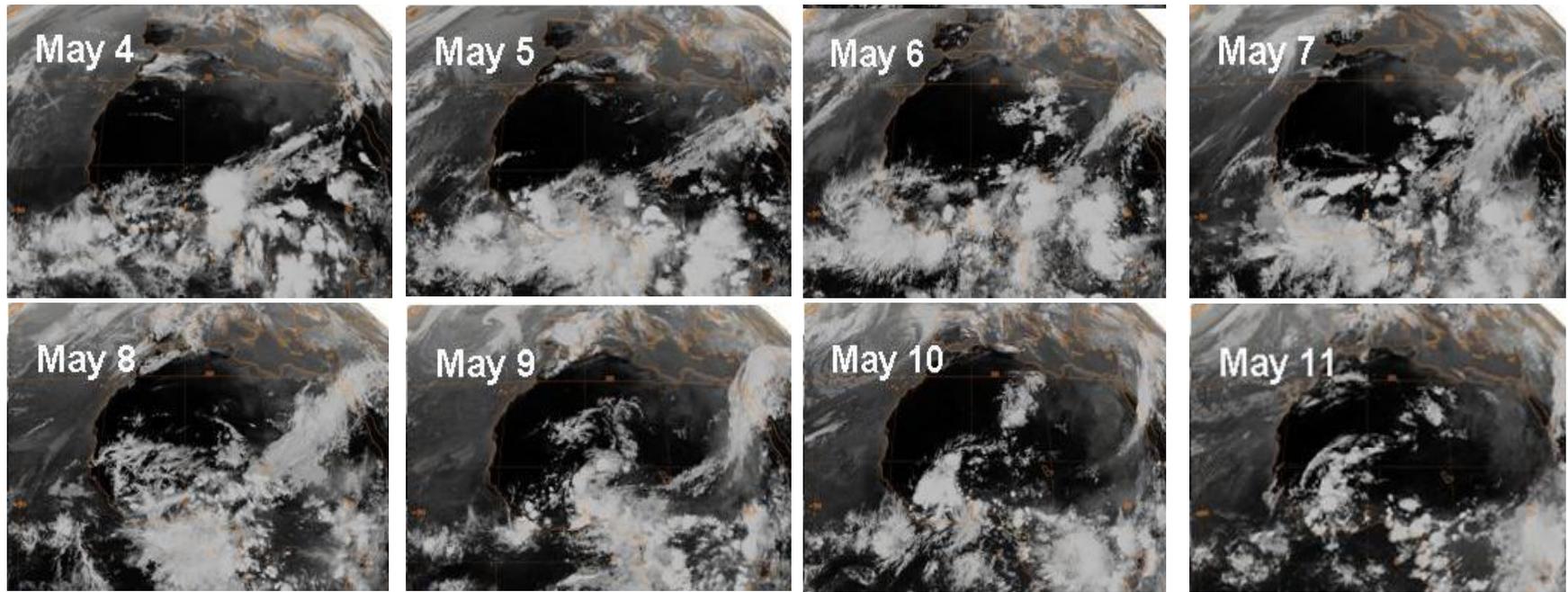


Figure 5.12: *Meteosat-7* IR images at 1800 UTC for the duration of the MME (May 4 – May 11). Dates are marked on the images.

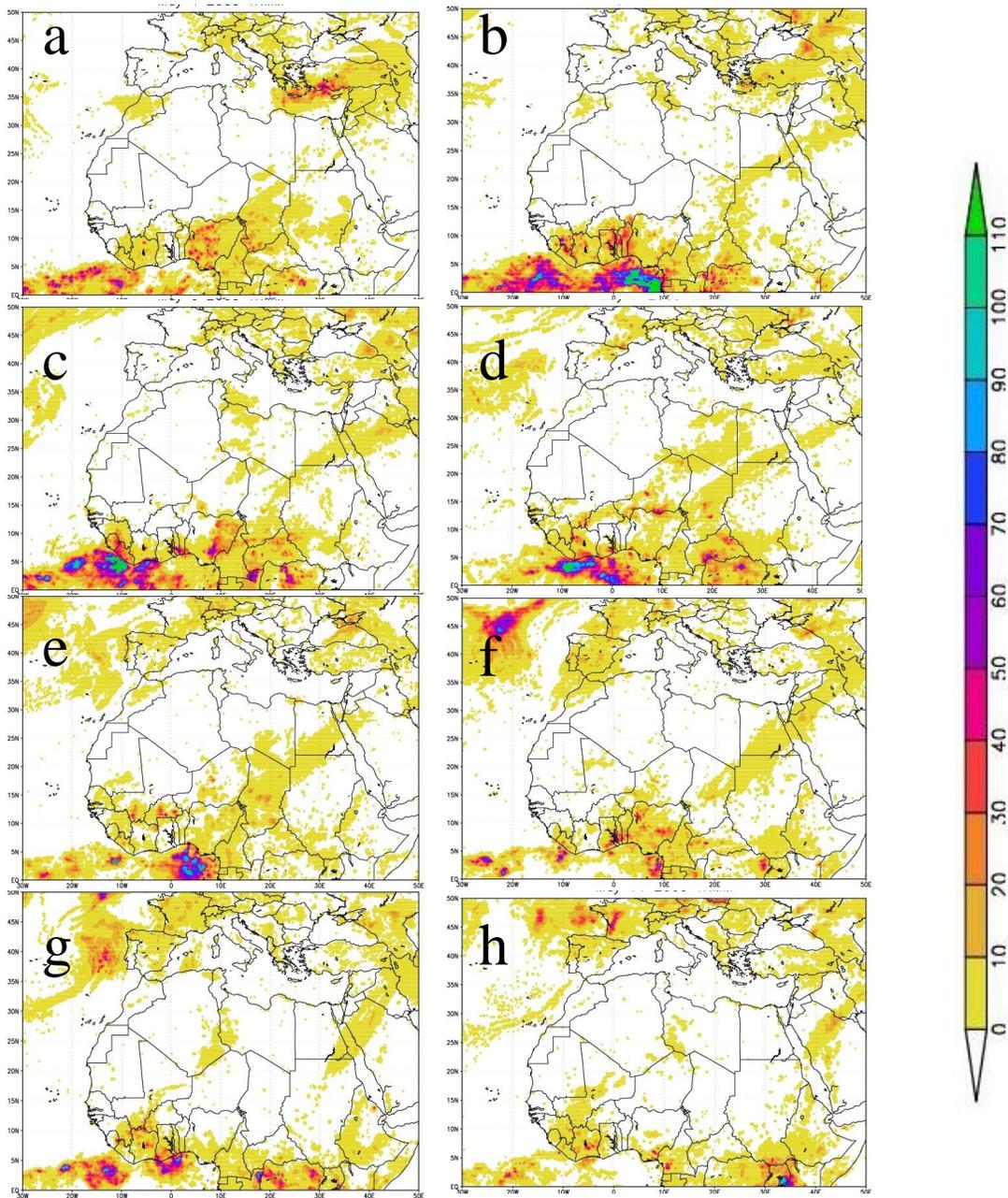


Figure 5.13: TRMM-derived view of mid-May tropical – extra-tropical interaction event. The dates shown are May 4 (a), 5 (b), 6 (c), 7 (d), 8 (e), 9 (f), 10 (g) and 11 (h).

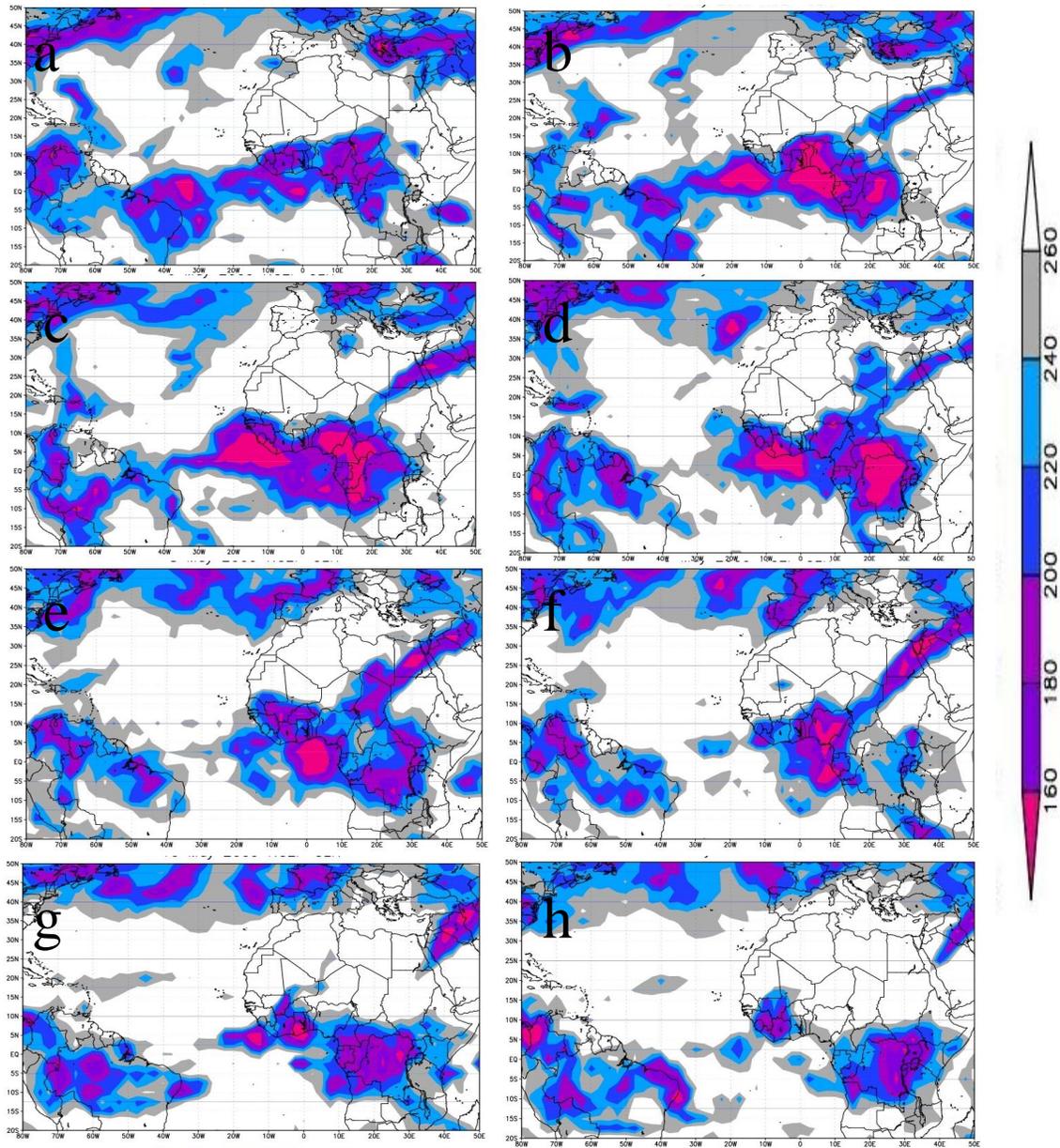


Figure 5.14: NCEP OLR-derived view of mid-May tropical – extra-tropical interaction event
 The dates shown are May 4 (a), 5 (b), 6 (c), 7 (d), 8 (e), 9 (f), 10 (g) and 11 (h).

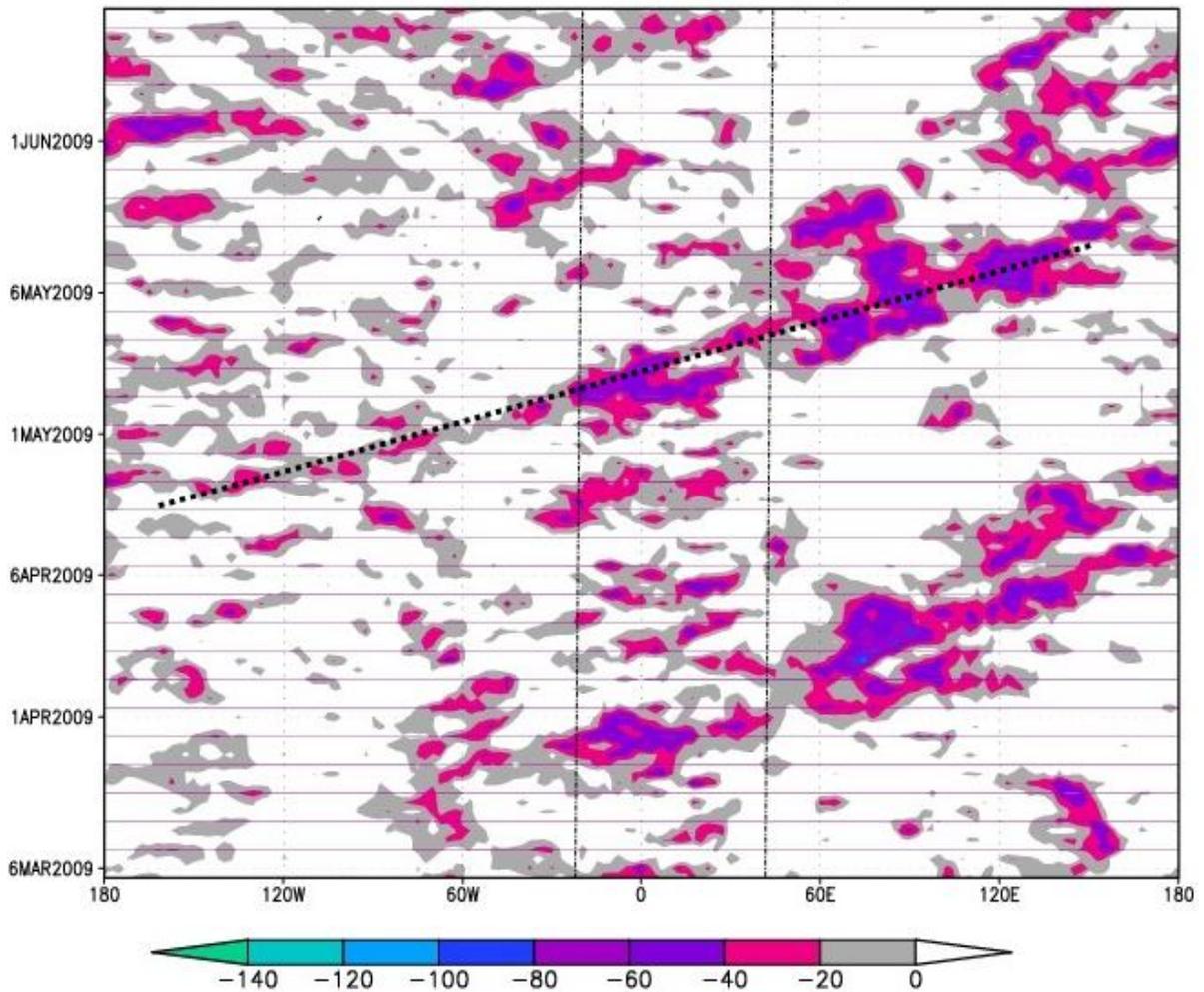


Figure 5.15: Time-longitude Hovmöller plot of NCEP OLR anomaly (2009 - recent climatology) for March 15 – June 15 2009 averaged for all points between 2.5°S and 7.5°S. Only negative values are shown for clarity.

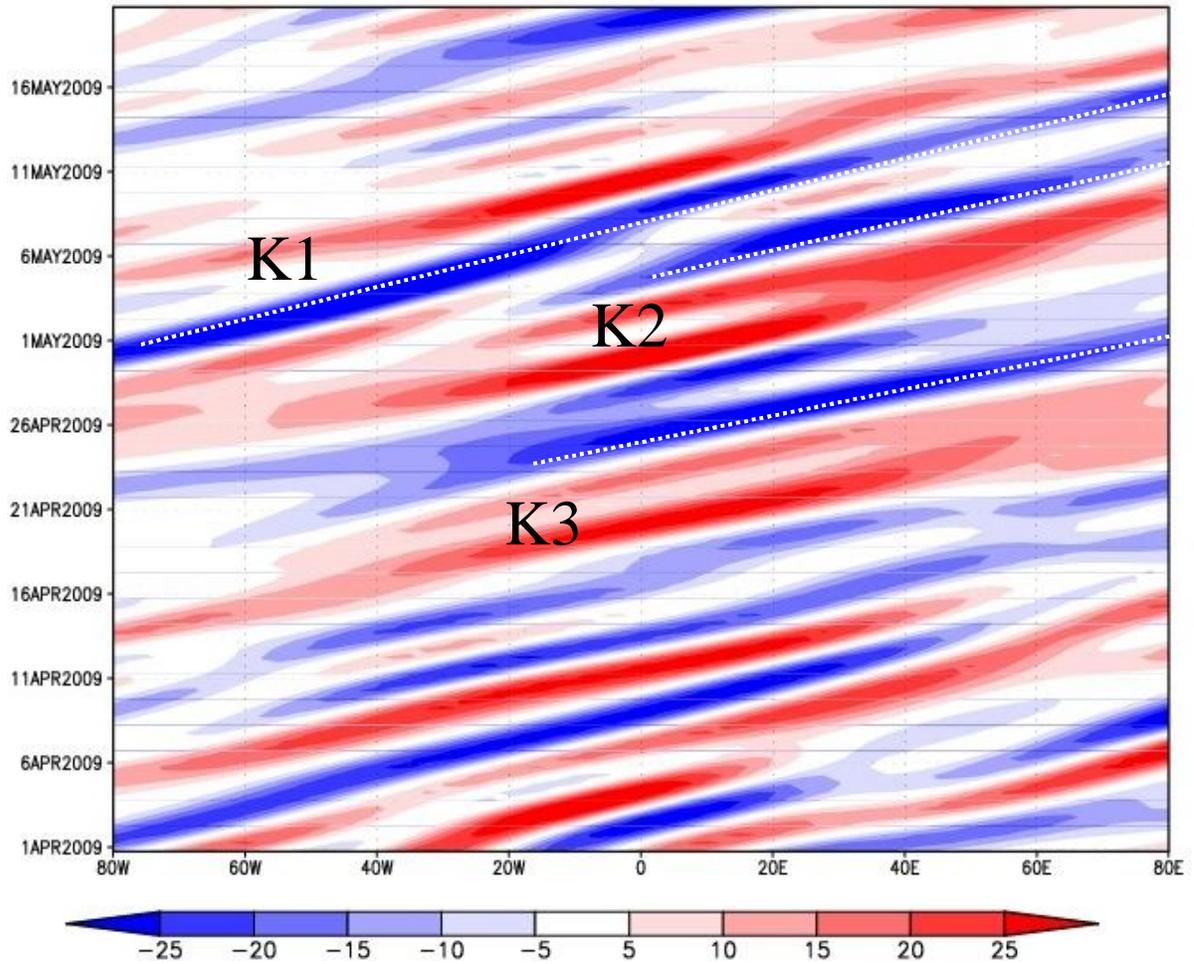


Figure 5.16: Kelvin-filtered OLR (W m⁻²) averaged for equator to 5°N from 80°W to 80°E for the period April 1 – May 20. Dashed diagonal line shows the eastward progression of the waves. Wave name designations are labeled accordingly.

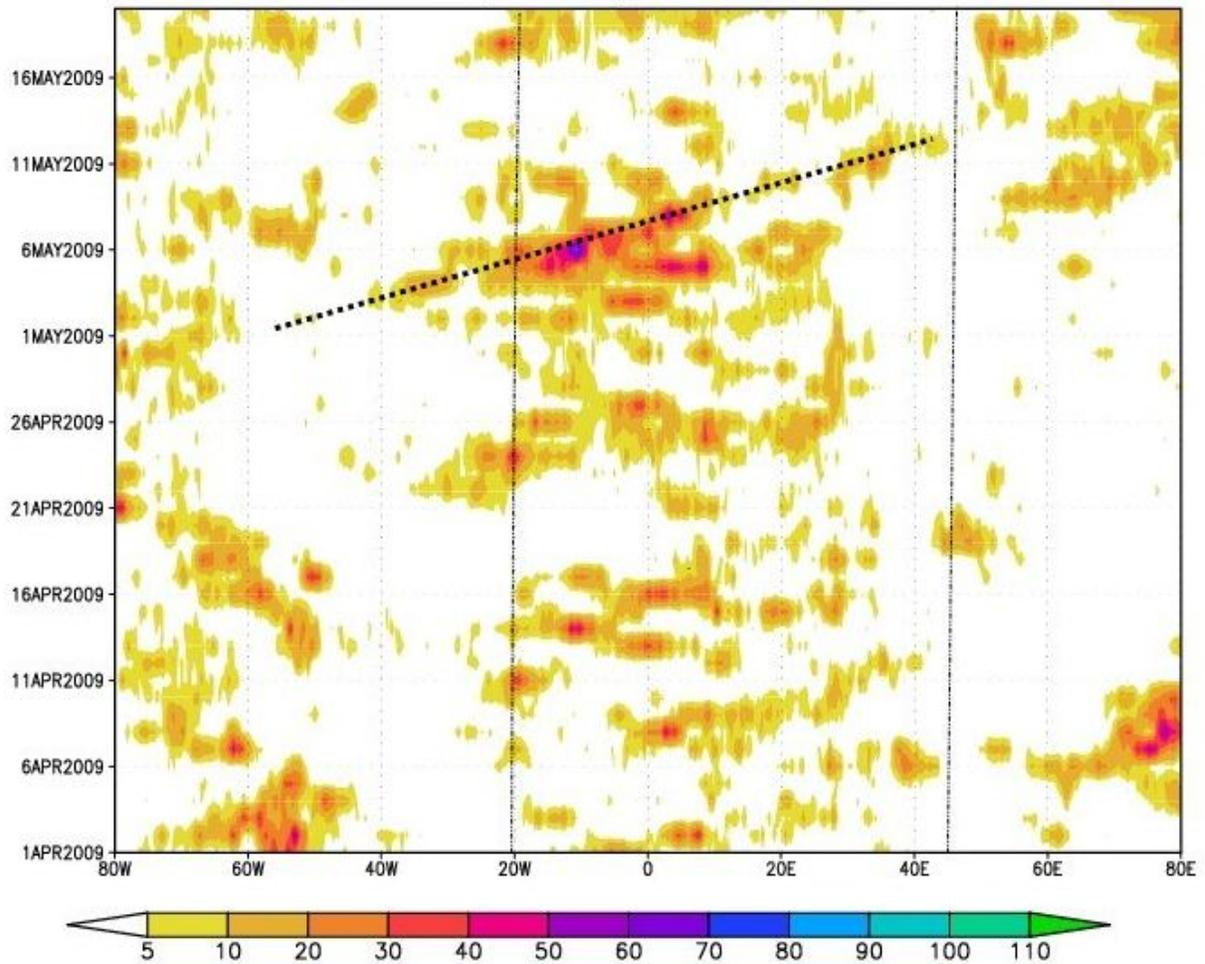


Figure 5.17: Unfiltered 3B43 TRMM daily accumulate precipitation (mm) averaged for equator to 7.5°N from 80°W to 80°E for the period April 1 – May 20. Vertical lines denote the approximate position of Africa. Dashed diagonal line shows the eastward progression of the wave.

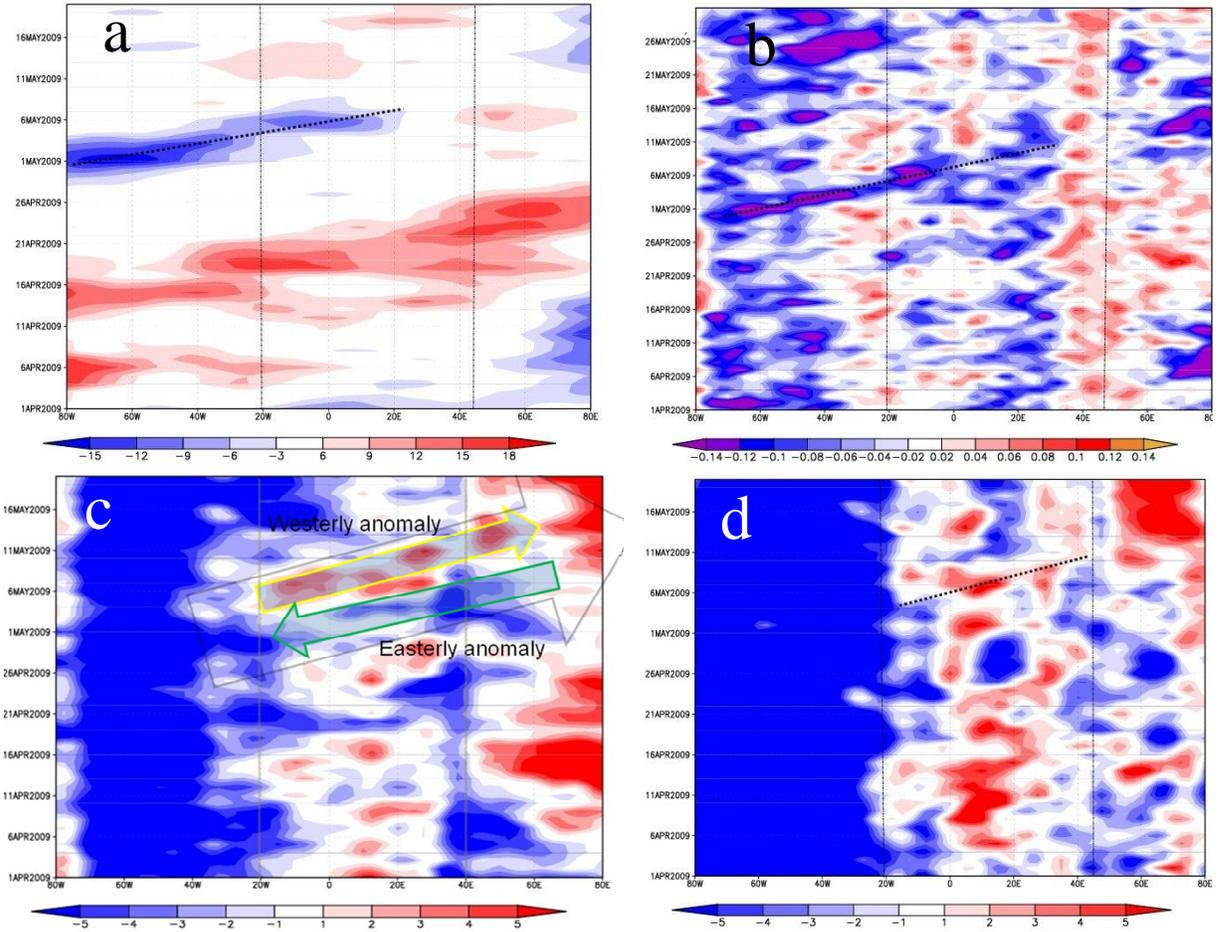


Figure 5.18: NNRP-derived (a) velocity potential at (200 hPa) at the equator, (b) FNL ω at 500 hPa at 1 Pa intervals, (c) zonal wind (m s^{-1}) at 850 hPa and (d) zonal wind (m s^{-1}) at 925 hPa averaged for 2.5°S to 7.5°N from 80°W to 80°E for the period April 1st – May 20th. Vertical lines denote the approximate position of Africa. Dashed diagonal line shows the eastward progression of the wave.

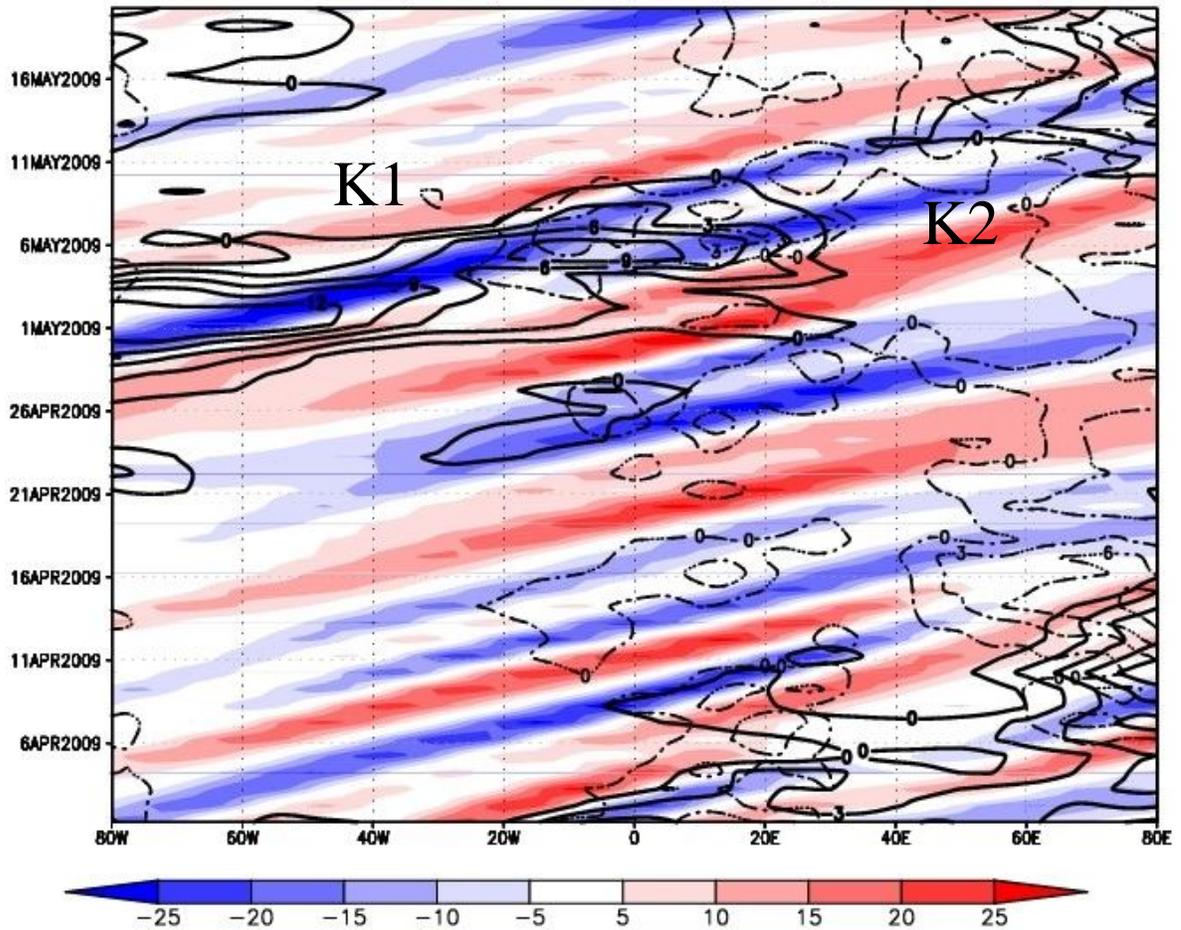


Figure 5.19: Time-longitude Hovmoller diagram of the MME Kelvin wave filtered from the OLR (shaded) averaged for $2.5^{\circ}\text{S} - 7.5^{\circ}\text{N}$ along with the 200 hPa velocity potential at the equator (solid contour) and westerly 850 hPa zonal wind (dash dot). Only positive values are shown for zonal winds and negative values for the velocity potential so that it corresponds with the convective signal.

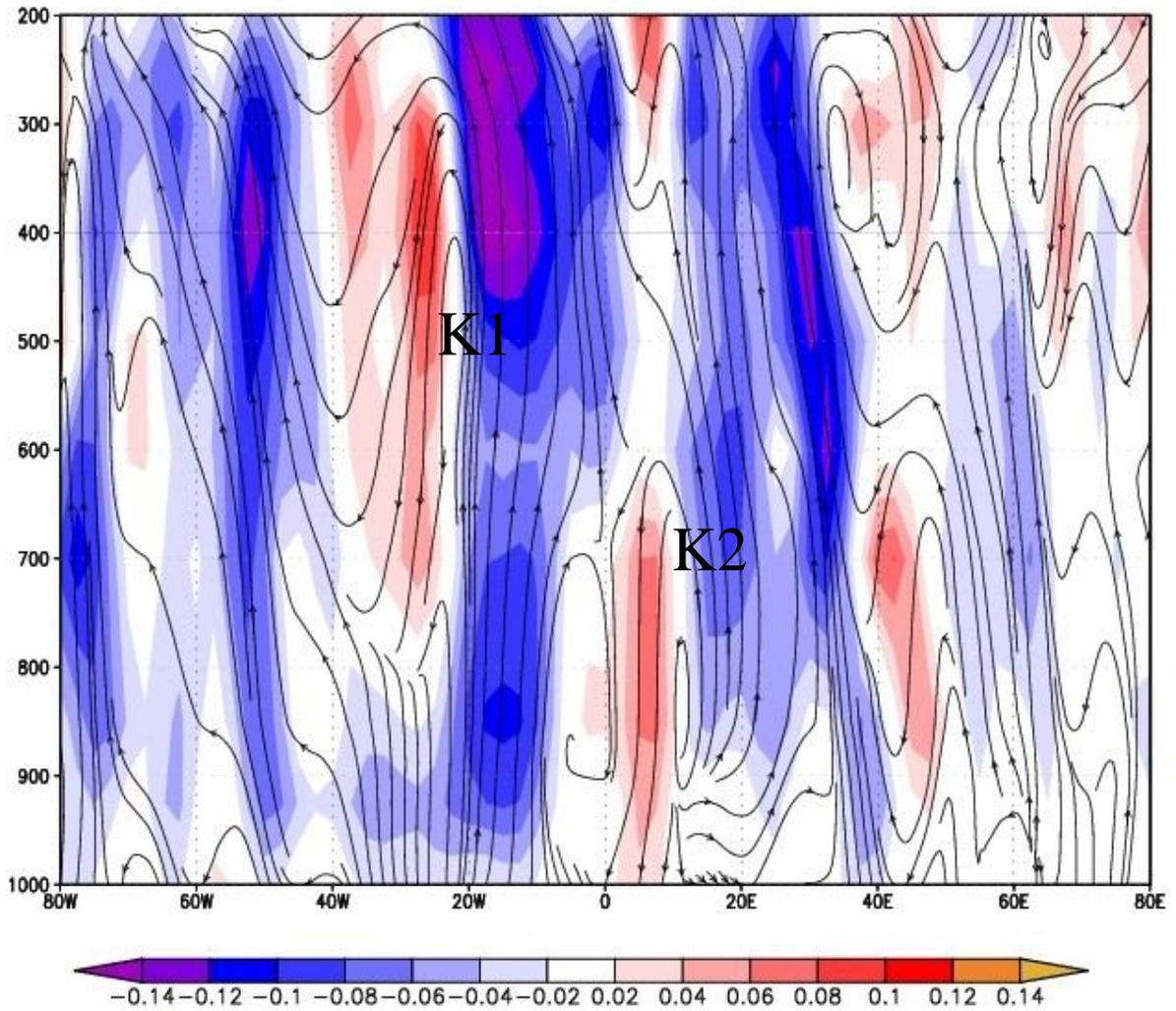


Figure 5.20: Vertical view of MME Kelvin wave (K1) on May 7 with the profile taken at the equator. Vertical velocity is shown (shaded) along with pseudo-vectors of zonal wind (m s^{-1}) and vertical velocity ($\text{Pa} \cdot 100$).

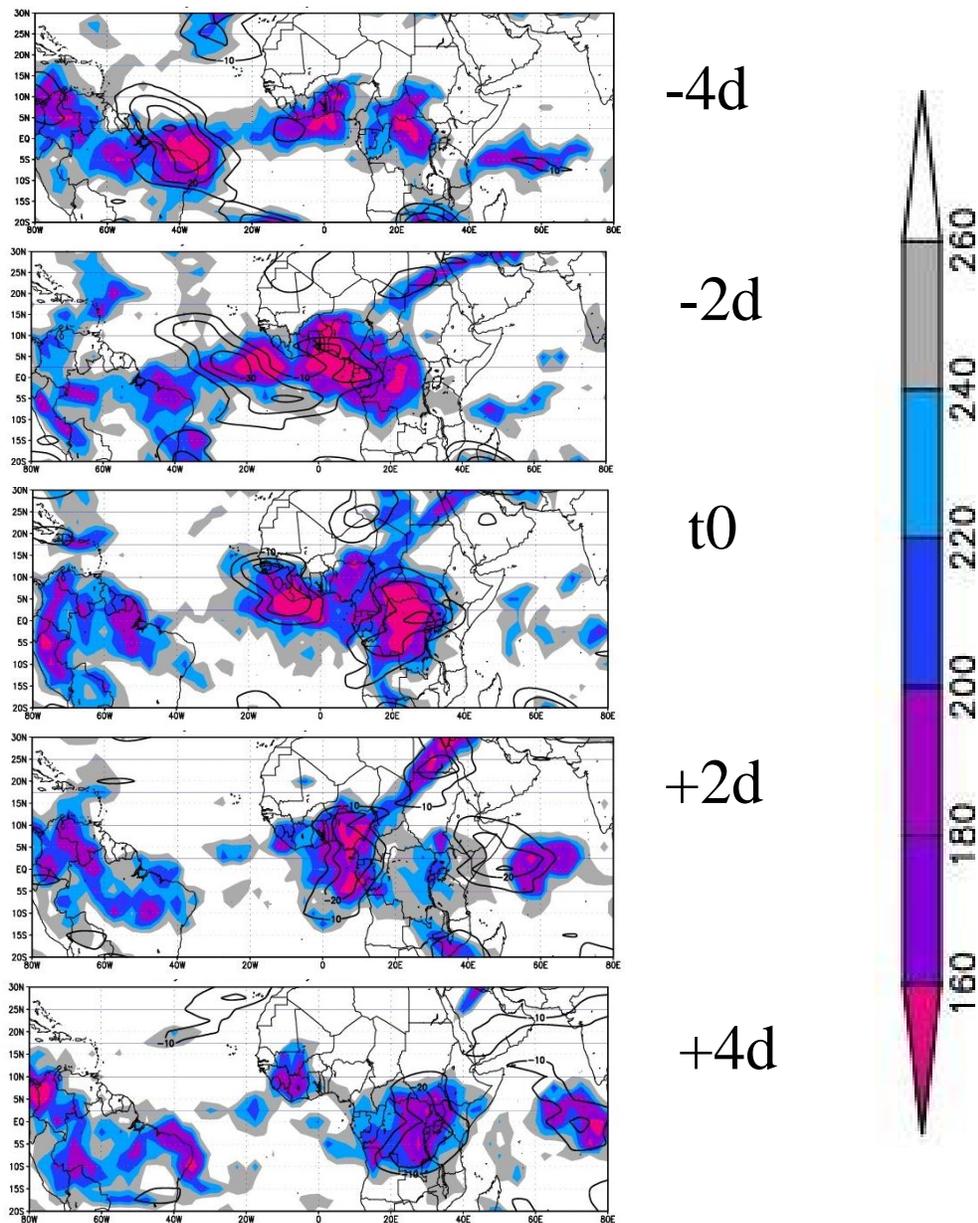


Figure 5.21: (top to bottom) Time sequences of NCEP OLR and Kelvin-filtered OLR. Date (t_0) is when the tropical-extratropical interaction is at its maximum. Kelvin-filtered positive anomalies are shown in contours; NCEP OLR is shaded for lower radiation values (i.e. strong convection).

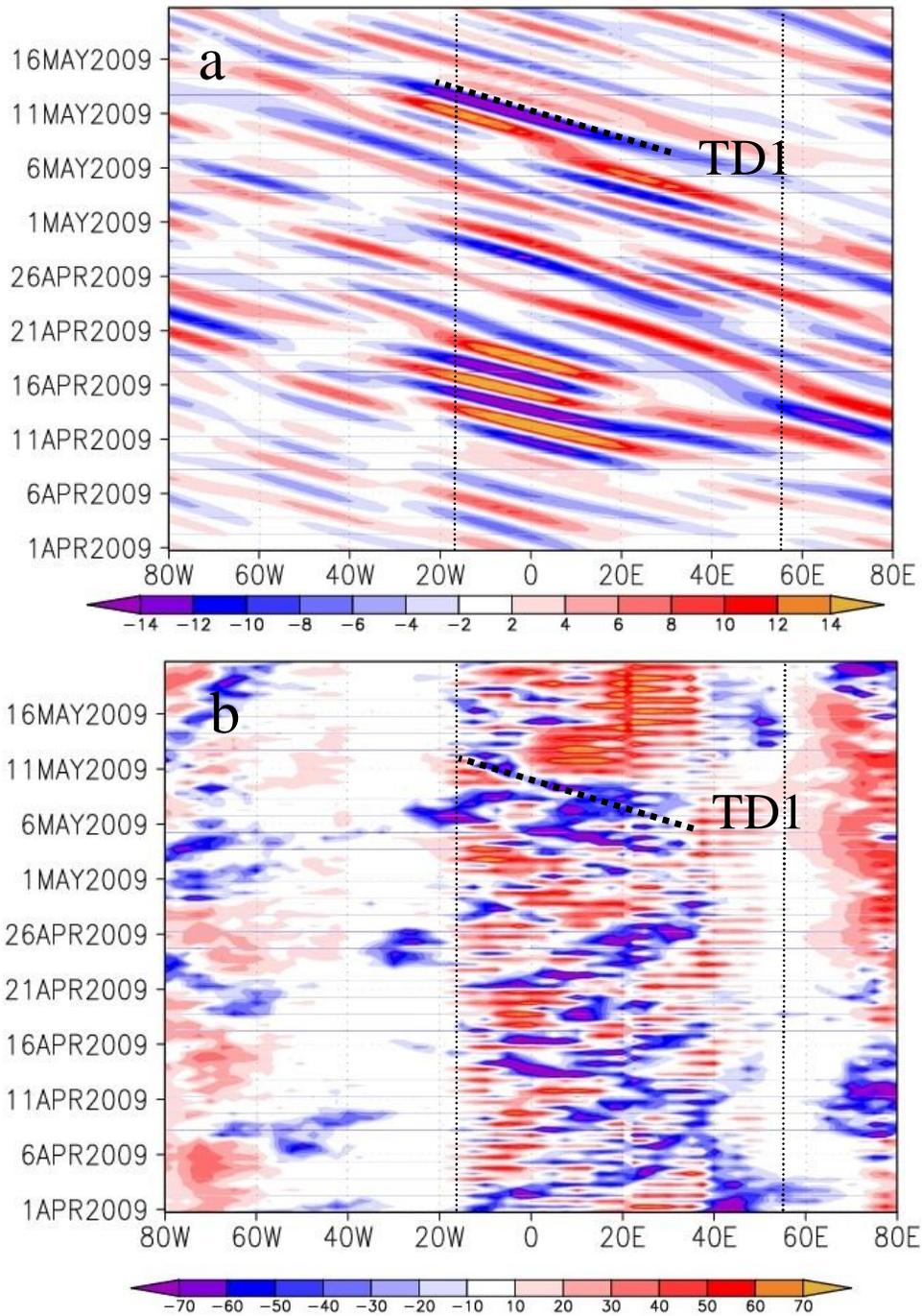


Figure 5.22: (a) TD-type filtered OLR ($W m^{-2}$) averaged for $10^{\circ}N - 15^{\circ}N$ from $80^{\circ}W$ to $80^{\circ}E$ for the period March 27 – May 20. Diagonal dashed line denotes convective portion of TD-types. Westward systems < 10 day period (b) also shown for perspective.

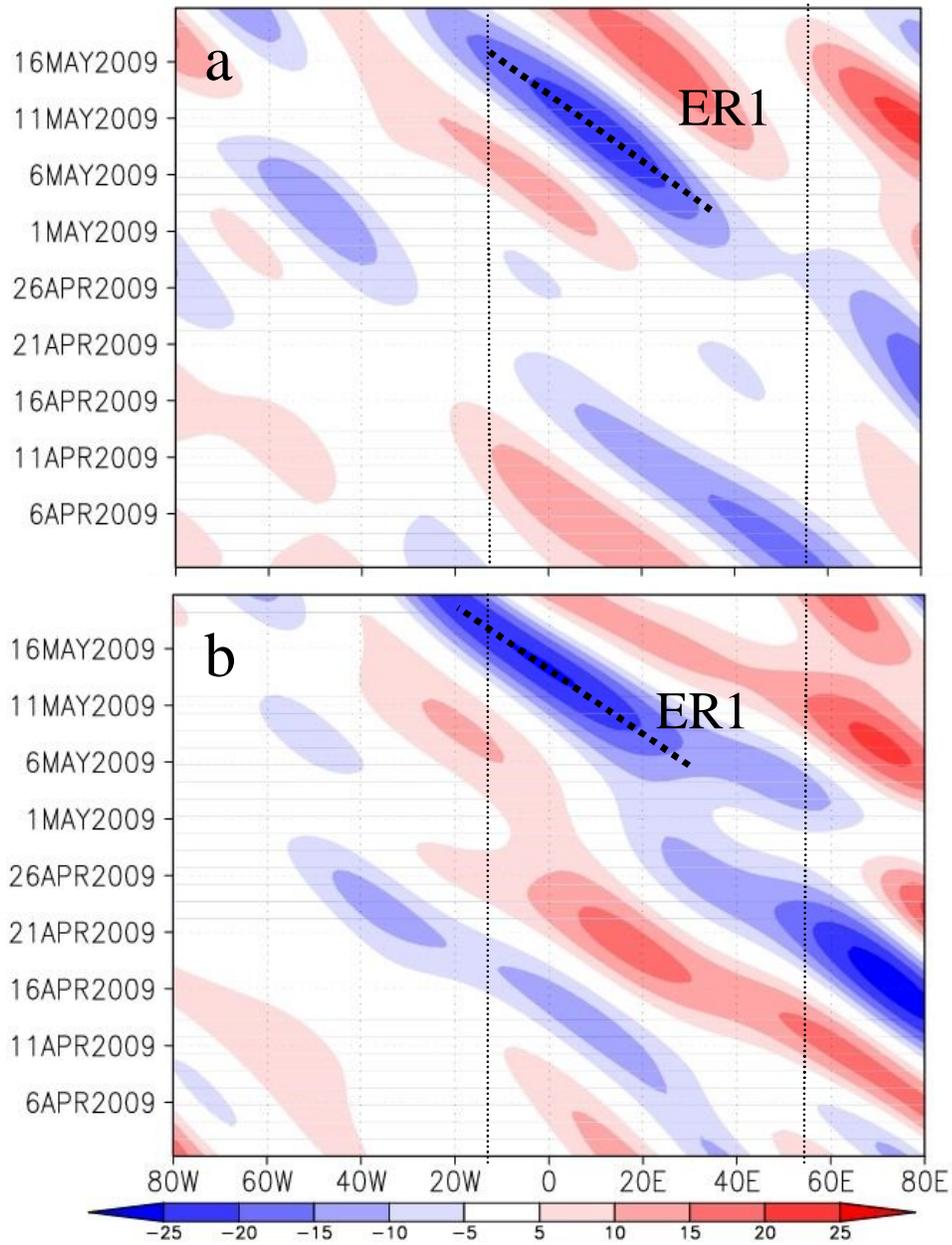


Figure 5.23: Time-longitude Hovmoller plot of ER-filtered OLR ($W m^{-2}$) for (a) 17.5°N and (b) 7.5°S from 80°W to 80°E for the period April 1 – May 20. Dashed diagonal line shows the westward progression of the wave. Wave name designation is labeled accordingly.

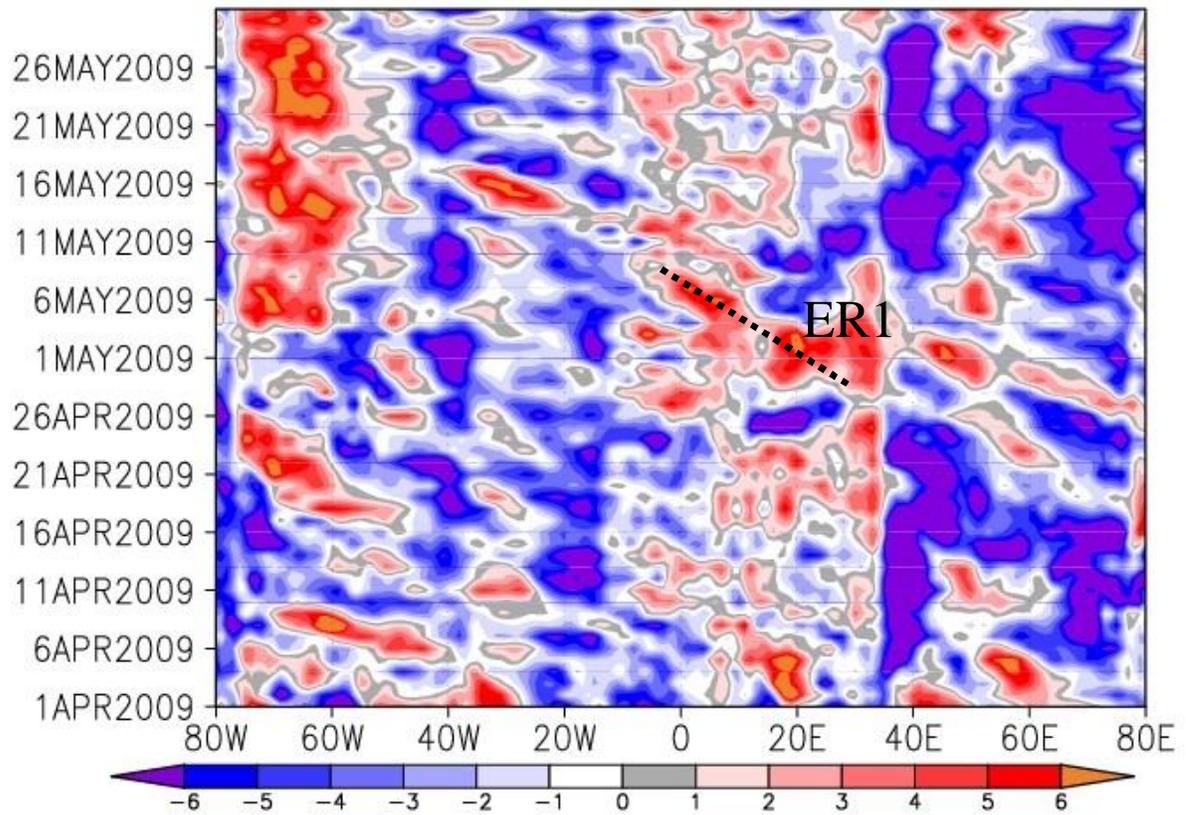


Figure 5.24: Time-longitude Hovmoller plot of 850 meridional wind (m s-1) 10°N - 10°S difference for April - May 2009 for 80°W to 80°E.

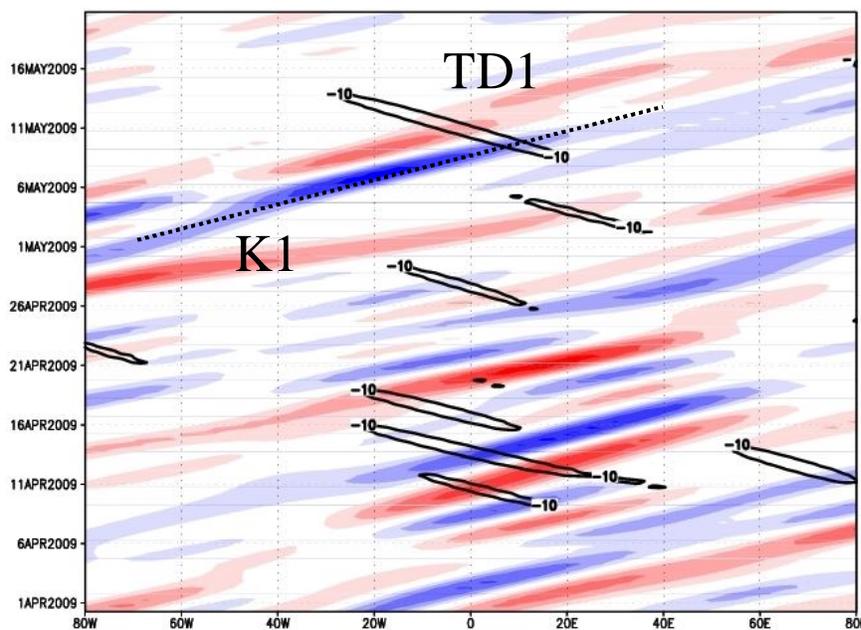
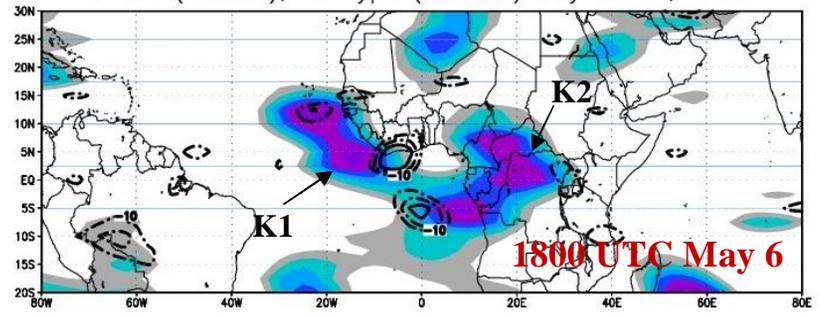
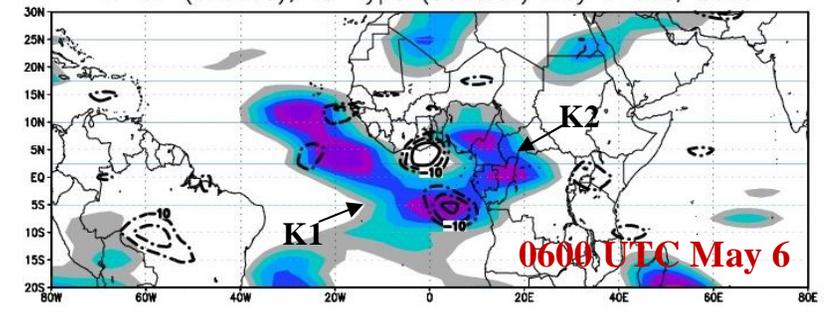
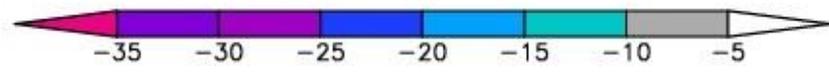
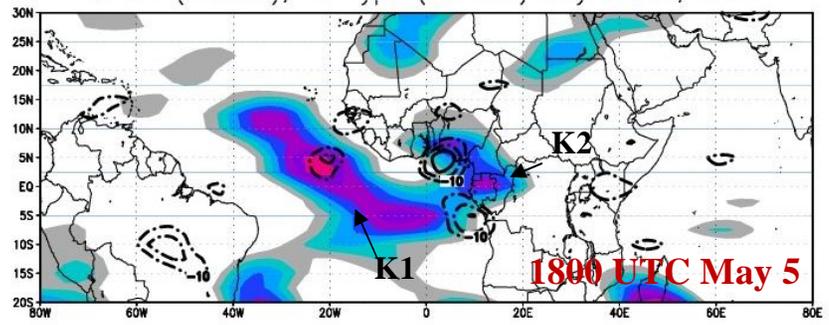
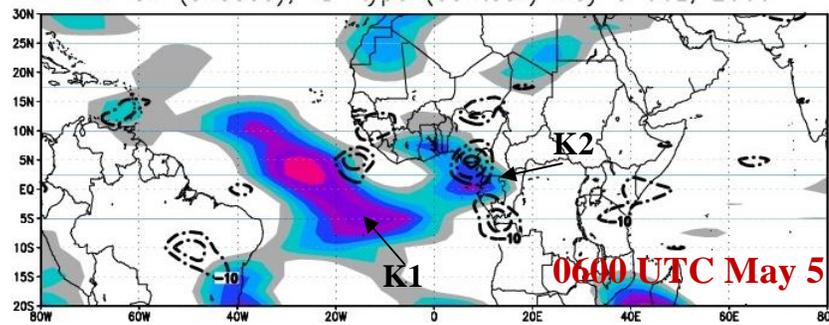
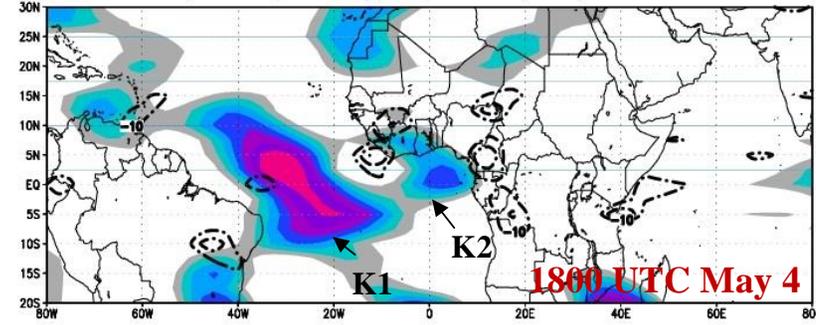
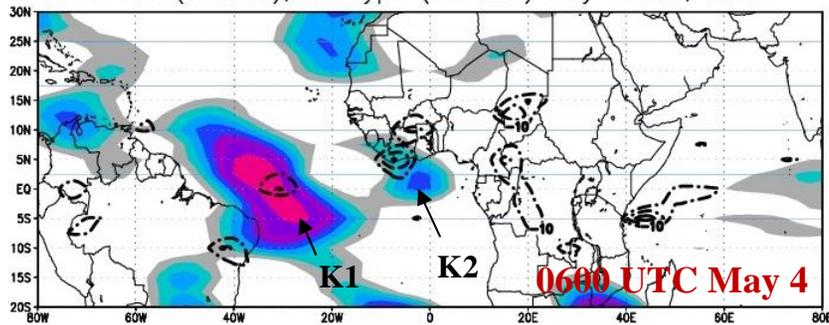
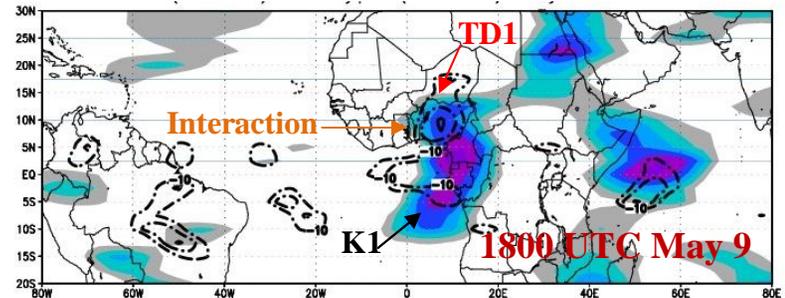
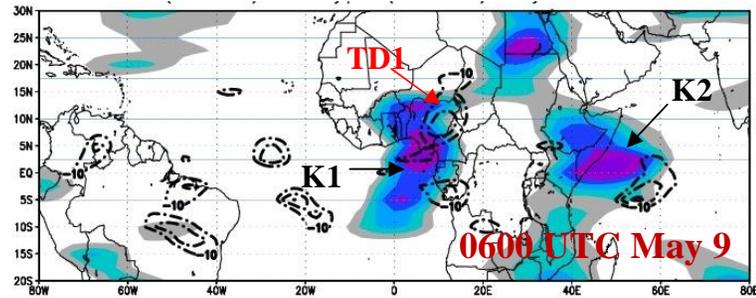
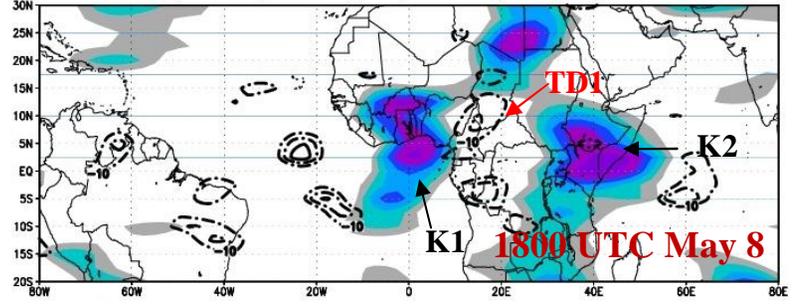
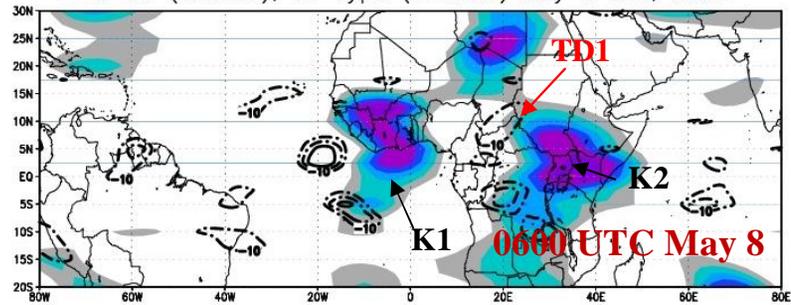
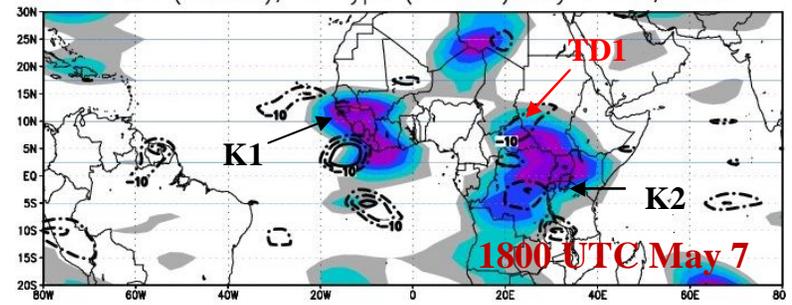
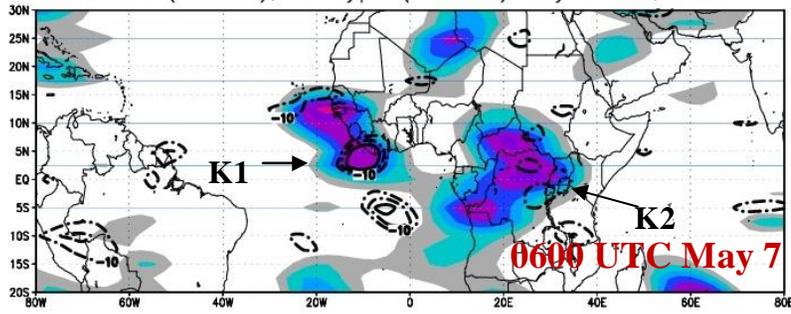
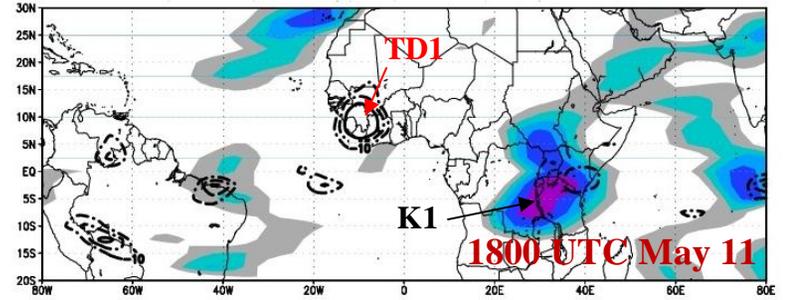
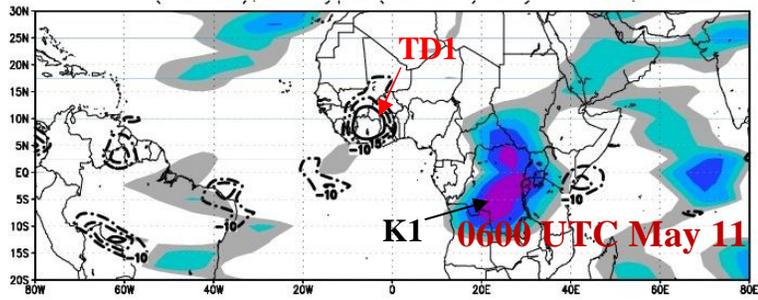
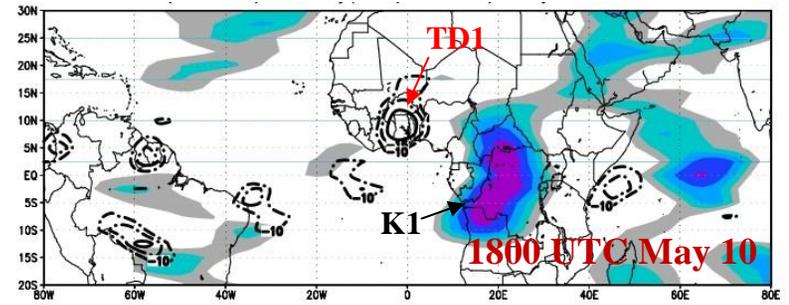
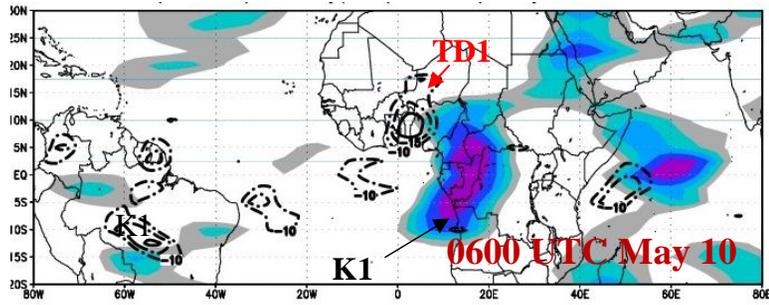


Figure 5.25: Time-longitude Hovmoller plot of TD-type (contour) and Kelvin (shaded) filtered OLR ($W m^{-2}$) averaged for $10^{\circ}N - 15^{\circ}N$ from $80^{\circ}W$ to $80^{\circ}E$ for the period April 1 – May 20 for 2009. TD1 is labeled and K1 is marked with a diagonal dashed line over the convective portion.

Figure 5.26: Time sequences of Kelvin-filtered OLR (shaded) and TD-type (contoured every 10 W m^{-2} from -10 W m^{-2} ; only negatives shown for clarity). TD-type activity was determined by filtering OLR in the period of 2–7.5 days with westward wavenumber of 6–20 used to capture easterly waves during the northern summer (see Kiladis et al. 2006). Weak and potentially spurious signals are suppressed, and only significant phases of both Kelvin waves and TD-types are displayed (i.e., magnitudes greater than one standard deviation). Dates and times are labeled on the bottom right (data is in twice daily format). K1 and K2 are labeled in black and TD1 is labeled in red.







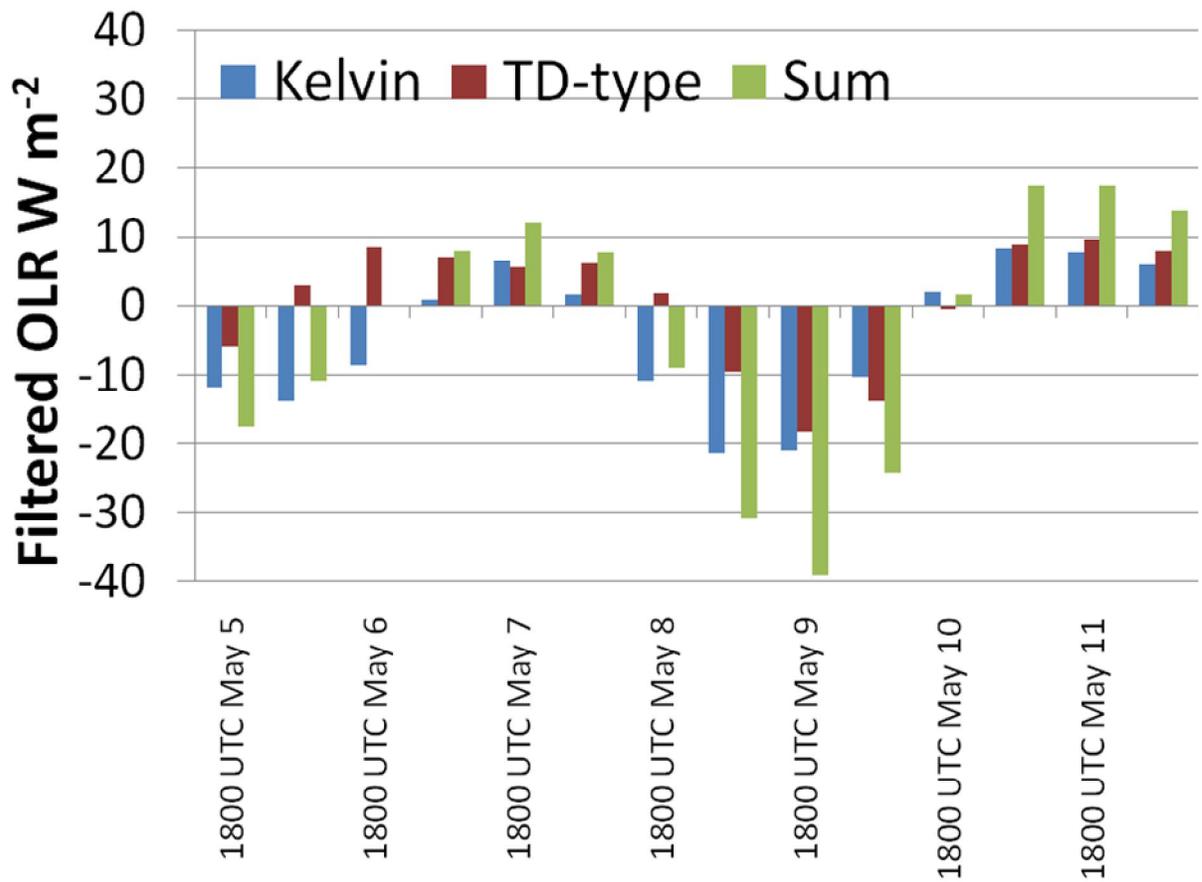


Figure 5.27: Time series for TD-type and Kelvin filtered OLR ($W m^{-2}$) along with the sum of the two taken as area averages for the period 1800 UTC May 5 – 1800 UTC May 11 of 2009.

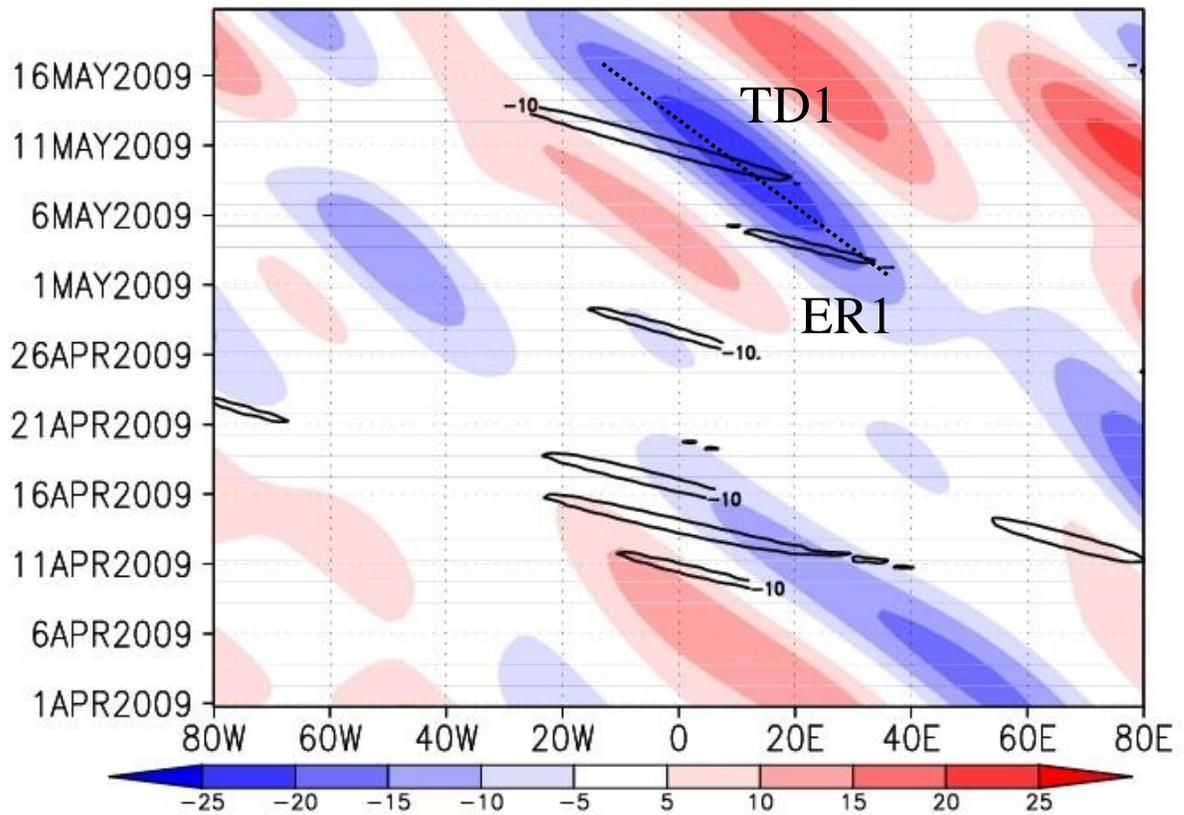
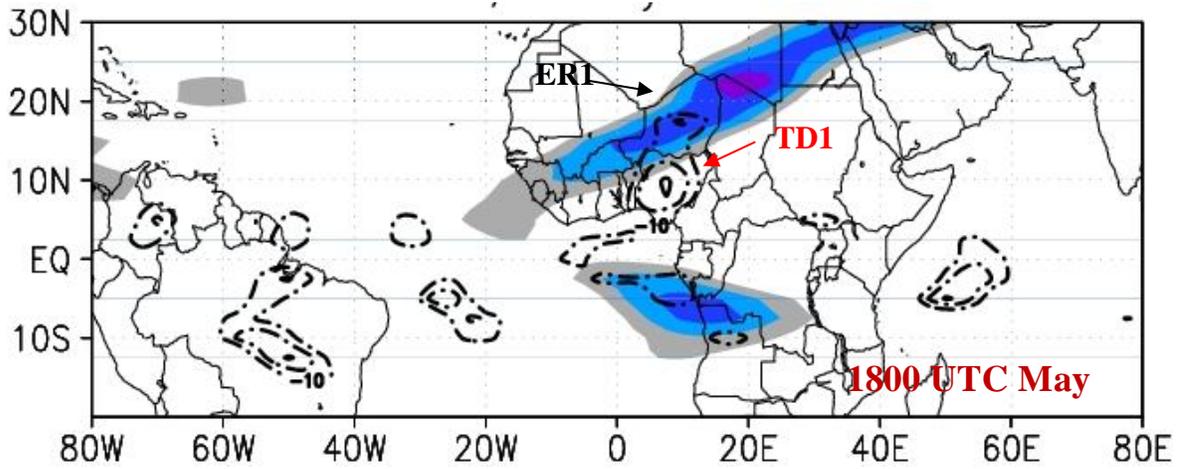
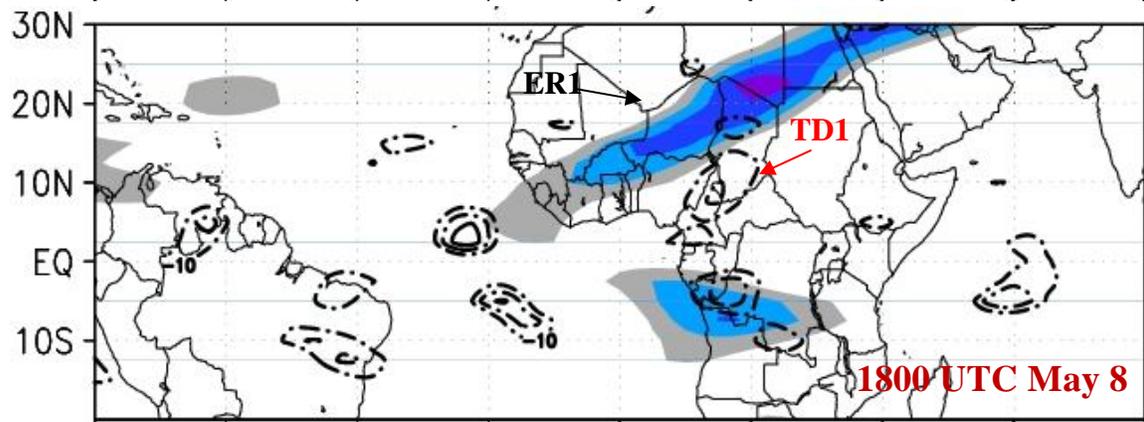
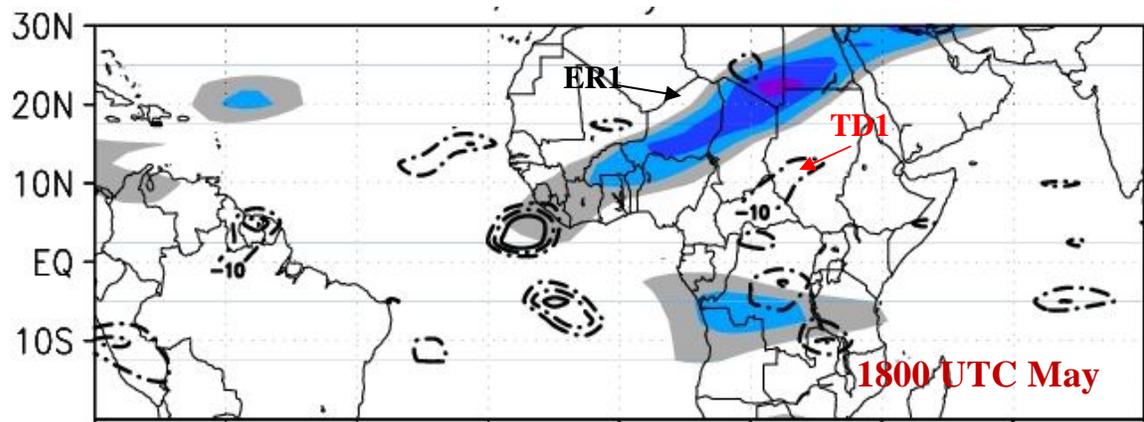
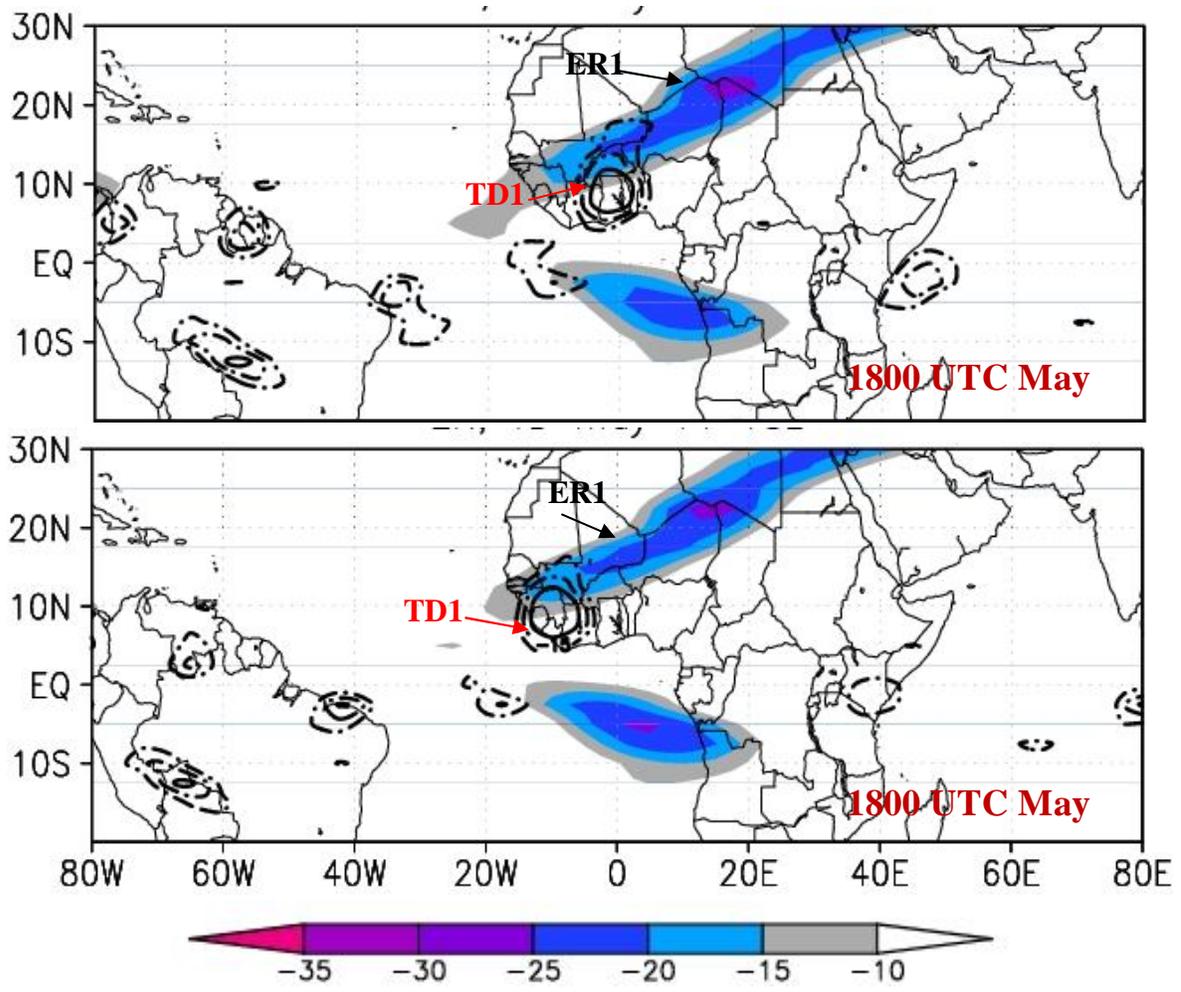


Figure 5.28: Time-longitude Hovmoller plot of TD-type (contour) and ER (shaded) filtered OLR (W m^{-2}) averaged for $10^{\circ}\text{N} - 15^{\circ}\text{N}$ from 80°W to 80°E for the period April 1 – May 20 for 2009. TD1 is labeled and ER1 is marked with a diagonal dashed line over the convective portion.

Figure 5.29: Time sequences of ER-filtered OLR (shaded) and TD-type (contoured every 10 W m^{-2} from -10 W m^{-2} ; only negatives shown for clarity). Weak and potentially spurious signals are suppressed, and only significant phases of both ER waves and TD-types are displayed (i.e., magnitudes greater than one standard deviation). Dates and times are labeled on the bottom right (data is in twice daily format). ER1 is labeled in black and TD1 is labeled in red.





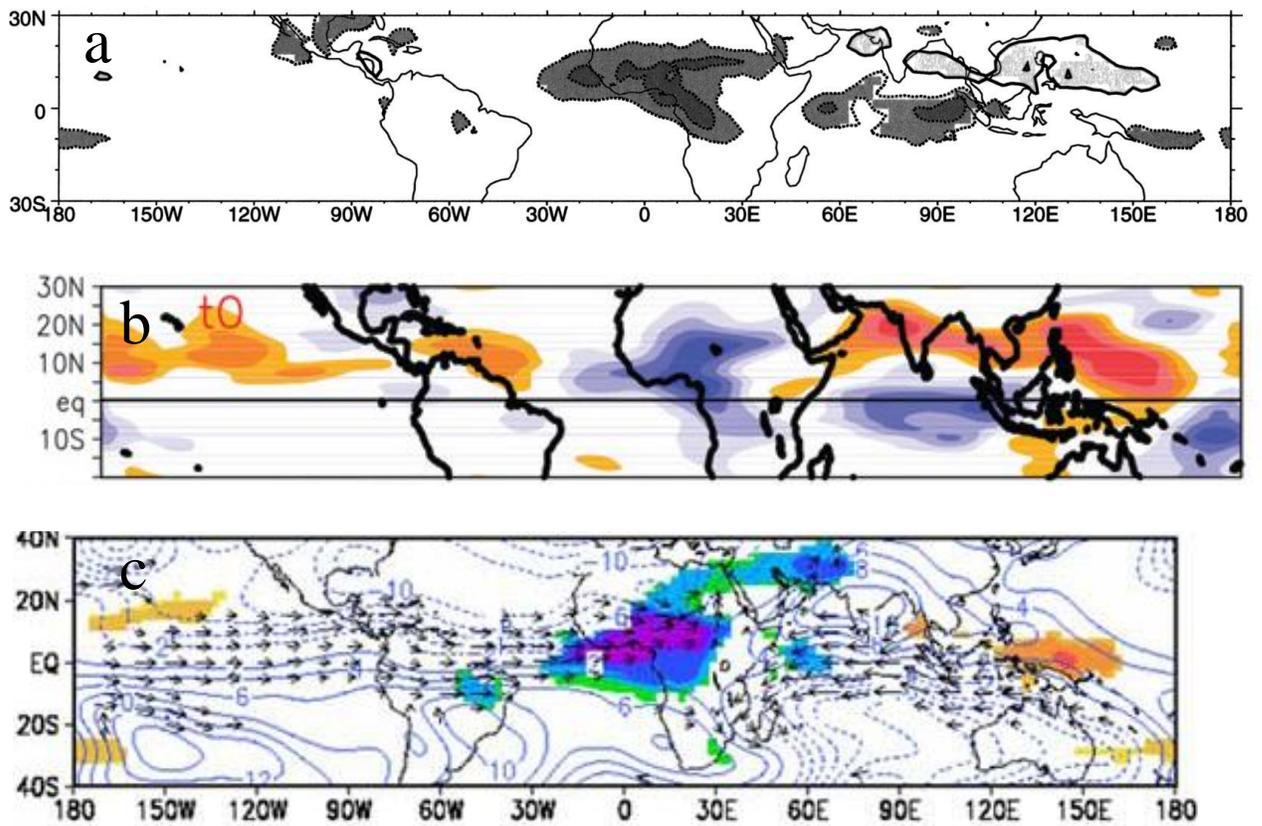


Figure 5.30: Day t0 of Time series for TD-type and Kelvin filtered OLR ($W m^{-2}$) along with the sum of the two taken as area averages for the period 1800 UTC May 5 – 1800 UTC May 11 of 2009.

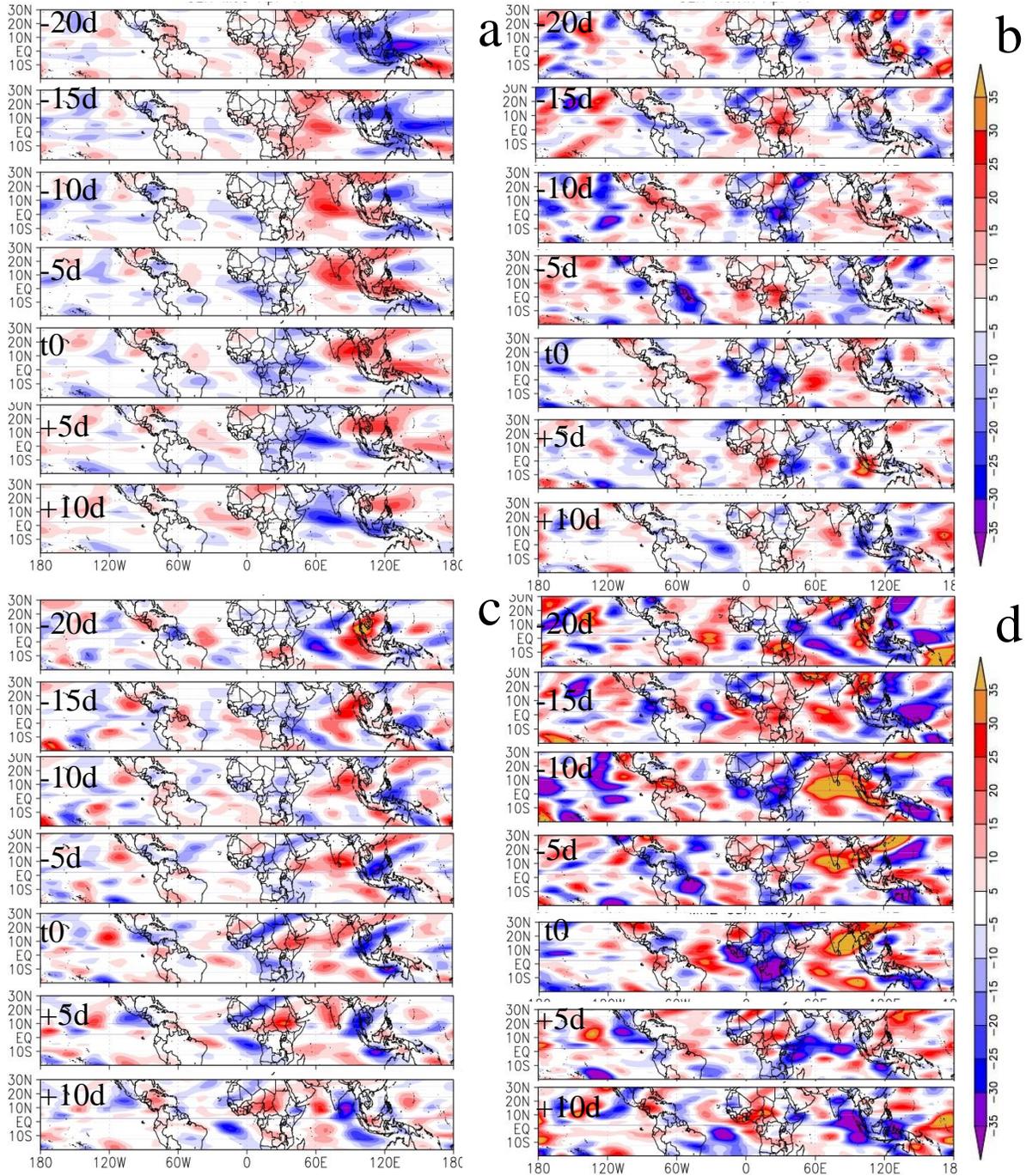


Figure 5.31: Time sequences of filtered OLR with the peak date (t_0) on May 7 2009. We show (a) the MJO-filtered OLR, (b) the Kelvin-filtered OLR, and (c) the equatorial Westward-propagating <30 day filtered OLR fields over the whole tropics from $t_0 - 20$ to $t_0 - 10$ days; (d) the sum of the three signals.

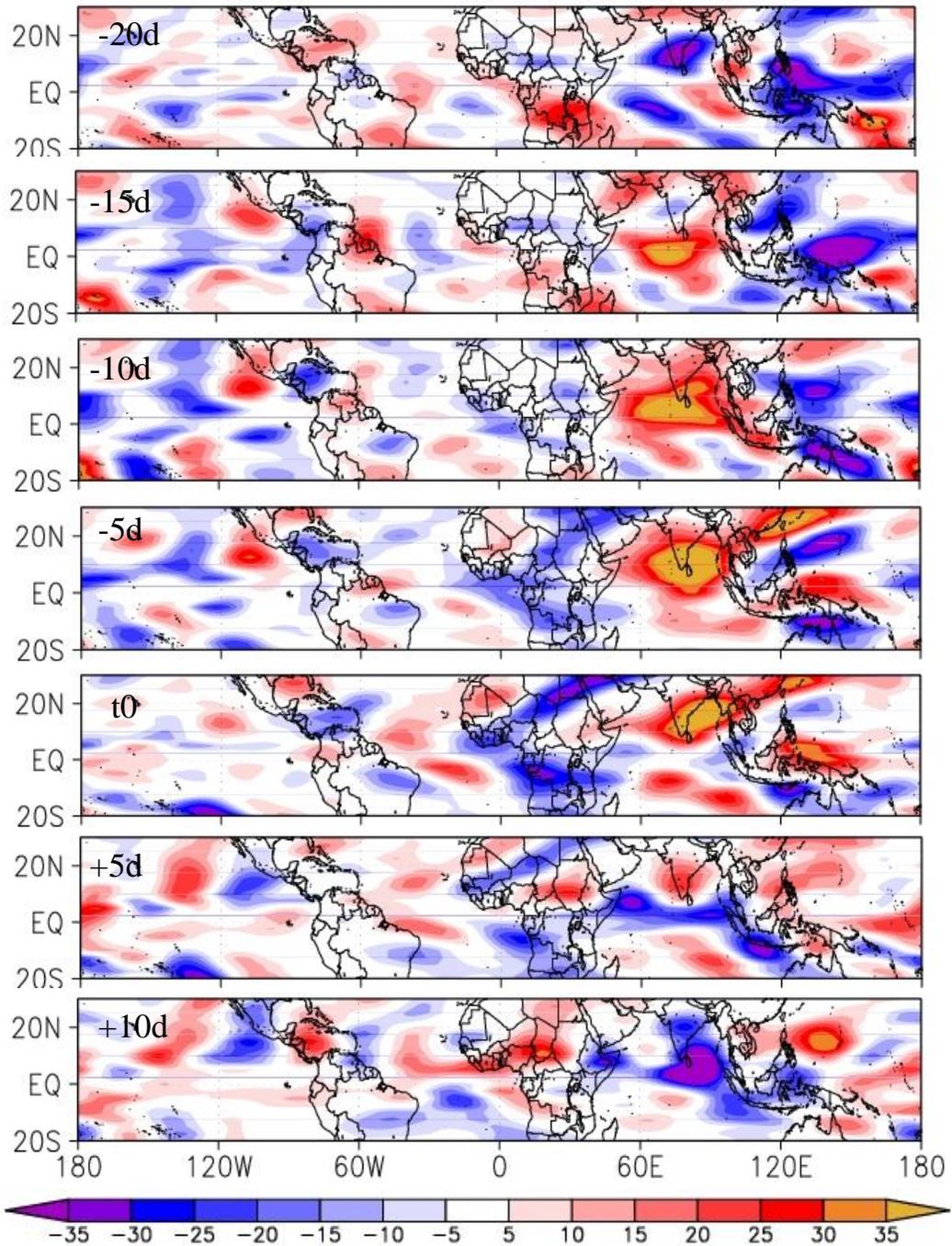


Figure 5.32: Time sequences of filtered OLR with the peak date (t_0) on May 7 2009 for the sum of ER and MJO over the whole tropics from $t_0 - 20$ to $t_0 - 10$ days.

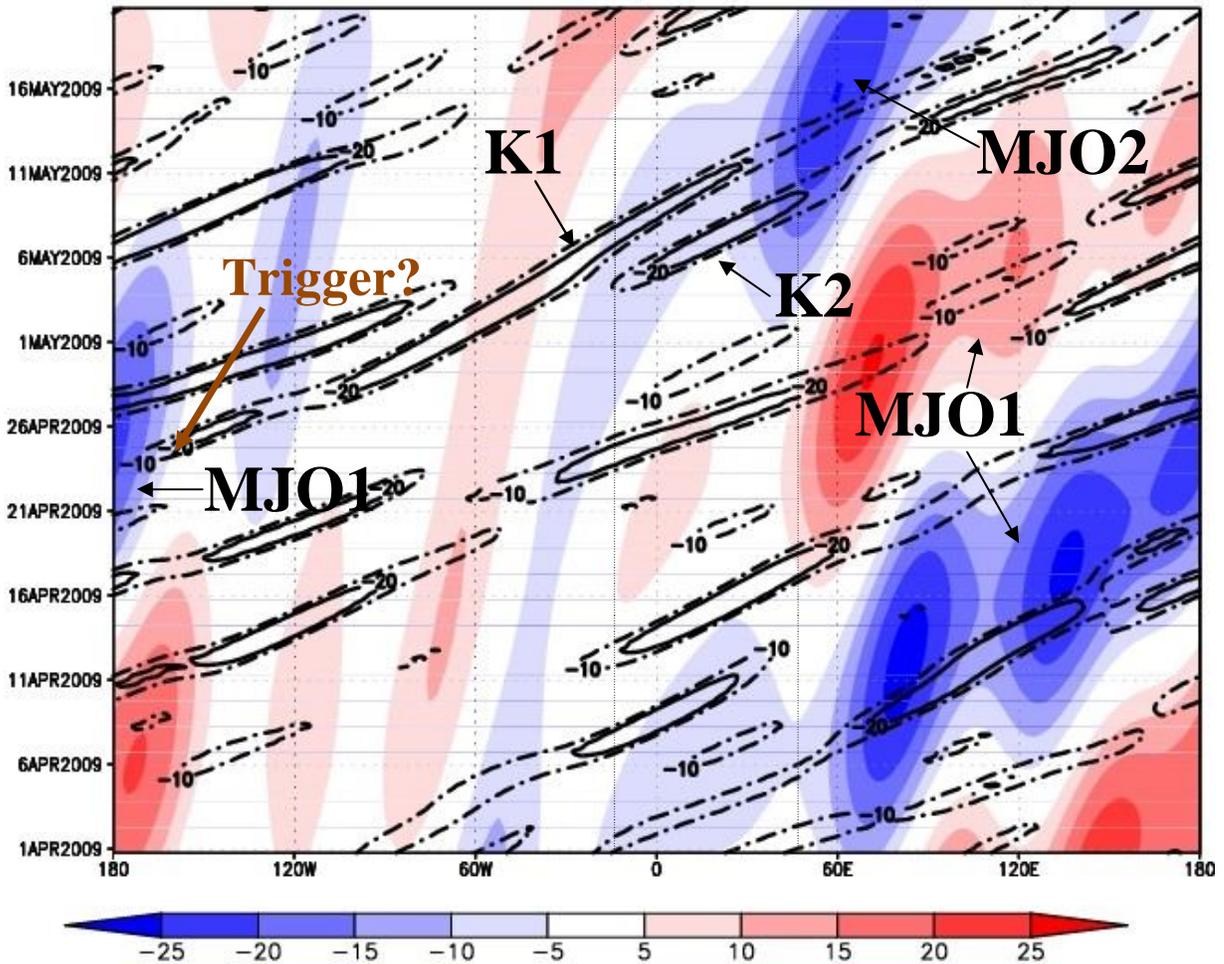
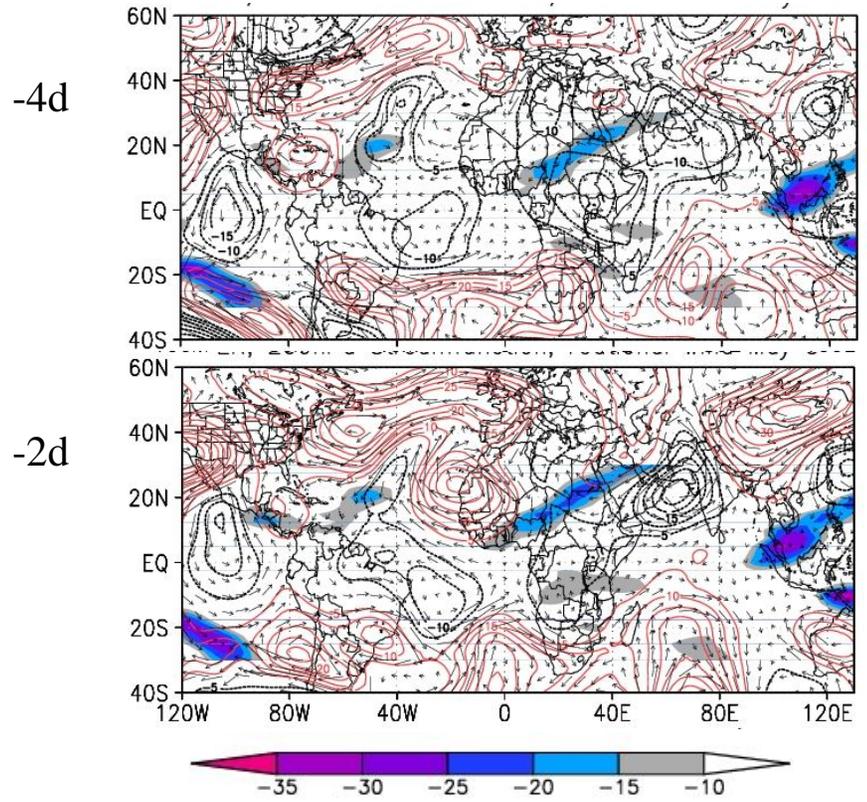
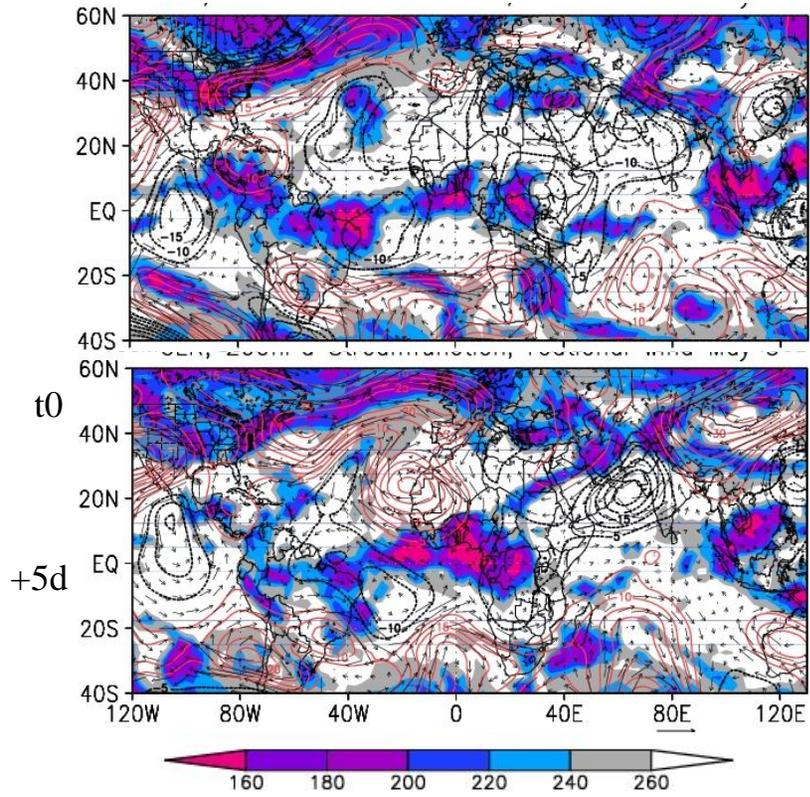
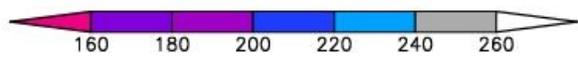
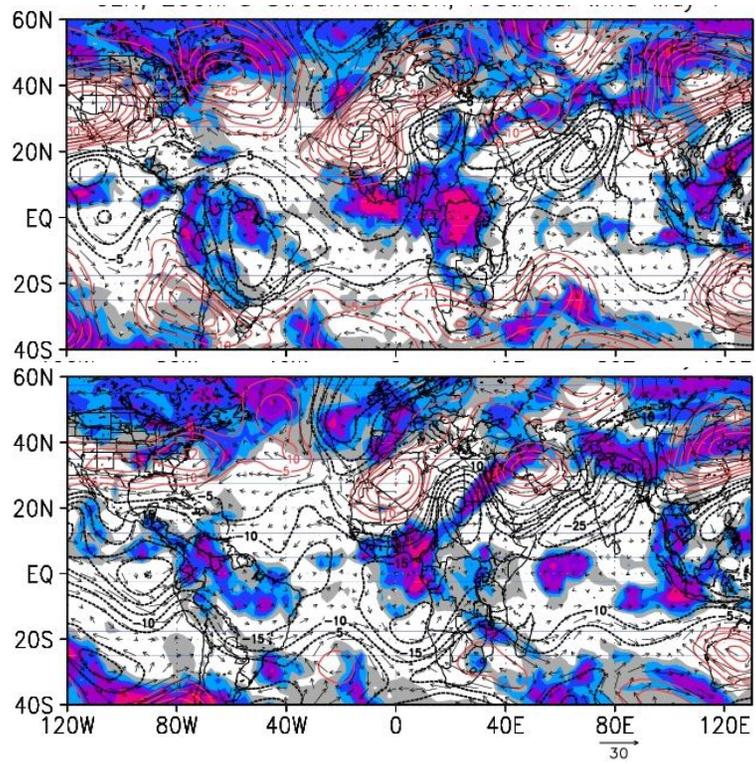


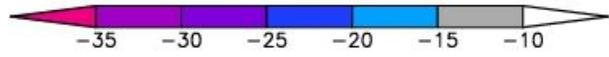
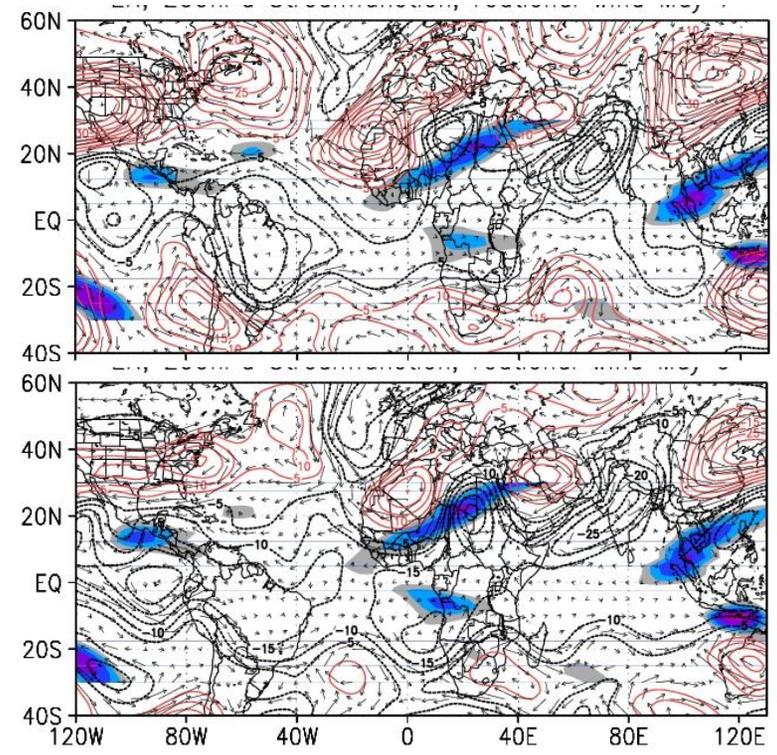
Figure 5.33: MJO (shaded) and Kelvin (contour) filtered NCEP OLR averaged for 2.5°S-7.5°N for April 1 – May 20 2009. K1, K2 and the April and May MJOs are labeled accordingly (MJO1 and MJO2 respectively). Vertical lines denote approximate location of Africa. Possible MJO Kelvin trigger is also labeled.

Figure 5.34: 200-mb streamfunction daily anomaly (contour), rotational wind, and OLR anomalies (shaded) for total OLR (left column) and ER-filtered OLR (right column). Dates are labeled. Contour interval is $10 \times 10 \text{ m}^2 \text{ s}^{-1}$, with negative contours dashed and in black and positive contours in red. Rotational wind anomalies are presented as vectors.

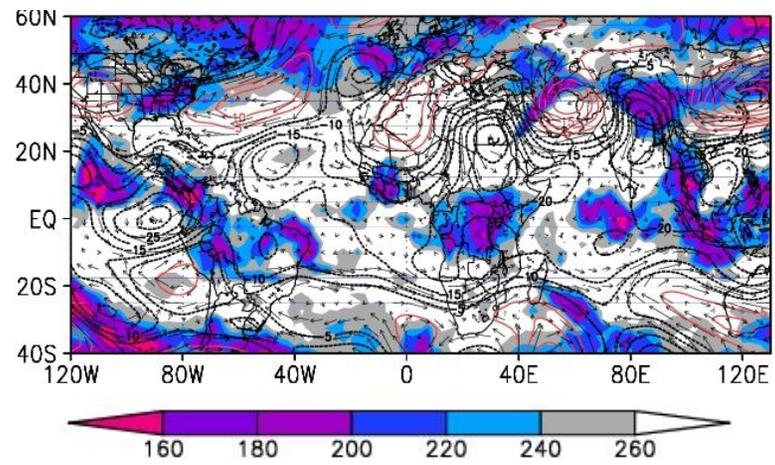




t0



+5d



+4d

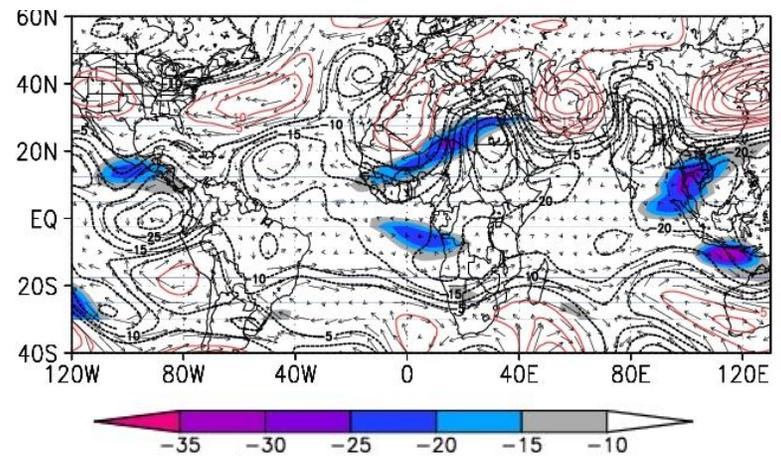
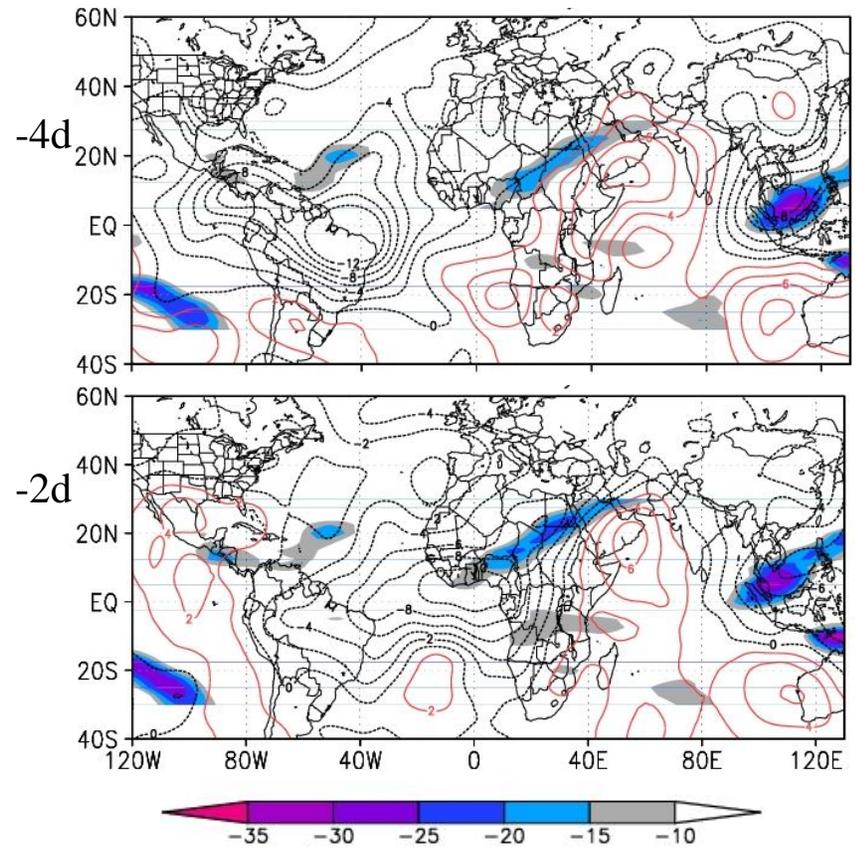
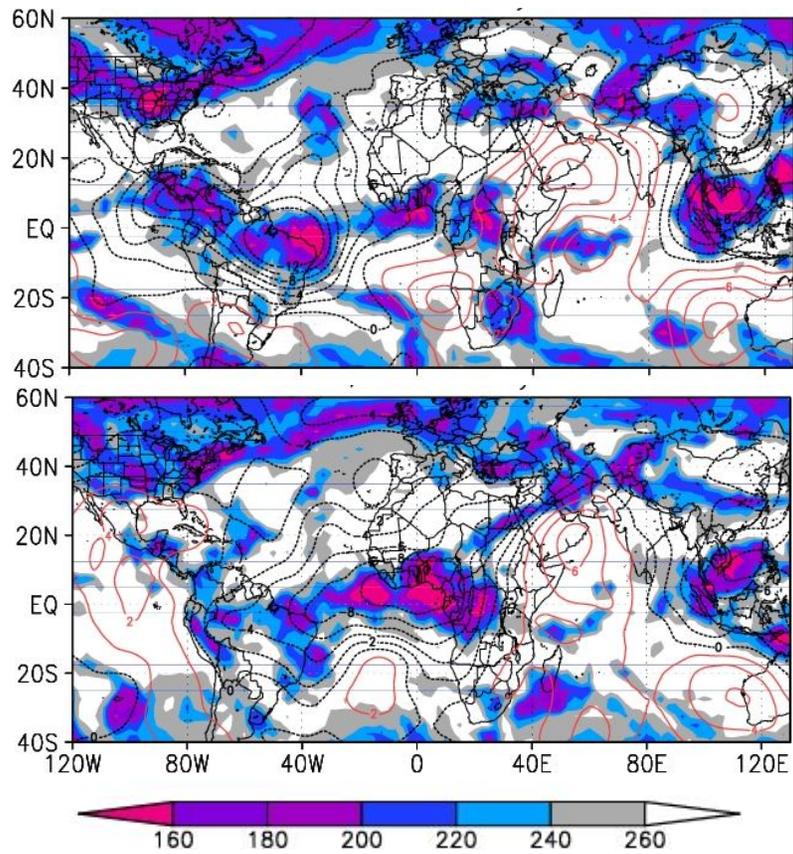
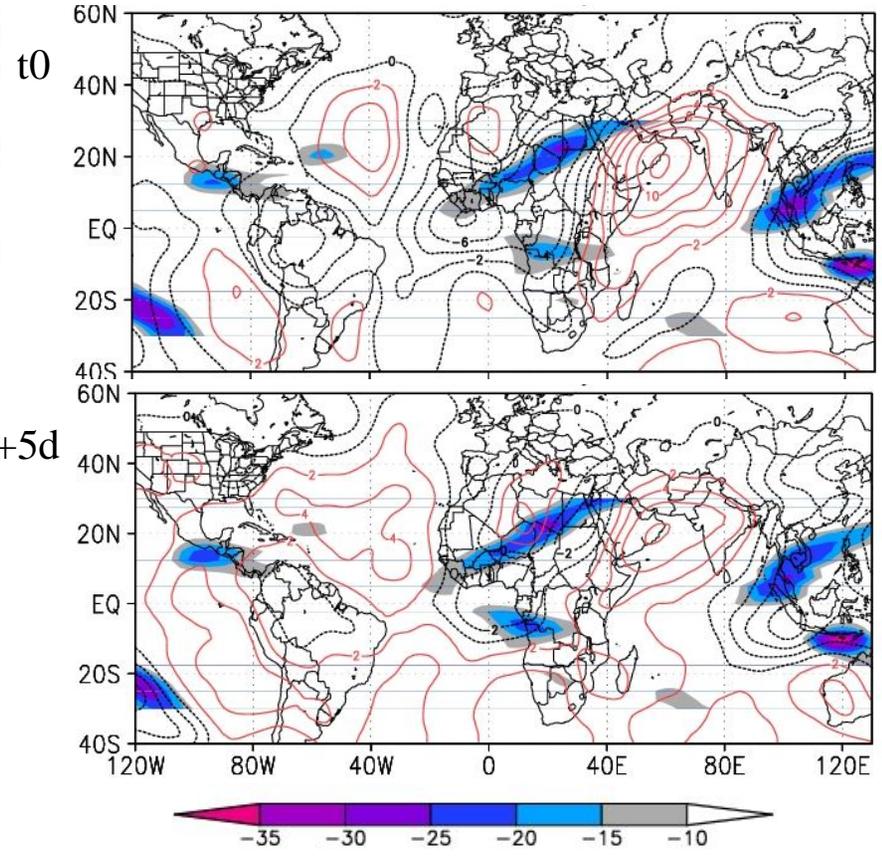
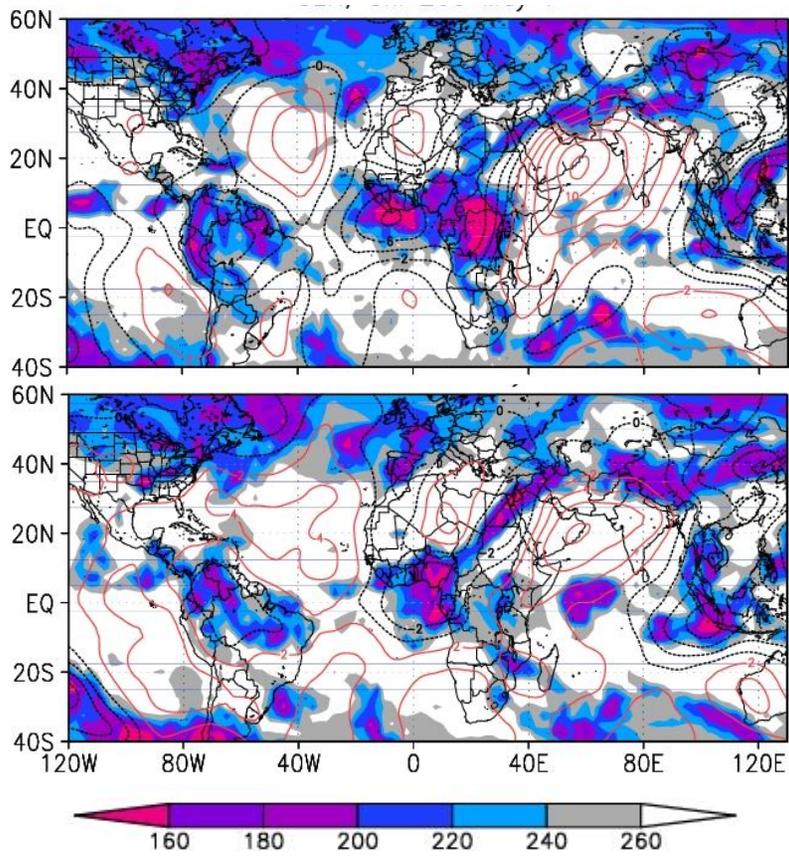
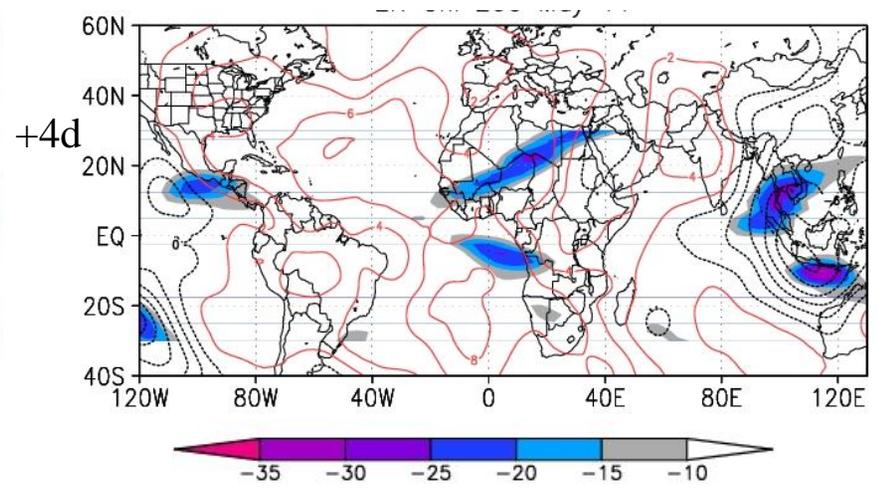
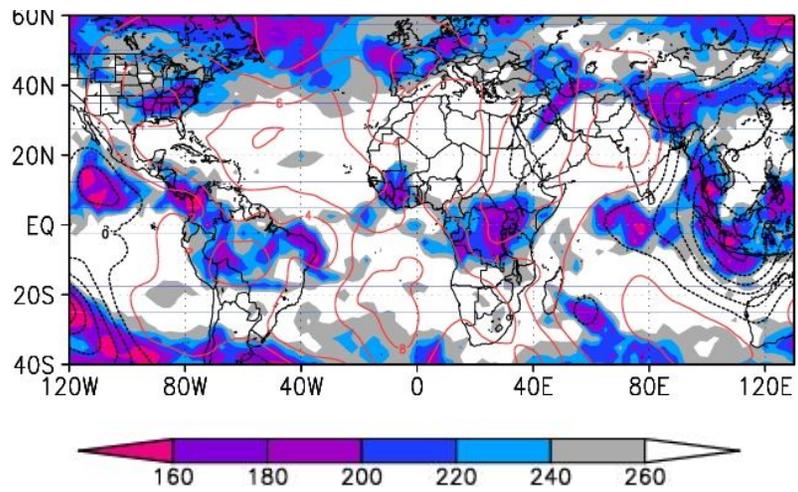


Figure 5.35: 200-mb velocity potential (contoured) and OLR anomalies (shaded) for total OLR (left column) and ER-filtered OLR (right column). Dates are labeled. Contour interval is $2 \times 10^5 \text{ m}^2 \text{ s}^{-1}$, with negative contours dashed and in black and positive contours in red. Rotational wind anomalies are presented as vectors.







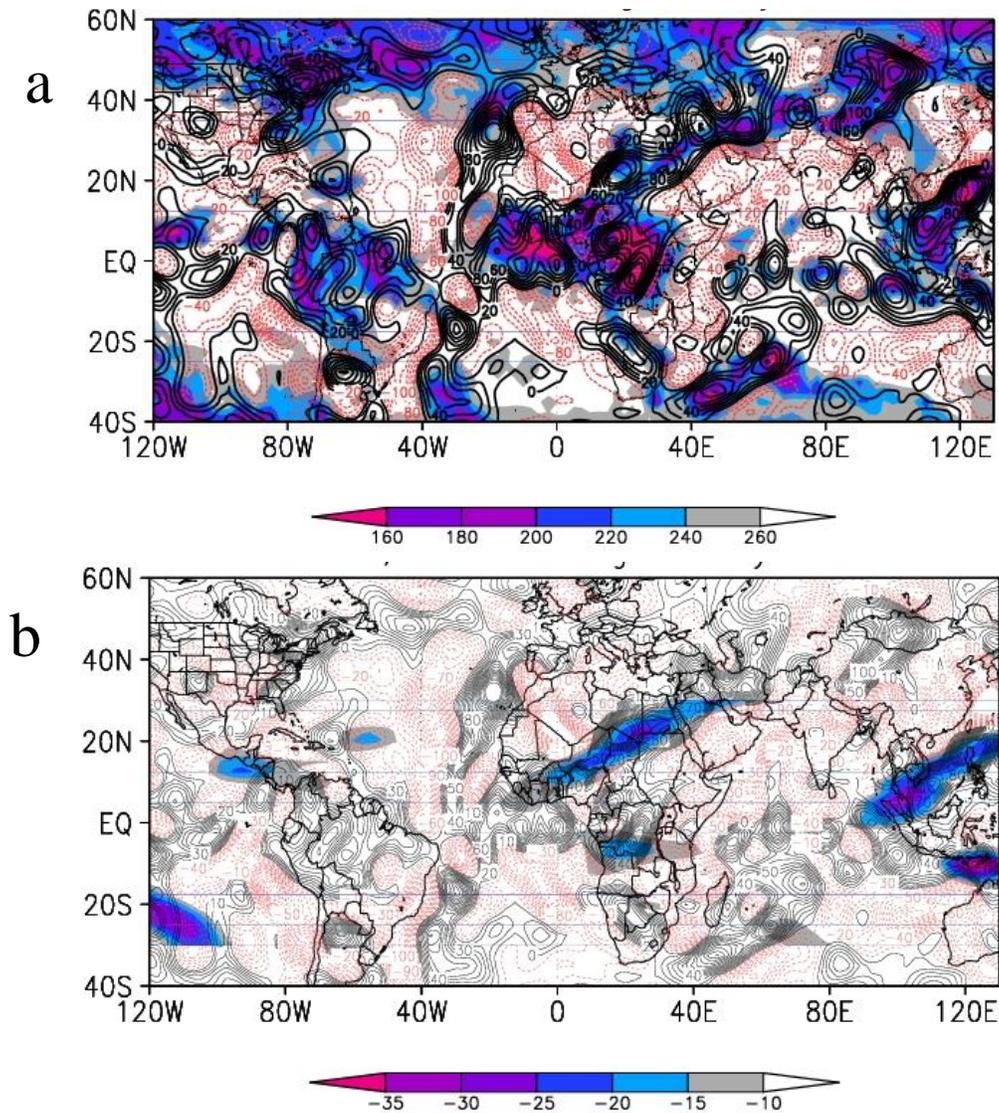


Figure 5.36: 200-mb divergence (contoured) and OLR anomalies (shaded) for total OLR (a) and ER-filtered OLR (b). Dates are labeled. Contour interval is $2 \times 10^5 \text{ m}^2 \text{ s}^{-1}$, with negative contours dashed and in black and positive contours in red. Rotational wind anomalies are presented as vectors.

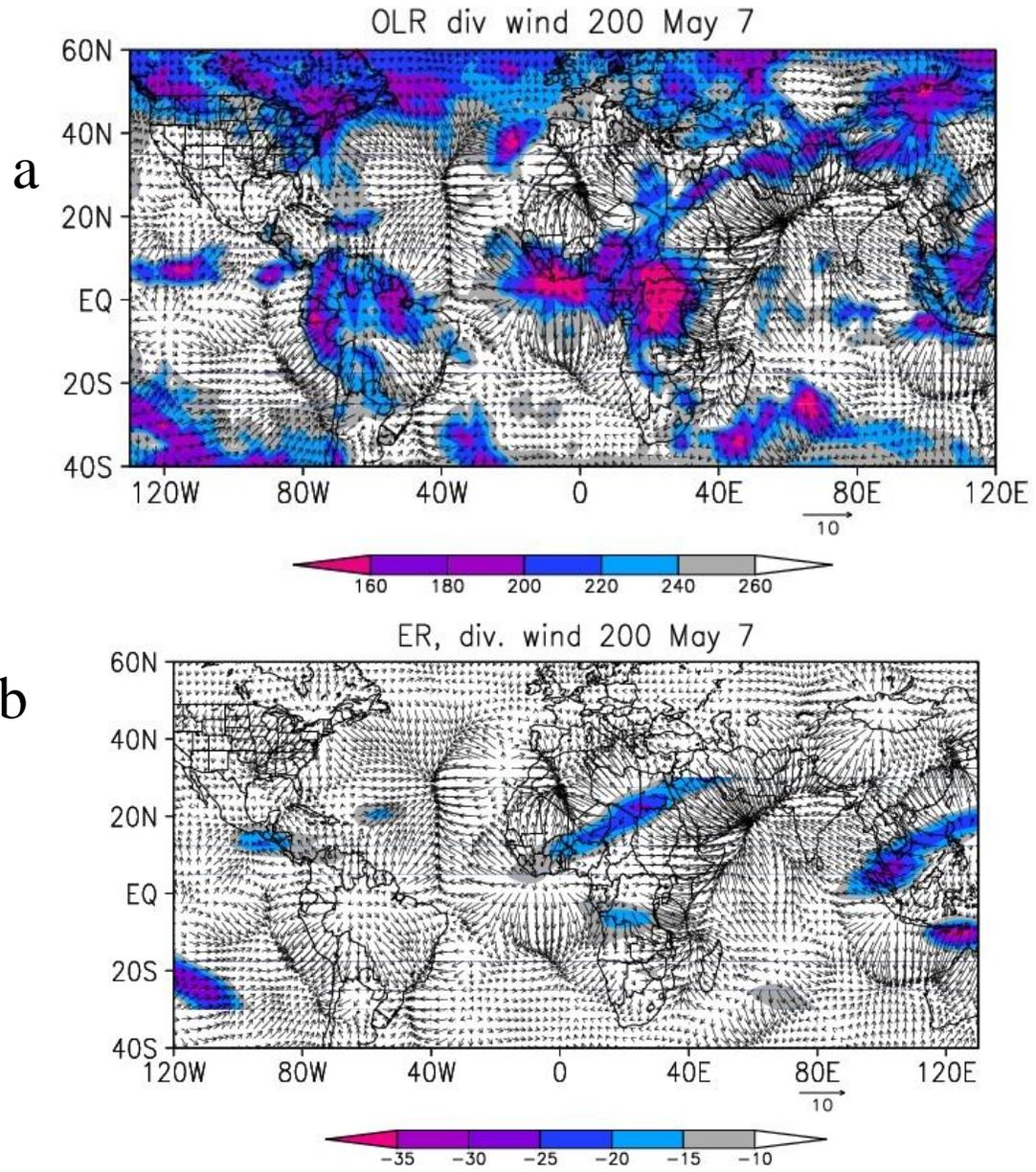


Figure 5.37: 200-mb divergent wind and OLR anomalies (shaded) for total OLR (a) and ER-filtered OLR (b) for t_0 .

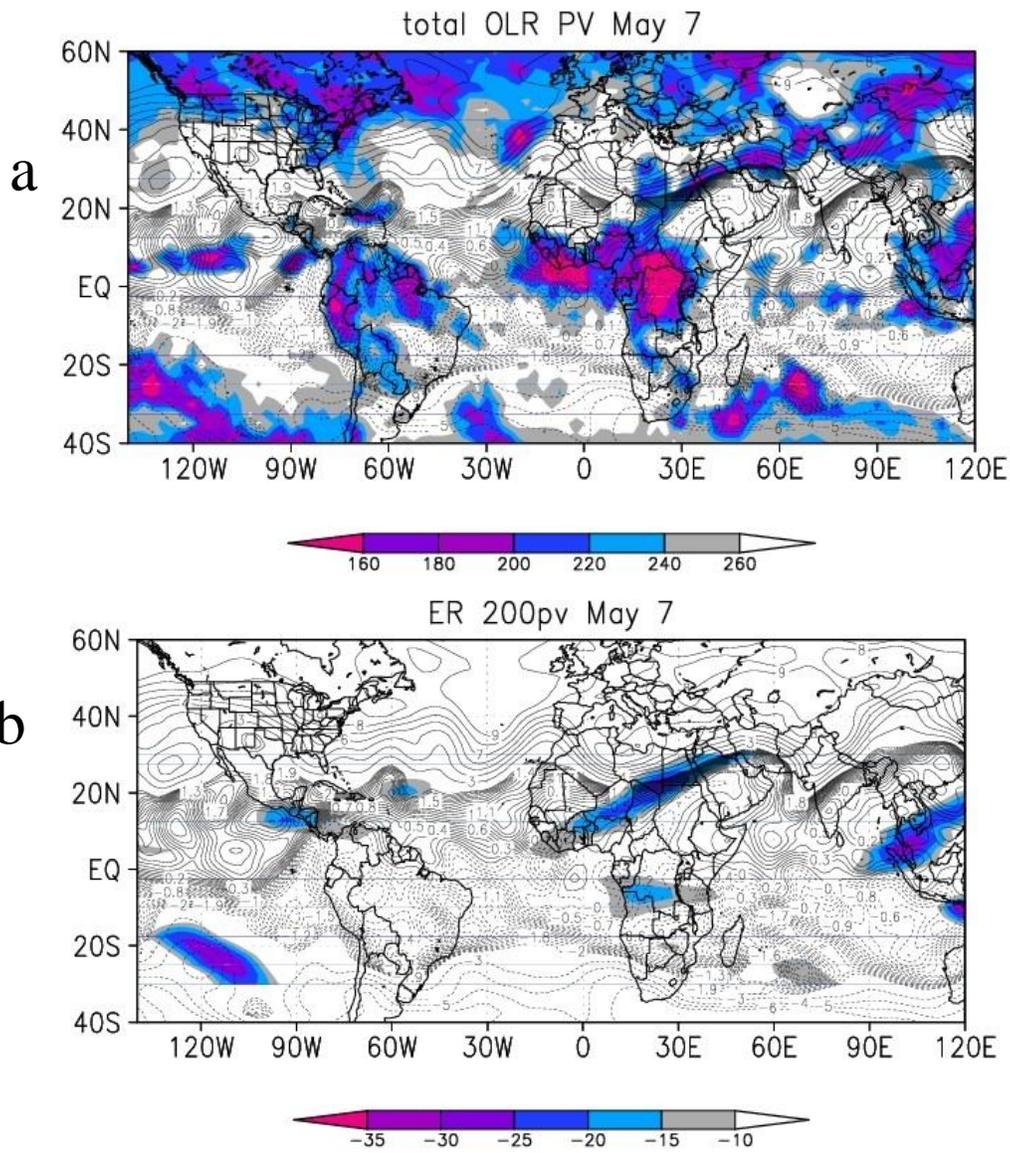


Figure 5.38: 200-mb PV in PV units ($= 1 \times 10^6 \text{ m}^2 \text{ s}^{-1} \text{ K kg}^{-1}$). Contour interval is 0.1 PV units between 22.0 and 12.0, and 1 PV unit otherwise wind and OLR anomalies (shaded) for total OLR (a) and ER-filtered OLR (b) for t_0 .

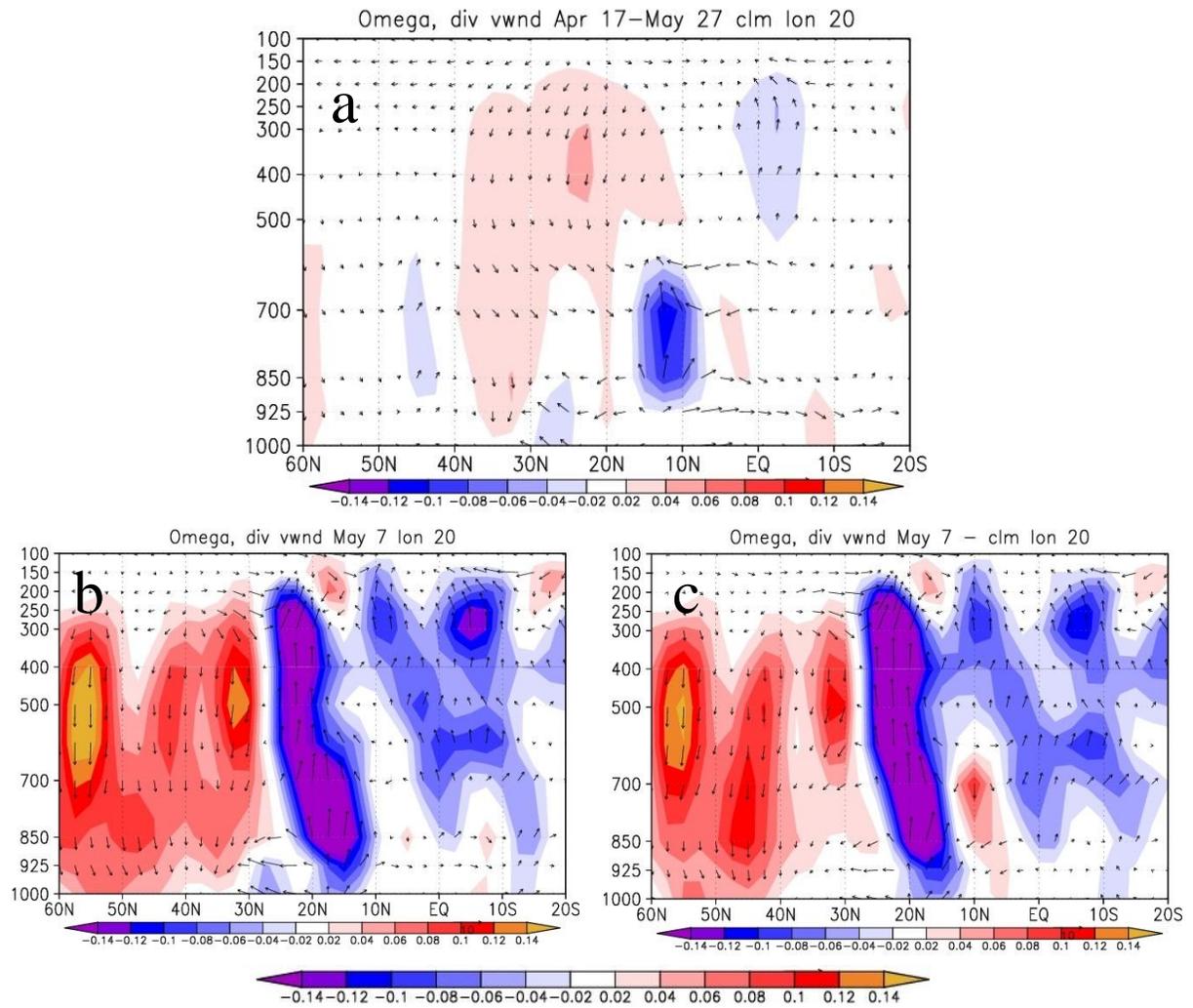


Figure 5.39: 200-mb mass circulation shown by the vectors. The contour interval is $1 \times 10^{-2} \text{ Pa s}^{-1}$, and the vectors are scaled such that a 1 m s^{-1} meridional divergent wind is equal to a $-5 \times 10^{-2} \text{ Pa s}^{-1}$ vertical motion. (a) Apr 17 – May 27 2000-2009. (b) Day t0 (c) t0-climatology.

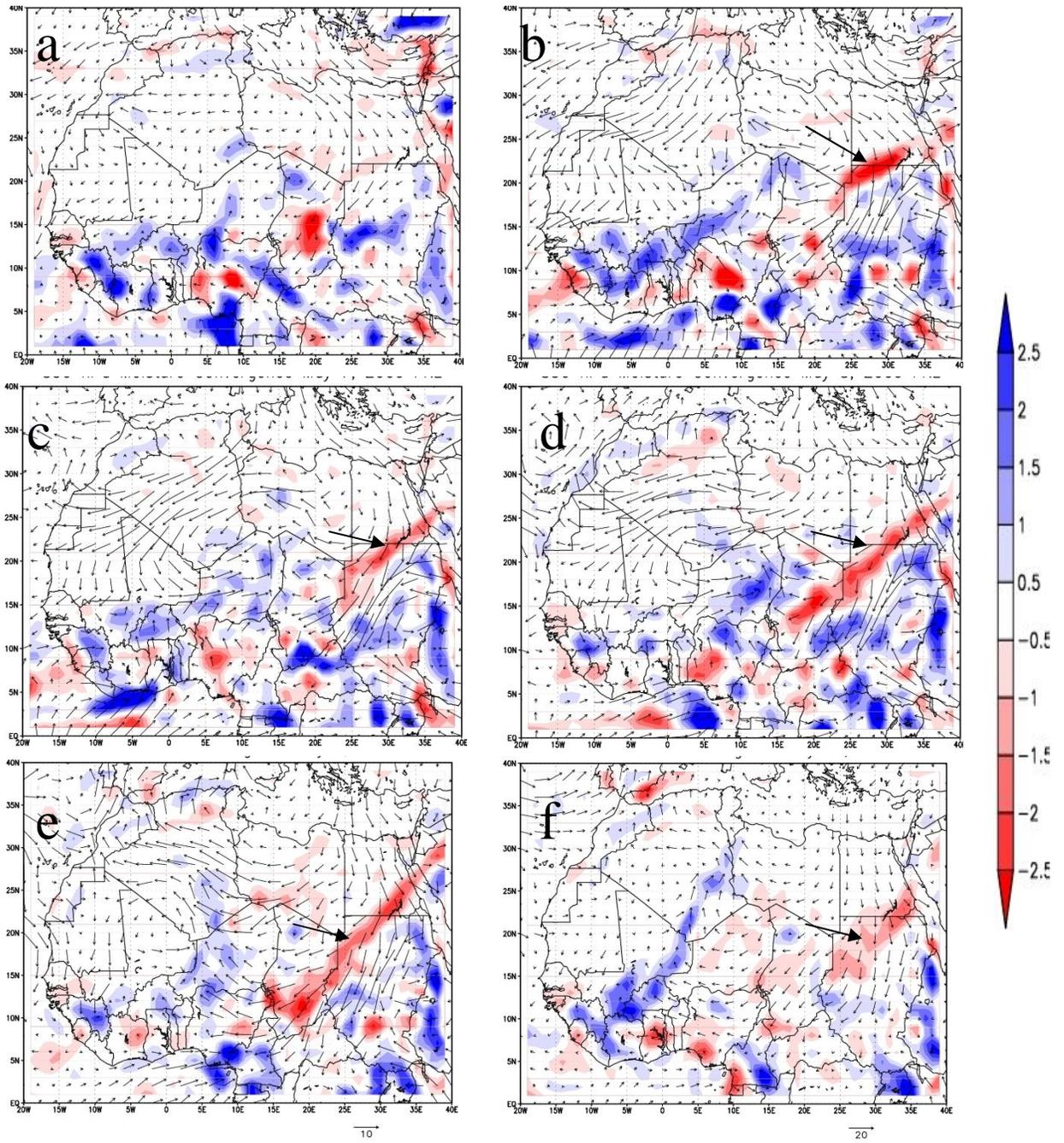


Figure 5.40: Moisture convergence at 850 hPa (shaded) and starting on May 5 (a), 6 (b), 7 (c), 8 (d), 9 (e) and 10 (f). Arrow denotes the tropical plume.

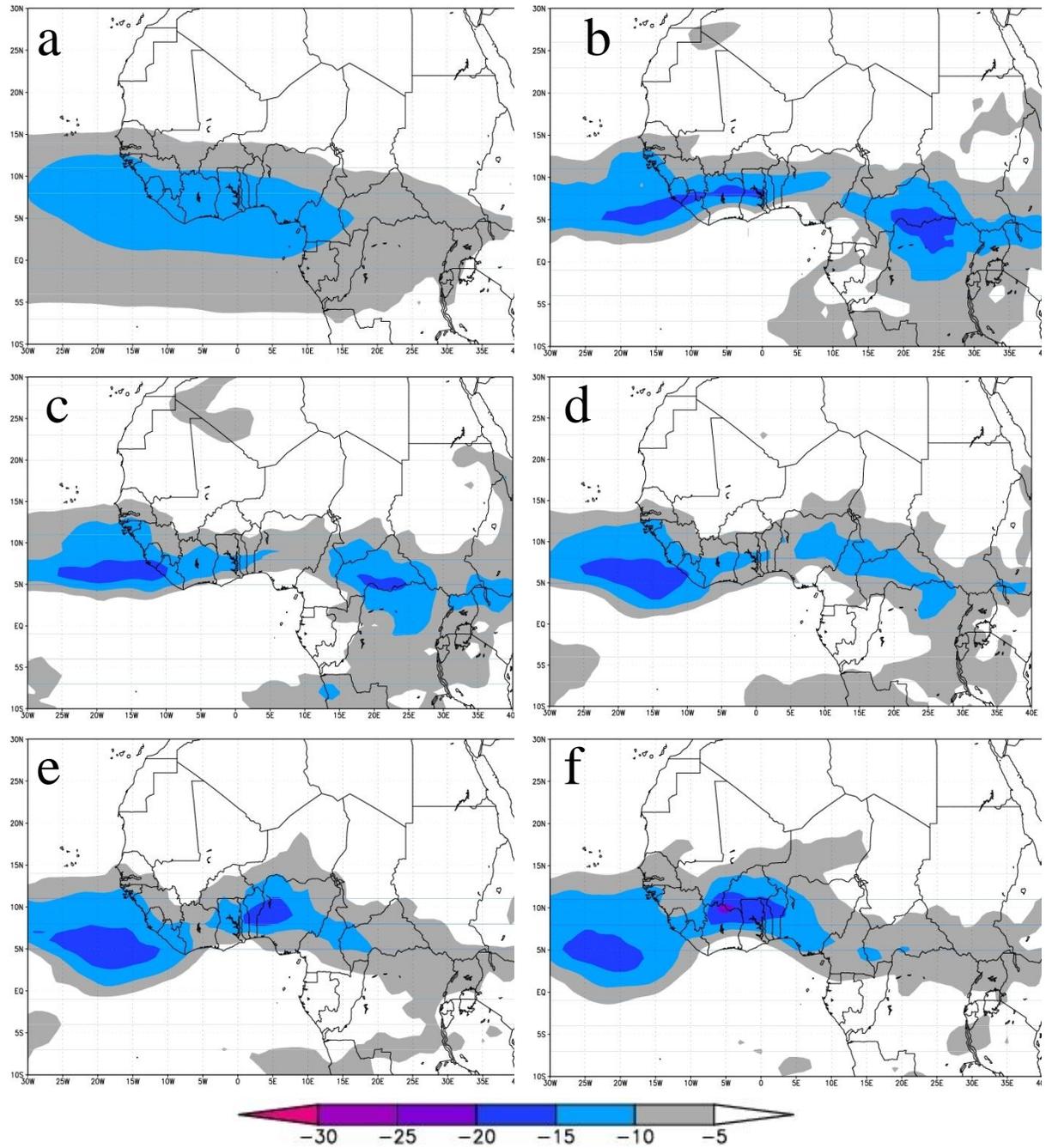


Figure 5.41: The African Easterly Jet at 700 hPa as given by FNL zonal wind (m s^{-1}) for the May climatology (2000-2009) (a), May 7 (b), 8 (c), 9 (d), 10 (e), 11 (f).

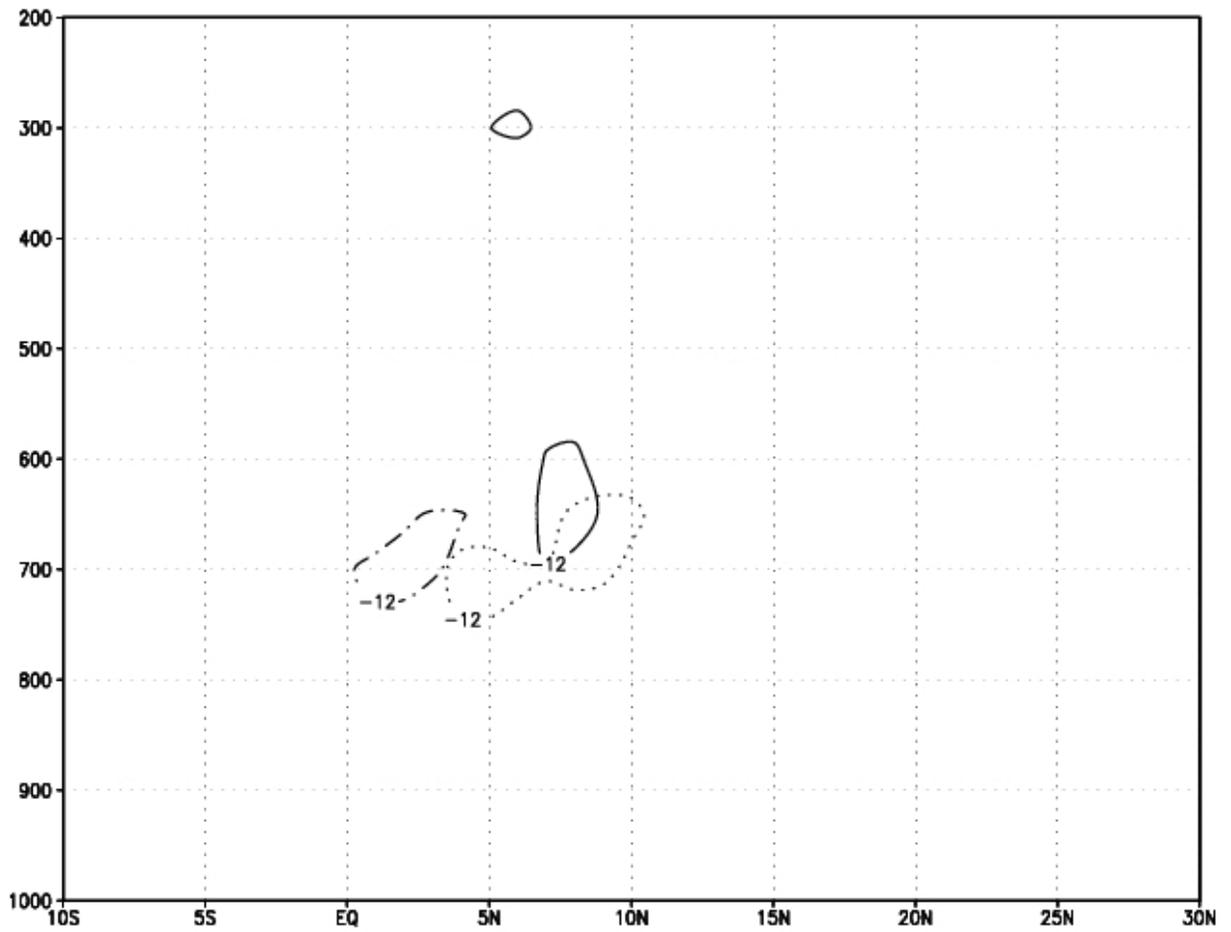


Figure 5.42: Representation of the AEJ core at 0°E as given by FNL zonal wind (m s^{-1}) for May 2 (dash-dot), May 8 (solid) and May 16 (dotted).

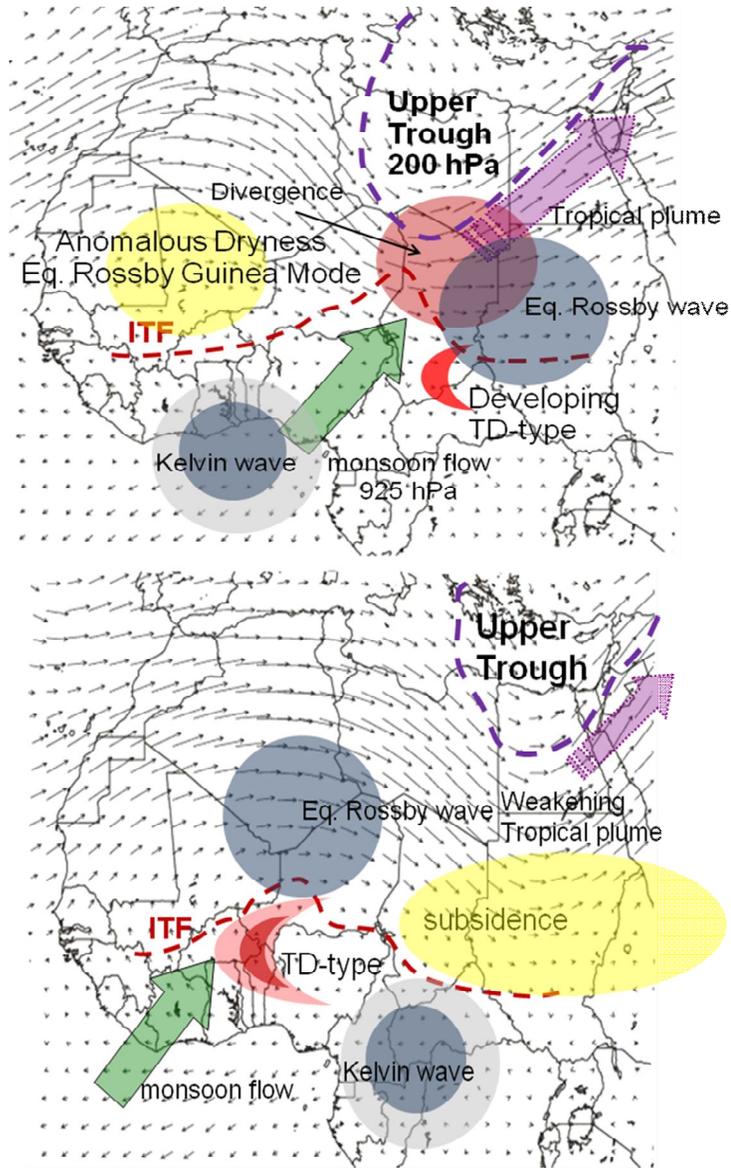


Figure 5.43: Schematic of MME during (a) the interaction between tropics and extratropics (-2d) and after the Kelvin/TD-type phasing (+2d).

Chapter 6

Simulation and Prediction of Moist

Events during the Boreal Spring

6.1 Introduction

Numerical prediction of weather and climate has been targeted as a method to predict conditions relevant to meningitis efforts in West Africa (Thomson et al. 2006; Diggle et al. 2009; Pandya et al. 2009; Trzaska et al. 2009). Short-term forecasts using large scale models are currently being evaluated for this purpose in order to provide 1-14 day weather forecasts to target dissemination of scarce vaccine (Pandya et al. 2009). Regional models have also been taken into consideration to help with meningitis efforts due to their ability to provide high resolution, district scale information relevant to inoculation and treatment of the disease. Figure 6.1 provides an example of the improvement made on coarse scale reanalysis. In this figure, we show the resolution for the majority of our model simulations (30 km) for relative humidity alongside the NNRP representation of the same time period. Also in this figure are geopolitical boundaries of states within the countries of Ghana, Burkina Faso

Although our study is primarily concerned with atmospheric moisture and temperature (as the main constituents defining relative humidity), it is important to acknowledge the role of correctly simulating precipitation patterns. Representing precipitation in regional models continues to be a challenge due to its importance for the generation of weather and climate prediction at scales that are relevant to the local population (agriculture, health) and for the study of important dynamical features that influence other parts of the world (African Easterly Waves). Rainfall over Sahelian West Africa is dependent of the northward propagation of precipitation associated to the Inter-Tropical Convergence Zone (ITCZ) and its displacement during the West Africa Monsoon (WAM) onset (Sultan and Janicot 2000; Le Barbe et al. 2002; Sultan and Janicot 2003). A second important feature is the intra-seasonal distribution of rainfall, characterized in recent studies by wet and dry sequences (Janicot and Sultan 2001; Sultan et al. 2003; Lebel et al. 2003). These constituents of precipitation dynamics, as well as the Saharan Heat Low (SHL), Madden-Julian Oscillation (MJO), and land characteristics and orography represent characteristics that should be tested within RCMs in order to gauge the value of undertaking downscaled simulations over the region.

Regional climate models (RCM) simulations combined with sensitivity tests have been used to study these features in the West Africa climate. Validation of parametrization schemes, in particular, is a challenge due to the lack of high resolution observations, both spatially and temporally, for much of the world (Vaidya, 2006) and especially over West Africa. Previous research applying RCMs over this portion of the continent include model

interpretation of moist static energy using the Modèle Atmosphérique Régional (MAR) (Gallee et al. 2006), WAM evolution from March to September with the Penn State/NCAR Mesoscale Model (MM5) (Sijikumar et al. 2006), influence of SST anomalies on the WAM using a modified version of MM5 (Vizy and Cook 2002), simulation the climatological period of 1992–2005 the regional climate model RegCM3 (Sylla et al. 2009).

In the aforementioned research, different RCM have been run over a period of several months but with different parameterizations and with different horizontal resolutions (coarser than 40 km). In the present study, the Advanced Research Weather Research and Forecasting (WRF-ARW) Model Version 3.0 (Skamarock et al., 2005) has been adapted for regional climate application and is used as an analytical and predictive tool. It has previously been tested over West Africa in studies such as Zhang (2007) and Flaounas et al. (2010). The work conducted by Flaounas et al. (2010) is especially important since they tested various physical schemes available in WRF on the WAM representation for 2006. Their results showed that the Kain-Fritsh cumulus scheme was appropriate for West Africa and this guided our approach. Our research builds on their results during the monsoon season by extending it to the transition period during April and May. The model was tested during the spring months of 2006 to compare output against a rich number of simulations and observations from the AMMA campaign (Redelsperger et al. 2006); we placed particular emphasis on simulating the moisture regime. The model was also tested during the 2009 season for real-time forecasts and downscaled reanalysis products in order to understand the model's ability to simulate conditions during the meningitis outbreaks in Nigeria.

Within the context of our work, we narrow the testing of the regional model to three main criteria: i) modeling boreal spring moist events, ii) assessing added value of downscaling for end-user purposes (i.e. meningitis efforts), and iii) capturing the shift in the moisture regime.

6.2 Model Description

For this study, the mesoscale non-hydrostatic WRF-ARW model (Versions 3.0 and 3.1) has been adapted for climate and real-time simulations. The WRF model is a numerical weather prediction (NWP) and atmospheric simulation system designed for both research and operational applications. The ARW is the ARW dynamics solver together with other components of the WRF system compatible with that solver and used in producing a simulation (Skamarock and Weisman 2008). The more recent improvements include vertical interpolation and memory improvements for the WRF-VAR system as well as the addition of spectral nudging starting with Version 3.1. In the following, we review the different model physics options utilized in our model validation tests.

6.2.1 Dynamical Core Model Physics

The WRF-ARW core utilized in this study is based on an Eulerian solver for fully compressible nonhydrostatic equations, cast in flux (conservative) form, using a mass (hydrostatic pressure) vertical coordinate. Prognostic variables are the column mass of dry air (μ), velocities u , v and w (vertical velocity), potential temperature, and geopotential. Non-

conserved variables such as temperature, pressure and density are diagnosed from the conserved prognostic variables. The solver uses a third-order Runge-Kutta time-integration scheme coupled with a split-explicit 2nd-order time integration scheme for the acoustic and gravity-wave modes. 5th-order upwind-biased advection operators are used in the fully conservative flux divergence integration; 2nd-6th order schemes are run-time selectable. The above description is based on work by Klemp et al (2007), Skamarock and Klemp (2007), Skamarock (2006), Skamarock et al (2005), Skamarock (2004), and Wicker and Skamarock (2002).

6.2.2 Atmospheric Radiation Schemes

6.2.2.1 Community Atmosphere Model

The CAM radiation scheme was used for our simulations since it has been shown to be especially suited for regional climate simulations by having a ozone distribution that varies during the simulation according to monthly zonal-mean climatological data. A spectral-band scheme used in the NCAR Community Atmosphere Model (CAM 3.0) is implemented for climate simulations for both short-wave and longwave radiation. It has the potential to handle several trace gases. It interacts with resolved clouds and cloud fractions, and is documented fully by Collins et al. (2004). It uses cloud fractions and overlap assumptions in unsaturated regions, and has a monthly zonal ozone climatology. It is documented fully by Collins et al. (2004).

6.2.2.2 Rapid Radiative Transfer Model (RRTM) Longwave

We tested the model for sensitivity to changes in radiation scheme via the Rapid Radiative Transfer Model (RRTM) Longwave, which is taken from the PSU-NCAR Mesoscale Model Version 5 (MM5). RRTM is based on Mlawer et al. (1997) and is a spectral-band scheme using the correlated- k method. It uses pre-set tables to accurately represent longwave processes due to water vapor, ozone, CO₂, and trace gases, as well as accounting for cloud optical depth.

6.2.2.3 Goddard Shortwave

The Goddard Shortwave scheme is based on Chou and Suarez (1994). It has a total of 11 spectral bands and considers diffuse and direct solar radiation components in a two-stream approach that accounts for scattered and reflected components. Ozone is considered with several climatological profiles available.

6.2.3 Land Surface Model Schemes

6.2.3.1 Noah Land Surface Model

The Noah Land Surface Model (LSM) is implemented in this study. The scheme was developed jointly by NCAR and NCEP, and is a unified code for research and operational purposes (Chen and Dudhia, 2001). The Noah LSM is a 4-layer soil temperature and moisture model with canopy moisture and snow cover prediction. The layer thickness are 10, 30, 60 and 100 cm (adding to 2 meters) from the top down. It includes root zone, evapotranspiration, soil drainage, and runoff, taking into account vegetation categories,

monthly vegetation fraction, and soil texture. The scheme provides sensible and latent heat fluxes to the boundary-layer scheme. The Noah LSM additionally predicts soil ice, and fractional snow cover effects, has an improved urban treatment, and considers surface emissivity properties.

6.2.3.2 5-layer Thermal Diffusion

Within our model testing, we employ the Thermal Diffusion model, which is a simple LSM based on the MM5 5-layer soil temperature model. Layers are 1, 2, 4, 8, and 16 cm thick. Temperature is fixed at a deep-layer average below these layers. The energy budget includes radiation, sensible, and latent heat flux. Thermal Diffusion (TD) also allows for snow cover fixed in time. Soil moisture is also fixed with a landuse- and season-dependent constant value, and there are no explicit vegetation effects.

6.2.3.3 Rapid Update Cycle (RUC) Model LSM

Also tested in this model is the Rapid Update Cycle (RUC) LSM, which has a multi-level soil model (capable of >9) with higher resolution in the top part of soil domain (0, 5, 20, 40, 160, 300 cm is default). The soil model solves heat diffusion and Richards moisture transfer equations, and also takes into account phase changes of soil water in colder climates (Smirnova et al., 1997, 2000). The RUC LSM also includes a multi-layer snow model with varying snow density, refreezing liquid water, snow depth and temperature dependent albedo, melting algorithms for snow-atmosphere interface and snow-soil interface, and simple

parameterization of fractional snow cover. The model also includes vegetation effects and canopy water. The RUC LSM employs a layer approach to the solution of energy and moisture budgets. An important aspect of this approach is that the layer spans the ground surface and includes half of the first atmospheric layer and half of the top soil layer with corresponding properties (density, heat capacity, etc.) Additionally, the residual of incoming fluxes (net radiation, latent and sensible heat fluxes, soil heat flux, precipitation contribution for heat storage, among others) modify the heat storage within this layer. An implicit technique is applied to the solution of these equations. Its treatment of the land surface is robust since it includes the following prognostic variables: volumetric liquid, soil temperature, frozen and total soil moisture contents, surface and sub-surface runoff, canopy moisture, evapotranspiration, latent, sensible and soil heat fluxes, skin temperature, heat of snow-water phase change, snow depth and density, and snow temperature.

6.2.4 Planetary Boundary Layer Schemes

6.2.4.1 Yonsei University (YSU) PBL

One of the choices for Planetary Boundary Layer (PBL) schemes of is the YSU scheme. The Yonsei University PBL (Hong et al., 2006) is the next generation of the MRF PBL, also using the countergradient terms to represent fluxes due to non-local gradients. This adds to the MRF PBL (Hong and Pan, 1996) an explicit treatment of the entrainment layer at the PBL top. The entrainment is made proportional to the surface buoyancy flux in line with results from studies with large-eddy models (Noh et al., 2003). The PBL top is defined using

a critical bulk Richardson number of zero (compared to 0.5 in the MRF PBL), so is effectively dependent on the buoyancy profile, in which the PBL top is defined at the maximum entrainment layer (compared to the layer at which the diffusivity becomes zero). A smaller magnitude of the counter-gradient mixing in the YSU PBL produces a well-mixed boundary-layer profile, whereas there is a pronounced over-stable structure in the upper part of the mixed layer in the case of the MRF PBL.

6.2.4.2 Mellor-Yamada-Janjic (MYJ) PBL

The second choice in PBL schemes is the Mellor-Yamada-Janjic (MYJ) (Janjic, 1990, 1996, 2002). This parameterization of turbulence in the planetary boundary layer as well as the free atmosphere (Janjic, 1990, 1996, 2002) corresponds to a nonsingular implementation of the Mellor-Yamada Level 2.5 turbulence closure model (Mellor and Yamada, 1982) through the full range of atmospheric turbulent regimes. An upper limit is imposed in this implementation on the master length scale. This upper limit depends on the turbulent kinetic energy (TKE) as well as buoyancy and shear of the driving flow. The functional form of the upper limit is derived in the unstable range from the requirement that the TKE production be nonsingular in growing turbulence. For the stable range, the upper limit is derived from the ratio of the variance of the vertical velocity deviation and TKE cannot be smaller than that corresponding to the regime of vanishing turbulence. The differential equation for the TKE production/dissipation is solved iteratively. Empirical constants are revised in Janjic (1996, 2002).

6.2.5 Microphysics Schemes

6.2.5.1 WRF Single-Moment 3-class (WSM3) scheme

We use the WRF single-moment microphysics scheme, which follows Hong et al. (2004) including ice sedimentation and other new ice-phase parameterizations. A major difference from other approaches is that a diagnostic relation is used for ice number concentration that is based on ice mass content rather than temperature. The computational procedures are described in Hong and Lim (2006). As with WSM5 and WSM6, the freezing/melting processes are computed during the fall-term sub-steps to increase accuracy in the vertical heating profile of these processes. The order of the processes is also optimized to decrease the sensitivity of the scheme to the time step of the model. During our testing of model parameters, it was found that WSM3 performed just as well as WSM5 and WSM6 given the 30km resolution. The WSM3 scheme predicts three categories of hydrometers: vapor, cloud water/ice, and rain/snow, which is a so-called simple-ice scheme. It follows Dudhia (1989) in assuming cloud water and rain for temperatures above freezing, and cloud ice and snow for temperatures below freezing. This scheme is computationally efficient for the inclusion of ice processes, but lacks supercooled water and gradual melting rates.

6.2.5.2 WSM6 scheme

Although more computationally expensive than WSM3, WSM6 was also tested in our sensitivity analysis in order to determine its merits over WSM3. The six-class scheme extends the WSM5 scheme to include graupel and its associated processes. Some of the graupel-related terms follow Lin et al. (1983), but its ice-phase behavior is significantly

different due to the changes of Hong et al. (2004). Mixed-phase particle fall speeds is also provided for the snow and graupel particles by assigning a single fallspeed to both that is weighted by the mixing ratios, which is then used for both sedimentation and accretion processes (Dudhia et al., 2008). The behavior of the WSM3, WSM5, and WSM6 schemes do not differ substantially for coarser mesoscale grids, but are vastly differently on cloud-resolving grids. Compared to WSM3 and WSM5, the WSM6 scheme is the most suitable for cloud-resolving grids, given the efficiency and theoretical backgrounds (Hong and Lim, 2006).

6.2.5.3 Kessler scheme

Also included in our analysis are more simple schemes such as the Kessler scheme (Kessler 1969), which was acquired from the COMMAS model (Wicker and Wilhelmson, 1995). The Kessler scheme is a simple warm cloud scheme that includes water vapor, cloud water, and rain. The microphysical processes included are: the production, fall, and evaporation of rain; the accretion and autoconversion of cloud water; and the production of cloud water from condensation.

6.2.5.4 Purdue Lin scheme

The final scheme utilized in this work is Purdue Lin scheme (Lin et al. 1983; Rutledge and Hobbs 1984). All parameterization production terms are based on the two studies along with some modifications, including saturation adjustment following Tao et al. (1989) and ice

sedimentation. Six classes of hydrometeors are included: water vapor, cloud water, rain, cloud ice, snow, and graupel. The scheme is taken from the Purdue cloud model, and the details can be found in Chen and Sun (2002). The Lin scheme is a relatively sophisticated microphysics scheme in the model, but it is found suitable for use in research studies such as the work performed in this chapter.

6.2.6 Cumulus Parameterization Schemes

6.2.6.1 Kain-Fritsch scheme

Numerous tests and previous research led to the use of the modified version of the Kain-Fritsch (KF) scheme (Kain, 2004) is based on Kain and Fritsch (1990) and Kain and Fritsch (1993), but has been modified based on testing within the Eta model. As with the original KF scheme, it utilizes a simple cloud model with moist updrafts and downdrafts, including the effects of detrainment, entrainment, and relatively simple microphysics. The KF scheme has been found to give realistic representation of the WAM onset in recent work by Flaounas et al. (2010).

6.2.6.2 Betts-Miller-Janjic scheme

Also tested in this study is the Betts-Miller-Janjic (BMJ) scheme (Janjic, 1994, 2000), which was derived from the Betts-Miller (BM) convective adjustment scheme (Betts, 1986; Betts and Miller, 1986). The BMJ scheme differs from the Betts-Miller scheme in several important aspects. For example, the deep convection profiles and the relaxation time are

variable and depend on the cloud efficiency, a nondimensional parameter that characterizes the convective regime (Janjic, 1994). Cloud efficiency depends on the entropy change, precipitation, and mean temperature of the cloud and the shallow convection moisture profile is derived from the requirement that the entropy change be small and nonnegative (Janjic, 1994).

6.2.6.3 Grell-Devenyi ensemble scheme

The third cumulus parameterization scheme tested in this study is the Grell-Devenyi Ensemble scheme (Grell and Devenyi 2002). The Grell ensemble scheme (GD) has a relatively simple approach of convective clouds. Clouds constitute a one dimensional system with a downdraft and an updraft branch. Mixing between the two branches as also between the convective system and the surrounding environment takes place only at the top and the bottom of the cloud. The schemes in the ensembles are mass-flux type schemes with differing updraft and downdraft entrainment and detrainment parameters, and precipitation efficiencies. These differences in static control are combined with differences in dynamic control, which is the method of determining cloud mass flux. Dynamic and trigger controls are applied as a combination of 144 ensemble members. Closure assumption is based on CAPE, low level vertical velocity or moisture convergence for which a quasi-equilibrium is applied for the available buoyant energy (large scale changes and changes due to convection are almost equal). Convective precipitation is proportional to the integral of the moisture advected by updraft. The total amount of cloud water due to condensation is removed by

rainfall leaving no residual. Another control is the trigger, where the maximum cap strength that permits convection can be varied.

6.2.7 Surface Layer Schemes

We use two different surface layer schemes in our analysis: Monin-Obukhov (MO) and Monin-Obukhov Janjic Eta (MOJE). Surface layer schemes calculate friction velocities and exchange coefficients that enable the calculation of surface heat and moisture fluxes by the land-surface models and surface stress in the planetary boundary layer scheme. The schemes do not provide tendencies, only the stability-dependent information about the surface layer for the land-surface and PBL schemes is given. Currently, each surface layer option is tied to particular boundary-layer options, but in the future more interchangeability and options may become available. For our purposes, the MYJ PBL scheme was tied to the MOJE and YSU to the MO scheme

6.2.8 Boundary Conditions

6.2.8.1 NCEP Final Analyses

A description of the NCEP Final Analyses is provided in Chapter 2, section 2.2.2. In order to circumvent redundancy, we only review model-specific information. For example, The vegetation/land-use and elevation data assimilated into the GFS model to develop FNL are based on the United States Geological Survey 24-category global 10-min dataset. Soil type is based on a combination of the 10-min 17-category United Nations Food and Agriculture

Organization soil data and U.S. State Soil Geographic 10-min soil data. The SST in the NCEP analysis are based on satellite and in situ observations and for mean daily $0.5^{\circ} \times 0.5^{\circ}$ fields. SST, fraction of vegetation and albedo are updated every 6 h following the diurnal and intraseasonal cycles.

6.2.8.1 GFS Real-time

The present study conducted a significant number of real-time WRF forecasts using NCEP GFS real-time boundary conditions. In the following, we explain some of the GFS model characteristics. The GFS adopts a spectral triangular truncation of 62 waves (T62) in the horizontal and a finite differencing in the vertical with 64 sigma layers. The model top is at 0.2 hPa. NCEP provides model data four times daily: 0000 UTC, 0600 UTC, 1200 UTC and 1800 UTC. The data range is 16 days.

6.3 Data and Methods

6.3.1 Validation Datasets

We used three types of data as validation tools for our experiments: in-situ, gridded observations and gridded reanalysis. In-situ data is necessary in order to analyze model predictions at the district scale that is relevant to meningitis efforts. Gridded information is useful for qualitative and quantitative spatial comparisons between model output and estimates of environmental conditions.

6.3.1.1 In-situ Observations

The documented decline in observational network and the ongoing communication problems of West Africa has negatively affected the monitoring and prediction of weather and climate in the region (Parker et al. 2008). Recent efforts through Africa Monsoon Disciplinary Analyses (AMMA) (Redelsperger et al. 2006) have been aimed at improving surface and upper air observations throughout this region of the continent beginning in 2004. This work has been undertaken in tandem with scientists from operational agencies throughout the breadth of West Africa by reactivating silent radiosonde stations, renovating unreliable stations, and installing new stations in regions of interest for the study of monsoon dynamics as well as of AEWs.

The present study benefits from the installation and upgrade of meteorological stations during the AMMA project, especially for the diagnosis of surface and upper level humidity and wind flow regimes. We note that there is a significant degree of uncertainty inherent in the use of upper level soundings from the AMMA stations (Bock et al. 2007) and that complementary datasets such as satellite soundings are necessary for better representation of the moisture in climate studies. The less reliable stations are used along with the more reliable sites to supplement model simulations and the examination of reanalysis products used to investigate intraseasonal phenomena in Chapters 4-5. The more reliable stations are also utilized to explore the climate-meningitis relationship during 2009. These include Ouagadougou (Burkina Faso; 12.37°N, 1.52°W), Niamey (Niger; 13.5°N, 2.2°E), Bamako

(Mali; 12.65°N, 8.0°W), Agadez (Niger; 17°N, 8.0°E), and N'Djamena (Chad; 12.1° N, 15.0° E). We acquired in-situ observations from the National Oceanic and Atmospheric Administration's (NOAA) National Climatic Data Center (NCDC, <http://www.ncdc.noaa.gov/oa/climate/climatedata.html#daily>) and the AMMA database: (<http://amma-international.org/data/>).

6.3.1.2 Gridded Reanalysis and Observations

In terms of precipitation, we compared the model results against satellite observations from the Tropical Rainfall Measurement Mission (TRMM) Multi-satellite Precipitation Analysis (Huffman et al. 2007), available for daily (3B43) and monthly (3B42) scales (Kummerow 1998, 2000). The monthly scale was used for the seasonal portion of our analysis, while the daily data was used for short-term simulations. Also utilized for seasonal comparison was the CPC Merged Analysis of Precipitation (CMAP), which has shown good results over tropical regions (Xie and Arkin, 1997). Mixing ratio at 925 and 850 hPa was acquire from the AIRS satellite to diagnose the model's ability to reproduce lower-tropospheric moisture at longer scales (weekly to monthly). Data from the AIRS Satellite is also utilized to derive mixing ratio at 925 and 850 hPa for the model validation portion of this study, presented in Chapter 4.

Gridded reanalysis fields were used as comparison tools for temperature, relative humidity and wind information. We use NNRP, FNL, and ECMWF data for this purpose. In-situ surface and upper level sounding datasets complemented the reanalysis and was

especially important for real-time forecasts and nowcasts during 2009. The cities shown in Fig. 6.2 represent locations for which we used meteorological observations data. Of the 7 presented, 4 had continuous sounding information: Agadez, Niamey, Tambacounda and N'Djamena.

Also utilized in this study, although to a lesser extent than NNRP and FNL, is the ECMWF AMMA reanalysis. The ECMWF data assimilation and forecasting system was rerun specifically for AMMA, using the specific AMMA archive of radio-sondes. The ECMWF re-analysis is available over a large Atlantic Africa area, limited to the period of May to September 2006, although some data is available for other time periods. ECMWF analyses generally compare well with independent integrated water vapor data derived from GPS (Bock et al., 2007), although important biases due to observational soundings has also been noted (Agustí-Panareda et al. 2009). The AMMA ECMWF has 25 vertical levels and covers the area 100°W to 50°E, 47°N to 25°S. The data is 4 times daily for analyses and 8 times for forecasts. This iteration of the model is based on Simmons et al. (2006).

6.3.2 Model Domains and Configuration

The WRF model configuration described here was chosen for long simulations at optimal computational rates while retaining the best physics schemes for the region. This study employs nested domains (Fig. 6.3a) for the model validation and real-time forecast experiments, where the outer domain has a 90km resolution and the inner domain is at 30km.

The outer domain ranges from 15°S to 38°N with 63 points in the south-north direction, and 39°W to 49°E and 97 points in the east-west direction. The inner domain ranges from 28°W to 21°E with 160 points in the east-west direction, and 8°S to 24°N with 103 points in the south-north direction. In our simulations, the top of the atmosphere is set at 50 hPa with 28 sigma levels which correspond to normalized pressure following topography.

6.3.3 Model Physics Parameterization Sensitivity Experiment

Initial tests in this study were aimed at choosing the best possible model physics configuration while at the same time retaining the capability to carry out long simulations at optimal computational rates. These tests followed a trial-and-error scheme and the different combinations are shown in Table 6.1. All model simulations were performed for the boreal spring of 2006 in order to take advantage of the rich AMMA database. Simulations were initiated in March of that year and ran through June. For our purposes, we analyze only April and May, given the specific application (meningitis project). There were 19 different physics combinations in which domains, start date, scalars and boundary conditions remained constant. This technique also allowed us to develop an ensemble of WRF simulations to test its useable skill in Chapter 7.

We used qualitative and quantitative methods to diagnose model error in this experiment. In our qualitative analysis, we performed visual side-by-side comparisons of model results against gridded observations and reanalysis. The fields tested are accumulated rainfall (mm) and surface temperature (°C). For the quantitative method, we chose to use correlation and

Mean Absolute Error (MAE) for the period of interest April-May. The motivation for using MAE for average model performance over the root mean square error (RMSE) stems from the fact that the RMSE is a function of three characteristics of a set of errors, rather than the average error. Further, it is found that the MAE is a more natural measure of error and is unambiguous (Willmott and Matsuura, 2005). The formula for MAE is as follows:

$$\text{MAE} = N^{-1} \sum \|P - O\| \quad (6.1)$$

where P is the model-predicted value and O is the observed value for N number of cases. Variables tested with the MAE include dewpoint temperature (C) and relative humidity as given by meteorological stations in Fig. 6.2.

The tests highlighted here are meant to answer two of the initial questions asked about regional model simulations with WRF: a) added value of dynamical downscaling and b) capturing the shift in the moisture regime.

6.3.4 Real-time Forecasts and Seasonal Hindcasts

The 2009 boreal spring provided a good test bed for gauging the model's capability to simulate atmospheric moisture. We took advantage of increased observational records in Kano, Nigeria, which was collocated with a major meningitis outbreak. Our simulations were carried out using the e1 physics combination (see Table 6.1) with FNL and NCEP GFS boundary conditions for seasonal (January – August) and short term forecasts, respectively.

The model forecasts are comprised of an ensemble of model predictions with 6-15 ensemble members, depending on the available data and computational considerations.

Forecasts were performed for April 1, 4, 6, 10, 15 and May 1 and 7 2009. The first 8 days of GFS boundary conditions provide information every 3 hrs, whilst days 9-16 only have information every 12 hrs. This paradigm allowed us to perform ensemble simulations such that each iteration of the model could be initialized at 0000 UTC and 0300 UTC for the 0000 UTC data source, for example, such that we acquire 8 different ensemble members at high temporal resolution. As an example, the data for April 1 2009 was provided for each of the 4 times listed above. The model would be initialized at 0000 and 0030 UTC for the 0000 UTC dataset, then 0600 and 0900 UTC for the 0600 UTC dataset and so on. Analysis of the data was started on April 2 so that all 8 possible ensemble members would have started the day before. However, this was not possible with longer-range (>8 days) forecasts because of the 12 hr interval between boundary conditions. Our method was then to use a 2-day buffer so that the 0000 UTC data source could have up to 4 iterations: 0000, 1200 UTC April 1 and 0000 and 1200 UTC April 2. This means that analyses must begin on the third date. The May 1 and 7 2009 simulations use this approach in order to capture the length of the MME.

We again employ MAE for the analysis of forecast and seasonal model cycles as well as correlation for the seasonal iteration only, given the short range of data (<16 days) for the real-time simulations. For 2009, all three goals outlined in the introduction are addressed, with particular attention to the simulation of moist events, including the MME investigated in Chapter 3 in both the seasonal and forecast runs. We compared the model results against satellite observations from TRMM and mixing ratio at 925 and 850 hPa from the AIRS satellite for weekly to sub-weekly scales. This allowed us to validate model simulations of

lower-tropospheric moisture. Particular emphasis is also placed on not just the progression of TD1 in the seasonal run but also to Kelvin waves throughout the length of the 2009 boreal spring.

6.4 Results

6.4.1 Simulations during 2006

6.4.1.1 Qualitative Analysis

The AMMA program in 2006 provided quality information through a variety of datasets, including a special ECMWF reanalysis product. We took advantage of this product to analyze how our simulations compared to it and to other datasets such as NNRP and FNL. This portion of the analysis is limited to precipitation and temperature due to the limited storage space for large number of seasonal ensembles. Relative humidity is also available and we will review it in the quantitative analysis.

We first review the simulation of precipitation in Fig. 6.4. We designate names for each physics parameter combination according to Table 6.1. Note that we refer to them as “ensemble members” since they will be utilized to determine the useable skill of the model in the seasonal scale. The figure represents accumulated precipitation during the month of April 2006. Software errors forced us to drop E13 from the analysis. We use TRMM and CMAP data as proxies for observed precipitation in terms of spatial distribution. TRMM has considerably higher resolution than CMAP but the latter is important to have as a reference

point. Main features during this time period are: i) pronounced ITCZ along 3N with heavier precipitation (>250 mm) west of the prime meridian. Significant amounts of rainfall were also experienced at 10°E along the equatorial coast of Africa (Cameroon, Gabon, Equatorial Guinea). This is confirmed by CMAP. Moderate amounts (>100 mm) are also found along the Gulf of Guinea (GOG) coast. Also, and perhaps more importantly, is a section of lighter precipitation values from the GOG to 10N from 10°W to 0°E. One additional feature worth noting is a secondary belt of moderate amounts (>150 mm) along 2S from 20°W to 10°W. This belt is connected to a larger shield of precipitation that spans 5S-4N and 5°W-15°E. This is a potentially important feature within our model testing.

There are three types of results in terms of precipitation: i) limited amounts over the GOG and adjacent regions, ii) heavy rainfall along the ITCZ, and iii) excessive rainfall throughout. E7, E9, E10, E12 and E15 all have excessive amounts of rainfall along the ITCZ and equatorial Africa. E15, in particular has amounts higher than 500 mm from the GOG south over the waters of the Atlantic Ocean. Of these ensemble members, 2 utilize the TD surface physics (E10 and E15), 2 utilize RUC surface physics (E7 and E9). Also note that E12 has RRTM-GODDARD radiation schemes instead of CAM, used in E1 (E1 is the base ensemble member since it is also used for other experiments, i.e. real-time forecasting, and in the initial domain setup).

Intense ITCZ precipitation is found in ensemble members E1, E2 and E17. E1 and E2 only differ in the microphysics scheme (WSM3 and WSM6, respectively). E17 also uses TD as surface physics. Other simulations produce rainfall in regions known to be dry, north of

10N (see CMAP and TRMM images): E11, E7, E15, E16, E17. Outside of E15, all other simulations use the RRTM-GODDARD radiation scheme. There are also ensemble members without precipitation overland: E4, E14 and E19. Of these, E14 uses TD, and E19 uses RRTM-GODDARD. E14 only varies from E1 in its surface layer physics: it uses MOJE instead of MO.

Precipitation distribution is a key factor in determining surface humidity, as convective events may advect moist air into drier climates by way of moisture fronts, as was the case with the MME. If we investigate precipitation patterns overland and, specifically, over West Africa, we find E1, E2, E10 and E16 have the better approximations from a qualitative point of view. The factors that determine this are a threshold of <250 mm accumulated precipitation over the GOG coast and agreeable representation of the >50 pocket of rainfall between 10°W to 0°E that reaches 10N. Of these, E10 uses TD and E16 utilizes RRTM-GODDARD schemes. We stress these factors because it could help determine the optimal choice for all simulations.

To further explicate the eventual choice of E1 as our base for the rest of the simulations in this project, we examine the distribution of average 2 meter temperatures (Fig. 6.5) throughout the region during May of 2006. We chose May because the ECMWF reanalysis was available for this month and allowed for further comparisons with the model data. Surface temperature is especially important since it is related to the calculation of relative humidity (%). We first point out the significant aspects of temperature distribution as given by the 3 reanalysis fields. Noteworthy is the slightly cooler climate displayed in the FNL data

west of 10°W, compared to the other two reanalyses. It also has pockets of >34C over portions of Chad and northeastern Nigeria. ECMWF is warmer than both NNRP and FNL, with >34C temperatures prevalent over Chad, Mali and Mauritania. All three agree on cooler conditions south of 10N. ECMWF does discriminate, however, in its distribution of temperatures <26C, as they are confined to the higher terrain of the Guinea and Cameroon Highlands and the Jos Plateau in Nigeria.

Model simulations are generally much warmer or much colder than the reanalysis. Typically, this is correlated with the choice of surface physics. For E10, E11, E14, E15 and E17, the markedly colder conditions (4-8 °C) correlate with the TD scheme. There are also much warmer conditions predicted by some of the ensemble members: E6, E7, E8, E12, E18 and E19. All, except for E8, use RRTM-GODDARD as the radiation scheme. Although E16 is not as warm as the above, it is still markedly warmer in a larger spatial range (north of 12N) than E1 and E2. Further, E1 and E2 are closer to ECMWF (regarded as a better model in the tropics and created specifically for AMMA). Thus, the better choice for simulating boreal spring climate is either E1 or E2, and since E2 is more computationally expensive, E1 became our default choice. The preceding has also served to show the model's capability to simulate the climate of the region, and we find that this is dependent on the chosen physics parameterizations.

6.4.1.2 Quantitative Analysis

A more complete assessment of model performance during our physics parameterization tests is to analyze the model's ability to simulate moisture at the surface, specifically, relative humidity (%). The motivation behind the choice of this variable is its documented relationship with the cessation of meningitis epidemics under the monsoonal, i.e. high humidity regime. In Table 6.2 we present MAE calculated for 4 cities: Agadez, Bamako, N'Djamena and Niamey. Notice that E1 outperforms most other ensemble members in terms of the mean for all 4 locations. However, this does not necessarily translate into the best result for all locations except for E16. Indeed, a closer look at the numbers for E16 reveals that E16 is nearly equivalent to E1 at Agadez, N'Djamena and Niamey. E5 is also very close to E1 and E16. It would seem from this analysis that E16 and E5 are viable options for simulations. Although the qualitative analysis showed E1 represented overall climate better than E5, the need to simulate conditions at the surface prompted us to explore the behavior of these physics combinations further.

Another method to gauge E1's performance versus a potentially equal option (E5, E16) is to investigate how they simulate conditions at a particular location throughout the period of interest. In Fig. 6.6a we show time series of relative humidity (%) during May 2006 over the city of Niamey using the 4-times daily averaged data acquired at the AMMA-enhanced station (black, solid contour) and ensemble members E1 (red, solid), E16 (purple, short dash), E5 (dark blue, dotted), E10 (long dash) and E14 (dash dot). The latter two are shown for perspective and allows us to understand the impact of the cold bias shown in Fig. 6.5

using the TD surface layer scheme. Also on Fig. 6.6a, we may discern how, near the end of the period (May 20), E5 and E16 are continuously more humid than both the observed and E1. Indeed, its overestimation begins on May 8, while E1 is closer to the observed. To further state our claim, we show the same time series but for the city of Bamako on Fig. 6.6b. Once again, E5 tends to overestimate the surface humidity. E16, however, is equivalent, if not better, than E1. We stress, however, that in the case of these two cities (equivalent latitude), May is the period with highest humidity flux as the moisture regime shifts from Harmattan to the monsoon. Further, the choice of E1 over E16 yields minimal difference in end results.

Given the importance of diurnal variability on monsoon dynamics (Parker et al 2005), we also analyzed the model's skill at this scale (Fig. 6.7). We use the rich AMMA dataset for the city of Niamey to compare two of the physics varying ensemble members with equivalent performance: E1 and E16. We concentrate our analysis on this figure on the fact that humidity in Niamey approached and crossed the RH40 threshold during late May (May 23-29 2006). Data from the meteorological station is acquired approximately every 6 hrs. We use model output for the same time periods in our comparison. We decided not to compute statistics due to the short time frame shown but visual analysis confirms that the model is able to effectively capture the diurnal variability over this location.

6.4.2 Simulations during 2009

6.4.2.2 Moist Events

One of the primary goals of the present study is to characterize the nature of moist events that occur during the transition from Harmattan to the monsoon. Using 2009 as a test bed, we now turn our attention to the simulation of these events throughout the months of April and May. We know, for example, that these short-term events are associated with mesoscale convection within synoptic systems such as TD-type (proxy for AEWs) and Kelvin waves. Thus, it becomes imperative to analyze the model's representation of precipitation during the months of April and May of 2009. We study the moist events in both the inner and the outer domain in order to see the advantage of higher resolution and also to analyze larger scale structures such as Kelvin waves.

Accumulated precipitation for the weeks of April 29 – May 5, May 6-12 and May 13-19 2009 is presented in Fig. 6.8. The inner domain model (Fig. 6.8b) captures the overall spatial structure of precipitation patterns over the region as portrayed by TRMM in Fig. 6.8a, but this positive result is limited to the continent. . The figure also shows that the model is unable to capture the ITCZ located over the GOG. As we move forward in time to May 6-12, we notice that there is increased precipitation in the northeastern side of our domain ($>15^{\circ}\text{E}$ and $>12^{\circ}\text{N}$), perhaps in a response to the TP that formed during May 7-9. The western side of the domain (west of 5°W), however, remains dry in this view as compared with TRMM. Since the period in Fig. 6.8c-d is during the height of the MME's TD1, we are left with the question of whether or not the model is able to capture this important feature. Finally, in Fig.

6.8e (TRMM), most of the precipitation totals have moved westward (west of 0°E) and also cover a larger meridional range (GOG to 15N). The model (Fig. 6.8f) does capture the westward movement of the rainfall except for southeastern regions of Senegal. However, the model fails to show the ITCZ off the GOG coast in Fig. 6.8d and Fig. 6.8f.

The preceding analysis showed that the model was unable to capture the significant amounts of precipitation associated with MME west of 5°E. This could be due, in part, to our threshold of 10 mm accumulation. We thus turn to another method to diagnose the propagation of the system: time-longitude Hovmoller diagrams. From this vantage point, the model actually shows the progression of TD1 with considerable clarity at 10N (Fig. 6.9b) compared to TRMM (Fig. 6.9a). This could be due to the inherent biases in TRMM due to its orbit configuration.

There are 3 events at 10N in Fig. 6.8b, which is consistent with the TD-type filtered OLR in Fig. 3.32a in Chapter 3. Notice that the May TD-type systems are not as prevalent in the TRMM data. Also consistent with TD-type systems is its speed: 8.44 m s⁻¹. However, the approximated speed of TD1 as given by TRMM is closer to 5.64 m s⁻¹, which could explain the faster observed propagation of the wave. This is only an estimate, however, so the time periods may be closer in actuality. This finding, however, is significant in the fact that a one-to-two day delay may have occurred with the simulation. Indeed, further inspection of the Hovmoller plot shows that there is no rainfall in the WRF simulation west of 5°W until May 12, even for the 10N plot Fig. 6.9b. The same is true for the meridional wind (Fig.4.10),

where no southerly flow is present before May 11 for points west of 0°E that are in association with TD1.

It is thus possible that the system is delayed in the simulation by at least two days compared to the observed. This could be due, in part, to the choice of domains. We illustrate this further with a daily sequence of WRF rainfall using the outer domain in Fig. 6.11. There is a clear TP in association with the mid-latitude system starting on May 6 that remains in place until May 10. Only limited precipitation is present west of 5°E . A factor at work in this instance may be the choice of domains. Indeed, the point of interaction between the mid-latitude system and tropical moisture is along the eastern and northern edges of the inner domain.

It is equally important to analyze the WRF model's ability to capture moisture throughout the vertical structure of the atmosphere. In Figure 6.12, mixing ratio data available from the AIRS satellite is compared against the same field from WRF for the 925 hPa level during the seven day periods of 6-12 and 13-19 May 2009, chosen due to highlight conditions before and after the MME. The observations from the satellite occur during 13:30 GMT (also local time). The model outputs data on a 6-hourly basis and the closest available occurs at 1200 UTC, so we use this in our comparison. As can be seen, the model captures a tropical plume that extends from the GOG into northern sectors of the country of Niger (into the Sahara Desert) for the 6-12 May period. There is a dry bias over the western portion of the domain from 5°E to 15°W , however. This bias also holds true for the 13-19 May period, but the westward propagation of the moisture is evident as portions east of 10°E and north of 10°N

that are visible in the AIRS observations are also captured. The model is also markedly moister ($+4-6 \text{ g kg}^{-1}$).towards the GOG.

Another aspect that had significant influence on the development of the MME is the propagation of CCEWs through the domain. In Fig. 6.13 we show accumulated precipitation values in the outer domain averaged for points between 2.5°S and 7.5°N (shaded) to elucidate the presence of Kelvin waves and the MJO and also for $10^{\circ}\text{N}-15^{\circ}\text{N}$ (contour) to highlight the MME TD1. We note that there is an eastward-moving feature during April, which could be related to the observed MJO (see Fig. 3.21 in chapter 3). The Kelvin wave that has the most impact on the MME (K1) is more difficult to discern in this figure, although there is a weak eastward-moving signal during this time. There is a link, however, with the westward-propagating systems through possible interactions for both eastward-moving signals. The most prominent aspect of this figure, however, is the significant lack of precipitation over the Atlantic Ocean that is in association with the ITCZ. This was also visible in our horizontal analysis in Fig. 6.8.

6.4.2.2 Surface Humidity

Following the same paradigm as simulations during 2006, the primary goal of this experiment is to test the model for its capability to reproduce surface moisture conditions. Thus, we analyze model output over particular locations. In this case, we have chosen Bamako, Kano, N'Djamena, Niamey, Ouagadougou and Tambacounda for our MAE analysis. Kano was chosen given the increase in surface information and the implications on

concurrent meningitis epidemics. Indeed, in the case of Kano, we find the model performs satisfactorily (Fig. 6.14) in its simulation of the peaks and valleys in relative humidity (%) associated with the short-term moist events. In Table 6.3 we show how WRF best performs over Tambacounda (6.71%) and Kano (8.73%). Niamey (12.56%) and Bamako (12.09%) are farther from the observed, as are Ouagadougou (13.25%) and N'Djamena (16.46%).

We can further explore the meaning behind the numbers above in Fig. 6.15 through simple time series of a main constituent in the calculation of relative humidity: the dewpoint temperature (T_d). In this case, we chose stations west of 5E (Niamey, Ouagadougou, Bamako and Tambacounda) given the poor performance in the simulation of the MME (section 4.3.2.2 above). The model is able to capture the overall pattern, especially the shift in the moisture regime from the variable spring conditions that are characterized by sharp moist spikes, to the more stable monsoon conditions once the moisture has reached the ITD (defined as the 15°C in the literature by Pospichal et al. 2009, among others). It should be noted, however, that some of the moisture spikes are not captured by the model. This becomes evident in the scatter plots (Figure 26), where a number of events are classified either as moist or dry when the opposite is true in the observations. In terms of correlations, Tambacounda has the highest (0.86), followed by Niamey (0.8), Ouagadougou (0.74) and Bamako (0.69). Tambacounda has the highest mainly due to the fact that, although the model has a dry bias, there are fewer instances where moisture spikes are misclassified as dry or moist. The opposite is true for Bamako, mainly due to a significant moist event that occurred

in mid April that was not captured by the model. This finding is also supported by the comparisons against the AIRS satellite observations (Fig. 6.17).

6.4.2.3 Real-time Forecasts

Numerous experimental model forecasts were performed for the period March-June 2009 using NCEP GFS boundary conditions. These forecasts were meant to diagnose the model's capability to predict surface moisture and to gauge the added value of utilizing dynamical downscaling for applications such as meningitis efforts. It was the forecast of the TD1 associated with the MME 10 days in advance that prompted further investigation of the event (Fig. 6.18). We highlight the prediction of moist events in this portion of the analysis.

A quantitative approach to determining the model's ability to simulate humidity is provided in Chapter 5. Our technique here will be more qualitative in nature. We limit this part of the analysis to three locations: Niamey, Kano and Bamako. As stated in section 4.3, there were different types of forecasts performed: short term (1-8 days) and long term (1-16 days). We chose to look at Kano first, given the meningitis epidemic and amelioration during this time period. Two different model iterations are presented in Fig. 6.19: (a) April 28 – May 4 and (b) May 1-7. Notice that the model captures the change in moisture on May 2-3 in Fig. 6.19a and all model simulations remain above the RH40 threshold for May 2-7 (b). Also, and perhaps more important in terms of model skill, is Fig. 6.20, where we show that the model captures the ascending moisture during (a) May 2-7 and also the spike associated with the MME (b). Noteworthy is the fact that model forecasts also estimate the MME to occur 1

to 2 days later than observed. This is in agreement with previous findings with the seasonal model simulations (section 4.3.2.2).

In terms of longer-period simulations, i.e. 1-16 days, the model performs reasonably well over the cities selected (we use quantitative measures to calculate this in Chapter 5). In Fig. 6.21, for instance, we present conditions as Bamako for the observed and predicted surface moisture. These model iterations were initiated on May 1 and stem from that particular set of GFS boundary conditions. This particular simulation is, perhaps, the most successful since it i) captures the timing of the MME, ii) remains below RH40 (WRF AVE) and iii) contains widely-varying model results. This last finding is particularly significant for ensemble prediction, as it gives a more probabilistic outcome for end-users.

Model forecasts for the city of Kano also contain a high degree of agreement with the observations (Fig. 6.22). Conditions remain above RH40 for most of the period, but the model is also able to capture the steep decline after May 10, when the subsidence to the east of the MME begins to influence the climate of the region. The last set of model simulations we present is over the city of Niamey (Fig. 6.23). The model once again has difficulty with the timing and strength of the MME over this particular location. The ensemble average (WRF AVE) has two distinct peaks on May 7 and May 10 that are above RH40. The observations show a single pulse of moisture that spans the length of May 8-10. There is also considerable model spread during this date, suggesting important dependency on the boundary conditions from GFS. If the global dataset was able to predict the event, then WRF had a better chance in doing so also. Further analysis revealed that certain forecast iterations

(i.e. 1200 UTC on May 1) were able to construct the sequence of events that led to the MME and its associated phenomena (mid-latitude system, equatorial waves). This study had only a limited amount of boundary conditions available for proper simulation of the event (May 1 and May 7 initial conditions). We propose that enriching the dataset with more iterations of the global model (May 2, 3, 4 and so on) could help ameliorate the situation.

6.5 Conclusions

Important findings in this chapter include the negative bias incurred by the use of Thermal Diffusion (TD) as a LSM. This cold bias (see Fig. 6.5) caused higher humidity throughout the region. This is also evident in a time series of an area average over the city of Niamey, Niger (Fig. 6.6a). We found two optimal physics parameter combinations that worked well over the region: E1 and E16. Most of the forecast and seasonal simulations for 2009 were carried out with this particular set of parameters (KF microphysics, YSU PBL, CAM radiation, etc.). We showed that E1 could be used to successfully investigate the dynamics of West Africa during the boreal spring, with a MAE of 6.06% for Niamey, for example.

As documented in Flaounas et al (2010), the KF cumulus scheme has the more robust results over the region during the summer months. The same holds true for the MYJ PBL scheme. However, within our tests over the region, the YSU scheme provided similar results and, given the performance of real-time simulations for 2009 with YSU, we saw no need to change our scheme. This may be due to the fact that we are more interested in the shift of the moisture regime and not on the monsoon itself. YSU had shown a positive bias in precipitation in Flaounas et al. (2010).

Our analysis also showed that the model is able to capture the shift in the moisture regime throughout the various locations used as proxies for this seasonal event (Fig. 6.15). It is shown how the model correctly approximates the highly variable, moist-event-dependent humidity regime before the crossing of the ITF (15°C). There is less variance in T_d and relative humidity once this point has been reached and the model simulates this with success.

There are important short-comings to the seasonal model simulation for 2009 in that it is unable to capture the timing of the westward-shifting MME and its associated TD1. WRF also has difficulty in developing and sustaining eastward-propagating CCEWs such as Kelvin waves and the MJO. There is qualitative evidence for a weak signal of the K1 wave analyzed in Chapter 3 as well as a more pronounced eastward signal during April (possibly associated with the MJO). A determining factor in this predicament could be the limit of the domains (39W-49E for the outer domain), which does not allow for the larger spatial range of Kelvin waves. Recent research on this front has, however, found that WRF is able to capture Kelvin and Equatorial Rossby waves (Tulich et al. 2009). We propose a widening of the outer domain in future simulations in order to get a better representation of intraseasonal variability in this part of the continent.

We have shown that the model can capture both moist events and the actual shift in the moisture regime for a given location. We address the second topic posed at the beginning of this chapter with Fig. 6.24. In this time series of weekly averages of observed relative humidity (blue), attack rates (grey-black), WRF (red) and NNRP (green), we show that the model can be a useful tool for meningitis efforts. In this figure, the link between observed

humidity and the collapse of epidemics occurs on the week of April 13-19 (see chapter 2 for details on data sources and the disease-climate interface). The season-long WRF simulation follows the observed humidity during the weeks of highest flux within a distance of <3%. In comparison, the coarse-scale reanalysis, shown to represent global models currently being employed for meningitis-climate research, tends to overestimate surface humidity by as much as 50%. Indeed, further inspection of NNRP in this plot shows that the humidity field is over RH40 for the first week of the analysis (March 30 – April 5) and only 1.6% below this threshold for the week of April 6-12. We propose that further resources should be invested in continuing the use of regional models, given the positive results, whilst addressing some of the shortcomings divulged in the present research. We have found that there is certain value in using limited-area models and we stress that they are a viable option for decision-makers in the region.

Table 6.1: List of Physics parameter sensitivity ensembles.

	Cumulus	Surface layer	Surface Physics	PBL	Soil layers	Microphysics	Radiation LW	Radiation SW
e1	KF	MO	Noah	YSU	Noah	WSM 3-class	CAM	CAM
e2	KF	MO	Noah	YSU	Noah	WSM 6-class	CAM	CAM
e3	KF	MOJE	Noah	MYJ	Noah	WSM 3-class	CAM	CAM
e4	BM	MOJE	Noah	MYJ	Noah	WSM 3-class	CAM	CAM
e5	GD	MOJE	Noah	MYJ	Noah	WSM 3-class	CAM	CAM
e6	KF	MOJE	RUC	MYJ	RUC	WSM 3-class	RRTM	GODDARD
e7	KF	MO	RUC	YSU	RUC	WSM 3-class	RRTM	GODDARD
e8	GD	MO	TD	YSU	TD	WSM 3-class	CAM	CAM
e9	KF	MO	RUC	YSU	RUC	WSM 3-class	CAM	CAM
e10	KF	MO	TD	YSU	TD	WSM 3-class	CAM	CAM
e11	KF	MOJE	TD	MYJ	TD	WSM 3-class	RRTM	GODDARD
e12	KF	MO	Noah	YSU	Noah	WSM 3-class	RRTM	GODDARD
e13	KF	MOJE	Noah	MYJ	Noah	WSM 3-class	RRTM	GODDARD
e14	KF	MO	TD	YSU	TD	Lin	CAM	CAM
e15	KF	MO	TD	YSU	TD	Kessler	CAM	CAM
e16	BM	MOJE	Noah	MYJ	Noah	WSM 3-class	RRTM	GODDARD
e17	KF	MO	TD	YSU	TD	WSM 3-class	RRTM	GODDARD
e18	KF	MOJE	RUC	MYJ	RUC	WSM 3-class	CAM	CAM
e19	GD	MOJE	RUC	MYJ	RUC	WSM 3-class	CAM	CAM

Table 6.2: MAE for each ensemble member at the cities listed.

	Agadez	Bamako	N'Djamena	Niamey	mean
e1	27.71	13.66	14.84	6.06	15.57
e2	15.96	21.52	20.51	7.06	16.26
e3	21.44	15.39	16.96	13.63	16.86
e4	22.20	14.99	15.17	11.35	15.93
e5	32.45	13.58	16.91	10.84	18.44
e6	19.14	17.83	16.43	24.09	19.37
e7	17.46	19.03	16.16	14.23	16.72
e8	50.20	16.94	22.63	46.44	34.05
e9	17.07	19.11	16.95	17.34	17.62
e10	49.56	16.32	22.12	47.42	33.86
e11	61.47	26.98	32.07	60.00	45.13
e12	14.11	22.42	18.89	10.02	16.36
e14	70.03	34.67	39.90	55.57	50.04
e15	61.53	26.67	32.17	52.43	43.20
e16	26.09	10.68	14.91	7.44	14.78
e17	47.59	17.19	19.12	46.04	32.48
e18	24.63	13.58	20.08	21.10	19.85
e19	26.25	12.72	15.47	16.92	17.84

Table 6.3: WRF MAE for relative humidity (%) at each city.

City	MAE
Bamako	12.09
Kano	8.73
N'Djamena	16.46
Niamey	12.56
Ouagadougou	13.25
Tambacounda	6.71

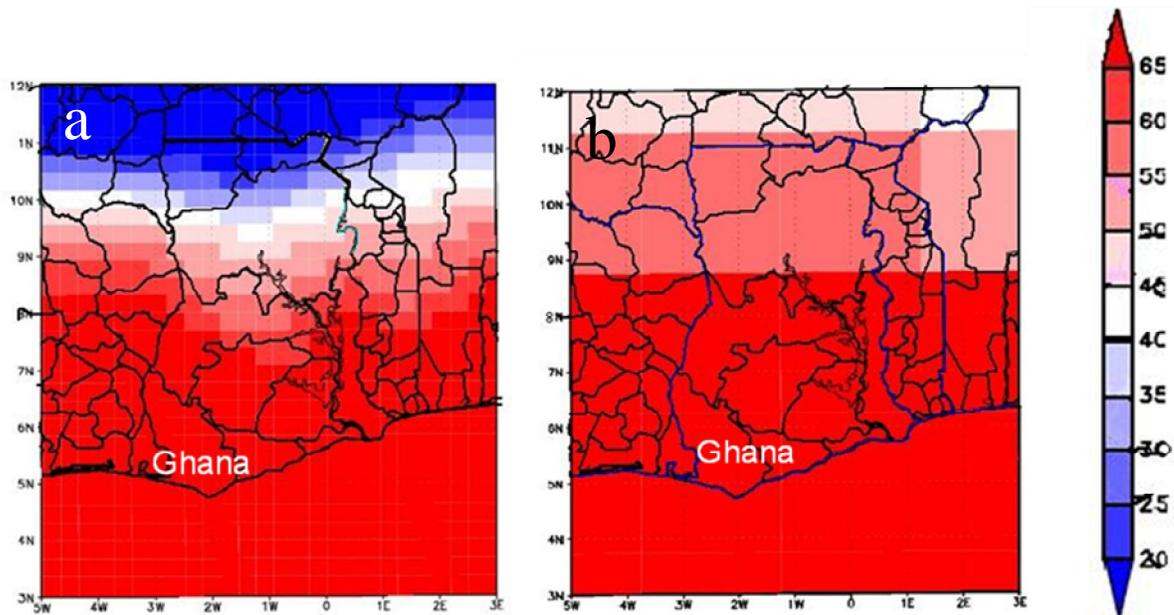


Figure 6.1: Model resolution of relative humidity (%) over Ghana for (a) WRF at 30 km and (b) NNRP at $2.5^{\circ} \times 2.5^{\circ}$. Blue outlines denote country boundaries. State boundaries are shown in black contours.

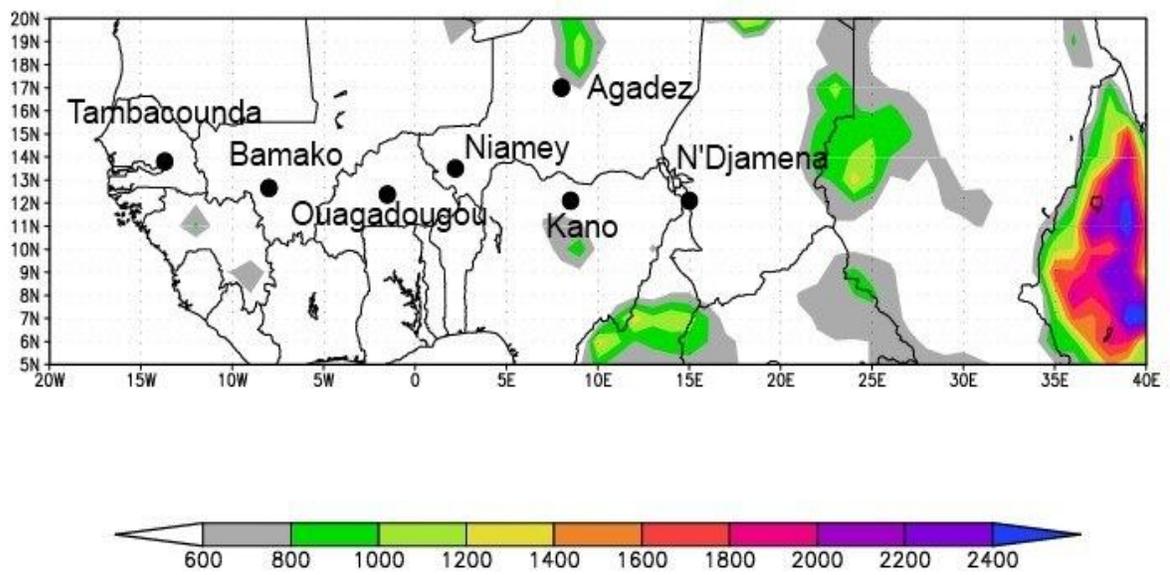


Figure 6.2: Locations chosen for comparative analysis with in-situ information.

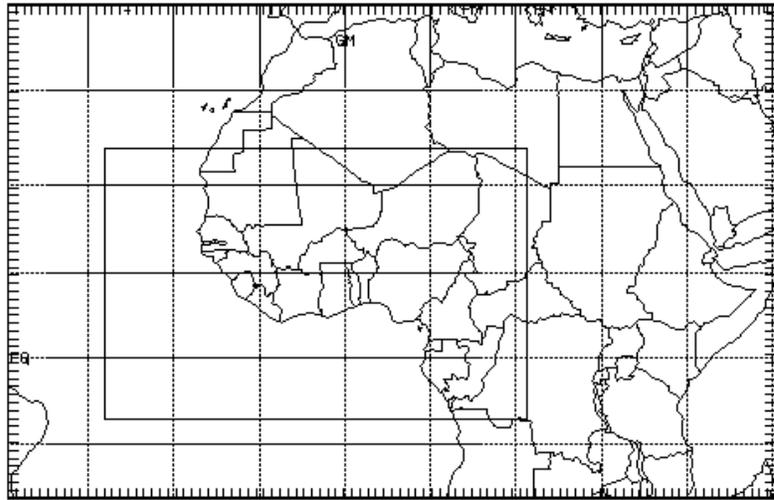


Figure 6.3: Model domain configuration showing inner and outer domain for seasonal and real-time simulations.

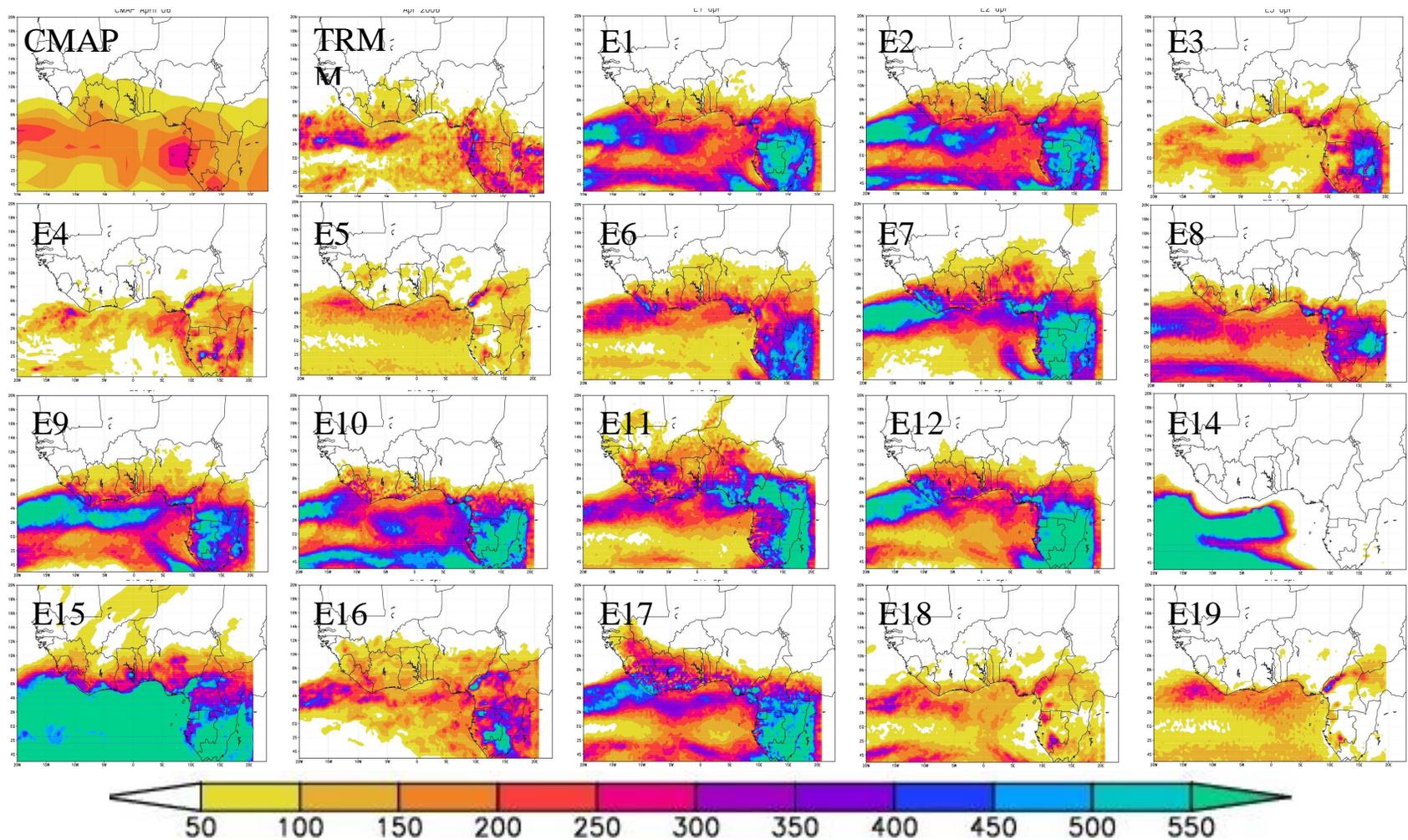


Figure 6.4: Accumulated precipitation (mm) for April 2006. Labels denote the data analyzed: TRMM, CMAP and physics parameterizaion ensemble members defined in Table 6.1.

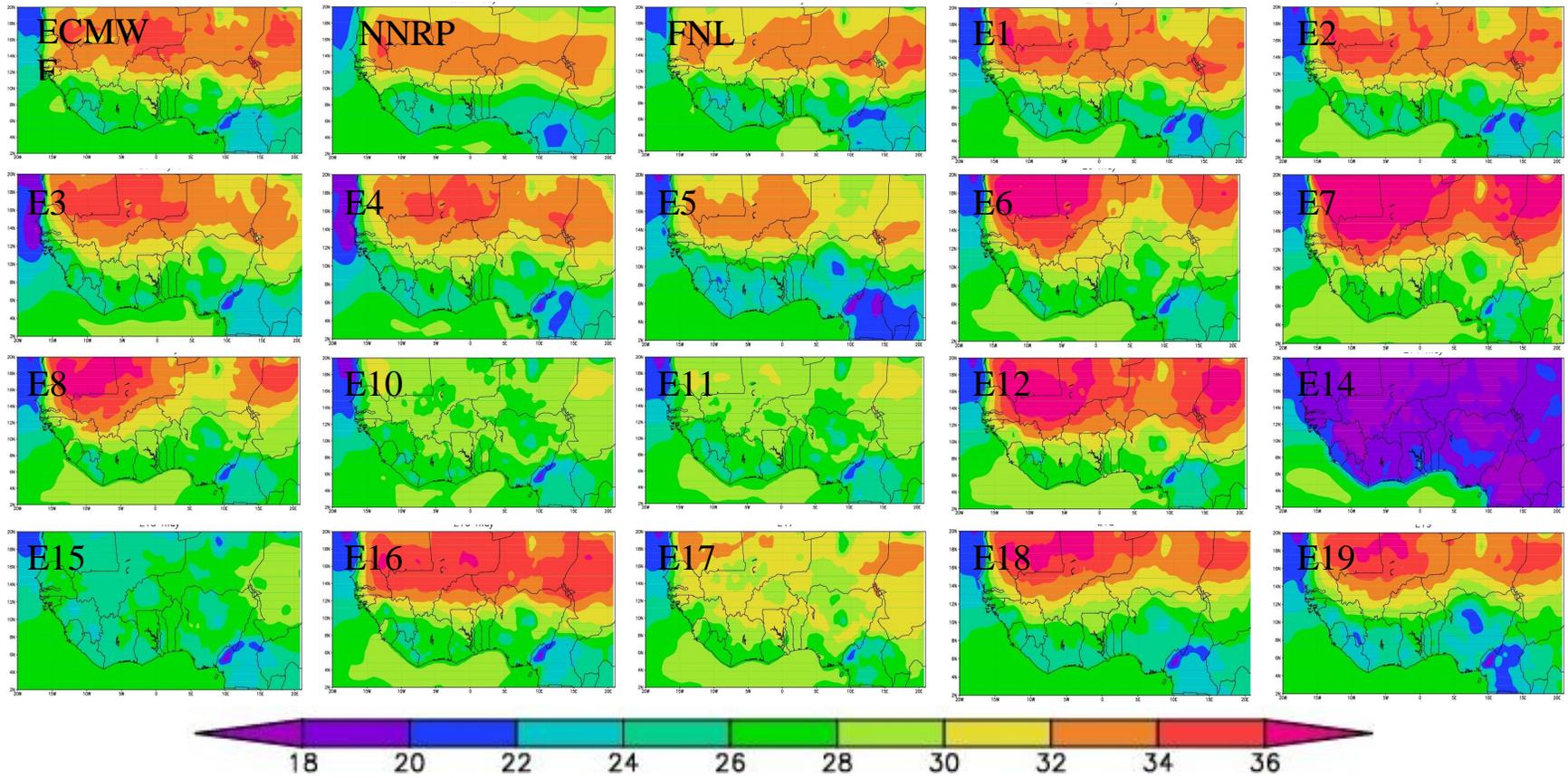


Figure 6.5: Average temperature ($^{\circ}\text{C}$) for April 2006. Labels denote the data analyzed: ECMWF, NNRP, FNL and physics parameterizaion ensemble members defined in Table 6.1

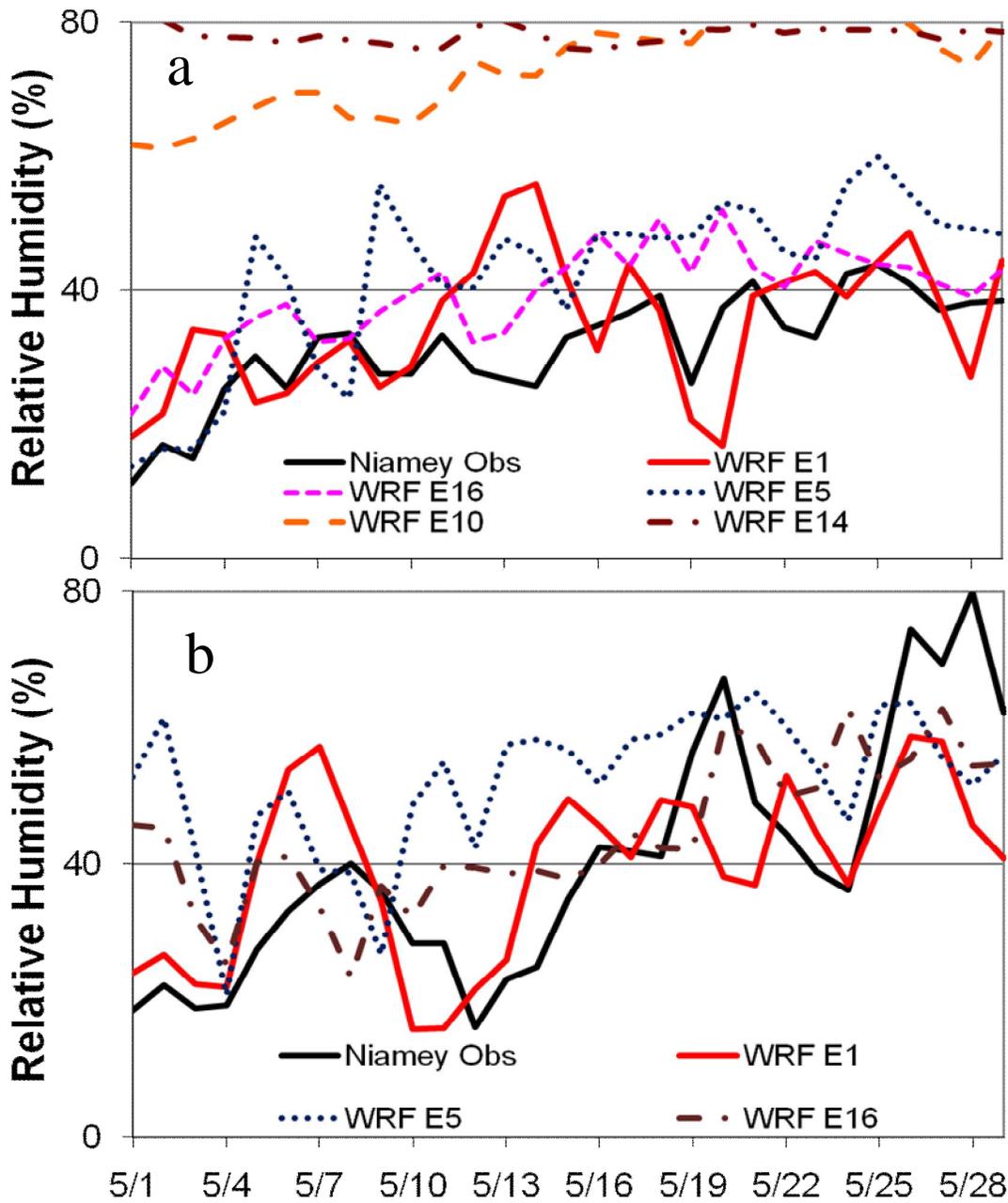


Figure 6.6: Time series of relative humidity (%) during May 2006 for in-situ observations over the city of (a) Niamey and (b) Bamako (black, solid), and area averages of ensemble members E1 (red, solid), E2 (purple, short dash), E5 (dark blue, dotted), E10 (long dash) and E14 (dash dot).

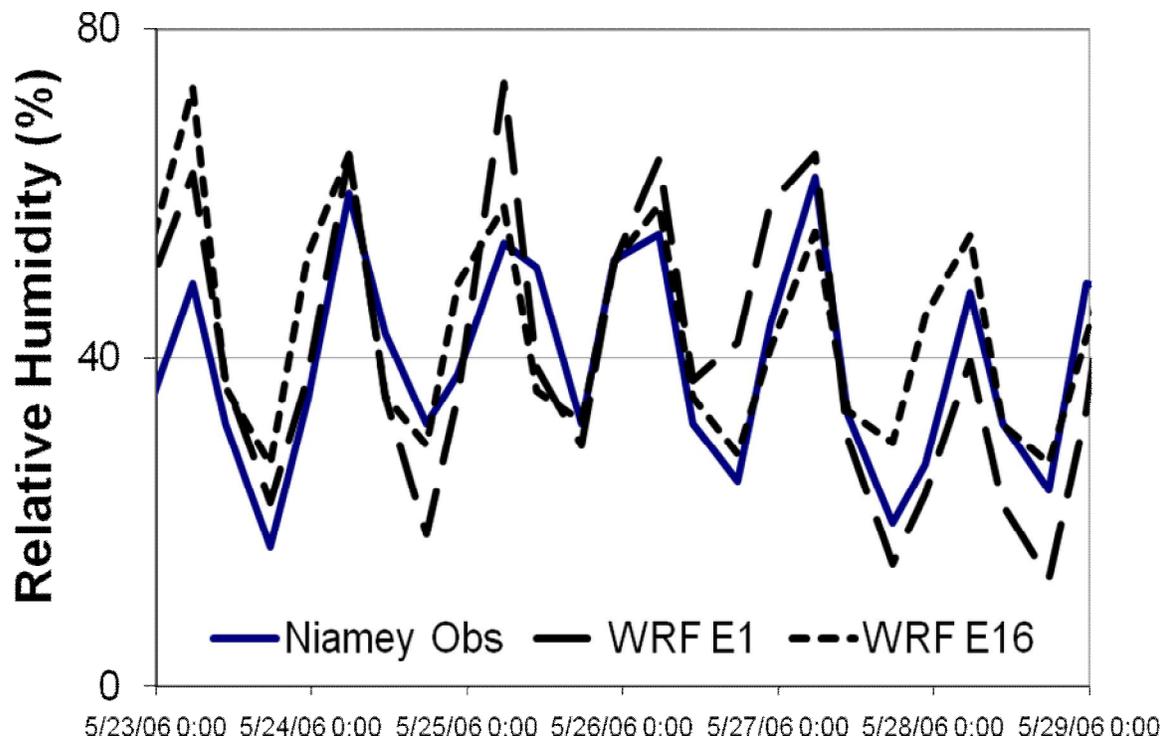


Figure 6.7: Time series of the diurnal variability of relative humidity (%) during May 23-28 2006 at 6 hr intervals for in-situ observations over the city of Niamey (black, solid), and area averages of ensemble members E1 (black, long dash) and E2 (purple, short dash).

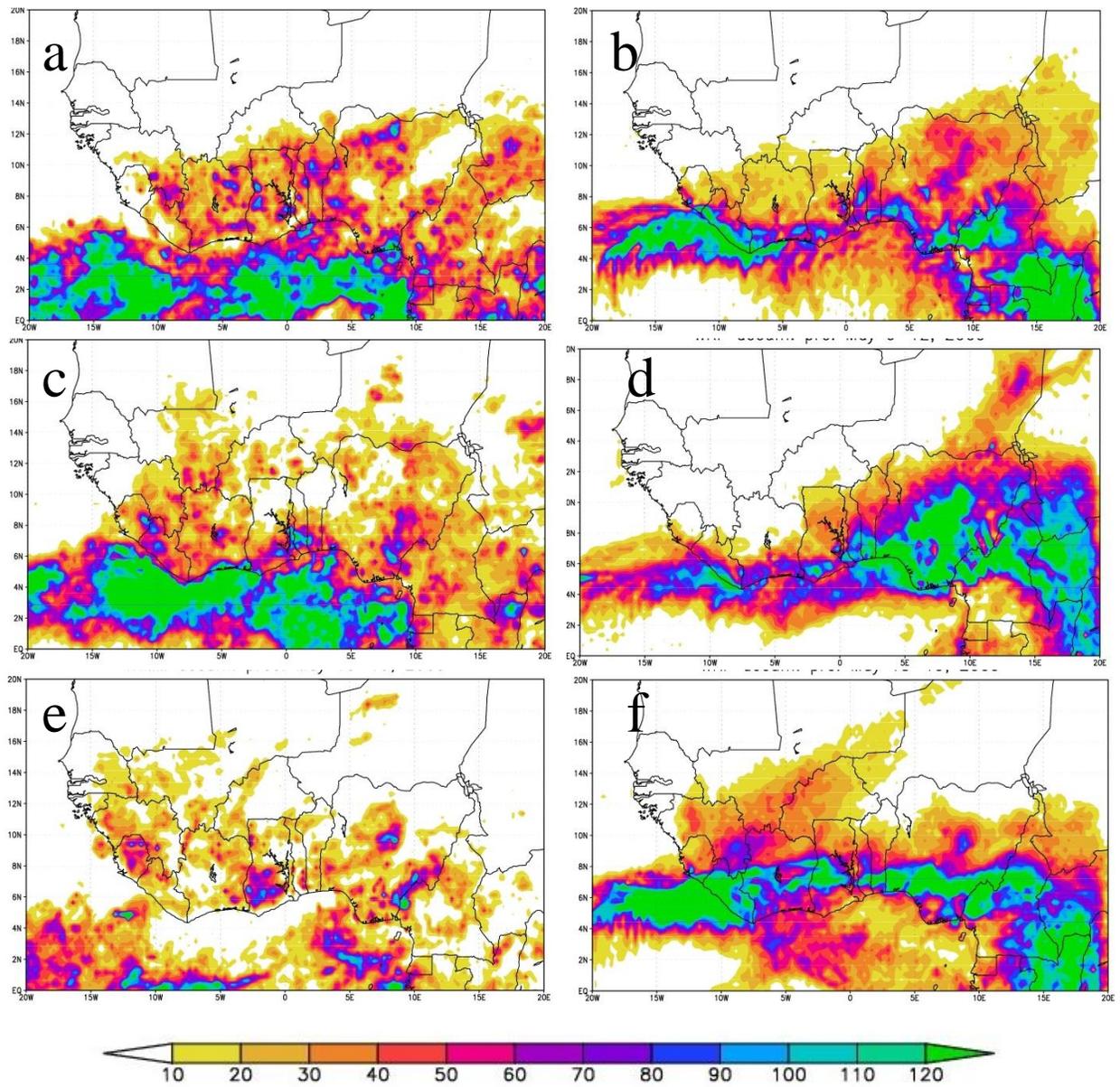


Figure 6.8: Accumulated precipitation during April 29 – May 5, May 6-12, May 13-19. TRMM is shown in (a), (c) and (e) while WRF is shown in (b), (d) and (f) for the dates shown.

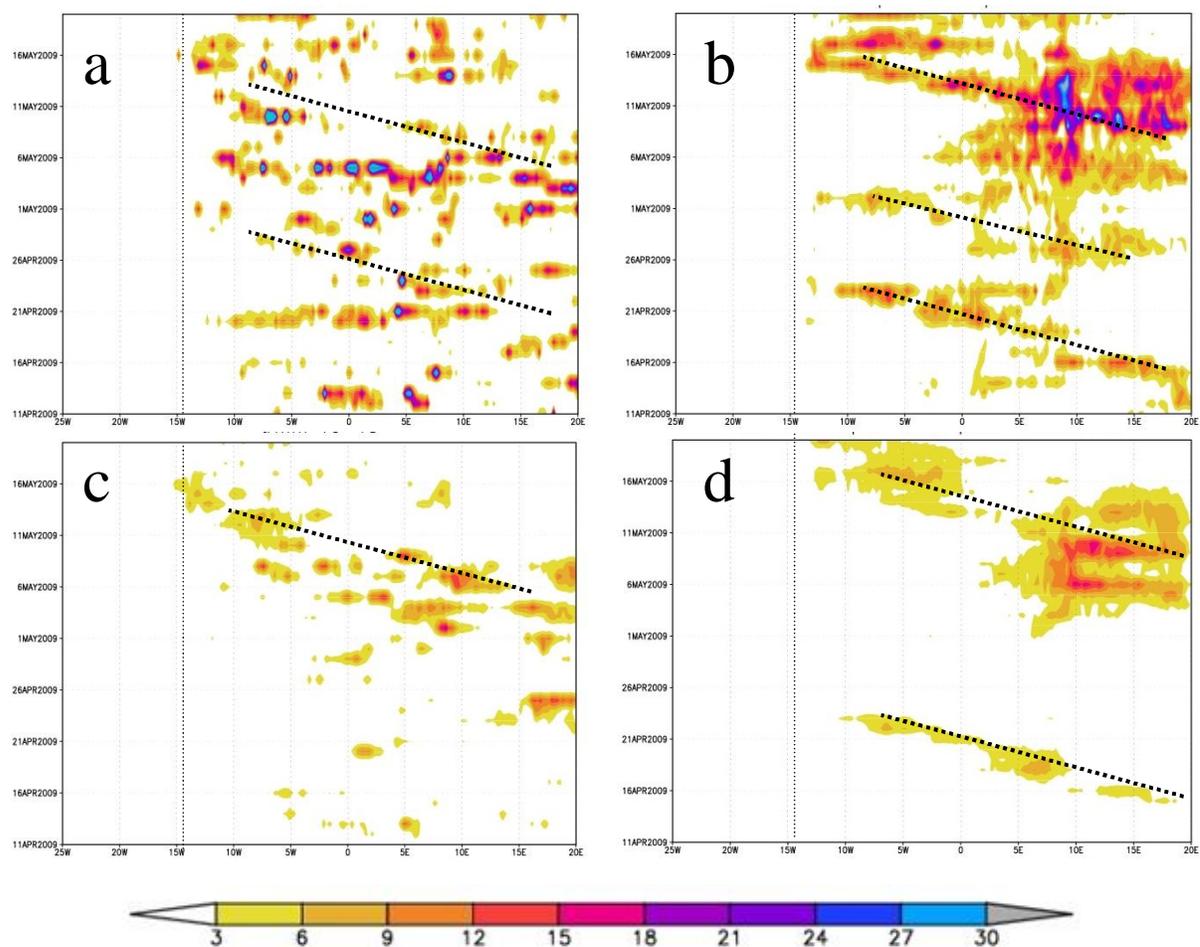


Figure 6.9: Time longitude Hovmoller diagram of accumulated precipitation during April 11 – May 20 for 20°W-20°E for all points spanning 25°W-20°E. Points along 10N are shown for (a) TRMM and (b) WRF and for 10-15N average for (c) TRMM and (d) WRF. Vertical line denotes approximate location of the coast of West Africa

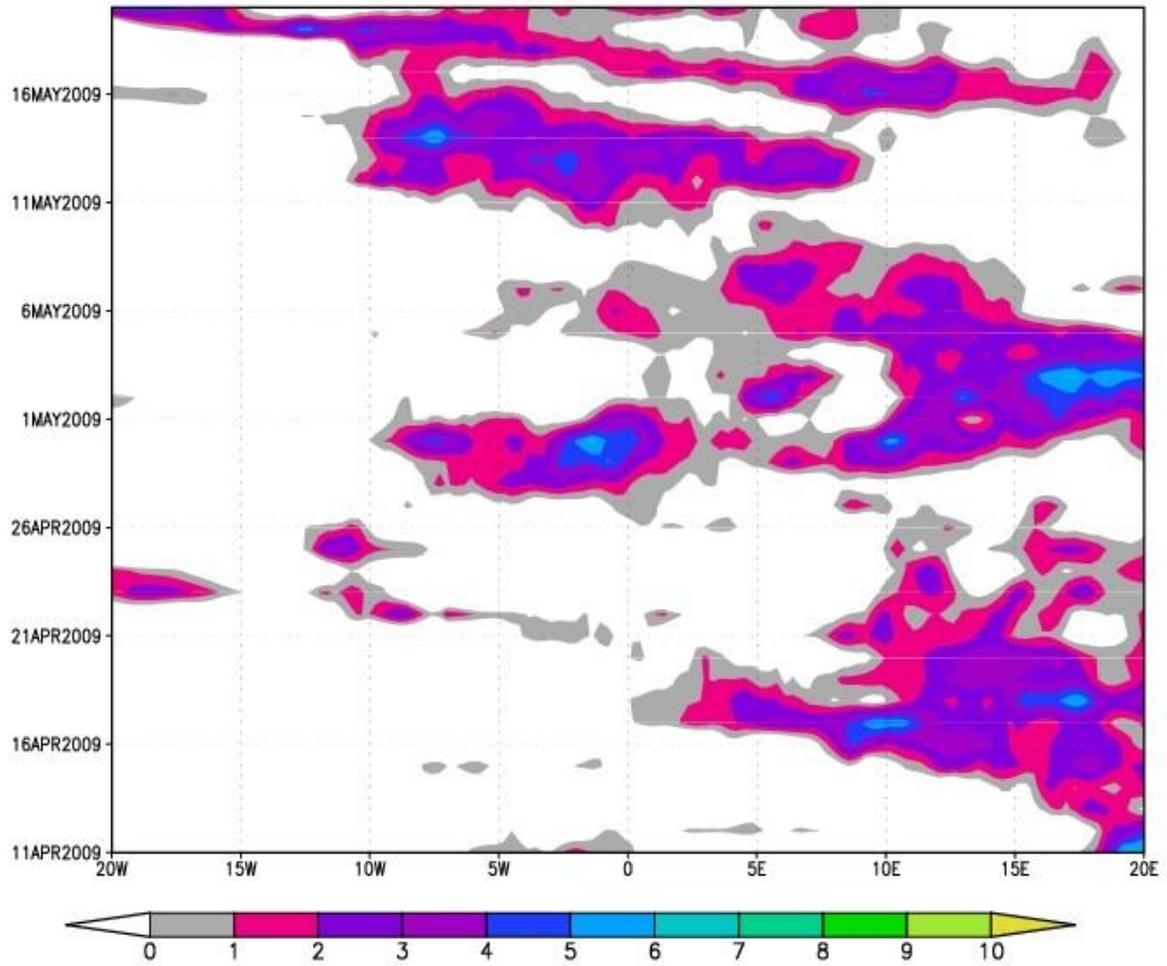


Figure 6.10: Time-longitude Hovmoller meridional wind (m s⁻¹) in the WRF inner domain for April 11 – May 20 2009 averaged for all points between 10N and 15N.

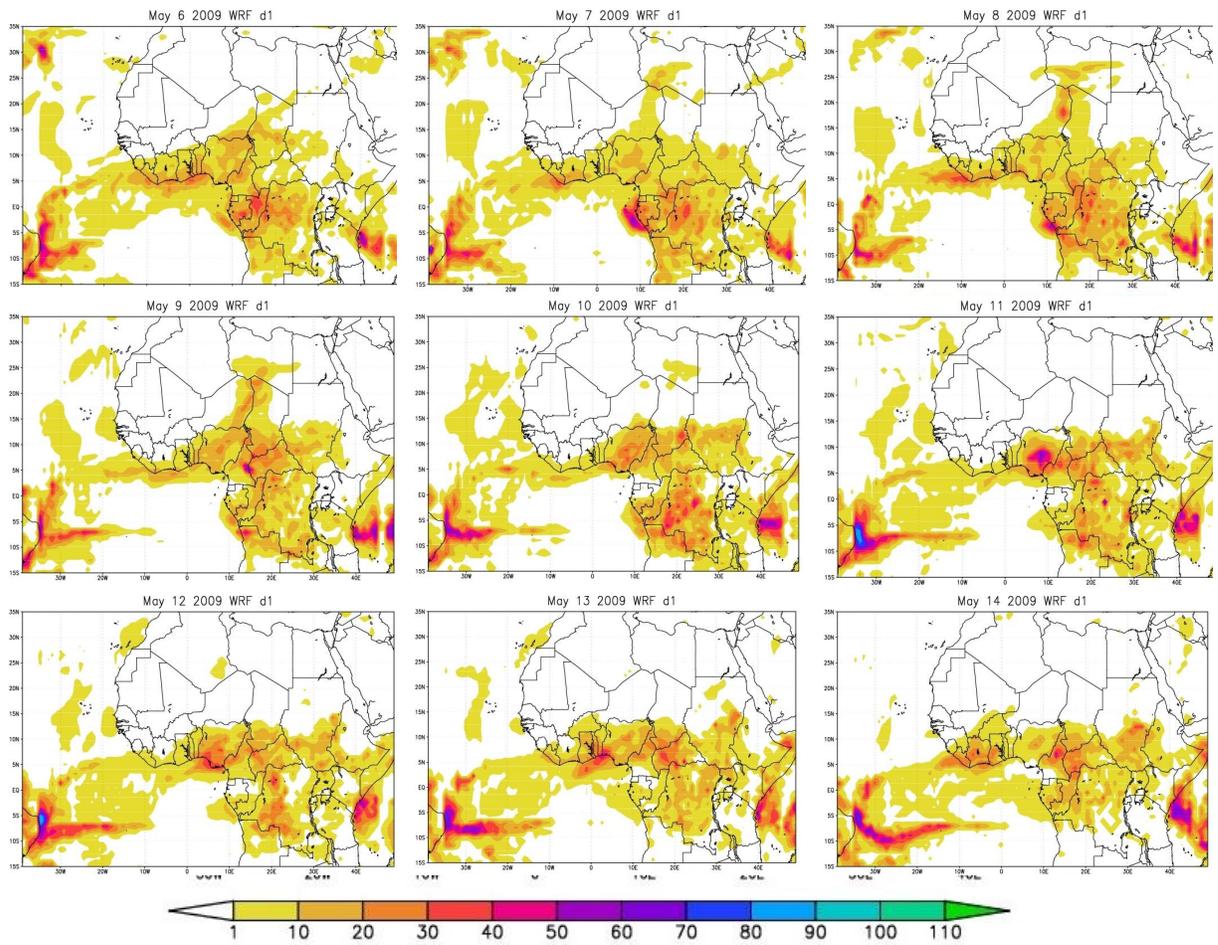


Figure 6.11: Sequence of accumulated precipitation (mm) from the WRF simulation. Dates are from May 6 to May 14 and are shown at the top of each figure. This vantage point shows the delayed progression of the TD1 event within the MME.

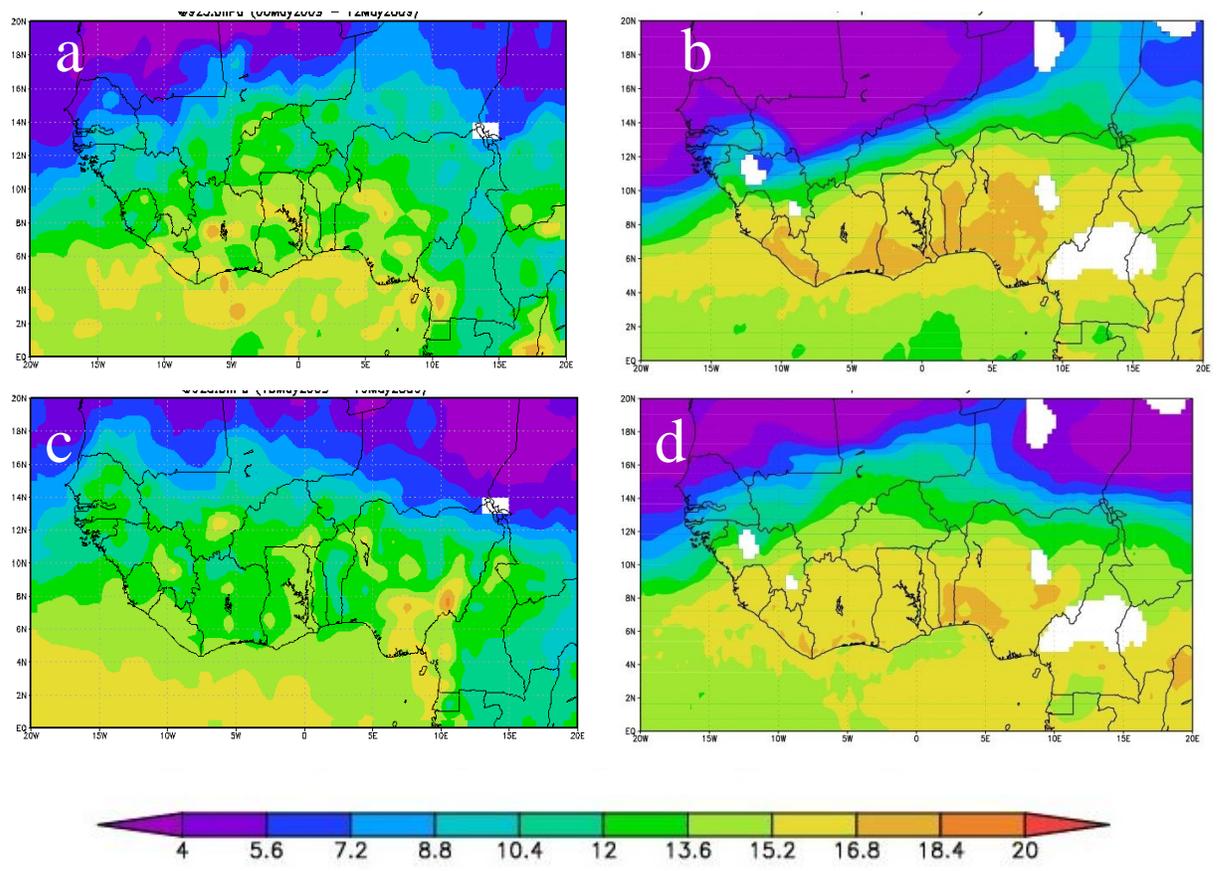


Figure 6.12: 925 hPa mixing ratio from (a) AIRS satellite for May 6-12 at 1330 UTC and WRF at 1200 UTC (b), AIRS for 1330 UTC May 13-19 (c) and WRF at 1200 UTC (d).

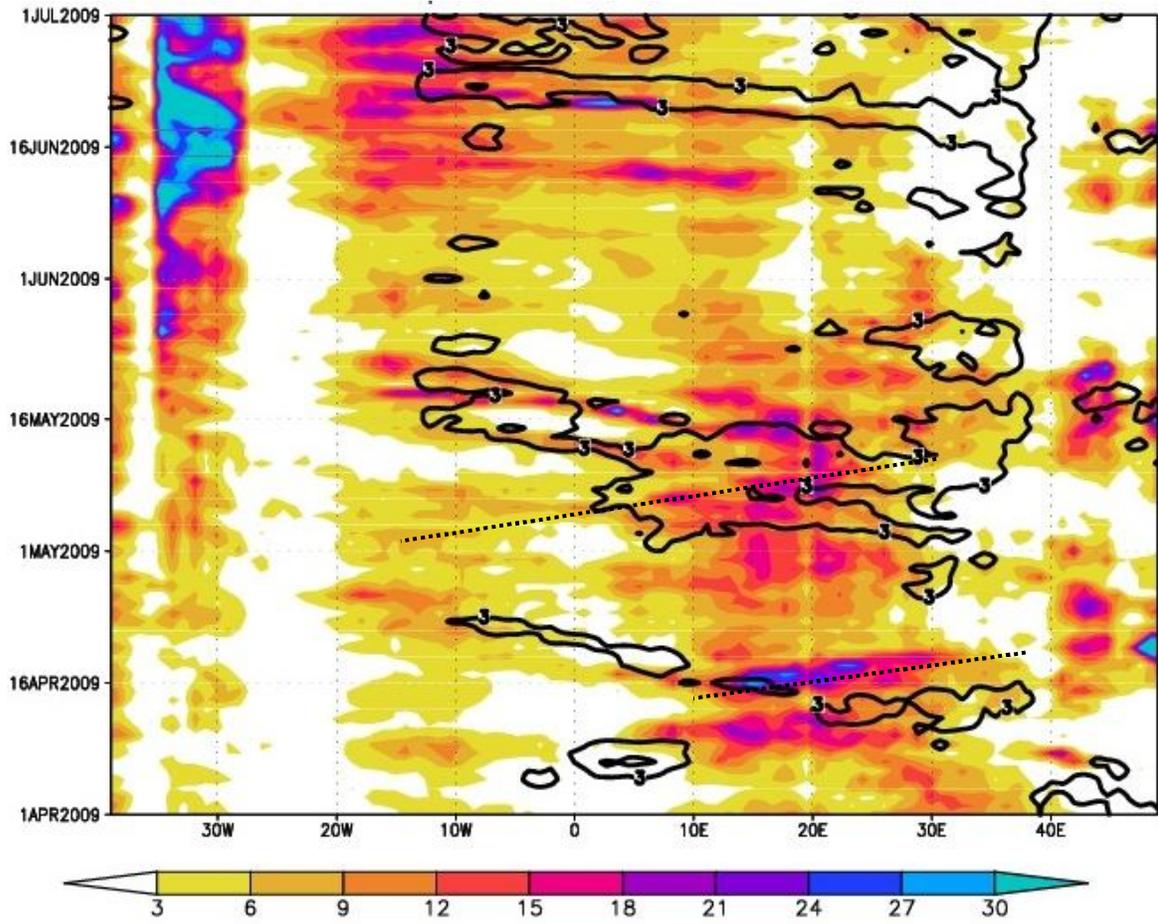


Figure 6.13: Time longitude Hovmoller diagram of accumulated precipitation in the outer domain averaged for points between 2.5S and 7.5N (shaded) and 10N-15N (contour). The domain spans longitudes 239W-49E.

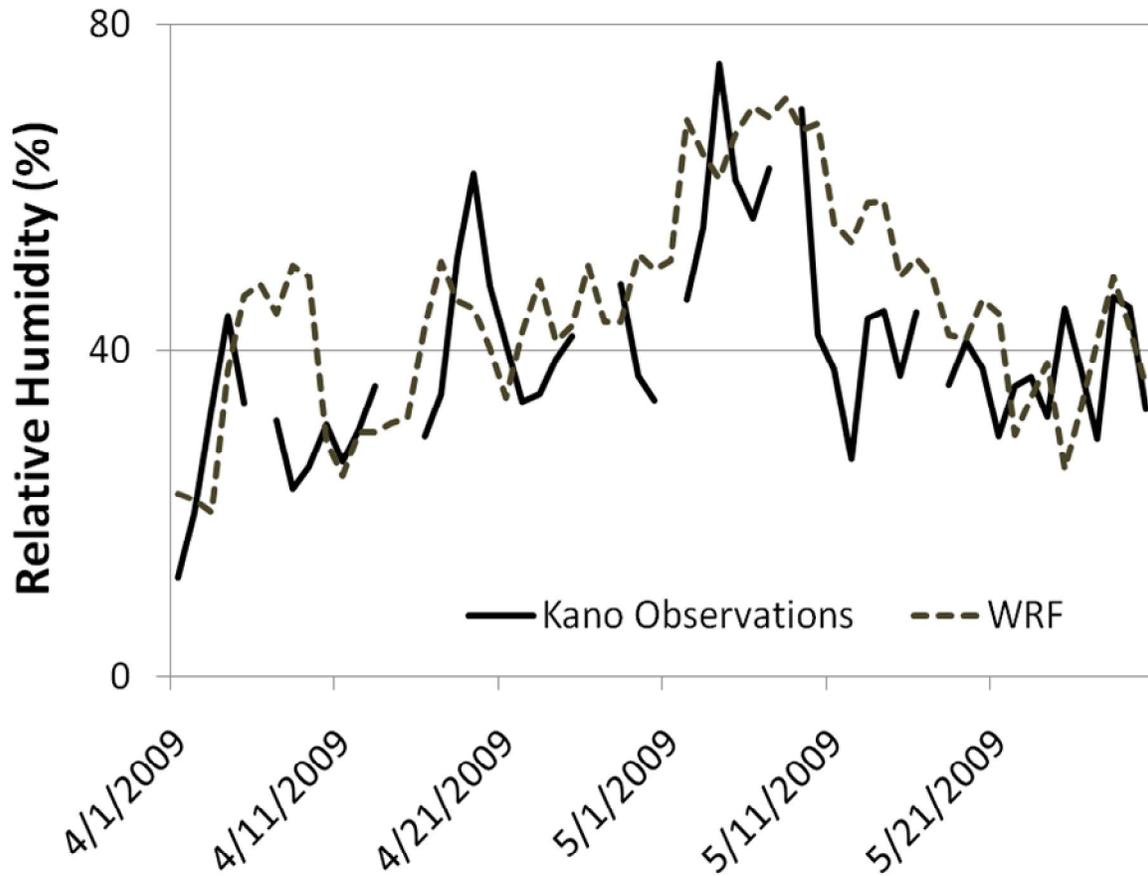


Figure 6.14: Time series of observed relative humidity (%) at Kano, Nigeria (solid) and area average of WRF output over the region (dash). The period shown is April 1 – May 30 2009.

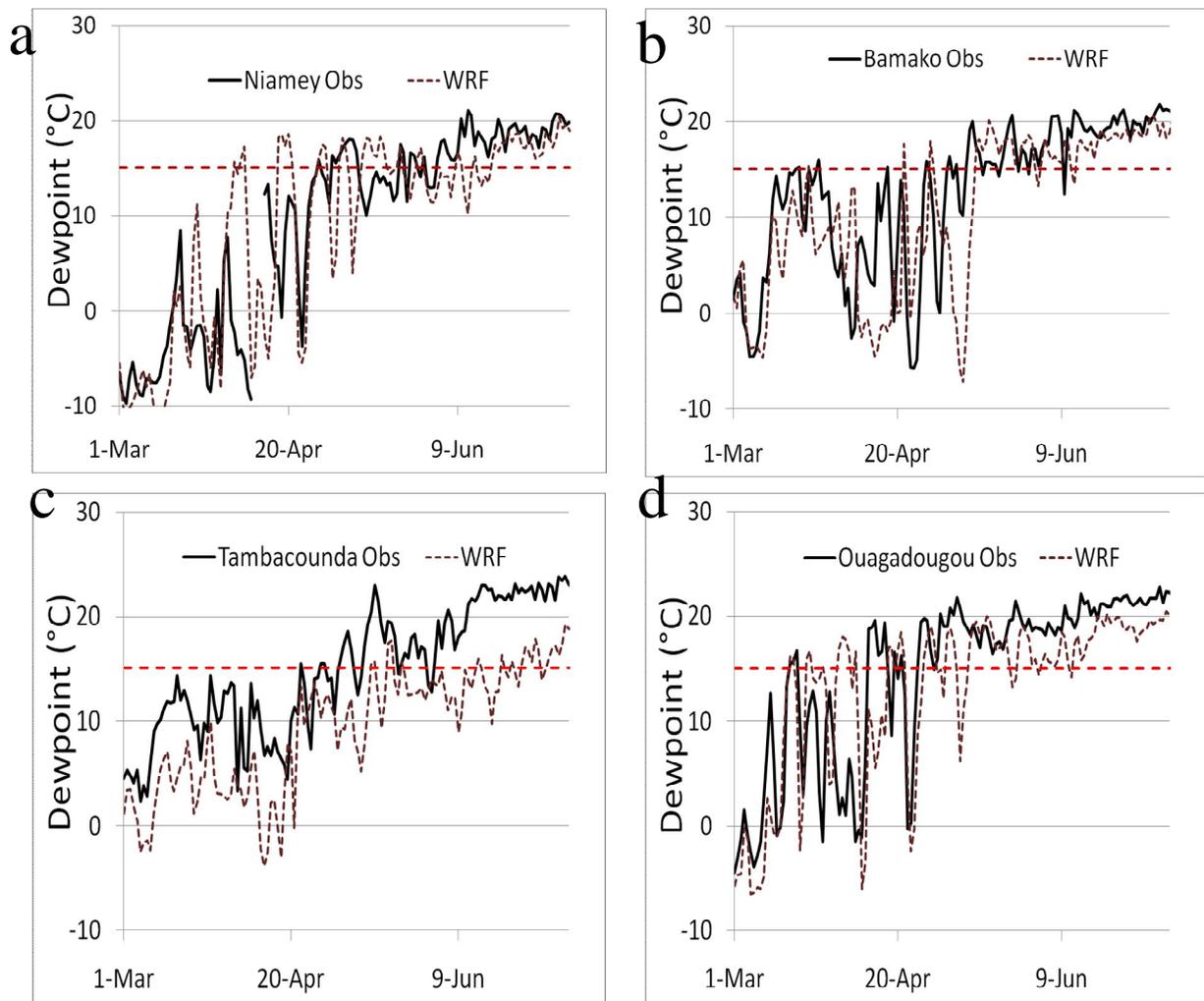


Figure 6.15: Time series of dewpoint temperature ($^{\circ}\text{C}$) for observed (solid) and WRF-simulated (dotted) for (a) Niamey, (b) Bamako, (c) Tambacounda and (d) Ouagadougou. Dashed red line denotes 15°C isoline for the ITD.

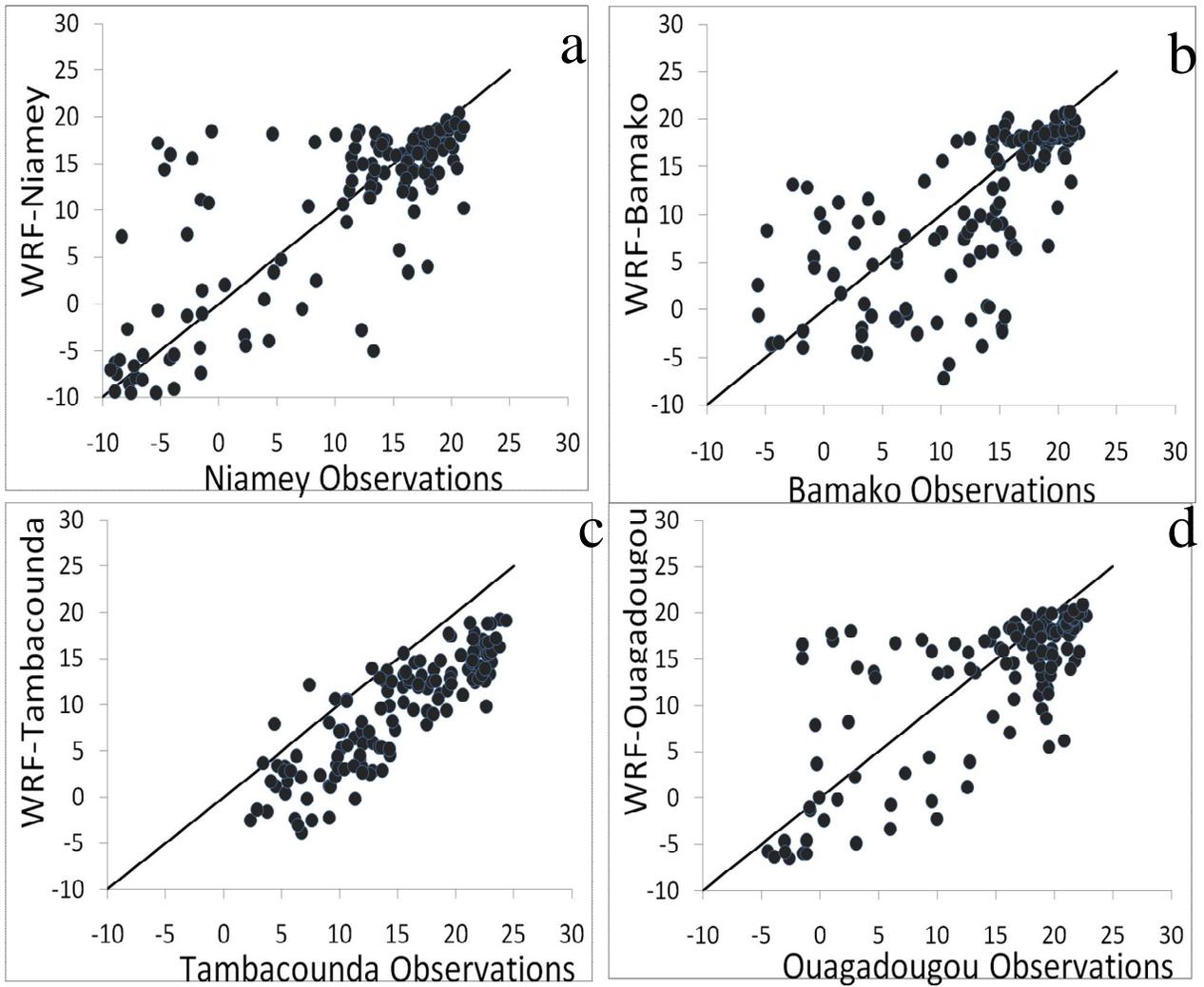


Figure 6.16: Scatter plots for WRF-derived dewpoint temperature versus observed for (a) Niamey, (b) Bamako, (c) Tambacounda and (d) Ouagadougou.

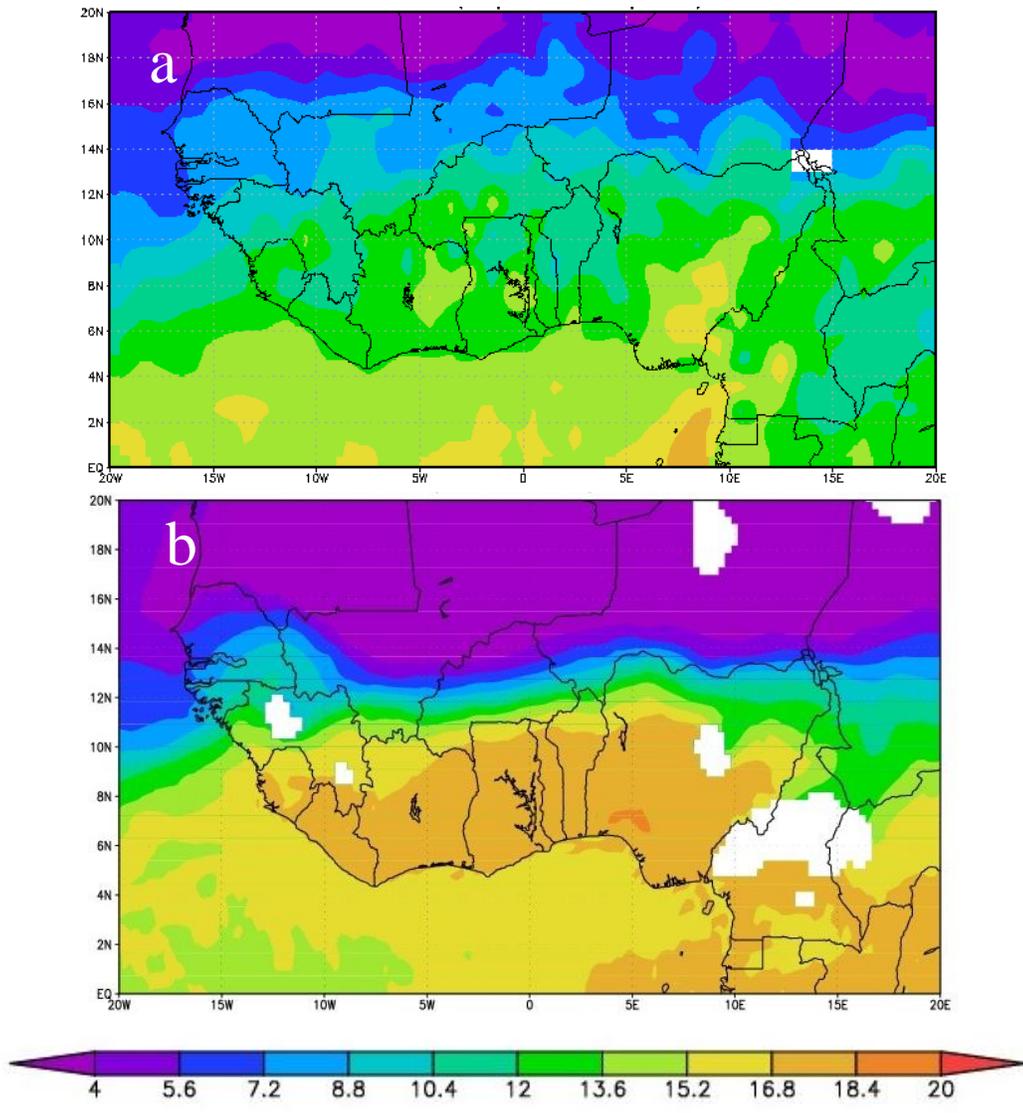


Figure 6.17: Mixing ratio at 925 hPa for April 15-22, 2009 for (a) AIRS 1330 UTC and (b) WRF 1200 UTC.

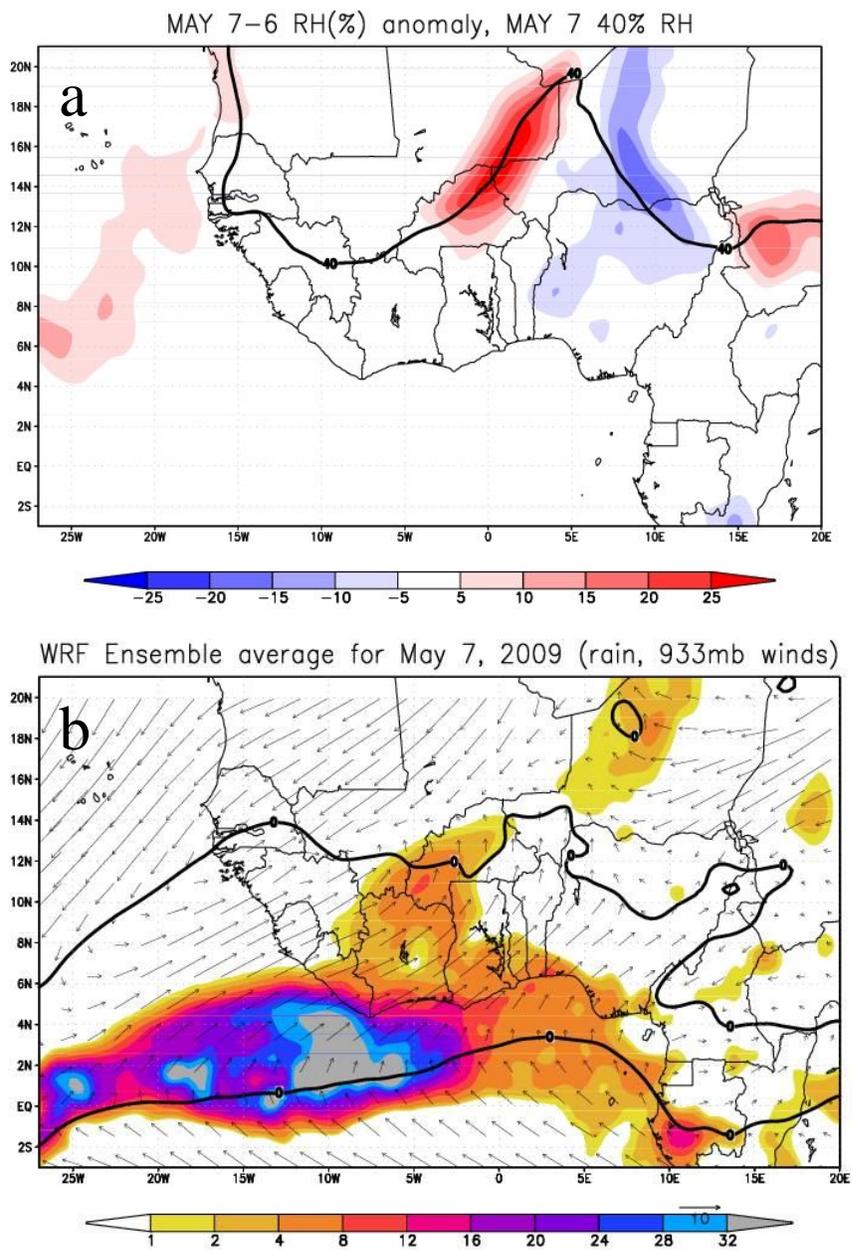


Figure 6.18: Forecasted westward-propagated event during May 7, 2009. (a) Change in RH (% , shaded) and 40% line (contour). (b) Daily accumulated precipitation and 933 hPa winds. Contour delineates the ITF.

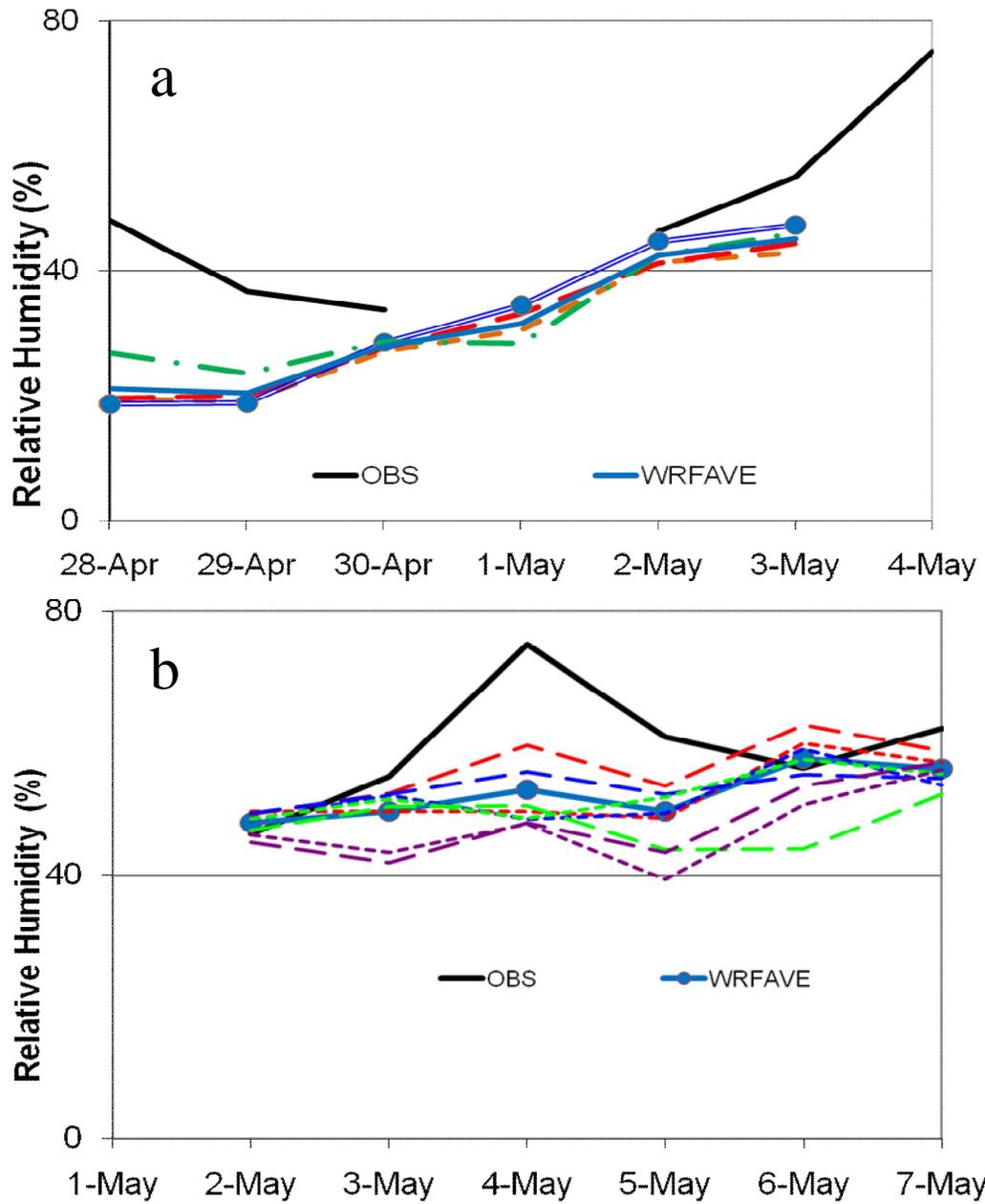


Figure 6.19: Time series of observed (solid) relative humidity (%) at Kano and area average of model output for WRF ensemble average (blue circles) for (a) April 28 – May 4 and (b) May 1–7. Unlabeled contours are individual ensemble members.

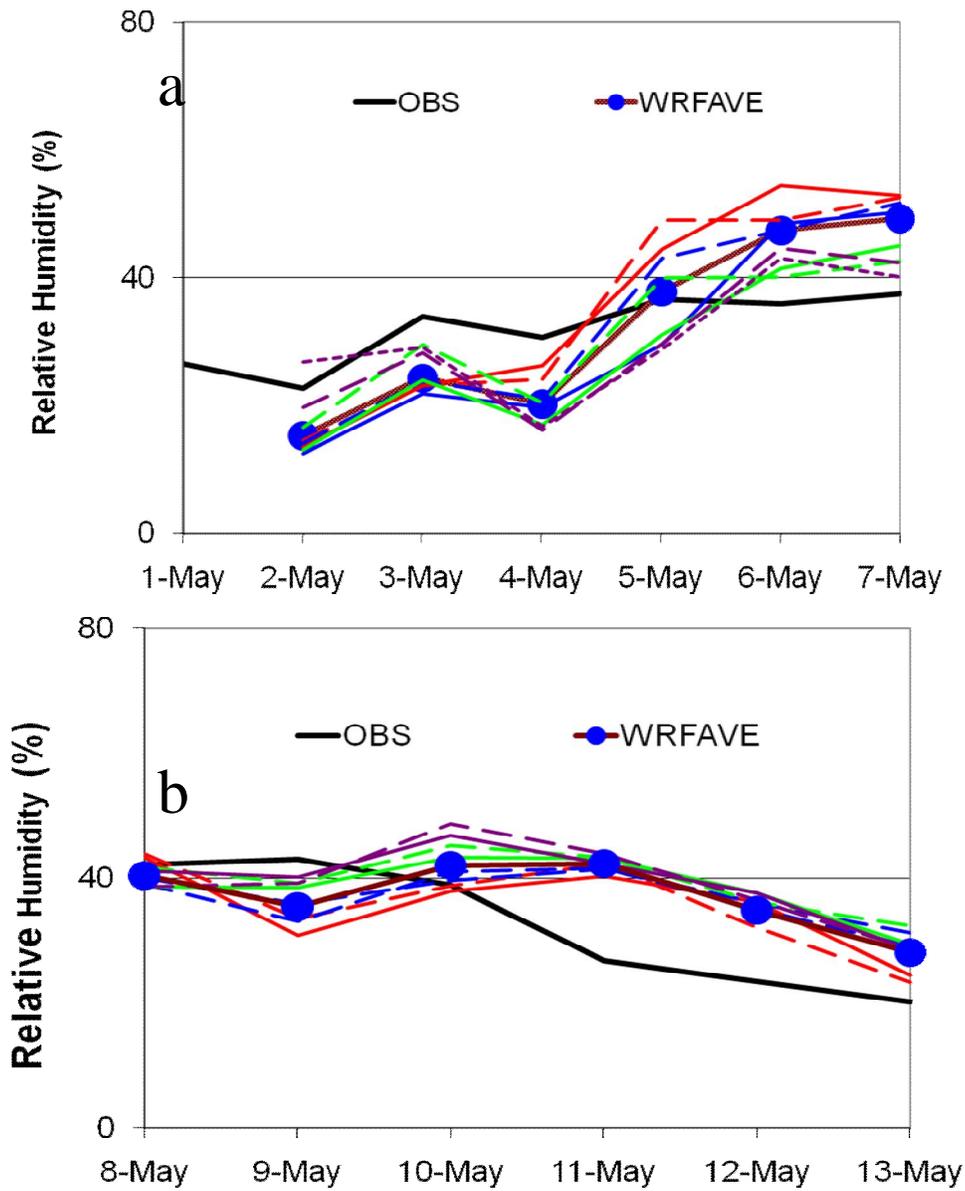


Figure 6.20: Time series of observed (solid) relative humidity (%) at Niamey and area average of model output for WRF ensemble average (blue circles) for (a) May 1-7 (b) May 8-13. Unlabeled contours are individual ensemble members.

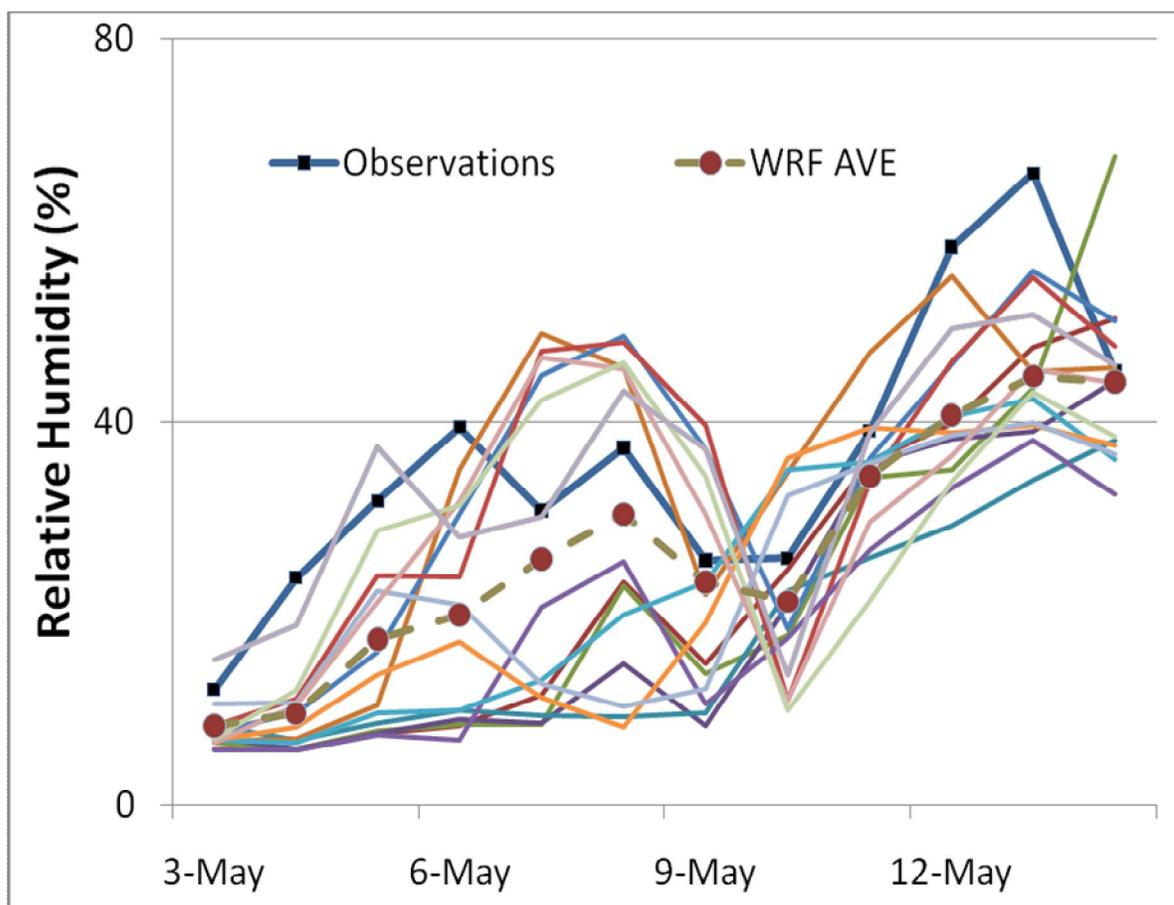


Figure 6.21: Time series of observed (solid, black squares) relative humidity (%) at Bamako and area average of model output for WRF ensemble average (tan, burgundy circles) for May 3-16. Unlabeled contours are individual ensemble members.

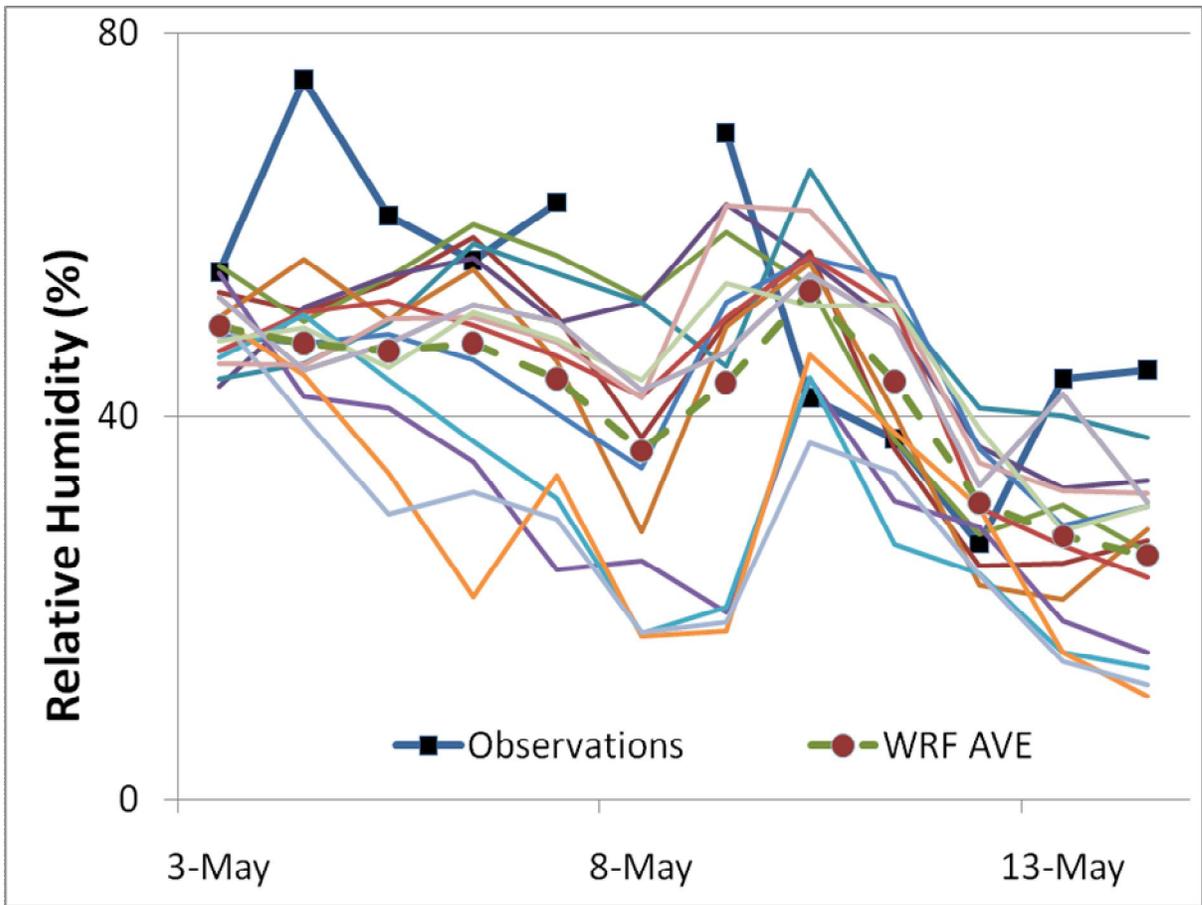


Figure 6.22: Time series of observed (solid, black squares) relative humidity (%) at Kano and area average of model output for WRF ensemble average (tan, burgundy circles) for May 3-16. Unlabeled contours are individual ensemble members.

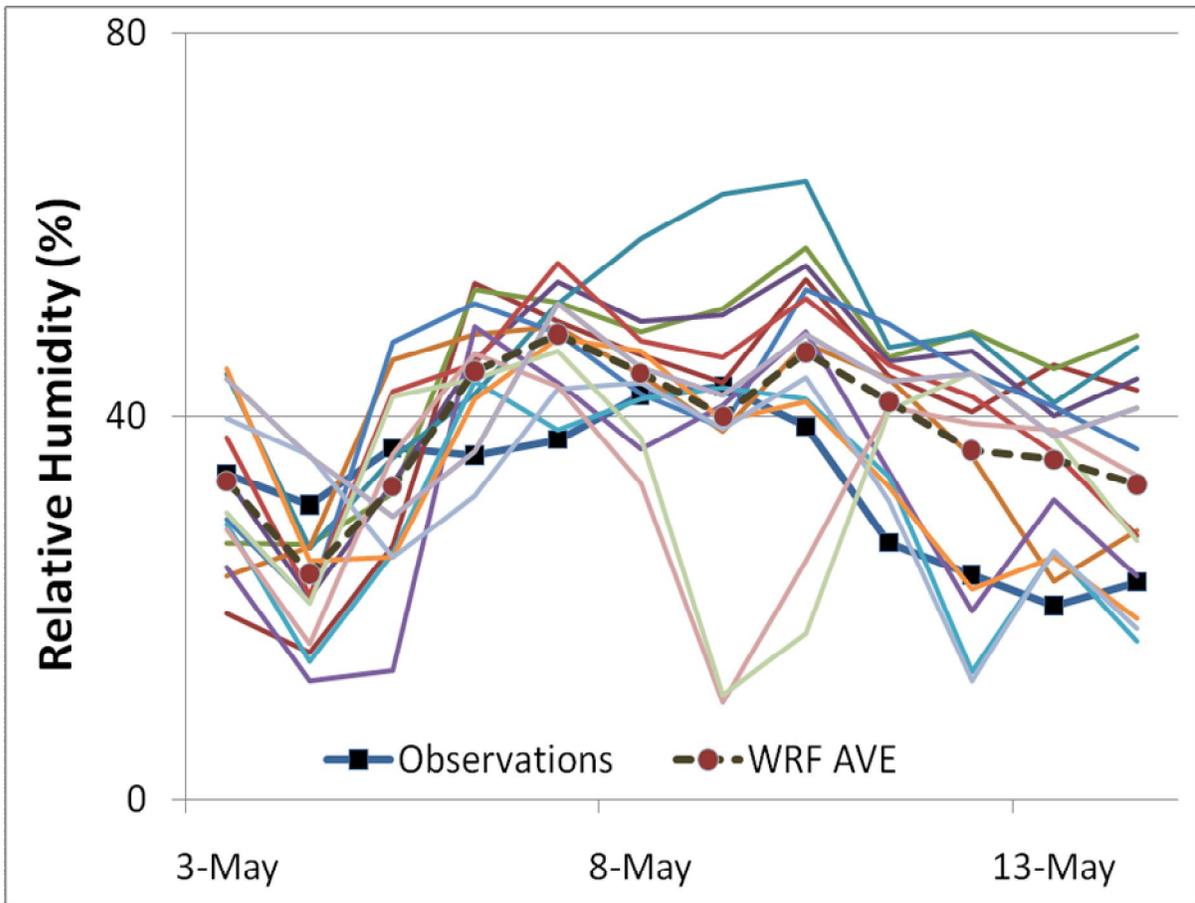


Figure 6.23: Time series of observed (solid, black squares) relative humidity (%) at Niamey and area average of model output for WRF ensemble average (tan, burgundy circles) for May 3-16. Unlabeled contours are individual ensemble members.

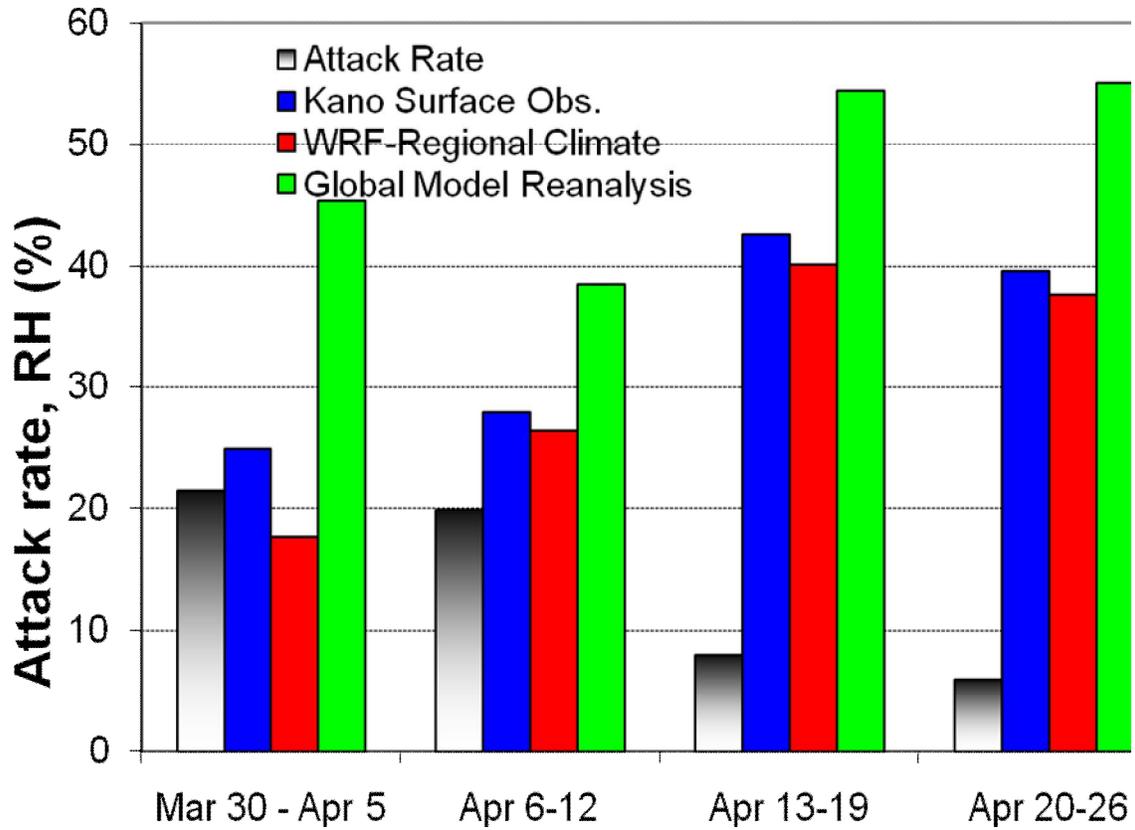


Figure 6.24: Time series showing attack rates (black/white), observed RH (blue), WRF-simulated RH (red) and NCEP/NCAR reanalysis RH (green) during March-April 2009.

Chapter 7

An Extended Procedure for

Implementing the Relative Operating

Characteristic Graphical Method

7.1 Introduction

Climate and weather forecasts are currently being considered as tools in the West Africa Google.org/UCAR meningitis project (Pandya et al. 2009) given the robust link between moisture and meningitis incidences (Molesworth et al., 2003). Short-term forecasts, in particular, have been targeted to minimize meningitis incidence by providing 1-14 day weather forecasts to target dissemination of scarce vaccine. During the 2009 boreal spring, numerous ensemble real-time forecasts simulations were carried out over the region to test

the Weather Research and Forecasting (WRF) model's performance. This real-time ensemble dataset as well as the distinctive application at hand (meningitis mitigation) serves as a source of motivation for the development of a new skill measurement technique that takes into account a given end-user's specific needs.

The relative (or receiver) operating characteristic (ROC) graphical method is widely used for estimating the skill of ensemble prediction systems (EPS) in climate and weather forecasting (Marzban 2004). However, the traditional procedure for its implementation suffers from a major limitation because it does not distinguish among different end-user applications. Although considerably more cumbersome to implement, the economic value (EV) graphical method is increasingly becoming an attractive option because of its ability to provide a measure of the EPS performance for a specific hypothetical end user (Richardson 2000a,b). Several studies have discussed the relationship between the ROC and the EV graphical methods (Mylne 1999; Richardson 2000b, 2001; Zhu et al. 2002). The ROC and EV methods are related through the hit and false alarm rates, thus raising the possibility of the existence of an explicit functional relationship between them. In this study we search for this relationship in order to develop a hybrid procedure that exploits both the ROC and EV methods. Our goal is to retain the basic characteristics of the traditional ROC method because of its appealing simplicity while also exploiting the ability of the EV method to provide user-specific model evaluation.

In the rest of Section 5.1 we review the main attributes of the traditional ROC and the EV graphical methods. Section 5.2 describes the EROC procedure and its relationship with the traditional ROC method. In Section 5.3 we apply the EROC method to obtain the useable skill for seasonal hindcasts for 2006 and real-time forecasts during 2009. Conclusions are presented in Section 5.4.

7.1.1 Traditional ROC graphical method

The ROC graphical method is extensively used in many disciplines, including the geosciences (Harvey et al. 1992), clinical epidemiology (Walter and Irwig 1988), clinical neurophysiology (Laman et al. 2005), nuclear medicine (McNeil and Adelstein 1976), radiology (Hanley and McNeil 1982, 1983), biomedical engineering (Jalihal and Nolte 1994), and psychology (Swets 1973; Swets and Pickett 1982). It has been used in meteorology for more than two decades (Mason 1982; Stanski et al. 1989; Harvey et al. 1992). The characteristics and merits of the ROC have been extensively discussed in literature (Wilks 2006; Buizza and Palmer 1998; Buizza et al. 1998; Mason and Graham 2002; Juras 2000; Wilson 2000; Kheshgi and White 2001; Kharin and Zwiers 2003; Marzban 2004; and many others). The World Meteorological Organization (1992) has recommended the ROC graphical method as one of the standards for model verification. Hamill and Juras (2006) have recently shown that simple averaging over a subset of model grid points, with significant differences in the observed average frequency of the relevant climate anomaly

event, may result in fictitiously high ROC skill even when there is negligible corresponding skill at the individual grid points. This and other interpretative advances over the years have resulted in the comprehensive understanding of the usefulness and limitations of the ROC method in meteorology (Wilks 2006).

The basic information required for the traditional implementation of the ROC graphical procedure in meteorology consists of the end-user definition of the relevant climate anomaly event E , historical record of the prediction of E by the EPS, and the corresponding observational record of the occurrence of E . We assume that E is forecast to occur if the forecast probability of the EPS exceeds some threshold, that is, of $p > p_t$ (and is forecast not to occur if $p < p_t$), where p is defined as probability given by the ratio (n/N) and n is the number of the runs in the ensemble for which E actually occurs and N is the size of the ensemble, and where p_t is defined as Threshold of p above which the event is forecast to occur. The basis of ROC can be further analyzed by looking at its components in 2x2 tabular format of the forecast-model contingency matrix (Table 7.1). The contingency matrix provides four important parameters: α , β , γ , δ , and we can define our hit rate H and false alarm F ratios:

$$H_{p_t} = \delta / (\beta + \delta), \quad (7.1)$$

where H_{p_t} is the ratio of correct forecasts δ against the total occurrences of $E = (\beta + \delta)$, and β represent errant forecasts. Similarly, we also present:

$$F_{p_t} = \gamma / (\alpha + \gamma), \quad (7.2)$$

where F_{pt} is defined as the ratio of incorrect forecasts γ against the total number of non-occurrences of $E = (\alpha + \gamma)$ and α represents a correct forecast for no E to occur. Within the ROC graphical method, each pt has a corresponding H_{pt} and F_{pt} that form the curve within the interval $[0,1]$ that is used to determine the amount of skill a given EPS has. The curve is then used to represent an area bounded by $(H_{pt}, F_{pt}, \text{solid line})$ against the diagonal $H=F$ (dashed) as seen on Fig. 7.1. This area is then used to calculate the skill using the standard skill score (Wilks 2006) or the ROC area-based skill score (ROCS; Richardson 2000a). We will derive the equations that generate the skill score in the last section of this study.

7.1.2 The EV Graphical Method

Use of EV was first introduced to the meteorological community as a graphical verification tool by Richardson (2000a,b), and it is therefore relatively more recent than the ROC method. In addition to the information required for implementing the ROC graphical method, the hypothetical end user provides information for two additional parameters L , the loss incurred if no action is taken but E occurs, and C , the cost of taking action based on the model prediction that E would occur (Palmer et al. 2000). The EV cost–loss decision problem therefore relates to a hypothetical decision maker for whom an adverse climate anomaly event may or may not occur. In assuming a binary mitigation strategy this approach therefore could result in some oversimplification of the actual situation for many users because in reality they may have an infinite range of available mitigation options. Despite

this simplicity, the economic value problem can nevertheless reasonably approximate some simple real-world decision problems (Roebber and Bosart 1996; Wilks 2006), and also serve a useful purpose for evaluating ensemble prediction systems.

The C and L variables can be further explored by enhancing our contingency matrix (Table 2) and developing a User Expense Matrix (UEM). Within the UEM, L is the loss suffered by the occurrence of E and C is the cost incurred by the user's preventive actions. Note that this C is present for all instances in which the EPS has forecasted E since the user has taken the EPS information to prepare for E. We can now represent the expected expense using the variables in table 2 with the following equation:

$$M = \frac{\beta L + C(\gamma + \delta)}{L} \quad (7.3)$$

The user-expected mean (M) is thus defined as the total number of events missed multiplied by the incurred loss (βL), added to the total cost of taking action ($C(\gamma + \delta)$), the sum of which is divided by the total loss (L) due to E .

From the relationships created by Eq. (7.3), we can develop and derive further associations among the variables presented in the tables. Over the course of time, the climatological occurrence of the event becomes:

$$\beta + \delta = \bar{o}, \quad (7.4)$$

where \bar{o} is defined as the climatology for all occurrences of E including hits and misses by the EPS. The definition of \bar{o} also allows us to derive further identities:

$$\beta = \bar{o} - \delta \quad (7.5)$$

$$\alpha + \gamma = 1 - \bar{o} \quad (7.6)$$

In Eq. (7.5) we define β as the difference between climatology \bar{o} and correct prediction and occurrence δ of E . For Eq. (7.6) to be true, the number of events has to be sufficiently large, and this enables the end user to make informed decisions concerning impending expenses.

Using Eq. (7.1) and Eq. (7.4) we find that:

$$H_{p_t} = \delta / \bar{o}$$

so that, when multiplying both sides by \bar{o} , we get:

$$\delta = H_{p_t} \bar{o} \quad (7.7)$$

We can now see that the cost of E occurring is equal to the climatology multiplied by the hit rate (H). Similarly, employing Eq. (7.2) and the identity in Eq. (7.6), we find that:

$$F_{p_t} = \gamma / (1 - \bar{o})$$

so that, when variables are rearranged, we arrive at the following formula:

$$\gamma = F_{p_t} (1 - \bar{o}) \quad (7.8)$$

Similar to (7.7), this identity allows us to gauge the interconnection between F and climatology.

Using equations (7.5) and (7.7) and substituting δ with $H_{p_t} \bar{o}$, we find:

$$\beta = \bar{o} - H_{p_t} \bar{o}, \quad (7.9)$$

which allows us to represent β as the hit rate-climatology relationship subtracted from climatology itself in order to analyze the losses due to errant forecasts relative to the climatology. Now that we have derived all variables in terms of their relationship with the average frequency of the event, \bar{o} , we rewrite (7.3) as:

$$M = \frac{(\bar{o} - \bar{o}H_{p_t})L}{L} + \frac{C(F_{p_t}(1 - \bar{o}) + \bar{o}H_{p_t})}{L},$$

where the L s cancel out and the Equation (reduces to

$$M = \bar{o} - \bar{o}H_{p_t} + \frac{C}{L}(F_{p_t}(1 - \bar{o}) + \bar{o}H_{p_t})$$

The C/L derived above now represents a hypothetical user for which there is a particular cost-loss ratio that they are willing to work with when utilizing EPS forecasts. Redistributing the C/L we get:

$$M = \bar{o} - \bar{o}H_{p_t} + \frac{C}{L}F_{p_t}(1 - \bar{o}) + \frac{C}{L}(\bar{o}H_{p_t}).$$

Rearranging the Equation (we have:

$$M = \frac{C}{L}F_{p_t}(1 - \bar{o}) + \frac{C}{L}H_{p_t}\bar{o} - \bar{o}H_{p_t} + \bar{o}$$

Grouping the $H_{p_t}\bar{o}$ terms together, the Equation (reduces to:

$$M = F_{p_t} \frac{C}{L} (1 - \bar{o}) + H_{p_t} \bar{o} \left(\frac{C}{L} - 1 \right) + \bar{o} ,$$

which becomes:

$$M = F_{p_t} \frac{C}{L} (1 - \bar{o}) - H_{p_t} \bar{o} \left(1 - \frac{C}{L} \right) + \bar{o} \quad (7.10)$$

Equation (7.10) above is related to Zhu et al (2002)'s Equation (7.5) and Richardson (2000a)'s Equation (7.7). Substituting μ for C/L we can rewrite our Equation (as follows:

$$M_{forecast} = F_{p_t} \mu (1 - \bar{o}) - H_{p_t} \bar{o} (1 - \mu) + \bar{o} \quad (7.11)$$

This is Equation (7.4) in Semazzi and Mera (2006) and defines the value of an EPS for a range of mitigation options (or users) μ . One special case of the M Equation (includes the perfect forecast, where $H_{p_t} = 1$ and $F_{p_t} = 0$. Thus, (7.11) becomes:

$$M = (0)\mu(1 - \bar{o}) - (1)\bar{o}(1 - \mu) + \bar{o}$$

and reduces to

$$M = -\bar{o}(1 - \mu) + \bar{o} .$$

Redistributing terms we get:

$$M = -\bar{o}(1 - \mu + 1) ,$$

which further reduces to:

$$M = -\bar{o}(-\mu)$$

Multiplying terms:

$$M_{perfect} = \bar{o}\mu \quad (7.12)$$

The value for a perfect forecast in Zhu et al. (2002) and references therein is represented in Eq. (7.12). Another special case for Eq. (7.11) occurs when we define the value for climatology so that M has two possible outcomes: One is $H = 0$ and $F = 0$, when the user never takes action and the other occurs when $H = F = 1$. When $H = F = 0$ we get:

$$M = (0)\mu(1 - \bar{o}) - (0)\bar{o}(1 - \mu) + \bar{o} ,$$

which reduces to

$$M_{cli} = \bar{o} . \quad (7.13)$$

In the case where $H = F = 1$, we get:

$$M = (1)\mu(1 - \bar{o}) - (1)\bar{o}(1 - \mu) + \bar{o} ,$$

which reduces to:

$$M = \mu(1 - \bar{o}) + \mu\bar{o} .$$

Redistributing, we get:

$$M = \mu - \mu\bar{o} + \mu\bar{o} ,$$

which reduces to:

$$M_{cli} = \mu \quad (7.14)$$

Thus, we have arrived at two possible outcomes of M_{cli} , which is defined by the hypothetical user. We now have the ability to define the value of an EPS forecast for a hypothetical user by utilizing the following formula:

$$V = \frac{M_{c\ lim\ ato\ log\ y} - M_{forecast}}{M_{c\ lim\ ato\ log\ y} - M_{perfect}}, \quad (7.15)$$

as defined by Richardson (2000a), Semazzi and Mera (2006) and Zhu et al. (2002). This formula can be employed for every point in the ROC graph. That is, every H_{p_i} and F_{p_i} has a corresponding value curve on the EV plot and, using Eq. (7.15) and combining it with (7.11), (7.12), (7.13) and (7.14) we define specific V_{p_i} for every H and F on the ROC figure:

$$V_{p_i} = \frac{\min(\mu, \bar{o}) - F_{p_i} \mu(1 - \bar{o}) + H_{p_i} \bar{o}(1 - \mu) - \bar{o}}{\min(\mu, \bar{o}) - \bar{o} \mu} \quad (7.16)$$

The $\min(\mu, \bar{o})$ can thus be defined as the user-determined climatology. The envelope curve may be obtained by plotting V against μ for discrete values of p_i appropriately covering the possible range of 0–1. Palmer et al. (2000) have shown that the end user with $\mu = \bar{o}$ should expect the maximum value $V = V_{max}$. This relationship allows us to construct EV (Fig. 7.2). Figure 7.3 schematically displays the main steps and considerations involved in the implementation of the ROC and EV graphical procedures and their relationship to the proposed extended ROC (EROC) method, which is introduced in Section 5.2.

7.2 EROC Procedure

Based on the ROC skill alone it is impossible to determine if a useful level of skill has been achieved for a specific end user. The goal is to develop an alternative procedure similar to the traditional implementation of the ROC graphical method, but one that also provides evaluation for a specific end user.

7.2.1 Construction of generalized baselines

Using Equation (7.16) derived above, we recognize that the V will change for each μ and that, as thus, the baseline for a non-optimal user would shift from its position at $H = F$ (climatology). It is possible, for instance, that the user may require a minimum amount of value for an EPS in order to employ it for their purposes. Thus, we find that $V > V_{min}$ and we rewrite (7.16):

$$V_{p_t} = \frac{\min(\mu, \bar{o}) - F_{p_t} \mu(1 - \bar{o}) + H_{p_t} \bar{o}(1 - \mu) - \bar{o}}{\min(\mu, \bar{o}) - \bar{o} \mu} \geq V_{min} ,$$

so that

$$\frac{\min(\mu, \bar{o}) - F_{p_t} \mu(1 - \bar{o}) + H_{p_t} \bar{o}(1 - \mu) - \bar{o}}{\min(\mu, \bar{o}) - \bar{o} \mu} \geq V_{min} ,. \quad (7.17)$$

In order to construct our baselines so that it reflects the $H = F$ for climatology, we solve for H_{p_t} to find a functional Equation (that will define H in terms of F . Dividing (7.17) on both sides by $\min(\mu, \bar{o}) - \bar{o}\mu$, we arrive at:

$$\min(\mu, \bar{o}) - F_{p_t} \mu(1 - \bar{o}) + H_{p_t} \bar{o}(1 - \mu) - \bar{o} \geq V_{\min} \min(\mu, \bar{o}) - \bar{o}\mu .$$

Moving the first, second and fourth terms on the left hand side (l.h.s) to the right hand side (r.h.s) to isolate H_{p_t} , we get:

$$H_{p_t} \mu(1 - \bar{o}) \geq V_{\min} \min(\mu, \bar{o}) - \bar{o}\mu + F_{p_t} \mu(1 - \bar{o}) - \min(\mu, \bar{o}) + \bar{o} ,$$

and dividing both sides by $\bar{o}(1 - \mu)$ we get:

$$H_{p_t} \geq \frac{V_{\min} \min(\mu, \bar{o}) - \bar{o}\mu + F_{p_t} \mu(1 - \bar{o}) - \min(\mu, \bar{o}) + \bar{o}}{\bar{o}(1 - \mu)} . \quad (7.18)$$

With (7.18) we are able to create base lines based on functions derived from the user-defined V_{\min} and \bar{o} given the choices $\mu < \bar{o}$ or $\mu \geq \bar{o}$. If the user chooses $\mu < \bar{o}$, then $\min(\mu, \bar{o})$ reduces to μ , to reflect the fact that μ can only have a functional forecast when its minimum climatological value condition is met. Thus, (7.18) becomes:

$$H_{p_t} \geq \frac{V_{\min} \mu - \bar{o}\mu + F_{p_t} \mu(1 - \bar{o}) - \mu + \bar{o}}{\bar{o}(1 - \mu)} .$$

Rearranging terms, we get:

$$H_{p_t} \geq \frac{V_{\min} \mu - \bar{o} \mu - \mu + \bar{o}}{\bar{o}(1 - \mu)} + \frac{F_{p_t} \mu(1 - \bar{o})}{\bar{o}(1 - \mu)}$$

With further simplification, we factor the μ out of $\mu - \bar{o} \mu$:

$$H_{p_t} \geq \frac{V_{\min} \mu(1 - \bar{o}) - \mu + \bar{o}}{\bar{o}(1 - \mu)} + \frac{F_{p_t} \mu(1 - \bar{o})}{\bar{o}(1 - \mu)} \quad (7.19)$$

We will return to (7.19) after the following derivation. If the user decides that $\mu \geq \bar{o}$, we return to (7.18), where $\min(\mu, \bar{o}) = \bar{o}$ and the function becomes:

$$H_{p_t} \geq \frac{V_{\min} \bar{o} - \bar{o} \mu + F_{p_t} \mu(1 - \bar{o}) - \bar{o} + \bar{o}}{\bar{o}(1 - \mu)}$$

The function reduces to:

$$H_{p_t} \geq \frac{V_{\min} \bar{o} - \bar{o} \mu + F_{p_t} \mu(1 - \bar{o})}{\bar{o}(1 - \mu)}.$$

Factoring \bar{o} out of $\bar{o} - \bar{o} \mu$, we get:

$$H_{p_t} \geq \frac{V_{\min} \bar{o}(1 - \mu) + F_{p_t} \mu(1 - \bar{o})}{\bar{o}(1 - \mu)},$$

and redistributing, the function becomes:

$$H_{p_t} \geq \frac{V_{\min} \bar{o}(1 - \mu)}{\bar{o}(1 - \mu)} + \frac{F_{p_t} \mu(1 - \bar{o})}{\bar{o}(1 - \mu)},$$

where the $\bar{o}(1 - \mu)$ cancels out in the first term and we get:

$$H_{p_t} \geq V_{\min} + \frac{F_{p_t} \mu(1-\bar{o})}{\bar{o}(1-\mu)}. \quad (7.20)$$

Note that both (7.19) and (7.20) have $\frac{F_{p_t} \mu(1-\bar{o})}{\bar{o}(1-\mu)}$ in common and that the first term on the right-hand-side has V_{\min} in common. Thus, we can condense (7.19) and (7.20) into one Equation (that defines H as a function of F :

$$H_{p_t} \geq \hat{\alpha} + \hat{\beta} F_{p_t}, \quad (7.21)$$

where we define $\hat{\alpha}$ and $\hat{\beta}$ as:

$$\text{where } \hat{\alpha} = \begin{cases} \frac{V_{\min} \mu(1-\bar{o}) - \mu + \bar{o}}{\bar{o}(1-\mu)}, & \text{for } \mu < \bar{o} \\ V_{\min} & \text{For } \mu \geq \bar{o} \end{cases}, \quad (7.22)$$

$$\text{and } \hat{\beta} = \frac{\mu(1-\bar{o})}{\bar{o}(1-\mu)} \quad (7.23)$$

In this case, (7.21) is represented in Semazzi and Mera (2006) in their Equation (7.8). The value for $\hat{\alpha}$ dictates the relationship between the user-defined climatology and the minimum value they are willing to accept from the EPS, V_{\min} . The $\hat{\beta}$ variable is defined as the ratio of the loss due to F against the cost inherent in taking action but for which E actually occurred. We note that $H=F$ is a special case of (7.21), and that (7.21) is a universal

form of base lines in EROC. In order to show this, we set $\mu = \bar{\sigma}$, and using (7.20) according to the $\mu \geq \bar{\sigma}$ identity, we find that, when setting $V_{min}=0$:

$$H_{p_t} = V_{min} + \frac{F_{p_t} \mu(1 - \mu)}{\mu(1 - \mu)}$$

which reduces to:

$$H_{p_t} = V_{min} + F_{p_t}$$

And since $V_{min}=0$,

$$H_{p_t} = F_{p_t}$$

Two simplified forms of (7.21) also provide important insight about the widely used model evaluation method based on the ROC graphical method. As derived above, and from (7.21) we also represent (7.21) as:

$$H_{p_t} > F_{p_t},$$

which is identical to the condition employed in the traditional application of the ROC graphical method. In this case the added value of the EPS based on the EV method is simply the difference between the ROC graph and the baseline $H_{p_t} = F_{p_t}$. It may be shown from (7.15) that these conditions correspond to the case in which V is maximum, $V_{max} = H_{p_t} - F_{p_t}$, which strictly corresponds only to a very specific end user when $\mu = \bar{\sigma}$. Using this metric as a general measure of the performance of an EPS ignores the rest of the idealized end users corresponding to $\mu \neq \bar{\sigma}$. This method of evaluating EPS where it is explicitly or implicitly

assumed that $\mu = \bar{o}$ is extensively employed by most of the major weather and climate prediction centers throughout the world to assess forecast skill (see Hamill and Juras 2006, and references therein).

Another simplified form of (7.8), however, which is more general than the one we have just described above, is obtained by requiring $V_{min}=0$ and $\mu \neq \bar{o}$. When $\mu > \bar{o}$ we find that $\hat{\alpha} = 0$ and $\hat{\beta} > 1$; thus, the graph of the modified baseline is $H_{p_t} > \hat{\beta}F_{p_t}$, which is a straight line also passing through the origin, but its slope is greater than that of $H_{p_t} = F_{p_t}$, as illustrated in Fig. 7.4a. For convenience, the ROC graph in Fig. 7.4 has been constructed from the synthetic values of H_{p_t} and F_{p_t} derived from a simple analytic parabolic function expressed as follows:

$$H_{p_t} = F_{p_t} (2 - F_{p_t}) \quad (7.24)$$

The function above features many characteristics similar to typical ROC graphs based on observed data, such as in Molesworth et al. (2003). To be specific, it passes through $H = F = 0$ and $H = F = 1$. its slope is relatively larger in the vicinity of (0, 0), and it approaches zero toward (1, 1). Near the conclusion of this study we came across a study by Marzban (2004) in which a variety of generic ROC graphs for theoretical analysis are investigated. Although the Marzban formulation is more flexible because it includes several free parameters that make it possible to control the concavity of the ROC graph, one of the shapes analytically generated by Marzban is very similar to ours in Fig. 7.4.

In the case of $\mu < \bar{o}$ we find that $\hat{\alpha} = 0$ and $\hat{\beta} < 1$ and the corresponding baselines satisfy $H_{p_t} \geq \hat{\alpha}(\mu) + \hat{\beta}(\mu)F_{p_t}$. This is a family of baselines, all of which pass through the point $(H, F) = (1,1)$ (see Fig. 7.4a). The most general form of (7.21) may be obtained by setting $V_{min} > 0$ and $\mu \neq \bar{o}$ (Fig. 7.4b). This generalization accommodates the full range of viable end-user applications. If V_{min} is large enough, then this condition imposed by users may render the EPS worthless to them.

7.2.2 End-user eligibility limits

We can further scrutinize the range of possible μ values by giving (7.21) a closer look. If, for example, we set $\mu > \bar{o}$, then, by definition, \bar{o} will be the minimum, i.e. $\min(\mu, \bar{o}) = \bar{o}$. In this case, the user has the choice to take a bigger cost than the climatological V_{max} of occurrences (such as terciles, when $\bar{o} = 0.33$). It is also possible that there may not be as much value, but the risk is acceptable for an end user that has a wider range of mitigation possibilities and a larger amount of resources at their disposal. We know from (7.20) and (7.21) that $\hat{\alpha} = 0$ and $\beta > 0$. Thus, starting with (7.17) and setting $(\mu, \bar{o}) = \bar{o}$:

$$\frac{\bar{o} - F_{p_t} \mu(1 - \bar{o}) + H_{p_t} \bar{o}(1 - \mu) - \bar{o}}{\bar{o} - \bar{o} \mu} \geq V_{min}$$

which reduces to:

$$\frac{\bar{\phi} - F_{p_t} \mu(1 - \bar{o}) + H_{p_t} \bar{o}(1 - \mu) - \bar{\phi}}{\bar{o} - \bar{o} \mu} \geq V_{\min}$$

$$\frac{-F_{p_t} \mu(1 - \bar{o}) + H_{p_t} \bar{o}(1 - \mu)}{\bar{o} - \bar{o} \mu} \geq V_{\min}$$

Multiplying both sides by $\bar{o} - \bar{o} \mu$, we get:

$$-F_{p_t} \mu(1 - \bar{o}) + H_{p_t} \bar{o}(1 - \mu) \geq V_{\min} (\bar{o} - \bar{o} \mu).$$

Distributing $H_{p_t} \bar{o}$ for the second term in the left hand side, and the V_{\min} on the right hand side, we get:

$$-F_{p_t} \mu(1 - \bar{o}) + H_{p_t} \bar{o} - H_{p_t} \bar{o} \mu \geq V_{\min} \bar{o} - V_{\min} \bar{o} \mu$$

Subtracting $H_{p_t} \bar{o} \mu$ from both sides and adding $V_{\min} \bar{o} \mu$ to both sides:

$$-\mu(F_{p_t} (1 - \bar{o})) - H_{p_t} \bar{o} \mu + V_{\min} \bar{o} \mu \geq V_{\min} \bar{o} - H_{p_t} \bar{o}.$$

Factoring for μ :

$$-\mu(F_{p_t} (1 - \bar{o})) - \mu(H_{p_t} \bar{o} + V_{\min} \bar{o}) \geq V_{\min} \bar{o} - H_{p_t} \bar{o},$$

and factoring for \bar{o} :

$$-\mu(F_{p_t} (1 - \bar{o})) - \mu(H_{p_t} \bar{o} + V_{\min} \bar{o}) \geq \bar{o}(V_{\min} - H_{p_t}),$$

so that the Equation (becomes:

$$-\mu[(F_{p_t}(1-\bar{o})) + \bar{o}(H_{p_t} + V_{\min})] \geq \bar{o}(V_{\min} - H_{p_t}).$$

Dividing through by $((F_{p_t}(1-\bar{o})) + \bar{o}(H_{p_t} + V_{\min}))$ and multiplying by -1, we get:

$$\mu \leq \frac{\bar{o}(H_{p_t} - V_{\min})}{(F_{p_t}(1-\bar{o})) + \bar{o}(H_{p_t} + V_{\min})}$$

Which, by the definition stating $\mu > \bar{o}$,

$$\bar{o} \leq \mu \leq \frac{\bar{o}(H_{p_t} - V_{\min})}{(F_{p_t}(1-\bar{o})) + \bar{o}(H_{p_t} + V_{\min})} \quad (7.25)$$

Since $\mu > \bar{o}$ for this user, we derive a baseline that oscillates about $H = F = 0$ so that μ can have more value for smaller H/F ratios, i.e. they are sensitive to high false alarm rates more than low hit rates.

For a user with $\mu < \bar{o}$, or being able to take on only a certain amount of cost for an event, then by definition, $\min(\mu, \bar{o}) = \mu$. This also means that the user has an upper limit in terms of value, \bar{o} . Thus, (7.17) reduces to

$$\frac{\mu - F_{p_t}\mu(1-\bar{o}) + H_{p_t}\bar{o}(1-\mu) - \bar{o}}{\mu - \bar{o}\mu} > V_{\min}$$

Dividing both sides by $\mu - \bar{o}\mu$ we get:

$$\mu - F_{p_t}\mu(1-\bar{o}) + H_{p_t}\bar{o}(1-\mu) - \bar{o} > V_{\min}(\mu - \bar{o}\mu).$$

Distributing the $H_{p_t} \bar{o}$ in the second term of the l.h.s, we have:

$$\mu - F_{p_t} \mu(1 - \bar{o}) + H_{p_t} \bar{o} - H_{p_t} \bar{o} \mu - \bar{o} > V_{\min} (\mu - \bar{o} \mu),$$

and rearranging terms:

$$\mu + H_{p_t} \bar{o} - \bar{o} - F_{p_t} \mu(1 - \bar{o}) - H_{p_t} \bar{o} \mu > V_{\min} (\mu - \bar{o} \mu).$$

Factoring out \bar{o} from $H_{p_t} \bar{o} - \bar{o}$:

$$\mu - \bar{o}(1 - H_{p_t}) - F_{p_t} \mu(1 - \bar{o}) - H_{p_t} \bar{o} \mu > V_{\min} (\mu - \bar{o} \mu),$$

and subtracting $\mu - F_{p_t} \mu(1 - \bar{o}) - H_{p_t} \bar{o} \mu$ from both sides:

$$-\bar{o}(1 - H_{p_t}) > V_{\min} (\mu - \bar{o} \mu) + F_{p_t} \mu(1 - \bar{o}) + H_{p_t} \bar{o} \mu - \mu.$$

Distributing V_{\min} on $(\mu - \bar{o} \mu)$ and $F_{p_t} \mu$ on $(1 - \bar{o})$:

$$-\bar{o}(1 - H_{p_t}) > V_{\min} \mu - V_{\min} \bar{o} \mu + F_{p_t} \mu - F_{p_t} \mu \bar{o} + H_{p_t} \bar{o} \mu - \mu,$$

and factoring out $-\mu$:

$$-\bar{o}(1 - H_{p_t}) > -\mu(-V_{\min} + V_{\min} \bar{o} - F_{p_t} + F_{p_t} \bar{o} - H_{p_t} \bar{o} + 1).$$

Rearranging terms:

$$-\bar{o}(1 - H_{p_t}) > -\mu(1 - V_{\min} + V_{\min} \bar{o} - F_{p_t} + F_{p_t} \bar{o} - H_{p_t} \bar{o})$$

Factoring:

$$-\bar{o}(1 - H_{p_t}) > -\mu[1 - (1 - \bar{o})(F_{p_t} + V_{\min}) - H_{p_t} \bar{o}]$$

Rewriting the Equation (we get:

$$-\mu[1 - (1 - \bar{o})(F_{p_t} + V_{\min}) - H_{p_t} \bar{o}] < -\bar{o}(1 - H_{p_t}),$$

and dividing both sides by $[1 - (1 - \bar{o})(F_{p_t} + V_{\min}) - H_{p_t} \bar{o}]$ and multiplying by -1 (which switches the $<$ to $>$):

$$\bar{o} > \mu > \frac{\bar{o}(1 - H_{p_t})}{[1 - (1 - \bar{o})(F_{p_t} + V_{\min}) - H_{p_t} \bar{o}]} \quad (7.26)$$

Since $\mu < \bar{o}$ for this user group and $\hat{\alpha}$ becomes important, the user-defined μ dictates the behavior of EROC so that the base line oscillates about the $H = F = 1$ point and the user is highly sensitive to H_{p_t} . Therefore, its EPS is only valuable, i.e. useable, given a specified minimum hit rate and to a higher degree than the V_{\min} they are willing to accept. Our μ range is thus bounded by the two inequalities so that:

$$\frac{\bar{o}(1 - H_{p_t})}{[1 - (1 - \bar{o})(F_{p_t} + V_{\min}) - H_{p_t} \bar{o}]} \leq \mu \leq \frac{\bar{o}(H_{p_t} - V_{\min})}{(F_{p_t} (1 - \bar{o})) + \bar{o}(H_{p_t} + V_{\min})} \quad (7.27)$$

This is consistent with the importance of H_{p_t} as defined by the user. Note that the lower limits are more sensitive to H_{p_t} (numerator) and the upper limits are highly bounded by V_{\min} since it is also present in the numerator. This correlates with the manner in which we define (7.25) and (7.26) and is the essence of (7.27).

The special case in which $H = 1$, $F = 0$, and $V_{\min} = 0$ corresponds to a perfect EPS and (7.27) reduces to $0 \leq \mu \leq 1$. Thus, as expected, all end users benefit from the EPS. The other interesting special case occurs when $H = F \neq 0$ or 1. In this case (7.27) reduces to $\mu = \bar{\mu}$ which we expect from the discussion in Section 5.3.1. The corresponding conditions for the end points of the ROC graph are $H = F = 0$ and $H = F = 1$, and (7.27) reduces to $\bar{\mu} < \mu < 1$ and $0 < \mu < \bar{\mu}$ respectively. Inspection of Fig. 7.4a shows that the points $H = F = 0$ and $H = F = 1$ lie on an infinite number of off-diagonal baselines corresponding to the two categories of end users defined by the inequalities $\mu > \bar{\mu}$ and $\mu < \bar{\mu}$ respectively.

7.2.3 Interpretation of EROC area under graph

The ROC graphical method is a function of H_{p_i} and F_{p_i} and, given the derivation of (7.21), we know that ROC is a special case of EROC for an optimal user. We found that when setting $\mu = \bar{\mu}$, (7.21) reduces to $H = F$, or the natural diagonal base line present in all ROC plots. We generalize this by the following equation:

$$H_{p_i} = \hat{\alpha}(\mu) + \hat{\beta}(\mu)F_{p_i} \quad (7.28)$$

so that all baselines can be derived from (7.28) as a function of a particular μ . This is also consistent with the manner in which we define (7.21). In the case of $\mu = \bar{\mu}$, (7.28) reduces to:

$$H_{p_i} = 0 + F_{p_i} \bar{\mu} ,$$

or simply, climatology.

Let us now calculate a baseline given a specific μ where H is now the point corresponding to the base line and also a function of F . To acquire the difference between ROC and the new baseline we set:

$$\Delta H = H_{p_t} - H, \quad (7.29)$$

where H is the baseline. Combining (7.28) with (7.29), we get:

$$\Delta H = H_{p_t} - \hat{\alpha}(\mu) - \hat{\beta}(\mu)F_{p_t} \quad (7.30)$$

To analyze the relationship between EROC and EV, we combine (7.30), (7.15) and (7.22) and (7.23). By simply equating the value (V) and the distance of ROC to the baseline (ΔH) for all hypothetical users, and assuming there is a one-on-one relationship, that is, assuming the value exactly matches the distance of H to the user-defined baseline, we have:

$$V = \Delta H \quad (7.31)$$

Because we are, indeed, bounded by the two types of user, we assume a constant $\hat{\gamma}$ that varies according to μ . Thus, (7.31) becomes:

$$V = (\hat{\gamma})\Delta H \quad (7.32)$$

Thus, we must solve for each type of equation. For $\mu < \bar{o}$, using (7.15) and (7.16) for the V and (7.30) for the ΔH and combining them together in (7.31), and assuming that $V_{min} = 0$, we have:

$$\Delta H = H_{p_t} - \frac{\bar{o} - \mu}{\bar{o}(1 - \mu)} - F_{p_t} \frac{\mu(1 - \bar{o})}{\bar{o}(1 - \mu)},$$

and V at $\mu < \bar{o}$, which when using (7.22) and (7.23) and recognizing that $\min(\mu, \bar{o}) = \mu$, becomes:

$$V = \frac{H_{p_t} \bar{o}(1 - \mu) - \bar{o} + \mu - F_{p_t} \mu(1 - \bar{o})}{\mu(1 - \bar{o})},$$

and combining equations we get

$$\frac{H_{p_t} \bar{o}(1 - \mu) - \bar{o} + \mu - F_{p_t} \mu(1 - \bar{o})}{\mu(1 - \bar{o})} = \hat{\gamma} \left(H_{p_t} - \frac{\bar{o} - \mu}{\bar{o}(1 - \mu)} - F_{p_t} \frac{\mu(1 - \bar{o})}{\bar{o}(1 - \mu)} \right)$$

Dividing through by $\left(H_{p_t} - \frac{\bar{o} - \mu}{\bar{o}(1 - \mu)} - F_{p_t} \frac{\mu(1 - \bar{o})}{\bar{o}(1 - \mu)} \right)$:

$$\frac{H_{p_t} \bar{o}(1 - \mu) - \bar{o} + \mu - F_{p_t} \mu(1 - \bar{o})}{\mu(1 - \bar{o})} * \frac{\bar{o}(1 - \mu)}{H_{p_t} \bar{o}(1 - \mu) - \bar{o} + \mu - F_{p_t} \mu(1 - \bar{o})} = \hat{\gamma}$$

Rearranging terms and multiplying both sides by $\frac{\mu(1 - \bar{o})}{\bar{o}(1 - \mu)}$, we have:

$$\frac{(H_{p_t} \bar{o}(1 - \mu) - \bar{o} + \mu - F_{p_t} \mu(1 - \bar{o})) \bar{o}(1 - \mu)}{(\mu(1 - \bar{o}))(H_{p_t} \bar{o}(1 - \mu))(\bar{o} - \mu - F_{p_t} \mu(1 - \bar{o}))} = \hat{\gamma} \frac{\mu(1 - \bar{o})}{\bar{o}(1 - \mu)}.$$

The Equation (then reduces to:

$$\frac{H_{p_t} \bar{o}(1 - \mu) - \bar{o} + \mu - F_{p_t} \mu(1 - \bar{o})}{H_{p_t} \bar{o}(1 - \mu) - \bar{o} - \mu - F_{p_t} \mu(1 - \bar{o})} = \hat{\gamma} \frac{\mu(1 - \bar{o})}{\bar{o}(1 - \mu)}$$

And after terms cancel out on the l.h.s., we are left with:

$$1 = \hat{\gamma} \frac{\mu(1 - \bar{o})}{\bar{o}(1 - \mu)} \quad (7.33)$$

From (7.23), we know that

$$\hat{\beta} = \frac{\mu(1 - \bar{o})}{\bar{o}(1 - \mu)}$$

so our equation further reduces to:

$$1 = \hat{\gamma}\hat{\beta}$$

And thus,

$$\hat{\gamma} = \frac{1}{\hat{\beta}} \quad (7.34)$$

In this case, we find that the relationship between V and ΔH is proportional only through the inverse of the $\hat{\beta}$ function. This suggests that V and ΔH are related by ratio of the cost inherent in taking action but for which E actually occurred against the loss due to F . We have also shown that (7.34) does not match the definition in Semazzi and Mera (2006) for (7.15) in their study, so we propose that the derivation for this Equation (be revised to match the derivation in the present study).

For the case in which $\mu \geq \bar{o}$, we once again explore the relationship by examining (7.32).

For this range of μ , $\min(\mu, \bar{o}) = \bar{o}$, so (7.30) becomes:

$$\Delta H = H_{p_t} - 0 - F_{p_t} \frac{\mu(1-\bar{o})}{\bar{o}(1-\mu)}$$

This reduces to

$$\Delta H = H_{p_t} - F_{p_t} \frac{\mu(1-\bar{o})}{\bar{o}(1-\mu)} \quad (7.35)$$

As with ΔH above, we employ the same relationship, $\min(\mu, \bar{o}) = \bar{o}$ for the range $\mu \geq \bar{o}$ for the value Equation (using (7.15) and (7.16) so that

$$V = \frac{-\bar{o} + \bar{o} - F_{p_t} \mu(1-\bar{o}) + H_{p_t} \bar{o}(1-\mu)}{\bar{o}(1-\mu)}$$

Which reduces to:

$$V = \frac{-F_{p_t} \mu(1-\bar{o})}{\bar{o}(1-\mu)} + H_{p_t}$$

or

$$V = H_{p_t} - \frac{F_{p_t} \mu(1-\bar{o})}{\bar{o}(1-\mu)} \quad (7.36)$$

We recognize that in this case V and ΔH are equivalent since (7.35) and (7.36) have the same result. Thus, we can show that (7.32) is true for $\mu \geq \bar{o}$ and the relationship between these functions becomes:

$$V = (\hat{\gamma})\Delta H \quad \text{where } \hat{\gamma} = \begin{cases} \frac{1}{\hat{\beta}}, & \text{for } \mu < \bar{o} \\ 1 & \text{For } \mu \geq \bar{o} \end{cases} \quad (7.37)$$

Again, we note that our findings are not in line with Semazzi and Mera (2006) Equation (7.15), but this is only the case when $\mu < \bar{o}$, and where the relationship between V and ΔH is only true if ΔH is divided by $\hat{\beta}$. To show graphically why this is the case, we present Fig. 7.5, in which $\Delta H/\hat{\beta}$ clearly has a linear one-to-one relationship (purple squares) as (7.32) suggests. For the case (7.15) in Semazzi and Mera (2006), we show that the two variables are not equivalent (blue diamonds), so that $V \neq \hat{\beta}\Delta H$.

We can now condense the implementation of the EROC graphical method into the following steps:

1. Construct the usual ROC graph based on the H_{pt} and F_{pt} values computed from the output from the EPS and the observed occurrence of E .
2. Identify a specific end user μ for whom we wish to evaluate the skill of the EPS.
3. Construct a customized baseline $H_{pt} = \hat{\alpha}(\mu) + \hat{\beta}(\mu)F_{pt}$ for a particular end user that is based on the inequality defined in (7.21).

4. Estimate the relative skill of an EPS by computing the difference between a point on the ROC graph and the corresponding value on the user-specific baseline constructed in step 3.

7.2.3 The Semazzi-Mera Skill Score

The derivation in Section 5.2.2 defines the important connection between EV and EROC graphical methods that we are seeking in this study. In Fig. 7.6 (left-hand panels) we have plotted V and ΔH against F for $\mu (= 0.25) < \bar{o}$ (Fig. 7.6, middle), $\mu (= 0.33) = \bar{o}$ (Fig. 7.6, top), $\mu (= 0.40) > \bar{o}$ (Fig. 7.6, bottom). We can see that in the case of $\mu \geq \bar{o}$ ΔH is identically equal to V ; however, when $\mu < \bar{o}$, $\Delta H \neq V$. Nevertheless and more importantly, Fig. (7.6, right-hand panels) confirm that for all values of μ the relationship between ΔH and V is linear. For illustration purposes we have adopted tercile stratification ($\bar{o} = 0.33$) which is widely used by the seasonal climate prediction community (American Meteorological Society, 2001). It is used by the International Climate Outlook Forum (ICOF), seasonal climate prediction system, the International Research Institute, and the United Kingdom Meteorological Office (UKMO), among other centers. For its experimental seasonal forecasts for various regions around the world IRI produces maps of forecast probabilities based on the “Above Normal”, “Near Normal”, or “Below Normal” tercile categories (Mason et al, 1999).

Another important use of ROC in EPS skill measurement is the Area Skill Score (ASS) or ROC Skill Score (ROCSS), as shown in Richardson (2000a) and references therein:

$$ROCS = \frac{A - A_{Clim}}{A_{Per} - A_{Clim}} \quad (7.38)$$

The area A under the ROC is used as an index of the accuracy of the forecast system (Mason 1982; Buizza et al. 1998, 1999). A perfect system would have $A = 1.0$, while no-skill systems ($H = F$) would have $A = 0.5$. Substituting $A_{per}=1$, and $A_{clim}=0.5$, we have:

$$ROCS = \frac{A - 0.5}{1 - 0.5},$$

which becomes:

$$ROCS = \frac{A - 0.5}{0.5},$$

and reduces to

$$ROCS = 2A - 1. \quad (7.39)$$

Because our baseline determines score for a particular user, then the skill score as determined by Richardson (2000a), Stanski, and Wilks (2006), will necessarily change to adapt to the corresponding values of a non-optimal user. We note that M_{clim} in the Equation (for V is $H = F$, which is also a special condition of EROC when $\mu = \bar{o}$, as we showed at the end of Section 5.3. Thus, if A_{clim} is also the $H=F$ baseline, then $A\mu$ is the base line in EROC,

so that A_{clim} becomes a special case of A_μ . Based on these assumptions, we present the Semazzi-Mera Skill Score (SMSS):

$$SMSS = \frac{A - A_\mu}{A_{per} - A_\mu}, \quad (7.40)$$

where A is the area under the ROC curve, $A_{per} = 1$, and A_μ is the appropriate area between the baseline and the ROC graph. In this case, A_μ is determined by the μ and thus by the baseline on the EROC plot. It is the “climatological” baseline for a hypothetical user.

The SMSS is a convenient and compact form of presenting forecast skill verification derived

from both the ROC and EV methods. To elucidate the relationship between SMSS and ROCS, we set A_μ for the special case where $\mu = \bar{\sigma}$ and $V_{min} = 0$. In this case, our baseline is computed using (7.21), where $\hat{\alpha} = V_{min}$ at $\mu \geq \bar{\sigma}$ and $\hat{\beta}$ reduces to 1. Thus, (7.21) reduces to $H = F$ and we can construct our baseline based on $H = F$, i.e. the diagonal from the origin [0,0] to unity [1,1]. Since A_μ is the total of the area under the baseline, based on (7.21) we have:

$$A_\mu = \int_0^1 [\hat{\alpha}(\mu) + \hat{\beta}(\mu)F]dF \quad (7.41)$$

Integrating (7.39), we have:

$$A_\mu = \hat{\alpha}(\mu) + \hat{\beta}(\mu)/2, \quad (7.42)$$

and we know that $\hat{\alpha} = V_{min} = 0$ and that $\hat{\beta} = 1$, (7.40) reduces to:

$$A_{\mu} = 1/2. \tag{7.43}$$

We find that (7.43) is consistent with A_{clim} , where $A_{\text{clim}} = 0.5$ or $1/2$. We can thus implement SMSS's derivative, ROCS or (7.39), which reduces to (7.40).

7.2.4 Further geometrical interpretation of the connection between the EV and ROC graphs

Our analysis may be used for the interpretation of the peculiar backward or forward “trails” observed in many previous studies based on the EV graphical method (Zhu et al. 2002). Inspection of the graph in Fig. 7.4 suggests that the forward trail arises when the following condition is satisfied:

$$\left. \begin{array}{l} F = 0 \\ H \neq 0 \end{array} \right\} \quad \text{For } \mu > \bar{o} \tag{7.44}$$

To confirm that this condition results in a forward trail we substitute (7.44) into (7.11), (7.12) and (7.14) and find that

$$M_{\text{forecast}} = -[H\bar{o}(1 - \mu) - \bar{o}] \tag{7.45}$$

$$M_{\text{cli}} = \bar{o} \tag{7.46}$$

$$M_{\text{perfect}} = \bar{o}\mu \tag{7.47}$$

Substituting (7.45)–(7.47) into (7.15) yields $V = H$, which corresponds to a horizontal forward trail on the EV graph since $\mu > \bar{o}$. In a similar way, we can assume that a backward trail occurs when

$$\left. \begin{array}{l} F \neq 1 \\ H = 1 \end{array} \right\} \quad \text{For } \mu < \bar{o} \quad (7.48)$$

Substitution of the condition in (7.46) into the definitions in (7.11), (7.12) and (7.14) gives

$$M_{forecast} = F\mu(1 - \bar{o}) + \mu\bar{o} \quad (7.49)$$

$$M_{cli} = \mu \quad (7.50)$$

$$M_{perfect} = \bar{o}\mu \quad (7.51)$$

Combining (7.49)–(7.51) with (7.15) yields $V = (1 - F)$, which is a horizontal straight line extending backward on the EV graph since $\mu < \bar{o}$. To illustrate the trail's geometrical behavior, we modified the ROC graph in Fig. 7.4 by imposing the conditions $F = 0$ and $H = 0.08$ and the condition $H = 1$ and $F = 0.92$. The corresponding extended ROC graphs are displayed in Figs. 4.7a and 4.8a, respectively. Inspection of the corresponding V graphs (Figs. 4.7b and 4.8b) reveals, as anticipated, that $V = 0.08$ in both cases, thus confirming that we obtain the forward and backward trails when $V = H$ and $V = 1 = F$, respectively.

5.3 Application of EROC

The goal of current meningitis mitigation efforts, in terms of the disease's link with atmospheric moisture, is to provide 1-14 day weather forecasts to target dissemination of scarce vaccine. In Chapter 4 we showed how regional model simulations of moist events over West Africa was successful in providing higher-resolution information and as well as prediction of these important systems. The physics parameter ensemble for the April-May period of 2006 provided a unique dataset with which to test the hypothetical use of EPS over West Africa for seasonal forecasts. Further, the numerous real-time forecasts used to test the model's short and mid range skill also present another opportunity to test EPS at this timescale. Finally and perhaps most importantly, is the existence of a direct societal application: meningitis. We thus devote this portion of the chapter to the testing of EPS skill using EROC with particular emphasis on addressing the economic impact of adopting limited-area model simulations by decision-makers.

7.3.1 Economic Benefits of Environmental Prediction for West Africa

The economic cost of weather and climate-related natural hazards is currently estimated to be \$100 billion globally (Konare 2009). Within these costs exist health factors associated with environmental conditions, such as the meningitis-humidity relationship. The value of weather and climate information is potentially high, but it has yet to be fully exploited by decision

makers. Recent research related to the WHO MERIT program also suggests that Easier to estimate costs of weather and climate service delivery than benefits (Konare 2009).

The majority of cost-benefit analyses related to meningitis efforts have been limited to the nature of vaccination campaigns: preventive and reactive. In Parent du Châtelet (2001), the authors investigated the cost-effectiveness of preventive and reactive mass immunization campaigns over West Africa from a theoretical modeling perspective and found that preventive strategy prevented 59% of cases compared to 49% for the emergency strategy. Monetary implications of preventive inoculation were significant: cost per case prevented was US\$59 for the preventive strategy and US\$133 for the reactive strategy. This study conceded that although preventive action would incur a lower cost, the model relies on prediction of epidemics at least 3 years in advance.

Until this point, the economic impact of utilizing environmental forecasting as a tool in the management of meningitis epidemics over sub-Saharan Africa has been limited to identification of factors relating the disease and climate (e.g. Molesworth et al. 2003) and overall evaluation of socio-economic benefits on the health sector (e.g. Konare 2009). An ongoing goal of international climate agencies like the World Climate Research Program (WCRP) is to develop a strategy for demonstration and assessment of socio-economic benefits and applications arising from advanced knowledge and predictive skill of multi-scale tropical weather/climate events on timescales of days to seasons (Moncrieff et al. 2007). The skill of statistically downscaled global model output over West Africa during the boreal

spring is currently being assessed as an application for meningitis mitigation (UCAR Africa Initiative, personal communication). Similar analyses of regional models such as WRF have yet to be undertaken and thus become the focus of this portion of our research.

We employ the EROC graphical procedure on seasonal and intraseasonal simulations in order to address two types of potential forecast impact: i) seasonal climate information may be applied for logistical consideration (distribution of vaccine stockpiles, transportation, personnel) ahead of changes in the environment that can influence epidemic patterns and ii) intraseasonal or short-term prediction could be used to minimize meningitis incidence by providing 1-14 day weather forecasts to target dissemination of scarce vaccine. Currently, the targeted aim of short-term forecasts is to diagnose environmental conditions a week in advance that could push a district in “alert” into a full “epidemic.” The knowledge may be used to shift resources from a high-humidity district (in which the disease spread is lessening) to a dry area still prone to disease spread. We hypothesize that good useable skill in model forecasts would allow for the integration of model predictions to enhance the World Health Organization’s Decision Tree for vaccination campaign, which, at the moment, does not include environmental factors as a main constituent of action threshold (Novak et al. 2009).

7.3.2 Datasets and Methodology

The present study offers a unique opportunity to analyze the climate-disease-economic interface given the high costs of immunization campaigns and the documented link between West African climate and meningitis outbreaks. Estimates of preventive care versus reactive efforts to control epidemics have been estimated to yield total costs of up to 55% in savings in terms of preventive/reactive methods (Parent du Châtelet et al. 2001). It is difficult to isolate particular cost-loss ratios for meningitis efforts due to the complexity of disease dynamics and the available resources to counter an epidemic. We thus employ hypothetical end-user ratios (μ) in our analysis. The chosen ratios shown in Table 7.3 are based on preventive/reactive vaccination costs from Parent du Châtelet et al. (2001) in order to maintain continuity with previous work with meningitis in Africa. We use the “base case” and “best case” scenario figures from their study (see Table 1 in their study), which they define as conditions during a mass vaccination campaign in Matam, Senegal in 1997 and the assumptions used in their model. Assumptions include variables such as attack rate, fatality rate, annual endemic incidence, proportion of neurological sequelae, endemic fatality rate, non-meningococcal meningitis incidence, vaccination coverage and costs, and meningitis surveillance and investigation campaigns.

As given by Table 7.3, the chosen μ parameters are 0.45 and 0.37 for base and best case scenarios (BC and BS hereafter, respectively). For our purposes, these numbers represent the cost-loss ratio for a decision-maker that chooses to utilize EPS to predict disease dynamics

based solely on the current state of the climate in a given region. The BC is chosen to represent a decision-making institution that is able to invest more resources into prevention of the disease, while BS represents a user with less capital.

The model tested is the Weather Research and Forecasting model (WRF, described in detail in Chapter 4) and we assess its seasonal simulation capability for April-May 2006 using FNL boundary conditions and short (16-day) forecast simulations during May 2009 with GFS real-time boundary conditions. Given the nature of our datasets (seasonal and real-time), we chose two approaches in order to create model ensembles: initial condition variation and model physics perturbations. Both methods have been tested in the literature (e.g. Mullen and Baumhefner 1988; Houtekamer and Derome 1995; Du et al. 1997) and also in comparison with each other (Stensrud et al. 2000).

For the seasonal experiment, 19 ensemble members are derived from the multi-physics parameterization experiment, which has a month of spin-up in March and runs through the end of June of 2006. We chose 2006 due to the high volume of comparative datasets available through the AMMA campaign (which includes ECMWF forecasts as well as a well-calibrated station in Niamey). The chosen event (E) is the observed RH40 at three locations: Niamey, Bamako and N'Djamena and there are 60 days (April 1 – May 30) for which the model makes a prediction. Climatology is assumed to be equal number of FA and H . We evaluate the model's overall ability to simulate moisture.

For the real-time experiment, one set of ensemble forecasts were chosen: May 1. The experiments have 15 sets of ensemble members each and the perturbation employed was varying initial conditions, i.e. model start-up with 12 hour increments. Boundary conditions from the NCEP GFS used for real-time simulations are supplied 4 times daily at 00z, 06z, 12z and 18z. This provides 4 different initial conditions that can be perturbed further by starting the model at 00z, 12z of the initial day (May 1) and 00z, 12z for the second day (May 2) in the 00z May 1 boundary conditions. The same method is used for 06z May 1 and so on, except for 18z May 1. The model is analyzed starting on the third day of the simulation (i.e. May 3 for May 1 initialization) in order to have at least 15 ensemble members for the experiment (note that 18z initialization only has 3 model iterations since a fourth would start at 06z of the third day). Model data for our analysis is acquired by taking a 0.2 degree area average over each of the locations utilized.

The chosen E for the real-time skill analysis is the actual occurrence of a moist event ($>RH40$ for a 3-day running mean) over a particular location for the entire domain. This differs from the seasonal analysis in that E is the number of stations that are either above or below the RH40 threshold instead of daily occurrences of RH40. In this instance, for example, the model may correctly predict 15 out of 20 locations to cross the threshold and may miss 3 plus 2 false alarms. This methodology allows us to inspect model performance at different daily intervals from an actual event: May 3, May 4, May 5, and so on would be 24, 48, 60 hours in advance.

7.3.3 Results

7.3.3.1 Seasonal simulations

We first examine the useable skill of WRF for seasonal model simulations. The model is evaluated over Niamey (Niger), Bamako (Mali) and N'Djamena (Chad) given the more continuous nature of observations at those locations. In Fig. 7.9 we present EROC plots for each one of the stations. For Bamako (Fig. 7.9a), there is considerable skill where a good number of ensemble members continuously predict the event. Note that the ROC curve for this location intercepts the y-axis at 0.53 and would induce a forward trail in the corresponding EV plot. Given the two μ parameters (0.37 and 0.45), $\mu < \bar{o}$ and the corresponding baseline is computed according to (7.21-5.23). Thus, the user-defined μ dictates the behavior of EROC so that the base line oscillates about the $H = F = 1$ point and the user is highly sensitive to H_{pr} . Therefore, its EPS is only useable given a specified minimum hit rate. For users in Bamako, this is highly favorable given the y-intercept highlighted above. The corresponding SMSS for Bamako is 0.49 for $\mu = 0.37$ and 0.63 for $\mu = 0.45$.

Useable skill was also computed for the cities of Niamey and N'Djamena. For Niamey (Fig. 7.9b), high hit rates also translated into increased skill and a SMSS of 0.52 for $\mu = 0.37$ and 0.65 for $\mu = 0.45$. Notice that there isn't enough information to complete the loop for Niamey so that the y or x axes are intercepted. We propose that a higher number of ensemble

members would alleviate the situation. Also notice that this drawback does not hamper our use of EROC since the ROC curve for Niamey falls within the $\mu = 0.37, 0.45$ baselines. For N'Djamena, the model has only limited skill (~ 0.04 for $\mu = 0.45$ and negative skill for $\mu = 0.37$).

The preceding analysis suggests that the model has good skill over important Meningitis Belt locations such as Niamey and Bamako. For N'Djamena, which lies farther east (15°E), model skill is appreciably lower and it suggests that more locations should be explored to test the model's performance further. However, quality observational data is notoriously difficult to acquire in this region and we propose that other methods be used to characterize the model's skill in simulating the moisture regime: skill over multiple locations and for specific occurrences such as moist events.

7.3.3.2 Real-time simulations

The boreal spring of 2009 is highlighted throughout the present study due to the increased amount of data on meningitis outbreaks, concurrent meteorological observations at Kano, Nigeria, and due to the wealth of real-time experimental model simulations. As described in Section 5.3.2, this portion of the analysis uses a different pathway to gauge the skill of WRF EPS: we isolate the occurrences of moist events over 21 different stations (Table 7.4). This method allows us to test for the primary purpose of dynamical modeling prediction: surface humidity. By choosing the occurrence of a 3-day running mean of RH40 we are effectively

customizing EROC analysis for meningitis mitigation. For the real-time cases, we opted for the more theoretical baselines used throughout the rest of the chapter: $\mu = 0.27$ and $\mu = 0.55$. The motivation behind this choice is that there are no available real-world numbers at this point on which to base short-term decisions and we hope this exercise can add to the body of knowledge on the matter. We also retain the bi-modal yes-no RH40 approach from the seasonal simulation, however, since this is still the event we are testing.

Although numerous modeling iterations occurred from April to May of 2009, we preferred to conduct our experiment around the time of the MME: May 5-12th. On this occasion, we use model data from May 1st (00z, 06z, 12z, 18z) as described in Section 7.3.2. Because we are using 3-day means and given the conditions in 5.3.2, the data begins on May 5th (average of May 2-5th). In Fig. 7.10 we present an EROC plot for the WRF real-time simulations. Notice that the available dataset does not form a closed loop, i.e. does not intercept the $H=1$ or $FA=1$ boundaries. This is due to the fact that the model only repeatedly produces a false alarm at one location and on 9 iterations. Outside of this isolated event, there are no false alarms. Further, the WRF model is unable to capture the moist event at 3 of the chosen locations repeatedly. However, the model is useful for the majority of the locations and, as can be seen by the data markers on the plot, hit rates are large compared to the false alarm rate. Also notice that the derived μ -specific baselines are computed only using the available FA information. Thus, we would measure its useable skill only relative to the provided baseline.

The work presented in this section of the study highlights the need for more data sources to either test the available model data or to perhaps increase the number of ensemble members. A change in the choice of parameters may also influence the final outcome of the plotted EROC. For example, using a date other than May 7th for our analysis may provide additional information. We find, however, that this may not be the case. For the majority of the dates, the model repeatedly failed to produce false alarms and we found May 7 to be more representative of what the majority of the calculations were showing. For the May 5 average, for instance, there was no FA reported and all points on the EROC plot would lie on the vertical axis. It is evident that additional experimentation with ensemble testing methodology would be beneficial for this study, especially given the high-impact nature of the underlying public health application.

7.4 Conclusions

An extended ROC procedure has been developed from the traditional ROC and the EV graphical methods used for evaluating the performance of ensemble climate/weather prediction systems. Based on the analysis of the formula for computing economic value we have derived an inequality defining the range for eligible hypothetical end users who would benefit from the EPS. Outside these limits the EPS yields no added benefits relative to the use of climatological persistence. In the proposed extended ROC approach we recommend construction of user-specific baselines. Unlike the implementation of the traditional ROC

method, which assumes a diagonal baseline, the extended ROC baselines do not necessarily pass through the origin and their slopes are, in general, different from unity. We show that the skill of an EPS based on the extended ROC method is proportional to the corresponding estimate based on the economic value graphical method. As a consequence, the extended ROC procedure may be used to provide the same primary information concerning the performance of an EPS as the EV method.

We propose the Semazzi–Mera skill score, which is function of the hit rate, the false alarm, and the cost–loss ratio that identifies the hypothetical decision maker. It is demonstrated that the usual ROCS skill ($= 2A - 1$), where A is the area under the ROC graph, is a special case of the SMSS. We show that forward and backward horizontal trails often observed in connection with economic value graphs correspond to special cases in which $V = H$ and $V = 1 = F$, respectively.

The EROC method has been applied to analyze the skill of ensemble forecasts for West Africa on seasonal and real-time scales in order to test the model's ability to capture important shifts in the moisture regime relative to health efforts. The EROC plots of WRF EPS show useable skill in both seasonal and real-time simulations. Further testing is required to analyze real-time ensemble data, as the available information does not capture the characteristic origin-to-unity loop seen in most ROC figures in the literature.

APPENDIX

List of Acronyms and Symbols

EV	Economic value
ROC	Relative operating characteristic
EROC	Extended ROC
EPS	Ensemble climate prediction system
E	Climate anomaly event
α	Number of correctly predicted non-occurrences of event E
β	Number of cases in which nonoccurrence of the event E was incorrectly predicted
γ	Number of ensemble runs in which event E was predicted to occur but did not materialize
δ	Number of ensemble runs in which occurrence of event E was correctly predicted
F_{pt}	False alarm, equal to $\gamma / (\alpha + \gamma)$
H_{pt}	Hit rate, equal to $\delta / (\beta + \delta)$
L	Loss incurred if E occurs and no preemptive action is taken
C	Cost of taking action based on the EPS that E would occur
μ	Ratio of C over L
M_{perfect}	User expected mean expenditure based on a perfect prediction model

M_{forecast}	User expected mean expenditure based on a credible EPS that we wish to evaluate
M_{clim}	User expected mean expenditure based on climatological persistence
p	Forecast probability
p_t	Threshold of p above which the event is forecast to occur
\bar{o}	Average frequency of the historical occurrence of E
V_{min}	Minimum V
$\hat{\alpha}$	Equal to $\frac{V_{\text{min}}\mu(1-\bar{o})-\mu+\bar{o}}{\bar{o}(1-\mu)}$ for $\mu < \bar{o}$ and equal to V_{min} for $\mu \geq \bar{o}$
$\hat{\beta}$	Equal to $\frac{\mu(1-\bar{o})}{\bar{o}(1-\mu)}$
$\hat{\gamma}$	Equal to $\hat{\beta}$ for $\mu < \bar{o}$ and equal to 1 for $\mu \geq \bar{o}$
ΔH	Relative skill of an EPS based on the difference between a point on the ROC graph and the corresponding value on the user-specific baseline

Table 7.1: Forecast model contingency matrix
Observations

		No	Yes
E	No	α	β
P	yes	γ	δ
S			

Table 7.2: User Expense Matrix
Observations

		No	Yes
E	No	α	βL
P	yes	$C\gamma$	$C\delta$
S			

Table 7.3: Predictive and Reactive vaccination costs from Parent du Châtelet et al. (2001) and derived ratios used in EROC.

	Preventive strategy	Reactive strategy	Ratio
Base case cost per case prevented	59.52	133.07	0.45
Best case cost per case prevented	23.62	63.83	0.37

Table 7.4: Locations of station observations used in the real-time simulation model skill analysis.

City	Country	Lat	Lon
Agadez	Niger	17.0°N	8.0°E
Aioun El Atrouss	Mauritania	16.7°N	9.6°W
Bamako	Mali	12.6°N	8.0°W
Bobo Dioulasso	Burkina-Fasso	11.2°N	4.3°W
Boromo	Burkina-Fasso	11.8°N	2.9°W
Bougouni	Mali	11.4°N	7.5°W
Gaoua	Burkina-Fasso	10.3°N	3.2°W
Gaya	Niger	11.9°N	3.5°E
Kano	Nigeria	12.1°N	8.5°E
Kiffa	Mauritania	16.5°N	11.4°W
Mango	Togo	10.4°N	0.5°E
Matam	Senegal	15.6°N	13.2°W
N'Djamena	Chad	12.1°N	15.0°E
Niamey	Niger	13.5°N	2.2°E
Ouagadougou	Burkina-Fasso	12.3°N	1.5°W
Ouahigouya	Burkina-Fasso	13.6°N	2.4°W
San	Mali	13.3°N	4.8°W
Tambacounda	Senegal	13.8°N	13.7°W
Tidjikja	Mauritania	18.6°N	11.4°W
Timbuktu	Mali	16.7°N	3.0°W
Wa	Ghana	10.1°N	2.5°W

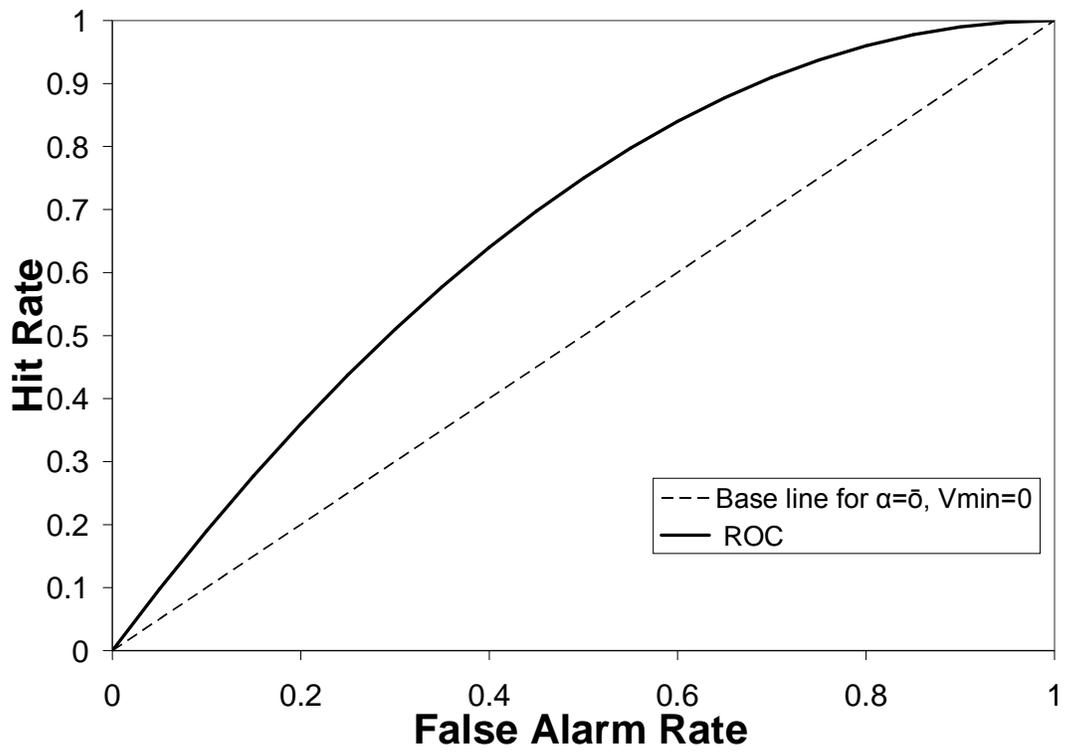


Figure 7.1: ROC Diagram based on synthetic hit-rate and false-alarm data computed from (7.24).

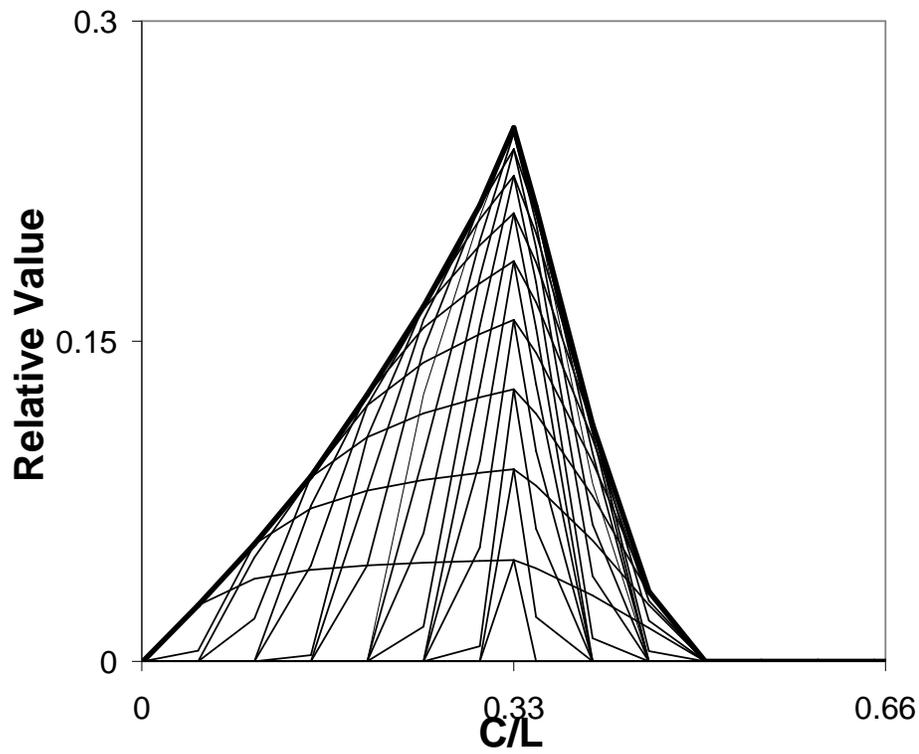


Figure 7.2: Economic value graph based on the ROC graph in Fig. 7.1.

Algorithm for the Extended ROC (EROC) Graphical Method

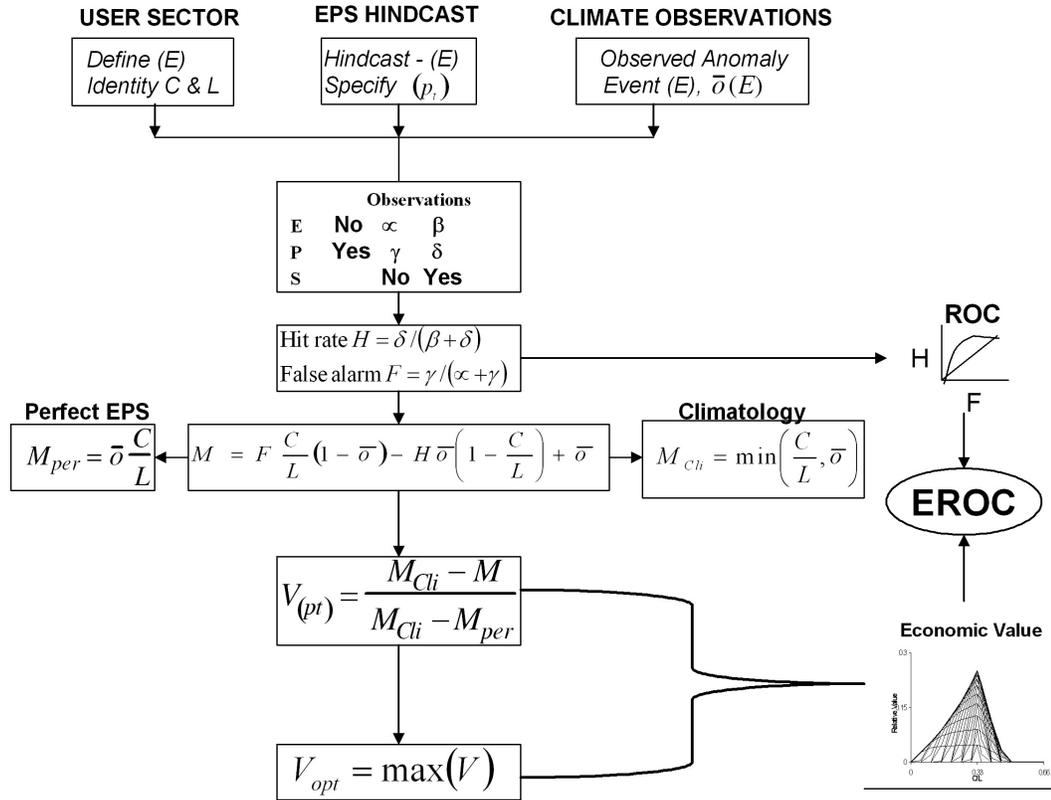


Figure 7.3: Algorithm for the EROC graphical method.

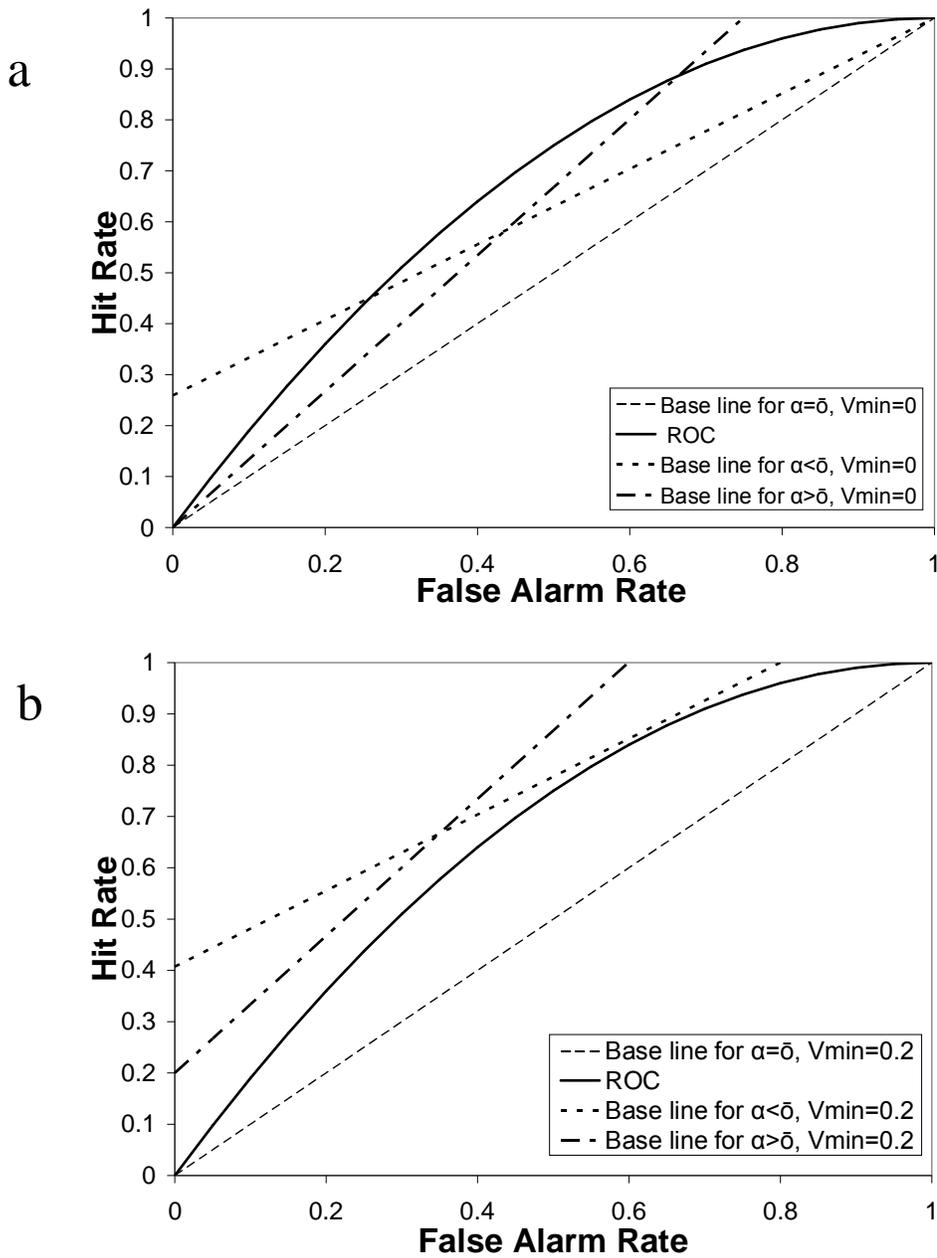


Figure 7.4: EROC diagram based on synthetic hit-rate and false-alarm data computed from (7.24): $V_{\min} =$ (a) 0 and (b) 0.2.

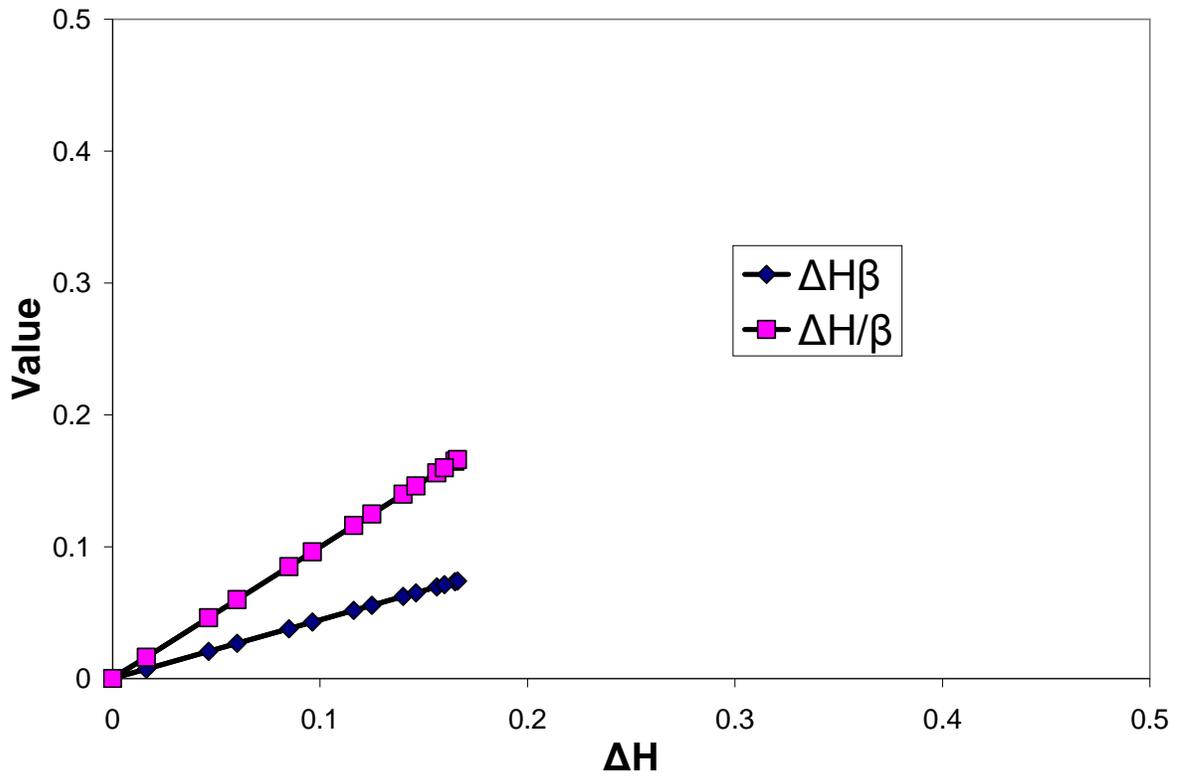


Fig. 7.5: Comparison of relationship between V and ΔH from $\Delta H\beta$ calculated in this study and $\Delta H/\beta$ from Semazzi and Mera (2006).

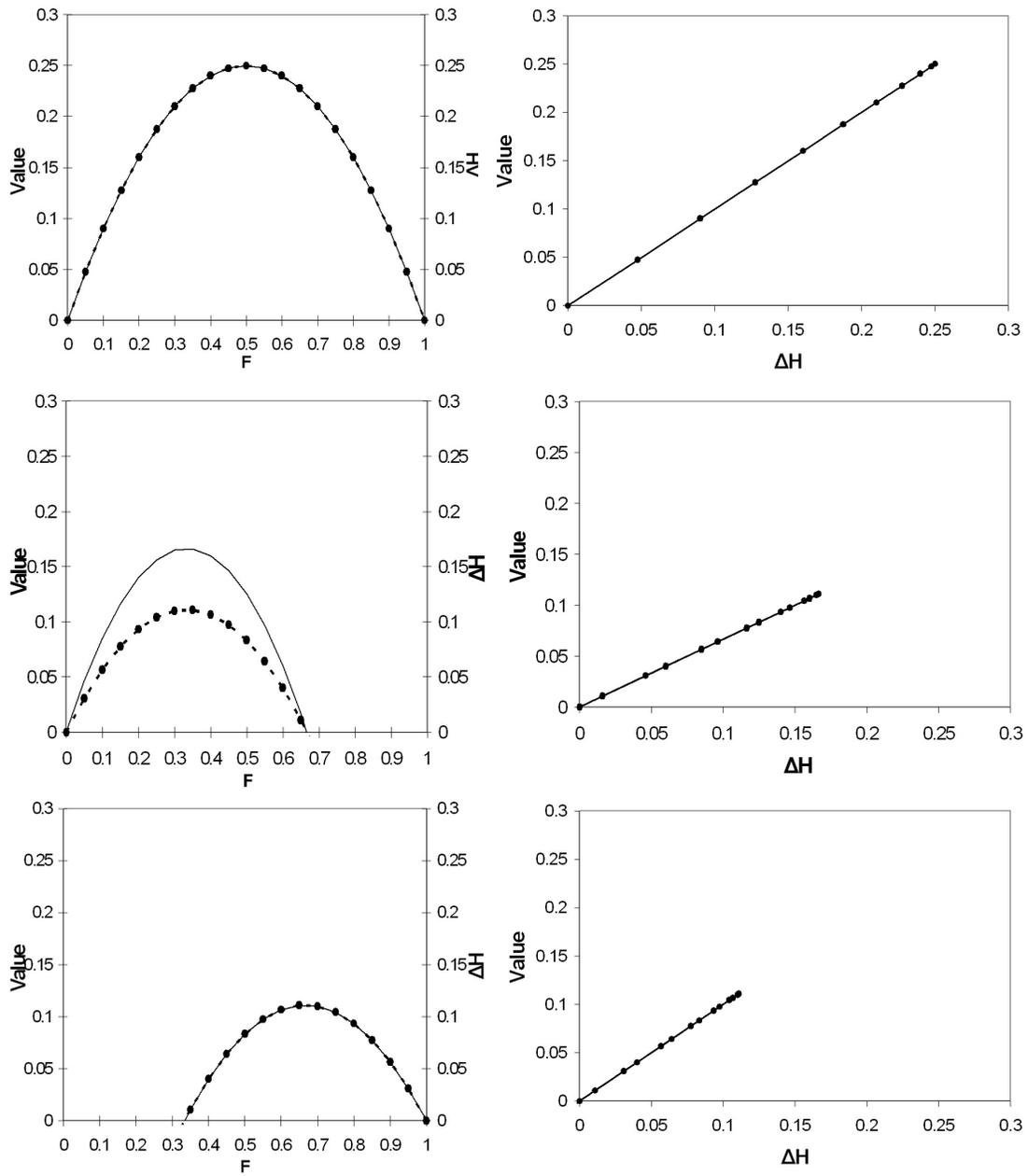


Fig. 7.6: (left) Plots of V (solid line) and ΔH (dotted line) vs. F for $\mu (=0.33) = \bar{\mu}$, $\mu (=0.25) < \bar{\mu}$, $\mu (=0.25) > \bar{\mu}$; (right) corresponding plots of value V vs ΔH .

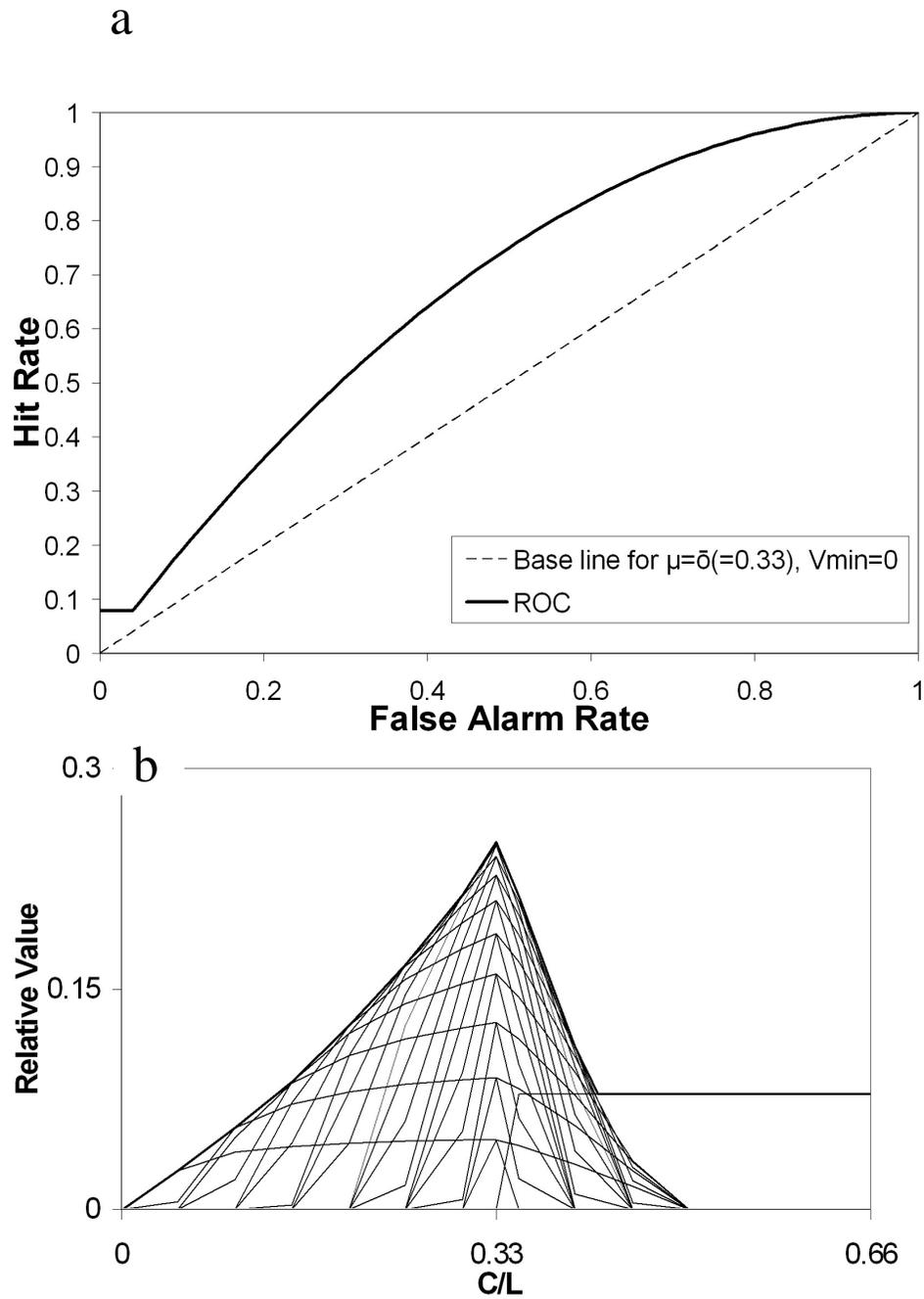


Fig. 7.7: (a) EROC graph based on modification of Fig. 4, and (b) corresponding economic value graph with forward trail.

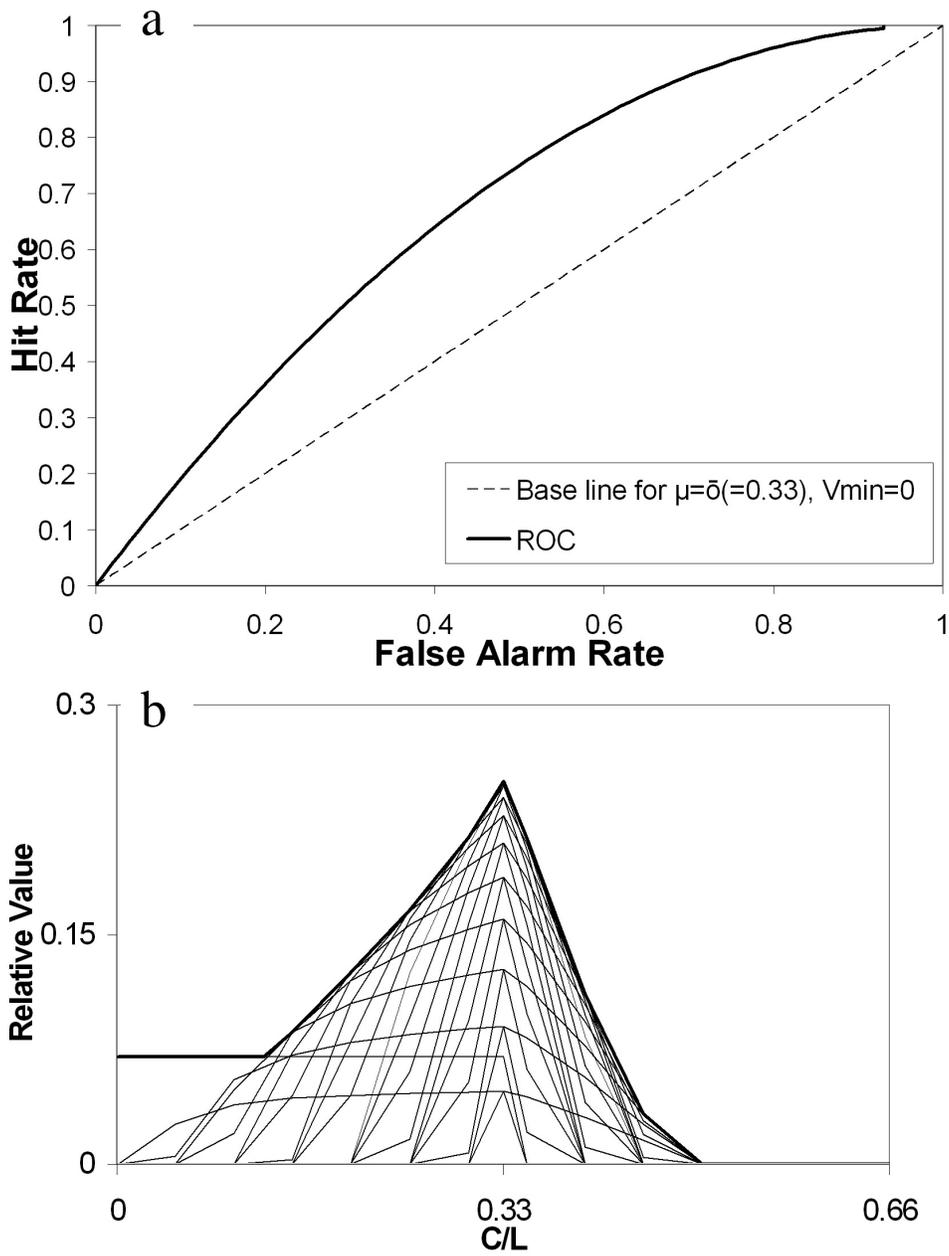


Figure 7.8: (a) EROC graph based on modification of Fig. 4, and (b) corresponding economic value graph with backward trail.

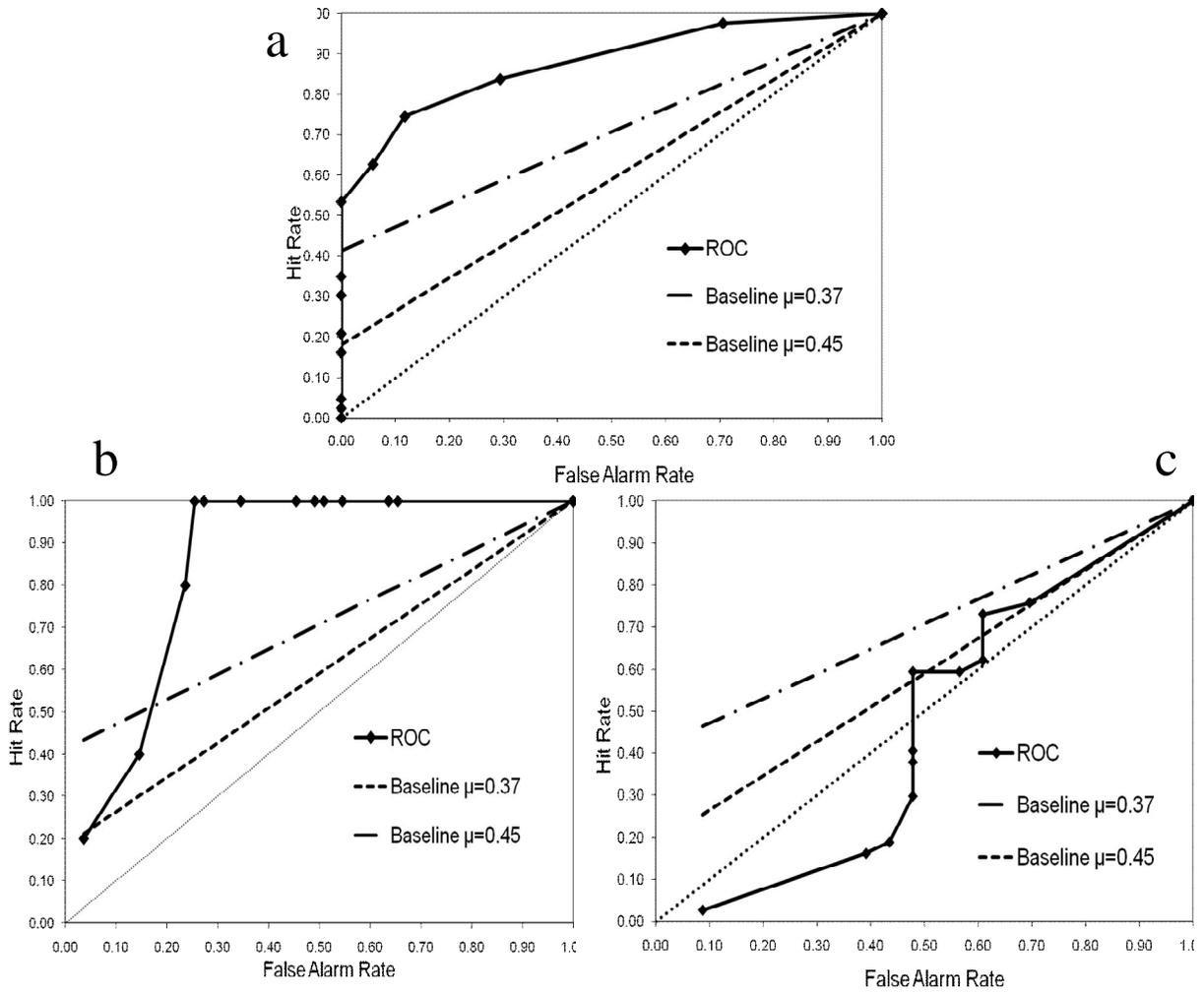


Figure 7.9: EROC plots for (a) Bamako, (b) Niamey and (c) N'Djamena.

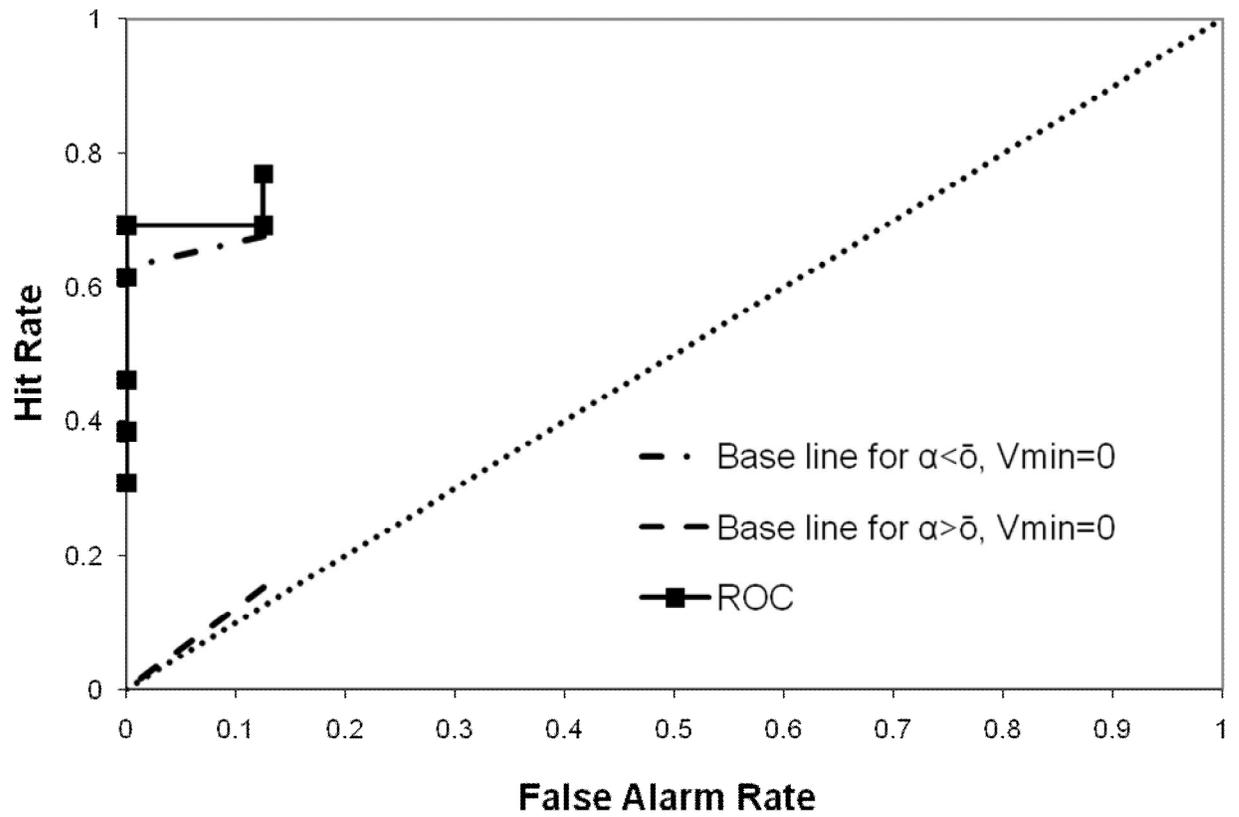


Figure 7.10: EROC graph for real-time WRF simulations of the 3-day running mean of RH40 over the stations listed in Table 7.4.

References

- Adedokun, J. A. 1978. West African Precipitation and Dominant Atmospheric Mechanisms. *Arch. Met. Geoph. Biokl., Ser. A*, **27**,289-310.
- Adeyewa, Z. Debo, Kenji Nakamura, 2003: Validation of TRMM Radar Rainfall Data over Major Climatic Regions in Africa. *J. Appl. Meteor.*, **42**, 331-347.
- Adler, Robert F., George J. Huffman, David T. Bolvin, Scott Curtis, Eric J. Nelkin, 2000: Tropical Rainfall Distributions Determined Using TRMM Combined with Other Satellite and Rain Gauge Information. *J. Appl. Meteor.*, **39**, 2007-2023.
- Adler, Robert F., and Coauthors, 2003: The Version-2 Global Precipitation Climatology Project (GPCP) Monthly Precipitation Analysis (1979–Present). *J. Hydrometeorol.*, **4**, 1147-1167
- Afiesimama, E. A., 2007: Annual cycle of the mid-tropospheric easterly jet over West Africa. *Theoretical and Applied Climatology*, **90**, 103-111
- Agustí-Panareda, A., Coauthors 2009: Radiosonde humidity bias correction over the West African region for the special AMMA reanalysis at ECMWF. *Quart. J. Roy. Meteor. Soc.*, **135**:595–617.
- American Meteorological Society, 2001: AMS Statement. Seasonal to Interannual Climate Prediction (Adopted by AMS Council 14 January 2001). *Bull. Amer. Meteor. Soc.*, **82**, 701–704.

- Ati, O. F., C. J. Stigter, and E. O. Oladipo, 2002: A comparison of methods to determine the onset of the growing season in northern Nigeria. *Int. J. Climatol.*, **22**, 731–742.
- Betts, A. K., 1986: A new convective adjustment scheme. Part I: Observational and theoretical basis. *Quart. J. Roy. Meteor. Soc.*, **112**, 677–691.
- Betts, A. K., and M. J. Miller, 1986: A new convective adjustment scheme. Part II: Single column tests using GATE wave, BOMEX, and arctic air-mass data sets. *Quart. J. Roy. Meteor. Soc.*, **112**, 693–709.
- Besancenot, J. P., M. Boko, P. C. Oke, 1997: Weather conditions and cerebrospinal meningitis in Benin (Gulf of Guinea, West Africa). *European Journal of Epidemiology* **13**: 807–815, 1997
- Bock, O., M.-N. Bouin, A. Walpersdorf, J. P. Lafore, S. Janicot, F. Guichard, and A. Agusti Panareda, 2007: Comparison of ground-based GPS precipitable water vapour to independent observations and NWP model reanalysis over Africa. *Quart. J. Roy. Meteor. Soc.*, **133**, 2011–2027.
- Breman, J. G., 2001: The ears of the Hippopotamus: Manifestations, determinants, and estimates of the malaria burden. *Amer. J. Trop. Med. Hyg.*, **64** (Suppl 1, 2), 1–11.
- Breman, J. G., M. S. Alilio, and A. Mills, 2004: Conquering the intolerable burden of malaria, what's new, what's needed: A summary. *Amer. J. Trop. Med. Hyg.*, **71**, 1-15.

- Broutin H, S. Philippon, G. Constantin de Magny, F. Courel, B. Sultan and J. F. Guegan, 2007: Comparative study of meningitis dynamics across nine African countries: a global perspective, *Int. J. Health Geo.*, **6**,29, doi:10.1186/1476-072X-6-29.
- Buckle, C., 1996: *Weather and Climate in Africa*. Longman, 312 pp.
- Buizza, R., and T. N. Palmer. 1998a: Impact of ensemble size on ensemble prediction. *Mon. Wea. Rev.*, **126**, 2503–2518.
- Buizza, R., T. Petroliaqis, T. N. Palmer, J. Barkmeijer, M. Hamrud, A. Hollingsworth, A. Simmons, and N. Wedi, 1998b: Impact of model resolution and ensemble size on the performance of an ensemble prediction system. *Quart. J. Royal Meteor. Soc.*, **124**, 1935-1960.
- Burpee, R. W. 1972. The origin and structure of easterly waves in the lower troposphere of North Africa. *J. Atmos. Sci.* **29**: 77–90.
- Chang, C. P. V. F. Morris, and J. M. Wallace, 1970: A statistical study of easterly waves in the western Pacific. *J. Atmos. Sci.*, **27**, 195–201.
- Charney, J. G., 1975: Dynamics of desert and drought in the Sahel. *Quart. J. Roy. Meteor. Soc.*, 101, 193–202.
- Chen, F., and J. Dudhia, 2001: Coupling an advanced land-surface/ hydrology model with the Penn State/ NCAR MM5 modeling system. Part I: Model description and implementation. *Mon. Wea. Rev.*, 129, 569–585.

- Chen, S.-H., and W.-Y. Sun, 2002: A one-dimensional time dependent cloud model. *J. Meteor. Soc. Japan*, 80, 99–118.
- Chou M.-D., and M. J. Suarez, 1994: An efficient thermal infrared radiation parameterization for use in general circulation models. NASA Tech. Memo. 104606, 3, 85pp
- Collins, W.D. et al., 2004: Description of the NCAR Community Atmosphere Model (CAM 3.0), NCAR Technical Note, NCAR/TN-464+STR, 226pp.
- Cook, K., 1999: Generation of the African Easterly Jet and Its Role in determining West African precipitation. *J. Climate*, 14, 1165-1184.
- de Chabalier F., M. H. Djingarey, A. Hassane and J. P. Chippaux, 2000: Meningitis seasonal pattern in Africa and detection of epidemics: a retrospective study in Niger, 1990-98. *Trans R Soc Trop Med Hyg*, **94**, 664-668.
- Dhonneur, G. 1970: General Circulation and Types of Weather Over Western and Central Africa. GATE Experimental Design Proposal Annex 11.
- Diedhiou A, Janicot S, Viltard A, de F'elice P, Laurent H. 1999. Easterly wave regimes and associated convection over West Africa and the tropical Atlantic: Results from the NCEP/NCAR and ECMWF reanalyses. *Clim. Dyn.* **15**: 795–822.
- Diggle P, Moyeed R, Rawlingson B, Thomson M. 2002: Childhood malaria in the Gambia: a case study in model-based geostatistics. *Appl Stat*, **51**, 493–506.
- Dilley, J., R. S. Chen, U. Deichmann, A. L. Lerner-Lam, and M. Arnold, 2005: Natural Disaster Hotspots: A Global Risk Analysis. The World Bank.

- Donald, A., H. Meinke, B. Power, A. H. N. Maia, M. C. Wheeler, N. White, R. C. Stone, and J. Ribbe, 2006: Near-global impact of the Madden–Julian oscillation on rainfall. *Geophys. Res. Lett.*, **33**, L09704, doi:10.1029/2005GL025155.
- Doswell, C. A. I. I. I, and E. N. Rasmussen, 1994: The effect of neglecting the virtual temperature correction on CAPE calculations. *Wea. Forecasting*, **9**, 625–629.
- Drake, V. A., and R. A. Farrow, 1988: The influence of atmospheric structure and motions on insect migration. *Ann. Rev. Entomol.*, **33**, 183–210.
- Drobinski, P., S. Bastin, S. Janicot, O. Bock, A. Dabas, P. Delville, O. Reitebuch, and B. Sultan, 2009: On the late northward propagation of the West African summer monsoon in summer 2006 in the region of Niger/Mali. *J. Geophys. Res.*, **114**, D09108, doi:10.1029/2008JD0011159.
- Du, J., S. L. Mullen, and F. Sanders, 1997: Short-range ensemble forecasting of quantitative precipitation. *Mon. Wea. Rev.*, **125**, 2427–2459.
- Dubief, J., and P. Queney, 1935: Les grands traits du climat du Sahara algérien. *La Météorologie*, 80–91.
- Dudhia, J., 1989: Numerical study of convection observed during the winter monsoon experiment using a mesoscale two-dimensional model, *J. Atmos. Sci.*, **46**, 3077–3107.

- Dudhia, J., S.-Y. Hong, and K.-S. Lim, 2008: A new method for representing mixed-phase particle fall speeds in bulk microphysics parameterizations. *J. Met. Soc. Japan*, in press.
- Dunkerton, T. J., and M. P. Baldwin, 1995: Observation of 3–6 day meridional wind oscillations over the tropical Pacific, 1973–1992: Horizontal structure and propagation, *J. Atmos. Sci.*, **52**, 1585–1601.
- Duvel, J.P., 1990: Convection over tropical Africa and the Atlantic ocean during northern summer. Part II: modulations by easterly waves. *Mon Weather Rev.* **118**, 1855-1868
- Eldridge, R. H., 1957: A synoptic study of West African Disturbance Lines. *Q. J. Roy. Meteorol. Soc.*, **83**, 303–314.
- Eltahir, E. A. B., Gong, 1996: Dynamics of wet and dry years in the West Africa. *J.Clim.* **9** 1030-1042
- Fink, A. H., and P. Knippertz, 2003: An extreme precipitation event in southern Morocco in spring 2002 and some hydrological implications. *Weather*, **58**, 377–387.
- Flamant, P. Knippertz, D. J. Parker, J.-P. Chaboureau, C. Lavaysse, A. Agusti-Panareda and L. Kergoat, 2009, The impact of a mesoscale convective system cold pool on the northward propagation of the intertropical discontinuity over West Africa. *Q. J. R. Meteorol. Soc.* **135**, 139–159.
- Flamant, C, J. P. Chaboureau, D. P. Parker, C.M. Taylor, J. P. Cammas, O. Bock, F. Timouk, J. Pelon, 2007: Airborne observations of the impact of a convective system on the

- planetary boundary layer thermodynamics and aerosol distribution in the intertropical discontinuity region of the West African Monsoon. *Q. J. R. Meteorol. Soc.* **133**, 1175–1189.
- Flaounas, E., S. Bastin, S. Janicot, 2010: Regional climate modelling of the 2006 West African monsoon: sensitivity to convection and planetary boundary layer parameterisation using WRF. *Clim Dyn.* 1432-0894
- Flohn, H., 1975: Tropische Zirkulationsformen im Lichte der Satellitenaufnahmen (Tropical circulation types as reflected in satellite imagery). *Bonner Meteorologische Abhandlungen*, No. 21, Westdeutscher Verlag, Opladen, Germany, 82 pp.
- Gallee H, Moufouma-Okia W, Bechtold P, Brasseur O, Dupays I, Marbaix P, Messenger C, Ramel R, Lebel T (2004) A highresolution simulation of a West African rainy season using a regional climate model. *J Geophys Res* **109**. doi:10.1029/2003JD004020
- Giannini, A., R. Saravanan, and P. Chang, 2003: Oceanic forcing of Sahel rainfall on interannual to interdecadal time scales. *Science*, **302**, 1027–1030.
- Gill, A. E., 1980: Some simple solutions for heat-induced tropical circulation. *Quart. J. Roy. Meteor. Soc.*, **106**, 447–462.
- Greenwood B.M., I. S. Blakebrough, A. K. Bradley, S. Wali, H. C. Whittle., 1984: Meningococcal disease and season in sub-Saharan Africa. *Lancet*, **1**, 1339-1342.
- Greenwood B., 1999: Meningococcal meningitis in Africa. *Trans R Soc Trop Med Hyg* **93**, 341–53.

- Grell, G. A., and D. Devenyi, 2002: A generalized approach to parameterizing convection combining ensemble and data assimilation techniques. *Geophys. Res. Lett.*, 29(14), Article 1693.
- Grist, J. 2002: Easterly Waves over Africa. Part I: The Seasonal Cycle and Contrasts between Wet and Dry Years. *Mon. Weath. Rev.* **130**, 197-211.
- Griffiths, J. F. and Soliman, K. H. 1972 The northern desert (Sahara). Pp. 75–132 in *World survey of climatology*. Ed. H. E. Landsberg. *Climates of Africa*, Volume 10, Elsevier, New York, USA.
- Gruber, A., 1974: The wavenumber-frequency spectra of satellite-measured brightness in the Tropics. *J. Atmos. Sci.*, **31**, 1675–1680.
- Gruber, A., A. F. Krueger, 1984: The Status of the NOAA Outgoing Longwave Radiation Data Set. *Bull. Amer. Meteor. Soc.*, **65**, 958-962.
- Gu, G. 2009. Intraseasonal variability in the equatorial Atlantic-West Africa during March–June. *Clim Dyn*, 32:457–471
- Gu G., R.F. Adler. 2004. Seasonal evolution and variability associated with the West African monsoon system. *J Clim* 17:3364–3377
- Hagos, S. M., and K. H. Cook, 2007: Dynamics of the West African monsoon jump. *J. Climate*, 20, 5264–5284.

- Hagos, and K. Cook, 2009. Development of a Coupled Regional Model and Its Application to the Study of Interactions between the West African Monsoon and the Eastern Tropical Atlantic Ocean. *J. Clim* 22: 2591-2604.
- Hall, N. M. J., G. N. Kiladis, and C. D. Thorncroft, 2006: Three dimensional structure and dynamics of African easterly waves. Part II: Dynamical modes, *J. Atmos. Sci.*, **63**, 2231–2245.
- Hamill, T. M., and J. Juras, 2006: Measuring forecast skill: Is it real skill or is it the varying climatology? *Quart. J. Roy. Meteor. Soc.*, **132**, 2905–2923.
- Hamilton, R. A., and J. W. Archbold, 1954: Meteorology of Nigeria and adjacent territory. *Q. J. Roy. Meteor. Soc.*, 71, 231-264.
- Hanley J. A., and B. J. McNeil, 1982: The meaning and use of the area under a receiver operating characteristic (ROC) curve. *Radiology*, **143**, 2936.
- Hanley J. A. and B. J. McNeil, 1983: A method of comparing the areas under Receiver Operating Characteristic curves derived from the same cases. *Radiology*, **148**, 839-43.
- Harvey, L. O., Jr., K. R. Hammond, C. M. Lusk, and E. F. Mross, 1992: The application of signal detection theory to weather forecasting behavior. *Mon. Wea. Rev.*, **120**, 863-883.
- Hare, F. K., 1977: Takoradi-Khartoum air route: General synoptic climate. *Climatic Change*, 1, 157-172.
- Hastenrath, S., 1995: *Climate Dynamics of the Tropics*. Kluwer, 488 pp.

- Hodges, K. I., and C. D. Thorncroft, 1997: Distribution and statistics of African mesoscale convective weather systems based on the ISCCP Meteosat imagery. *Mon. Wea. Rev.*, **125**, 2821–2837.
- Holton, J. R., 2004: *An Introduction to Dynamic Meteorology*, 4th ed., 535 pp., Elsevier Academic, Burlington, Mass
- Hong, S.-Y., and H.-L. Pan, 1996: Nonlocal boundary layer vertical diffusion in a medium-range forecast model, *Mon. Wea. Rev.*, **124**, 2322–2339.
- Hong, S.-Y., J. Dudhia, and S.-H. Chen, 2004: A Revised Approach to Ice Microphysical Processes for the Bulk Parameterization of Clouds and Precipitation, *Mon. Wea. Rev.*, **132**, 103–120.
- Hong, S.-Y., and J.-O. J. Lim, 2006: The WRF Single-Moment 6-Class Microphysics Scheme (WSM6), *J. Korean Meteor. Soc.*, **42**, 129–151.
- Hong, S.-Y., and H.-L. Pan, 1996: Nonlocal boundary layer vertical diffusion in a medium-range forecast model, *Mon. Wea. Rev.*, **124**, 2322–2339.
- M. E. McIntyre, and A. W. Robertson, 1985: On the use and significance of isentropic potential vorticity maps. *Quart. J. Roy. Meteor. Soc.*, **111**, 877–946.
- Hoskins, B. J., I. N. James, and G. H. White, 1983: The shape, propagation and mean-flow interaction of large-scale weather systems. *J. Atmos. Sci.*, **40**, 1595–1612.
- Hoskins, B. J., and T. Ambrizzi, 1993: Rossby wave propagation on a realistic longitudinally varying flow. *J. Atmos. Sci.*, **50**, 1661–1671.

- Hoskins, B. J., and G.-Y. Yang. 2000: The equatorial response to higher-latitude forcing, *J. Atmos. Sci.*, **57**, 1197 – 1213, doi:10.1175/1520-0469(2000)057<1197:TERTHL>2.0.CO;2.
- Houtekamer, P. L., and J. Derome, 1995: Methods for ensemble prediction. *Mon. Wea. Rev.*, **123**, 2181–2196.
- Houze, R. A. and A. K. Betts, 1981: Convection in GATE. *Rev. Geophys. Space Phys.*, **19**, 541–576.
- Hsieh J.-S., Cook K. H. 2005. Generation of African easterly wave disturbances: Relationship to the African easterly jet. *Mon. Weather Rev.* 133: 1311–1327.
- Hsu, H.-H., and S.-H. Lin, 1992: Global teleconnections in the 250- mb streamfunction field during the Northern Hemisphere winter. *Mon. Wea. Rev.*, **120**, 1169–1190.
- Huffman, G. J., R. F. Adler, B. R. Rudolf, U. Schneider, and P. R. Keehn, 1995: Global precipitation estimates based on a technique for combining satellite-based estimates, rain gauge analysis, and NWP model precipitation information. *J. Climate*, **8**:1284–1295.
- Huffman, George J., and Coauthors, 2007: The TRMM Multisatellite Precipitation Analysis (TMPA): Quasi-Global, Multiyear, Combined-Sensor Precipitation Estimates at Fine Scales. *J. Hydrometeorol.*, **8**, 38-55.
- Jalihal, D., and L.W. Nolte 1994: Signal detection theory and reconstruction algorithms-performance for images in noise. *IEEE Trans. on Biomed. Eng.*, **41**, 501-4.

- Janicot, S., 1992: Spatiotemporal variability of West African rainfall. Part I: Regionalizations and typings. *J. Climate*, **5**, 489–497.
- Janicot, S., and B. Sultan, 2001a: Intra-seasonal modulation of convection in the West African monsoon. *Geophys. Res. Lett.*, **28**, 523–526.
- Janicot, S., S. Trzaska, and I. Pocard, 2001b: Summer Sahel-ENSO teleconnection and decadal time scale SST variations. *Climate Dyn.*, **18**, 303–320.
- Janicot, S., F. Mounier, N. M. J. Hall, S. Leroux, B. Sultan, G. N. Kiladis, 2009: Dynamics of the West African Monsoon. Part IV: Analysis of 25–90-Day Variability of Convection and the Role of the Indian Monsoon. *J. Climate*, **22**, 1541–1565
- Janjic, Z. I., 1990: The step-mountain coordinate: physical package, *Mon. Wea. Rev.*, **118**, 1429–1443.
- Janjic, Z. I., 1994: The step-mountain eta coordinate model: further developments of the convection, viscous sublayer and turbulence closure schemes, *Mon. Wea. Rev.*, **122**, 927–945.
- Janjic, Z. I., 1996: The surface layer in the NCEP Eta Model, *Eleventh Conference on Numerical Weather Prediction*, Norfolk, VA, 19–23 August; Amer. Meteor. Soc., Boston, MA, 354–355.
- Janjic, Z. I., 2000: Comments on "Development and Evaluation of a Convection Scheme for Use in Climate Models", *J. Atmos. Sci.*, **57**, p. 3686.

- Janjic, Z. I., 2002: Nonsingular Implementation of the Mellor–Yamada Level 2.5 Scheme in the NCEP Meso model, *NCEP Office Note*, No. 437, 61 pp.
- Jeffreys, H., 1926: On the dynamics of geostrophic winds. *Quart. J. Roy. Meteor. Soc.*, **52**, 85–104.
- Juras, J., 2000: Comments on “probabilistic predictions of precipitation using the ECMWF ensemble prediction system.” *Wea. Forecasting*, **15**, 365-366.
- Kain, J. S., and J. M. Fritsch, 1990: A one-dimensional entraining/ detraining plume model and its application in convective parameterization, *J. Atmos. Sci.*, **47**, 2784–2802.
- Kain, J. S., and J. M. Fritsch, 1993: Convective parameterization for mesoscale models: The Kain-Fritsch scheme, The representation of cumulus convection in numerical models, K. A. Emanuel and D.J. Raymond, Eds., Amer. Meteor. Soc., 246 pp.
- Kain, J. S., 2004: The Kain-Fritsch convective parameterization: An update. *J. Appl. Meteor.*, **43**, 170–181.
- Kalnay, E., and Coauthors, 1996: The NCEP/NCAR 40-Year Reanalysis Project. *Bull. Amer. Meteor. Soc.*, **77**, 437–471.
- Kessler, E., 1969: On the distribution and continuity of water substance in atmospheric circulation, *Meteor. Monogr.*, **32**, Amer. Meteor. Soc., 84 pp.
- Kharin, V. V., and F. W. Zwiers, 2003: On the ROC score of probability forecasts. *J. Climate*, **16**, 4145–4150.

- Kheshgi, H. S., and B. S. White, 2001: Testing distributed parameter hypotheses for the detection of climate change. *J. Climate*, **14**, 3464–3481.
- Kiladis, G. N., and K. M. Weickmann, 1992b: Extratropical forcing of tropical Pacific convection during northern winter. *Mon. Wea. Rev.*, **120**, 1924–1938.
- Kiladis, G. N., and K. M. Weickmann Extratropical forcing of tropical Pacific convection during northern winter. *Mon. Wea. Rev.*, **120**, 1924–1938.
- Kiladis, G. N., and S. B. Feldstein, 1994: Rossby wave propagation into the tropics in two GFDL general circulation models. *Climate Dyn.*, **9**, 245–252.
- Kiladis, G. N., and M. Wheeler, 1995: Horizontal and vertical structure of observed tropospheric equatorial Rossby waves. *J. Geophys. Res.*, **100**, 22 981–22 997.
- Kiladis, G. N., and K. M. Weickmann, 1997: Horizontal structure and seasonality of large-scale circulations associated with tropical convection. *Mon. Wea. Rev.*, **125**, 1997–2013.
- Kiladis, G. N. 1998: Observations of Rossby waves linked to convection over the eastern tropical Pacific, *J. Atmos. Sci.*, **55**, 321 – 339.
- Kiladis, G. N., C. D. Thorncroft, and N. M. J. Hall, 2006: Three-Dimensional Structure and Dynamics of African Easterly Waves. Part I: Observations, *J. Atmos. Sci.*, **63**, 2212-2230.
- Kiladis, G. N., M. C. Wheeler, P. T. Haertel, and P. E. Roundy, 2009: Convectively coupled equatorial waves, *Rev. Geophys.* **47**, RG2003, doi:10.1029/2008RG000266

- Kistler, R., et al., 2001: The NCEP-NCAR 50-Year Reanalysis: Month Means CD-ROM and Documentation. *Bulletin of the American Meteorological Society*, 82 (2), 247–268
- Klemp, J. B., W. C. Skamarock, and J. Dudhia, 2007: Conservative split-explicit time integration methods for the compressible nonhydrostatic equations. *Mon. Wea. Rev.*, accepted..
- Knippertz, P., 2004: A Simple Identification Scheme for Upper-Level Troughs and Its Application to Winter Precipitation Variability in Northwest Africa. *J. Climate*, 17, 1411–1418.
- Knippertz, P., and J. E. Martin, 2005: Tropical plumes and extreme precipitation in subtropical and tropical West Africa. *Quart. J. Roy. Meteor. Soc.*, **131**, 2337–2365.
- Knippertz, P., 2005: Tropical–extratropical interactions associated with an Atlantic tropical plume and subtropical jet streak. *Mon. Wea. Rev.*, **133**, 2759–2776.
- Knippertz, P. and Fink, A. H. 2006. Synoptic and dynamic aspects of an extreme springtime Saharan dust outbreak. *Quart. J. R. Meteorol. Soc.* **132**, 1153–1177.
- Knippertz and A. H. Fink, 2008: Dry-season precipitation in tropical West Africa and its relation to forcing from the extratropics. *Mon. Wea. Rev.*, 136 (9), 3579–3596
- Knippertz and A. H. Fink, 2009: Prediction of Dry-Season Precipitation in Tropical West Africa and its Relation to Forcing from the Extratropics. *Weather and Forecasting*.
- Konare, K. 2009: Evaluation of the socio-economic benefits of weather and climate services (the Health sector). *Third MERIT Technical Meeting*. Niamey, Niger.

- Kong, K.-Y., 2006: Understanding the genesis of Hurricane Vince through the surface pressure tendency equation. Preprints, *27th Conf. on Hurricanes and Tropical Meteorology*, Monterey, CA, Amer. Meteor. Soc., 9B.4. [Available online at <http://ams.confex.com/ams/pdfpapers/108938.pdf>.]
- Kuettner, J. P., and D. E. Parker, 1976: GATE: report of the field phase. *Bull. Amer. Met. Soc.*, **57**, 11-27.
- Kummerow, Christian, William Barnes, Toshiaki Kozu, James Shiue, Joanne Simpson, 1998: The Tropical Rainfall Measuring Mission (TRMM) Sensor Package. *J. Atmos. Oceanic Technol.*, **15**, 809-817.
- Kummerow and Coauthors, 2000: The status of the Tropical Rainfall Measuring Mission (TRMM) after two years in orbit. *J. Appl. Meteor.*, **39**, 1965–1982.
- Laing AG, Fritsch JM. 1993. Mesoscale convective complexes in Africa. *Mon. Weather Rev.* **121**: 2254–2263.
- Laing, A. G., Carbone, R. E., Levizzani, V., Tuttle, J. D., 2008: The propagation and diurnal cycles of deep convection in northern tropical Africa. *Quarterly Journal of the Royal Meteorological Society*, **134**, doi: 10.1002/qj.194, 93-109.
- Laman, D. M.; Wieneke, G. H, van Duijn H, Veldhuizen, R. J, van Huffelen, A. C., 2005: QEEG Changes During Carotid Clamping in Carotid Endarterectomy: Spectral Edge Frequency Parameters and Relative Band Power Parameters. *J. of Clinical Neurophysiology*. **22(5.4)**, 244-252.

- Lamb, P. J., 1978a: Large-scale tropical surface circulation patterns associated with sub-Saharan weather anomalies. *Tellus*, **30**, 240–251.
- Lamb, P. J., 1978b: Case studies of tropical Atlantic surface circulation patterns during recent sub-Saharan weather anomalies: 1967 and 1968. *Mon. Wea. Rev.*, **106**, 482–491.
- Lamb and R. A. Pepler, 1990: West Africa. Teleconnections: Linkages between ENSO, Worldwide Climate Anomalies, and Societal Impacts, M. H. Glantz, R. W. Katz, and N. Nicholls, Eds. Cambridge University Press, 121–189.
- Lapeyssonnie L. La méningite cérébro-spinale en Afrique, 1963: *Bull World Health Organ.* **28**(Suppl 1), 3–114.
- Lebel, T., J. D. Taupin, and N. D'Amato, 1997: Rainfall monitoring during HAPEX-Sahel: 1. General rainfall conditions and climatology. *J. Hydrol*, **188–189**:74–96.
- Le Barbe', L., T. Lebel, and D. Tapsoba, 2002: Rainfall variability in West Africa during the years 1950– 90. *J. Clim.*, **15**, 187– 202.
- Lélé, M.I., and P.J.Lamb, 2010. Variability of InterTropical Front (ITF) and Rainfall over West African Soudano-Sahel. *J. Clim.*. *In press*.
- Leroux, M., 1983a: *Le climat de l'Afrique tropicale*. Vol. 1. Champion-Slatkine, 636 pp.
- Leroux, M., 1983b: *Le climat de l'Afrique tropicale*. Vol. 2. Champion-Slatkine, 24 pp, with 250 plates.
- Leroux, M. 2001: *The Meteorology and Climate of Tropical Africa*. Springer, 493 pp.

- Lezine, A. M., and J. Casanova, 1991: Correlated oceanic and continental records demonstrate past climate and hydrology of North Africa (0–140 ka). *Geology*, **19**, 307–310.
- Lin, Y.-L., R. D. Farley, and H. D. Orville, 1983: Bulk parameterization of the snow field in a cloud model. *J. Climate Appl. Meteor.*, **22**, 1065–1092.
- Lin Y-L, Robertson KE, Hill CM. 2005. Origin and propagation of a disturbance associated with an African easterly wave as a precursor of Hurricane Alberto (2000). *Mon. Weather Rev.* **133**: 3276–3298.
- Lindzen, R. S., 1967: Planetary waves on beta planes. *Mon. Wea. Rev.*, **95**, 441–451.
- Lindzen, R. S., and A. Y. Hou, 1988: Hadley circulations for zonally averaged heating centered off the equator. *J. Atmos. Sci.*, **45**, 2416–2427.
- Madden, R. A. and P.R. Julian. 1994. Observations of the 40–50-day tropical oscillation—A review. *Monthly Weather Review* **122** (5): 814–37.
- Magaña, V., and M. Yanai, 1995: Mixed Rossby–gravity waves triggered by lateral forcing. *J. Atmos. Sci.*, **52**, 1473–1486.
- Maiga, I. H., 2005: Rôle du climat sur la dynamique des populations acridiennes au Sahel: Influence de la mousson sur l’écologie du criquet Sénégalais. Proc. AMMA-CIRAD Workshop, CERAAS, Thiès, Sénégal.
- Mak, M. K., 1969: Laterally driven stochastic motions in the tropics. *J. Atmos. Sci.*, **26**, 41–64.

- Marzban, C. 2004: The ROC curve and its area under it as performance measures. *Wea. Forecasting*, **19**, 1106-1114.
- Mason, I., 1982: A model for assessment of weather forecasts. *Aust. Meteor. Mag.*, **30**, 291–303.
- Mason, S. J., and N. E. Graham, 2002: Areas beneath the relative operating characteristics (ROC) and levels (ROL) curves: statistical significance and interpretation. *Quart J. Roy. Meteor. Soc.*, **128**, 2145-2166.
- Mason, S. J., L. Goddard, N. E. Graham, E. Yulaeva, L. Sun, and P. A. Arkin, 1999: The IRI seasonal climate prediction system and the 1997/98 El Niño event. *Bull. Amer. Meteor. Soc.*, **80**, 1853–1873.
- Matthews, M., 2004: Intraseasonal variability over tropical Africa during northern summer, *J. Clim., J. Climate*, **17**, 2427–2440.
- Mathon, V. and H. Laurent. 2001. Life cycle of the Sahelian mesoscale convective cloud systems. *Quart. J. Roy. Meteor. Soc.* 127:377–406.
- Mathon, V., H. Laurent, T. Lebel, 2002: Mesoscale Convective System Rainfall in the Sahel. *J. Appl. Meteor.*, 41, 1081-1092.
- Matsuno, T., 1966: Quasi-geostrophic motions in the equatorial area. *J. Meteor. Soc. Japan*, **44**, 25–43.
- McGuirk, J. P., A. H. Thompson, and J. R. Schaefer, 1988: An eastern Pacific tropical plume. *Mon. Wea. Rev.*, **116**, 2505–2521.

- McNeil, B. J., and S.J. Adelstein, 1976: Determining the value of diagnostic and screening tests. *J. of Nuclear Medicine*, **17**, 439-448.
- Meehl, G. A., G. N. Kiladis, K. M. Weickmann, M. Wheeler, D. S. Gutzler, and G. P. Compo, 1996: Modulation of equatorial subseasonal convective episodes by tropical–extratropical interaction in the Indian and Pacific Ocean regions. *J. Geophys. Res.*, **101**, 15 033–15 049.
- Mejia, J. F., J. Murillo, J. M. Galvez, M. W. Douglas. 2006: Accuracy of the NCAR Global Tropospheric Analysis (FNL) over Central South America based upon upper air observations collected during the SALJEX. Proceedings of 8 ICSHMO, Foz do Iguaçu, Brazil, April 24-28, 2006, INPE, p. 1759-1764.
- Mekonnen, A., 2006: The role of Kelvin wave activity on convection and rainfall over tropical Africa. Preprints, *27th Conf. on Hurricanes and Tropical Meteorology*, Monterey, CA, Amer. Meteor. Soc., 4D.2. [Available online at <http://ams.confex.com/ams/pdfpapers/108508.pdf>.]
- Mekonnen, A., C. D. Thorncroft, A. R. Aiyyer, and G. N. Kiladis. 2008: Convectively coupled Kelvin waves over tropical Africa during the boreal summer: Structure and variability, *J. Clim.*, 21, 6649–6667.
- Mitchell, T., and J. M. Wallace, 1992: The annual cycle in equatorial convection and sea surface temperature. *J. Climate*, 5, 1140–1156.

- Mlawer, E. J., S. J. Taubman, P. D. Brown, M. J. Iacono, and S. A. Clough, 1997: Radiative transfer for inhomogeneous atmosphere: RRTM, a validated correlated-k model for the longwave. *J. Geophys. Res.*, 102 (D14), 16663–16682.
- Mohr, K.I., 2004: Interannual, Monthly, and Regional Variability in the Wet Season Diurnal Cycle of Precipitation in Sub-Saharan Africa. *J. Climate*, **17**, 2441–2453.
- Molesworth, A. M., 2003: Environmental risk and meningitis epidemics in Africa. RESEARCH Emerging Infections Diseases, 9, 1287-1293.
- Moncrieff, M. W., M. A. Shapiro, J. M. Slingo and F. Molteni, 2007: Collaborative research at the intersection of weather and climate. *WMO Bulletin*, **56** (3), 204-211.
- Mounier, F., G. N. Kiladis, and S. Janicot, 2007: Analysis of the dominant mode of convectively coupled Kelvin waves in the West African monsoon. *J. Climate*, **20**, 1487–1503.
- Mounier, F., S. Janicot, and G. N. Kiladis, 2008: The West African monsoon dynamics. Part III: The quasi-biweekly zonal dipole. *J. Climate*, **21**, 1911–1928.
- Molesworth, A. M., 2003: Environmental risk and meningitis epidemics in Africa. RESEARCH Emerging Infections Diseases, 9, 1287-1293.
- Moore, P. S., 1992: Meningococcal meningitis in Sub-Saharan Africa – A Model for the epidemic process. *Clin. Infect. Diseases*, 14, 515-525.

- Mullen, S. L., and D. P. Baumhefner, 1988: Sensitivity to numerical simulations of explosive oceanic cyclogenesis to changes in physical parameterizations. *Mon. Wea. Rev.*, **116**, 2289–2329.
- Mylne, K. R., 1999: *The use of forecast value calculations for optimal decision making using probability forecasts*. Preprints, 17th Conf. on Weather Analysis and Forecasting, Denver, CO, Amer. Meteor. Soc., 235239.
- Neelin, J. D., and I. M. Held, 1987: Modeling tropical convergence based on the moist static energy budget. *Mon. Wea. Rev.*, **115**, 3–12.
- Newell, R. E., and J. E. Kidson, 1984: African mean wind changes between Sahelian wet and dry periods. *J. Climatol.*, **4**, 27–33.
- Nguyen, H. and J. P. Duvel: 2008, Synoptic wave perturbations and convective systems over equatorial Africa. *J. Clim.*, **21**, 6372–6388.
- Nicholson, S. E., 1978: Climatic variations in the Sahel and other African regions during the past five centuries. *J. Arid Environ.*, **1**, 3–24.
- Nicholson, S. E., 1981: Rainfall and atmospheric circulation during drought periods and wetter years in West Africa. *Mon. Wea. Rev.*, **109**, 2191–2208.
- Nicholson, S.E., J.P. Grist. 2003. The Seasonal Evolution of the Atmospheric Circulation over West Africa and Equatorial Africa. *J. of Climate*. **16**: 1013-1030.
- Nicholson, S.E., P.J. Webster. 2007. A physical basis for the interannual variability of rainfall in the Sahel. *Q. J. R. Meteorol. Soc.* **133**: 2065–2084

- Nicholson SE, Webster PJ. 2008. A physical basis for the interannual variability of rainfall in the Sahel. *Quarterly Journal of the Royal Meteorological Society* 133: 2065–2084.
- Nigam, Sumant, Chul Chung, Eric DeWeaver, 2000: ENSO Diabatic Heating in ECMWF and NCEP–NCAR Reanalyses, and NCAR CCM3 Simulation. *J. Climate*, **13**, 3152-3171
- Noh, Y., W.G. Cheon, S.-Y. Hong, and S. Raasch, 2003: Improvement of the K-profile model for the planetary boundary layer based on large eddy simulation data. *Bound.-Layer Meteor.*, 107, 401–427.
- Okumura, Y. and S. Xie 2004: Interaction of the Atlantic equatorial cold tongue and the African monsoon. *J.Clim.* 17 3589-3601.
- Omosho, B., A.A. Balogun, K. Ogunjobi. 2000: Predicting monthly and seasonal rainfall, onset and cessation of the rainy season in West Africa using only surface data. *Int. J. Climatol.* **20**, 865–880.
- Palmer, T. N., C. Brankovic and D. S. Richardson, 2000: A PROVOST probability and decision-model analysis of PROVOST seasonal multi-model ensemble integrations. *Quart J. Roy. Meteor. Soc.*, **126**, 2013-2034.
- Pandya, R. and coauthors, 2009: Short-term weather forecasts to help allocate meningitis vaccine. *Third MERIT Technical Meeting*. Niamey, Niger.
- Panofsky, H., 1956: *Introduction to Dynamic Meteorology*. The Pennsylvania State University, 243 pp.

- Parent du Châtelet, I., B. D. Gessner and A. da Silva. 2001: Comparison of cost-effectiveness of preventive and reactive mass immunization campaigns against meningococcal meningitis in West Africa: a theoretical modeling analysis. *Vaccine*, **19**, 3420–3431
- Parker, D. J., Thorncroft, C. D., Burton, R., and Diongue, A., 2005a: Analysis of the African easterly jet using aircraft observations from the JET2000 experiment. *Q. J. R. Meteorol. Soc.*, **131**, 1461-1482
- Parker, D. J., R. R. Burton, A. Diongue-Niang, R. J. Ellis, M. Felton, C. M. Taylor, C. D. Thorncroft, P. Bessemoulin and A. M. Tompkins. 2005b: The diurnal cycle of the West African monsoon circulation. *Q. J. R. Meteorol. Soc.*, **131**, 2839–2860.
- Parker D.J., Fink A, Janicot S, Ngamini J-B, Douglas M, Afiesimama E, Agusti-Panareda A, Beljaars A, Dide F, Diedhiou A, Lebel T, Polcher J, Redelsperger J-L, Thorncroft CD, Wilson GA. 2008. The AMMA radiosonde program and its implications for the future of atmospheric monitoring over Africa. *Bull. Am. Meteorol. Soc.* **89**, 1015–1027.
- Pires, P., J.-L. Redelsperger, and J.-P. Lafore, 1997: Equatorial atmospheric waves and their association to convection. *Mon. Wea. Rev.*, **125**, 1167–1184.
- Pospichal, B., D.B. Karam, S. Crewell, C. Flamant, A. Hunerbein, O. Bock and F. Said. 2009. Diurnal cycle of the intertropical discontinuity over West Africa analysed by remote sensing and mesoscale modeling. *Quarterly Journal of the Royal Meteorological Society*, DOI: 10.1002/qj.435.

- Ramel R, Gallée H, Messenger C. 2006. On the northward shift of the West African monsoon. *Clim. Dyn.* 26(4): 429–440.
- Redelsperger J-L et al, 2002. Multi-scale description of a sahelian synoptic weather system representative of the West African monsoon. *Q J R Meteorol Soc* 128:1229–1257.
- Redelsperger, J-L., C. D. Thorncroft, A. Diedhiou, T. Lebel, D. J. Parker, and J. Polcher, 2006: African Monsoon Multidisciplinary Analysis: An international research project and field campaign. *Bull. Amer. Meteor. Soc.*, **87**:1739–1746.
- Reed, R. J., and E. E. Recker, 1971: Structure and properties of synoptic-scale wave disturbances in the equatorial western Pacific, *J. Atmos. Sci.*, **28**, 1117–1133,
- Reed, R. J., D. C. Norquist, and E. E. Recker 1977: The structure and properties of African wave disturbances as observed during phase III of GATE, *Mon. Weather Rev.*, 105, 317–333.
- Richman, M. B., 1986: Rotation on principal component. *J. Climatol.*, **6**, 293–335.
- Richardson, D. S., 2000a: Skill and economic value of the ECMWF ensemble prediction system. *Quart J. Roy. Meteor. Soc.*, **126**, 649-668.
- Richardson, D. S., 2000b: Applications of costloss models. *Proc. Seventh ECMWF Workshop on Meteorological Operational Systems*, Reading, United Kingdom, ECMWF, 209213.

- Richardson, D. S., 2001: Measures of skill and value of ensemble prediction systems, their interrelationship and the effect of ensemble size. *Quart J. Roy. Meteor. Soc.*, **127**, 2473-2489.
- Roebber, P. J., and L. F. Bosart, 1996: The complex relationship between forecast skill and forecast value: A real world analysis. *Wea. Forecasting*, **11**, 544–559.
- Rodwell, M.J. and B.J. Hoskins, 2001: Subtropical anticyclones and summer monsoons. *J. of Climate*, **14**, 3192–3211.
- Rodwell, M.J. and B.J. Hoskins, 1996: Monsoons and the dynamics of deserts. *Quart. J. Roy. Meteor. Soc.*, **122**, 1385–1404.
- Roffey, J., and J. I. Magor, 2003: Desert locust population dynamics parameters. FAO Desert Locust Technical Series No. AGP/DL/TS/30, Rome.
- Ross, Robert S., T. N. Krishnamurti, S. Pattnaik, A. Simon, 2009: Energy Transformation and Diabatic Processes in Developing and Nondeveloping African Easterly Waves Observed during the NAMMA Project of 2006. *Weather and Forecasting*, **24**, 1524-1548
- Roundy, P.E. and W. M. Frank, 2004: A climatology of waves in equatorial region. *J. Atmos. Sci.*, **61**, 2105–2132.
- Rowell, D. P., and J. R. Milford, 1993: On the generation of African squall lines. *J. Climate*, **6**, 1181–1193.

- Rowell, D. P., C. K. Folland, K. Maskell, and M. N. Ward, 1995: Variability of summer rainfall over tropical North Africa (1906–1992): Observations and modeling. *Quart. J. Roy. Meteor. Soc.*, **121**, 669–704.
- Rowell, D. P., 2001: Teleconnections between the tropical Pacific and the Sahel. *Quart. J. Roy. Meteor. Soc.*, **127**, 1683–1706.
- Rutledge, S. A., and P. V. Hobbs, 1984: The mesoscale and microscale structure and organization of clouds and precipitation in midlatitude cyclones. XII: A diagnostic modeling study of precipitation development in narrow cloud-frontal rainbands. *J. Atmos. Sci.*, **20**, 2949–2972.
- Sijikumar S, Roucou P, Fontaine B. 2006. Monsoon onset over Sudan-Sahel: Simulation by the regional scale model MM5. *Geophys. Res. Lett.* **33**: L03814. doi:10.1029/2005GL024819.
- Simmons, A. J. 2006: Observations, assimilation and the improvement of global weather prediction – some results from operational forecasting and ERA-40. *Predictability of Weather and Climate*, pp 459–488, Palmer TN and Hagedorn R (eds). Cambridge University Press.
- Skamarock, W. C., and J. B. Klemp, 2007: A time-split nonhydrostatic atmospheric model for research and NWP applications. *J. Comp. Phys.*, special issue on environmental modeling. Accepted

- Skamarock, W. C., 2006: Positive-Definite and Monotonic Limiters for Unrestricted-Timestep Transport Schemes. *Mon. Wea. Rev.*, 134, 2241-2250.
- Skamarock, W. C., J. B. Klemp, J. Dudhia, D. O. Gill, D. M. Barker, W. Wang, and J. G. Powers, 2005: A description of the Advanced Research WRF Version 2. NCAR Tech Notes-468+STR
- Skamarock, W. C., 2004: Evaluating Mesoscale NWP Models Using Kinetic Energy Spectra. *Mon. Wea. Rev.*, 132, 3019-3032.
- Skamarock W. C. and M. L. Weisman, 2008: The impact of positive-definite moisture transport on NWP precipitation forecasts, *Mon. Wea. Rev.*: submitted.
- Smith, R. K., G. Garden, J. Molinari, and B. R. Morton (2001), Proceedings of an International Workshop on the Dynamics and Forecasting of Tropical Weather Systems, *Bull. Am. Meteorol. Soc.*, **82**, 2825–2829.
- Smirnova, T. G., J. M. Brown, and S. G. Benjamin, 1997: Performance of different soil model configurations in simulating ground surface temperature and surface fluxes. *Mon. Wea. Rev.*, 125, 1870–1884.
- Smirnova, T. G., J. M. Brown, S. G. Benjamin, and D. Kim, 2000: Parameterization of cold season processes in the MAPS land-surface scheme. *J. Geophys. Res.*, 105 (D3), 4077–4086.
- Stanski, H. R., L. J. Wilson, and W. R. Burrows, 1989: Survey of common verification methods in meteorology. *Environ. Can. Res. Report 89-5*, **114**, pp. 29 Available from

- Atmospheric Environment Service, Forecast Research Division, 4905 Dufferin St., Downsview, ON M3H 5T4, Canada.
- Stensrud, David J., Jian-Wen Bao, Thomas T. Warner, 2000: Using Initial Condition and Model Physics Perturbations in Short-Range Ensemble Simulations of Mesoscale Convective Systems. *Mon. Wea. Rev.*, 128, 2077-2107
- Straub, K. H., and G. N. Kiladis, 2002: Observations of a convectively coupled Kelvin wave in the eastern Pacific ITCZ. *J. Atmos. Sci.*, **59**, 30–53
- Straub, K. H., and G. N. Kiladis, 2003a: Extratropical forcing of convectively coupled Kelvin waves during austral summer. *J. Atmos. Sci.*, **60**, 526–543.
- Straub, K. H., and G. N. Kiladis, 2003b: Interaction between the boreal summer intraseasonal oscillation and higher-frequency tropical wave activity. *Mon. Wea. Rev.*, **131**, 945–960.
- Sultan, S. and S. Janicot, 2000: Abrupt shift of the ITCZ over West Africa and intra-seasonal variability. *Geophys. Res. Lett.*, **27**, 3353–3356.
- Sultan, S. Janicot and A. Diedhiou, 2003a: West African monsoon dynamics. Part I: Documentation of intraseasonal variability. *J. Climate*, **16**, 3389–3406.
- Sultan B, Janicot S. 2003b. The West African monsoon dynamics. Part II: The “Preonset” and “Onset” of the summer monsoon. *J. Climate* 16: 3407–3427.
- Sultan B, K. Labadi, J. F. Guegan and S. Janicot, 2005: Climate drives the meningitis epidemics onset in west Africa. *PLoS Med*, 2, e6.

- Swets, J. A., 1973: The relative operating characteristic in psychology. *Science*, **182**, 990-999.
- Swets, J.A. and Pickett, R.M. 1982: *Evaluation of Diagnostic Systems - Methods from Signal Detection Theory*. Academic Press.
- Sylla M.B., Coppola E., Mariotti L., Giorgi F., Ruti P. M., Dell'Aquila A., Bi X. 2009: Multiyear simulation of the African climate using a regional climate model (RegCM3) with the high resolution ERA-interim reanalysis. *Clim Dyn.* doi:10.1007/s00382-009-0613-9
- Takayabu, Y. N., 1994: Large-scale cloud disturbances associated with equatorial waves. Part I: Spectral features of the cloud disturbances. *J. Meteor. Soc. Japan*, **72**, 433–448.
- Takayabu, Y. N. and T. Nitta, 1993: 3–5 day period disturbances coupled with convection over the tropical Pacific Ocean. *J. Meteor. Soc. Japan*, **71**, 221–246.
- Tao, W.-K., J. Simpson, and M. McCumber 1989: An ice-water saturation adjustment, *Mon. Wea. Rev.*, 117, 231–235.
- Tetzlaff G, Peters M. 1988. A composite study of early summer squall lines and their environment over West Africa. *Meteorol. Atmos. Phys.* 38: 153–163.
- Thomson, M. C., A. M. Molesworth, M. H. Djingarey, K. R. Yameogo, F. Belanger, and L. E. Cuevas, 2006: Potential of environmental models to predict meningitis epidemics in Africa. *Trop. Med. and Int. Health*, 11, 781-788.

- Thorncroft, C.D., B. J. Hoskins, and M. E. McIntyre, 1993: Two paradigms of baroclinic-wave life-cycle behaviour. *Quart. J. Roy. Meteor. Soc.*, **119**, 17–55.
- Thorncroft, C.D., B.J. Hoskins, 1994a: An idealized study of African easterly waves. Part I: a linear view. *Q J R Meteorol Soc*, **120**, 953-982
- Thorncroft, C.D., B.J. Hoskins, 1994b: An idealized study of African easterly waves. Part II: a nonlinear view. *Q J R Meteorol Soc*, **120**, 983-1015
- Thorncroft, C. D., and H. A. Flocas, 1997: A case study of Saharan cyclogenesis. *Mon. Wea. Rev.*, **125**, 1147–1165.
- Tipping, C., 1995: The Longest Migration. Chapter 11 in University of Florida Book of Insect Records (<http://ufbir.ifas.ufl.edu/>).
- Tomas, R. A., and P. J. Webster, 1994: Horizontal and vertical structure of cross-equatorial wave propagation. *J. Atmos. Sci.*, **51**, 1417–1430.
- Trenberth, K. E., 1998: and C. J. Guillemot, 1998: Evaluation of the atmospheric moisture and hydrological cycle in the NCEP/NCAR reanalyses. *Climate Dyn.*, **14**, 213–231.
- Trenberth, Kevin E., David P. Stepaniak, James W. Hurrell, Michael Fiorino, 2001: Quality of Reanalyses in the Tropics. *J. Climate*, **14**, 1499-1510
- Trzaska, S., C. Perez, M. C. Thomson. 2009: Climate Information for Meningitis. *Third MERIT Technical Meeting*. Niamey, Niger.

- Tulich, S. N., G. N. Kiladis, A. Suzuki-Parker. 2009: Convectively coupled Kelvin and easterly waves in a regional climate simulation of the tropics. *Clim. Dyn.* DOI 10.1007/s00382-009-0697-2
- Vaidya, S. S., 2006: The performance of two convective parameterization schemes in a mesoscale model over the Indian region. *Meteorology and Atmospheric Physics*, **92** (3 -4), 175–190.
- Vizy, E. K, and K. H. Cook, 2001: Mechanisms by which Gulf of Guinea and Eastern North Atlantic Sea Surface Temperature anomalies can influence African rainfall. *J. Climate*, 14, 795-821.
- Vizy E. K., Cook K. H. 2002: Development and application of a mesoscale climate model for the tropics: influence of sea surface temperature anomalies on the West African monsoon. *J Geophys Res* 107(D3):40223.
- Walker, Sir G. T. 1924. Correlation in Seasonal Variations of Weather, IX. A Further Study of World Weather (World Weather II). *Mere. India Met. Dept.* 24, 275-332
- Walker, J., and P. R. Rowntree, 1977: The effect of soil moisture on circulation and rainfall in a tropical model. *Quart. J. Roy. Meteor. Soc.*, 103, 29–46.
- Walter, S. D., and L.M. Irwig, 1988: Estimation of test error rates, disease prevalence, and relative risk from misclassified data. *J. of Clinical Epidemiology*, **41**, 923-38.
- Wang, H., and R. Fu, 2007: The influence of Amazon rainfall on the Atlantic ITCZ through convectively coupled Kelvin waves. *J. Climate*, 20, 1188–1201.

- Ward, M. N., 1998: Diagnosis and short-lead time prediction of summer rainfall in tropical North Africa at interannual and multidecadal timescales. *J. Climate*, **11**, 3167–3191
- Weickmann, K. M., G. N. Kiladis, and P. D. Sardeshmukh, 1997: The dynamics of intraseasonal atmospheric angular momentum oscillations. *J. Atmos. Sci.*, **54**, 1445–1461.
- Wheeler, M., G. N. Kiladis, 1999: Convectively coupled equatorial waves: Analysis of clouds and temperature in the wavenumber–frequency domain. *J. Atmos. Sci.*, **56**, 374–399.
- Wheeler, M., G. N. Kiladis, and P. J. Webster, 2000: Large-scale dynamical fields associated with convectively coupled equatorial waves. *J. Atmos. Sci.*, **57**, 613–640.
- Wheeler, M., and K. M. Weickmann, 2001: Real-time monitoring and prediction of modes of coherent synoptic to intraseasonal tropical variability, *Mon. Weather Rev.*, **129**, 2677–2694.
- Wicker, L. J., and W. C. Skamarock, 2002: Time splitting methods for elastic models using forward time schemes. *Mon. Wea. Rev.*, **130**, 2088–2097.
- Wicker, L. J., and R. B. Wilhelmson, 1995: Simulation and analysis of tornado development and decay within a three-dimensional supercell thunderstorm. *J. Atmos. Sci.*, **52**, 2675–2703.
- Wicker, L. J., and W. C. Skamarock, 2002: Time splitting methods for elastic models using forward time schemes. *Mon. Wea. Rev.*, **130**, 2088–2097.

- Wilks, D. S., 1995: *Statistical Methods in the Atmospheric Sciences*. Cambridge Press. 547 pp.
- Willmott, C. and K. Matsuura, 2005: Advantages of the mean absolute error (MAE) over the root mean square error (RMSE) in assessing average model performance. *Climate Research*, **30**, 79–82.
- Wilson, J. D., and M. K. Mak, 1984: Tropical response to lateral forcing with a latitudinally and zonally nonuniform basic state. *J. Atmos. Sci.*, **41**, 1187–1201.
- Wilson, L. J., 2000: Comments on “probabilistic predictions of precipitation using the ECMWF ensemble prediction system.” *Wea. Forecasting*, **15**, 361-364.
- Winstanley, D., 1970: The North African flood disaster, September 1969. *Weather*, **25**, 390–403.
- World Meteorological Organization, 1992: Manual on the Global Data Processing System, section III, Attachment II.7 and II.8, (revised in 2002). Available from <http://www.wmo.int/web/www/DPS/Manual/WMO485.pdf>.
- World Health Organization, 2000: Detecting meningococcal meningitis epidemics in highly-endemic African countries. *Weekly Epidemiological Record*, 38.
- World Health Organization, 2009: Meningococcal Disease: situation in the African Meningitis Belt. Available from http://www.who.int/csr/don/2009_03_25/en/index.html.

- Wu, M.-L. C., O. Reale, S. D. Schubert, M. J. Suarez, R. D. Koster, P. J. Pegion, 2009: African Easterly Jet: Structure and Maintenance. *J. Climate*, in press.
- Xie, P., P. A. Arkin, 1997: Global Precipitation: A 17-Year Monthly Analysis Based on Gauge Observations, Satellite Estimates, and Numerical Model Outputs. *Bull. Amer. Meteor. Soc.*, **78**, 2539-2558.
- Xie, S.-P., J.A. Carton, 2004: Tropical Atlantic Variability: Patterns, Mechanisms, and Impacts. In: in Earth Climate: The Ocean-Atmosphere Interaction. C. Wang, S.-P. Xie, and J. A. Carton (eds.), Geophysical Monograph, AGU, Washington, D.C., 2004.
- Yang, G.-Y., B. Hoskins, and J. Slingo. 2007: Convectively coupled equatorial waves. Part III: Synthesis structures and their forcing and evolution, *J. Atmos. Sci.*, 64, 3438 – 3451, doi:10.1175/JAS4019.1.
- Yaka, P., B. Sultan, H. Broutin, S. Janicot, S. Philippon, N. Fourquet. 2008: Relationships between climate and year-to-year variability in meningitis outbreaks: a case study in Burkina Faso and Niger. *International Journal of Health Geographics*, 7, 34.
- Yanai, M., and M.-M. Lu, 1983: Equatorially trapped waves at the 200-mb level and their association with meridional convergence of wave energy flux. *J. Atmos. Sci.*, **40**, 2785–2803
- Yang, G. and J. Slingo, 2001: The diurnal cycle in the tropics. *Mon. Weather Rev.*, **129**, 784–801.

- Yang, G.-Y., B. Hoskins, J. Slingo, 2003: Convectively coupled equatorial waves: A new methodology for identifying wave structures in observational data, *J. Atmos. Sci.*, **60**, 1637–1654.
- Yang, G.-Y., B. Hoskins, J. Slingo, 2007: Convectively coupled equatorial waves. Part II: Propagation characteristics, *J. Atmos. Sci.*, **64**, 3424–3437, doi:10.1175/JAS4018.1.
- Yeh, T.-C., R. T. Wetherald, and S. Manabe, 1984: The effect of soil moisture on the short-term climate and hydrology change—A numerical experiment. *Mon. Wea. Rev.*, **112**, 474–490.
- Uppala, S. M., Coauthors 2005: The ERA-40 Re-analysis. *Quart. J. Roy. Meteor. Soc.*, **131**:2961–3012.
- Zangvil, A., 1975: Temporal and spatial behavior of large-scale disturbances in tropical cloudiness deduced from satellite brightness data. *Mon. Wea. Rev.*, **103**, 904–920.
- Zangvil, A., and M. Yanai, 1980: Upper tropospheric waves in the tropics. Part I: Dynamical analysis in the wavenumber-frequency domain. *J. Atmos. Sci.*, **37**, 283–298.
- Zhang, C., and P. J. Webster, 1992: Laterally forced equatorial perturbations in a linear model. Part I: Stationary transient forcing. *J. Atmos. Sci.*, **49**, 585–607.
- Zhang, X. 2007: Adapting the Weather Research and Forecasting Model for the Simulation of Regional Climate in East Africa. PhD Thesis. North Carolina State University.
- Zheng, and E. Eltahir, 1997: The response to deforestation and desertification in a model of West African monsoons. *Geophys. Res. Lett.*, **24**, 155–158.

Zhu, Y., Z. Toth, R. Wobus, D. Richardson, and K. Mylne, 2002: The economic value of ensemble weather forecasts. *Bull. Amer. Meteor. Soc.*, **83**, 73-83